



**Πανεπιστήμιο Κύπρου**  
**University of Cyprus**

**DEPARTMENT OF CHEMISTRY**

**Development of New Catalysts for the Utilization of Natural Gas  
Towards Synthesis Gas and Liquid Fuels Production: The  
Contribution of Transient Isotopic Techniques**

**DOCTOR OF PHILOSOPHY DISSERTATION**

**Michalis A. Vasiliades**

**2018**



**Πανεπιστήμιο Κύπρου**  
**University of Cyprus**

**DEPARTMENT OF CHEMISTRY**

**Development of New Catalysts for the Utilization of Natural Gas  
Towards Synthesis Gas and Liquid Fuels Production: The  
Contribution of Transient Isotopic Techniques**

**Michalis A. Vasiliades**

**A dissertation submitted to the University of Cyprus in partial fulfillment of  
the requirements for the degree of Doctor of Philosophy**

**January 2018**

Michalis A. Vasiliades

## VALIDATION PAGE

**PhD Candidate:** Michalis A. Vasiliades

**Thesis Subject:** Development of New Catalysts for the Utilization of Natural Gas Towards Synthesis Gas and Liquid Fuels Production: The Contribution of Transient Isotopic Techniques

*The present Doctoral Dissertation was submitted in partial fulfillment of the requirements for the degree of Doctor of Philosophy at the Department of Chemistry and was approved on the ..... by the members of the Examination Committee.*

**Examination Committee:**

Dr. Angelos M. Efstathiou, Professor, University of Cyprus

**(Research Supervisor)** \_\_\_\_\_

Dr. Ioannis Paschalides, Professor, University of Cyprus

**(Internal Member, Coordinator)** \_\_\_\_\_

Dr. Agapios Agapiou, Lecturer, University of Cyprus

**(Internal Member)** \_\_\_\_\_

Dr. Albin Pintar, Professor, National Institute of Chemistry, Slovenia

**(External Member)** \_\_\_\_\_

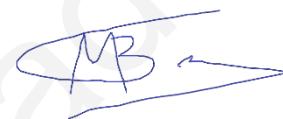
Dr. Kyriaki Polychronopoulou, Associate Professor, Khalifa University of Science, Technology and Research

**(External Member)** \_\_\_\_\_



**The present doctoral dissertation was submitted in partial fulfillment of the requirements for the degree of Doctor of Philosophy of the University of Cyprus. It is a product of original work of my own, unless otherwise mentioned through references, notes, or any other statements.**

**Michalis A. Vasiliades**

A handwritten signature in blue ink, consisting of the letters 'M' and 'A' intertwined, followed by a long horizontal stroke that tapers to a point on the right. Below the signature is a dotted line.

## ΠΕΡΙΛΗΨΗ

Η παρούσα Διδακτορική Διατριβή διαπραγματεύεται την ανάπτυξη, χαρακτηρισμό και μελέτη καινοτόμων καταλυτικών συστημάτων που αφορούν δύο σημαντικές διεργασίες για αξιοποίηση του φυσικού αερίου προς παραγωγή αερίου σύνθεσης και υγρών καυσίμων. Η πρώτη διεργασία αφορά τη ξηρή αναμόρφωση του μεθανίου (Dry Reforming of Methane, DRM:  $\text{CH}_4 + \text{CO}_2 \leftrightarrow 2\text{CO} + 2\text{H}_2$ ) η οποία έχει μελετηθεί εκτενώς από την επιστημονική κοινότητα, αφού προσφέρει αρκετά πλεονεκτήματα για την αξιοποίηση τόσο του φυσικού αερίου, πλούσιου σε διοξείδιο του άνθρακα (Natural Gas rich in  $\text{CO}_2$  (>30 vol%)), όσο και του βιοαερίου (μίγμα κυρίως  $\text{CH}_4/\text{CO}_2$ ) προς παραγωγή αερίου σύνθεσης (μίγμα  $\text{CO}/\text{H}_2 \sim 1$ ). Η δεύτερη διεργασία αφορά τη σύνθεση Fischer-Tropsch, FTS ( $(2n + 1) \text{H}_2 + n \text{CO} \rightarrow \text{C}_n\text{H}_{2n+2} + n \text{H}_2\text{O}$ ) η οποία χρησιμοποιείται ήδη σε βιομηχανική κλίμακα για παραγωγή ανώτερης αξίας και φιλικότερων προς το περιβάλλον υγρών καυσίμων.

Το πλέον σημαντικό μειονέκτημα που παρουσιάζει η διεργασία DRM ( $\Delta H^\circ = + 247 \text{ kJ mol}^{-1}$ ) για ευρεία εφαρμογή στη βιομηχανία, χρησιμοποιώντας χαμηλού κόστους στηριζόμενους καταλύτες Ni, είναι η μη αποδεκτή απενεργοποίηση των καταλυτών με το χρόνο αντίδρασης, κυρίως λόγω της εναπόθεσης “άνθρακα” και της σύντηξης τόσο των σωματιδίων του υποστρώματος όσο και αυτών του μετάλλου (κυρίως η ενεργή φάση) στις υψηλές θερμοκρασίες αντίδρασης ( $T > 700 \text{ }^\circ\text{C}$ ) που απαιτούνται. Η δημιουργία άνθρακα κατά την διεργασία DRM οφείλεται κυρίως στη διάσπαση του  $\text{CH}_4$  στην επιφάνεια του μετάλλου ( $\text{CH}_4(\text{g}) + \text{s} \rightarrow \text{C-s} + 2\text{H}_2(\text{g})$ ) και στην αντίδραση Boudouard ( $2\text{CO}(\text{g}) + \text{s} \leftrightarrow \text{C-s} + \text{CO}_2(\text{g})$ ), όπου “s” ορίζεται το ενεργό κέντρο στην καταλυτική επιφάνεια.

Στην παρούσα εργασία έχουν αναπτυχθεί μονομεταλλικοί (Ni) και διμεταλλικοί (Ni-Co) καταλύτες εναποτιθέμενοι σε ευκόλως ανάξιμα μικτά υποστρώματα  $\text{Ce}_{1-x}\text{M}_x\text{O}_{2-\delta}$  ( $\text{M} = \text{Zr}^{4+}, \text{Pr}^{3+}$ ), οι οποίοι επέδειξαν σημαντική μείωση στη δημιουργία άνθρακα στην επιφάνεια των στερεών καταλυτών σε σχέση με τη χρήση  $\text{CeO}_2$  ως υπόστρωμα (μέχρι και 120 φορές μικρότερη εναπόθεση άνθρακα). Το σημαντικό αυτό αποτέλεσμα οδηγεί σε αύξηση της σταθερότητας του καταλύτη με το χρόνο αντίδρασης (> 50 h). Για την κατανόηση του μηχανισμού εναπόθεσης του άνθρακα κατά την αντίδραση DRM, πραγματοποιήθηκαν τα πιο κάτω: (i) μελέτη της κινητικής δημιουργίας και απομάκρυνσης του άνθρακα από την επιφάνεια του καταλύτη, (ii) κατανόηση της προέλευσης ( $\text{CH}_4$  ή/και  $\text{CO}_2$ ) του ενεργού (active) άνθρακα ο οποίος οδηγεί στην παραγωγή αερίου CO, όπως και του ανενεργού (inactive) άνθρακα, ο οποίος οδηγεί στην απενεργοποίηση του καταλύτη, και (iii) κατανόηση της επίδρασης του

ευκίνητου οξυγόνου του υποστρώματος στην απομάκρυνση του άνθρακα προς παραγωγή CO, η οποία εξαρτάται απόλυτα από τη χημική σύσταση του υποστρώματος, το είδος του μετάλλου, το μέγεθος και τη μορφολογία των σωματιδίων του μετάλλου, όπως και της θερμοκρασίας αντίδρασης.

Για την επίτευξη των πιο πάνω στόχων, σχεδιάστηκαν και εφαρμόστηκαν για πρώτη φορά ένας σημαντικός αριθμός δυναμικών και ισοτοπικών πειραμάτων, όπως: Steady State Isotopic Transient Kinetic Analysis (SSITKA, χρήση  $^{13}\text{CO}_2$ ), Transient Isothermal Reaction (TIR) με χρήση  $^{18}\text{O}_2$  και  $^{13}\text{CO}$ , Transient Isothermal Hydrogenation (TIH) και Temperature Programmed Oxidation (TPO) (χρήση  $^{13}\text{CO}$  και  $^{13}\text{CO}_2$ ). Οι τεχνικές HR-TEM, HAADF/STEM και SEM χρησιμοποιήθηκαν για τη συσχέτιση της επίδρασης του μεγέθους των σωματιδίων και της μορφολογίας των Ni και Co στη δημιουργία του μη ενεργού άνθρακα. Έχει βρεθεί ότι η εναπόθεση άνθρακα μέσω  $\text{CH}_4$  προχωρεί στην επιφάνεια Ni και Co, ενώ μέσω της ενεργοποίησης του  $\text{CO}_2$  προχωρεί τόσο στο Ni και Co όσο και στη διεπιφάνεια μετάλλου-υποστρώματος με τη συμμετοχή κενών θέσεων οξυγόνου του υποστρώματος. Η δημιουργία άνθρακα είναι απόλυτα συνδεδεμένη με τη θερμοκρασία της αντίδρασης, όπως επίσης και με τη χημική σύσταση του μετάλλου και του υποστρώματος (Ni ή Ni-Co και Ce/Zr ή Ce/Pr).

Ο πολύπλοκος μηχανισμός που διέπει την FTS σε βιομηχανικούς στηριζόμενους καταλύτες Co (SASOL, South Africa) απαιτεί βαθιά κατανόηση, αφού η μέθοδος σύνθεσης των καταλυτών (π.χ. μέγεθος σωματιδίων Co, χημική τροποποίηση του υποστρώματος, ενεργοποίηση του καταλύτη), επηρεάζουν σημαντικά κρίσιμες κινητικές παραμέτρους και τη σταθερότητα των καταλυτών με το χρόνο αντίδρασης. Για το σκοπό αυτό, σχεδιάστηκαν και εφαρμόστηκαν, για πρώτη φορά, πειράματα SSITKA στους 230 °C, ούτως ώστε να υπολογιστούν σε συνθήκες αντίδρασης: (i) η επιφανειακή κάλυψη ( $\theta$ ) των ενεργών  $\text{CH}_x$ -s ( $\text{C}_\alpha$ ) και αντιστρεπτά προσροφημένων CO-s ενδιάμεσων ειδών της αντίδρασης, (ii) ο μέσος χρόνος παραμονής τους ( $\tau_{\text{CH}_x}$  και  $\tau_{\text{CO}}$  ( $\text{s}^{-1}$ )) στην καταλυτική επιφάνεια, και (iii) ο κινητικός ρυθμός  $\text{TOF}_{\text{CH}_4}$ ,  $\text{ITK}$  ( $\text{s}^{-1}$ ). Ο τελευταίος υπολογίζεται με βάση τη συγκέντρωση των ενεργών ενδιάμεσων ειδών που οδηγούν στην παραγωγή  $\text{CH}_4$  ( $\text{H}_2/\text{CO} = 2; 5 \text{ vol}\% \text{ CO}$ ). Πειράματα δυναμικής ισοθερμοκρασιακής και θερμο-προγραμματιζόμενης υδρογόνωσης έχουν σχεδιαστεί και εφαρμοστεί τα οποία έχουν αναδείξει: (i) την παρουσία ενός λιγότερο ενεργού είδους  $\text{CH}_x$  ( $\text{C}_\beta$ ) που παράχθηκε κατά την αντίδραση FTS στους 230 °C και το οποίο δεν οδηγεί στην παραγωγή αέριου  $\text{CH}_4$  υπό συνθήκες FTS. Αντίθετα, το είδος αυτό ( $\text{C}_\beta$ ) υδρογονώνεται στους 230 °C ( $\text{CO}/\text{H}_2 \rightarrow \text{He} \rightarrow 50\% \text{ H}_2/\text{He}$  (t)) προς παραγωγή μεθανίου, και (ii) την παρουσία διαφόρων μη

ενεργών ενδιάμεσων ειδών που περιέχουν άνθρακα τα οποία υδρογονώνονται προς παραγωγή μεθανίου σε θερμοκρασίες  $T > 230$  °C (χρήση TPH). Επιπλέον, όταν η τεχνική SSITKA συνδυάστηκε με άλλες φασματοσκοπικές τεχνικές (SSITKA-DRIFTS), έγινε εφικτός ο προσδιορισμός της χημικής σύστασης και δομής των ενεργών ενδιάμεσων ειδών αλλά και των μη ενεργών ειδών που δημιουργούνται σε συνθήκες FTS. Επίσης, εφαρμόστηκαν συμπληρωματικές τεχνικές χαρακτηρισμού των εν λόγω καταλυτών, όπως: powder XRD, TPO, H<sub>2</sub>-TPR και HAADF/STEM για τον υπολογισμό του μέσου μεγέθους των σωματιδίων Co και τη μελέτη της μορφολογίας τους, όπως και των οξειδοαναγωγικών χαρακτηριστικών του υποστρώματος.

## ABSTRACT

The present Doctoral Thesis is referred to the development, characterization and in-depth study of novel catalytic systems related with two major processes concerning the utilization of Natural Gas (NG) towards the production of synthesis gas (CO/H<sub>2</sub> gas mixture) and liquid fuels. The first process is that of Dry Reforming of Methane, DRM ( $\text{CH}_4 + \text{CO}_2 \leftrightarrow 2\text{CO} + 2\text{H}_2$ ), which has been extensively studied, especially by the research community, since it offers several advantages for the *catalytic utilization both of natural gas, rich in CO<sub>2</sub> (> 30 vol%) and biogas (mainly CH<sub>4</sub>/CO<sub>2</sub> mixture)* towards the production of synthesis gas (CO/H<sub>2</sub> ~ 1). The second process is that of Fischer-Tropsch Synthesis, FTS ( $(2n + 1) \text{H}_2 + n \text{CO} \rightarrow \text{C}_n\text{H}_{2n+2} + n \text{H}_2\text{O}$ ), which is already used on industrial scale for the production of cleaner and more environmentally friendly liquid fuels by using the synthesis gas as a feedstock.

The main disadvantage of DRM ( $\Delta H^\circ = + 247 \text{ kJ mol}^{-1}$ ) for wide industrial applications over low-cost Ni-based catalysts, is the non-acceptable extent of catalyst deactivation with time on stream, mainly due to “carbon” deposition and sintering of both the support and active metal particles at the high reaction T’s (> 700 °C) required. The carbon formed under DRM is mainly the result of CH<sub>4</sub> decomposition ( $\text{CH}_4 (\text{g}) \rightarrow \text{C-s} + 2\text{H}_2 (\text{g})$ ) on the metal surface and the Boudouard reaction ( $2\text{CO} (\text{g}) \leftrightarrow \text{C-s} + \text{CO}_2 (\text{g})$ ), where “s” refers to an active surface catalytic site.

In the present work, Ni and bimetallic Ni-Co catalysts deposited on reducible Ce<sub>1-x</sub>M<sub>x</sub>O<sub>2-δ</sub> (i.e. M = Zr<sup>4+</sup>, Pr<sup>3+</sup>) mixed metal oxides were developed, which were found to significantly reduce carbon formation rate on the catalytic surface (ca. by a factor of 120), in comparison with the case where CeO<sub>2</sub> support was used. This important result leads to the increase of catalyst stability with time-on-stream (> 50 h). With aim of understanding the carbon deposition mechanism under DRM reaction conditions, the following were performed: (i) kinetics studies of carbon formation and removal, (ii) revealing the origin of carbon formation (CH<sub>4</sub> vs. CO<sub>2</sub> activation route) towards *active* carbon species (CO gas product) and *inactive* carbon (catalyst deactivation), and (iii) understanding the role of support lattice oxygen in removing carbon towards CO formation (carbon gasification process), as a function of the chemical composition of support, metal phase, the size and morphology of metal particles and the reaction temperature.

To achieve all the aforementioned goals, several transient isotopic and temperature-programmed techniques alone or in combination were designed and conducted for the first time,

namely: (i) Steady State Isotopic Transient Kinetic Analysis (SSITKA-MS/DRIFTS, use of  $^{13}\text{CO}_2$ ), (ii) Transient Isothermal Reaction (TIR) with the use of  $^{18}\text{O}_2$  and  $^{13}\text{CO}$ , (iii) Transient Isothermal Hydrogenation (TIH), and (iv) Temperature Programmed Oxidation (TPO) (use of  $^{13}\text{CO}$  and  $^{13}\text{CO}_2$ ). Moreover, HR-TEM, HAADF/STEM and SEM techniques were implemented in order to correlate the effect of particle size and morphology of Ni and Co towards *inactive carbon* deposition. It was found that carbon deposition via the  $\text{CH}_4$  molecular route proceeds on Ni and Co surfaces, while via the  $\text{CO}_2$  activation route proceeds on both Ni and Co but also on the metal-support interface via the participation of support's *oxygen vacant sites*. The carbon formation is found to strongly depend on reaction temperature, and the chemical composition of both the metal and support (Ni or Ni-Co and Ce/Zr or Ce/Pr).

The complex mechanism underlying FTS over industrial Co-based catalysts (SASOL, South Africa) seeks deep understanding, as the various preparation and aftertreatment methods of the working catalyst (e.g., Co particle size, support modification, catalyst activation) strongly affects important kinetic parameters and catalyst's stability over reaction time. For the purpose of the present work, SSITKA experiments were designed for the first time over Co-based industrial catalysts for the *in situ* evaluation of (i) the surface coverage ( $\theta$ ) of active  $\text{CH}_x$ -s ( $C_\alpha$ ) and CO-s reversibly chemisorbed intermediates, (ii) the residence time  $\tau_{\text{CH}_x}$  and  $\tau_{\text{CO}}$  ( $\text{s}^{-1}$ ) associated with the  $\text{CH}_x$ -s and CO-s, respectively, and (iii) the  $\text{TOF}_{\text{CH}_4, \text{ITK}}$  ( $\text{s}^{-1}$ ) (estimated based on the concentration of *active* carbon-containing intermediates leading to  $\text{CH}_4$ ) for the methanation reaction at 230 °C. Moreover, transient isothermal and temperature-programmed hydrogenation experiments were performed to elucidate: (i) the presence of a *less active*  $\text{CH}_x$  species ( $C_\beta$ ) formed during FTS ( $\text{CO}/\text{H}_2$ ) at 230 °C, which does not lead to  $\text{CH}_4$  under FTS but is readily hydrogenated at 230 °C to methane, and (ii) the presence of various kinds of refractory carbon-containing *inactive* species towards hydrogenation to methane at  $T > 230$  °C (use of TPH). Furthermore, when SSITKA was combined with a spectroscopic technique (SSITKA-DRIFTS), the *chemical composition and the structure* of the *active* reaction intermediates but also of the *inactive* (spectator) ones were determined. Complementary characterization techniques, such as powder XRD, TPO,  $\text{H}_2$ -TPR and HAADF/STEM were used for estimating the mean Co particle size and their morphology, as well as the redox characteristics for the investigated supported metal catalysts.

## ACNOWLEDGEMENTS

There were not only four years of research within twenty-eight years of studies, but I can wholeheartedly say that this chapter was one of the most important so far in my life, thus I would like to thank every and each one that was a part of this fairytale. It might be a typical procedure, whereas for me it is a sincere soul deposit.

First and foremost, I feel honored and I should thank my supervisor Professor Dr. Angelos M. Efstathiou which has accepted in full extent to convey me all that high-level scientific and engineering knowledge acquired in his long carrier. With his support, advice and the confidence showed on my person in parallel with his uncompromised do-it-yourself way of thinking he is the one developed my strong academic skills and one of those who decisively contributed to the completion of this thesis.

I would like to thank Professor Dr. Ioannis Paschalides and Lecturer Dr. Agapios Agapiou from the Department of Chemistry of the University of Cyprus for their involvement, fruitful discussions and instructive comments during all my scientific examinations.

Special thanks go to Professor Dr. Albin Pintar from the National Institute of Chemistry, in Slovenia, for kindly accept my invitation to participate as an external examiner, but especially for providing me with catalysts, HR-TEM photos and for the constructive collaboration through his post-doctoral fellow Dr. Petar Djinovic.

I warmly thank Associate Professor Dr. Kyriaki Polychronopoulou from the Department of Mechanical Engineering of the Khalifa University of Science, Technology and Research, in Abu Dhabi, UAE, for kindly accept my invitation to participate as an external examiner, as well as for his valuable knowledge on the improvement of my catalysis background and my thesis.

Special thanks are due to Dr. Theodora Kiratsi and her post-doctoral fellow Dr. Ioannis Rigopoulos from the Department of Mechanical and Manufacture Engineering of the University of Cyprus, for the easy-going and productive collaboration through all these years, giving me a multidiscipline knowledge. Moreover, I would like to thank Dr. Magdalini Theodoridou from the Department of Civil and Environmental Engineering of the University of Cyprus for providing me with SEM photos.

I would like to thank former and present HCL research group members, especially Dr. Christos M. Kalamaras and Liliya F. Davlyatova, I had the pleasure to work with, for their

companionship and help and all the academic, administrative and technical staff of the Department of Chemistry of the University of Cyprus for their support.

Thanks, are due to MEL Chemicals (UK) and SASOL (South Africa), especially Dr. Gregory Govender, that rise this research with their financial support and industrial know-how and are gratefully acknowledged.

My sincere thanks go also to my childhood friends, for help and support, both in academic and life problems, making my life less stressful and more enjoyable. So many of them but I would like to thank at least: Andreas, Michalis, Simos, Omiros, Christos, George and Stella; I am glad that you are next to me.

Last but not least, I would and should thank my parents, sisters and all my relatives, who were wishing me all the best during my academic carrier, and I am more than sure that, behind my back, they were giving me all their positive energy. Without their tolerance, continuous love, encouragement and support, the completion of my dreams would not have been possible.

Ευχαριστώ  
ηορσϋ



***Dedication:***

*to my father Andreas,*

*to my mother Patricia,*

*to my sisters Myria and Elina*

*and to my childhood friends*

## Table of Contents

Chapter 1: Literature Review.....	1
1.1. State of the art – Syngas production .....	1
1.2. Catalytic technologies to syngas production.....	4
1.2.1. Steam Methane Reforming (SMR) .....	5
1.2.2. Dry Reforming of Methane (DRM).....	6
1.2.3. Partial Oxidation (POX) .....	7
1.2.4. Autothermal Reforming of Methane (ATR).....	7
1.3. Dry Reforming of Methane over supported metal catalysts .....	10
1.3.1. Thermodynamics of DRM .....	10
1.3.2. Catalytic performance studies.....	12
1.3.3. Deactivation of catalysts .....	17
1.3.4. Mechanistic studies .....	19
1.4. Fischer-Tropsch synthesis on Co-based supported catalysts .....	22
1.4.1 Catalytic performance studies.....	23
1.4.2 Kinetic and Mechanistic studies .....	25
1.4.3 Modelling on FT – SSITKA technique.....	26
References .....	31
Chapter 2: Theoretical Background .....	45
2.1. Fundamental physicochemical properties of supported metal catalysts .....	45
2.1.1. Bulk and surface structural defects .....	45
2.1.2. Crystal structures of CeO <sub>2</sub> and doped-CeO <sub>2-x</sub> solids .....	47
2.2. Chemical adsorption (chemisorption).....	49
2.2.1. Chemisorption of CO.....	50
2.2.2. Chemisorption of H <sub>2</sub> .....	51
2.2.3. Chemisorption of CO <sub>2</sub> .....	52
2.3. Catalysts synthesis .....	53
2.3.1. Support synthesis via sol-gel (modified citrate) method .....	53
2.3.2. Supported metal catalysts synthesis - The wet impregnation method .....	55
2.4. Diffuse Reflectance Infrared Fourier Transform Spectroscopy (DRIFTS) .....	56
2.5. Steady State Isotopic Transient Kinetic Analysis – SSITKA .....	58

2.5.1.	Introduction.....	58
2.5.2.	Mathematical modelling of SSITKA.....	59
2.6.	SSITKA Modeling of Methanation Reaction .....	63
	References .....	66
Chapter 3: Experimental .....		73
3.1.	Synthesis of catalysts support – Dry Reforming of Methane .....	73
3.1.1.	Ce <sub>1-x</sub> M <sub>x</sub> O <sub>2-δ</sub> (M = Zr <sup>4+</sup> , Pr <sup>3+</sup> ) mixed metal oxides .....	73
3.1.2.	Ce <sub>0.75</sub> Zr <sub>0.25</sub> O <sub>2-δ</sub> mixed metal oxides .....	73
3.1.3.	Activated γ-Al <sub>2</sub> O <sub>3</sub> - Fischer-Tropsch synthesis .....	74
3.2.	Supported metal catalysts.....	74
3.2.1.	5% Ni/Ce <sub>1-x</sub> M <sub>x</sub> O <sub>2-δ</sub> (M = Zr <sup>4+</sup> , Pr <sup>3+</sup> ) .....	74
3.2.2.	3 wt.% Ni/Ce <sub>0.75</sub> Zr <sub>0.25</sub> O <sub>2-δ</sub> - EG.....	75
3.2.3.	3 wt.% NiCo/Ce <sub>0.75</sub> Zr <sub>0.25</sub> O <sub>2-δ</sub> - EG/HT.....	75
3.2.4.	20 wt.% Co with platinum over uncoated and carbon-coated Sasol's γ-Al <sub>2</sub> O <sub>3</sub> for the Fischer-Tropsch Synthesis.....	75
3.3.	Physicochemical characterization of catalysts .....	76
3.3.1.	Specific surface area (BET), pore volume and mean pore size (BJH) .....	76
3.3.2.	Powder X-ray Diffraction (PXRD).....	76
3.3.3.	Mass Spectrometry (MS) .....	77
3.3.4.	In situ Diffuse Reflectance Infrared Fourier Transform Spectroscopy (in situ DRIFTS).....	78
3.3.5.	Field Emission-Scanning Electron Microscopy (FE-SEM).....	81
3.3.6.	High Resolution Transmission Electron Microscopy-Energy Dispersive X-Ray Analysis (HRTEM-EDX) and High Angle Annular Dark Field-Scanning Transmission Electron Microscopy (HAADF-STEM).....	81
3.3.7.	X-Ray Photoelectron Spectroscopy (XPS) .....	82
3.4.	Transient experiments for catalyst characterization.....	83
3.4.1.	H <sub>2</sub> Temperature-Programmed Desorption (H <sub>2</sub> -TPD) .....	83
3.4.2.	H <sub>2</sub> Temperature-Programmed Reduction (H <sub>2</sub> -TPR).....	84
3.4.3.	Oxygen Storage Capacity measurements (OSC).....	85
3.5.	Catalytic performance studies .....	85
3.5.1.	5% Ni/Ce <sub>1-x</sub> M <sub>x</sub> O <sub>2-δ</sub> (M = Zr <sup>4+</sup> , Pr <sup>3+</sup> ) - Dry Reforming of Methane .....	85
3.5.2.	3 wt.% Ni and NiCo supported on Ce <sub>1-x</sub> Zr <sub>x</sub> O <sub>2-δ</sub> - Dry Reforming of Methane ..	86
3.5.3.	Checking for mass transport resistances .....	87

3.6. Characterization of deposited carbonaceous species in DRM – Use of transient methods .....	88
3.6.1. Transient Isothermal Hydrogenation (TIH) and Temperature - Programmed Hydrogenation (TPH).....	88
3.6.2. Temperature-Programmed Oxidation (TPO).....	89
3.6.3. TGA-Temperature-Programmed Oxidation (TPO) – CHNS.....	90
3.7. Mechanistic studies - DRM.....	90
3.7.1. The Contribution of CO <sub>2</sub> and CH <sub>4</sub> activation routes towards the formation of inactive carbon.....	90
3.7.2. Probing the participation of support lattice oxygen in the carbon path .....	91
3.7.3. Probing the gasification of carbon by CO <sub>2</sub> (C-s + CO <sub>2</sub> ↔ 2CO + s) .....	93
3.7.4. SSITKA studies – Tracing the carbon path of CO <sub>2</sub> activation .....	93
3.8. Mechanistic studies – Fischer-Tropsch (Methanation).....	96
3.8.1. SSITKA studies – <sup>13</sup> CO/H <sub>2</sub> gas switch.....	96
3.8.2. SSITKA studies – CO/D <sub>2</sub> switch.....	99
3.9. Experimental apparatus for catalyst testing and characterization and in situ DRIFTS and operando studies .....	99
References .....	102
Chapter 4: Dry Reforming of Methane over Ce <sub>1-x</sub> M <sub>x</sub> O <sub>2-δ</sub> (M=Zr <sup>4+</sup> , Pr <sup>3+</sup> )-supported Ni catalysts .....	105
4.1. The effect of support composition in the origin and reactivity of carbon.....	106
4.1.1. Catalyst characterization.....	106
4.1.2. Characterisation of “carbon” formed during DRM by various transient techniques .....	114
4.1.3. In situ DRIFTS-CO chemisorption studies.....	122
4.1.4. Estimation of inactive “carbon” formed during RWGS reaction .....	123
4.1.5. SEM studies of fresh and spent catalysts.....	124
4.1.6. Discussion.....	126
4.2. Performance and characterization studies of active and inactive carbon over Ni/Ce <sub>1-x</sub> Pr <sub>x</sub> O <sub>2-δ</sub> catalysts .....	134
4.2.1. Catalyst characterization.....	134
4.2.2. Characterization of “carbon” formed during DRM by various transient techniques .....	143
4.2.3. SSITKA – Mechanistic Studies .....	149
4.2.4. Discussion.....	154

References .....	165
Chapter 5: Dry Reforming of Methane over $Ce_{1-x}Zr_xO_{2-\delta}$ – supported Ni and NiCo bimetallic catalysts.....	169
5.1. 3 wt.% Ni/ $Ce_{0.75}Zr_{0.25}O_2$ catalyst (3Ni EG code).....	170
5.1.1. Powder XRD and H <sub>2</sub> -TPR characterization.....	170
5.1.2. Catalytic DRM performance of 3 wt.% Ni/ $Ce_{0.75}Zr_{0.25}O_{2-\delta}$ .....	171
5.1.3. Transient evolution rates of CH <sub>4</sub> /He and CH <sub>4</sub> /CO <sub>2</sub> /He (DRM) reactions .....	173
5.1.4. Characterisation of “carbon” formed during CH <sub>4</sub> /He and DRM reactions .....	174
5.1.5. Probing the participation of support lattice oxygen in DRM.....	177
5.1.6. SSITKA - Quantifying the active carbon present in the CO <sub>2</sub> reaction path .....	179
5.1.7. Probing the gasification of “carbon” by CO <sub>2</sub> .....	181
5.1.8. Discussion.....	182
5.2. The effect of synthesis method of $Ce_{0.75}Zr_{0.25}O_{2-\delta}$ and that of Co in the carbon-path of DRM over NiCo/ $Ce_{0.75}Zr_{0.25}O_{2-\delta}$ catalysts .....	188
5.2.1. Catalyst characterization studies.....	188
5.2.2. Transient evolution rates of CH <sub>4</sub> /He reaction and characterization of the deposited “carbon” .....	192
5.2.3. Transient evolution rates of CH <sub>4</sub> /CO <sub>2</sub> /He (DRM) reaction and characterization of deposited “carbon” .....	196
5.2.4. Quantifying the origin of inactive “carbon” (CH <sub>4</sub> vs CO <sub>2</sub> activation route) ....	197
5.2.5. Probing the participation of support lattice oxygen in DRM.....	199
5.2.6. Quantifying the active carbon present in the CO <sub>2</sub> activation route - SSITKA .	203
5.2.7. Relationship between active and inactive carbon formation and long-term catalyst stability in DRM.....	204
References .....	212
Chapter 6: Elucidation of Kinetic and Mechanistic Aspects of Fischer-Tropsch Synthesis over Industrial Co-based Catalysts .....	215
6.1 Introduction.....	215
6.2 Catalysts characterization.....	217
6.3 SSITKA – Mass Spectrometry studies.....	221
6.3.1 Probing the carbon-path of methanation reaction.....	221
6.3.2 Probing higher hydrocarbons pathways (C <sub>2</sub> 's and C <sub>3</sub> 's) .....	225
6.3.3 Transient Isothermal Hydrogenation (TIH) and Temperature-Programmed Hydrogenation (TPH).....	226

6.3.4	Probing the H-path in Fischer-Tropsch .....	231
6.3.5	Modeling of $^{12}\text{CH}_4$ -SSITKA transients .....	234
6.4	In situ DRIFTS studies.....	239
6.4.1	Surface intermediates formed under CO/H <sub>2</sub> .....	239
6.4.2	Surface reaction intermediates behaviour during the SSITKA switch .....	240
6.4.3	Transient isothermal DRIFTS hydrogenation of CO.....	244
6.5	Effect of adsorbed carbon on the CO chemisorption .....	246
6.6	Conclusions .....	248
	References .....	250
	Chapter 7: Future Work .....	255

## List of Figures

**Figure 1.1:** Global mitigation on Greenhouse Gas Emissions.

**Figure 1.2:** From natural gas towards the production of more valuable chemicals [12].

**Figure 1.3:** Syngas ( $H_2/CO$ ) ratio derived from different reforming routes [21].

**Figure 1.4:** DRM and side reactions equilibrium in the 500-900 °C range [53].

**Figure 1.5:** Carbon formation (mol/mol of TC, %) (a) and syngas ( $H_2/CO$ ) ratio (b) formation on different  $CH_4/CO_2$  ratio obtained in the range of 550-1200 °C [55].

**Figure 1.6:** Temperature programmed hydrogenation (TPH) over 3 wt.% Ni/MgO at different contact times [109].

**Figure 1.7:** Schematic representation of a FTS plant [133].

**Figure 1.8:** Schematic representation of the three basic FT reaction mechanisms [156].

**Figure 1.9:** Mechanistic models, transient responses, and kinetic parameters obtained by SSITKA technique [167].

**Figure 1.10:** Comparison of the SSITKA transient response  $F(t)$  (a) and of the logarithmic transient response (b) of single pool, two pools in series and two pools in parallel [167].

**Figure 1.11:** Schematic illustration of the DRIFT cell single bed reactor [200].

**Figure 2.1:** Defects present in a surface of metal oxide [12].

**Figure 2.2:** Crystal structure of defective (oxygen vacancies)  $CeO_2$  [27].

**Figure 2.3:** Crystal structure of  $CeO_2$  under (a) oxidized and (b) reduced conditions [33].

**Figure 2.4:** Electron transfer from the  $5\sigma$  to the  $2\pi^*$  orbitals of CO: gas phase state (left), and adsorbed CO state (right).

**Figure 2.5:** CO chemisorption related to the nature of transition metal.

**Figure 2.6:** CO chemisorption over a catalytic surface (a) linear, (b) bridged, and (c) gem-dicarbonyl (or twin) type [64].

**Figure 2.7:** Electron transfer processes during  $H_2$  chemisorption.

**Figure 2.8:** Molecular chemisorption of  $CO_2$  over metal oxide surfaces [64].

**Figure 2.9:** Citric acid structure (left) and metal-citric acid complex (right).

**Figure 2.10:** Electric double layer of the surface support in contact with the metal impregnation solution [64].

**Figure 2.11:** DRIFTS cell apparatus [105].

**Figure 2.12:** Isotopic distribution of active intermediate pools ( $n$ ), under (a) steady state reaction conditions, (b) after a step gas change in the isotopic composition of reactant R.

**Figure 2.13:** Normalized transient response curves of the inert gas (I) and the products (P and P\*) derived from the SSITKA switch ( $R \rightarrow R^*$ ).

**Figure 2.14:** Reaction methanation sequence over Raney nickel catalysts [120].

**Figure 2.15:** Normalized transient responses of  $\text{CH}_4$  [120].

**Figure 2.16:** Different mechanistic pathways of the two pool intermediates [120].

**Figure 3.1:** Experimental apparatus used for the implementation of transient studies.

**Figure 3.2:** Experimental apparatus used for the operando SSITKA-DRIFTS studies [31].

**Figure 4.1:** Powder X-ray diffractograms of (a) 5 wt.% Ni/ $\text{Ce}_{0.8}\text{Zr}_{0.2}\text{O}_{2-\delta}$ , (b) 5 wt.% Ni/ $\text{Ce}_{0.5}\text{Zr}_{0.5}\text{O}_{2-\delta}$  and (c) 5 wt.% Ni/ $\text{Ce}_{0.8}\text{Pr}_{0.2}\text{O}_{2-\delta}$  solids following calcination of the fresh samples in air (750 °C/4 h). Inset graph shows a magnification of the Ni (111) diffraction peak (★) obtained for the 5 wt.% Ni/ $\text{Ce}_{0.5}\text{Zr}_{0.5}\text{O}_{2-\delta}$  catalyst.

**Figure 4.2:** Transient isothermal reduction rates obtained over the  $\text{Ce}_{0.8}\text{Zr}_{0.2}\text{O}_{2-\delta}$ ,  $\text{Ce}_{0.5}\text{Zr}_{0.5}\text{O}_{2-\delta}$  and  $\text{Ce}_{0.8}\text{Pr}_{0.2}\text{O}_{2-\delta}$  solid supports at 600 °C (a) and 700 °C (b) following the step gas switch: He  $\rightarrow$  0.5%  $\text{H}_2$ /1% Kr/Ar/He.

**Figure 4.3:**  $\text{H}_2$ -TPD traces obtained over 5 wt.% Ni/ $\text{Ce}_{0.8}\text{Pr}_{0.2}\text{O}_{2-\delta}$  (a) and 5 wt.% Ni/ $\text{Ce}_{1-x}\text{Zr}_x\text{O}_{2-\delta}$  ( $x = 0.2, 0.5$ ) catalysts (b)-(c). Deconvoluted  $\text{H}_2$ -TPD trace obtained over the 5 wt.% Ni/ $\text{Ce}_{0.8}\text{Zr}_{0.2}\text{O}_{2-\delta}$  catalyst (d).  $F_{\text{He}} = 50 \text{ NmL min}^{-1}$ ;  $\beta = 30 \text{ °C min}^{-1}$ ;  $W = 0.5 \text{ g}$ .

**Figure 4.4:** Conversion (%) of  $\text{CH}_4$  and  $\text{CO}_2$  (a) and  $\text{H}_2$ -yield (%) and  $\text{H}_2/\text{CO}$  gas product ratio (b) obtained after 1 h of dry reforming of methane in the 550-750 °C range over the 5 wt.% Ni/ $\text{Ce}_{0.8}\text{Pr}_{0.2}\text{O}_{2-\delta}$  catalyst;  $\text{GHSV} = 30,000 \text{ h}^{-1}$ .

**Figure 4.5:** Stability test of the dry reforming of methane reaction in terms of  $\text{CO}_2$  and  $\text{CH}_4$  conversion (%) and  $\text{H}_2$ -yield (%) performed at  $T = 550$  and  $750 \text{ °C}$  over the 5 wt.% Ni/ $\text{Ce}_{0.8}\text{Pr}_{0.2}\text{O}_2$  catalyst for 50 h on reaction stream;  $\text{GHSV} = 30,000 \text{ h}^{-1}$ .

**Figure 4.6:** (a) Transient response curves of  $\text{CH}_4$  concentration obtained during isothermal hydrogenation (TIH) of “carbon” formed after 1 h of dry reforming at 550 °C ( $\text{GHSV} = 30,000 \text{ h}^{-1}$ ) over 5 wt.% Ni supported on (A)  $\text{Ce}_{0.8}\text{Pr}_{0.2}\text{O}_2$ , (B)  $\text{Ce}_{0.8}\text{Zr}_{0.2}\text{O}_2$  and (C)  $\text{Ce}_{0.5}\text{Zr}_{0.5}\text{O}_2$  carriers. Gas delivery sequence: 20%  $\text{CH}_4$ /20%  $\text{CO}_2$ /He (550 °C, 1 h)  $\rightarrow$  He (550 °C, 15 min)  $\rightarrow$  20%  $\text{H}_2$ /He (550 °C, t); (b) TPH following TIH over the 5 wt.% Ni/ $\text{Ce}_{0.8}\text{Pr}_{0.2}\text{O}_2$  catalyst.

**Figure 4.7:** Transient response curves of  $\text{CO}_2$  and CO concentrations (mol%) obtained during TPO of “carbon” formed after 1 h (a) and 50 h (b) of dry reforming of methane conducted at



750 °C (GHSV = 30,000 h<sup>-1</sup>) over a 5 wt.% Ni/Ce<sub>0.8</sub>Pr<sub>0.2</sub>O<sub>2</sub> catalyst. Gas delivery sequence: DRM (750 °C, 1 h or 50 h) → He gas flow, increase T to 800 °C and stay until no CO/CO<sub>2</sub> are measured in the MS → cool down in He gas flow to 100 °C → 10% O<sub>2</sub>/He (50 NmL min<sup>-1</sup>), T is increased to 800 °C (β = 30 °C min<sup>-1</sup>).

**Figure 4.8:** Temperature-programmed oxidation (TPO) to <sup>12</sup>CO<sub>2</sub> and <sup>13</sup>CO<sub>2</sub> of “carbon” formed after 30 min of DRM at 550 °C (a) and 750 °C (b) over the 5 wt.% Ni/Ce<sub>0.5</sub>Zr<sub>0.5</sub>O<sub>2</sub> catalyst. Gas delivery sequence: 5% <sup>13</sup>CO<sub>2</sub>/5% <sup>12</sup>CH<sub>4</sub>/45% Ar/45% He (T, 30 min) → He (800 °C, 15 min) → cool down in He flow to 100 °C → 10% O<sub>2</sub>/He (50 NmL min<sup>-1</sup>), T is increased to 800 °C (TPO, β = 30 °C min<sup>-1</sup>); DRM reaction conditions: F<sub>T</sub> = 100 NmL min<sup>-1</sup>; W = 0.5 g.

**Figure 4.9:** Temperature-programmed oxidation (TPO) to <sup>12</sup>CO<sub>2</sub> and <sup>13</sup>CO<sub>2</sub> of “carbon” formed after 30 min of DRM at 550 °C (a) and 750 °C (b) over the 5 wt.% Ni/Ce<sub>0.8</sub>Pr<sub>0.2</sub>O<sub>2</sub> catalyst. Gas delivery sequence: 5% <sup>13</sup>CO<sub>2</sub>/5% <sup>12</sup>CH<sub>4</sub>/45% Ar/45% He (T, 30 min) → He (800 °C, 15 min) → cool down in He flow to 100 °C → 10% O<sub>2</sub>/He (50 NmL min<sup>-1</sup>), T is increased to 800 °C (TPO, β = 30 °C min<sup>-1</sup>); DRM reaction conditions: F<sub>T</sub> = 100 NmL min<sup>-1</sup>; W = 0.5 g.

**Figure 4.10:** (a) Transient response curves of H<sub>2</sub>, <sup>12</sup>CO, <sup>13</sup>CO, <sup>12</sup>CO<sub>2</sub> and <sup>13</sup>CO<sub>2</sub> obtained at 750 °C during the gas switch: He (100 NmL min<sup>-1</sup>, 750 °C) → 5% <sup>13</sup>CO/5% <sup>12</sup>CH<sub>4</sub>/45% Ar/45% He (100 NmL min<sup>-1</sup>, 750 °C, t); (b) Transient response curves of <sup>12</sup>CO, <sup>13</sup>CO, <sup>12</sup>CO<sub>2</sub> and <sup>13</sup>CO<sub>2</sub> obtained during TPO (10% O<sub>2</sub>/He, 50 NmL min<sup>-1</sup>) following (a) over the 5 wt.% Ni/Ce<sub>0.8</sub>Pr<sub>0.2</sub>O<sub>2</sub> catalyst. Gas delivery sequence: 5% <sup>13</sup>CO/5% <sup>12</sup>CH<sub>4</sub>/45% Ar/45% He (750 °C, 30 min) → He (800 °C, 15 min) → cool down in He flow to 100 °C → 10% O<sub>2</sub>/He (50 NmL min<sup>-1</sup>), T is increased to 800 °C (TPO, β = 30 °C min<sup>-1</sup>); W = 0.5 g.

**Figure 4.11:** (a) Transient response curves of H<sub>2</sub>, <sup>12</sup>CO, <sup>13</sup>CO, <sup>12</sup>CO<sub>2</sub> and <sup>13</sup>CO<sub>2</sub> obtained at 750 °C during the gas switch: He (100 NmL min<sup>-1</sup>, 750 °C) → 5% <sup>13</sup>CO/5% <sup>12</sup>CH<sub>4</sub>/45% Ar/45% He (100 NmL min<sup>-1</sup>, 750 °C, t); (b) Transient response curves of <sup>12</sup>CO, <sup>13</sup>CO, <sup>12</sup>CO<sub>2</sub> and <sup>13</sup>CO<sub>2</sub> obtained during TPO (10% O<sub>2</sub>/He, 50 NmL min<sup>-1</sup>) following (a) over the Ce<sub>0.8</sub>Pr<sub>0.2</sub>O<sub>2</sub> carrier alone. Gas delivery sequence: 5% <sup>13</sup>CO/5% <sup>12</sup>CH<sub>4</sub>/45% Ar/45% He (750 °C, 30 min) → He (800 °C, 15 min) → cool down in He flow to 100 °C → 10% O<sub>2</sub>/He (50 NmL min<sup>-1</sup>), T is increased to 800 °C (TPO, β = 30 °C min<sup>-1</sup>); W = 0.5 g.

**Figure 4.12:** (A) DRIFT spectrum recorded in the 2250-1800 cm<sup>-1</sup> range over the 5 wt.% Ni/Ce<sub>0.5</sub>Zr<sub>0.5</sub>O<sub>2</sub> catalyst after 30-min treatment in 5% CO/Ar gas at 25 °C; IR bands obtained after deconvolution are also shown. IR bands of adsorbed CO obtained in the 2200-1800 cm<sup>-1</sup>

range after deconvolution of the spectra recorded at 25 °C after 30-min treatment in 5% CO/Ar gas at 25 °C (B) and 550 °C (C) for the 5 wt.% Ni supported on Ce<sub>0.8</sub>Pr<sub>0.2</sub>O<sub>2</sub> (a), Ce<sub>0.5</sub>Zr<sub>0.5</sub>O<sub>2</sub> (b) and Ce<sub>0.8</sub>Zr<sub>0.2</sub>O<sub>2</sub> (c) carriers.

**Figure 4.13:** Transient concentration response curves of CO and CO<sub>2</sub> obtained during TPO of “carbon” formed after 1 h of reverse water-gas shift (RWGS) reaction performed at 750 °C. Reaction feed gas composition: 20% CO<sub>2</sub>/7% H<sub>2</sub>/He; W<sub>cat</sub> = 0.3 g; GHSV = 30,000 h<sup>-1</sup>.

**Figure 4.14:** SEM micrographs of the fresh 5 wt.% Ni/Ce<sub>0.8</sub>Pr<sub>0.2</sub>O<sub>2-δ</sub> catalyst.

**Figure 4.15:** SEM micrographs of the spent 5 wt.% Ni/Ce<sub>0.8</sub>Pr<sub>0.2</sub>O<sub>2-δ</sub> catalyst (after 1 h of dry reforming of methane at 750 °C; 20% CH<sub>4</sub>/20% CO<sub>2</sub>/He; GHSV = 30,000 h<sup>-1</sup>).

**Figure 4.16:** Representation of the main chemical reaction steps of the CH<sub>4</sub> and CO<sub>2</sub> activation routes on the 5 wt.% Ni/Ce<sub>0.8</sub>Pr<sub>0.2</sub>O<sub>2-δ</sub> catalyst towards dry reforming of methane for syngas (CO/H<sub>2</sub>) production.

**Figure 4.17:** Powder X-ray diffractograms of (a) 5 wt.% Ni/CeO<sub>2</sub>, (b) 5 wt.% Ni/Ce<sub>0.8</sub>Pr<sub>0.2</sub>O<sub>2</sub>, (c) 5 wt.% Ni/Ce<sub>0.5</sub>Pr<sub>0.5</sub>O<sub>2</sub>, (d) 5 wt.% Ni/Ce<sub>0.35</sub>Pr<sub>0.65</sub>O<sub>2</sub> and (e) 5 wt.% Ni/Ce<sub>0.2</sub>Pr<sub>0.8</sub>O<sub>2</sub> fresh catalysts after calcination in 20% O<sub>2</sub>/He at 750 °C for 4 h. Inset graph shows a magnification of the NiO (200) diffraction peak (★) related to the 5 wt.% Ni/Ce<sub>0.5</sub>Pr<sub>0.5</sub>O<sub>2-δ</sub> solid.

**Figure 4.18:** TEM (left-hand side) and HAADF/STEM micrographs (right-hand side) with corresponding EDXS elemental mapping for (a) 5 wt.% Ni/CeO<sub>2</sub> and (b) 5 wt.% Ni/Ce<sub>0.2</sub>Pr<sub>0.8</sub>O<sub>2-δ</sub> catalysts.

**Figure 4.19:** (a) TEM micrograph of nickel particle formed in the 5 wt.% Ni/Ce<sub>0.2</sub>Pr<sub>0.8</sub>O<sub>2</sub> catalyst, where polysynthetic twin crystals are clearly visible as brighter and darker areas; (b) STEM micrograph of the same nickel particle with the highlighted twin crystal boundary, where carbon layers are also clearly shown; (c) a model of polysynthetic cubo-octahedral twin crystal.

**Figure 4.20:** H<sub>2</sub>-TPD traces obtained over the 5 wt.% Ni/Ce<sub>1-x</sub>Pr<sub>x</sub>O<sub>2-δ</sub> (x = 0, 0.5, 0.8) catalysts. F<sub>He</sub> = 50 N mL min<sup>-1</sup> He; β = 30 °C min<sup>-1</sup>; W = 0.5 g.

**Figure 4.21:** (A) CH<sub>4</sub>-conversion (%) and H<sub>2</sub> yield (%), (B) CO<sub>2</sub>-conversion (%) and CO yield (%) and (C) H<sub>2</sub>/CO gas product ratio obtained after 30 min in dry reforming of methane in the 550-750 °C range over 5 wt.% Ni supported on (a) CeO<sub>2</sub>; (b) Ce<sub>0.8</sub>Pr<sub>0.2</sub>O<sub>2-δ</sub>; (c) Ce<sub>0.5</sub>Pr<sub>0.5</sub>O<sub>2-δ</sub>; (d) Ce<sub>0.35</sub>Pr<sub>0.65</sub>O<sub>2-δ</sub> and (e) Ce<sub>0.2</sub>Pr<sub>0.8</sub>O<sub>2-δ</sub> carriers; P<sub>CH<sub>4</sub></sub> = 0.2 bar, P<sub>CO<sub>2</sub></sub> = 0.2 bar, P<sub>T</sub> = 1.0 bar; GHSV = 30,000 h<sup>-1</sup>.

**Figure 4.22:** Stability test (25 h) in the dry reforming of methane reaction performed at 750 °C in terms of CO<sub>2</sub>-conversion (%) (A), CH<sub>4</sub>-conversion (%) (B) and H<sub>2</sub>/CO gas-product ratio (C)

over 5 wt.% Ni supported on (a) CeO<sub>2</sub>; (b) Ce<sub>0.8</sub>Pr<sub>0.2</sub>O<sub>2-δ</sub>; (c) Ce<sub>0.5</sub>Pr<sub>0.5</sub>O<sub>2-δ</sub>; (d) Ce<sub>0.35</sub>Pr<sub>0.65</sub>O<sub>2-δ</sub> and (e) Ce<sub>0.2</sub>Pr<sub>0.8</sub>O<sub>2-δ</sub> catalysts; P<sub>CH<sub>4</sub></sub> = 0.2 bar, P<sub>CO<sub>2</sub></sub> = 0.2 bar, P<sub>T</sub> = 1.0 bar; GHSV = 30,000 h<sup>-1</sup>.

**Figure 4.23:** Effect of Pr atom-% composition (Pr/(CePr) x 100) on (a) CH<sub>4</sub>-conversion (%), (b) CO<sub>2</sub>-conversion (%) and (c) H<sub>2</sub>/CO gas-product ratio obtained after 0.5 h (▲) and 25 h (●) of dry reforming of methane at 750 °C over 5 wt.% Ni/Ce<sub>1-x</sub>Pr<sub>x</sub>O<sub>2-δ</sub> catalysts (x = 0, 0.2, 0.5, 0.65 and 0.8); GHSV = 30,000 h<sup>-1</sup>.

**Figure 4.24:** Transient response curves of CO<sub>2</sub> and CO obtained during TPO of “carbon” formed after 25 h of dry reforming of methane at 750 °C (GHSV = 30,000 h<sup>-1</sup>) over the 5 wt.% Ni/Ce<sub>1-x</sub>Pr<sub>x</sub>O<sub>2-δ</sub> (x = 0.0, 0.2, 0.5) catalysts. Gas delivery sequence: DRM (750 °C, 25 h) → He, increase T to 800 °C until no CO and CO<sub>2</sub> are measured in the MS → cool down in He flow to 300 °C → T is increased to 800 °C (β = 30 °C min<sup>-1</sup>).

**Figure 4.25:** TGA-TPO relative weight-% vs temperature profiles for the spent 5 wt.% Ni/Ce<sub>1-x</sub>Pr<sub>x</sub>O<sub>2-δ</sub> catalysts following 25 h of dry reforming at 750 °C.

**Figure 4.26:** SEM micrographs obtained on the fresh and spent (after 25 h on stream in DRM at 750 °C) catalysts: (a) 5 wt.% Ni/CeO<sub>2</sub>, (b) 5 wt.% Ni/Ce<sub>0.8</sub>Pr<sub>0.2</sub>O<sub>2-δ</sub>, (c) 5 wt.% Ni/Ce<sub>0.5</sub>Pr<sub>0.5</sub>O<sub>2-δ</sub>, (d) 5 wt.% Ni/Ce<sub>0.35</sub>Pr<sub>0.65</sub>O<sub>2-δ</sub> and (e) 5 wt.% Ni/Ce<sub>0.2</sub>Pr<sub>0.8</sub>O<sub>2-δ</sub>.

**Figure 4.27:** Powder X-ray diffractograms of fresh 5 wt.% Ni/CeO<sub>2</sub> (a) and aged (after 25 h in dry reforming of methane at 750 °C) 5 wt.% Ni/CeO<sub>2</sub> catalyst (b).

**Figure 4.28:** Temperature-programmed oxidation (TPO) of “carbon” formed during dry reforming of <sup>12</sup>CH<sub>4</sub> with <sup>13</sup>CO<sub>2</sub> at 550 and 750 °C over 5 wt.% Ni/CeO<sub>2</sub> (a, b) and 5 wt.% Ni/Ce<sub>0.2</sub>Pr<sub>0.8</sub>O<sub>2-δ</sub> (c, d) catalysts. Gas delivery sequence: 5% <sup>13</sup>CO<sub>2</sub>/5% <sup>12</sup>CH<sub>4</sub>/Ar/He (T, 30 min, F<sub>T</sub> = 100 N mL min<sup>-1</sup>) → He (750 °C, 10 min) → cool in He flow to 100 °C → 10% O<sub>2</sub>/He, TPO (F<sub>T</sub> = 50 N mL min<sup>-1</sup>, β = 30 °C min<sup>-1</sup>); W = 0.2 g (fresh catalyst).

**Figure 4.29:** Kr, <sup>13</sup>CO and <sup>13</sup>CO<sub>2</sub> SSITKA response curves obtained after 2 h of dry reforming of methane at 750 °C over (a) 5 wt.% Ni/CeO<sub>2</sub> and (b) 5 wt.% Ni/Ce<sub>0.8</sub>Pr<sub>0.2</sub>O<sub>2-δ</sub> catalysts. SSITKA switches: 5% <sup>12</sup>CO<sub>2</sub>/5% <sup>12</sup>CH<sub>4</sub>/Ar/He (2 h) → 5% <sup>13</sup>CO<sub>2</sub>/5% <sup>12</sup>CH<sub>4</sub>/2% Kr/Ar/He (20 min) → 5% <sup>12</sup>CO<sub>2</sub>/5% <sup>12</sup>CH<sub>4</sub>/Ar/He (t); W<sub>cat</sub> (200 mg) = 30 mg diluted with 170 mg SiC; F<sub>T</sub> = 100 N mL min<sup>-1</sup>.

**Figure 4.30:** Kr, <sup>13</sup>CO and <sup>13</sup>CO<sub>2</sub> SSITKA response curves obtained after 2 h in dry reforming of methane at 550 °C over 5 wt.% Ni/CeO<sub>2</sub> catalyst. SSITKA switches: 5% <sup>12</sup>CO<sub>2</sub>/5% <sup>12</sup>CH<sub>4</sub>/Ar/He (2 h) → 5% <sup>13</sup>CO<sub>2</sub>/5% <sup>12</sup>CH<sub>4</sub>/2% Kr/Ar/He (20 min) → 5% <sup>12</sup>CO<sub>2</sub>/5% <sup>12</sup>CH<sub>4</sub>/Ar/He (t); W<sub>cat</sub> = 0.25 g; F<sub>T</sub> = 50 NmL min<sup>-1</sup>; X<sub>CH<sub>4</sub></sub> = 40%; X<sub>CO<sub>2</sub></sub> = 55%.

**Figure 4.31:** The SSITKA formalism applied for the activation path of CO<sub>2</sub> towards the formation of CO in the DRM reaction over the 5 wt.% Ni/Ce<sub>1-x</sub>Pr<sub>x</sub>O<sub>2-δ</sub> catalysts. “C”-s is the pool of active carbon-containing species, CO-s is the pool of adsorbed CO, and CO<sub>3</sub><sup>2-</sup>-s is the pool of non-active and reversibly adsorbed carbonate-type species on the Ce<sub>1-x</sub>Pr<sub>x</sub>O<sub>2-δ</sub> support.

**Figure 4.32:** Isothermal transient rates of hydrogen formation obtained at the switch He → 5% <sup>12</sup>CO<sub>2</sub>/5% <sup>12</sup>CH<sub>4</sub>/Ar/He (t) at 550 °C (a) and 750 °C (b) over the 5 wt.% Ni/Ce<sub>1-x</sub>Pr<sub>x</sub>O<sub>2-δ</sub> (x = 0.0, 0.2 and 0.8) catalysts; W<sub>cat</sub> = 0.1 g mixed with 0.1 g SiC (550 °C) and W<sub>cat</sub> = 0.03 g mixed with 0.17 g SiC (750 °C); F<sub>T</sub> = 100 N mL min<sup>-1</sup>.

**Figure 4.33:** TEM image of Ni crystallite at the tip of carbon nanotubes showing detachment of the Ni metal clusters from the CeO<sub>2</sub> support observed after 25 h of methane dry reforming reaction at 750 °C.

**Figure 5.1:** Powder XRD pattern of the 3 wt.% Ni/Ce<sub>0.75</sub>Zr<sub>0.25</sub>O<sub>2-δ</sub> (3 Ni EG) catalyst.

**Figure 5.2:** H<sub>2</sub>-TPR traces recorded over the (a) 3 wt.% Ni/Ce<sub>0.75</sub>Zr<sub>0.25</sub>O<sub>2-δ</sub> catalyst and (b) the Ce<sub>0.75</sub>Zr<sub>0.25</sub>O<sub>2-δ</sub> support.

**Figure 5.3:** CH<sub>4</sub> and CO<sub>2</sub> conversions and the H<sub>2</sub>/CO product gas ratio as a function of time on stream (TOS) for the 3 wt.% Ni/Ce<sub>0.75</sub>Zr<sub>0.25</sub>O<sub>2-δ</sub> catalyst at 750 °C. Feed gas composition: 44.2% CH<sub>4</sub>, 44.2% CO<sub>2</sub>, balance N<sub>2</sub>; W<sub>cat</sub> = 50 mg; F<sub>T</sub> = 56.5 NmL min<sup>-1</sup>.

**Figure 5.4:** (a) Transient rates (μmol g<sup>-1</sup> s<sup>-1</sup>) of H<sub>2</sub>, CO and CO<sub>2</sub> formation as a function of time obtained after the gas switch He → 20% CH<sub>4</sub>/He at 750 °C was made; (b) transient rates (μmol g<sup>-1</sup> s<sup>-1</sup>) of H<sub>2</sub> and CO formation as a function of time obtained after the gas switch He → 20% CH<sub>4</sub>/20% CO<sub>2</sub>/He (DRM) at 750 °C was made. F<sub>T</sub> = 100 NmL min<sup>-1</sup>; W<sub>cat</sub> = 25 mg.

**Figure 5.5:** (a) TPH trace and (b) TIH response curves (T = 600, 645, 670 and 700 °C) of the “carbon” formed after 30-min treatment of the catalyst in 20% CH<sub>4</sub>/He at 750 °C. Gas delivery sequence (TPH): He (750 °C) → 20% CH<sub>4</sub>/He (750 °C, 30 min) → He (750 °C, 10 min) → cool in He flow to 100 °C → 20% H<sub>2</sub>/He, TPH (100 to 750 °C, F<sub>He</sub> = 50 NmL min<sup>-1</sup>, β = 30 °C min<sup>-1</sup>) → TIH at 750 °C for 10 min; (b) He (750 °C) → 20% CH<sub>4</sub>/He (750 °C, 30 min, F<sub>T</sub> = 100 NmL min<sup>-1</sup>) → He (10 min) → cool in He flow to the lowest T (600 °C) → 20% H<sub>2</sub>/1% Kr/Ar (10 min, F<sub>T</sub> = 100 NmL min<sup>-1</sup>) → increase T to 750 °C and stay for 30 min → repeat the same procedure for the next highest T; W<sub>cat</sub> = 25 mg.

**Figure 5.6:** Temperature-programmed oxidation (TPO) of “carbon” formed during dry reforming of methane (<sup>13</sup>CO<sub>2</sub>/<sup>12</sup>CH<sub>4</sub>/He) at 750 °C. Gas delivery sequence: 5% <sup>13</sup>CO<sub>2</sub>/5%

$^{12}\text{CH}_4/\text{He}$  (750 °C, 30 min,  $F_T = 50 \text{ NmL min}^{-1}$ )  $\rightarrow$  He (750 °C, 10 min) cool in He flow to 100 °C  $\rightarrow$  10%  $\text{O}_2/\text{He}$ , TPO (100 to 750 °C,  $F_T = 50 \text{ NmL min}^{-1}$ ,  $\beta = 30 \text{ °C min}^{-1}$ );  $W_{\text{cat}} = 50 \text{ mg}$ .

**Figure 5.7:** Transient rates of  $^{16}\text{O}_2$  and  $^{16}\text{O}^{18}\text{O}$  ( $\mu\text{mol g}^{-1} \text{ s}^{-1}$ ) formation as a function of time due to the isotopic exchange of lattice  $^{16}\text{O}$  with  $^{18}\text{O}$  after treatment of the catalyst with 2%  $^{18}\text{O}_2/\text{He}$  for 10 min at 750 °C. Gas delivery sequence: He (750 °C)  $\rightarrow$  2%  $^{18}\text{O}_2/\text{He}$  (750 °C, 10 min);  $W_{\text{cat}} = 25 \text{ mg}$ .

**Figure 5.8:** Transient concentration (mol%) response curves of  $\text{C}^{18}\text{O}$ ,  $\text{C}^{16}\text{O}^{18}\text{O}$  and  $\text{C}^{18}\text{O}_2$  obtained at 750 °C after (a) dry reforming of methane (20%  $\text{CH}_4/20\% \text{ CO}_2/\text{He}$ ), (b) 20%  $\text{CO}_2/\text{He}$  gas treatment and (c) 1%  $\text{CO}/\text{He}$  gas treatment, following catalyst pre-treatment with 2%  $^{18}\text{O}_2/\text{He}$  (10 min) at 750 °C and He purge. Gas delivery sequence: He (750 °C)  $\rightarrow$  2%  $^{18}\text{O}_2/\text{He}$  (10 min)  $\rightarrow$  He (5 min)  $\rightarrow$  20%  $\text{CO}_2/20\% \text{ CH}_4/\text{He}$  (t) or 20%  $\text{CO}_2/\text{He}$  (t) or 1%  $\text{CO}/\text{He}$  (t);  $W_{\text{cat}} = 25 \text{ mg}$ .

**Figure 5.9:** Transient dimensionless response curves of Kr,  $^{13}\text{CO}$  and  $^{13}\text{CO}_2$  obtained during SSITKA at 750 °C after 30 min of dry reforming of methane. SSITKA gas switches: 5%  $^{12}\text{CO}_2/5\% \text{ }^{12}\text{CH}_4/\text{He}$  (30 min)  $\rightarrow$  5%  $^{13}\text{CO}_2/5\% \text{ }^{12}\text{CH}_4/\text{Kr}/\text{He}$  (20 min)  $\rightarrow$  5%  $^{12}\text{CO}_2/5\% \text{ }^{12}\text{CH}_4/\text{He}$  (t);  $W_{\text{cat}} = 50 \text{ mg}$ ;  $F_T = 100 \text{ NmL min}^{-1}$ .

**Figure 5.10:** Transient response curves of (a) dimensionless concentrations of Kr and  $^{13}\text{CO}_2$  and (b)  $^{12}\text{CO}$  and  $^{13}\text{CO}$  concentrations obtained at 750 °C following 30 min of dry reforming of methane at 750 °C according to the following sequence of gas switches: 5%  $\text{CO}_2/5\% \text{ CH}_4/\text{He}$  (30 min)  $\rightarrow$  He (5 min)  $\rightarrow$  5%  $^{13}\text{CO}_2/\text{Kr}/\text{He}$  (t).  $W_{\text{cat}} = 50 \text{ mg}$ ;  $F_T = 100 \text{ NmL min}^{-1}$ .

**Figure 5.11:** SEM images of spent 3 wt.% Ni/Ce<sub>0.75</sub>Zr<sub>0.25</sub>O<sub>2- $\delta$</sub>  catalyst focusing on carbon structures.

**Figure 5.12:** XRD profiles of 3NiCo EG and 3NiCo HT powder samples. Red bars show the peak positions of Ce<sub>0.75</sub>Zr<sub>0.25</sub>O<sub>2- $\delta$</sub>  (PDF 28-0271), black bars of CeO<sub>2</sub> (PDF 034-0394) and green bars of ZrO<sub>2</sub> (PDF 01-089-6976).

**Figure 5.13:** HAADF/STEM micrograph with corresponding EDXS elemental mapping of cobalt, nickel and their overlay on a fresh reduced 3NiCo EG catalyst prior to catalytic tests.

**Figure 5.14:** SAED pattern of a fresh reduced 3NiCo EG catalyst prior to catalytic tests.

**Figure 5.15:** HR-TEM micrograph on a fresh and reduced 3NiCo EG catalyst prior to catalytic tests.

**Figure 5.16:** Transient rate of solid reduction by hydrogen ( $\mu\text{mol g}^{-1} \text{ s}^{-1}$ ) as a function of time at 750 °C over 3NiCo EG (a) and 3NiCo HT (b) catalysts.  $W_{\text{cat}} = 25 \text{ mg}$ .

**Figure 5.17:** Transient rates ( $\mu\text{mol g}^{-1} \text{s}^{-1}$ ) of (A)  $\text{H}_2$ , (B)  $\text{CO}$  and (C)  $\text{CO}_2$  formation as a function of time obtained during methane decomposition (20%  $\text{CH}_4/\text{He}$ ) at 750 °C over 3NiCo EG (a), 3NiCo HT (b),  $\text{CeZrO}_2$  EG (c) and  $\text{CeZrO}_2$  HT (d) solids.  $W_{\text{cat}} = 25$  mg.

**Figure 5.18:** Temperature programmed hydrogenation (TPH) traces of “carbon” to  $\text{CH}_4$  obtained following 30-min treatment in 20%  $\text{CH}_4/\text{He}$  at 750 °C over the 3NiCo EG (a) and 3NiCo HT (b) catalysts.  $W_{\text{cat}} = 25$  mg.

**Figure 5.19:** Transient response curves of  $\text{CH}_4$  concentration at 645 °C (A) and 700 °C (B) obtained during transient isothermal hydrogenation (TIH); (C) Total amount ( $\mu\text{mol g}^{-1}$ ) of “carbon” formed after 30-min treatment of the catalyst in 20%  $\text{CH}_4/\text{He}$  at 750 °C.  $W_{\text{cat}} = 25$  mg; a: 3NiCo EG, b: 3NiCo HT.

**Figure 5.20:** Transient rates ( $\mu\text{mol g}^{-1} \text{s}^{-1}$ ) of  $\text{CO}$  (A) and  $\text{H}_2$  (B) formation as a function of time obtained during dry reforming of methane at 750 °C over 3NiCo EG (a) and 3NiCo HT (b) catalysts.  $W_{\text{cat}} = 25$  mg.

**Figure 5.21:** TPO of “carbon” formed during DRM with labeled  $^{13}\text{CO}_2$  at 750 °C for the 3NiCo EG (A) and 3NiCo HT (B) catalysts.  $W_{\text{cat}} = 50$  mg.

**Figure 5.22:** Transient rates ( $\mu\text{mol g}^{-1} \text{s}^{-1}$ ) of  $^{16}\text{O}_2$  (A) and  $^{16}\text{O}^{18}\text{O}$  (B) formation as a function of time, estimated from the transient isotopic exchange of lattice  $^{16}\text{O}$  with  $^{18}\text{O}$  experiment according to the gas switch  $\text{He} \rightarrow 2\% \text{ }^{18}\text{O}_2/\text{He}$  performed at 750 °C over the 3NiCo EG (a) and 3NiCo HT (b) catalysts.  $W_{\text{cat}} = 25$  mg.

**Figure 5.23:** Transient concentration (mol%) response curves of  $\text{C}^{16}\text{O}^{18}\text{O}$  (A),  $\text{C}^{18}\text{O}_2$  (B) and  $\text{C}^{18}\text{O}$  (C) obtained during dry reforming of methane at 750 °C following treatment with 2%  $^{18}\text{O}_2/\text{He}$  at 750 °C for 10 min over the 3NiCo EG (a) and 3NiCo HT (b) catalysts.  $W_{\text{cat}} = 25$  mg.

**Figure 5.24:** Transient concentration (mol%) response curves of  $\text{C}^{18}\text{O}$ ,  $\text{C}^{16}\text{O}^{18}\text{O}$  and  $\text{C}^{18}\text{O}_2$  obtained at 750 °C after the gas switch  $\text{He} \rightarrow 20\% \text{ CO}_2/\text{He}$  is made over the 3NiCo EG (A) and 3NiCo HT (B) catalysts, following catalyst pre-treatment with 2%  $^{18}\text{O}_2/\text{He}$  (10 min) at 750 °C. Gas delivery sequence:  $\text{He}$  (750 °C)  $\rightarrow$  2%  $^{18}\text{O}_2/\text{He}$  (10 min)  $\rightarrow$   $\text{He}$  (5 min)  $\rightarrow$  20%  $\text{CO}_2/\text{He}$  (t);  $W_{\text{cat}} = 25$  mg.

**Figure 5.25:** Transient concentration (mol%) response curves of  $\text{C}^{18}\text{O}$ ,  $\text{C}^{16}\text{O}^{18}\text{O}$  and  $\text{C}^{18}\text{O}_2$  obtained at 750 °C after the gas switch x%  $\text{CO}/\text{He}$  made over 3NiCo EG (A) and 3NiCo HT (B) catalysts, following pre-treatment with 2%  $^{18}\text{O}_2/\text{He}$  (10 min) at 750 °C. Gas delivery sequence:  $\text{He}$  (750 °C)  $\rightarrow$  2%  $^{18}\text{O}_2/\text{He}$  (10 min)  $\rightarrow$   $\text{He}$  (5 min)  $\rightarrow$  x%  $\text{CO}/\text{He}$  (t);  $W_{\text{cat}} = 25$  mg; x = 0.65 and 0.85, respectively, for 3NiCo EG and 3NiCo HT catalysts.

**Figure 5.26:** SSITKA dimensionless concentration response curves (Z) of Kr,  $^{13}\text{CO}$  and  $^{13}\text{CO}_2$  obtained after 30 min of dry reforming of methane at 750 °C performed over the 3NiCo HT catalyst.  $W_{\text{cat}} = 50$  mg;  $F_T = 100$  NmL min $^{-1}$ . SSITKA switches: 5%  $^{12}\text{CO}_2/5\%$   $^{12}\text{CH}_4/\text{He}$  (30 min)  $\rightarrow$  5%  $^{13}\text{CO}_2/5\%$   $^{12}\text{CH}_4/\text{He}$  (3 min)  $\rightarrow$  5%  $^{12}\text{CO}_2/5\%$   $^{12}\text{CH}_4/\text{He}$  (t).

**Figure 5.27:**  $\text{CH}_4$ -conversion (%) as a function of time on stream (TOS) for the DRM at 750 °C over the 3 NiCo EG (a) and 3NiCo HT (b) catalysts. Feed gas composition: 44.2%  $\text{CH}_4$ , 44.2%  $\text{CO}_2$ , 11.5%  $\text{N}_2$ ;  $W_{\text{cat}} = 50$  mg;  $F_T = 56.5$  NmL min $^{-1}$ .

**Figure 5.28:** (A)  $\text{CO}_2$  conversion and (B)  $\text{H}_2/\text{CO}$  gas product ratio as a function of time on stream (TOS) obtained during DRM at 750 °C over the 3 NiCo EG (a) and 3NiCo HT (b) catalysts. Feed gas composition: 44.2%  $\text{CH}_4$ , 44.2%  $\text{CO}_2$ , balance  $\text{N}_2$ ;  $W_{\text{cat}} = 50$  mg;  $F_T = 56.5$  NmL min $^{-1}$ .

**Figure 5.29:** SEM image of spent (20 h in DRM) 3NiCo EG catalyst, where the growth of carbon nano-filaments is clearly shown.

**Figure 5.30:** HAADF/STEM micrographs of 3NiCo EG catalyst after 20 h of DRM reaction (44.2%  $\text{CO}_2/44.3\%$   $\text{CH}_4/11.5\%$   $\text{N}_2$ ) at 750 °C; a progressive magnification is provided.

**Figure 5.31:** HAADF/STEM micrographs of 3NiCo EG catalyst after DRM reaction at 750 °C for 20 h. The image is focused on the NiCo bimetallic particle (top left) with corresponding EDXS elemental mapping: top right nickel; bottom right cobalt (Co); and bottom left nickel (Ni) and cobalt (Co) overlaid.

**Figure 5.32:** High-energy resolution of Co2p spectra for the 3NiCo EG catalyst recorded at different TOS (Fresh, 5, 10 and 20 h).

**Figure 5.33:** High-energy resolution Zr3d spectra for the 3NiCo EG catalyst recorded at different TOS (Fresh, 5, 10 and 20 h).

**Figure 5.34:** High-energy resolution O 1s spectra for the 3NiCo EG catalyst recorded at different TOS in DRM (Fresh, 5, 10 and 20 h).

**Figure 5.35:** Normalized high-energy resolution Ce 3d spectra for the 3NiCo EG catalyst recorded at different TOS in DRM (Fresh, 5, 10 and 20 h).

**Figure 6.1:** Powder X-ray diffractograms of CY-A and CY-C solid catalysts.

**Figure 6.2:**  $\text{NO}_2$  concentration during calcination in air for CY-A (solid black) and CY-C (dotted red) impregnated with cobalt nitrate (Ref. [46]).

**Figure 6.3:**  $\text{NO}_2$  (red) and  $\text{CO}_2$  (green) concentration traces obtained during calcination in air of the CY-C catalyst (Ref. [46]).

**Figure 6.4:** Hydrogen temperature programmed reduction (H<sub>2</sub>-TPR) profile recorded over the CY-C catalyst (Ref. [46]).

**Figure 6.5:** Transmission electron microscopy images (HAADF-TEM) with a schematic distribution of Co crystallites over (a) CY-A and (b) CY-C solid catalysts (Ref. [46]).

**Figure 6.6:** Normalized concentration (Z) transient response curves of <sup>13</sup>CO and <sup>13</sup>CH<sub>4</sub> obtained during SSITKA (<sup>12</sup>CO/H<sub>2</sub> (32 h) → <sup>13</sup>CO/H<sub>2</sub> (t)) at 230 °C on CY-A (a, c) and CY-C (b, d) catalysts. Feed composition: <sup>12</sup>CO = 5%, <sup>13</sup>CO = 5%, H<sub>2</sub> = 10%, 1% Kr, balance He. Total flow rate: 100 NmL min<sup>-1</sup>, W<sub>CY-A</sub> = 0.4 g; W<sub>CY-C</sub> = 0.3 g.

**Figure 6.7:** Schematic modelling of a single C<sub>n</sub> (n ≥ 2) surface intermediate [59].

**Figure 6.8:** Experimental MS response curves of <sup>13</sup>CH<sub>4</sub> (m/z = 17) and m/z = 30 and 31 signals recorded during SSITKA (<sup>12</sup>CO/H<sub>2</sub> → <sup>13</sup>CO/H<sub>2</sub>) over the CY-A and CY-C catalysts.

**Figure 6.9:** (a) Transient isothermal hydrogenation of carbonaceous species formed during FT reaction conditions at 230 °C towards CH<sub>4</sub> formation on the CY-A catalyst; (b) Temperature-programmed hydrogenation of carbonaceous species following (a); (c) deconvolution of TPH trace shown in (b).

**Figure 6.10:** (a) Transient isothermal hydrogenation of carbonaceous species formed during FT reaction conditions at 230 °C towards CH<sub>4</sub> formation on the CY-C catalyst; (b) Temperature-programmed hydrogenation of carbonaceous species following (a); (c) deconvolution of TPH trace shown in (b).

**Figure 6.11:** (a) HD transient response curves obtained during the SSITKA-MS switch over CY-A according to the gas delivery sequence: 3.5% CO/7% H<sub>2</sub>/Ar/He → 3.5% CO/7% D<sub>2</sub>/Ar/Kr/He at 230 °C; (b) transient response of HD obtained during the gas switch: 7% H<sub>2</sub>/Ar/He (230 °C, 15 min) → 7% D<sub>2</sub>/Ar/Kr/He (t).

**Figure 6.12:** (a) HD transient response curves obtained during the SSITKA-MS switch over CY-C according to the gas delivery sequence: 3.5% CO/7% H<sub>2</sub>/Ar/He → 3.5% CO/7% D<sub>2</sub>/Ar/Kr/He at 230 °C; (b) transient response of HD obtained during the gas switch: 7% H<sub>2</sub>/Ar/He (230 °C, 15 min) → 7% D<sub>2</sub>/Ar/Kr/He (t).

**Figure 6.13:** Model C (Ref. [53]) describing the carbon-path of methanation reaction after considering the participation of *two kinds* of active CH<sub>x</sub>-s which are formed via two different kinds of adsorbed CO-s.



**Figure 6.14:** Experimental (left) and simulated (right) transient normalized concentration (Z) response curves of Kr and  $^{12}\text{CH}_4$  obtained during the SSITKA switch: 5%  $^{12}\text{CO}/10\% \text{H}_2/1\% \text{Kr}/\text{Ar}/\text{He}$  (16 h)  $\rightarrow$  5%  $^{13}\text{CO}/10\% \text{H}_2/\text{Ar}/\text{He}$  at 230 °C over the two catalysts.

**Figure 6.15:** Transient normalized concentration (Z) response curves of Kr and  $^{12}\text{CH}_4$  (Experimental and Simulated) obtained during the SSITKA switch: 5%  $^{12}\text{CO}/10\% \text{H}_2/1\% \text{Kr}/\text{Ar}/\text{He}$  (16 h)  $\rightarrow$  5%  $^{13}\text{CO}/10\% \text{H}_2/\text{Ar}/\text{He}$  at 230 °C over CY-A catalyst.

**Figure 6.16:** Model A mechanism of Methanation Reaction after considering the participation of two kinds of active  $\text{CH}_x$ -s which are formed via the same active adsorbed CO-s.

**Figure 6.17:** Transient normalized concentration (Z) response curves of Kr,  $^{13}\text{CH}_4$  experimental and  $^{13}\text{CH}_4$  simulated by Model A and Model C based on the SSITKA switch: 5%  $^{12}\text{CO}/10\% \text{H}_2/1\% \text{Kr}/\text{Ar}/\text{He}$  (30 min)  $\rightarrow$  5%  $^{13}\text{CO}/10\% \text{H}_2/\text{Ar}/\text{He}$  at 230 °C over CY-A (left) and CY-C (right).

**Figure 6.18:** *In situ* DRIFTS spectra recorder under  $\text{CO}/\text{H}_2/\text{Ar}$  gas flow in the 3000-2800  $\text{cm}^{-1}$  (a) and 2250-1800  $\text{cm}^{-1}$  (b) range over the CY-C catalyst sample.

**Figure 6.19:** Integral band area (Abs units) development of each of the three kinds of adsorbed CO-s species (two linear and one bridged) identified with TOS in  $\text{CO}/\text{H}_2$  reaction for the CY-C catalyst.

**Figure 6.20:** SSITKA-DRIFTS ( $^{12}\text{CO}/\text{H}_2 \rightarrow ^{13}\text{CO}/\text{H}_2$ ) performed at 230 °C over the CY-A and CY-C catalysts.

**Figure 6.21:** SSITKA-DRIFTS spectra recorded under  $^{12}\text{CO}/\text{H}_2$  and  $^{13}\text{CO}/\text{H}_2$  at 230 °C in the 3000-2800  $\text{cm}^{-1}$  range over the CY-C catalyst.

**Figure 6.22:** *In situ* DRIFTS spectra recorded in 5%  $\text{H}_2/\text{Ar}$  flow at 230 °C over the CY-A and CY-C catalysts as a function of time in 5%  $\text{H}_2/\text{Ar}$  gas flow.

**Figure 6.23:** Dimensionless surface concentration of adsorbed CO as a function of time during the 5%  $\text{H}_2/\text{Ar}$  gas treatment for the CY-A and CY-C catalysts.

**Figure 6.24:** Effect of carbon deposition on CO chemisorption (5%  $\text{CO}/\text{Ar}$ ) at 25 °C over the fresh CY-C sample and that after treated with  $\text{CO}/\text{Ar}$  at 230 °C.

**Figure 6.25:** *In situ* DRIFTS spectra recorded in the 2800-3000  $\text{cm}^{-1}$  range under 50%  $\text{H}_2/\text{Ar}$  gas flow at (a)  $T = 230$  °C and (b) TPH ( $T = 300, 400, 500, 600$  °C) following  $^{12}\text{CO}/\text{H}_2$  reaction at 230 °C (1 h) over the CY-C catalyst. Spectra for  $T = 300-600$  °C were recorded after 5-min  $\text{H}_2/\text{Ar}$  treatment of the catalyst at the given T.

## List of Tables

**Table 1.1:** Natural Gas resources in the Eastern Mediterranean are, as of the EIA 2013 report [7].

**Table 1.2:** Syngas production from natural gas using different kinds of reforming reactions.

**Table 2.1:** Types of defects of a crystal structure [7].

**Table 4.1:** BET surface area (SSA,  $\text{m}^2 \text{g}^{-1}$ ), specific pore volume ( $V_p$ ,  $\text{cm}^3 \text{g}^{-1}$ ), average pore size ( $d_p$ , nm), primary crystallite size ( $d_c$ , nm), lattice constant ( $\alpha$ , Å) and Oxygen Storage Capacity Complete (OSCC,  $\mu\text{mol g}^{-1}$ ) obtained over the  $\text{Ce}_{0.8}\text{Pr}_{0.2}\text{O}_2$  and  $\text{Ce}_{1-x}\text{Zr}_x\text{O}_{2-\delta}$  ( $x = 0.2$  and  $0.5$ ) solids.

**Table 4.2:**  $\text{H}_2$  desorption ( $\mu\text{mol g}^{-1}$ ) and Ni dispersion (D, %) obtained during  $\text{H}_2$ -TPD performed on fresh 5 wt.% Ni supported on  $\text{Ce}_{0.8}\text{Pr}_{0.2}\text{O}_{2-\delta}$  and  $\text{Ce}_{1-x}\text{Zr}_x\text{O}_{2-\delta}$  ( $x = 0.2, 0.5$ ) carriers.

**Table 4.3:** Conversion of  $\text{CH}_4$  and  $\text{CO}_2$  (%),  $\text{H}_2$  and  $\text{CO}$  yield (%) and  $\text{H}_2/\text{CO}$  gas product ratio obtained during Dry Reforming of Methane ( $T = 550\text{-}750 \text{ }^\circ\text{C}$ ; 1 h on stream; GHSV =  $30,000 \text{ h}^{-1}$ ) over 5 wt.% Ni/ $\text{Ce}_{0.8}\text{Pr}_{0.2}\text{O}_2$  and 5 wt.% Ni/ $\text{Ce}_{1-x}\text{Zr}_x\text{O}_{2-\delta}$  ( $x = 0.2, 0.5$ ) catalysts.  $P_{\text{CH}_4} = 0.2$  bar;  $P_{\text{CO}_2} = 0.2$  bar;  $P_{\text{He}} = 0.6$  bar.

**Table 4.4:**  $^{12}\text{CO}_2$  and  $^{13}\text{CO}_2$  ( $\mu\text{mol g}^{-1}$ ) and  $^{12}\text{CO}_2/^{13}\text{CO}_2$  product gas ratio obtained during temperature-programmed oxidation (TPO) to  $^{12}\text{CO}_2$  and  $^{13}\text{CO}_2$  of “carbon” formed after 1 h of dry reforming using 5%  $^{13}\text{CO}_2/5\% \text{ }^{12}\text{CH}_4/45\% \text{ Ar}/45\% \text{ He}$  at 550 and 750  $^\circ\text{C}$  over the 5 wt.% Ni/ $\text{Ce}_{0.8}\text{Pr}_{0.2}\text{O}_2$  and 5 wt.% Ni/ $\text{Ce}_{1-x}\text{Zr}_x\text{O}_{2-\delta}$  ( $x = 0.2, 0.5$ ) catalysts.

**Table 4.5:** BET surface area (SSA,  $\text{m}^2 \text{g}^{-1}$ ), specific pore volume ( $V_p$ ,  $\text{cm}^3 \text{g}^{-1}$ ), average pore size ( $d_p$ , nm), primary crystallite size ( $d_c$ , nm) and lattice constant ( $\alpha$ , Å) obtained over  $\text{Ce}_{1-x}\text{Pr}_x\text{O}_{2-\delta}$  ( $x = 0.0, 0.2, 0.5, 0.65, 0.8$ ) solids. The mean crystallite size of NiO ( $d_{\text{NiO}}$ , nm) for the corresponding supported nickel catalysts is also reported.

**Table 4.6:**  $\text{H}_2$  desorption ( $\mu\text{mol g}^{-1}$ ), Ni dispersion ( $D_{\text{Ni}}$ , %) and Ni mean particle size ( $d_{\text{Ni}}$ , nm) obtained from  $\text{H}_2$ -TPD performed on the fresh 5 wt.% Ni/ $\text{Ce}_{1-x}\text{Pr}_x\text{O}_{2-\delta}$  ( $x = 0.0, 0.2, 0.5, 0.65, 0.8$ ) catalysts.  $T_M$  ( $^\circ\text{C}$ ) is the temperature at which maximum  $\text{H}_2$  desorption rate occurs.

**Table 4.7:** Temperature-programmed oxidation (TPO) of “carbon” ( $\text{CO}$  and  $\text{CO}_2$  formation,  $\mu\text{mol g}^{-1}$ ) formed after 25 h of DRM at 750  $^\circ\text{C}$  over the 5 wt.% Ni/ $\text{Ce}_{1-x}\text{Pr}_x\text{O}_{2-\delta}$  ( $x = 0.0, 0.2, 0.5, 0.8$ ) catalysts. The amount of “carbon” (wt.%) measured by TGA-TPO is also reported.

**Table 4.8:**  $^{12}\text{CO}_2$  and  $^{13}\text{CO}_2$  ( $\mu\text{mol g}^{-1}$ ) and  $^{12}\text{CO}_2/^{13}\text{CO}_2$  product ratio obtained during temperature-programmed oxidation (TPO) of “carbon” formed after 30 min of dry reforming (5%  $^{13}\text{CO}_2/5\%$   $^{12}\text{CH}_4/45\%$  Ar/45% He) at 550 and 750 °C over the 5 wt.% Ni/CeO<sub>2</sub> and 5 wt.% Ni/Ce<sub>0.2</sub>Pr<sub>0.8</sub>O<sub>2- $\delta$</sub>  catalysts. DRM reaction conditions:  $F_T = 100 \text{ N mL min}^{-1}$ ;  $W_{\text{cat}} = 0.2 \text{ g}$  (no SiC as dilution was used).

**Table 4.9:** Steady-state concentration ( $\mu\text{mol g}^{-1}$  or  $\theta$ ) of active “carbon” ( $N_C$ ) and reversibly adsorbed CO<sub>2</sub> ( $N_{\text{CO}_2}$ ,  $\mu\text{mol g}^{-1}$  or  $\theta$ ) measured by SSITKA after 2 h of dry reforming (5% CH<sub>4</sub>/5% CO<sub>2</sub>/He) at 550 and 750 °C.

**Table 5.1:** Amounts of H<sub>2</sub>, CO and CO<sub>2</sub> ( $\text{mmol g}^{-1}$ ) produced after 5 min of methane decomposition (20% CH<sub>4</sub>/He reaction) at 750 °C.

**Table 5.2:**  $^{12}\text{CO}_2$  and  $^{13}\text{CO}_2$  ( $\mu\text{mol g}^{-1}$ ) and  $^{12}\text{CO}_2/^{13}\text{CO}_2$  ratio obtained during temperature-programmed oxidation (TPO) of carbon species formed during 30-min reforming in 5%  $^{13}\text{CO}_2/5\%$   $^{12}\text{CH}_4/\text{He}$  at 750 °C over the 3NiCo EG and 3NiCo HT catalysts.

**Table 5.3:** Amounts ( $\text{mmol g}^{-1}$ ) of C<sup>16</sup>O<sup>18</sup>O, C<sup>18</sup>O<sub>2</sub> and C<sup>18</sup>O formed during the various gas switches applied over the 3NiCo EG and 3NiCo HT catalysts after 10-min <sup>18</sup>O<sub>2</sub>/He treatment at 750 °C.

**Table 6.1:** Primary crystallite size of Co<sub>3</sub>O<sub>4</sub> ( $d_{\text{Co}_3\text{O}_4}$ , nm) and Co ( $d_{\text{Co}}$ , nm) dispersion of Co (D, %), Active Co metal surface area ( $\text{m}^2 \text{g}^{-1}$ ), BET specific surface area (SSA,  $\text{m}^2 \text{g}^{-1}$ ), specific pore volume ( $V_p$ ,  $\text{cm}^3 \text{g}^{-1}$ ) and average pore size ( $d_p$ , nm) obtained over CY-A and CY-C solids.

**Table 6.2:** Amount (N,  $\mu\text{mol g}^{-1}$ ) and surface coverage ( $\theta$ ) of adsorbed CO and active CH<sub>x</sub> (leading to CH<sub>4</sub>), mean residence time ( $\tau$ ), kinetic rates of methane formation ( $\mu\text{mol g}^{-1} \text{ s}^{-1}$  or TOF) and effective rate constant ( $k_{\text{eff}}$ ,  $\text{s}^{-1}$ ) of methane formation over CY-A and CY-C catalysts pertain to 32 h of continuous FT reaction.

**Table 6.3:** Deconvoluted TPH traces obtained over the CY-A and CY-C catalysts.

**Table 6.4:** Amount and surface coverage of non-exchangeable  $^{12}\text{CH}_x\text{-s}$  hydrogenated to  $^{12}\text{CH}_4$  at 230 °C (TIH), exchangeable  $^{13}\text{CH}_x\text{-s}$  and  $^{13}\text{CO-s}$  hydrogenated to  $^{13}\text{CH}_4$  at 230 °C (TIH), as well as of  $^{12}\text{C}_x\text{H}_y\text{-s}$  hydrogenated to  $^{12}\text{CH}_4$  under TPH after 32 h in FT over the CY-A and CY-C catalysts.

**Table 6.5:** Quantities of HD formed during the two different SSITKA and H/D exchange experiments performed over the CY-A and CY-C catalysts.

**Table 6.6:** CO conversion (%) under CO/H<sub>2</sub>, CO/D<sub>2</sub> and the KIE estimated over the CY-A and CY-C catalysts.

**Table 6.7:** Model C – SSITKA kinetic parameters estimated for the experiment performed after 16 h of FT reaction.  $\tau_1$  and  $\tau_2$  (s) reflect the mean lifetime of  $\text{CH}_x^1$ -s and  $\text{CH}_x^2$ -s, respectively, active intermediates, and  $R^2$  is the value of mathematical regression of the experimental vs simulated data.

**Table 6.8:** Model A – SSITKA performed after 16 h of FT reaction, where  $\tau_1$  and  $\tau_2$  (s), reflect the mean lifetime of  $\text{CH}_x^1$ -s and  $\text{CH}_x^2$ -s, respectively, and  $R^2$  is the value of mathematical regression of the experimental vs simulated data.

**Table 6.9:** Peak position ( $\text{cm}^{-1}$ ) appeared after deconvolution of the CO-region IR bands (2250-1800  $\text{cm}^{-1}$ ) recorded under  $^{12}\text{CO}/\text{H}_2$  and  $^{13}\text{CO}/\text{H}_2$  feed streams.

**Table 6.10:** IR bands recorded in the 2250-1800  $\text{cm}^{-1}$  range after CO chemisorption at 25 °C over the CY-C (fresh) and CO/Ar treated at 230 °C (CY-C used) samples.

## Nomenclature

CSTR	Continuous stirred-tank reactor
D	Dispersion of metal supported catalyst
$d_p$	Average pore diameter
DFT	Density Functional Theory
DRIFTS	Diffuse Reflectance Infrared Fourier Transform Spectroscopy
DRM	Dry Reforming of Methane
$E_a$	Activation Energy
EDX	Energy Dispersive X-ray analysis
et al.	et alia (and others)
FTS	Fischer-Tropsch Synthesis
$F_T$	Total molecular flow
FWHM	Full Width Half Maximum
GHSV	Gas Hourly Space Velocity
HAADF	High Angle Annular Dark Field
HC	Hydrocarbons
HOMO	Highest Occupied Molecular Orbital
HRTEM	High Resolution Transmission Electron Microscopy
KIE	Kinetic Isotopic Effect
KM	Kubelka-Munk units
LUMO	Lowest Unoccupied Molecular Orbital
MS	Mass Spectrometer
$M_w$	Molecular weight
NG	Natural Gas
$N_i$	Amount of reaction intermediates
$O_L$	Lattice Oxygen
OSC	Oxygen Storage Capacity
Ppm	part per million
RWGS	Reverse Water Gas Shift Reaction
SEM	Scanning Electron Microscopy
SSITKA	Steady State Isotopic Transient Kinetic Analysis

T	Temperature
t	time
TEM	Transmission Electron Microscopy
TIH	Transient Isothermal Hydrogenation
TIR	Transient Isothermal Reduction
TOF	Turn Over Frequency
TOS	Time on Stream
TPD	Temperature-Programmed Desorption
TPH	Temperature-Programmed Hydrogenation
TPO	Temperature-Programmed Oxidation
TPR	Temperature-Programmed Reduction
$W_{\text{cat}}$	Weight of catalytic bed
XPS	X-ray Photoelectron Spectroscopy
XRD	X-ray Diffraction
$\beta$	Heating ramp
$\theta$	Surface coverage
$\tau$	mean life time

## Chapter 1: Literature Review

### 1.1. State of the art – Syngas production

The overpopulation and growth of industrialization in earth planet requires high energy demands, which are expected to be increased 57% by 2030 [1]. For several decades, the use of coal and oil were the primary sources of energy. This energy production, based mainly on fossil fuels, and the emissions of gaseous pollutants (i.e. CO<sub>2</sub>, NO<sub>x</sub>, CH<sub>4</sub>) associated with the use of these energy sources with significant environmental impacts are concepts completely interwoven [2,3]. Important impacts include the overheating of the earth and oceans due to the retreated energy, melting of the ices and other extreme climate phenomena.

The most important and abundant greenhouse gas is water vapor with its concentration to be controlled by the local climate (more in warm tropical seas but less at poles). As of the report published in 2017 from the United States Environmental Protection Agency (EPA) and the Greenhouse Gas Reporting Program (GHGRP), by 2015, CO<sub>2</sub> and CH<sub>4</sub> present in the atmosphere (~ 82% and 10%) and contribute 75% of the total greenhouse gases (GHG), with NO<sub>x</sub> and CFC's to follow (~ 5% and 3%). Although CH<sub>4</sub> concentration in the atmosphere (~ 2 ppm) it is much less than CO<sub>2</sub> (~ 405 ppm), it is contributing about 20% on the global warming [4]. CH<sub>4</sub> and CO<sub>2</sub> emissions could come from natural (lakes, grass, etc.) and anthropogenic (landfills, oil and gas processing, wastewater treatment, etc.) activities. Atmospheric CO<sub>2</sub> content modelling was performed by Budzianowski et al. [5], which they expect that its concentration will be increased and stabilised at ~ 610 ppm (~ 2 times than today). Carbon dioxide as a waste by-product of fossil fuel combustion, should be prevented or reduced, thus, new technologies to capture it for subsequent sequestration or convert it into valuable chemicals should be developed.

Considering that, and in conjunction with both the expected depletion of oil and the fluctuation of its price, it is necessary to find alternative energy sources (non-oil-based) that will lead to the mitigation of GHG intensity [5]. In a positive manner, most of the countries have been harmonized with laws (i.e. Europe 2020) that promote the reduction of GHG (especially European and Asian), whereas some others (i.e. Turkey, Cyprus and Malta), they have increased their emissions compared to 1990 (Fig. 1.1).

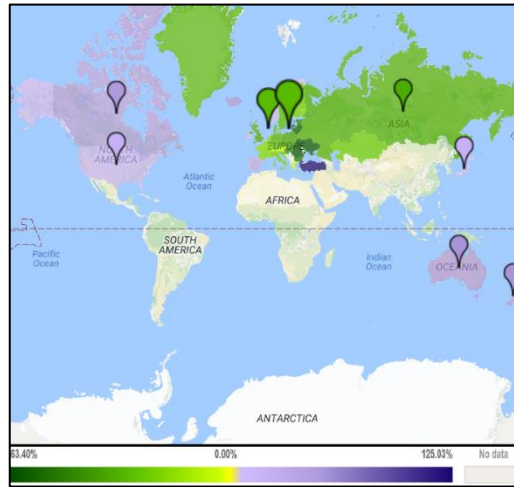


**Figure 1.1:** Global mitigation on Greenhouse Gas Emissions.

Natural gas (NG), even though is a non-renewable fossil fuel, seems to be an *alternative promising solution*, since: i) it can be converted into many valuable products, including liquid fuels, by existing chemical and petrochemical industries [6], and ii) abundant deposits were found around the world. As shown in Table 1.1, from the last report of the European Information Administration (EIA) in 2013, findings in Eastern Mediterranean Region (30<sup>th</sup> world's largest reserves of NG), even though are small, ~ 40 Tscf compared to the nearby Mediterranean North African reserves (ca. 239 Tscf), they might transform the geopolitical relationships between the beneficiaries. Despite that there is not any infrastructure for the transportation of the NG in the area, a conversion of it into more valuable chemicals (i.e. energy, fuels and chemicals), it will be a financial miracle for the region.

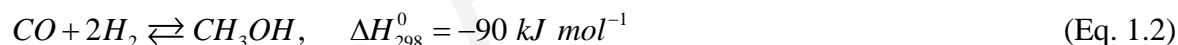
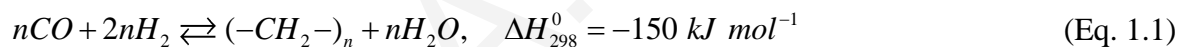
**Table 1.1:** Natural Gas resources in the Eastern Mediterranean are, as of the EIA 2013 report [7].

Country	Estimated reserves (Trillion standard cubic feet, Tscf)	Discovery date	First volumes
Cyprus	7	2011	2018
Israel	33.42	1999-2013	2012-2016
Palestinian Territories	1	2000	unknown
Egypt	30	2015	2017



NG resources mainly consist of ~ 80% hydrocarbons (HC) (mostly CH<sub>4</sub> and less C<sub>2</sub>H<sub>6</sub>, C<sub>3</sub>H<sub>8</sub>, C<sub>4</sub>H<sub>10</sub>) and ~ 15% CO<sub>2</sub>, with the higher CO<sub>2</sub>/CH<sub>4</sub> to be preferable for the production of higher HC [8] and high-purity H<sub>2</sub>. In fact, discoveries of NG resources with CO<sub>2</sub> content exceeding even well above 30 vol% have been reported [9].

The concept of converting Natural Gas to Liquids (GTL) is not new, and it is considered necessary because most of NG resources are far from industrial infrastructures, with the transportation of it through pipelines not to be always possible [10]. Acknowledge that, converting natural gas (methane) into more valuable products [11], as seen in Fig. 1.2 [12], gained the attention of many scientists. Some of these routes lead to the direct production of more valuable products via O<sub>2</sub> or CO<sub>2</sub> usage as an oxidant [8,13,14], whereas others by an indirect way via the intermediate production of syngas, a mixture of CO and H<sub>2</sub>, by using O<sub>2</sub>, H<sub>2</sub>O or CO<sub>2</sub> [15,16]. *Syngas* (mixture of CO and H<sub>2</sub> gases) can be the feed stock in several chemical and petrochemical companies in order to produce liquid fuels, methanol, olefins, gasoline, etc. To a commercial scale, two methods have successfully been developed, namely the Fischer-Tropsch [17] and the methanol synthesis [18], which are represented by Eq. (1.1) and Eq. (1.2), respectively:



Noteworthy to be mentioned that both H<sub>2</sub> and CO can be used independently. On the one hand, H<sub>2</sub> can mainly be used for ammonia synthesis but also as an energy carrier in fuel cells, for urea and heavy water production, etc. On the other hand, CO can be used in the production of plastics, paints, acetic acids, etc [11].

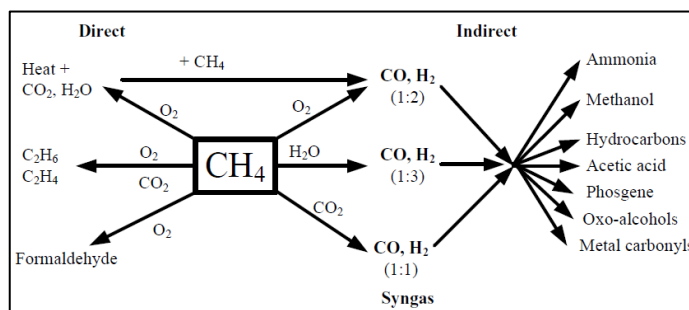


**Figure 1.2:** From natural gas towards the production of more valuable chemicals [12].

## 1.2. Catalytic technologies to syngas production

Nowadays, on-going research on the catalytic reforming of methane, mainly derived from natural gas or biogas towards the generation of syngas, it has gained the interest of industry [19,20]. Efforts to commercialize high carbon dioxide content (>30 vol%) have traditionally been unsuccessful due to high processing costs. However, increased demand for Natural Gas (NG) can make development of high carbon dioxide content gas fields an attractive proposition [9]. Monetisation of high carbon dioxide content NG becomes increasingly viable with higher NG costs and, especially, as far as gas processors are concerned, if technology developments can reduce gas processing costs. However, NG processing plants that produce very large quantities of carbon dioxide will have to consider disposal of CO<sub>2</sub> to underground storage, which inevitably requires high pressure dense phase carbon dioxide, thus adds significant cost [9]. A very attractive and alternative utilisation of CO<sub>2</sub>-rich NG reserves is its catalytic chemical transformation into synthesis gas ( $\text{CH}_4 + \text{CO}_2 \rightarrow 2 \text{CO} + 2 \text{H}_2$ ) to be used for the synthesis of fuels (Gas to Liquid technology) and other important high-added value chemicals [21].

The current stationary use of biogas (50-75% CH<sub>4</sub>, 25-45% CO<sub>2</sub>, 2-7% H<sub>2</sub>O, traces of H<sub>2</sub>S, N<sub>2</sub>, NH<sub>3</sub>) production units (organic wastes from landfill sites; industrial, domestic or commercial organic waste; agricultural waste materials) is the combined heat and power generation, where the electricity produced via stationary internal combustion engines (ICEs) can be fed into the public grid or used as an independent power supply for industrial and commercial areas. One of the challenges of this biogas (fuel) utilisation is the *increase in the energy efficiency* of ICE. Recent investigations [22] reported that syngas-fuelled engines with direct injection system, is expected to have better power engine output. The latter makes future efforts for the conversion of biogas into syngas with overall energy efficiency better than the existing one a very challenging topic of investigation and technological interest. The successful accomplishment of such an effort requires first the development of a robust catalytic system for the conversion of biogas into an appropriate syngas composition for boosting the overall energy efficiency of the operation of a biogas plant towards power/heat generation.

Reforming of methane into syngas contributes therefore indisputably to the large-scale production of liquid fuels [23], and minimize greenhouse gas emissions. Notwithstanding, all reforming of methane processes give high yield of syngas and appeal high conversion of methane, but different reforming processes producing different H<sub>2</sub>/CO ratio (Fig. 1.3), which is very important for syngas downstream exploitation towards different end products [24].

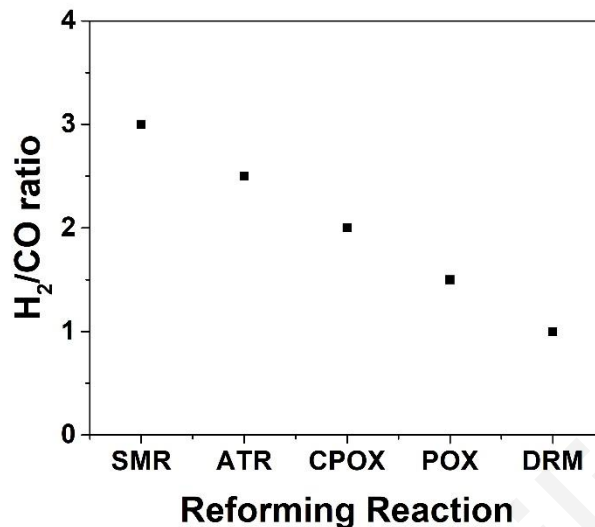
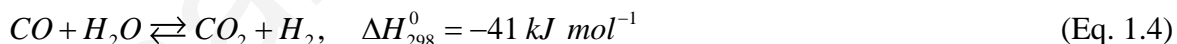
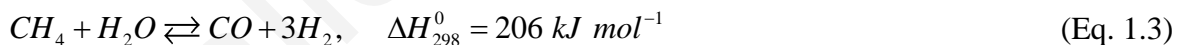


**Figure 1.3:** Syngas (H<sub>2</sub>/CO) ratio derived from different reforming routes [21].

### 1.2.1. Steam Methane Reforming (SMR)

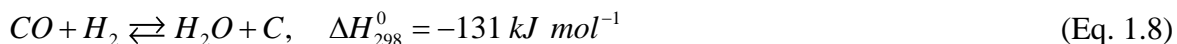
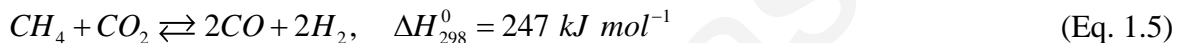
Steam Methane Reforming with H<sub>2</sub>O (Eqs. (1.3) - (1.4)) is a well-established and commercialized technology for syngas production (H<sub>2</sub>/CO ~ 3), where as a high endothermic reaction, it is highly energy intensive. Heat and excess steam should be supplied in order to produce higher yields of H<sub>2</sub>. Due to this, the reforming reactor (reformer), which is loaded with a metal based catalyst (e.g., Ni, Ru), is exposed to temperatures ~ 900 °C and pressures ~ 30 bar [25].



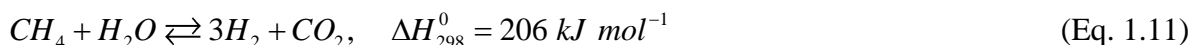
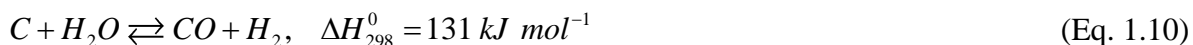
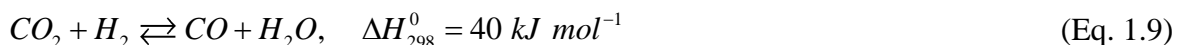
SMR is followed by downstream Water-Gas Shift (WGS) reaction (Eq. (1.4)), a slightly exothermic reaction, where CO is converted into CO<sub>2</sub> and the H<sub>2</sub>O to H<sub>2</sub>. Due to the WGS, the CO selectivity is very low and after further purification, the produced H<sub>2</sub> it can be used in fuel cells and petroleum refining [26,27] but not for FT synthesis towards long chain HCs. The latter is due to the fact that H<sub>2</sub> suppresses chain growth and decreases the selectivity to HCs [28]. Another drawback of SMR is the corrosion due to steam. Thus, desulphurization, which increases the capital investment, is required.

### 1.2.2. Dry Reforming of Methane (DRM)

Dry Reforming of Methane with CO<sub>2</sub> (Eq. (1.5)) yields syngas (H<sub>2</sub>/CO) with a theoretical molar ratio of unity. As a highly endothermic reaction, it therefore requires large amounts of heat but it can operate at 1 atm total pressure. A modelling performed by Beguerba et al. [26] explained at least five reactions, including several thermodynamically favourable side reactions, which are due to *carbon formation and deposition* over the catalyst surface, such as methane decomposition (Eq. (1.6)), Boudouard reaction (Eq. (1.7)) and CO reduction by hydrogen (Eq. (1.8)) [29]. Methane decomposition (or dehydrogenation) is a highly endothermic reaction, thus requiring large amounts of energy to proceed, whereas Boudouard reaction (CO disproportionation) is considered highly exothermic and is therefore favourable at lower temperatures.



The Reverse Water Gas Shift Reaction (RWGS) is also a side reaction of DRM, and is responsible for the production of H<sub>2</sub>O and CO, with in parallel consumption of H<sub>2</sub> according to Eq. (1.9). This reaction is usually the reason for obtaining a lower than unity H<sub>2</sub>/CO gas product ratio. Moreover, the water formed is able to react with the carbon formed towards syngas (H<sub>2</sub>/CO) according to Eq. (1.10) (coke gasification). The carbon species originating from CH<sub>4</sub> decomposition are more reactive and easily oxidized by CO<sub>2</sub> than those derived from the Boudouard reaction. The SMR reaction (Eq. (1.11)) could also take place but with lower reaction rates than the RWGS, and, therefore, due to both the RWGS and the SMR, the CO<sub>2</sub> conversion appears always greater than that of CH<sub>4</sub> in a DRM catalytic reaction system.



The main advantage of DRM, where it considers two greenhouse gases ( $\text{CH}_4$  and  $\text{CO}_2$ ) to produce syngas with a  $\text{H}_2/\text{CO}$  molar ratio close to unity, is the fact that appears very suitable for the FT synthesis of fuels since the latter requires  $\text{H}_2/\text{CO}$  close to unity for higher HCs production [28]. Disadvantage of DRM is considered the fact that there is no suitable product species in the reaction mixture for carbon gasification, as opposed to the case of SMR, and carbon deposition on the catalytic surface takes place with high rates. Thus, the development of *active and stable* catalysts (metal and support) with *coke resistance* and the adjustment of process parameters (ca. temperature and flow rate) are considered essential for the near future commercialization of the DRM process [30].

### 1.2.3. Partial Oxidation (POX)

Partial Oxidation of Methane (Eq. (1.12)), as opposed to DRM and SMR, is an exothermic reaction and it can convert, via a catalytic route (CPOX) and non-catalytic route (POX), methane to a  $\text{H}_2/\text{CO}$  (syngas) gas mixture with a ratio of  $\sim 2$ , after reacting with pure oxygen [26,31] at  $\sim 1300$  °C (POX) and  $\sim 850$  °C (CPOX).



CPOX over metal based catalysts (Pt, Rh, Ir, Pd, Ni, Co) requires less amount of thermal energy and that is why it has attracted the interest of FTS (heavy HC) and chemical (methanol and naphtha) synthesis related industries [32]. The advantages of POX are the high conversion rates, the high selectivity and the short residence time used [10]. Despite that, the use of pure oxygen increases the cost of the process, due to the requirement of a cryogenic oxygen production unit (air separation), and presents safety related issues when  $\text{CH}_4$  reacts with  $\text{O}_2$ , with the danger of explosion to be possible [33]. Moreover, the high exotherm of reaction induces active sites of the catalyst, thus making the process uncontrollable [34].

### 1.2.4. Autothermal Reforming of Methane (ATR)

Owing to the fact that DRM and SMR reactions are highly endothermic, they require energy supported from the burning of substantial fraction of the natural gas, thus showing inefficiency to the process. Autothermal Reforming of Methane is a combination of SMR, DRM

and POX, resulting to a thermal neutrality ( $\Delta H \sim 0.0 \text{ kJ mol}^{-1}$ ) and a  $\text{H}_2/\text{CO}$  ratio close to 1.0 for DRM/POX [35,36] and 2.5 for SMR/POX at  $\sim 1300 \text{ }^\circ\text{C}$ . This flexibility of the process makes it attractive to industries [37]. Nevertheless, only few commercial sites exist today.

Wood et al. [35] in their review compare the main natural gas exploitation technologies towards syngas production. The scale-up process, including reactor design and operating conditions are greatly affected by catalyst performance. All the aforementioned reforming technologies are of a catalytic nature (Table 1.2), with the research community to overwhelm an extensive work, whether supported noble metals or non-noble transition metals were used. More precisely, rhodium (Rh), ruthenium (Ru), platinum (Pt), palladium (Pd), Iridium (Ir), Nickel (Ni) and Cobalt (Co) are known to be very active as reforming of methane metal catalysts [38–43]. Bearing in mind that such catalysts need to assist in commercialization, noble metals, such as Rh and Ru, even though are the most active and stable with less prone to deactivation, are very expensive [44]. On the other hand, non-noble metals such as Ni and Co are preferred due to their low cost, however, due to coke and carbon deposition reveal rapid deactivation [45]. The lower O/C and H/C ratio appear as the controllable parameters for the tendency towards carbon deposition. In DRM with a ratio of  $\text{CO}_2/\text{CH}_4 = 1$ , the O/C equals to 1 and the H/C equals to 2, as opposed to that of SMR, which is 1 and 6, respectively. In the case of POX, the O/C equals to 1 and the H/C equals to 4 [46,47]. Considering that, it is obvious that DRM shows higher tendency towards carbon formation among the other known reforming processes. In particular, the most important topic is the inhibition of carbon deposition, which is being ranked as:  $\text{Ni} > \text{Co} > \text{Pd} > \text{Ir} > \text{Pt} > \text{Ru} > \text{Rh}$ .

**Table 1.2:** Syngas production from natural gas using different kinds of reforming reactions.

Reforming Reaction	Benefits	Drawbacks
<b>Dry Reforming of Methane (DRM)</b>	<ul style="list-style-type: none"> <li>• ~100% X<sub>CO2</sub> instead of releasing it into the atmosphere.</li> <li>• Best syngas (~1) for long chain HC production - FT synthesis.</li> </ul>	<ul style="list-style-type: none"> <li>• Heat should be supplied due to endothermicity.</li> <li>• Coke formation on the catalyst.</li> </ul>
<b>Steam Methane Reforming (SMR)</b>	<ul style="list-style-type: none"> <li>• Extensive commercial experience.</li> <li>• Lowest needs for additional energy.</li> <li>• Oxygen not required.</li> <li>• Optimum syngas ratio (~3) for liquid fuels production.</li> </ul>	<ul style="list-style-type: none"> <li>• High air emissions.</li> <li>• Costlier than POX and ATR.</li> <li>• CO recycle and H<sub>2</sub> excess removal.</li> </ul>
<b>Partial Oxidation (POX)</b>	<ul style="list-style-type: none"> <li>• Desulfurization of feed stock not required.</li> </ul>	<ul style="list-style-type: none"> <li>• Very high operating temperatures.</li> <li>• Oxygen should be supplied.</li> </ul>
<b>Autothermal Reforming (ATR)</b>	<ul style="list-style-type: none"> <li>• Lowest process temperatures than POX.</li> </ul>	<ul style="list-style-type: none"> <li>• Limited commercial experience.</li> <li>• Oxygen should be supplied.</li> </ul>

The active metals are usually dispersed as nanoparticles over promoted porous-ceramic oxide supports, with the propensity over Ni catalysts, based on stability, to be: CeZrO<sub>2</sub> > CeO<sub>2</sub> > ZrO<sub>2</sub> > La<sub>2</sub>O<sub>3</sub> > TiO<sub>2</sub> > Al<sub>2</sub>O<sub>3</sub> [48]. By controlling the particle size and increasing the basicity of catalysts, carbon deposition seems to be decreased. Passos et al. [47,48] found that the inhibition of carbon deposition in terms of carbonaceous species removal from the active sites can be promoted from the higher reducibility and oxygen storage/release availability of catalysts. In general, a novel catalytic system should comply with high conversion, selectivity and yield to the desired product. This can be achieved if the catalyst can operate at low temperatures, low cost and reveals low coke formation, high-poisoning and mechanical tolerance, with in parallel rapid reaction rate [49].

To conclude, even though Ni-based catalysts are mostly used because of their low cost, the development of optimum catalyst compositions is completely related to the catalyst

preparation method, the reforming method, and in particular the desired syngas ratio and its use. Higher syngas ( $H_2/CO$ ) ratio, where  $H_2$  is predominant, SMR should be used with the appropriate catalyst to be carefully chosen based on the literature. ATR and POX are extensively investigated for the production of liquid fuels, whereas syngas optimization is required. To produce higher HCs, DRM has been gaining prominent research and industrial interest due to the syngas generation with a  $H_2/CO$  close to unity, and the fact that two greenhouse gases,  $CO_2$  and  $CH_4$  are used as raw materials. In any case, heterogeneous catalysis and its concept that govern it should be followed in order to develop novel catalytic systems in the near future.

### 1.3. Dry Reforming of Methane over supported metal catalysts

As previously mentioned, reforming of methane by  $CO_2$  has received much attention because of the suitable utilization of natural gas-rich  $CO_2$  (>30 vol%) and biogas towards the production of a desired syngas ratio for the GTL technology ( $H_2/CO \sim 1$ ) and for the upgrading of stationary gas engines (electricity production) towards better energy efficiencies by using syngas than NG.

#### 1.3.1. Thermodynamics of DRM

Dry Reforming of Methane by  $CO_2$  (Eq. (1.5)) is a reversible and highly endothermic ( $\Delta H^\circ = +247 \text{ kJ mol}^{-1}$ ) reaction. Thermodynamic equilibrium analysis at  $CH_4/CO_2$  ratio of 1 and constant pressure was simulated and reported by several scientific teams [50–52] by minimizing the total Gibbs free energy ( $\Delta G^\circ$ ) and maximizing the entropy ( $\Delta S^\circ$ ) of reaction. This analysis could be used for the identification of possible reactions occurring during DRM and at which temperatures. As shown in Fig. 1.4, the equilibrium state for which  $\Delta G^\circ$  is negative (spontaneous reaction) for the DRM occurs at  $T < 643 \text{ }^\circ\text{C}$ . This shows that DRM is favoured at temperatures higher than  $643 \text{ }^\circ\text{C}$ . As of the side reactions described previously (Eqs. (1.6) - (1.8)), which mainly contribute in carbon formation,  $CH_4$  decomposition ( $\Delta H^\circ = +75 \text{ kJ mol}^{-1}$ ) occurs in the  $500 - 1000 \text{ }^\circ\text{C}$  range, while the Boudouard reaction ( $\Delta H^\circ = -171 \text{ kJ mol}^{-1}$ ) at  $T < 700 \text{ }^\circ\text{C}$ . In the case of RWGS reaction, this takes place at  $T > 800 \text{ }^\circ\text{C}$ . In addition, a challenge is to find the optimum DRM operating conditions with minimum carbon deposition and  $H_2/CO$  ratio close to unity.



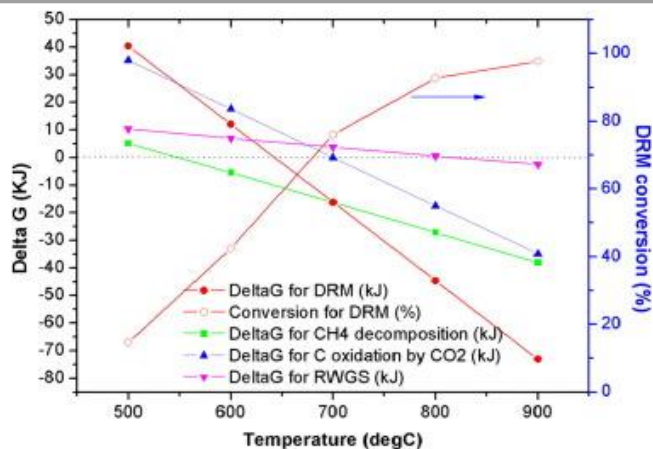


**Figure 1.4:** DRM and side reactions equilibrium in the 500-900 °C range [53].

Based on all the above mentioned thermodynamic considerations, it has been transpired that carbon formation and deposition takes place in the range of  $550 < T < 700$  °C due to  $\text{CH}_4$  cracking and the Boudouard reaction, with temperatures over 1000 °C to be optimum with no carbon formation. More precisely, Fig. 1.4 ( $T = 700$  °C,  $\Delta G_{\text{CH}_4\text{-d}} < \Delta G_{\text{C-CO}_2}$ ) and Fig. 1.5a illustrate that using a lower  $\text{CH}_4/\text{CO}_2$  ratio and higher reaction temperatures could minimize carbon formation. However, as shown in Fig. 1.5b, at lower temperatures the  $\text{H}_2/\text{CO}$  ratio is higher than 2, leading to the synthesis of short chain HCs ( $\text{C}_1\text{-C}_5$ ), and even though the  $\text{CH}_4$  conversion obtained is higher, it is not practical because the excess of  $\text{CO}_2$  can reduce the  $\text{H}_2$  yield and increase energy consumption. To produce long chain HCs, oxygenates and olefins via FT synthesis, the  $\text{H}_2/\text{CO}$  ratio should be close to unity. This can be achieved when the reaction temperatures are higher than 800 °C and at the same time the  $\text{CH}_4/\text{CO}_2$  ratio is 1, with  $\text{CH}_4$  conversions to be increased with increasing reaction temperature; however, it is not possible to be greater than 99% [54]. It should be considered though that high reaction temperatures required to overcome the endothermicity of DRM are responsible for metal sintering, which cause severe catalyst deactivation.

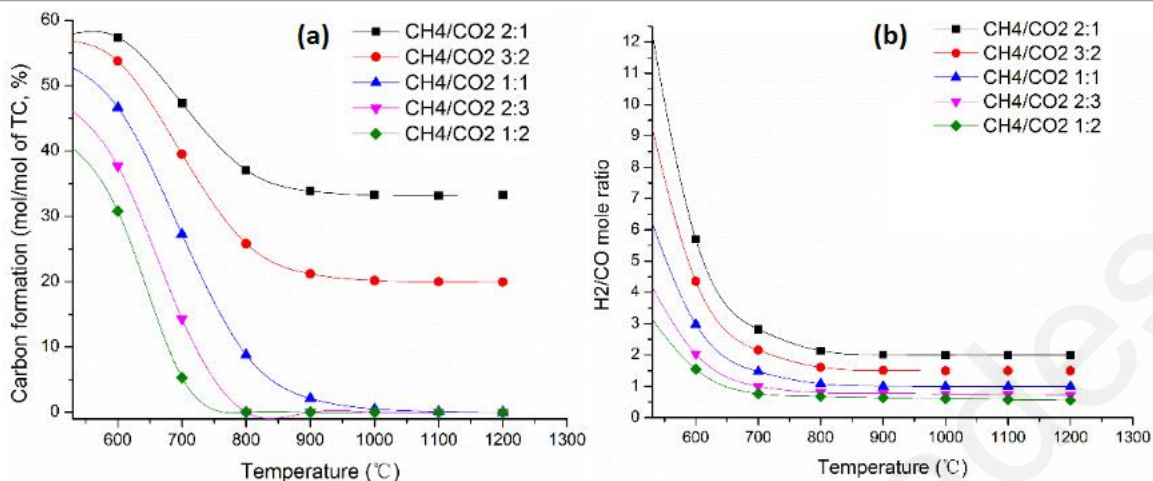


**Figure 1.5:** Carbon formation (mol/mol of TC, %) (a) and syngas (H<sub>2</sub>/CO) ratio (b) formation on different CH<sub>4</sub>/CO<sub>2</sub> ratio obtained in the range of 550-1200 °C [55].

### 1.3.2. Catalytic performance studies

The main drawbacks of running DRM at high reaction temperatures are the carbon deposition and the metal sintering. Thus, the development of novel catalytic systems of low cost and high activity and stability at these high T's becomes of paramount importance. Extensive efforts have been devoted concerning the development of optimum catalyst compositions by using different synthesis methods, calcination temperatures, various types of active metals, supports and promoters, which are comprehensively listed below.

#### 1.3.2.1. Effect of active metal

Scientific publications in the field of catalytic DRM appeared for more than 30 years. Usman et al. [55] have shown the influence of the chemical nature of active metals over different supports, on the catalytic activity. The first investigations were concerning catalysts with noble metals as active components (e.g. Rh, Ru, Pd, Ir, Au and Pt), which revealed higher activity and stability and coke resistance under DRM conditions compared to other metals (e.g. Ni). Despite their high cost, it has been found that over  $\alpha$ -Al<sub>2</sub>O<sub>3</sub> and MgAlO<sub>x</sub> supports, the impregnation of 5 wt.% of such noble metal can lead to more stable and coke resistant catalyst, with the trend to be: Rh > Ru > Ir > Pd > Pt > Au [28]. In particular, all catalysts showed no carbon deposition except Pd, whereas in terms of stability, Pd and Pt showed sintering of the metal particles due to high temperatures. These results were explained both after using powder XRD and TEM

measurements, which showed highly dispersed and smaller metal particles (1.5nm) that assist the reduction of carbon and metal agglomeration and sintering [56].

In recent years, non-noble active metals (Ni, Co and Fe) gain more attention because of their low-cost compared with noble metals, with Ni and Co to show also higher catalytic activity. The former metals revealed 5 times more coke deposition while the latter showed almost 10 times more compared to Pd supported catalysts. The increasing of Ni content imparts larger metal surface area, which imparts higher catalytic rates (in terms of CH<sub>4</sub> conversion) in DRM [57] by decreasing the primary crystallite size (ca. 25 nm), whereas catalysts with less than 10 mol % of Ni formed the lowest amount of carbon. In general, Ni-based catalysts show higher catalytic activity than Co-based ones, and therefore they have been investigated more. This higher catalytic activity can be explained as due to the smaller particle size and higher dispersion (ca. 9.5%) achieved for Ni compared to Co [58,59].

Since carbon deposition is linked to catalyst deactivation, it could be overcome by the development of non-noble metal catalysts with the addition of promoters (ca. very low loading of noble metals) [60] or dopants (alkali or alkaline) [61], where metal will be highly dispersed and the support will be suitable in terms of synergy [38,62].

### **1.3.2.2. Effect of promoter**

The addition of metal oxides or noble metals as promoters of Ni-based catalysts has been found to improve catalyst's performance. In particular, with the addition of 0.5% Rh as a promoter of Ni/ $\gamma$ -Al<sub>2</sub>O<sub>3</sub> catalysts, higher activity and lower carbon deposition were achieved [28,61], and this was explained as due to the formation of Rh-Ni clusters. Same behaviour was detected with the addition of Pt, where Pt-Ni alloy was formed with enrich surface in Pt, thus minimizing the metal particle size (10 nm) with increasing Pt content (0.4 wt.%) [63,64]. This increase in catalytic activity, stability and minimization of carbon deposition were also observed when non-noble (e.g. Co, Ce or Mo) or noble (e.g. Rh, Ru, Pd or Pt) metal was added as promoter in different supports ( $\alpha$ -Al<sub>2</sub>O<sub>3</sub>, ZrO<sub>2</sub>, MgO, SiO<sub>2</sub>, TiO<sub>2</sub> and CeZrO<sub>2</sub>), showing clearly that bimetallic catalysts lead to better metal dispersion, smaller particle size and good synergy between the metals [60,65–67] when compared to the monometallic ones.

The addition of Mo and W as promoters of 2 wt.% Ni/Al<sub>2</sub>O<sub>3</sub> catalyst was found to decrease carbon deposition compared to the unpromoted catalyst. Whereas increase to the amount of the former leads to deactivation due to its low melting point (T = 795 °C), which

spread the  $\text{MoO}_3$  over the Ni metal particle. In case of the latter though, higher stability was achieved due to its highest melting point ( $T = 1473\text{ }^\circ\text{C}$ ), which alter the solubility and dissociation of carbon in metal [68]. When K was added as promoter of  $\text{Co}/\text{Al}_2\text{O}_3$  catalyst, lower conversions were achieved, but the ability to gasify the carbon and partially cover the metal active sites for  $\text{CH}_4$  dehydrogenation was increased [69]. This was found to be a result of its strong metal-support interactions due to the increment of the reducibility of metal particles. Y-promoted catalysts showed superior catalytic activity with inhibition of carbon deposition due to great metal-support interactions, small metal particles and resistance to sintering [70]. Addition of La over  $\text{Ni}/\text{BaTiO}_3$  catalyst showed low carbon deposition with high catalytic activity and stability, a result of the highly dispersed active components and small metal particle size formation.

Several scientists were reported the addition of  $\text{CeO}_2$  or  $\text{CeO}_2\text{-ZrO}_2$  as promoters of  $\text{Ni}/\text{Al}_2\text{O}_3$  catalyst, where prevention of  $\text{NiAl}_2\text{O}_4$  and smaller metal particles formation [71,72] increased the  $\text{CO}_2$  dissociation, which leads to gasification of carbon species [73]. The gasification (continuous removal) of these carbon species from the active sites and prevention of their deposition is due to the superior oxygen transfer rate from the Ce and Ce-Zr mixed oxides. Moreover, such catalysts exhibit high activity and stability because of their higher reducibility and higher oxygen storage capacity, OSC [74].

Doping  $\text{Ni}/\text{Mg-Al-O}$  catalysts with Ce, long thermal stability of the basic sites was achieved, leading to a great enhancement of  $\text{CO}_2$  chemisorption. This ability is translated to the decrease of carbon deposition due to its gasification from dissociated oxygen and unsaturated reaction intermediates, even though the selectivity and activity were not increased. By increasing the Ce content (wt.%), even better results were obtained as illustrated via SEM images, where filamentous carbon was observed over 1 wt.% of Ce but when 3 wt.% was added on  $\text{Ni}/\text{Mg-Al-O}$ , no carbon formation was noticed [75]. Similar results were also reported on several studies using other promoters (e.g. Sn, Co, Mn) over the  $\text{Ni}/\text{MgO}$  and  $\text{Ni}/\text{Al}_2\text{O}_3$  catalysts, where great catalytic activity, stability and coke resistance were obtained. Sn and Co owed their highest catalytic activity and coke resistance to the high affinity for oxygen species, whereas Mn with lower catalytic activity, resulted in catalyst agglomeration, leading to the formation of large metal particles [76–78]. Superior results were reported when  $\text{MgO}$  was added as promoter of the  $\text{Ru}/\text{C}$  (activated carbon) catalyst, where carbon deposition is limited due to the formation of  $\text{MgCO}_3$  and the removal of carbon species by the provision of oxygen species [79]. Addition

of MgO or CeO<sub>2</sub> and La<sub>2</sub>O<sub>3</sub> over mesoporous materials (Ni/SBA-15) was also exhibited excellent catalytic activity, stability and minimal carbon deposition and metal agglomeration due to the formation of solid solution, basic active sites with strong CO<sub>2</sub> adsorption and small metal particles [80].

### 1.3.2.3. Effect of support

DRM's high temperature conditions affect the SSA of metal oxides, which depends on the properties of catalysts such as the melting point and phase transformation. Hence, it has been raised that coke formation is influenced by the nature of support, which should be able to gasify the carbon species for the prevention of carbon deposition and sintering [81].

Talkhonchek and Haghghi [82] developed and investigated the effect of support over Ni-based nanocatalysts (based on FESEM analysis) used for DRM. These catalytic materials, including different supports, such as CeO<sub>2</sub>, Al<sub>2</sub>O<sub>3</sub> and NH<sub>4</sub>NO<sub>3</sub> (clinoptilolite), were prepared by the wet impregnation method and characterized based on their physicochemical properties, their activity and stability. Different techniques including: BET, XRD, FTIR, EDX and FESEM were used for the physicochemical characterization. BET analysis illustrated that Ni/Al<sub>2</sub>O<sub>3</sub> catalyst had the highest SSA (m<sup>2</sup> g<sup>-1</sup>) among the other two catalytic materials. Based on the XRD and EDX results, the authors concluded that Ni was homogeneously dispersed over CeO<sub>2</sub> and Al<sub>2</sub>O<sub>3</sub>, with the best NiO dispersion to be on Ni/CeO<sub>2</sub> nanocatalyst. Regarding the activity and stability tests for DRM, which were in harmony with physicochemical results, Ni species are potential active sites providing to the Ni/Al<sub>2</sub>O<sub>3</sub> catalyst the fastest and highest conversions at 850 °C (~ 95% CH<sub>4</sub> and CO<sub>2</sub>) and yields (~ 90% H<sub>2</sub> and CO), and in parallel demonstrated stability for over 24 h [82]. Besides that, due to the high temperatures, alumina is unstable due to its thermal deterioration and phase transformation to  $\alpha$ -Al<sub>2</sub>O<sub>3</sub> [83]. As of Ni/NH<sub>4</sub>NO<sub>3</sub>, even though it is cheaper and demonstrated good activity, the generation of syngas and the H<sub>2</sub> and CO yields obtained were low.

Previous studies over reducible metal oxides such as CeO<sub>2</sub> and TiO<sub>2</sub> revealed the redox properties (ca. Ce<sup>4+</sup>/Ce<sup>3+</sup>), the oxygen mobility and the high oxygen storage capacity, which improves metal dispersion and resist sintering at high temperatures [84–88] as compared to irreducible metal oxides (e.g. Al<sub>2</sub>O<sub>3</sub> and SiO<sub>2</sub>). By modifying the CeO<sub>2</sub> with ZrO<sub>2</sub> provides better thermal stability, highest initial activity and better oxygen mobility for the CeO<sub>2</sub>-ZrO<sub>2</sub> supported metal catalysts. These characteristics improve the DRM activity of the catalysts

mainly due to the strong metal-support interactions by provision of oxygen from the support to the metal. Highest catalytic activity and excellent thermal stability exhibited when 0.5 wt.% of Pt, Rh or Ru was added over Ni/CeZr catalysts.

MgO-based catalysts, due to their high thermal stability (melting point, 2850 °C) and SSA were extensively studied as supports of DRM catalysts [89–91]. More specific, 8 wt.% Ni added to an MgO support showed the highest methane conversion among other loadings [92]. Noteworthy that Ni particles supported on MgO were found to be very small, preventing carbon deposition due to the formation of solid solution (NiO-MgO) with limited available amount of NiO for reduction [93]. Moreover, this stability was proved by XRD studies, where Ni<sup>2+</sup> was incorporated into the MgO support lattice, thus leading to the formation of NiO-MgO. This high stability though is not only related to the solid solution phase but also from the suppression of water (WGS) and the high basicity of the catalyst [94]. The latter reduces carbon deposition due to the enhancement of CO<sub>2</sub> chemisorption. Solid-solutions based on ZrO<sub>2</sub> with MgO, CaO, TiO<sub>2</sub>, Ta<sub>2</sub>O<sub>5</sub> and NbO<sub>2</sub> showed high activity, great metal-support interactions with superior oxygen vacant sites concentration and small metal particle size, which reduced coke formation and deposition [95–99].

#### **1.3.2.4. Effect of calcination temperature**

It has been found that loading and calcination temperature over non-noble metal supported catalysts strongly affect the activity and stability of the catalyst. Specifically, changes in calcination temperature (T<sub>C</sub>) from 300 to 750 °C over Ni-based catalysts affect the particle size of Ni, which increases by increasing T<sub>C</sub>. The calcination of catalysts causes the NiO to coalesce, creates inactive Ni sites, mould transformations, regulates the metal-support and oxide-support interactions, as well as the solid state reactions of CH<sub>4</sub> decomposition [100–102], revealing in that way higher conversions.

Calcination of MgO-supported Co-based (4-48 wt.%) catalysts in the range of 500-700 °C resulted to the reconstruction of the metal oxide and O<sup>2-</sup> donating centres and to higher catalytic activity, influencing in that way the basicity of the catalyst. It was found [103] that suppression of sintering of MgO and thus of its increase of particle size occurred when the catalyst was calcined at higher temperatures and for the highest Co loading used (48 wt.%). Under these conditions, sintering and carbon deposition resulted in lower catalytic activity and stability. Concerning Co-based catalysts over different supports, T<sub>C</sub> strongly affects the

chemical composition of the Co-oxide phase, from  $\text{Co}_3\text{O}_4$  at 500 °C to  $\text{Co}_2\text{AlO}_4$  and  $\text{CoAl}_2\text{O}_4$  at 1000 °C. The  $\text{Co}_3\text{O}_4$  phase due to its higher reducibility implies higher Co surface area, resulting in lower deactivation during DRM. It was shown that deactivation on high Co loadings (> 12 wt.%) is due to carbon formation, whereas on low loadings (~ 2 wt.%) is due to carbon deposition ( $T_C = 500$  °C) and metal oxidation ( $T_C = 1000$  °C). By this, it is shown that there is a  $T_C$  limit where the higher catalytic activity and stability is not always achieved with higher  $T_C$ . In general, though, several studies confirmed that  $T_C \sim 800$  °C and low metal loading lead to more stable and active catalysts [104], whereas there is no direct relationship.

### 1.3.3. Deactivation of catalysts

Deactivation of a catalyst is expressed as loss of catalytic activity or the reaction rate. In general, catalyst deactivation can be the result of chemical, mechanical and thermal reasons. Chemical's nature deactivation might be occurred due to poisoning, vapour formation and reaction with the solid, whereas fouling is of a mechanical nature [105,106].

#### 1.3.3.1. Deactivation due to carbon deposition

The carbon formation on the DRM catalysts it can be in various forms with different characteristics and reactivity, all largely related to the reaction temperature [107]. The carbon may deposit as graphitic carbon (coke) growing as a film on the catalyst surface.

On Ni-based catalysts, the carbon is formed firstly on Ni particles, followed by carbon nanotube growth with Ni at its tip, commonly referred as “whisker”, which is mechanically strong and deactivates the catalyst. This deactivation leading to degradation and preventing the regeneration of the catalyst is due to the creation of catalyst pellets that fracture and break apart. Over Ni/ $\text{Al}_2\text{O}_3$  catalysts, three types of carbonaceous species are presented, namely:  $C_\alpha$ ,  $C_\beta$  and  $C_\gamma$ . It was found that the most active carbon ( $C_\alpha$ ) leads to the formation of CO, as an active reaction intermediate, while  $C_\beta$  and  $C_\gamma$  lead to the deactivation of the catalyst, with less reactivity and ability for oxidation. Chen et al. [109] revealed these properties by performing temperature-programmed hydrogenation (TPH) experiments over a Ni/MgO catalyst, as it can be seen in Fig. 1.6.

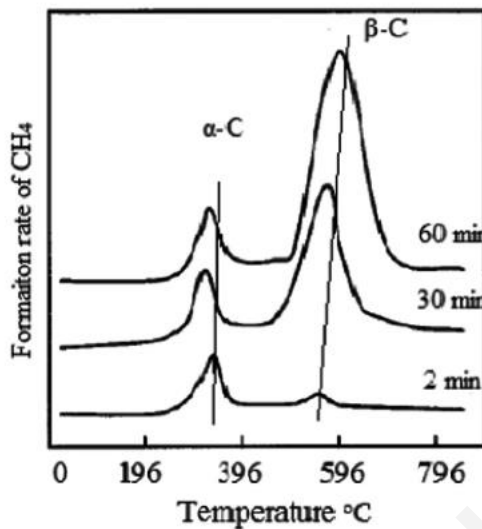


**Figure 1.6:** Temperature programmed hydrogenation (TPH) over 3 wt.% Ni/MgO at different contact times [109].

At low temperatures, an encapsulated film of  $\text{CH}_x$  accumulated on the metal surface and after its polymerization, block and deactivate the metal surface. At high temperatures, pyrolytic coke formed due to thermal cracking of  $\text{CH}_x$ , which encapsulates and deactivates the catalyst particles, as it diffuses in the form of graphitic film across the metal particles. At these temperatures, whisker carbon (amorphous polymeric graphite) also formed, firstly by diffusion of carbon through metal crystals, then by nucleation and growth as a filament with the metal presented at whisker's tip. This type of carbon is responsible for the plugging of catalytic pores, rather than the deactivation of it [108]. XPS studies over Ni-based catalyst on  $\text{Al}_2\text{O}_3$  showed three transition peaks which can be associated with  $-\text{C}-\text{C}-$ ,  $-\text{C}-\text{O}-\text{C}-$  and  $\text{CO}^{3-}$ . The former describes the filamentous carbon (graphitic form), which leads to catalyst deactivation, with the latter to be amorphous carbon which as more reactive can easily be gasified [109].

### 1.3.3.2. Deactivation due to other reasons

The carbon formation and deposition is one of the main chemical reasons that causes catalyst deactivation but not the only one. Degradation due to chemical, thermal, and mechanical phenomena can be reversible, allowing the catalyst to be regenerated, whereas in some cases it can be irreversible leading to catalyst deactivation. Of chemical nature reasons, transformations of the metal or the support via solid state reaction(s) might be considered. Ordinarily, the interaction of  $\gamma\text{-Al}_2\text{O}_3$  support with Ni under steam environment, can form  $\text{NiAl}_2\text{O}_4$  and remove



Al (dealumination), leading the catalyst to an irreversibly loss of its crystallinity and activity. Moreover, the redox ability of the catalysts is reversible but of high operating cost. Specifically, for the high temperatures required for the endothermic reforming reactions, Ni catalysts can be oxidized under oxidative conditions (Ni to NiO) and reduced under reductive conditions (NiO to Ni).

Depending on the downstream process, the lower limit of impurities it differs, whereas in any case, the lowest concentration of impurities is preferred (ppb level is desirable), to ensure longer lifetime of catalyst. The main challenge is to remove them from the feed gas by purification prior to the reaction. Sulphur compounds ( $\sim 20$  ppm), and specifically  $H_2S$  ( $\sim 4$  ppm), are the most important impurities contained in the natural gas, which they can poison the catalysts. Also, other impurities, such as moisture, inert  $N_2$  ( $\sim 3$  vol%), As and Hg ( $\sim 14$  ppm) may be present in the feed gas stream. Even though some of the impurities are inert, present in low amounts and have no detrimental effects, they might dilute the final syngas and form other species such as  $NH_3$  and HCN in the reactor. Moreover, oxygenates in biogas or from the methanol addition in the natural gas, for avoidance of hydrate formation might be considered. Sulphur compounds removal can be achieved via the use of activated carbon, which adsorb and oxidize  $H_2S$  into elemental sulphur and  $SO_2$  [110]. This process, which might be affected by humidity and alkali-impregnation, allows activated carbon pore structure and its surface characteristics (acidity) and  $N_2$  content to influence  $H_2S$  breakthrough capacity and selectivity towards elemental sulphur formation [111,112]. In particular, high humidity enhances water adsorption and in assistant with alkali-impregnation with  $Na_2CO_3$ , promotes dissociation and removal of  $H_2S$ . Micoli et al. [115] suggested the use of zeolite-based materials, which with their basicity induce acid-base and redox reactions for the removal of  $H_2S$ . Desulfurization can also be achieved with biological processes, which are very effective and environmental friendly. This includes the use of bio-filters, bio-trickling filters, bio-scrubbers and sulphide-oxidizing bacteria [113–117].

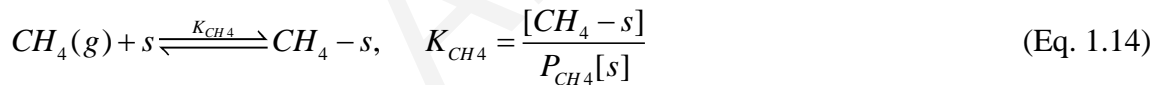
### 1.3.4. Mechanistic studies

As mentioned in previous sections, deactivation is one of the main drawbacks of DRM catalysts, thus it is essential to understand the mechanism of coke formation both from  $CO_2$  and  $CH_4$  reaction paths in order to develop novel catalytic materials in the near future. There are three main models describing the reaction paths in DRM.

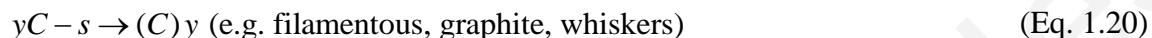
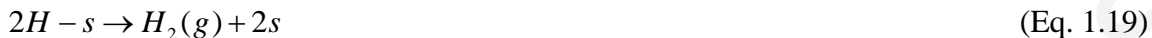
The usual empirical power law model is simple and covers the kinetic rate of DRM in wider range, based on the two reaction order parameters estimation (Eq. (1.13)) with respect to reactants, whereas it does not consider the various catalytic surface reaction steps and the rate-determining step (RDS) in order to estimate the reaction rate.

$$r = k[P_{CH_4}]^m[P_{CO_2}]^n \quad (\text{Eq. 1.13})$$

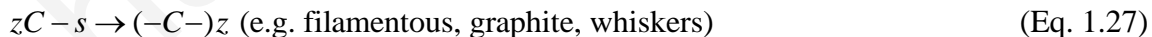
Mark and Maier [121] suggested a more rigorous model which follows the Eley-Rideal (E-R) mechanism, where  $CH_4$  is adsorbed and decomposed on the metal sites towards adsorbed carbon and hydrogen atomic species, with the carbon species to further react directly towards CO, by the reactant  $CO_2$ , as shown in Eq. (1.14) and Eq. (1.15), respectively. Few studies support that  $CH_4$  adsorption should be considered as the RDS, providing trustful simulation over experimental data, with Akpan et al. [122,123] to have further developed four different rate-determining step models. Theoretically, both reactants ( $CO_2$  and  $CH_4$ ) can be adsorbed or directly reacting towards CO formation, whereby it is shown from other E-R simulations that gaseous  $CO_2$  react with adsorbed  $CH_4$  [118].



Several research groups have investigated both E-R and Langmuir-Hinshelwood-Hougen-Watson (LHHW) models, and they concluded that in the operated DRM temperature range, LHHW model fits in a more-realistic way the reaction kinetics of the experimental data. In particular,  $CH_4$  adsorbs and decomposes (Eqs. (1.16) – (1.22)) on the metallic sites towards reactive adsorbed  $CH_x$  ( $x = 0-3$ ) and atomic hydrogen species, where the  $CH_x$  species are further oxidised towards  $CO(g)$  by oxygen species derived from the dissociation (Eqs. (1.23) – (1.27)) of the reactant  $CO_2$  [119–122], which is firstly adsorbed on the catalytic surface [123]. When methane decomposition rate is faster than the rate of carbon oxidation, there is carbon formation and deposition on the catalyst [38,124]. It is noteworthy to be mentioned that the formation of carbon is mainly occurred on the metallic sites, to the metal-support interface and less to the support itself [125].

**(a) CH<sub>4</sub> decomposition towards H<sub>2</sub> on metallic sites**

where “-s” and “O<sub>L</sub>” represent unoccupied active sites and lattice oxygen on the support surface, respectively. CO<sub>2</sub> dissociation, as opposed to CH<sub>4</sub> decomposition, occurs not only on metallic sites but also on support’s sites. This is due to the fact that metal oxide supports, such as CeO<sub>2</sub> and CeO<sub>2</sub>-ZrO<sub>2</sub> previously described have a large concentration of oxygen vacant sites ( $\square_L$ ), where the CO<sub>2</sub> can be dissociated.

**(b) CO<sub>2</sub> dissociation on metallic sites and metal-oxides supports**

Based on the LHHW model and focusing on the CH<sub>4</sub> decomposition and CO<sub>2</sub> dissociation steps, the carbon species derived from Eq. (1.7) (Boudouard reaction) and participating in Eq. (1.27) are considered as *inactive carbon*, which has filamentous, graphitic and whisker form [125]. It should be clarified that the inactive carbon (zC-s or yC-s) does not lead to the formation of CO, whereas the *active carbon* (C-s) can be gasified by O-s and O<sub>L</sub> derived from the CO<sub>2</sub> dissociation towards the formation of CO.

As a conclusion for the interesting reaction of DRM, kinetic modelling requires more experimental data to be validated, where several side reactions affect and play an important role, with the catalyst nature and temperature range contributing to the complexity of DRM's network and thus its simulation. It is essential to develop a novel catalytic system which will illustrate high catalytic activity, long-time stability, inhibition of sintering and practically no carbon accumulation. This could be achieved by carefully controlling several parameters, such as the nature and loading of active metal, the chemical composition of promoter and support, and catalyst activation, as described previously.

#### **1.4. Fischer-Tropsch synthesis on Co-based supported catalysts**

The Fischer-Tropsch synthesis (FTS) is a heterogeneous non-reversible, exothermic and complicated polymerization process ( $n(\text{CO} + 2\text{H}_2) \rightarrow (\text{CH}_2)_n + n\text{H}_2\text{O}$ ,  $\Delta H^\circ = -167 \text{ kJ mol}^{-1}$ ) [126], which is widely commercialized after the pioneering work of Franz Fischer and Hans Tropsch in the 1920's and 1930's. As such, FTS can be used for the production of a large variety of chemicals and fuels (i.e. alcohols, aldehydes, paraffins and olefins) [127] by using the synthesis gas ( $\text{CO}/\text{H}_2$ ) as a feedstock, which is derived from natural gas, coal or biomass, as illustrated in Fig. 1.7. Depending on the desired products, FTS can be separated into two routes: (i) the High Temperature FTS (300 – 350 °C) which is used for the production of gasoline and linear low-molecular weight olefins, and (ii) the Low Temperature FTS (200 – 240 °C) for the production of diesel and high molecular weight linear waxes [128]. Different FTS products could be produced based on different important parameters, such as the catalyst composition, the FTS reaction conditions (T, P) and other process parameters (i.e. reactor design, space velocity) [129–132].

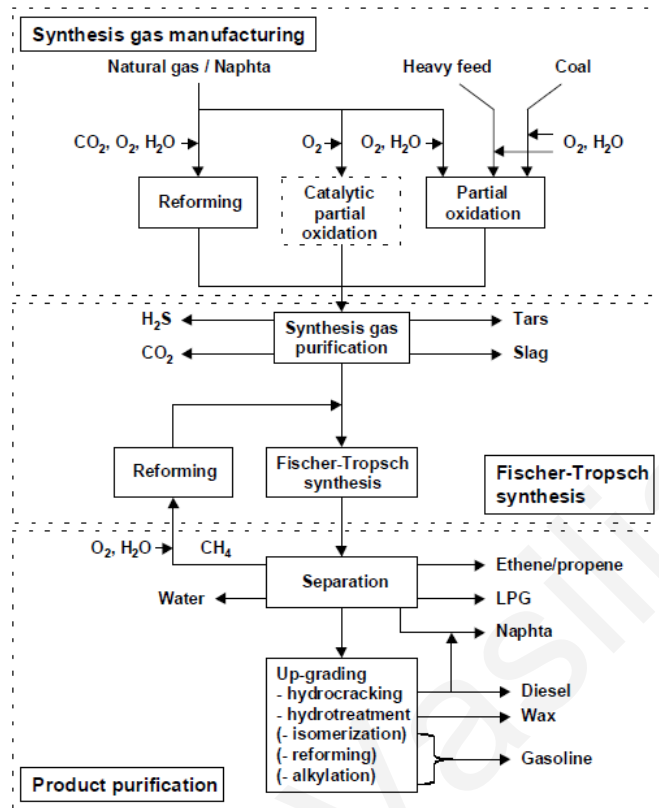


**Figure 1.7:** Schematic representation of a FTS plant [133].

Alongside with the main FTS reaction, several other reactions occur, which are responsible for the deactivation of the catalyst, mainly due to carbon formation (Eqs. (1.28) - (1.31)), such as: (i) the Water-Gas shift reaction (WGS) (Eq. (1.28)), (ii) the carbon deposition via reduction of CO (Eq. (1.29)), (iii) the Boudouard reaction (Eq. (1.30)), and (iv) the metal carbide formation (Eq. (1.31), e.g.  $\text{Co}_2\text{C}$  or  $\text{Fe}_3\text{C}$ ).



#### 1.4.1 Catalytic performance studies

Many physical and chemical processes (i.e. diffusion, adsorption, desorption, reaction and surface reconstruction) might influence the catalytic performance [134,135]. Although all

group VIII metals display some activity under FTS conditions, Co- and Fe-based catalysts are mainly used in commercial FTS scale, due to their high catalytic activity under FTS conditions, but also due to their wide availability and low-cost, in comparison to noble metals (i.e. Ru, Rh and Pt) [136–138]. Unpromoted Ru-based catalysts appear as the most active and stable catalysts under FTS conditions, with high selectivity on waxes with high molecular weight, whereas due to their high cost, they have been studied only on the academic level [139]. In the case that higher HC's ( $> C_{4+}$ ) are desirable, then Co-based catalysts are predominant, whereas Fe-based catalysts are mainly used for the production of olefins and oxygenates [140,141]. As well described in the open literature, there is a linear correlation between the metal loading and the kinetic rate of FTS reaction [142,143]. However, the metal-support interactions play an important role in the catalytic chemistry, as they can affect the structure and electron density of Co particles. For that reason, several supports have thoroughly studied (i.e.  $\gamma$ -Al<sub>2</sub>O<sub>3</sub>, TiO<sub>2</sub>, SiO<sub>2</sub>, CeO<sub>2</sub> and ZrO<sub>2</sub>) [144–147]. A great support shows high surface area (minimizes metal sintering) and hydrothermal stability, like in the cases of mixed metal oxides [148,149], and can significantly affect the FTS performance, due to its acidity and porosity [150], with the latter to significantly affect Co dispersion, reducibility, activity, and selectivity under FTS conditions [151]. Acidic supports could lead to olefin isomerization, lower chain growth, and higher selectivity to lighter hydrocarbons. Last but not least, the preparation method of the catalyst plays also an important role for the FTS reaction [148].

Fe-based catalysts, promoted with P and Cu, and supported over  $\gamma$ -Al<sub>2</sub>O<sub>3</sub> and SiO<sub>2</sub>, exhibit structural stabilization leading to high activity, selectivity and higher activity for the WGS reaction, mainly due to the presence of *Fe-carbide* as *active* phase and the formation of Fe-oxides. The high activity towards the WGS reaction, even though decrease the FT catalytic activity, thus the water should be removed, it is helpful for the utilisation of syngas with lower than unity H<sub>2</sub>/CO ratios (i.e. derived from coal or biomass), which ratios are flexibly controllable. However, the WGS reaction results in low carbon efficiency due to the consumption of CO towards CO<sub>2</sub>. The main advantage of Fe-based catalysts is their resistance under H-T FTS conditions, and their selectivity for light olefins, linear alkane fuels, alkenes and oxygenates, while in parallel exhibit low selectivity to methane and heavy wax formation [152]. Co-based catalysts supported over metal oxides, exhibit better stability, high activity and low activity towards WGS (resistance to deactivation by water) due to the formation of cobalt carbide (Co<sub>2</sub>C). Co metal is usually poorly dispersed over its support, thus, promoters such as

Pt, Ru and Re are used to inhibit catalyst deactivation due to carbon formation or oxidation. In contrast with the Fe-based catalysts, the olefins on Co-based catalysts tend to get readsorbed, increasing in this way the chain growth towards the formation of heavy HC's [139]. However, a major disadvantage of Co/ $\gamma$ -Al<sub>2</sub>O<sub>3</sub> catalysts is that Co is reducible only at high temperatures, due to strong metal-support interactions, as opposed to Co/SiO<sub>2</sub>, where the interactions are weak but is difficult to get high Co dispersion.

It is well known in the literature that in order to achieve high Co dispersion, and consequently optimum FTS performance, the synthesis of carbon-supported Co catalysts is very productive, due to the easier reducibility of the Co oxide species formed. Moreover, this kind of support has the consequence of decreasing the metal-support interactions, due to the hydrophobic characteristics and inertness of the graphitic surface [153,154].

#### 1.4.2 Kinetic and Mechanistic studies

Due to the complexity of the FTS reaction mechanism, it is required to identify the key initiator and its propagation for good understanding. According to the literature [155–157], after the adsorption and dissociation of CO on the catalyst surface, the following three major reaction mechanisms are considered to proceed under FTS conditions (Fig. 1.8):

##### (a) The carbene mechanism (carbide or alkyl mechanism)

The *carbene mechanism*, is one of the first FT reaction mechanism proposed by Fischer and Tropsch in 1926 [158], where the initiation steps consist of (i) the adsorption of gaseous reactant CO, (ii) its dissociation on the catalytic surface, (iii) its hydrogenation towards surface carbide formation (-C<sub>ads</sub>) and H<sub>2</sub>O, and (iv) the hydrogenation (-H<sub>ads</sub>) of the surface carbides (-C<sub>ads</sub>) towards the formation of the -CH<sub>ads</sub>, and thereafter to -CH<sub>2,ads</sub> and -CH<sub>3,ads</sub>. The methylene groups (-CH<sub>2,ads</sub>) are considered as the *key intermediate* (monomer), whereas the -CH<sub>3,ads</sub> are considered as the *chain growth initiator*, where polymerization towards surface alkyl species (R-CH<sub>2,ads</sub>-CH<sub>2,ads</sub>) takes place until their hydrogenation and release as a product (R-CH<sub>2,ads</sub>-CH<sub>3,ads</sub>) [159].

##### (b) The hydroxycarbene mechanism

The *hydroxycarbene mechanism* defines the mechanism where after CO adsorption on the catalyst surface and its partial hydrogenation towards surface hydroxycarbene species

( $\text{CHOH}_{\text{ads}}$ ), the chain growth proceeds via a condensation reaction of two  $\text{CHOH}_{\text{ads}}$  species, towards  $\text{C}_2\text{H}_5\text{OH}$  and water. The hydroxycarbene species is considered as the monomer, and the whole mechanism illustrates the formation of alcohols via the hydrogenation, aldehydes via desorption and hydrocarbons via the H-assisted elimination of the OH group [156].

### (c) The CO-insertion mechanism

As of its name, the *CO-insertion mechanism* [160] describes the insertion of  $\text{CO}_{\text{ads}}$  intermediate (key intermediate) into the metal-alkyl bond ( $\text{M}-\text{CH}_3$ ), where the resulting ( $\text{M}-\text{C}_2\text{H}_3\text{O}$ ) surface acyl species is first hydrogenated to an alkyl chain ( $\text{M}-\text{C}_2\text{H}_5$ ) and water, where the alkyl chain is further grown [161]. This mechanism illustrates the formation of alcohols, aldehydes and hydrocarbons, whereas there is not any experimental evidence describing it as the key mechanism for HC's formation under FTS conditions, where it was found that it could be the key mechanism for oxygenates formation [162].

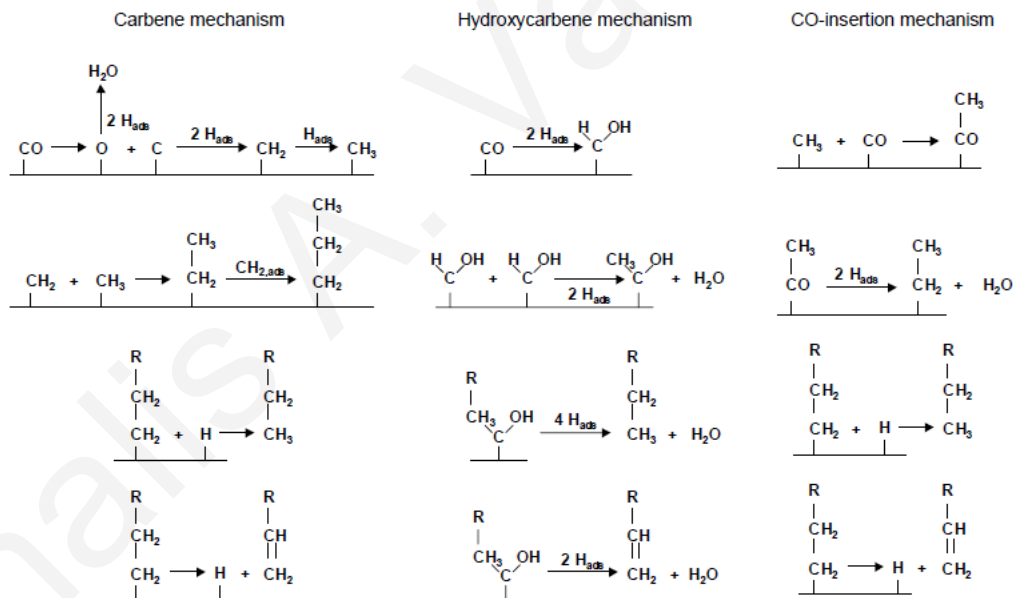


**Figure 1.8:** Schematic representation of the three basic FT reaction mechanisms [156].

### 1.4.3 Modelling on FT – SSITKA technique

The Steady State Isotopic Transient Kinetic Analysis (SSITKA) is a well-known and established advanced technique that allows to obtain, in a molecular level, important information over catalysed heterogeneous reactions [163], using either a continuous-stirred tank reactor (CSTR) or a plug-flow reactor (PFR). FT synthesis has been largely investigated by using the SSITKA technique for obtaining the concentration (surface coverage) and site



reactivity of reaction intermediates that participate in the complex mechanistic pathway described in the previous section [164]. Under steady-state reaction conditions and by combining the transient technique (SSITKA), one is able to deeply investigate and estimate the catalytic performance, the reaction order, the activation energy [135,165,166] but also the concentration (mol/g) and surface coverage ( $\theta$ ) of the *active reaction intermediates*, the *surface residence time* and the *intrinsic turnover frequency* of reaction based on the measured *active* only reaction intermediates (TOF<sub>ITK</sub>) [163]. Shannon and Goodwin [167] and recently Efstathiou et al. [168] have well reviewed the SSITKA technique and its benefits over several chemical reactions. The main advantage of the SSITKA technique is that it is applied under isothermal and isobaric conditions and without changing the overall composition of reaction, thus, the composition of the adsorbed phase does not change, and mechanistic studies can be made in the most accurate way. Further on this issue are given in Chapter 2.

	reaction	adsorption	pool system	model	transient responses and kinetic parameters
1	irreversible	irreversible	single	$R \xrightarrow{r_R} X \xrightarrow{\frac{r_P}{F_p(t)}} P$	$F_p(t) = e^{-t/\tau_X}; r_R = r_P$ $\tau_X = \frac{N_X}{r_P}; k = \tau_1^{-1}$ $TOF_i = \frac{r_i}{N_S} = \tau_1^{-1} \frac{N_i}{N_S} = k \cdot \theta_i$
2	irreversible	reversible	single	$R \xrightleftharpoons[r_R^d]{r_R^a} X \rightarrow P$	$F_p(t) = e^{-t/\tau_P}; r_P = r_R - r_R^d$ $\tau_X = \frac{N_X}{r_P + r_R^d} = \tau_P$
3	irreversible	irreversible	multiple in series	$R \rightarrow X_1 \rightarrow P$	$F_p(t) = \sum_{i=1}^n \frac{\tau_i^{n-1}}{\prod_{j=1, j \neq i}^n (\tau_i - \tau_j)} e^{-t/\tau_i}$ $\tau_P = \sum_{i=1}^n \tau_i$
4	irreversible	reversible	multiple in series	$R \xrightleftharpoons[r_R^d]{r_R^a} X_1 \rightarrow X_i \rightarrow P$	$F_p(t) = \sum_{i=1}^n \frac{\tau_i^{n-1}}{\prod_{j=1, j \neq i}^n (\tau_i - \tau_j)} e^{-t/\tau_i}$ $\tau_1 = \frac{N_1}{r_P + r_R^d}; \tau_{i>1} = \frac{N_i}{r_P}$ $\tau_P = \sum_{i=1}^n \tau_i$
5	irreversible	irreversible	multiple in parallel	$R \rightarrow X_1 \rightarrow P$ $R \rightarrow \vdots \rightarrow P$ $R \rightarrow X_n \rightarrow P$	$F_p(t) = \sum_{i=1}^n \alpha_i e^{-t/\tau_i}$ $\alpha_i = \frac{N_i}{\sum_{j=1}^n N_j}; \tau_P = \sum_{i=1}^n \alpha_i \tau_i$
6	irreversible	reversible	multiple in parallel	$R \xrightleftharpoons[r_{R,i}^d]{r_{R,i}^a} X_i \xrightarrow{r_{iP}} P$ $R \rightleftharpoons \vdots \rightarrow P$ $R \rightleftharpoons X_n \rightarrow P$	$F_p(t) = \sum_{i=1}^n \alpha_i e^{-t/\tau_i}$ $\alpha_i = \frac{N_i}{\sum_{j=1}^n N_j}; \tau_i = \frac{N_i}{r_{iP} + r_{R,i}^d}$ $\tau_P = \sum_{i=1}^n \alpha_i \tau_i$

**Figure 1.9:** Mechanistic models, transient responses, and kinetic parameters obtained by SSITKA technique [167].

A summary of the mechanistic models, based on the irreversible reaction, adsorption (either reversible or irreversible) and pool system in the formalism of SSITKA technique can be seen in Fig. 1.9 [42]. In all cases, the reactions presented in Fig. 1.9 are considered irreversible, condition that allows one to obtain analytical solutions for the SSITKA response of product P. In the case of a single pool system (Models 1 and 2), the intermediates are converted towards products, thus, by using appropriate material balances, the intermediate accumulation rate can be calculated as the difference between reactants and products. Moreover, the  $\tau$  and rate constant ( $k$ ) can be estimated, as well as the TOF of the active reaction intermediate based on the product rate and its surface coverage, which is estimated from the amount of reaction intermediates ( $N_i$ ) and the overall active sites ( $N_s$ ) [169]. It should be noted though, that in the case that there is reversible adsorption (Models 2, 4 and 6), the rate constants should be included in the calculations for the different parameters. In the cases of multiple in series pool systems (Models 3 and 4), the output of the first intermediate pool acts as feed to the following intermediate pool. The total  $\tau$  can be estimated from the summation of the individual  $\tau$ 's of each pool. Models 5 and 6 show the multiple in parallel pool systems, where catalytic surface is not homogeneous, having multiple sites or pathways to the same product, with different activity. In both cases, the overall transient response,  $F_p(t)$  can be estimated, based on the fractional number ( $x_i$ ) of the intermediates ( $N_i$ ) in the  $i^{\text{th}}$  pool. The total  $\tau$  can be calculated based on the summation of the individual  $\tau$ 's of each pool multiplied by  $x_i$ . Fig. 1.10 shows the differences in the SSITKA  $F(t)$  response between the kinetic models. The differences become distinguished especially in the logarithmic plot of the transient response (Fig. 1.10b), where the single pool model gives a straight line of higher slope than the case of two-pools models [167].

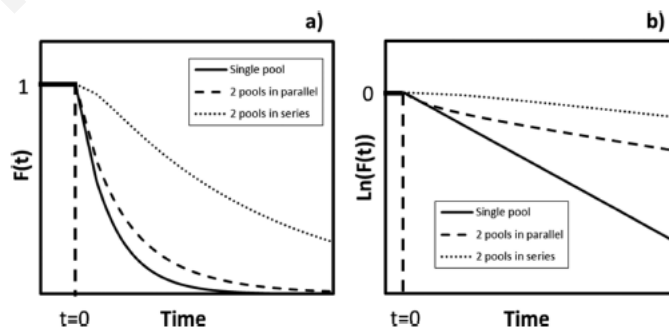


**Figure 1.10:** Comparison of the SSITKA transient response  $F(t)$  (a) and of the logarithmic transient response (b) of single pool, two pools in series and two pools in parallel [167].

A wide discussion and comparison of numerical methods considering reversible reaction steps, and the kinetic parameters obtained could be found in Kao et al. [170]. In these cases, several limitations come up. Firstly, the chromatographic effect should be considered, as the reactants are adsorbed on the catalytic surface, leading to delay in the changes of the isotopic composition in the gas phase, and this could create overestimation on the intrinsic kinetics of reaction steps. This effect could be avoided by increasing the space velocity of the reactants (increase flow and decrease the mass of catalyst) [171–173]. Secondly, the reversible adsorption of the product might also occur under real SSITKA conditions, and this reveal a delay in the transient responses [174]. The total  $\tau$  includes both the  $\tau$  of reaction intermediates but also the one of the reversible adsorption, and this could be corrected via Eq. (1.32) as proposed by Biloen et al. [175], where  $x$  is equal to 0.5 (empirical constant).

$$\tau_{real} = \tau_{exp.} - x\tau_{reac.} \quad (\text{Eq. 1.32})$$

A relative problem of SSITKA technique, which, however, at the same time turning it into its advantage, is that in some cases, is not possible to maintain steady-state reaction conditions upon SSITKA (no change in the overall reaction rate), thus the estimation of the intrinsic kinetic parameters becomes more challenging. This is the case of the isotopic exchanges of  $H_2$  to  $D_2$  [174,176]. The former can provide information for the characterization of the active surface, such as to evaluate the number of active sites participating during the exchange. In the case of oxygen isotopic exchange, quantitative information of the lattice oxygen diffusivity and the total oxygen storage capacity could be accomplished [177–179].

Many researchers have used effectively the SSITKA technique in order to reveal the effects of different catalytic properties (i.e. active metal, support, promoter, particle size) and operating conditions (i.e. space velocity, pre-treatment, activation,  $H_2$  partial pressure, temperature,  $H_2/CO$  ratio) to the catalytic performance (activity, selectivity and stability) and the reaction kinetics ( $\tau$ ,  $k$ , TOF,  $\theta$ ,  $N$ ) of the intermediates. Co- and Fe-based catalysts are the most studied in FTS by using the SSITKA technique, whereas there are several studies in the literature where noble metals were used for the SSITKA methanation reaction (i.e. Rh, Ru, Pt, Pd). An extensive review is presented by Ledesma et al. [180].

At this point, it is worthy to mention that by *SSITKA-Mass Spectrometry* alone it is not possible to investigate the whole mechanistic pathway of the FTS reaction due to the inability to *quantitatively follow* the evolution of all the labelled hydrocarbon gaseous species during the experiment. This is possible only by *GC-Mass Spectrometry* analysis as reported in detail

elsewhere [160,176,181]. Furthermore, SSITKA studies in FTS should be performed at similar pressures as those encountered in practice (25-35 bar). However, due to the proportional consumption of isotope gas compared to the application at  $P = 1$  bar, the requirements of more complex analytical and flow-gas systems, and the drawback and difficulty in interpreting correctly the  $C_2^+$ -hydrocarbons transient responses due to retainment and readsorption phenomena within the porous support system, high-pressure SSITKA studies on FT synthesis are very limited. Additionally, similar results' trend was reported for FT-SSITKA performed at 1 bar and 35 bar [182]. Thus, SSITKA technique for the FT synthesis is used at  $\sim 1$  bar total pressure, where methanation reaction predominates. It is important, however, to appreciate that by studying even methanation reaction mechanism, the important *active* intermediates of CO-s and  $CH_x$ -s and those of *inactive* carbon ( $-C_xH_y$ ) derived from  $-CH_x$  can be well investigated in order to understand how important catalyst design parameters and process reaction parameters as well, influence these kinetic parameters ( $k$ ,  $\theta$ ) and mechanism of methanation. It should be stated at this point that CO-s and  $CH_x$ -s intermediate species largely concern the chain-growth of FTS, thus their investigation at  $\sim 1$  bar pressure is of paramount importance for the design of better FTS catalysts.

There are several publications regarding the investigation of FT (methanation) reaction kinetics and mechanisms using both the experimental approach (CSTR/PFR reactor - SSITKA analysis) and the theoretical one, namely: density functional theory (DFT) [183–185], (ii) isotopic tracing [186,187], and (iii) theoretical modelling of SSITKA [188–191].

A drawback of SSITKA-Mass Spectrometry technique is that it lacks determination of the *composition (structure) of the adsorbed active reaction intermediates*. However, the latter becomes feasible when SSITKA is combined with other suitable spectroscopic techniques, such as FTIR spectroscopy, which is used for the direct investigation of the chemical composition of the adsorbed *active and inactive* reaction intermediates [192]. Moreover, *operando* SSITKA-MS-FTIR methodology, in a single [193–195] or dual-bed cell reactor ( $\sim 300$  mg) is a very powerful tool that provides at the same time the structure and concentration of the *active* reaction intermediates (*red isotopic shift*), and the structure of inactive ones (*no isotopic shift*) [196–198]. The former could also be achieved by comparing the isotopic exchange transient rate curves of the surface species derived from FTIR to those derived from the MS. The *active* reaction intermediates are expected to reveal fast isotopic exchange, whereas spectator species reveal slow or no isotopic exchange as discussed by Meunier et al. [199]. Goguet et al. [74]

presented an *operando* SSITKA-DRIFTS set-up, where the single DRIFTS bed cell (Fig. 1.11) is used as reactor to estimate quantitatively and qualitatively the reactivity of the adsorbed surface intermediate species under reaction conditions. Ledesma et al. [180] presented an extensive chronological compilation of studies carried out by coupling the SSITKA and FTIR spectroscopic technique under FTS reaction conditions.

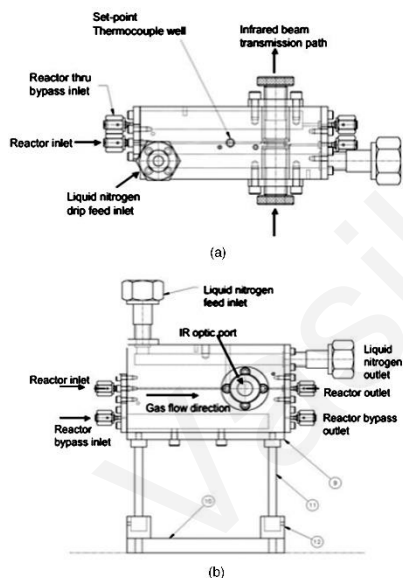


**Figure 1.11:** Schematic illustration of the DRIFT cell single bed reactor [200].

Microkinetic studies enhanced with SSITKA combined with in situ FTIR under methanation conditions were presented by Bobin et al. [201], where further studies by other groups [170,194,202] revealed important issues of the reaction mechanism, where different adsorbed CO species (linear and bridged) bonded over the catalytic surface of different Ni and Rh-based catalysts were probed. Furthermore, the CO activation mechanism, over the catalytic surface, its H-assisted (no reactive H-C-O species), where CO is reversibly adsorbed and the hydrogenation of  $\text{CH}_x$  intermediate towards  $\text{CH}_4$  is the rate-limiting step were probed [194,202]. Schweicher et al. [79] have presented SSITKA-DRIFTS experiments under FTS reaction conditions, where formate ( $\text{HCOO}^-$ ) and methylene ( $-\text{CH}_2$ ) adsorbed species act as *spectators*.

## References

- [1] F. Umbach, Energy Policy 38 (2010) 1229–1240.
- [2] K. Li, B. Lin, Renew. Sustain. Energy Rev. 52 (2015) 1107–1122.

- [3] M.E. Popa, M.K. Vollmer, A. Jordan, W.A. Brand, S.L. Pathirana, M. Rothe, T. Röckmann, *Atmos. Chem. Phys.* 14 (2014) 2105–2123.
- [4] D.J. Wuebbles, K. Hayhoe, *Earth-Science Rev.* 57 (2002) 177–210.
- [5] V. Andreoni, S. Galmarini, *Energy* 44 (2012) 682–691.
- [6] C. Perego, R. Bortolo, R. Zennaro, *Catal. Today* 142 (2009) 9–16.
- [7] U.S. Energy Information Administration, *Overview of Oil and Natural Gas in the Caspian Sea Region*, 2013.
- [8] T. Suhartanto, A.P.E. York, A. Hanif, H. Al-Megren, M.L.H. Green, *Catal. Letters* 71 (2001) 49–54.
- [9] L.S. Tan, K.K. Lau, M.A. Bustam, A.M. Shariff, *J. Nat. Gas Chem.* 21 (2012) 7–10.
- [10] C. He, F. You, *Ind. Eng. Chem. Res.* 53 (2014) 11442–11459.
- [11] C. Karakaya, R.J. Kee, *Prog. Energy Combust. Sci.* 55 (2016) 60–97.
- [12] J.R.H. Ross, A.N.J. van Keulen, M.E.S. Hegarty, K. Seshan, *Catal. Today* 30 (1996) 193–199.
- [13] S.M. Al-Zahrani, *Catal. Today* 64 (2001) 217–225.
- [14] Z. Guo, B. Liu, Q. Zhang, W. Deng, Y. Wang, Y. Yang, *Chem. Soc. Rev.* 43 (2014) 3480.
- [15] A. Holmen, *Catal. Today* 142 (2009) 2–8.
- [16] M.C. Alvarez-Galvan, N. Mota, M. Ojeda, S. Rojas, R.M. Navarro, J.L.G. Fierro, *Catal. Today* 171 (2011) 15–23.
- [17] H. Jahangiri, J. Bennett, P. Mahjoubi, K. Wilson, S. Gu, *Catal. Sci. Technol.* 4 (2014) 2210–2229.
- [18] A. Galadima, O. Muraza, *J. Nat. Gas Sci. Eng.* 25 (2015) 303–316.

- [19] D.A. Wood, *J. Nat. Gas Sci. Eng.* 26 (2015) 772–779.
- [20] K. Aasberg-Petersen, I. Dybkjær, C. V. Ovesen, N.C. Schjødt, J. Sehested, S.G. Thomsen, *J. Nat. Gas Sci. Eng.* 3 (2011) 423–459.
- [21] M.E. Dry, *Catal. Today* 71 (2002) 227–241.
- [22] F.Y. Hagos, A.R.A. Aziz, S.A. Sulaiman, *Adv. Mech. Eng.* 2014 (2014) 401587.
- [23] J. Baltrusaitis, W.L. Luyben, *ACS Sustain. Chem. Eng.* 3 (2015) 2100–2111.
- [24] J.R. Rostrup-Nielsen, *Catal. Rev. - Sci. Eng.* 46 (2004) 247–270.
- [25] A. Ricca, V. Palma, M. Martino, E. Meloni, *Fuel* 198 (2017) 175–182.
- [26] M. Oertel, J. Schmitz, W. Weirich, D. Jendrysek, Neumann, R. Schulten, *Chem. Eng. Technol.* 10 (1987) 248–255.
- [27] M. Sinaei Nobandegani, M.R. Sardashti Birjandi, T. Darbandi, M.M. Khalilipour, F. Shahraki, D. Mohebbi-Kalhari, *J. Nat. Gas Sci. Eng.* 36 (2016) 540–549.
- [28] Z. Hou, P. Chen, H. Fang, X. Zheng, T. Yashima, *Int. J. Hydrogen Energy* 31 (2006) 555–561.
- [29] Y. Benguerba, L. Dehimi, M. Virginie, C. Dumas, B. Ernst, *React. Kinet. Mech. Catal.* 114 (2015) 109–119.
- [30] C.A. Schwengber, F.A. Da Silva, R.A. Schaffner, N.R.C. Fernandes-Machado, R.J. Ferracin, V.R. Bach, H.J. Alves, *J. Environ. Chem. Eng.* 4 (2016) 3688–3695.
- [31] G. Iaquaniello, E. Antonetti, B. Cucchiella, E. Palo, A. Salladini, A. Guarinoni, A. Lainati, L. Basini, in: S.B. Gupta (Ed.), *Nat. Gas - Extr. to End Use*, InTech, Rijeka, 2012.
- [32] R.C. Ramaswamy, P.A. Ramachandran, M.P. Dudukovic, *Ind. Eng. Chem. Res.* 46 (2007) 8638–8651.
- [33] P. Djinović, I.G. Osojnik črnivec, B. Erjavec, A. Pintar, *Appl. Catal. B Environ.* 125

- (2012) 259–270.
- [34] D.J. Wilhelm, D.R. Simbeck, A.D. Karp, R.L. Dickenson, *Fuel Process. Technol.* 71 (2001) 139–148.
- [35] A. Moral, I. Reyero, C. Alfaro, F. Bimbela, L.M. Gandía, *Catal. Today* 299 (2018) 280–288.
- [36] M. Akri, S. Pronier, T. Chafik, O. Achak, P. Granger, P. Simon, M. Trentesaux, C. Batiot-Dupeyrat, *Appl. Catal. B Environ.* 205 (2017) 519–531.
- [37] J. Pasel, R.C. Samsun, A. Tschauder, R. Peters, D. Stolten, *Appl. Energy* 198 (2017) 88–98.
- [38] J.R. Rostrup-Nielsen, J.H. Bak Hansen, *J. Catal.* 144 (1993) 38–49.
- [39] J.H. Ryu, K.Y. Lee, H.J. Kim, J. Il Yang, H. Jung, *Appl. Catal. B Environ.* 80 (2008) 306–312.
- [40] F.V.D. Souza, B. Garcia-Sogo, A.D.S. Souza, A.P. San-Juán, V. Moreno, *Brazilian Arch. Biol. Technol.* 49 (2006) 21–27.
- [41] A. Shamsi, *Catal. Today* 139 (2009) 268–273.
- [42] A. Ishihara, E.W. Qian, I.N. Finahari, I.P. Sutrisna, T. Kabe, *Fuel* 84 (2005) 1462–1468.
- [43] R. Horn, K.A. Williams, N.J. Degenstein, L.D. Schmidt, *J. Catal.* 242 (2006) 92–102.
- [44] J. Barbero, M.A. Peña, J.M. Campos-Martin, J.L.G. Fierro, P.L. Arias, *Catal. Letters* 87 (2003) 211–218.
- [45] M. Zeppieri, P.L. Villa, N. Verdone, M. Scarsella, P. De Filippis, *Appl. Catal. A Gen.* 387 (2010) 147–154.
- [46] J.H. Edwards, A.M. Maitra, *Fuel Process. Technol.* 42 (1995) 269–289.
- [47] M.A. Peña, J.P. Gómez, J.L.G. Fierro, *Appl. Catal. A Gen.* 144 (1996) 7–57.



- [48] M.A. Naeem, A.S. Al-Fatesh, A.E. Abasaheed, A.H. Fakeeha, *Fuel Process. Technol.* 122 (2014) 141–152.
- [49] T. Inui, in: *CO<sub>2</sub> Convers. Util.*, 2002, pp. 130–152.
- [50] B. Cañete, C.E. Gigola, N.B. Brignole, *Ind. Eng. Chem. Res.* 53 (2014) 7103–7112.
- [51] R.Y. Chein, Y.C. Chen, C.T. Yu, J.N. Chung, *J. Nat. Gas Sci. Eng.* 26 (2015) 617–629.
- [52] Y. Sun, T. Ritchie, S.S. Hla, S. McEvoy, W. Stein, J.H. Edwards, *J. Nat. Gas Chem.* 20 (2011) 568–576.
- [53] Y. Kathiraser, U. Oemar, E.T. Saw, Z. Li, S. Kawi, *Chem. Eng. J.* 278 (2015) 62–78.
- [54] C. Song, *Catal. Today* 115 (2006) 2–32.
- [55] P. Cao, S. Adegbite, T. Wu, *Energy Procedia* 105 (2017) 1864–1869.
- [56] A.I. Tsyganok, M. Inaba, T. Tsunoda, S. Hamakawa, K. Suzuki, T. Hayakawa, *Catal. Commun.* 4 (2003) 493–498.
- [57] K. Mette, S. Kühn, A. Tarasov, M.G. Willinger, J. Kröhnert, S. Wrabetz, A. Trunschke, M. Scherzer, F. Girgsdies, H. Düdder, K. Kähler, K.F. Ortega, M. Muhler, R. Schlögl, M. Behrens, T. Lunkenbein, *ACS Catal.* 6 (2016) 7238–7248.
- [58] Z. Hao, Q. Zhu, Z. Jiang, H. Li, *Powder Technol.* 183 (2008) 46–52.
- [59] Z. Hao, Q. Zhu, Z. Lei, H. Li, *Powder Technol.* 182 (2008) 474–479.
- [60] C. Crisafulli, S. Scire, S. Minico, L. Solarino, *Appl. Catal. a-General* 225 (2002) 1–9.
- [61] M. Ocsachoque, F. Pompeo, G. Gonzalez, *Catal. Today* 172 (2011) 226–231.
- [62] J. Gao, Z. Hou, H. Lou, X. Zheng, in: *Fuel Cells Technol. Fuel Process.*, 2011, pp. 191–221.
- [63] M. García-Diéguez, I.S. Pieta, M.C. Herrera, M.A. Larrubia, L.J. Alemany, *Appl. Catal. A Gen.* 377 (2010) 191–199.

- [64] M. García-Diéguez, M.C. Herrera, I.S. Pieta, M.A. Larrubia, L.J. Alemany, *Catal. Commun.* 11 (2010) 1133–1136.
- [65] B. Pawelec, S. Damyanova, K. Arishtirova, J.L.G. Fierro, L. Petrov, *Appl. Catal. A Gen.* 323 (2007) 188–201.
- [66] W.K. Józwiak, M. Nowosielska, J. Rynkowski, *Appl. Catal. A Gen.* 280 (2005) 233–244.
- [67] M.-S. Fan, A.Z. Abdullah, S. Bhatia, *Appl. Catal. B Environ.* 100 (2010) 365–377.
- [68] A.P.E. York, T. Suhartanto, M.L.H. Green, in: *Stud. Surf. Sci. Catal.*, 1998, pp. 777–782.
- [69] D. San José-Alonso, M.J. Illán-Gómez, M.C. Román-Martínez, *Catal. Today* 176 (2011) 187–190.
- [70] C. Shi, P. Zhang, *Appl. Catal. B Environ.* 115–116 (2012) 190–200.
- [71] I. Luisetto, S. Tuti, C. Battocchio, S. Lo Mastro, A. Sodo, *Appl. Catal. A Gen.* 500 (2015) 12–22.
- [72] T.Y. Kim, S.M. Kim, W.S. Lee, S.I. Woo, *Int. J. Hydrogen Energy* 38 (2013) 6027–6032.
- [73] S. Therdthianwong, C. Siangchin, A. Therdthianwong, *Fuel Process. Technol.* 89 (2008) 160–168.
- [74] S.M. Stagg-Williams, F.B. Noronha, G. Fendley, D.E. Resasco, *J. Catal.* 194 (2000) 240–249.
- [75] C.E. Daza, J. Gallego, F. Mondragón, S. Moreno, R. Molina, *Fuel* 89 (2010) 592–603.
- [76] H. Xiao, Z. Liu, X. Zhou, K. Zhu, *Catal. Commun.* 34 (2013) 11–15.
- [77] M. Yu, K. Zhu, Z. Liu, H. Xiao, W. Deng, X. Zhou, *Appl. Catal. B Environ.* 148–149 (2014) 177–190.

- [78] X. Li, M. Wu, Z. Lai, F. He, *Appl. Catal. A Gen.* 290 (2005) 81–86.
- [79] Y. Schuurman, C. Mirodatos, P. Ferreira-Aparicio, I. Rodríguez-Ramos, A. Guerrero-Ruiz, *Catal. Letters* 66 (2000) 33–37.
- [80] B. Huang, X. Li, S. Ji, B. Lang, F. Habimana, C. Li, *J. Nat. Gas Chem.* 17 (2008) 225–231.
- [81] A.F. Lucrédio, J.M. Assaf, E.M. Assaf, *Appl. Catal. A Gen.* 400 (2011) 156–165.
- [82] J.L. Rogers, M.C. Mangarella, A.D. D’Amico, J.R. Gallagher, M.R. Dutzer, E. Stavitski, J.T. Miller, C. Sievers, *ACS Catal.* 6 (2016) 5873–5886.
- [83] Z. Cheng, Q. Wu, J. Li, Q. Zhu, *Catal. Today* 30 (1996) 147–155.
- [84] D.H. Kim, S.Y. Kim, S.W. Han, Y.K. Cho, M.-G. Jeong, E.J. Park, Y.D. Kim, *Appl. Catal. A Gen.* 495 (2015) 184–191.
- [85] W. Chen, G. Zhao, Q. Xue, L. Chen, Y. Lu, *Appl. Catal. B Environ.* 136–137 (2013) 260–268.
- [86] T. Odedairo, J. Chen, Z. Zhu, *Catal. Commun.* 31 (2013) 25–31.
- [87] H. Ay, D. Üner, *Appl. Catal. B Environ.* 179 (2015) 128–138.
- [88] A. Kambolis, H. Matralis, A. Trovarelli, C. Papadopoulou, *Appl. Catal. A Gen.* 377 (2010) 16–26.
- [89] E. Ruckenstein, Y.H. Hu, *Appl. Catal. A, Gen.* 133 (1995) 149–161.
- [90] E. Ruckenstein, H.Y. Wang, *J. Catal.* 205 (2002) 289–293.
- [91] K.C. Mondal, V.R. Choudhary, U.A. Joshi, *Appl. Catal. A Gen.* 316 (2007) 47–52.
- [92] Y. Wang, M. Berrill, F. Pedaci, M.M. Shakya, S. Gilbertson, Z. Chang, E. Granados, B.M. Luther, M.A. Larotonda, J.J. Rocca, *Opt. Photonics News* 20 (2009) 44.
- [93] Y.H. Hu, *Catal. Today* 148 (2009) 206–211.

- [94] Y.H. Wang, H.M. Liu, B.Q. Xu, *J. Mol. Catal. A Chem.* 299 (2009) 44–52.
- [95] S. Liu, L. Guan, J. Li, N. Zhao, W. Wei, Y. Sun, *Fuel* 87 (2008) 2477–2481.
- [96] A.A. Lemonidou, M.A. Goula, I.A. Vasalos, *Catal. Today* 46 (1998) 175–183.
- [97] A. Ranjbar, M. Rezaei, *J. Nat. Gas Chem.* 21 (2012) 178–183.
- [98] V. Choque, N. Homs, R. Cicha-Szot, P.R. de la Piscina, *Catal. Today* 142 (2009) 308–313.
- [99] X. Tian, Y. Zeng, T. Xiao, C. Yang, Y. Wang, S. Zhang, *Microporous Mesoporous Mater.* 143 (2011) 357–361.
- [100] J.L. Ewbank, L. Kovarik, F.Z. Diallo, C. Sievers, *Appl. Catal. A Gen.* 494 (2015) 57–67.
- [101] S.K. Shaikhutdinov, L.B. Avdeeva, O. V. Goncharova, D.I. Kochubey, B.N. Novgorodov, L.M. Plyasova, *Appl. Catal. A, Gen.* 126 (1995) 125–139.
- [102] Q.G. Yan, C.R. Luo, W.Z. Weng, L.F. Yang, H.L. Wan, T.H. Wu, *Acta Phys. - Chim. Sin.* 17 (2001) 737–738.
- [103] J.M. Montero, D.R. Brown, P.L. Gai, A.F. Lee, K. Wilson, *Chem. Eng. J.* 161 (2010) 332–339.
- [104] H. Wang, E. Ruckenstein, *Appl. Catal. A Gen.* 209 (2001) 207–215.
- [105] C.H. Bartholomew, *Appl. Catal. A Gen.* 212 (2001) 17–60.
- [106] J.A. Moulijn, A.E. Van Diepen, F. Kapteijn, *Appl. Catal. A Gen.* 212 (2001) 3–16.
- [107] J.R. Rostrup-Nielsen, *Catal. Today* 37 (1997) 225–232.
- [108] J.M. Ginsburg, J. Piña, T. El Solh, H.I. De Lasa, *Ind. Eng. Chem. Res.* 44 (2005) 4846–4854.
- [109] A. Carrero, J.A. Calles, A.J. Vizcaíno, *Chem. Eng. J.* 163 (2010) 395–402.

- [110] J. Kwaśny, W. Balcerzak, *Polish J. Environ. Stud.* 25 (2016) 37–43.
- [111] S. Bashkova, F.S. Baker, X. Wu, T.R. Armstrong, V. Schwartz, *Carbon N. Y.* 45 (2007) 1354–1363.
- [112] A. Bagreev, T.J. Bandosz, *Carbon N. Y.* 39 (2001) 2303–2311.
- [113] P.L.F. Van Den Bosch, D.Y. Sorokin, C.J.N. Buisman, A.J.H. Janssen, *Environ. Sci. Technol.* 42 (2008) 2637–2642.
- [114] N. Abatzoglou, S. Boivin, *Biofuels, Bioprod. Biorefining* 3 (2009) 42–71.
- [115] K. Tang, V. Baskaran, M. Nemati, *Biochem. Eng. J.* 44 (2009) 73–94.
- [116] G. Rodriguez, A.D. Dorado, M. Fortuny, D. Gabriel, X. Gamisans, *Process Saf. Environ. Prot.* 92 (2014) 261–268.
- [117] P. Oyarzún, F. Arancibia, C. Canales, G.E. Aroca, *Process Biochem.* 39 (2003) 165–170.
- [118] A.M. Becerra, M.E. Iriarte, A.E. Castro-Luna, *React. Kinet. Catal. Lett.* 79 (2003) 119–125.
- [119] S.-G. Wang, D.-B. Cao, Y.-W. Li, J. Wang, H. Jiao, *J. Phys. Chem. B* 110 (2006) 9976–9983.
- [120] X.E. Verykios, *Chem. Ind. Chem. Eng. Q.* 8 (2002) 238–255.
- [121] S. Sokolov, E. V. Kondratenko, M.M. Pohl, U. Rodemerck, *Int. J. Hydrogen Energy* 38 (2013) 16121–16132.
- [122] M.-S. Fan, A.Z. Abdullah, S. Bhatia, *ChemCatChem* 1 (2009) 192–208.
- [123] A. Erdöhelyi, J. Cserényi, F. Solymosi, *J. Catal.* 141 (1993) 287–299.
- [124] N. Matsui, K. Anzai, N. Akamatsu, K. Nakagawa, N. Ikenaga, T. Suzuki, *Appl. Catal. A Gen.* 179 (1999) 247–256.
- [125] C.G. Rotaru, G. Postole, M. Florea, F. Matei-Rutkovska, V.I. Pârvulescu, P. Gelin,

- Appl. Catal. A Gen. 494 (2015) 29–40.
- [126] A.Y. Khodakov, Catal. Today 144 (2009) 251–257.
- [127] C.H. Bartholomew, Catal. Letters 7 (1990) 303–315.
- [128] I. Wender, Fuel Process. Technol. 48 (1996) 189–297.
- [129] B. Todic, W. Ma, G. Jacobs, B.H. Davis, D.B. Bukur, J. Catal. 311 (2014) 325–338.
- [130] J. Patzlaff, Y. Liu, C. Graffmann, J. Gaube, Appl. Catal. A Gen. 186 (1999) 109–119.
- [131] A.Y. Krylova, Solid Fuel Chem. 48 (2014) 22–35.
- [132] J. Yang, W. Ma, D. Chen, A. Holmen, B.H. Davis, Appl. Catal. A 470 (2014) 250–260.
- [133] V. Dijk, The Fischer-Tropsch Synthesis : A Mechanistic Study Using Transient Isotopic Tracing Proefschrift Henricus Adrianus Johannes van Dijk, Eindhoven Univeristy of Technology, 2001.
- [134] H. Chuan Kang, W.H. Weinberg, Chem. Rev. 95 (1995) 667–676.
- [135] R.J. Berger, F. Kapteijn, J.A. Moulijn, G.B. Marin, J. De Wilde, M. Olea, D. Chen, A. Holmen, L. Lietti, E. Tronconi, Y. Schuurman, Appl. Catal. A Gen. 342 (2008) 3–28.
- [136] M. Ostadi, E. Rytter, M. Hillestad, Chem. Eng. Res. Des. 114 (2016) 236–246.
- [137] R. Oukaci, A.H. Singleton, J.G. Goodwin, Appl. Catal. A Gen. 186 (1999) 129–144.
- [138] M.A. Vannice, J. Catal. 37 (1975) 449–461.
- [139] M. Trépanier, A. Tavasoli, A.K. Dalai, N. Abatzoglou, Appl. Catal. A Gen. 353 (2009) 193–202.
- [140] P. Biloen, W.M.H. Sachtler, in: D.D. Eley, H. Pines, P.B. Weisz (Eds.), Adv. Catal., Academic Press, 1981, pp. 165–216.
- [141] R.C. Brady, R. Pettit, J. Am. Chem. Soc. 102 (1980) 6181–6182.

- [142] J.P. Den Breejen, P.B. Radstake, G.L. Bezemer, J.H. Bitter, V. Frøseth, A. Holmen, K.P. De Jong, *J. Am. Chem. Soc.* 131 (2009) 7197–7203.
- [143] R. Luque, A.R. de la Osa, J.M. Campelo, A.A. Romero, J.L. Valverde, P. Sanchez, *Energy Environ. Sci.* 5 (2012) 5186–5202.
- [144] M. Trépanier, A. Tavasoli, A.K. Dalai, N. Abatzoglou, *Fuel Process. Technol.* 90 (2009) 367–374.
- [145] Fischer, V. Steen, Claeys, J. *Catal.* 299 (2013) 67–80.
- [146] G. Jacobs, K. Chaudhari, D. Sparks, Y. Zhang, *Fuel* 82 (2003) 1251–1260.
- [147] W. Ma, G. Jacobs, D.E. Sparks, M.K. Gnanamani, V.R.R. Pendyala, C.H. Yen, J.L.S. Klettlinger, T.M. Tomsik, B.H. Davis, *Fuel* 90 (2011) 756–765.
- [148] E. Iglesia, *Appl. Catal. A Gen.* 161 (1997) 59–78.
- [149] J. Wang, P.A. Chernavskii, Y. Wang, A.Y. Khodakov, *Fuel* 103 (2013) 1111–1122.
- [150] V.R. Surisetty, A.K. Dalai, J. Kozinski, *Ind. Eng. Chem. Res.* 49 (2010) 6956–6963.
- [151] H. Xiong, Y. Zhang, S. Wang, J. Li, *Catal. Commun.* 6 (2005) 512–516.
- [152] A.Y. Khodakov, W. Chu, P. Fongarland, *Chem. Rev.* 107 (2007) 1692–1744.
- [153] Y. Yang, K. Chiang, N. Burke, *Catal. Today* 178 (2011) 197–205.
- [154] P. Trogadas, T.F. Fuller, P. Strasser, *Carbon N. Y.* 75 (2014) 5–42.
- [155] A. Kiennemann, J.P. Hindermann, *Catal. Rev.* 35 (1993) 1–127.
- [156] R. Anderson, *The Fischer-Tropsch Synthesis*, Academic Press, Orlando, Florida, 1984.
- [157] M.E. Dry, *Appl. Catal. A Gen.* 138 (1996) 319–344.
- [158] F. Fischer, H. Tropsch, *Brennstoff-Chem* 7 (1926) 97–104.
- [159] J.L.C. Rowsell, O.M. Yaghi, in: A. Steynberg, M. Dry (Eds.), *Angew. Chemie - Int.*

Ed., Elsevier, 2005, pp. 4670–4679.

- [160] N.S. Govender, *Mechanistic Study of the High-Temperature Fischer-Tropsch Synthesis Using Transient Kinetics*, Eindhoven University of Technology, 2010.
- [161] S.L. Brown, S.G. Davies, *J. Chem. Soc. Chem. Commun.* 1986 (1986) 84.
- [162] F. Zaera, *J. Mol. Catal.* 86 (1994) 221–242.
- [163] C. Mirodatos, *Catal. Today* 9 (1991) 83–95.
- [164] B. Todic, W. Ma, G. Jacobs, B.H. Davis, D.B. Bukur, *Catal. Today* 228 (2014) 32–39.
- [165] G. Le Cardinal, *Chem. Eng. Sci.* 33 (1978) 1568–1569.
- [166] P. Biloen, *J. Mol. Catal.* 21 (1993) 17–24.
- [167] S.L. Shannon, J.G. Goodwin, *Chem. Rev.* 95 (1995) 677–695.
- [168] A.M. Efstathiou, J.T. Gleaves, G.S. Yablonsky, in: *Charact. Solid Mater. Heterog. Catal. From Struct. to Surf. React. Vol. 1&2*, Wiley-VCH Verlag GmbH & Co. KGaA, 2012, pp. 1013–1073.
- [169] J.G. Goodwin, S. Kim, W.D. Rhodes, in: *J.J. Spivey, G.W. Roberts (Eds.), Catalysis*, The Royal Society of Chemistry, 2007, pp. 320–347.
- [170] J.Y. Kao, H. Piet-Lahanier, E. Walter, J. Happel, *J. Catal.* 133 (1992) 383–396.
- [171] M. Agnelli, H.M. Swaan, C. Marquez-Alvarez, G.A. Martin, C. Mirodatos, *J. Catal.* 175 (1998) 117–128.
- [172] C.J. Bertole, C.A. Mims, G. Kiss, *J. Catal.* 221 (2004) 191–203.
- [173] H.A.J. Van Dijk, J.H.B.J. Hoebink, J.C. Schouten, *Top. Catal.* 26 (2003) 111–119.
- [174] S. Pansare, A. Sirijaruphan, J.G. Goodwin, in: *Isot. Heterog. Catal.*, 2006, pp. 183–211.
- [175] P. Biloen, J.N. Helle, F.G.A. van den Berg, W.M.H. Sachtler, *J. Catal.* 81 (1983) 450–463.



- [176] N.S. Govender, M.H.J.M. de Croon, J.C. Schouten, *Appl. Catal. A Gen.* 373 (2010) 81–89.
- [177] O. Ovsitser, E. V. Kondratenko, *Catal. Today* 142 (2009) 138–142.
- [178] E. V. Kondratenko, O. Ovsitser, J. Radnik, M. Schneider, R. Kraehnert, U. Dingerdissen, *Appl. Catal. A Gen.* 319 (2007) 98–110.
- [179] M.A. Brundage, S.S.C. Chuang, *J. Catal.* 164 (1996) 94–108.
- [180] C. Ledesma, J. Yang, D. Chen, A. Holmen, *ACS Catal.* 4 (2014) 4527–4547.
- [181] J. Schweicher, A. Bundhoo, A. Frennet, N. Kruse, H. Daly, F.C. Meunier, *J. Phys. Chem. C* 114 (2010) 2248–2255.
- [182] B.C. Enger, V. Froseth, J. Yang, E. Rytter, A. Holmen, *J. Catal.* 297 (2013) 187–192.
- [183] J. Yang, Y. Qi, J. Zhu, Y.A. Zhu, D. Chen, A. Holmen, *J. Catal.* 308 (2013) 37–49.
- [184] Y. Qi, J. Yang, X. Duan, Y.-A. Zhu, D. Chen, A. Holmen, *Catal. Sci. Technol.* 4 (2014) 3534–3543.
- [185] J. Xie, J. Yang, A.I. Dugulan, A. Holmen, D. Chen, K.P. De Jong, M.J. Louwerse, *ACS Catal.* 6 (2016) 3147–3157.
- [186] M. Pontes, G.H. Yokomizo, A.T. Bell, *J. Catal.* 104 (1987) 147–155.
- [187] M. Otarod, J. Happel, Y. Soong, E. Walter, L. Pronzato, *Appl. Catal. A Gen.* 151 (1997) 97–107.
- [188] M. Rothaemel, K.F. Hanssen, E.A. Blekkan, D. Schanke, A. Holmen, *Catal. Today* 40 (1998) 171–179.
- [189] S. Storsæter, D. Chen, A. Holmen, *Surf. Sci.* 600 (2006) 2051–2063.
- [190] R.A. van Santen, A.J. Markvoort, *Faraday Discuss.* 162 (2013) 267.
- [191] R.A. van Santen, M.M. Ghouri, S. Shetty, E.M.H. Hensen, *Catal. Sci. Technol.* 1 (2011) 891.

- [192] S. Van Doorslaer, D.M. Murphy, in: M. Drescher, G. Jeschke (Eds.), *Top. Curr. Chem.*, Springer Berlin Heidelberg, Berlin, Heidelberg, 2012, pp. 1–40.
- [193] S.S.C. Chuang, F. Guzman, *Top. Catal.* 52 (2009) 1448–1458.
- [194] M.W. Balakos, S.S.C. Chuang, G. Srinivas, *J. Catal.* 140 (1993) 281–285.
- [195] G. Srinivas, S.S.C. Chuang, M.W. Balakos, *AIChE J.* 39 (1993) 530–532.
- [196] A. Ueno, T. Onishi, K. Tamaru, *Trans. Faraday Soc.* 66 (1970) 756.
- [197] R.D. O'Brien, *Can. J. Biochem. Physiol.* 35 (1957) 45–54.
- [198] K. Tamaru, in: D.D. Eley, H. Pines, P.B. Weisz (Eds.), *Adv. Catal.*, Academic Press, 1965, pp. 65–90.
- [199] F.C. Meunier, *Catal. Today* 155 (2010) 164–171.
- [200] Y. Yang, R.S. Disselkamp, J. Szanyi, C.H.F. Peden, C.T. Campbell, J.G. Goodwin, *Rev. Sci. Instrum.* 77 (2006) 94104.
- [201] A.S. Bobin, V.A. Sadykov, V.A. Rogov, N. V. Mezentseva, G.M. Alikina, E.M. Sadovskaya, T.S. Glazneva, N.N. Sazonova, M.Y. Smirnova, S.A. Veniaminov, C. Mirodatos, V. Galvita, G.B. Marin, *Top. Catal.* 56 (2013) 958–968.
- [202] D.M. Stockwell, J.S. Chung, C.O. Bennett, *J. Catal.* 112 (1988) 135–144.

---

## Chapter 2: Theoretical Background

### 2.1. Fundamental physicochemical properties of supported metal catalysts

The selection of an appropriate solid catalyst, which is of great scientific, technological and economic interest, in controlling the rate and selectivity of a chemical reaction at both the laboratory and industrial scale, is one of the most difficult tasks in the field of heterogeneous catalysis. In general, maximum reaction rate could be achieved when the chemical bonds between the surface adsorbed intermediate complexes and the atoms (or group of atoms) of the catalytic surface are neither strong enough nor too loose [1]. The most applied industrial-scale catalysts are those of supported metals (active phase) over a porous metal oxide (support). The active phase is the one mostly related to the catalytic activity, whereas the choice of the right support is of paramount importance, as the latter should be resistant to high pressures, temperatures, poisoning from impurities and should promote homogeneous dispersion of small metal particles [2]. In addition, tuning (or engineering) the metal-support interface (metal-support interactions, e.g. electronic nature) is now well understood how this could boost the activity of a given catalytic reaction by providing different in nature catalytic sites with significantly higher site reactivity,  $k$  ( $s^{-1}$ ) [3–5]. The structural and electronic properties of the catalytic surface of a given solid, are, therefore, of a great interest and importance since they both control the mechanism and kinetics of the catalytic reaction. The most important structural properties of solid catalysts are their crystal structure, primary particles morphology, and the local structure of their surface active sites. These properties are affected by the grid defects of the bulk of the support (metal oxide) but also from the active phase (metal), as well as the presence of foreign ions in the bulk and surface of the catalyst [6].

Over the past few years, there has been a fast growth in the number of published papers towards the characterization of ceria-based supported metal catalysts, and the understanding of how ceria as support affects the mechanism of different catalytic reactions, due to the influence of oxygen storage and release (OSR) kinetics of ceria-based supports [7].

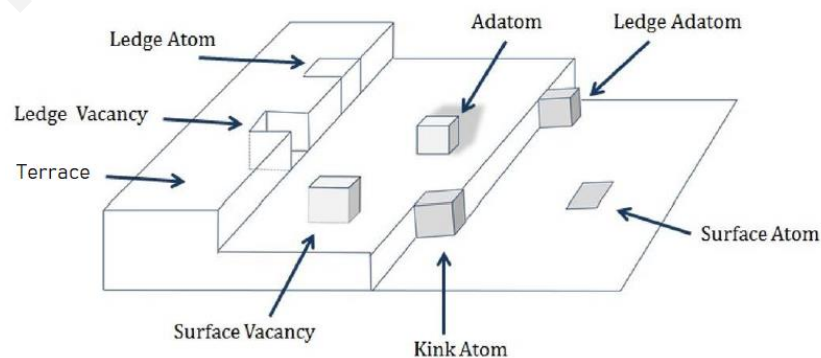
#### 2.1.1. Bulk and surface structural defects

Defects in a crystal structure [8] could increase the free energy and the entropy of the system, and these could be ionic or structural as presented in Table 2.1 [7].

**Table 2.1:** Types of defects of a crystal structure [7].

Defects	Physical Nature
<b>Ionic</b>	<ul style="list-style-type: none"> <li>• Interstitial ions in positions that should not be reserved</li> <li>• Contaminated ions</li> <li>○ Lattice ion impurities</li> <li>○ Bulk modifiers and dopants</li> <li>○ Oxygen vacant sites</li> </ul>
<b>Structural</b>	<ul style="list-style-type: none"> <li>• Volume defects</li> <li>• Planar defects</li> <li>• Line defects</li> <li>• Point defects (closed-packed crystal structure)</li> <li>○ Frenkel (in position movement of an atom)</li> <li>○ Schottky (pair of vacant sites in the bulk due to absence of ion)</li> </ul>

During this PhD thesis, it was necessary to understand the defects that are present on the bulk of the metal oxides (e.g.,  $\text{CeO}_2$  and doped- $\text{CeO}_2$  materials) and which are affected by the nature of them and the partial pressure of oxygen. Such defects are categorized to: (a) genetic, which are dependent to the nature of the metal oxide and not to the partial pressure of oxygen, (b) intrinsic (sub-lattice oxygen) and (c) extrinsic (ion impurities), which are dependent both to the partial pressure of oxygen and the nature of the metal oxide [6,9–11]. Figure 2.1 shows surface defects which are related to metal oxides, such as empty spaces (*vacancies*), extra atoms (*adatoms*), multiple layers (*terraces*), which in many cases differs by one atomic level (*steps*), and if are not smoothly grown, lead to *kinks*.

**Figure 2.1:** Defects present in a surface of metal oxide [12].

### 2.1.2. Crystal structures of CeO<sub>2</sub> and doped-CeO<sub>2-x</sub> solids

The metal-oxide supports of CeO<sub>2</sub> and doped-ceria were used as supports of Ni and Co metals (supported metal catalysts) in the present PhD thesis. CeO<sub>2</sub> based catalysts are used as supports in several industrial catalytic processes, the most important one being the automotive three-way catalysis [13–15]. On the other hand, these materials are of great interest at a research level for several other applications (e.g., water-gas shift, reforming and oxidation reactions), mainly due to their ability to be used as catalysts (redox potential that allows labile lattice oxygen to be formed, creation of oxygen vacancies that could potentially act as new catalytic sites), structural and electronic promoters, and to their electronic interaction (semiconductors) with both the metal [16] and other small molecules (H<sub>2</sub>, CO, O<sub>2</sub>) [17–21]. Furthermore, ceria is known for its following properties related to the catalytic effect [7,22–26]:

- (i) influence on the dispersion of metals over the support,
- (ii) increase of the thermal stability of support,
- (iii) storage and release of oxygen,
- (iv) formation of surface and bulk oxygen vacancies (imperfections of crystal structure), and
- (v) creation of active sites.

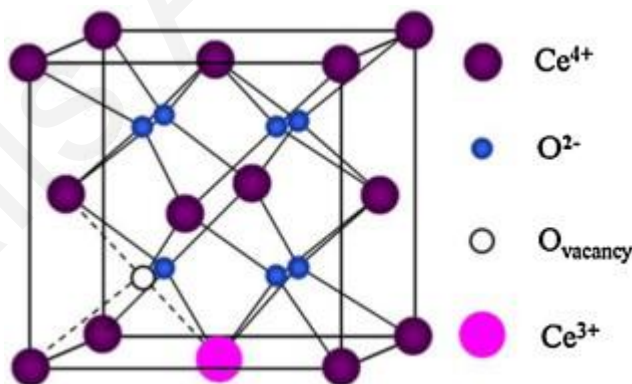


**Figure 2.2:** Crystal structure of defective (oxygen vacancies) CeO<sub>2</sub> [27].

The crystal structure of CeO<sub>2</sub> (Fig. 2.2) is that of face centered cubic (fcc) of CaF<sub>2</sub> type-structure [28], with a melting temperature,  $T = 2400$  °C. In this fcc cubic structure, each Ce<sup>4+</sup> cation is coordinated by eight equivalent adjacent oxygen anions (O<sup>2-</sup>), whereas each oxygen anion is tetrahedrally coordinated with four Ce<sup>4+</sup> cations [29]. It is noteworthy to be mentioned that CeO<sub>2</sub> has the ability for storage and release oxygen under oxidized (Ce<sup>4+</sup>) and reduced

(Ce<sup>3+</sup>) conditions, and in parallel, it keeps its CaF<sub>2</sub> structure even after the loss of lattice oxygen to leave behind oxygen vacant sites. The stoichiometry of CeO<sub>2</sub> is only applied in theory. CeO<sub>2</sub> shows several non-stoichiometric but stable phases, CeO<sub>2-x</sub> (x < 0.2) between CeO<sub>2</sub> (Ce<sup>4+</sup>) and Ce<sub>2</sub>O<sub>3</sub> (Ce<sup>3+</sup>); under reduced conditions, an oxygen atom is removed and the two electrons left behind are placed at the d-orbitals of two neighbor Ce<sup>4+</sup> cations, thus transforming them to Ce<sup>3+</sup> [30,31]. The formation of an oxygen vacancy in the crystal structure of CeO<sub>2-x</sub> leads to a decrease in the Gibbs free energy of the system ( $\Delta G^{\circ}$ ), due to the increase of the entropy ( $\Delta S^{\circ}$ ), which finally stabilizes the crystal structure [32].

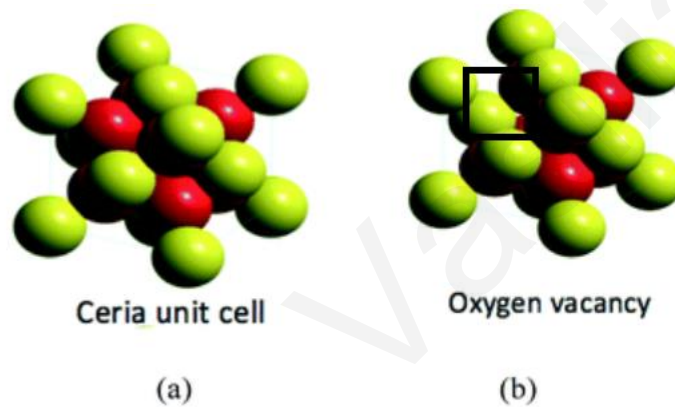


**Figure 2.3:** Crystal structure of CeO<sub>2</sub> under (a) oxidized and (b) reduced conditions [33].

The chemistry behind the fast changes in the oxidation states of Ce<sup>4+</sup> ↔ Ce<sup>3+</sup> can be assigned via Eq. (2.1) and as depicted in Fig. 2.3 [7,34].



where, Ce<sup>x</sup> and Ce<sup>'</sup> refer to Ce<sup>4+</sup> and Ce<sup>3+</sup> at cation lattice point, respectively, O<sup>x</sup> refers to O<sup>2-</sup> at anion lattice point and V<sub>O</sub> refers to an oxygen vacant site formed after the release of O<sub>2</sub> in the gas phase.

The doped-ceria supports are of great interest due to their very important oxygen storage capacity (OSC) and mobility properties, where as a result of this the increase of the catalytic activity obtained through the insertion of smaller (Zr<sup>4+</sup>) or larger (Pr<sup>3+</sup>) ions into the ceria lattice structure. This phenomenon is attributed to the effect of each dopant on the surface and bulk properties of CeO<sub>2</sub> [35–39], which can lead to three different crystal structures based on the temperature and composition in CeO<sub>2-x</sub>.

The insertion of larger than  $\text{Ce}^{4+}$  ions (e.g.,  $\text{Pr}^{3+} = 1.226 \text{ \AA}$ ) into the  $\text{CeO}_2$  ( $\text{Ce}^{4+} = 0.97 \text{ \AA}$ ) lattice ( $\text{Ce}_{1-x}\text{Pr}_x\text{O}_{2-\delta}$ ,  $x < 50 \text{ mol\%}$ ) leads to the increase of the oxygen vacant sites (more structural defects), as shown by Eq. (2.2) [7,40]. More specific, for every two  $\text{Pr}^{3+}$  cations that substitute two  $\text{Ce}^{4+}$  cations, an oxygen vacant site is created in order to keep the charge balance in the lattice [41,42]. The latter leads to an increase of the available labile O-s, thus towards the increase of the OSC, the mobility of the oxygen, and better thermal stability of the catalyst. This is due to the ability of both Ce and Pr oxides to easily change oxidative states ( $\text{Pr}^{3+} \leftrightarrow \text{Pr}^{4+}$  and  $\text{Ce}^{3+} \leftrightarrow \text{Ce}^{4+}$ ) [43–45], and as a result of this, the observed increase of the lattice constant (due to the larger ionic radius of Pr) seen by the powder X-ray diffraction technique [44].



On the other hand, the insertion of smaller than  $\text{Ce}^{4+}$  cations (e.g.,  $\text{Zr}^{4+} = 0.84 \text{ \AA}$ ) into the  $\text{CeO}_2$  lattice ( $\text{CeO}_2\text{-ZrO}_2$  solid solution), leads to the creation of labile oxygen due to structural disorders [46–48]. In particular, there is a 50% increase in the  $\text{Zr}^{4+}$  solubility into the  $\text{CeO}_2$  lattice due to [49–51]: (i) the decrease of the lattice constant (smaller ionic radius of  $\text{Zr}^{4+}$ ) leading to a decrease of the Ce-O distance, (ii) increase of the lattice channel diameter (enhance of oxygen diffusion), and (iii) increase of the structural defects.

## 2.2. Chemical adsorption (chemisorption)

Chemical adsorption ( $\Delta H_{\text{ads}}^\circ = 40 - 800 \text{ kJ mol}^{-1}$ ) is the process during which gas molecules impinging onto a catalytic surface are able to form chemical bonding [52] due to the *unsaturation* of the catalytic surface atoms (available unpaired electrons or free orbital bonding electrons). The latter simply arises by the missing neighbors over the first surface atomic layer, in comparison with the atoms in the subsurface/bulk region. During chemisorption of one or more reactants onto the catalytic surface, rearrangement of chemical bonds takes place, and the products formed can desorb from the surface, not able (in most of the cases) to form stable chemical bonding. As opposed to the physisorption (or physical adsorption) process, chemical adsorption does not exceed the one surface monolayer. In the case that chemical adsorption becomes an activated process, the energy demand needed for the creation of bonding between the gas molecules and the surface is referred to as the activation energy of adsorption ( $E_{\text{ads}}$ ) [52]. In most cases, chemical adsorption is a non-activated process.

The amount of a gas molecules adsorbed onto the catalytic surface is driven by the Gibbs free energy law ( $\Delta G^0 = \Delta H^0 - T\Delta S^0$ ), and considering the fact that irreversible and exothermic reactions do take place, this is determined by (i) the nature, preparation method and pre-treatment of the catalytic surface, and (ii) the nature, partial pressure and temperature of the gas molecules [52,53].

### 2.2.1. Chemisorption of CO

CO is thermodynamically unstable with free energy of  $\Delta G^0 = -60.6 \text{ kJ mol}^{-1}$ , and for that reason, it can only dissociate at high temperatures [54]. It should be mentioned though that for the dissociation of CO an electron should be transferred from the  $5\sigma$  (HOMO) to the  $2\pi^*$  (LUMO), which leads to an increase of its energy and then to its instability, something that can only take place when CO is chemisorbed on a catalytic surface and not in the gas phase. More specific, a two-step model can lead to the latter due to the small difference in energy between the Fermi metal level and the  $2\pi^*$  antibonding orbital of CO, which allows an electron transfer from the metal (bonding orbitals) to the CO ( $2\pi^*$ ), followed by an electron back-donation from the  $5\sigma$  of CO to the bonding orbitals of the metal [54,55], as schematically shown in Fig. 2.4.

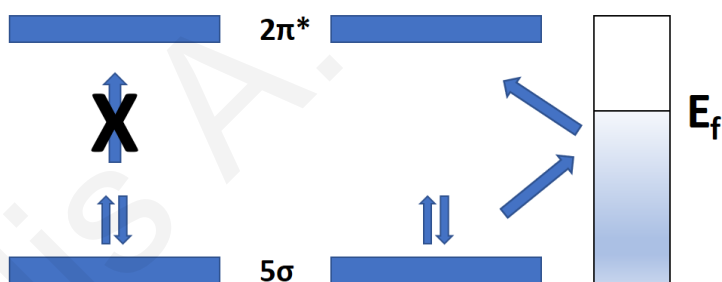


**Figure 2.4:** Electron transfer from the  $5\sigma$  to the  $2\pi^*$  orbitals of CO: gas phase state (left), and adsorbed CO state (right).

The chemisorption of CO (molecularly or dissociatively) over supported catalysts depends on the type of transition metal (i.e. Ni, Co, Ir, Cu, Ru, Rh, Pt, Pd), as extensively reported in the literature [56–61]. More precisely, based on the periodic Table (Fig. 2.5), CO is chemisorbed dissociatively ( $\text{CO}(\text{g}) + 2 \text{ s} \rightarrow \text{C-s} + \text{O-s}$ ) over transition metals in blue (e.g., Ni, Co, Rh), whereas it is chemisorbed molecularly ( $\text{CO}(\text{g}) + \text{s} \leftrightarrow \text{CO-s}$ ) over transition metals in white (e.g., Ir, Pt, Cu, Au, Ag).



Cr	Mn	Fe	Co	Ni	Cu
Mo	Tc	Ru	Rh	Pd	Ag
W	Re	Os	Ir	Pt	Au

**Figure 2.5:** CO chemisorption related to the nature of transition metal.

Molecular chemisorption of CO over a metal surface via carbon-metal chemical bonding could be possible in three different ways, as shown in Fig. 2.6: (a) linear, (b) bridged, and (c) gem-dicarbonyl (or twin) [62]. These chemical bonds can be identified by using the FTIR (transmittance or DRIFTS technique) in the range of 2200-1850  $\text{cm}^{-1}$  [63].

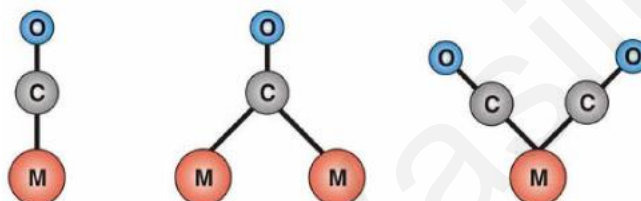


**Figure 2.6:** CO chemisorption over a catalytic surface (a) linear, (b) bridged, and (c) gem-dicarbonyl (or twin) type [64].

### 2.2.2. Chemisorption of H<sub>2</sub>

The chemisorption of H<sub>2</sub> over a catalytic metal surface is largely dissociatively ( $\text{H}_2(\text{g}) + 2 \text{ s} \leftrightarrow 2 \text{ H-s}$ ) and could be considered either activated or not based on the metal [65]. More precisely, the small energy difference between the Fermi energy level of the metal and the  $1\sigma^*$  (LUMO) of molecular H<sub>2</sub>, allows an electron back-donation transfer from the metal to the H<sub>2</sub> approaching the metal surface (in close to atomic distance) and in parallel there is an electron transfer from the  $1\sigma$  (HOMO) of H<sub>2</sub> to the d orbitals of the metal. In this way, the H-H bond becomes weak and a hydrogen-metal bond is made [66], as shown in Fig. 2.7 [64]. The dissociative chemisorption of H<sub>2</sub> and the binding energy of M-H formed over supported metal catalysts depend on the type of transition metal (e.g., Ni, Cu, Ru, Rh, Pt, Pd) and support composition, which all have well reported in the literature [65–69]. It is worthy to mention that during hydrogen chemisorption over a reducible metal oxide-supported metal catalyst (e.g. Pt/CeO<sub>2</sub>, Pt/La<sub>2</sub>O<sub>3</sub>), it is very common to observe a spillover (surface diffusion) of chemisorbed M-H from the metal surface to the metal-support interface and further to the support surface even at room temperature [70,71], which leads to an overestimation of the metal surface

(dispersion) during isothermal chemisorption and TPD studies. The rate of H-spillover was reported to be reduced significantly after using a very low partial pressure of H<sub>2</sub> (e.g. <0.002 bar or 2000 ppm H<sub>2</sub>) and adsorption temperatures below 25°C [72,73].

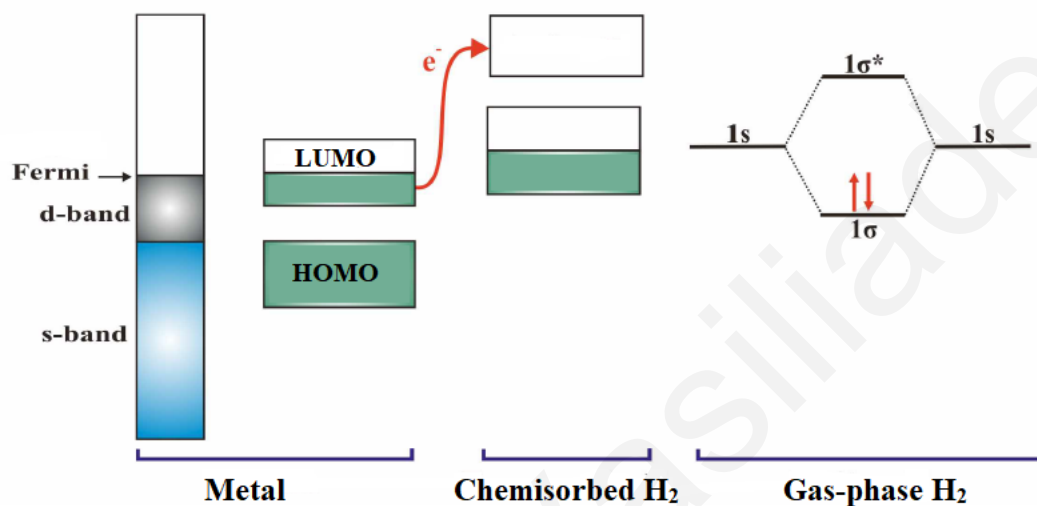


**Figure 2.7:** Electron transfer processes during H<sub>2</sub> chemisorption.

### 2.2.3. Chemisorption of CO<sub>2</sub>

The dissociation of CO<sub>2</sub> over a metal oxide surface is thermodynamically favored, and it could be done over (i) metal cation, (ii) oxygen anion, and (iii) oxygen vacant sites. Molecular adsorption of CO<sub>2</sub> over metal oxides could be achieved under certain conditions and could lead to the formation of (a) carbonate, (b) carboxylate, (c) acid carboxylate, (d) formate and (e) carbonite adsorbed species as depicted in Fig 2.8 [74–76]. All these kinds of chemisorbed carbon dioxide could be identified using the FTIR (or DRIFTS) technique in the range of 1000-1750 cm<sup>-1</sup> [77–79]. This molecular adsorption of CO<sub>2</sub> is mainly due to the interaction of CO<sub>2</sub> with O<sup>n-</sup> of the metal oxide surface, where there is electron transfer from the 2p<sub>z</sub> (HOMO) of O<sup>n-</sup> to the π\*<sub>2p</sub> (LUMO) of CO<sub>2</sub> [80,81].

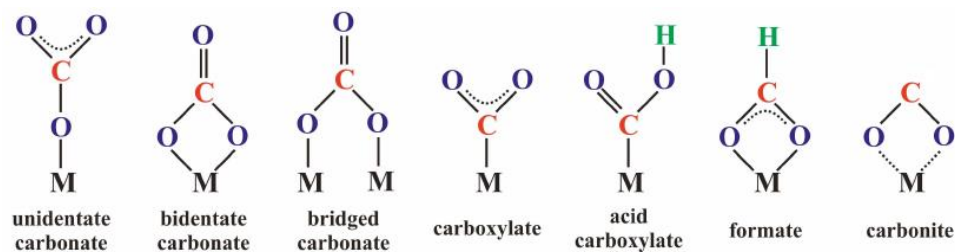


**Figure 2.8:** Molecular chemisorption of CO<sub>2</sub> over metal oxide surfaces [64].

In the opposite side, the dissociative chemisorption derived from the interaction of CO<sub>2</sub> with the metal cations leads to an electron transfer from the oxygen of CO<sub>2</sub> to a free orbital of the metal oxide cation, which further leads to its dissociation and the formation of a bridged CO and atomic oxygen. It should be mentioned that the atomic oxygen can make bonding either with the metal of the surface or it can diffuse and fill in an oxygen vacant site in the mixed metal oxides [80].

### 2.3. Catalysts synthesis

#### 2.3.1. Support synthesis via sol-gel (modified citrate) method

The sol-gel method is used to synthesize high purity powders, starting with the creation of a solution, towards its transformation to a gel, at particularly low temperatures, leading to a better control of stoichiometry homogenization [82]. As well described in the literature [83], this particular synthesis method has drawn the attention of the research community mainly due to its important advantages, such as: (a) the creation of a homogeneous solid solution from the molecular point of view, (b) the creation of high surface meso- and micro-porous solids, and (c) the high dispersion of dopants achieved in the case of doped-mixed metal oxides.

During the sol-gel method, the organic (or inorganic) metal precursors in the form of metal alkoxides M(RO)<sub>x</sub> [84] are dissolved in water (or other organic diluents). Particularly, as shown in Eqs. (2.3) - (2.4), the metal alkoxides are hydrolysed (acidic, basic or neutral) followed by several condensation reactions among the hydroxyl groups. The hydrolysis and condensation steps still occur, while the aging (gel to drying) period is in progress. Both mechanisms occur spontaneously, with several intermediate species present in solution, and these are sensitive on several parameters, such as: amount and type of diluent, amount of acid or base, temperature and time as reported by Hench and West [85].



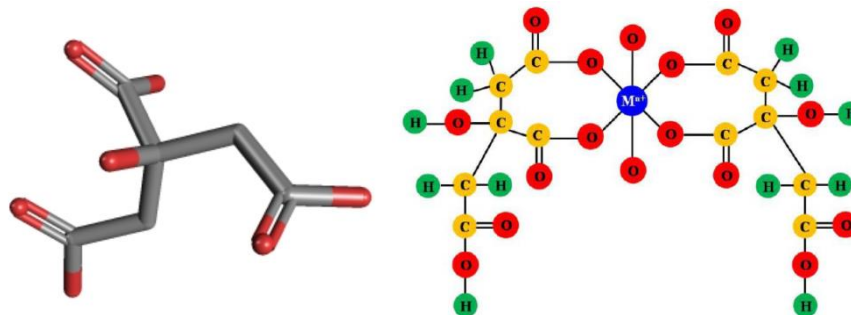
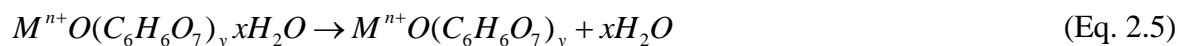


**Figure 2.9:** Citric acid structure (left) and metal-citric acid complex (right).

In the present PhD thesis, the *modified citrate sol-gel* method was used for the preparation of mixed metal oxides, where citric acid (C.A.,  $C_6H_8O_7$ ) was the complexing agent [86]. It has been reported [87,88] that the proportion of complexing agent in relation to the metal is very important for the final structural properties of the solid. In comparison with the traditional sol-gel method, citrate sol-gel method takes less time and requires cheaper metal precursor compounds (e.g., nitrate hydrate) [82], while it yields powders with high purity, surface area and homogeneity [89,90]. Citric acid is described as a strong ligand, having in its molecular structure three carboxyl groups (Fig. 2.9, left). Under acidic conditions (pH  $\sim$  2) these carboxyl groups can form complexes with free metal cations ( $M^{n+}$ ,  $M = Ce^{4+}$ ,  $Zr^{4+}$ ,  $Pr^{3+}$ ) in solution, and prevent the precipitation of the metal ions from solution in the form of metal hydroxides [91–93]. The complex of M-C.A. anion formed (Fig 2.9, right) can be transformed [94–96] towards a metal oxide solid powder form ( $M_xO_{2-\delta}$ ) as follows:

- (i) Dehydration at 180 °C (Eq. (2.5)),
- (ii) Dehydration of citric acid group at 240 °C followed by C.A. decomposition towards carbonaceous species formation in the range of 240 – 460 °C (Eq. (2.6)),
- (iii) Carbonaceous metal species ( $M_xO(CO_3)_y$ ) formation (350 – 550 °C), with in parallel production of CO, CO<sub>2</sub> and H<sub>2</sub>O, and
- (iv) Decomposition of the  $M_xO(CO_3)_y$  (550 – 650 °C) to form  $M_xO_{2-\delta}$ .



### 2.3.2. Supported metal catalysts synthesis - The wet impregnation method

The wet impregnation method was used to impregnate the active metal phase (Ni or NiCo) onto the porous support (CeO<sub>2</sub>-based materials) [83]. It is worth mentioning that H<sub>2</sub>O was used as diluent, since it diffuses faster than the precursor compound, leading to a gradient concentration of the latter, longwise of the spherical support particle [83]. While heating, the latter solution is evaporated and becomes more concentrated with the active metal ions to precipitate and deposit over the surface within the pore system of support, leading to the formation of metal salt particles or metal oxide-type of surface species. To achieve all the above mentioned, several parameters should be considered, and these are related to: (i) the impregnation temperature and time, (ii) the nature of precursor compound, (iii) the diluent and any extra compounds (ligands), and (iv) the *pH* of the solution.

The *pH* value of solution during impregnation plays a very important role and controls the interactions of the active “metal phase” with the surface of the metal oxide support, especially in the case that the diluent is H<sub>2</sub>O. The surface of the metal oxide support consists of M<sup>x+</sup> cations and O<sup>y-</sup> anions, thus, during impregnation of support with the aqueous metal-containing solution, the support is covered with hydroxyl groups as the result of the interactions of the H<sub>2</sub>O with M<sup>x+</sup> and/or the O<sup>y-</sup> according to Eq. (2.7):

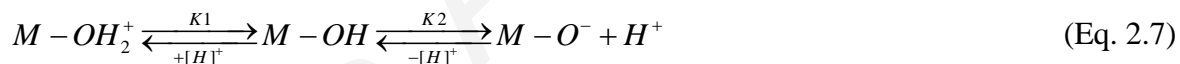
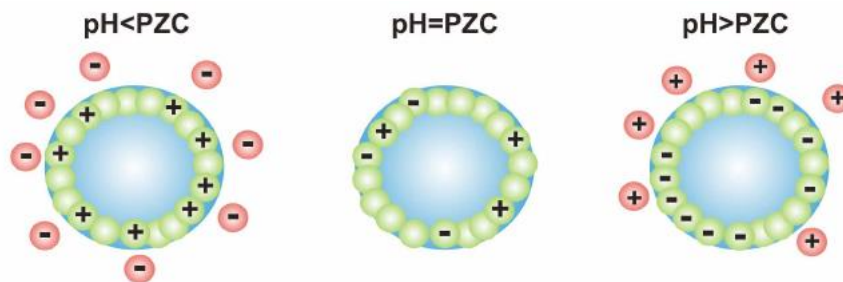


Figure 2.10 illustrates that the support surface is charged, leading to the formation of an electric double layer across the surface of a metal oxide support particle due to the interactions with the aqueous impregnation solution (Eq. (2.7)), which all these are interconnected with the point of zero charge (PZC) of the support metal oxide surface (acidic or basic) [97]. When the *pH* value of the impregnated solution within the pore volume of support is equal to the PZC value, the surface of the support reveals a *neutral* charge. For *pH* values (acid solution) lower than the PZC (basic surface), the surface of the metal oxide support it has a positive charge, whereas when the *pH* value is higher than the PZC, the surface of support has a negative charge. Thus, ions appeared across the metal oxide surface particle are pushed to compensate the charge of the surface in a way to create a neutralization of the system [98].



**Figure 2.10:** Electric double layer of the surface support in contact with the metal impregnation solution [64].

#### 2.4. Diffuse Reflectance Infrared Fourier Transform Spectroscopy (DRIFTS)

DRIFTS is well-applied technique in the field of heterogeneous catalysis which allows the *in situ* characterization (qualitative and semi-quantitative) of the adsorbed species over a catalytic surface by using the infrared (IR) radiation, in the wavenumber range of  $4000 - 400 \text{ cm}^{-1}$  [99,100]. However, the DRIFTS technique has the following limitations among other IR techniques (e.g., transmission mode) [101,102]:

- (i) *DRIFTS cell related*
  - a. Relatively high cost
  - b. Temperature ( $< 900 \text{ }^\circ\text{C}$ )
- (ii) *Catalyst related*
  - a. Porous or granular powder form
  - b. Low adsorption coefficient
  - c. High scattering of IR radiation (dark color sample to be diluted with inert KBr)
- (iii) *Analysis related*
  - a. Quantitative analysis of the absorbed spectrum is not recommended
  - b. Gas phase peaks should be subtracted and removed from the spectrum.

The advantage of the DRIFTS technique among the other IR-based techniques is that the small amount of catalyst used in the DRIFTS cell, which acts as a reactor, does not require any special treatment, and that the spectrum could be received in a very short time ( $< 10 \text{ s}$ ) with the least signal-to-noise (S/N) ratio [103]. As shown in Fig. 2.11, the IR radiation interacts with the catalyst's surface (diffuses within some  $\mu\text{m}$ 's depth in the solid sample bed) in a wide angle

through an ellipsoid window, from which the reflected IR beam is collected from the ellipsoid mirror and analyzed by the MCT detector.

The signal which is collected from the MCT detector is analysed, where the intensity of the IR could be given in Kubelka-Munk (K-M) units on the basis of the corresponding theory (Eqs. (2.8) – (2.10)), which correlates the concentration of the adsorbed species (vibrators) and the intensity. By using K-M units, one is able to compare more reliably adsorbed species between different samples, not only qualitatively but also quantitatively, where these two samples should be of a similar nature and granulation, in a way to have common scattering coefficient ( $s$ ) [104].

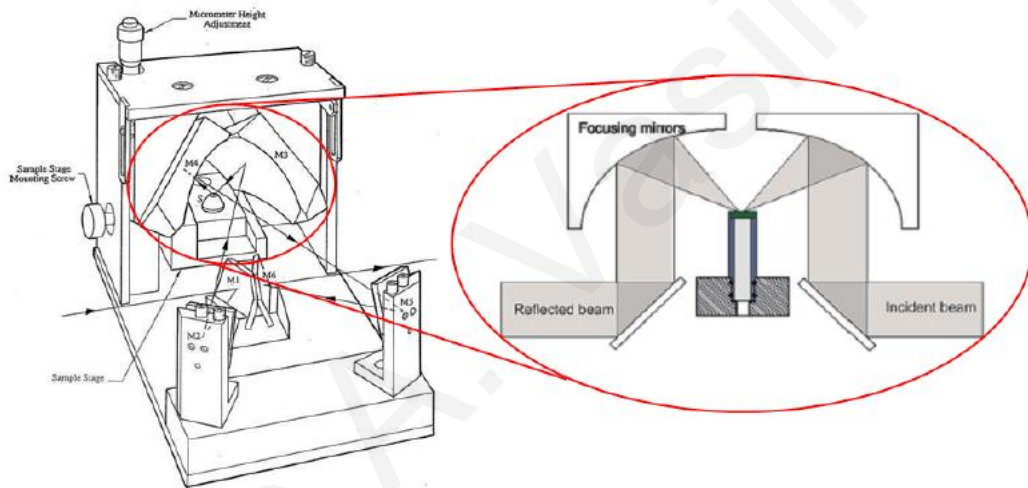


**Figure 2.11:** DRIFTS cell apparatus [105].

$$KM = \frac{(1 - R_{\infty})^2}{R_{\infty}} = \frac{k}{s} \quad (\text{Eq. 2.8})$$

$$k = 2.303ac \quad (\text{Eq. 2.9})$$

$$R_{\infty} = \frac{R_{\text{samp.}}}{R_{\text{ref.}}} \quad (\text{Eq. 2.10})$$

On the basis of the K-M theory,  $R_{\infty}$  refers to the reflectivity of a solid with “infinite” thickness, and is equal to the reflectance of a given sample with regards to the one of the reference sample (inert to IR radiation, KBr),  $k$  is the absorbance coefficient of the solid sample related to the given vibration within the molecular structure of adsorbed species,  $s$  is the

scattering coefficient,  $\alpha$  is the absorptivity of the chemical bond in that species, and  $c$  is the concentration of that species in the solid sample.

## 2.5. Steady State Isotopic Transient Kinetic Analysis – SSITKA

### 2.5.1. Introduction

SSITKA is an *in situ* technique, first proposed by Happel [106], Bennett [107,108] and Biloen [109] based on Tamaru [110] inspiration, which provides in-depth information and correlation between mechanistic and micro-kinetic parameters (i.e. surface concentration of *active* species, rate constants of elementary reaction steps involving the *active* intermediates) of a given heterogeneous catalytic reaction [94,95]. This detailed mechanistic/kinetic information cannot be obtained in a more accurate way by using *steady-state rate analysis data and modeling*. This is because of the further restrictions imposed during modeling of SSITKA data (e.g., surface coverage of reaction intermediates, not measured by steady-state rate measurements, significantly larger amount of data to be fitted in SSITKA compared to the steady-state rate analysis approach, various features of the transient response curves in SSITKA should be fitted, not the case with steady-state catalytic measurements).

During application of the SSITKA experiment, one is able to monitor on-line, under *steady state* reaction conditions, the tracing of a mechanistic path of a reaction followed by the reactants towards products formation over time, after switching (step change) the composition of one of the reactant gases to its equivalent stable chemical isotope (e.g., the step gas switch 5%  $^{12}\text{CO}/10\% \text{H}_2/\text{He} \rightarrow 5\% \text{}^{13}\text{CO}/10\% \text{H}_2/\text{He}$ ). In this particular isotopic gas switch, the rate of the overall surface catalytic reaction does not change, since the partial pressures of reactant components, temperature and space velocity are kept unaffected [108]. Mainly, one records by on line mass spectrometry (30-50 ms acquisition rate/cycle) the transient evolution of the concentration of the isotopic labeled gaseous reactant and product species due to the transient replacement of only the *active* non-labeled with labeled reaction intermediates. In this SSITKA experiment, therefore, no information about the inactive species formed under the non-labeled reactant feed treatment of the catalyst is obtained [111].

Based on the gas-phase transient isotopic response curves recorded and appropriate material balances (see Section 2.6 and Chapter 3), it is able to determine several important kinetic parameters under working catalyst reaction conditions, such as: (i) the concentration ( $N_i$ , mol/g) and the surface coverage ( $\theta_i$ ) of the *active* reaction intermediates, (ii) the mean life time

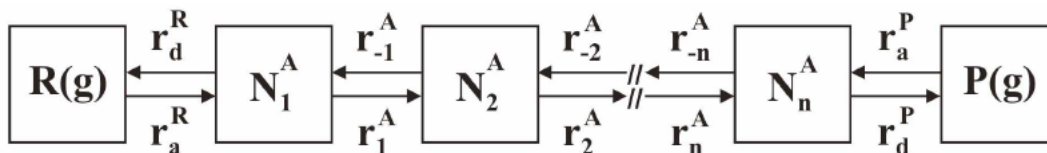
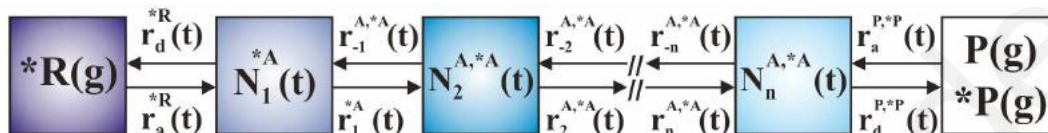


( $\tau_i, s$ ) of the *active* intermediates on the catalytic surface, and (iii) kinetic rate constants ( $k_i$ ) of individual mechanistic reaction steps [112]. These SSITKA results can be highlighted and correlated from results derived by the *operando methodology* using spectroscopic techniques (e.g. DRIFTS and Raman) coupled with mass spectrometry, where it is able to determine the *chemical structure* of the *active and inactive* (spectator) species [113].

### 2.5.2. Mathematical modelling of SSITKA

A nice approach to describe the SSITKA technique was first well described by Happel et al. [90] and later reviewed by Shannon and Goodwin [114] and Efstathiou et al. [98]. In this approach, a reversible catalytic heterogeneous reaction at steady-state (Fig. 2.12) is seen as a series of pools, each pool representing an individual *active* reaction intermediate having a mean life-time on the surface. Two consecutive pools are interconnected reversibly (micro-kinetic reversibility) in order to meet the general case of a reversible reaction. Figure 2.12a shows the series of pools of the *active* reaction intermediate species under steady-state reaction conditions for the reaction  $R(g) \leftrightarrow P(g)$ , where the concentration of each active species is named  $N_i$  ( $\mu\text{mol/g}$ ). Here we follow the reaction path of a given reactant R molecular species to its product molecular species P. The kinetic rate of the reaction ( $r_R, \text{mol R s}^{-1}$ ) at steady state is simply estimated from a material balance for an open once-through reactor. At this condition, a surface coverage (or concentration,  $N_i$ ) for each pool is established based on the governed kinetics, which stays constant with time on stream.

At  $t = 0$ , a step gas change (use of four way valve actuator, see Chapter 3) is performed, where the feed stream with the non-isotopic R reactant gas changes to the equivalent isotopic  $R^*$  one, having kept the same chemical composition (partial pressures) and gas flow-rate [115]. In the case that product P is reversibly adsorbed on the same active sites, the surface coverage of the various active intermediates (Fig. 2.12) includes that of adsorbed P. However, if the product P is re-adsorbed on non-active surface sites, the estimation of the concentration of the active reaction intermediates is overestimated. A typical example of this has been recently demonstrated in the case of water-gas shift reaction over reducible metal oxides-supported Pt catalysts [116].

(a) Steady state conditions,  $t \leq 0$ 

 (b)  $0 < t < \tau_i$ 


**Figure 2.12:** Isotopic distribution of active intermediate pools ( $n$ ), under (a) steady state reaction conditions, (b) after a step gas change in the isotopic composition of reactant  $R$ .

Figure 2.12b depicts the dynamics of replacement of the isotope in reactant  $R^*$  in all associated active intermediates that eventually lead to the formation of the product  $P^*$  when a non-ideal step change to the concentration of  $R^*$  is made. The distribution of the isotope in each individual active reaction intermediate species is related to the steady state kinetic rates ( $r_i/r_{-i}$ ) between the pools as depicted in Fig. 2.12b.

During the SSITKA switch, the transient response of  $P$  should be expected to decrease, while that of  $P^*$  to increase, until the new steady-state is reached ( $r_p = r_{p^*}$ ). At this point, the total rate of product  $P$  at steady-state ( $r_p^{s.s}$ ,  $\text{mol s}^{-1}$ ) should be equal to the sum of the transient rates (at a given time) of  $P$  and  $P^*$  (Eq. (2.11)). For a flow-type reactor,  $r_p^{s.s}$  is given by Eq. (2.12), where  $F_T$  ( $\text{mol s}^{-1}$ ) is the total molecular flow of the product gas mixture at the exit of the reactor. A very similar expression to Eq. (2.12) applies for the  $r_p$  (t).

$$r_p^{s.s} = r_p(t) + r_{p^*}(t) \quad (\text{Eq.2.11})$$

$$r_p^{s.s} = F_T y_p^{s.s} \quad (\text{Eq. 2.12})$$

Based on Eqs. (2.11) - (2.12), it is able to calculate via Eq. (2.13) a normalized transient response ( $Z_P$ ) curve, which at  $t = 0$  (step change) is equal to  $Z_P = 1.0$ , and at  $t \rightarrow t_{s,s}^*$  (new steady state after the isotopic switch) is equal to  $Z_P = 0$ .

$$Z_P(t) = \frac{y_p(t)}{y_p^{s.s}} \quad (\text{Eq. 2.13})$$

During the accurate execution of a SSITKA experiment, in terms of pressure, temperature and flow surges, and in the absence of any kinetic isotopic effects, the transient responses of  $Z_P(t)$  and  $Z_{P^*}(t)$  should behave as mirror images, and are crossing each other at  $Z = 0.5$ . Thus, Eq. (2.14) applies [112]:

$$Z_P(t) + Z_{P^*}(t) = 1.0 \quad (\text{Eq. 2.14})$$

Figure 2.13 shows the transient response curves  $Z_P$  and  $Z_{P^*}$  of the products P and P\*, respectively, as developed during the SSITKA switch, whereas  $Z_I(t)$  refers to the dimensionless response curve of an inert gas (i.e. Kr) present in the non-isotopic feed gas stream. This  $Z_I(t)$  response curve describes the hydrodynamics of the system from the chromatographic switching valve through the tubing and the micro-reactor towards the MS detector [98].

An important kinetic parameter that the SSITKA technique can measure is the *mean life time* ( $\tau$ , s) of *all the active intermediate species* present in the reaction path from the reactant to the given product, and which can be estimated from the transient response curves  $Z_I$  and  $Z_P$  via Eq. (2.15). In a way to examine whether or not the product P readsorbs on the catalyst surface, SSITKA experiments using the same space velocity but different amount of catalyst could be used [114]. In this case, it is possible to account for the readsorption of product P at the external surface sites of the powder particles within the catalyst bed in the micro-reactor, but not within the internal surface sites of the solid particles. This remains a problem in evaluating correctly the concentration of active species leading to the product P if the latter readsorbs to a large extent on non-active catalytic surface sites [116].

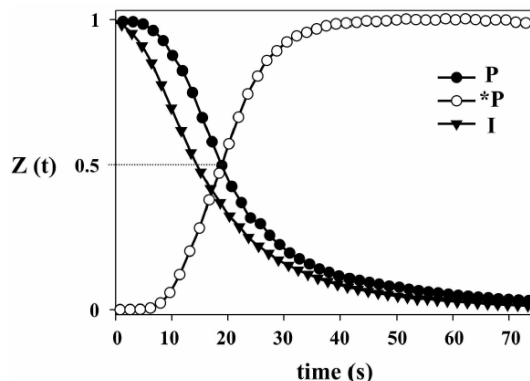


**Figure 2.13:** Normalized transient response curves of the inert gas (I) and the products (P and P\*) derived from the SSITKA switch ( $R \rightarrow R^*$ ).

$$\tau_p(s) = \int_0^{t_{s,s}^*} [Z_p(t) - Z_l(t)] dt \quad (\text{Eq. 2.15})$$

The concentration of the *active* reaction intermediates,  $N_p$  ( $\text{mol g}^{-1}$ ) formed in the reaction path of R towards P (Fig. 2.12) can be estimated using the appropriate material balance and the normalized transient response curves of  $Z_l(t)$  and  $Z_p(t)$ , as shown in Eq. (2.16). It should be pointed out that this estimation does not make use of any kinetic or mechanistic information/modeling of reaction. Furthermore, mathematical simulation of the normalized transient response curves of product P/P\* (see Chapter 6) allows to estimate the concentration of *each individual active reaction intermediate* [117]. The two important kinetic parameters  $N_p$  and  $\tau_p$  are related via Eq. (2.17).

$$N_p(\text{mol g}_{cat}^{-1}) = \frac{F_T y_P^{s,s}}{W} \int_0^{t_{s,s}^*} [Z_p(t) - Z_l(t)] dt \quad (\text{Eq. 2.16})$$

$$R_p = \frac{N_p}{\tau_p} \quad (\text{Eq. 2.17})$$

where,  $R_p$  ( $\text{mols s}^{-1}$ ) refers to the kinetic reaction rate of P formation under steady-state reaction conditions.

Michel Boudart [118] first proposed the term “turnover frequency, TOF” for the catalytic rate, which refers the number of product molecules produced per unit time and per “site” on the catalytic surface at a given temperature and partial pressures of reactants (Eq. 2.18). The “site” here refers to the measured atoms on the whole catalytic surface per gram basis, where for a metal surface this parameter is estimated from selective gas chemisorption measurements [ref]. This is usually referred as the number of catalytic cycles per unit time. Thus, TOF obviously underestimates the real turnover frequency of the reaction since not all the exposed surface atoms could participate in the reaction path, or in other words could accommodate *active* reaction intermediates. The parameter  $\text{TOF}_{\text{ITK}}$  (larger than TOF), refers then to the TOF estimated based on the *number of active reaction intermediates* measured during SSITKA [119] according to Eq. (2.18):

$$TOF_{ITK} = \frac{R_p}{N_p} \quad (\text{Eq. 2.18})$$

This  $TOF_{ITK}$  ( $s^{-1}$ ) is therefore larger than that of TOF (based on the *total* surface atoms exposed to the reaction mixture).

## 2.6. SSITKA Modeling of Methanation Reaction

Soong et al. [120] in their pioneering study of the causes of activity decline in the methanation over Raney nickel catalyst have implemented the steady-state isotopic transient kinetics analysis (SSITKA) technique. Based on the obtained SSITKA response curves, it was inferred that the methanation proceeds via at least two parallel pathways and the relative contribution of the two pathways changes with catalyst aging [120]. It was also concluded that the gradual development of a less reactive carbonaceous overlayer alone is insufficient to explain the observed experimental results and that aging affected the Ni metal catalytic surface itself.

A Raney nickel aluminum-based catalyst (SSA:  $60 \text{ m}^2 \text{ g}^{-1}$ ) was used for the purposes of their study, which was exposed for 320 h under hydrogen-lean syngas conditions ( $\text{H}_2/\text{CO} = 10$ ). The authors considered that methanation proceeds via two carbon-derived surface  $\text{CH}_x$  intermediates with different rate constants ( $k_a$  and  $k_b$ , where  $k_a < k_b$ ) as shown in Fig. 2.14, leading to  $\text{CH}_4$  production but also to a *slow buildup* of graphite.

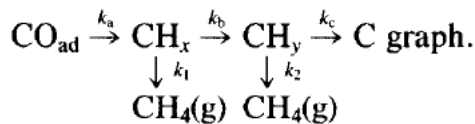


**Figure 2.14:** Reaction methanation sequence over Raney nickel catalysts [120].

SSITKA-MS experiments were performed during the aging of the catalyst, where the feed stream repeatedly changed from  $^{12}\text{CO}/\text{H}_2/\text{Ar}$  to  $^{13}\text{CO}/\text{H}_2$  at  $210 \text{ }^\circ\text{C}$ . During the changes, important kinetic and mechanistic information ( $k$ ,  $\theta$ ) was obtained, where they concluded that the general methanation mechanism (Fig. 2.14) was not the case.

From the  $^{12}\text{CO}$  to  $^{13}\text{CO}$  switch, they observed the well-known chromatographic effect, where the  $^{12}\text{CO}$  response lags behind that of inert gas (Ar), which is due to the reversibly adsorbed ( $^{12}\text{CO}_{\text{ad}}$ ). This behaviour led to the estimation of CO surface coverage ( $\theta$ ), which was

close to one monolayer and increased with aging [120]. Normalized responses (F) of the  $^{12}\text{CH}_4$  and  $^{13}\text{CH}_4$  products are illustrated in Fig. 2.15. Two are the main features should be mentioned: (i) in any case the sum of  $F^{12}\text{CH}_4$  and  $F^{13}\text{CH}_4$  should be equal to 1, and (ii) the two curves are crossing each other at  $F = 0.5$ . It is worthy to mention that during aging, several SSITKA switches were performed, with practically identical features.

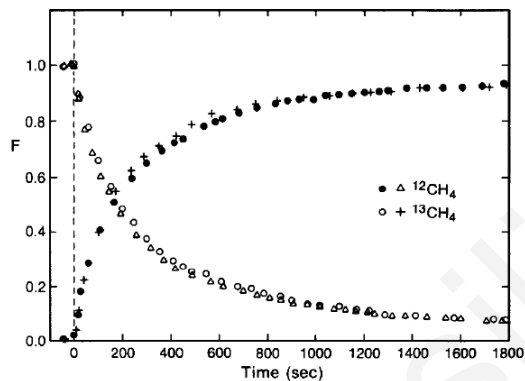


**Figure 2.15:** Normalized transient responses of  $\text{CH}_4$  [120].

Based on the above SSITKA experimental observations, Soong et al. [120] trying to put certain demands on the reaction pathway(s), at first, they have considered a reaction pathway with only one type of intermediate ( $I^*$ ), and considering that all reactant and products contain one carbon atom only, as shown in Eq. (2.19). Here,  $I^*$  is a carbon-derived surface adsorbed intermediate species.



After performing mathematical analysis and considering the appropriate initial condition at  $t = 0$  (is the time when the switch from  $^{12}\text{CO}/\text{H}_2$  to  $^{13}\text{CO}/\text{H}_2$  performed) and that  $t > 0$ , they concluded that both a partially and completely exchanged pool relax with a single relaxation constant ( $\tau$ ), which becomes distinguishable only experimentally. The latter led to the conclusion that at least *two pools* of surface intermediates should participate in the reaction path of methane formation (Fig. 2.16).

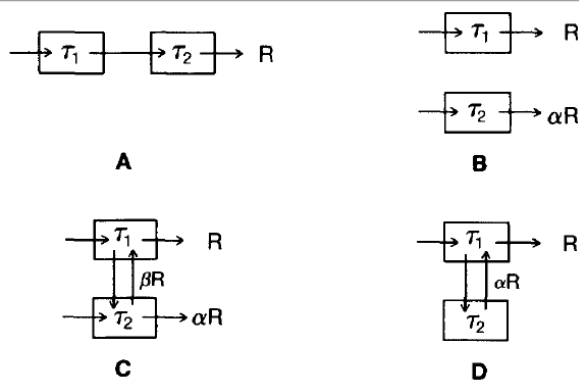


**Figure 2.16:** Different mechanistic pathways of the two pool intermediates [120].

Figure 2.16 shows four different mechanistic models (two-pool model), with the case of Model A to be *two pools in series* and in all other cases (Models B-D) the *two pools are in parallel and/or interconnected*. As reported [120], Model A could not be the case explaining their experimental results. In the cases of Models B-D, they illustrated that pool 1 and pool 2 are independent, and the combined relaxation is practically the sum of the two. To identify which of the three remaining Models (B-D) best describe the observed SSITKA responses, they expanded their mathematical analysis and compared it with the experimental data, considering the relaxation time of the pools during several SSITKA gas switches. By following this analysis, they concluded that Model B could not also simulate their experimental results. Thus, the next step was to consider the two-pool scheme in parallel (rather than in series), such as Model C or D, where analytical solutions of  $F(t)$  as a function of four adjustable parameters were derived. For that reason, instead of Fig. 2.14 and the typical methanation reaction scheme, they considered alternative reaction paths, as shown in Fig. 2.16C and D. This implies that  $\text{CH}_y$  ( $\tau_2$ ), a less reactive carbon, builds up with time, and that lining out is caused by a  $\text{CH}_y$ -removal reaction balancing the  $\text{CH}_y$ -formation reaction, which equilibrates in about 120 h of aging (as of catalytic experiments). Considering these possibilities and the transient SSITKA responses obtained from which they calculated the lifetime of  $\text{CH}_y$  that equilibrates at about 850 s, they ruled out Model C (Fig. 2.16 C) and concluded that Model D (Fig. 2.16 D) simulates better their experimental data.

It should be mentioned at this point that the analytical solutions provided to the various models depicted in Fig. 2.16 [120] consider that the SSITKA isotopic  $^{12}\text{CO}/^{13}\text{CO}$  gas switch is described by an ideal step function. Also, it is considered that that  $\text{CO}(g)$  gas pool exchanges

very fast with CO-s, thus, an almost *step change of CO-s* is introduced in the pools of Models A-D (Fig. 2.16).

In the present doctoral thesis work, methanation reaction over the Co-based SASOL industrial catalysts (see Chapter 6) was modeled based on the work of Soong et al. [120], where the reaction path reflected via the two-pool model (Fig. 2.16) was found to be supported by SSITKA-DRIFTS experimental evidence. More precisely, two kinds of adsorbed CO-s (linear bonded) were identified, and one bridged-type one. Each of the two linearly bonded CO-s provides the  $\text{CH}_x$  ( $\tau_1$ ) and  $\text{CH}_y$  ( $\tau_2$ ) active reaction intermediates. Evidence for this consideration was recently provided in our laboratory, where Petalidou et al. [121] have investigated the kinetics of hydrogenation of the various adsorbed CO-s formed on  $\text{Co}/\gamma\text{-Al}_2\text{O}_3$  by *in situ* DRIFTS. It was concluded that the two linear adsorbed CO-s were significantly more active than the bridged-type CO-s.

### References

- [1] H. Öström, *Chemical Bonding of Hydrocarbons to Metal Surfaces*, Fysikum, 2004.
- [2] C.H. Bartholomew, R.J. Farrauto, in: *Fundam. Ind. Catal. Process.*, John Wiley & Sons, Inc., 2010, pp. 118–196.
- [3] M. VANNICE, *J. Catal.* 56 (1979) 236–248.
- [4] A. Kumar, V. Ramani, *ACS Catal.* 4 (2014) 1516–1525.
- [5] J. Yong, X. Luan, X. Dai, X. Zhang, H. Qiao, Y. Yang, X. Huang, *Catal. Sci. Technol.* 7 (2017) 4206–4215.
- [6] V. E. Henrich and P.A. Cox, *The Surface Science of Metal Oxides*, Cambridge University Press, 1996.
- [7] A. TROVARELLI, *Catal. Rev.* 38 (1996) 439–520.
- [8] H.L. Tuller, *J. Electrochem. Soc.* 126 (1979) 209.
- [9] Z. Zhang, X.E. Verykios, M. Baerns, *Catal. Rev.* 36 (1994) 507–556.
- [10] M.V. Ganduglia-Pirovano, A. Hofmann, J. Sauer, *Surf. Sci. Rep.* 62 (2007) 219–270.
- [11] G. Munuera, A. Fernandez, A.R. Gonzalez-Elipe, in: A. Crucq (Ed.), *Stud. Surf. Sci. Catal.*, Elsevier, 1991, pp. 207–219.
- [12] G. Zangari, *Coatings* 5 (2015) 195–218.
- [13] J. Wang, H. Chen, Z. Hu, M. Yao, Y. Li, *Catal. Rev. - Sci. Eng.* 57 (2015) 79–144.
- [14] M. Boaro, M. Vicario, C. De Leitenburg, G. Dolcetti, A. Trovarelli, *Catal. Today* 77



- (2003) 407–417.
- [15] J. Kašpar, P. Fornasiero, M. Graziani, *Catal. Today* 50 (1999) 285–298.
- [16] Z. Liu, D.C. Grinter, P.G. Lustemberg, T.-D. Nguyen-Phan, Y. Zhou, S. Luo, I. Waluyo, E.J. Crumlin, D.J. Stacchiola, J. Zhou, J. Carrasco, H.F. Busnengo, M.V. Ganduglia-Pirovano, S.D. Senanayake, J.A. Rodriguez, *Angew. Chemie Int. Ed.* 55 (2016) 7455–7459.
- [17] R.K. Herz, in: A. Crucq, A. Frennet (Eds.), *Stud. Surf. Sci. Catal.*, Elsevier, 1987, pp. 427–444.
- [18] R.K. Herz, E.J. Shlnouskls, *Ind. Eng. Chem. Prod. Res. Dev.* 24 (1985) 385–390.
- [19] R.K. Herz, J.A. Sell, *J. Catal.* 94 (1985) 166–174.
- [20] R.K. Herz, J.B. Klela, J.A. Sell, *Ind. Eng. Chem. Prod. Res. Dev.* 22 (1983) 387–396.
- [21] R.K. Herz, *Ind. Eng. Chem. Prod. Res. Dev.* 20 (1981) 451–457.
- [22] M. Pijolat, M. Prin, M. Soustelle, O. Touret, P. Nortier, *J. Chem. Soc. Faraday Trans.* 91 (1995) 3941.
- [23] Y.P. Fu, C.H. Lin, *J. Alloys Compd.* 354 (2003) 232–235.
- [24] A. Bensalem, F. Bozon-Verduraz, M. Delamar, G. Bugli, *Appl. Catal. A, Gen.* 121 (1995) 81–93.
- [25] M. Ozawa, M. Kimura, A. Isogai, *J. Alloys Compd.* 193 (1993) 73–75.
- [26] R. Di Monte, J. Kašpar, *Catal. Today* 100 (2005) 27–35.
- [27] L. Wang, F. Meng, K. Li, F. Lu, *Appl. Surf. Sci.* 286 (2013) 269–274.
- [28] M. Fernández-García, A. Martínez-Arias, J.C. Hanson, J.A. Rodriguez, *Chem. Rev.* 104 (2004) 4063–4104.
- [29] J.P.Y. Tan, H.R. Tan, C. Boothroyd, Y.L. Foo, C. Bin He, M. Lin, *J. Phys. Chem. C* 115 (2011) 3544–3551.
- [30] N. V. Skorodumova, S.I. Simak, B.I. Lundqvist, I.A. Abrikosov, B. Johansson, *Phys. Rev. Lett.* 89 (2002) 166601/1-166601/4.
- [31] A.M. Duarte de Farias, D. Nguyen-Thanh, M.A. Fraga, *Appl. Catal. B Environ.* 93 (2010) 250–258.
- [32] H. Nörenberg, J.H. Harding, *Surf. Sci.* 477 (2001) 17–24.
- [33] K. Reed, A. Cormack, A. Kulkarni, M. Mayton, D. Sayle, F. Klaessig, B. Stadler, *Environ. Sci. Nano* 1 (2014) 390–405.
- [34] A.M. Efstathiou, S.Y. Christou, in: A. Trovarelli, P. Fornasiero (Eds.), *Catal. Sci. Ser.*,

- 2nd ed., Imperial College Press, 2012, pp. 1–84.
- [35] C. Papadopoulou, H. Matralis, X. Verykios, in: L. Guzzi, A. Erd helyi (Eds.), *Catal. Altern. Energy Gener.*, Springer New York, New York, NY, 2012, pp. 57–127.
- [36] A. Wolfbeisser, O. Sophiphun, J. Bernardi, J. Wittayakun, K. F ttinger, G. Rupprechter, *Catal. Today* 277 (2016) 234–245.
- [37] S. Damyanova, B. Pawelec, K. Arishtirova, M.V.M. Huerta, J.L.G. Fierro, *Appl. Catal. B Environ.* 89 (2009) 149–159.
- [38] T. Sukonket, A. Khan, B. Saha, H. Ibrahim, S. Tantayanon, P. Kumar, R. Idem, *Energy and Fuels* 25 (2011) 864–877.
- [39] M.S. Aw, M. Zorko, P. Djinovi c, A. Pintar, *Appl. Catal. B Environ.* 164 (2015) 100–112.
- [40] T. Miki, T. Ogawa, M. Haneda, N. Kakuta, A. Ueno, S. Tateishi, S. Matsuura, M. Sato, *J. Phys. Chem.* 94 (1990) 6464–6467.
- [41] S. Bernal, G. Blanco, M.A. Cauqui, A. Mart n, J.M. Pintado, A. Galtayries, R. Sporken, *Surf. Interface Anal.* 30 (2000) 85–89.
- [42] L. Jiang, S. Fernandez-Garcia, M. Tinoco, Z. Yan, Q. Xue, G. Blanco, J.J. Calvino, A.B. Hungria, X. Chen, *ACS Appl. Mater. Interfaces* 9 (2017) 18595–18608.
- [43] B.M. Reddy, G. Thrimurthulu, L. Katta, Y. Yamada, S.E. Park, *J. Phys. Chem. C* 113 (2009) 15882–15890.
- [44] S. Rossignol, F. G rard, D. Mesnard, C. Kappenstein, D. Duprez, *J. Mater. Chem.* 13 (2003) 3017–3020.
- [45] S. Mahapatra, G. Madras, T.N. Guru Row, *J. Phys. Chem. C* 111 (2007) 6505–6511.
- [46] C.F. Oliveira, F.A.C. Garcia, D.R. Ara jo, J.L. Macedo, S.C.L. Dias, J.A. Dias, *Appl. Catal. A-Gen.* 413–414 (2012) 292–300.
- [47] G.W. Graham, H.W. Jen, W. Chun, R.W. McCabe, *J. Catal.* 182 (1999) 228–233.
- [48] E. Aneggi, C. De Leitenburg, A. Trovarelli, *Catal. Today* 181 (2012) 108–115.
- [49] M. Yashima, K. Morimoto, N. Ishizawa, M. Yoshimura, *J. Am. Ceram. Soc.* 76 (1993) 1745–1750.
- [50] M. Yashima, H. Takashina, M. Kakihana, M. Yoshimura, *J. Am. Ceram. Soc.* 77 (1994) 1869–1874.
- [51] M. Yashima, in: A. Trovarelli, P. Fornasiero (Eds.), *Catal. by Ceria Relat. Mater.*, 2nd ed., Imperial College Press, 2013, pp. 1–45.

- [52] W.J.T. John Meurig Thomas, *Principles and Practice of Heterogeneous Catalysis*, John Wiley & Sons, 1997.
- [53] G. Öhlmann, *Handbook of Heterogeneous Catalysis*, 2nd ed., Wiley-VCH Verlag GmbH, 1999.
- [54] J.T. Yates, *Surf. Sci.* 299–30 (1994) 731–741.
- [55] G. Blyholder, *J. Phys. Chem.* 68 (1964) 2772–2777.
- [56] C.W. Olsen, R.I. Masel, *Surf. Sci.* 201 (1988) 444–460.
- [57] R.R. Cavanagh, J.T. Yates, *J. Chem. Phys.* 74 (1981) 4150–4155.
- [58] R. Monteiro, *Catal. Today* 65 (2001) 77–89.
- [59] A.D. Crowell, *J. Chem. Phys.* 32 (1960) 1576–1577.
- [60] M.M. Baker, E.K. Rideal, *Trans. Faraday Soc.* 51 (1955) 1597.
- [61] J. Bagg, F.C. Tompkins, *Trans. Faraday Soc.* 51 (1955) 1071.
- [62] R.R. Ford, in: D.D. Eley, H. Pines, P.B. Weisz (Eds.), *Academic Press*, 1935, pp. 51–150.
- [63] M. Kappers, C. Dossi, R. Psaro, S. Recchia, A. Fusi, *Catal. Letters* 39 (1996) 183–189.
- [64] C.M. Kalamaras, *Mechanistic and Kinetic Studies of Water-Gas Shift Reaction by Using Operando Methodologies and Transient Isotopic Techniques*, University of Cyprus, 2011.
- [65] K. Christmann, *Surf.~Sci.~Rep.~(Netherlands)~* 9 (1988) 1–163.
- [66] K. Nobuhara, H. Kasai, W.A. Diño, H. Nakanishi, *Surf. Sci.* 566–568 (2004) 703–707.
- [67] S.H. Payne, H.J. Kreuzer, W. Frie, L. Hammer, K. Heinz, *Surf. Sci.* 421 (1999) 279–295.
- [68] U. Bischler, P. Sandl, E. Bertel, T. Brunner, W. Brenig, *Phys. Rev. Lett.* 70 (1993) 3603–3606.
- [69] C. Zupanc, A. Hornung, O. Hinrichsen, M. Muhler, *J. Catal.* 209 (2002) 501–514.
- [70] C.N. Costa, A.M. Efstathiou, *J. Phys. Chem. C* 111 (2007) 3010–3020.
- [71] R.P. Smith, in: G.M. Pajonk, S.J. Teichner, J.E. Germain (Eds.), *Am. Sci.*, Elsevier, 2017, pp. 20–22.
- [72] S.K. Beaumont, S. Alayoglu, C. Specht, N. Kruse, G.A. Somorjai, *Nano Lett.* 14 (2014) 4792–4796.
- [73] B.H. Kim, H.Y. Yu, W.G. Hong, J. Park, S.C. Jung, Y. Nam, H.Y. Jeong, Y.W. Park, Y. Jun, H.J. Kim, *Chem. Asian J.* 7 (2012) 684–7.

- [74] F. Bozon-Verduraz, A. Bensalem, *J. Chem. Soc. Faraday Trans.* 90 (1994) 653.
- [75] E.A. Gordon, M. Lambert, *Surf. Sci.* 288 (1993) 114–118.
- [76] G. Busca, V. Lorenzelli, *Mater. Chem.* 7 (1982) 89–126.
- [77] G. Jacobs, L. Williams, U. Graham, G.A. Thomas, D.E. Sparks, B.H. Davis, *Appl. Catal. A Gen.* 252 (2003) 107–118.
- [78] T. Shido, K. Asakura, Y. Iwasawa, *J. Catal.* 122 (1990) 55–67.
- [79] O. Pozdnyakova, D. Teschner, A. Wootsch, J. Kröhnert, B. Steinhauer, H. Sauer, L. Toth, F.C. Jentoft, Z. Paál, R. Schlögl, *J. Catal.* 237 (2006) 1–16.
- [80] D. Ochs, B. Braun, W. Maus-Friedrichs, V. Kempter, *Surf. Sci.* 417 (1998) 406–414.
- [81] G. Pacchioni, *Surf. Sci.* 281 (1993) 207–219.
- [82] S. Zhuang, Y. Liu, S. Zeng, J. Lv, X. Chen, J. Zhang, *J. Sol-Gel Sci. Technol.* 77 (2016) 109–118.
- [83] J.W. Geus, in: G. Poncelet, P. Grange, P.A. Jacobs (Eds.), *Stud. Surf. Sci. Catal.*, Elsevier, 1983, pp. 1–33.
- [84] C.J. Brinker, G.W. Scherer, in: C.J. Brinker, G.W. Scherer (Eds.), *Sol-Gel Sci.*, Academic Press, San Diego, 1990, pp. 234–301.
- [85] L.L. Hench, J.K. West, *Chem. Rev.* 90 (1990) 33–72.
- [86] K.C. Petallidou, K. Polychronopoulou, S. Boghosian, S. Garcia-Rodriguez, A.M. Efstathiou, *J. Phys. Chem. C* 117 (2013) 25467–25477.
- [87] H.F. Yu, P.C. Liu, *J. Alloys Compd.* 416 (2006) 222–227.
- [88] W.J. Lee, T.T. Fang, *J. Mater. Sci.* 30 (1995) 4349–4354.
- [89] B.J. Hwang, R. Santhanam, D.G. Liu, *J. Power Sources* 97–98 (2001) 443–446.
- [90] Z. Haijun, J. Xiaolin, Y. Yongjie, L. Zhanjie, Y. Daoyuan, L. Zhenzhen, *Mater. Res. Bull.* 39 (2004) 839–850.
- [91] M.-F. Luo, Z.-L. Yan, L.-Y. Jin, M. He, *J. Phys. Chem. B* 110 (2006) 13068–13071.
- [92] Y. Han, S. Li, X. Wang, X. Chen, *Mater. Res. Bull.* 39 (2004) 25–32.
- [93] P. Vaqueiro, M.A. López-Quintela, *Chem. Mater.* 9 (1997) 2836–2841.
- [94] N.S. Gajbhiye, U. Bhattacharya, V.S. Darshane, *Thermochim. Acta* 264 (1995) 219–230.
- [95] S.G. Kim, W.N. Wang, T. Iwaki, A. Yabuki, K. Okuyama, *J. Phys. Chem. C* 111 (2007) 10175–10180.
- [96] M. Rajendran, M.S. Rao, *J. Solid State Chem.* 113 (1994) 239–247.

- [97] D.C. Grahame, *Chem. Rev.* 41 (1947) 441–501.
- [98] D.J. A, L.J. O, *J. Colloid. Interface. Sci.* 67 (1978) 90.
- [99] F.C. Meunier, D. Tibiletti, A. Goguet, R. Burch, *Oil Gas Sci. Technol.* 61 (2006) 497–502.
- [100] T. Armaroli, T. Bécue, S. Gautier, *Oil Gas Sci. Technol.* 59 (2004) 215–237.
- [101] F.C. Meunier, *RSC Adv.* 6 (2016) 17288–17289.
- [102] J. Sirita, S. Phanichphant, F.C. Meunier, *Anal. Chem.* 79 (2007) 3912–3918.
- [103] M.B. Mitchell, in: *Struct. Relations Polym.*, 1993, pp. 351–375.
- [104] M. Che, C.O. Bennett, in: *Adv. Catal.*, 1989, pp. 55–172.
- [105] S.L. Scott, *Spectroscopy in Catalysis: An Introduction*, 3rd ed., Wiley-VCH Verlag GmbH & Co. KGaA, 2008.
- [106] G. Le Cardinal, *Chem. Eng. Sci.* 33 (1978) 1568–1569.
- [107] C.O. BENNETT, in: *Catal. Under Transient Cond.*, 1982, pp. 1–32.
- [108] C.O. Bennett, in: W.O. Haag, B.C. Gates, H. Knözinger (Eds.), *Adv. Catal.*, Academic Press, 1999, pp. 329–416.
- [109] P. Biloen, *J. Mol. Catal.* 21 (1993) 17–24.
- [110] K. Tamaru, in: D.D. Eley, H. Pines, P.B. Weisz (Eds.), *Adv. Catal.*, Academic Press, 1965, pp. 65–90.
- [111] H. Chuan Kang, W.H. Weinberg, *Chem. Rev.* 95 (1995) 667–676.
- [112] A.M. Efstathiou, J.T. Gleaves, G.S. Yablonsky, in: *Charact. Solid Mater. Heterog. Catal. From Struct. to Surf. React. Vol. 1&2*, Wiley-VCH Verlag GmbH & Co. KGaA, 2012, pp. 1013–1073.
- [113] M.A. Bañares, *Catal. Today* 100 (2005) 71–77.
- [114] S.L. Shannon, J.G. Goodwin, *Chem. Rev.* 95 (1995) 677–695.
- [115] A.M. Efstathiou, X.E. Verykios, *Appl. Catal. A Gen.* 151 (1997) 109–166.
- [116] A.M. Efstathiou, in: *Catalysis*, The Royal Society of Chemistry, 2016, pp. 175–236.
- [117] A. EFSTATHIOU, *J. Catal.* 120 (1989) 118–136.
- [118] M. Boudart, G. Djega-Mariadassou, *Kinetics of Heterogeneous Catalytic Reactions*, Princeton University Press, 1984.
- [119] J.G. Goodwin, S. Kim, W.D. Rhodes, in: J.J. Spivey, G.W. Roberts (Eds.), *Catalysis*, The Royal Society of Chemistry, 2007, pp. 320–347.
- [120] Y. Soong, K. Krishna, P. Biloen, *J. Catal.* 97 (1986) 330–343.

[121] K.C. Petallidou, M.A. Vasiliades, A.M. Efstathiou, ACS Catal. (2018).

Michalis A. Vasiliades

---

## Chapter 3: Experimental

### 3.1. Synthesis of catalysts support – Dry Reforming of Methane

#### 3.1.1. $\text{Ce}_{1-x}\text{M}_x\text{O}_{2-\delta}$ ( $\text{M} = \text{Zr}^{4+}, \text{Pr}^{3+}$ ) mixed metal oxides

The  $\text{Ce}_{1-x}\text{M}_x\text{O}_{2-\delta}$  ( $x = 0.0, 0.2, 0.5, 0.65, 0.8, \text{M} = \text{Zr}^{4+}, \text{Pr}^{3+}$ ) mixed metal oxide supports were synthesized using the citrate sol-gel method [1], where citric acid (CA) (Scharlau 99.5%) in the ratio of  $\text{M}:\text{CA} = 1:1.5$  was used as ligand. The metal precursors used were  $\text{Ce}(\text{NO}_3)_3 \cdot 6\text{H}_2\text{O}$ ,  $\text{Pr}(\text{NO}_3)_3 \cdot 6\text{H}_2\text{O}$  and  $\text{ZrO}(\text{NO}_3)_2 \cdot x\text{H}_2\text{O}$  (Sigma-Aldrich 99%), where each of them were dissolved in 50 ml of deionised water. For each solid composition, Ce precursor was mixed with Pr or Zr salt precursor to form a 0.175 M metal ions solution. The pH of solution was kept at the value of 2 after using  $\text{HNO}_3$  (5 M), and subsequently the citric acid was added to the solution. The solution was heated under continuous stirring at 70 °C for 4 h, and a solid in the gel form was finally produced. The resulting material was dried at 120 °C for 17 h, where a spongy material was received. Heating of the material in a furnace (ELF 11/6, Carbolite) from room T to 400 °C in static air (2 °C min<sup>-1</sup>) was then applied, where self-ignition took place at ~ 350 °C. The material was kept at 400 °C for 30 min. After cooling of the sample to room T and grinding, the resulting powder solid was calcined at 500 °C for 6 h (static air, 2 °C min<sup>-1</sup> from room T to 500 °C) and then at 750 °C for additional 4 h.

#### 3.1.2. $\text{Ce}_{0.75}\text{Zr}_{0.25}\text{O}_{2-\delta}$ mixed metal oxides

The  $\text{Ce}_{0.75}\text{Zr}_{0.25}\text{O}_{2-\delta}$  solid support was prepared in collaboration with the group of Dr. Albin Pintar (National Institute of Chemistry, Department of Environmental Sciences, Ljubljana-Slovenia). The former solid support ( $\text{CeO}_2:\text{ZrO}_2 = 80:20$  w/w) was prepared by the ethylene glycol sol-gel method, coded EG. In particular, after 1 g of cerium (III) nitrate hexahydrate (Fluka, p.a.) and zirconium (IV) oxynitrate hydrate (Sigma Aldrich, > 99% purity) in the appropriate ratio were dissolved in 1 mL of ultrapure water and mixed with 1 mL of propionic acid (Merck, > 99% purity) and 30 mL of *ethylene glycol* (EG) (Merck, > 99% purity). The solution was transferred to a PTFE-clad autoclave and aged for 200 min at 180 °C. The precipitated solid was separated from the solution by 15-min centrifugation at 9000 rpm, washed with ultrapure water and ethanol and dried overnight in a laboratory drier at 70 °C. After drying, the material was calcined for 4 h at 400 °C in air (heating ramp of 5 °C min<sup>-1</sup>).

The  $\text{Ce}_{0.75}\text{Zr}_{0.25}\text{O}_{2-\delta}$  ( $\text{Ce}/\text{Zr} = 2.87$ ) solid support was prepared by *two different* methods. During the *hydrothermal method* (coded HT), 4.04 g of  $\text{Ce}(\text{NO}_3)_3 \cdot 6\text{H}_2\text{O}$  (Fluka, p.a.) and 1.1 g  $\text{ZrO}(\text{NO}_3)_2 \cdot 6\text{H}_2\text{O}$  (Sigma Aldrich, > 99% purity) were dissolved in 100 ml of distilled water. The solution was added drop-wise to 250 ml of 25%  $\text{NH}_4\text{OH}$  (Merck, p.a.) under stirring. The produced suspension was transferred to PTFE-lined autoclave and aged for 6 h at 120 °C. The aged product was filtered, washed with distilled water and ethanol and dried overnight in a laboratory drier at 70 °C.

During the *ethylene glycol method* (coded EG), 4.04 g of  $\text{Ce}(\text{NO}_3)_3 \cdot 6\text{H}_2\text{O}$  and 1.1 g of  $\text{ZrO}(\text{NO}_3)_2 \cdot 6\text{H}_2\text{O}$  were dissolved in 5 ml of ultrapure water and mixed with 5 ml of propionic acid (Merck, > 99% purity) and 154 ml of ethylene glycol (Merck, > 99% purity). The solution was transferred to PTFE-clad autoclave and aged for 200 min at 180 °C. The precipitated solid was separated from the solution by 15-min centrifugation at 8950 rpm, washed with distilled water and ethanol and dried overnight in a laboratory drier at 70 °C. After drying, the material was calcined at 400 °C for 4 h in air with a heating ramp of 5 °C  $\text{min}^{-1}$ .

### 3.1.3. Activated $\gamma\text{-Al}_2\text{O}_3$ - Fischer-Tropsch synthesis

In the present work, Sasol's Germany Puralox SCCa  $\gamma$ -alumina support was used as described in the patent (JL 2000 EP 1 299 593 B1). Carbon-coated alumina supports with different carbon layers were prepared via the chemical vapour polymerisation of acetone. More precisely, 5-330 mL of acetone were vaporised by bubbling 600  $\text{mL min}^{-1}$  of Ar at room T. The produced acetone vapour was passed over 70 g of Sasol's activated  $\gamma\text{-Al}_2\text{O}_3$ . The latter was performed at 400 °C in a fluidized bed reactor, where carbon-coated supports were produced with various carbon levels (0, 0.3, 1.5, 5.0, 8.1, 10 mol-%). Activation of the carbon-coated supports was done with 2.5  $\text{ml min}^{-1}$  of air, increase of temperature to 250 °C ( $\beta = 1 \text{ °C min}^{-1}$ ), and held for 10 min before cool-down at 25 °C.

## 3.2. Supported metal catalysts

### 3.2.1. 5% Ni/ $\text{Ce}_{1-x}\text{M}_x\text{O}_{2-\delta}$ ( $\text{M} = \text{Zr}^{4+}, \text{Pr}^{3+}$ )

The 5% Ni-supported catalysts were prepared by using the *wet impregnation* method with controlled pH (~ 9.5) via the use of  $\text{NH}_3$  solution (25 vol%) until the evaporation of the solvent [2,3]. 2.0 g of support were added in 100 mL of distilled water and the solid was impregnated with a given amount of aqueous  $\text{Ni}(\text{NO}_3)_3 \cdot 6\text{H}_2\text{O}$  (Sigma-Aldrich, 99%) so as to



yield a 5 wt.% Ni nominal loading. The aqueous solution was heated at 70 °C for 4 h until total evaporation of water, and the resulting slurry was dried overnight and calcined in static air for 4 h at 750 °C. The fresh catalyst obtained, prior to any catalytic measurements was in situ reduced in H<sub>2</sub> (1 bar, 50 NmL min<sup>-1</sup>) at 700 °C for 2 h.

### 3.2.2. 3 wt.% Ni/Ce<sub>0.75</sub>Zr<sub>0.25</sub>O<sub>2-δ</sub> - EG

The Ce<sub>0.75</sub>Zr<sub>0.25</sub>O<sub>2-δ</sub>-EG supported nickel (3 wt.%) catalyst was prepared using the *homogeneous deposition-precipitation* method [4]. 0.318 g of aqueous Ni(NO<sub>3</sub>)<sub>3</sub>·6H<sub>2</sub>O (Merck, p.a.) was added in 100 mL of ultrapure water, where 2.1 g of CeZrO<sub>2</sub> powder support was mixed with 1.68 g of urea (Merck, p.a.) so as to achieve a yield of 3 wt.% Ni nominal loading.

### 3.2.3. 3 wt.% NiCo/Ce<sub>0.75</sub>Zr<sub>0.25</sub>O<sub>2-δ</sub> - EG/HT

A total amount of 3 wt.% cobalt and nickel metals (1.8 wt.% Co, 1.2 wt.% Ni) was deposited over both supports in an identical manner, namely: 0.129 g of Ni(NO<sub>3</sub>)<sub>2</sub>·6H<sub>2</sub>O (Merck, p.a.), 0.193 g of Co(NO<sub>3</sub>)<sub>2</sub>·6H<sub>2</sub>O (Merck, p.a.), 2.1 g of CeZrO<sub>2</sub> powder and 1.68 g urea (Merck, p.a.) were dispersed in 100 ml of distilled water. One drop of concentrated HNO<sub>3</sub> was added in order to decrease the initial pH value below 3. The suspension was heated in a slow and controlled manner from room T to 90 °C and maintained under reflux for 22 h. Afterwards, the suspension was filtered, washed with ethanol and water and dried overnight in air at 70 °C. The catalysts were calcined at 750 °C for 4 h in air. For simplicity, the two prepared catalysts are named 3NiCo HT and 3NiCo EG, respectively, the supports of which were prepared by the hydrothermal and ethylene glycol sol-gel methods. The fresh catalyst obtained, prior to any catalytic measurements was in situ reduced in H<sub>2</sub> (1 bar, 50 NmL min<sup>-1</sup>) at 700 °C for 2h.

### 3.2.4. 20 wt.% Co with platinum over uncoated and carbon-coated Sasol's γ-Al<sub>2</sub>O<sub>3</sub> for the Fischer-Tropsch Synthesis

The 20% Co with platinum (wt.% Co / wt.% Pt = 400) supported catalysts were prepared by using the slurry phase impregnation method [5] of given amount of aqueous Co(NO<sub>3</sub>)<sub>3</sub>·6H<sub>2</sub>O (Sigma-Aldrich, 99%) over uncoated or carbon-coated alumina support [5]. The resulting slurry was dried under vacuum and calcined in static air at 250 °C. Sequential impregnation and calcination steps were performed in a way to get a 20 wt.% Co nominal loading. The fresh

catalysts obtained, prior to any catalytic measurements were in situ reduced in H<sub>2</sub> (1 bar, 50 NmL min<sup>-1</sup>) at 425 °C.

### 3.3. Physicochemical characterization of catalysts

#### 3.3.1. Specific surface area (BET), pore volume and mean pore size (BJH)

The specific surface area (SSA, m<sup>2</sup> g<sup>-1</sup>), pore volume (cm<sup>3</sup> g<sup>-1</sup>) and mean pore diameter (nm) of the solids (textural properties) were measured by the Brunauer, Emmett, and Teller developed method (BET), in 1938 [6]. The BET method relies on the natural multilayer adsorption of N<sub>2</sub> (inert gas) on the surface of a solid at its boiling temperature (77 K). In the present work, the Micromeritics Gemini III Surface Area and Pore Size Analyzer was used for textural characterization of the solids following an *in-situ* degassing of samples at 300 °C for 4 h in N<sub>2</sub> gas-flow, in order to remove any adsorbed atmospheric H<sub>2</sub>O and most of CO<sub>2</sub>. For the SSA calculation, seven N<sub>2</sub> partial pressures (P/P<sup>0</sup>) in the linear BET range of 0.05-0.35 were applied. The BJH method was then used to estimate the total pore volume and the mean pore diameter based on the adsorption/desorption isotherms, where 40 points in the P/P<sup>0</sup> range of 0.0-1.0 were taken [7].

#### 3.3.2. Powder X-ray Diffraction (PXRD)

The powder X-ray Diffraction (PXRD) technique was applied after using a Shimadzu 6000 Series diffractometer with a CuKα (λ = 1.5418 Å) radiation source, in order to identify crystallite phase(s) and estimate the mean volume size (d<sub>c</sub>, nm) of the primary crystallites of support of a given solid powder catalyst (sieved to less than d<sub>p</sub> = 106 μm) but also that of the metal (Ni, Co) catalytic phase. Powder XRD diffractograms were recorded in the 2θ range of 20-80° with a scan speed of 2° min<sup>-1</sup>. The identification of the derived crystallite phases was done by crosschecking diffractograms available in the JCPDS (Joint Committee on Powder Diffraction Standards) library, but also from various publications with powder XRD results similar to this work's mixed metal oxides.

For the cubic structure pertaining to ceria or ceria-zirconia (pseudo cubic structure), the lattice parameter (a, Å) can be calculated by using Eq. (3.1) and the crystallite volume (V) according to the Equation 3.2.

$$\alpha = d_{hkl} \sqrt{h^2 + k^2 + l^2} \quad (\text{Eq. 3.1})$$

$$V = a^3 \quad (\text{Eq. 3.2})$$

where,  $d_{hkl}$  is the distance between two successive atomic levels and h, k, and l are the Miller indices. In the present case of cubic symmetry,  $\alpha = d_{111} \sqrt{3}$  was calculated by using the crystallite face (111) of pure CeO<sub>2</sub>.

The Scherrer equation (Eq. (3.3)) [8] was used to estimate the mean volume crystallite size of the support metal-oxide single phase and that for the reduced Ni ( $d_c$ , nm) and oxidized cobalt (Co<sub>3</sub>O<sub>4</sub>).

$$\langle d_c \rangle = \frac{K\lambda}{\beta \cos \theta} \quad (\text{Eq. 3.3})$$

where,  $\lambda$  refers to the wavelength of the X-ray irradiation used, K is a constant (~ 0.9, for spherical shape crystallites), which depends on the shape and size distribution of the crystallites,  $\beta$  is the line broadening (rad) of the full width at half maximum (FWHM) intensity of the diffractogram peak ( $\beta_{1/2}$ ), and  $\theta$  is the angle between the incident X-Ray beam and its reflectance on the vertical plane.

According to Equation 3.4 and the particle size of Co<sub>3</sub>O<sub>4</sub>, estimated via Eq. 3.3, the particle size of metallic cobalt was estimated [9].

$$d_{Co} = 0.75d_{Co_3O_4} \quad (\text{Eq. 3.4})$$

The Co dispersion was calculated based on Equation 3.5.

$$D(\%) = \left( \frac{0.96}{d_{Co}} \right) \times 100 \quad (\text{Eq. 3.5})$$

### 3.3.3. Mass Spectrometry (MS)

Mass spectrometry, is a powerful instrumental technique based on Eugen Goldstein in 1886 (and Wilhelm Wien in 1897) [10,11] observation over canal rays in gas discharges under

low pressure, which traveled away from the anode and through channels in a perforated cathode and allows the on-line display and recording of transient responses. This technique separates and detects, based on the mass to charge ratio ( $m/z$ ), the positive ions derived from the collisions of gas phase molecules, diffusing through a heated silica capillary tube and a leak diaphragm (SVI 050, Balzers Instruments) in the ultra-vacuum ion chamber ( $\sim 1 \times 10^{-6} - 5 \times 10^{-7}$  mbar; use of an integrated diaphragmatic and turbomolecular pump), with an electron beam generated by passing an electric current through a W metal filament.

A quadrupole mass spectrometer appears today as the most powerful instrumentation to use in recording the change in composition of a gas stream with real time. It has the ability to record 16 ( $m/z$ ) / sec. In the case of recording 1  $m/z$  only, an acquisition rate every 10 ms (100 data points / sec) is possible with a good S/N ratio. In the present work, an Omnistar Balzers Quadstar 422 (1-200 amu) mass spectrometer coupled with a *quadrupole mass filter* (QMS), and a secondary electron multiplier detector (SEM) was used, and several mass numbers ( $m/z$ ) vs time were able to be recorded and saved for further analysis (Quadstar 32-bit). Calibration of the MS signals ( $\mu\text{A}$ ) to concentrations (mol% or ppm) was performed using certified calibration gas mixtures. Optimisation of the MS peak shape (flat-topped peak) and mass scale alignment in the ion-source of the mass spectrometer was performed regularly by the provided software (Quadstar 422, Omnistar<sup>TM</sup>, Balzers Instruments).

#### **3.3.4. In situ Diffuse Reflectance Infrared Fourier Transform Spectroscopy (in situ DRIFTS)**

In situ DRIFTS used in catalytic science provides information for the *chemical structure* of the different adsorbed species formed on the catalytic surface either under reaction conditions or after chemisorption of the gas of interest [12]. In this specific application, of interest is the *adsorbed phase* established under reaction conditions or chemisorption of a gas alone, and not of the solid catalyst itself. This is accomplished after recording the DRIFT spectrum of the solid under the inert gas atmosphere used in the reaction gas mixture or the chemisorption gas mixture at the temperature of interest. The in-situ DRIFTS technique becomes even more powerful in the field of investigation of heterogeneous catalytic mechanisms (gas/solid interactions), when this is coupled with the SSITKA technique (see Ch. 2, Section 2.5). This combination allows one to differentiate between adsorbed species formed under reaction conditions as being true *active* reaction intermediates or simply inactive or *spectator* species [13,14]. This is based on

the fact that only the active reaction intermediates during the SSITKA switch should provide a red isotopic shift (due to the labeling of an atom in the group of atoms present in the adsorbed species and which are responsible for the given IR vibrational modes. For example, an adsorbed  $^{12}\text{CO}$ -s on a metal surface when is replaced by  $^{13}\text{CO}$ -s, a red isotopic shift in the  $\nu_s$  (C-O) stretching vibrational mode of about  $35\text{ cm}^{-1}$  would take place [15]. However, this expected behavior could be violated in certain cases, if the adsorbed reaction intermediate *is not an active* one but it is *reversibly chemisorbed* on the catalyst surface. In this case the red isotopic shift should also be observed and the interpretation then would be wrong. This scenario has been recently well described [13] in the case of water-gas shift reaction, and reference to other transient isotopic experiments needed to be designed and conducted in order to identify the true active intermediate species was provided. Today's progress in the design of FTIR instruments allow the recording of an averaged IR spectrum with good S/N ratio every about 10 s (use of MCT detector), thus this technique become so important in the field of transient catalysis and kinetics, in general, for gas-solid interactions.

During this PhD thesis work, a Perkin-Elmer Frontier FT-IR spectrometer (256 scans per averaged spectrum recorded) with a resolution of  $4\text{ cm}^{-1}$ , a scanning speed of  $2\text{ cm s}^{-1}$  (MCT detector) and equipped with a high-temperature/high pressure temperature controllable DRIFTS cell reactor (Harrick Scientific, Praying Mantis) with  $\text{CaF}_2$  windows was used. In all cases, a fine powder catalyst ( $\sim 80\text{-}100\text{ mg}$ , depending on the density of the solid and the packing) was placed firmly into the ceramic cup of the DRIFTS cell reactor. Following its pre-treatment (e.g. calcination or reduction), a background/reference spectrum of the solid catalyst was collected under Ar flow at the temperature of interest, prior to any adsorption or reaction step. The spectrum recorded under reaction or adsorption conditions was *subtracted* from the relevant background spectrum. Thus, all the spectra presented in this PhD thesis work represent only the *adsorption phase of the solid* under investigation. Noteworthy to be mentioned that the collected DRIFT spectra ( $400 - 4000\text{ cm}^{-1}$ ) were smoothed to remove possible high frequency noise and further analyzed using Spectrum 10 for Windows software. Below, the necessary information *related to the pretreatment conditions* applied for each of the catalytic systems investigated by the DRIFTS technique (before DRIFT spectra were collected) is described.

- Ni/Ce<sub>1-x</sub>M<sub>x</sub>O<sub>2-δ</sub> catalytic system

The sample was first reduced (30% H<sub>2</sub>/Ar) at 700 °C for 2 h and a reference spectrum was then taken under Ar gas flow at 25 and 550 °C. DRIFT spectra were collected under 5% CO/Ar at 25 °C or 550 °C for the investigation of the structure of adsorbed CO (e.g. linear, bridged or gem-dicarbonyl) and the relative concentration of the kinds of adsorbed CO formed.

- Co-based FT catalytic system (SASOL)

In the case of FT catalyst sample, the latter was taken from the catalytic bed of the passivated catalyst sample (1% O<sub>2</sub>/He gas mixture, 75 cc min<sup>-1</sup> at 35 °C for 2 h), which was previously used in the quartz micro-reactor for conducting SSITKA-MS, TIH and TPH experiments. The sample in a very finely powder form was first diluted with KBr (KBr/sample: 5:1 w/w) before placed in the DRIFTS cell, reduced *in situ* at 450 °C for 2 h (50% H<sub>2</sub>/He gas mixture, 50 cc min<sup>-1</sup>) and then cooled in H<sub>2</sub>/He gas flow to 230 °C. The DRIFTS cell was then purged with Ar at 230 °C for 20 min, and a background spectrum was then recorded in Ar gas flow. Averaged DRIFTS spectra with good S/N ratio were collected every 30 s. DRIFT spectra were recorded before and after the SSITKA switch 5% <sup>12</sup>CO/10% H<sub>2</sub>/Ar (230 °C, 2 h) → 5% <sup>13</sup>CO/10% H<sub>2</sub>/Ar (5 min). It is noted that the KBr used was necessary in order to substantially increase the energy reaching the MCT detector due to the large absorbance of IR by the “black” color of FT solid catalyst.

Deconvolution and curve fitting procedures of IR spectra were performed considering Gaussian peaks. Due to an inherent observed overlapping of the gaseous CO (Q branch, 2116 cm<sup>-1</sup>) with the high-frequency linear adsorbed CO formed on the Ni and cobalt surface at the conditions of the experiments, the following blank experiment was performed in order to estimate the ratio of the band areas of the two gas-phase CO absorption bands (R and Q branches of gas-phase CO), where this information was later used in the deconvolution procedure of the CO-DRIFT spectra. A mixture of 5 vol% CO/Ar was passed through the DRIFTS cell containing only KBr (dry powder) at 230 °C and the spectrum was recorded. The ratio of Area(R)/Area(Q) was found to be 1.46, where R (centered at 2182 cm<sup>-1</sup>) and Q (centered at 2116 cm<sup>-1</sup>) are the IR absorption branches of gas-phase CO. During the deconvolution procedure of the whole IR CO-region (including gas-phase CO), the ratio of Area(R)/Area(Q), the position of maximum absorbance and the FWHM of the two gaseous R and Q bands were kept constant.

Isothermal hydrogenation (TIH) of adsorbed CO-s was performed following Fischer-Tropsch reaction at 230 °C (5% CO/10% H<sub>2</sub>/Ar) for 2 h, followed by an Ar purge (50 cc min<sup>-1</sup>) for 3 min, followed by a 5 vol% H<sub>2</sub>/Ar gas treatment (100 mL min<sup>-1</sup>). The TIH was followed by a temperature hydrogenation (TPH) run at 300, 400, 500 and 600 °C, where after 1 min of reaching the desired temperature a spectrum was recorded. In the case of TIH, spectra were collected at various times in the H<sub>2</sub>/Ar gas flow.

### **3.3.5. Field Emission-Scanning Electron Microscopy (FE-SEM)**

Scanning Electron Microscopy (SEM) is a very well-known technique widely used for the morphological study of the secondary particles (agglomerates) of solid materials. Today's SEM instruments use a Field Emission (FE) gun, called a cold cathode field emitter, in order to create the required electron beam, thus avoiding thermionic emitters for the generation of the electron beam from the filament (e.g. W wire fashioned into a sharp point). In the case of FE-SEM, the emission is reached by placing the filament in a huge electrical potential gradient. Fresh or spent (after DRM or FT reaction) catalysts were investigated by depositing the sample on a conductive carbon tape. The Supra 35 VP (20 kV) field emission scanning electron microscope (Carl Zeiss), based on the National Institute of Chemistry in Slovenia, was used for the FE-SEM measurements of this PhD thesis work.

### **3.3.6. High Resolution Transmission Electron Microscopy-Energy Dispersive X-Ray Analysis (HRTEM-EDX) and High Angle Annular Dark Field-Scanning Transmission Electron Microscopy (HAADF-STEM)**

Transmission Electron Microscopy with atomic resolution coupled with EDX analysis was used for the study of the morphology (3D structural information) and chemical composition of the metal phase (Ni or Co) of the supported metal catalysts. Energy Dispersive X-Ray (EDX) analysis was combined with the HRTEM for elemental chemical analysis in the case of Ni-Co bimetallic supported catalysts in order to examine their homogeneity (solid solution). A JEOL ARM 200 CF scanning transmission electron microscope, equipped with a cold field-emission gun, probe spherical aberration corrector (CESCOR unit from CEOS, Germany) and JEOL Centurio EDXS system with 100 mm<sup>2</sup> SDD detector was used for these studies. Prior to analysis, samples were ultrasonically dispersed in ethanol and deposited on a copper grid covered with carbon film. High-angle annular dark-field scanning transmission electron

microscopy (HAADF-STEM) analysis was also performed. The latter provides direct information on the local chemistry of nano-materials at the atomic scale. HAADF-STEM shows atomic number contrast for high scattering angles of the electrons, owing to predominant electron scattering at the potential of the nucleus similar to Rutherford scattering [16,17]. The characterization of materials by STEM helps to identify microstructures and nanostructures within a sample and to analyse defects in samples. HAADF STEM imaging is capable of resolving atomic structures with better than 2 Å lateral resolution.

The HRTEM-EDX analyses presented in this PhD thesis were performed during collaboration with the Slovenian National Institute of Chemistry (Dr. Albin Pintar research group). Also, for the FT catalysts investigated in this PhD thesis, HRTEM images were taken from SASOL S.A.

### **3.3.7. X-Ray Photoelectron Spectroscopy (XPS)**

The X-ray photoelectron spectroscopy (XPS) was used for the identification of the chemical composition of the surface (0-40 Å from the top atomic layer of the surface) of the solid catalysts and the oxidation state of elements of interest on the surface of solids [18]. XPS analyses were carried out on a PHI-TFA XPS spectrometer (physical Electronics Inc.). Samples were placed on a metallic sample holder and introduced in the ultra-high vacuum chamber of the spectrometer ( $10^{-9}$  mbar). The analyzed area was 0.4 mm in diameter, and the sample surface was excited by X-ray radiation from a monochromatic Al source at 1486.6 eV. The survey wide-energy spectra were taken over the energy range of 0 – 1400 eV with analyzer pass energy of 187 eV in order to perform surface elemental quantitative analysis. High-energy resolution XP spectra were acquired with the energy analyzer operating at a resolution of  $\sim 0.6$  eV and pass energy of 29 eV. During data processing, the spectra were aligned by setting the C 1s peak at 284.8 eV. The accuracy of binding energies reported was  $\pm 0.3$  eV. Quantification of surface composition (at.%) was performed from XP peak intensities taking into account relative sensitivity factors provided by the instrument's manufacturer. XP spectra were analyzed using the Multipak software provided by the instrument (version 8.1, Physical Electronics Inc.). The relative error of the calculated surface concentrations for the supported Ni catalysts investigated is  $\sim 15\%$ . The XPS work was carried out at the National Institute of Chemistry in Slovenia during collaboration with the research group of Dr. Albin Pintar.



### 3.4. Transient experiments for catalyst characterization

#### 3.4.1. H<sub>2</sub> Temperature-Programmed Desorption (H<sub>2</sub>-TPD)

The H<sub>2</sub>-TPD technique reveals important information related to the heterogeneity of a metal catalytic surface in the case of supported metal catalysts [19,20]. For example, different desorption peaks could be associated with different M-H binding states on the metal surface simply due to the different exposed metal faces (e.g. (100) and (111)) or defects (kinks, corners) on the surface of a metal nanoparticle. Also, metal adsorption sites at the metal-support interface could give rise to different electron density on such metal sites, thus leading to different binding energies than metal sites on the surface of the nanoparticle. After considering very carefully the conditions of hydrogen selective chemisorption to avoid the well-known H spill-over effect [21] (diffusion of atomic H from the metal to the support surface), it is possible to estimate good values for the metal dispersion (%), and thus to obtain the mean metal crystallite (particle) size (nm) based on an assumed particle's geometry.

During the present PhD thesis work, the use of the following experimental protocol was applied, and the TPD transient H<sub>2</sub> signal from the micro-reactor was continuously recorded with an on-line mass spectrometer (MS, Balzers, Omnistar 1–200 amu) at  $m/z = 2$ . A calibration gas mixture of 0.3 vol% H<sub>2</sub>/He was used to convert the hydrogen transient response signal into concentration (mol%) vs time response curve.

H<sub>2</sub> (1 bar, 700 °C, 2 h) → He (50 mL min<sup>-1</sup>, 750 °C, 10 min) → cool-down in He flow (25 °C) → He (10 min) → 0.3 vol% H<sub>2</sub>/He (50 mL min<sup>-1</sup>, 25 °C, 30 min) → He (50 mL min<sup>-1</sup>, 10 min) → **TPD run to 750 °C** ( $\beta = 30$  °C min<sup>-1</sup>).

In particular, the following are noted. A 0.5-g sample of the supported 5 wt.% Ni catalyst was introduced into the CSTR quartz micro-reactor [22] and first reduced in H<sub>2</sub> (1 bar) at 700 °C for 2 h. The catalyst was then purged in He flow to 750 °C to remove any hydrogen that might have been spilled over the support (until MS hydrogen signal reached the background value in He), and then cooled in He flow to room temperature. Hydrogen chemisorption was performed at room temperature using a 0.3 vol% H<sub>2</sub>/He gas mixture for 30 min; these conditions minimized hydrogen spillover. Following hydrogen chemisorption step, the catalyst sample was purged in He for 10 min to remove hydrogen from the gas phase of the reactor and the gas lines. The catalyst was then heated to 750 °C in He gas flow (50 NmL min<sup>-1</sup>) with a heating rate of

30 °C min<sup>-1</sup>. Ni metal dispersion (D, %) was estimated from the H<sub>2</sub> desorption peaks associated with desorbed H<sub>2</sub> up to 600 °C, and after assuming an H<sub>2</sub> chemisorption stoichiometry of H/M<sub>s</sub>= 1, where M = Ni. The Ni mean primary particle size,  $d_{Ni}$  (nm), was estimated based on the dispersion measurements (H<sub>2</sub>-TPD) and after applying the following Eq. (3.6) [23]:

$$\langle d_{Ni} \rangle = \frac{0.97}{D(\%)} \times 100 \quad (\text{Eq. 3.6})$$

### 3.4.2. H<sub>2</sub> Temperature-Programmed Reduction (H<sub>2</sub>-TPR)

The H<sub>2</sub>-TPR technique applied over supported metal catalysts provides valuable information related to the reduction of support lattice oxygen, thus the formation of oxygen vacancies, the reduction of support's lattice oxygen at the metal-support interface, and reduction of the metal oxide (supported metal particles). Proper kinetic analysis could provide the energetics of such reduction processes [24]. During the present application of H<sub>2</sub>-TPR over the supported Ni and Co catalysts, the H<sub>2</sub> signal was continuously recorded via the mass spectrometer ( $m/z = 2$ ) and calibrated by a 2 vol% H<sub>2</sub>/He certified gas mixture. By calculating the amount of H<sub>2</sub> consumption and subtracting that due to the full NiO reduction (theoretical case), one can estimate a lower limit for the extent of CeO<sub>2</sub>-based support reduction.

A 5 vol% H<sub>2</sub>/Ar gas was used for the application of TPR over 0.1 g of ceria-based mixed metal oxides (e.g. Ce<sup>4+</sup> → Ce<sup>3+</sup>) supported Ni (5 wt.%) and the following protocol was performed:

10% O<sub>2</sub>/He (50 mL min<sup>-1</sup>, 500 °C, 20 min) → Ar (50 mL min<sup>-1</sup>, 500 °C) → cool-down in Ar flow (50 mL min<sup>-1</sup>, 30 °C, 30 min) → 5% H<sub>2</sub>/Ar (50 mL min<sup>-1</sup>) → **H<sub>2</sub>-TPR run to 750 °C** ( $\beta = 10$  °C min<sup>-1</sup>).

For the FT catalysts (SASOL), H<sub>2</sub>-TPR was performed over 50 mg of sample, whereas the H<sub>2</sub> consumption was measured after using a thermal conductivity detector (TCD), while calibration was done by Ag<sub>2</sub>O powder reduction measurements.

Increase temperature in 20% O<sub>2</sub>/He flow (2500 mL min<sup>-1</sup>, 250 °C,  $\beta = 1$  °C min<sup>-1</sup>) → 20% O<sub>2</sub>/He (10 min) → cool-down in 20% O<sub>2</sub>/He (50 mL min<sup>-1</sup>, 30 °C, 30 min) → Ar (50 mL min<sup>-1</sup>, 30 °C, 30 min) → 10% H<sub>2</sub>/Ar (50 mL min<sup>-1</sup>) → **H<sub>2</sub>-TPR run to 900 °C** ( $\beta = 10$  °C min<sup>-1</sup>).

### 3.4.3. Oxygen Storage Capacity measurements (OSC)

The oxygen storage capacity complete, OSCC ( $\mu\text{mol O g}_{\text{cat}}^{-1}$ ) of the  $\text{Ce}_{1-x}\text{M}_x\text{O}_{2-\delta}$  solid supports was measured using the  $\text{H}_2/\text{O}_2$  pulse injection technique [23], in a specific range of temperatures (600 – 800 °C). The concentration ( $\mu\text{mol O g}_{\text{cat}}^{-1}$ ) of reactive and readily available oxygen species present in the solid (50 mg in powder form; < 106  $\mu\text{m}$  in diameter) was estimated based on the amount of  $\text{O}_2$  consumed during the re-oxidation step by successive oxygen pulses, the number of which is dependent on the size of the pulse and the kinetics of oxygen storage (surface/bulk diffusion) at the given temperature of treatment.

Increase Temperature under 20%  $\text{O}_2/\text{He}$  (50  $\text{mL min}^{-1}$ ,  $T_{\text{OSC}}$  (600-800 °C)) → 20%  $\text{O}_2/\text{He}$  ( $T_{\text{OSC}}$ , 1 h) → He (50  $\text{mL min}^{-1}$ ,  $T_{\text{OSC}}$ , 15 min) →  **$\text{H}_2$  pulses** until no further  $\text{H}_2$  consumption →  **$\text{O}_2$  pulses** until no further  $\text{O}_2$  consumption.

## 3.5. Catalytic performance studies

### 3.5.1. 5% Ni/ $\text{Ce}_{1-x}\text{M}_x\text{O}_{2-\delta}$ (M = $\text{Zr}^{4+}$ , $\text{Pr}^{3+}$ ) - Dry Reforming of Methane

Prior to any catalytic measurements, the solid was reduced in  $\text{H}_2$  (1 bar, 50  $\text{mL min}^{-1}$ ) at 700 °C for 2 h. The reaction feed composition consisted of 20%  $\text{CO}_2/20\%$   $\text{CH}_4/60\%$  He, the total volume flow rate was 150  $\text{mL min}^{-1}$ , and the amount of catalyst used was 0.3 g (catalyst (0.15 g) + SiC (0.15 g); particle size  $0.1 < d_p < 0.3$  mm), resulting in a GHSV of  $\sim 30,000$   $\text{h}^{-1}$  ( $\text{L}/\text{L}_{\text{cat}}/\text{h}$ ). Internal and external mass transport effects were checked (see Section 3.5.4) and found negligible, whereas heat mass transport effects ( $\Delta T$  gradient) within the catalyst bed were minimized due to the presence of SiC. Thus, reaction rates estimated and reported in this PhD thesis work refer to intrinsic kinetic rates of the Dry Reforming of Methane reaction.

The outlet feed gas stream from the reactor was directed to a mass spectrometer (Omnistar 1-300 amu, Balzer) for the on-line monitoring of  $\text{CH}_4$  ( $m/z = 15$ ),  $\text{H}_2$  ( $m/z = 2$ ) and  $\text{C}_2\text{H}_6$  ( $m/z = 30$ ), and to an infrared gas analyzer (Horiba, Model VA-3000) for CO and  $\text{CO}_2$ . The catalytic performance of the Ni/ $\text{Ce}_{1-x}\text{M}_x\text{O}_{2-\delta}$  solids was evaluated in the 550-750 °C range based on the  $\text{CO}_2$  ( $X_{\text{CO}_2}$ , %) and  $\text{CH}_4$  ( $X_{\text{CH}_4}$ , %) conversions, via the following Eqs. (3.7) - (3.8):

$$X_{\text{CO}_2} (\%) = \frac{(F_{\text{CO}_2}^{\text{in}} - F_{\text{CO}_2}^{\text{out}})}{F_{\text{CO}_2}^{\text{in}}} \times 100 \quad (\text{Eq. 3.7})$$

$$X_{\text{CH}_4} (\%) = \frac{(F_{\text{CH}_4}^{\text{in}} - F_{\text{CH}_4}^{\text{out}})}{F_{\text{CH}_4}^{\text{in}}} \times 100 \quad (\text{Eq. 3.8})$$

where,  $F_{CO_2}^{in}$  and  $F_{CH_4}^{in}$  are the molar flow rates (mols  $s^{-1}$ ) of  $CO_2$  and  $CH_4$  at the reactor inlet, respectively, and  $F_{CO_2}^{out}$  and  $F_{CH_4}^{out}$  are the molar flow rates (mols  $s^{-1}$ ) of  $CO_2$  and  $CH_4$  at the reactor outlet, respectively. Calibration of the MS and infrared  $CO/CO_2$  analyzer signals to concentration (mol%) was performed using standard calibration gas mixtures diluted in He gas.

The  $H_2$  and  $CO$  product yield (%) was estimated using Eqs. (3.9) - (3.10):

$$Y_{H_2} (\%) = \frac{F_{H_2}^{out}}{2F_{CH_4}^{in}} \times 100 \quad (\text{Eq. 3.9})$$

$$Y_{CO} (\%) = \frac{F_{CO}^{out}}{F_{CH_4}^{in} + F_{CO_2}^{in}} \times 100 \quad (\text{Eq. 3.10})$$

where,  $F_{H_2}^{out}$  and  $F_{CO}^{out}$  are the molar flow rates (mols  $s^{-1}$ ) of  $H_2$  and  $CO$  at the reactor outlet, respectively. Catalytic measurements were obtained according to the following protocol:

**20%  $CO_2$ /20%  $CH_4$ /60% He** (150 mL  $min^{-1}$ , T (550-750  $^{\circ}C$ , 1 h)  $\rightarrow$  20%  $H_2$ /He (750  $^{\circ}C$ ) until no methane was recorded in the MS  $\rightarrow$  cool-down in 20%  $H_2$ /He flow at the next T  $\rightarrow$  switch to the DRM feed gas stream.

A catalytic experiment using 0.15 g of *pure powder SiC* revealed no activity towards the DRM at the experimental conditions applied. The stability performance of all 5 wt.% Ni/ $Ce_{1-x}Pr_xO_{2-\delta}$  catalysts was examined at 550 and 750  $^{\circ}C$  for 25 h of continuous reaction (time-on-stream, TOS) and for the 5 wt.% Ni/ $Ce_{0.8}Pr_{0.2}O_{2-\delta}$  catalyst for 50 h on TOS.

### 3.5.2. 3 wt.% Ni and NiCo supported on $Ce_{1-x}Zr_xO_{2-\delta}$ - Dry Reforming of Methane

Catalytic tests were performed using a Microactivity Reference reactor system (MA-Ref PID Eng&Tech, Spain) equipped with a tubular quartz reactor (i.d. = 10 mm). Reaction feed stream was comprised of 25 mL  $min^{-1}$   $CH_4$ , 25 mL  $min^{-1}$   $CO_2$  and 6.5 mL  $min^{-1}$   $N_2$  (44.24 vol%  $CH_4$ , 44.24 vol%  $CO_2$ , 11.52 vol%  $N_2$ ). The operating pressure was maintained at  $\sim$ 1.2 bar during catalytic testing. The catalyst bed was comprised of 0.05-g solid, which was fixed between two quartz wool flocks. A K-type thermocouple was positioned inside the catalyst bed for temperature recording. The effluent gas stream from the reactor was fed through a heated

capillary (1/8 in. at 200 °C) to the GC (Agilent Technologies, model 7890A) for a quantitative and qualitative composition analysis. Prior to catalytic tests, the powdered catalyst sample was reduced *in situ* in a 20% H<sub>2</sub>/N<sub>2</sub> gas mixture (50 mL min<sup>-1</sup>) by heating from room T to 750 °C with a 10 °C min<sup>-1</sup> ramp rate, followed by an isothermal step at 750 °C for 1 h. These catalytic performance experiments were conducted in collaboration with the National Institute of Chemistry in Slovenia (research group of Dr. Albin Pintar).

### 3.5.3. Checking for mass transport resistances

A given amount of catalyst used in each catalytic performance experiment was placed in a ceramic mortar for further reduction of its grain size by exerting gentle pressure. It was then sieved, and the fraction of solid with grain particles size ( $d_p$ ) of less than 0.1 mm (100  $\mu$ m) was used. This grain size of powder particles was found suitable for the minimization of internal mass transport resistances according to the suggested experimental testing procedure reported elsewhere [23]. More precisely, the absence of intraparticle (internal) concentration gradients was verified by using two catalyst particle sizes,  $d_p$  (mm). The first one was in the range  $0.1 < d_p < 0.3$  mm and the second particle size was made smaller than 0.1 mm. The reactant conversion was estimated at a constant GHSV (constant volume flow rate). The obtainment of similar conversions for the different sized particles verifies the absence of internal (diffusion) mass transport resistances. The required amount of sieved sample was weighed in a microbalance (ABS 80-4 with 0.0001 g accuracy, KERN & Sohn GmbH) and then loaded in the quartz CSTR micro-reactor.

The absence of interparticle (external) concentration gradients (within the solid bed) was also verified by the testing procedure described in Perego et al. [25]. The linear velocity through the catalytic bed and the solid mass of catalyst sample were varied so as to keep the same gas hourly space velocity (GHSV, h<sup>-1</sup>). The obtainment of similar reactant conversions for the different flow rates verifies the absence of external mass transport resistances.

### 3.6. Characterization of deposited carbonaceous species in DRM – Use of transient methods

#### 3.6.1. Transient Isothermal Hydrogenation (TIH) and Temperature - Programmed Hydrogenation (TPH)

Kinetic features of the interaction of hydrogen with the “carbon” formed after 1 h of DRM and estimation of its deposited amount ( $\mu\text{mol g}^{-1}$ ) were investigated as follows. The fresh catalyst sample (catalyst (0.15 g) + SiC (0.15 g)) was first reduced in  $\text{H}_2$  (1 bar) at  $700\text{ }^\circ\text{C}$  for 2 h and then exposed to the DRM reaction feed stream for 1 h at  $550\text{ }^\circ\text{C}$ . The reactor was then purged in He gas flow for 15 min, and the feed was then switched to 20%  $\text{H}_2/\text{He}$  ( $50\text{ mL min}^{-1}$ ) for 10 min to carry out a transient isothermal hydrogenation (TIH) of the “carbon” formed during DRM. After the end of the 10-min TIH at  $550\text{ }^\circ\text{C}$ , the temperature was increased to  $750\text{ }^\circ\text{C}$  at the heating rate of  $\beta = 30\text{ }^\circ\text{C min}^{-1}$  to carry out a temperature-programmed hydrogenation (TPH) experiment. The mass numbers  $m/z = 2, 15, 18$  and  $30$  were used for  $\text{H}_2, \text{CH}_4, \text{H}_2\text{O}$  and  $\text{C}_2\text{H}_6$ . No ethane signal ( $m/z = 30$ ) was recorded in all hydrogenation experiments conducted. Quantification of the  $\text{CH}_4$  signal was made using a standard calibration gas (0.998%  $\text{CH}_4/\text{He}$ ).

TIH and TPH experiments were also performed over the Ni and NiCo/Ce<sub>1-x</sub>Zr<sub>x</sub>O<sub>2</sub> series of catalysts, following 30-min treatment of the fresh catalyst sample (25 mg) with **20 vol% CH<sub>4</sub>/He** gas mixture at  $750\text{ }^\circ\text{C}$ . More precisely, the following protocol was applied:

$\text{H}_2$  (1 bar,  $750\text{ }^\circ\text{C}$ , 1h)  $\rightarrow$  20%  $\text{CO}_2/20\%$   $\text{CH}_4/60\%$  He ( $100\text{ mL min}^{-1}$ ,  $750\text{ }^\circ\text{C}$ , 1h)  $\rightarrow$  Purge in He flow ( $50\text{ mL min}^{-1}$ ,  $30\text{ }^\circ\text{C}$ )  $\rightarrow$  He (20 min) until  $\text{H}_2, \text{CH}_4, \text{CO}$  and  $\text{CO}_2$  MS signals reached their respective background values  $\rightarrow$  20%  $\text{CH}_4/\text{He}$  ( $100\text{ mL min}^{-1}$ ,  $750\text{ }^\circ\text{C}$ , 30 min)  $\rightarrow$  Purge in He ( $50\text{ cc min}^{-1}$ ,  $750\text{ }^\circ\text{C}$ , 10 min) until no  $\text{CH}_4$  signal was recorded in the MS  $\rightarrow$  cool-down in He flow ( $50\text{ mL min}^{-1}$ ;  $T_{\text{TIH}}$  ( $600, 645, 670$  and  $700\text{ }^\circ\text{C}$ ))  $\rightarrow$  **TIH run with 20%  $\text{H}_2/\text{He}$  at  $T_{\text{TIH}}$  ( $100\text{ mL min}^{-1}$ ).**

In the case of TPH, the catalyst sample after the 30-min CH<sub>4</sub>/He treatment at 750 °C was exposed to the following gas treatments:

20% CH<sub>4</sub>/He (100 mL min<sup>-1</sup>, 750 °C, 30 min) → Purge in He flow (50 mL min<sup>-1</sup>, 750 °C, 10 min) until no CH<sub>4</sub> signal was recorded in the MS → cool-down in He (50 mL min<sup>-1</sup>, 100 °C) → 20% H<sub>2</sub>/He (100 mL min<sup>-1</sup>) → **TPH run to 750 °C** (100 mL min<sup>-1</sup>, β = 10 °C min<sup>-1</sup>) → 20% H<sub>2</sub>/He (TIH) (100 mL min<sup>-1</sup>, 10 min).

During the TIH and TPH characterization of “carbon” experimental procedures, CH<sub>4</sub> (m/z = 15) was continuously monitored in the mass spectrometer (MS) and quantification of the “carbon” hydrogenated to methane was performed using a certified methane gas mixture (ca. 0.998% CH<sub>4</sub>/He). During the transient CH<sub>4</sub> decomposition step, H<sub>2</sub> (m/z = 2), CO (m/z = 28) and CO<sub>2</sub> (m/z = 44) MS signals were continuously monitored and their conversion to mol% composition was made using standard calibration gas mixtures: 2 vol% H<sub>2</sub>/He, 2 vol% CO/He and 985 ppm CO<sub>2</sub>/He, respectively. The signal contribution of CO<sub>2</sub> (m/z = 44) to the m/z = 28 signal was considered in order to quantitatively estimate the concentration of CO (based on m/z = 28).

### 3.6.2. Temperature-Programmed Oxidation (TPO)

The reactivity towards oxygen and the amount (μmol g<sup>-1</sup>) of the “carbon” formed after 1 h, 25 h and 50 h of **dry reforming at 750 °C** were investigated by TPO over a 0.3-g catalyst sample bed without SiC or over a 0.15-g SiC and 0.15-g catalyst sample. The experimental procedure was as follows:

20% CO<sub>2</sub>/20% CH<sub>4</sub>/He (100 mL min<sup>-1</sup>, 750 °C, t (1, 25 or 50 h)) → Purge in He flow (50 mL min<sup>-1</sup>, 750 °C, 20 min) → Increase T in He to 800 °C (50 mL min<sup>-1</sup>) until no CO<sub>2</sub>, CO, H<sub>2</sub> and CH<sub>4</sub> signal were recorded in the MS → cool-down in He flow to 100 °C (100 mL min<sup>-1</sup>) → 10% O<sub>2</sub>/He (100 mL min<sup>-1</sup>) → **TPO run to 800 °C** (100 mL min<sup>-1</sup>, β = 30 °C min<sup>-1</sup>).

The CO (m/z = 28) and CO<sub>2</sub> (m/z = 44) signals in the MS were continuously monitored, and their quantification was made using certified calibration gas mixtures (2 vol% CO and 945 ppm CO<sub>2</sub> in He diluent).

### 3.6.3. TGA-Temperature-Programmed Oxidation (TPO) – CHNS

The amount of “carbon” accumulated on the surface of 5 wt.% Ni/Ce<sub>1-x</sub>Pr<sub>x</sub>O<sub>2-δ</sub> catalysts after 25 h of dry reforming at 750 °C, while using 0.3 g of catalyst (no SiC, same reactor as that used in TPO experiments) was also determined by means of CHNS elemental (Perkin Elmer, model 2400 Series II) and thermogravimetric analysis (TGA) (Perkin Elmer, model STA 6000). Prior to TGA, the sample was dried *in situ* in air flow (50 mL min<sup>-1</sup>) at 80 °C for 30 min. Subsequently, the sample temperature was increased maintaining the same gas flow rate to 900 °C with a heating rate of 10 °C min<sup>-1</sup>. The TGA/TPO analyses were performed in collaboration with the National Institute of Chemistry in Slovenia (research group of Dr. Albin Pintar).

## 3.7. Mechanistic studies - DRM

### 3.7.1. The Contribution of CO<sub>2</sub> and CH<sub>4</sub> activation routes towards the formation of inactive carbon

Temperature-programmed oxidation (TPO), following dry reforming of methane reaction having labelled the carbon of CO<sub>2</sub> in the feed stream (<sup>12</sup>CH<sub>4</sub>/ <sup>13</sup>CO<sub>2</sub>/ He), has been conducted in order to quantify the relative contribution of the CO<sub>2</sub> and CH<sub>4</sub> activation routes towards the formation of inactive “carbon” over the supported Ni and NiCo DRM catalysts (0.5 g sample) investigated. The experimental procedure was as follows:

5% <sup>12</sup>CO<sub>2</sub>/5% <sup>12</sup>CH<sub>4</sub>/45% Ar/45% He (50 or 100 mL min<sup>-1</sup>, T (550 or 750 °C), 30 min) → purge in He flow (50 mL min<sup>-1</sup>, 10 min) → increase T in He flow to 800 °C until background values were reached for the CO and CO<sub>2</sub> MS signals → cool-down in He to 100 °C → 10% O<sub>2</sub>/He (50 mL min<sup>-1</sup>, 230 °C, 7 min) → **TPO run to 800 °C** (50 mL min<sup>-1</sup>, β = 30 °C min<sup>-1</sup>).

The mass numbers (m/z) 2 (H<sub>2</sub>), 28 (<sup>12</sup>CO), 29 (<sup>13</sup>CO), 44 (<sup>12</sup>CO<sub>2</sub>) and 45 (<sup>13</sup>CO<sub>2</sub>) in the mass spectrometer were continuously monitored. The amount (μmol g<sup>-1</sup>) of “carbon” derived from the CO<sub>2</sub> molecular species (CO<sub>2</sub> activation route) were estimated after integrating the <sup>13</sup>CO- and <sup>13</sup>CO<sub>2</sub>-TPO traces, while that derived from the CH<sub>4</sub> molecular species (CH<sub>4</sub> activation route) after integrating the <sup>12</sup>CO- and <sup>12</sup>CO<sub>2</sub>-TPO traces. It should be mentioned that the “carbon” estimated by the TPO experiment includes both the *inactive* and *active* “carbon” formed during DRM, the latter estimated by the SSITKA experiment (see Section 3.7.4) but for the CO<sub>2</sub> activation route only.



In order to further investigate the chemical steps responsible for the deposition of inactive “carbon” during DRM reaction, the following experiment was conducted *for the first time*, to our knowledge, over 0.5 g of catalyst:

5%  $^{13}\text{CO}$ /5%  $^{12}\text{CH}_4$ /45% Ar/45% He (100 mL min<sup>-1</sup>, 750 °C, 30 min) → Purge in He flow (50 mL min<sup>-1</sup>, 10 min) → increase T under He to 800 °C until background values were reached for the CO and CO<sub>2</sub> MS signals → cool-down in He to 100 °C → 10% O<sub>2</sub>/He (50 mL min<sup>-1</sup>, 230 °C, 7 min) → **TPO run to 800 °C** (50 mL min<sup>-1</sup>, β = 30 °C min<sup>-1</sup>).

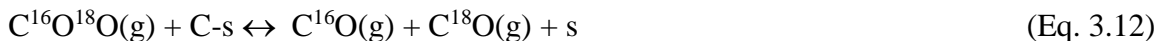
Analysis of the effluent gas stream in the MS during TPO was made in a similar manner as mentioned in the previous Section 3.6.2. During the  $^{13}\text{CO}/^{12}\text{CH}_4/\text{Ar}/\text{He}$  gas treatment, the transient evolution of H<sub>2</sub> (m/z = 2),  $^{12}\text{CO}$  (m/z = 28),  $^{12}\text{CO}_2$  (m/z = 44) and  $^{13}\text{CO}_2$  (m/z = 45) were recorded continuously with mass spectrometry.

### 3.7.2. Probing the participation of support lattice oxygen in the carbon path

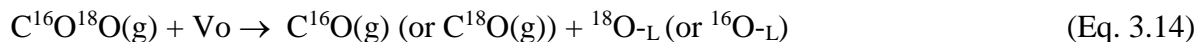
The participation of support lattice oxygen in the carbon pathway of the DRM reaction was probed after performing partial exchange of lattice  $^{16}\text{O}$  with  $^{18}\text{O}$  at 750 °C followed by DRM. The formation of C<sup>18</sup>O(g) might be an indication of the participation of lattice  $^{18}\text{O}$  present in the catalyst via the reaction of surface carbon, “C-s”, the latter derived from both the CH<sub>4</sub> and CO<sub>2</sub> activation routes, as also previously presented in Ch. 2, Section 2.2.



where, s is a catalytic site at the metal-support interface, the support or both,  $^{18}\text{O-L}$  is a lattice  $^{18}\text{O}$  and Vo is an oxygen vacancy of support. However, the possibility of C<sup>16</sup>O<sub>2</sub>(g) (present in the DRM feed stream) for an exchange of its oxygen(s) with surface  $^{18}\text{O-L}$  forming C<sup>16</sup>O<sup>18</sup>O(g) and C<sup>18</sup>O<sub>2</sub>(g) and the formation of C<sup>18</sup>O by the following reaction steps (3.12) - (3.14) should be examined:



Formation of  $C^{18}O(g)$  might also proceed via the dissociation of  $C^{16}O^{18}O(g)$  or  $C^{18}O_2(g)$  on an oxygen vacant site (Vo) of support [26,27]:



In order to correctly interpret the transient evolution of  $C^{18}O(g)$  upon the switch to the DRM reaction gas mixture (20%CH<sub>4</sub>/20%CO<sub>2</sub>/He) at 750 °C, the following gas switches after the <sup>16</sup>O/<sup>18</sup>O isotopic exchange at 750 °C were performed: (i) 20% CH<sub>4</sub>/He, (ii) 20% CO<sub>2</sub>/He or (iii) x% /He; x is the value of steady-state CO concentration formed under 20% CH<sub>4</sub>/20% CO<sub>2</sub>/He gas treatment of the catalyst. Based on several features of the transient response curves of  $C^{18}O(g)$ ,  $C^{16}O^{18}O(g)$  and  $C^{18}O_2(g)$ , such as time delays, peak maximum appearance ( $t_{\max}$ , s) and its shape, and estimation of the amount of <sup>18</sup>O ( $\mu\text{mol g}^{-1}$ ) incorporated in these species, it is possible to justify whether part of  $C^{18}O(g)$  is produced, as will be illustrated in Chapters 4 and 5.

The NiCo/Ce<sub>0.75</sub>Zr<sub>0.25</sub>O<sub>2-δ</sub> fresh catalyst samples (25 mg) were first reduced in 20% H<sub>2</sub>/He at 750 °C for 1 h and then purged in He flow until the H<sub>2</sub> ( $m/z = 2$ ), <sup>16</sup>O<sub>2</sub> ( $m/z = 32$ ) and <sup>16</sup>O<sup>18</sup>O ( $m/z = 34$ ) MS signals reached their respective background values. The catalyst was then exposed to 2% <sup>18</sup>O<sub>2</sub>/1%Kr/He gas mixture at 750 °C for 10 min during which exchange of <sup>16</sup>O-lattice oxygen of support and oxidation of Ni/NiO to Ni<sup>18</sup>O with <sup>18</sup>O<sub>2</sub>(g) took place. The signals of <sup>16</sup>O<sub>2</sub> ( $m/z = 32$ ), <sup>16</sup>O<sup>18</sup>O ( $m/z = 34$ ), <sup>18</sup>O<sub>2</sub> ( $m/z = 36$ ) and Kr ( $m/z = 84$ ) were recorded continuously with on line mass spectrometer (MS).

The amount of oxygen exchanged ( $\mu\text{mol } {}^{16}O \text{ g}^{-1}$ ) was estimated from the <sup>16</sup>O<sub>2</sub>(g) and <sup>16</sup>O<sup>18</sup>O(g) transient response curves (up to 10 min) after calibration of the  $m/z = 32$  and 34 signals in the mass spectrometer and the use of appropriate material balances. The 10-min treatment of the catalyst with <sup>18</sup>O<sub>2</sub>(g) was followed by a 10-min He purge at 750 °C before the switch to each of the three gas streams (i)-(iii) indicated above.

Calibration of the  $C^{18}O_2$  ( $m/z = 48$ ) and  $C^{16}O^{18}O$  ( $m/z = 46$ ) MS signals was made based on the natural abundance of <sup>18</sup>O in a certified 54.3% CO<sub>2</sub>/He gas mixture. Furthermore, contributions of  $C^{18}O_2$  ( $m/z = 48$ ) and  $C^{16}O^{18}O$  ( $m/z = 46$ ) to the  $m/z = 30$  ( $C^{18}O$ ) MS signals were estimated using a standard  $C^{16}O_2$ /He gas mixture and after considering the same contribution of  $m/z = 44$  to  $m/z = 28$  (CO<sub>2</sub>) for the  $m/z = 48$  to  $m/z = 30$  ( $C^{18}O_2$ ) and  $m/z = 46$  to  $m/z = 30$  ( $C^{16}O^{18}O$ ). Calibration of the  $C^{18}O$  ( $m/z = 30$ ) signal to concentration (mol%) was

made after considering a standard  $C^{16}O/He$  gas mixture (use of  $m/z = 28$  signal) and assuming similar sensitivities for the  $C^{16}O$  ( $m/z = 28$ ) and  $C^{18}O$  ( $m/z = 30$ ) gases.

### 3.7.3. Probing the gasification of carbon by $CO_2$ ( $C-s + CO_2 \leftrightarrow 2CO + s$ )

In order to probe the formation of  $CO(g)$  via gasification of carbon (“C-s”) by the  $CO_2$  reactant (reverse Boudouard reaction), the following gas switches were designed and performed at  $750\text{ }^\circ\text{C}$  over a fresh 0.05-g catalyst sample:

5%  $^{12}CO_2/5\%$   $^{12}CH_4/45\%$  Ar/45% He ( $100\text{ mL min}^{-1}$ ,  $750\text{ }^\circ\text{C}$ , 30 min)  $\rightarrow$  Purge in He flow ( $50\text{ mL min}^{-1}$ , 10 min) until background signals of  $^{12}CO$  ( $m/z = 28$ ),  $^{13}CO$  ( $m/z = 29$ ) and  $^{13}CO_2$  ( $m/z = 45$ ) are obtained  $\rightarrow$  **5%  $^{13}CO_2/1\%$  Kr/Ar/He** ( $100\text{ mL min}^{-1}$ ,  $750\text{ }^\circ\text{C}$ , t).

During the last gas switch, the  $^{12}CO$ ,  $^{13}CO$ ,  $^{13}CO_2$  and Kr signals were continuously monitored by on line MS. Conversion of  $^{12}CO$ ,  $^{13}CO$  and  $^{13}CO_2$  signals to concentrations (mol %) was made by using certified gas mixtures (2 vol%  $^{12}CO/He$ , 10 vol%  $^{13}CO/Ar$  and 10 vol%  $^{13}CO_2/Ar$ ). The amounts ( $\mu\text{mol g}^{-1}$ ) of  $^{12}CO$  and  $^{13}CO$  obtained at the switch to 5%  $^{13}CO_2/Kr/He$  were estimated using the concentration versus time response curves and the appropriate material balances for a flow-reactor.

### 3.7.4. SSITKA studies – Tracing the carbon path of $CO_2$ activation

Steady-state isotopic transient kinetic analysis (SSITKA) experiments using  $^{13}CO_2$  in the DRM feed gas stream (5%  $^{13}CO_2/5\%$   $^{12}CH_4/45\%$  Ar/45% He;  $100\text{ mL min}^{-1}$ ) were conducted over the fresh 5 wt.% Ni/Ce<sub>1-x</sub>Pr<sub>x</sub>O<sub>2- $\delta$</sub>  and 3 wt.% NiCo/Ce<sub>0.75</sub>Zr<sub>0.25</sub>O<sub>2- $\delta$</sub>  catalyst samples at low  $CH_4$  conversions at  $550\text{ }^\circ\text{C}$  (lower than 15%,  $W_{\text{cat}} = 0.1\text{ g}$ ) and at high  $CH_4$  conversions at  $750\text{ }^\circ\text{C}$  (integral reaction conditions,  $W_{\text{cat}} = 0.03\text{ g}$ ), in order to trace the carbon path of the  $CO_2$  activation route. After 30 min and 2 h of DRM, the following SSITKA switches were performed:

5%  $^{12}CO_2/5\%$   $^{12}CH_4/45\%$  Ar/45% He ( $100\text{ mL min}^{-1}$ ,  $750\text{ }^\circ\text{C}$ , 30 min)  $\rightarrow$  5%  $^{13}CO_2/5\%$   $^{12}CH_4/2\%$  Kr/43% Ar/45% He ( $100\text{ mL min}^{-1}$ ,  $750\text{ }^\circ\text{C}$ , 10 min)  $\rightarrow$  **5%  $^{12}CO_2/5\%$   $^{12}CH_4/45\%$  Ar/45% He** ( $100\text{ mL min}^{-1}$ ,  $750\text{ }^\circ\text{C}$ , 90 min)  $\rightarrow$  5%  $^{13}CO_2/5\%$   $^{12}CH_4/2\%$  Kr/43% Ar/45% He ( $100\text{ mL min}^{-1}$ ,  $750\text{ }^\circ\text{C}$ , 10 min)  $\rightarrow$  **5%  $^{12}CO_2/5\%$   $^{12}CH_4/45\%$  Ar/45% He** ( $100\text{ mL min}^{-1}$ ,  $750\text{ }^\circ\text{C}$ , t)

During the gas switch from the isotopic to the non-isotopic DRM feed gas stream, the decay of  $^{13}\text{CO}$  ( $m/z = 29$ ),  $^{13}\text{CO}_2$  ( $m/z = 45$ ) and Kr ( $m/z = 84$ ) signals were continuously monitored by on line mass spectrometer. Quantification of the *concentration of active carbon-containing* reaction intermediates over  $\text{NiCo/Ce}_{0.7}\text{Zr}_{0.25}\text{O}_2$ ,  $N_C$  ( $\mu\text{mol g}^{-1}$ ) present in the carbon path from the  $\text{CO}_2$  reactant to the  $\text{CO}$  gas product was estimated based on the following material balance Eq. (3.15):

$$N_C (\text{mol g}_{\text{cat}}^{-1}) = \frac{F_T y_{^{13}\text{CO}}^{s,s}}{W} \int_0^{t_f} [Z_{^{13}\text{CO}}(t) - Z_{\text{Kr}}(t)] dt \quad (\text{Eq. 3.15})$$

where  $F_T$  is the total molar flow rate ( $\text{mol s}^{-1}$ ) of the  $^{13}\text{CO}_2/^{12}\text{CH}_4/\text{Kr}/\text{Ar}/\text{He}$  feed gas stream and  $y_{^{13}\text{CO}}$  (s.s.) is the mole fraction of  $^{13}\text{CO}(\text{g})$  formed at steady-state in the  $^{13}\text{CO}_2/^{12}\text{CH}_4/\text{Kr}/\text{Ar}/\text{He}$  feed gas stream.  $Z_{^{13}\text{CO}}$  and  $Z_{\text{Kr}}$  are the dimensionless concentrations of  $^{13}\text{CO}(\text{g})$  and Kr tracer gas [28];  $t = 0$  is the time that the Kr signal at the switch  $^{13}\text{CO}_2/^{12}\text{CH}_4/\text{Kr}/\text{Ar}/\text{He} \rightarrow ^{12}\text{CO}_2/^{12}\text{CH}_4/\text{Ar}/\text{He}$  starts to decay, whereas  $t^f$  is the final time at which the new steady-state under the non-isotopic feed is obtained. It should be pointed out that  $N_C$  according to Eq. (3.15) includes any *adsorbed  $\text{CO}_2$ -s that truly participates in the carbon-path of  $\text{CO}$  formation* via the  $\text{CO}_2$  activation route.

According to the SSITKA theory and its interconnected pools formalism (see Ch. 2, Section 2.5), it is expected that the gaseous  $\text{CO}_2$  pool (reactant) forming first an active  $\text{CO}_2$ -s pool which feeds with “carbon” the following pools (in series) of active reaction intermediates, responsible for the formation of  $\text{CO}(\text{g})$  product, should produce a transient  $^{13}\text{CO}(\text{g})$  response upon the switch  $^{13}\text{CO}_2/^{12}\text{CH}_4 \rightarrow ^{12}\text{CO}_2/^{12}\text{CH}_4$  lagging behind that of  $^{13}\text{CO}_2(\text{g})$ . In the opposite case, (e.g.  $\text{Ni/Ce}_{1-x}\text{Pr}_x\text{O}_{2-\delta}$ ), when the  $^{13}\text{CO}_2(\text{g})$  transient curve lags behind that of  $^{13}\text{CO}(\text{g})$ , this difference is likely to be associated with the fact that another pool of reversibly adsorbed  $\text{CO}_2$ -s exists on the catalyst surface which does not participate in the formation of  $\text{CO}(\text{g})$ . The concentration ( $\mu\text{mol g}^{-1}$ ) of such *inactive reversibly adsorbed  $\text{CO}_2$*  formed on the catalyst surface under dry reforming can be estimated via the following material balance Eq. (3.16):

$$N_C (\text{mol g}_{\text{cat}}^{-1}) = \frac{F_T y_{^{13}\text{CO}}^{s,s}}{W} \int_0^{t_f} [Z_{^{13}\text{CO}}(t) - Z_{^{13}\text{CO}_2}(t)] dt \quad (\text{Eq. 3.16})$$

where,  $Z_{^{13}\text{CO}_2}$  is the dimensionless concentration of gaseous  $^{13}\text{CO}_2$ .

In the case of Ni/Ce<sub>1-x</sub>Pr<sub>x</sub>O<sub>2-δ</sub> catalysts, it is possible to estimate the amount (mol g<sub>cat</sub><sup>-1</sup>) of reversibly adsorbed CO<sub>2</sub> formed on the catalyst surface (e.g., CO<sub>2</sub> - s<sub>1</sub> (Ni) and/or CO<sub>3</sub><sup>2-</sup> - s<sub>2</sub> (support)) under dry reforming, which is considered as *spectator (inactive) species* after using the following relationship (Eq. (3.17)):

$$N_{CO_2} (\text{mol g}_{cat}^{-1}) = \frac{F_T y_{13CO_2}^{s,s} (1 - X_{13CO_2})}{W} \int_0^{t_f} [Z_{13CO_2}(t) - Z_{Kr}(t)] dt \quad (\text{Eq. 3.17})$$

where,  $y_{13CO_2}^f$  and  $X_{13CO_2}$  are the mole fraction of <sup>13</sup>CO<sub>2</sub> in the isotopic feed gas stream and the steady-state <sup>13</sup>CO<sub>2</sub> conversion, respectively.  $Z_{Kr}$  is the dimensionless concentration of Kr tracer gas; s<sub>1</sub> and s<sub>2</sub> represent catalytic sites on the nickel and metal oxide support surfaces, respectively.

The average residence time of the active carbon-containing species (C-pool) present in the CO<sub>2</sub> activation path to form CO,  $\tau_C$  (s), is calculated as the area between the normalized transient response curve of <sup>13</sup>CO(g) and that of <sup>13</sup>CO<sub>2</sub>(g) in the down-step SSITKA switch <sup>13</sup>CO<sub>2</sub>/<sup>12</sup>CH<sub>4</sub>/Ar/Kr/He → <sup>12</sup>CO<sub>2</sub>/<sup>12</sup>CH<sub>4</sub>/Ar/He, after using the following relationship (Eq. (3.18)):

$$\tau_C (s) = \int_0^{t_f} [Z_{13CO}(t) - Z_{13CO_2}(t)] dt \quad (\text{Eq. 3.18})$$

Based on the SSITKA theory and its formalism (see Ch. 2, Section 2.5), the specific kinetic rate of reaction (mol g<sub>cat</sub><sup>-1</sup> s<sup>-1</sup>) at steady-state is related to the TOF<sub>TK</sub> (s<sup>-1</sup>) by the following relationship (Eq. (3.19)):

$$\text{Rate}(\mu\text{mol g}^{-1} \text{ s}^{-1}) = \text{TOF}_{TK} N_C = N_C \left( \frac{1}{\tau_C} \right) \quad (\text{Eq. 3.19})$$

where  $N_C$  is the concentration (μmol g<sup>-1</sup>) of *active reaction intermediates* found in the carbon-path probed, and which is estimated according to Eq. (3.15).

### 3.8. Mechanistic studies – Fischer-Tropsch (Methanation)

#### 3.8.1. SSITKA studies – $^{13}\text{CO}/\text{H}_2$ gas switch

For the SSITKA experiments, FT (SASOL) catalyst was loaded into the quartz micro-reactor and pre-treated as follows:

He ( $50 \text{ mL min}^{-1}$ ,  $27 \text{ }^\circ\text{C}$ , 15 min)  $\rightarrow$  increase T in  $\text{H}_2$  flow to  $425 \text{ }^\circ\text{C}$  ( $50 \text{ mL min}^{-1}$ ,  $\beta = 1 \text{ }^\circ\text{C min}^{-1}$ )  $\rightarrow$   $\text{H}_2$  ( $425 \text{ }^\circ\text{C}$ , 10 h)  $\rightarrow$  cool-down in  $\text{H}_2$  to  $230 \text{ }^\circ\text{C}$  (30 min).

The Steady-State Isotopic Transient Kinetic Analysis (SSITKA) technique coupled with mass spectrometry (SSITKA-MS) was used to follow the carbon-path of the FT reaction, mainly for  $\text{CH}_4$  formation ( $\text{C}_2$ 's and  $\text{C}_3$ 's pathways were also followed in some cases), and which was carried out at  $230 \text{ }^\circ\text{C}$  and  $\sim 1.3$  bar total pressure in the reactor according to the following sequence of gas switches:

$5\% \text{ }^{12}\text{CO}/10\% \text{ H}_2/\text{Ar}$  ( $100 \text{ mL min}^{-1}$ ,  $230 \text{ }^\circ\text{C}$ , 32 h)  $\rightarrow$   **$5\% \text{ }^{13}\text{CO}/10\% \text{ H}_2/1\% \text{ Kr}/\text{Ar}$**  ( $100 \text{ mL min}^{-1}$ ,  $230 \text{ }^\circ\text{C}$ , 7 min)  $\rightarrow$  purge in Ar flow ( $100 \text{ mL min}^{-1}$ ,  $230 \text{ }^\circ\text{C}$ , 3 min).

The mass of the catalyst and the volume flow rate used were adjusted so as to keep the *CO conversion below 15%* and minimize external mass transport resistances. The amount of catalyst sample used was 0.4 g and 0.3 g for the CY-A and CY-C catalyst, respectively. After a given time-on-stream, the SSITKA gas switch was performed and the mass numbers 15 ( $^{12}\text{CH}_4$ ), 17 ( $^{13}\text{CH}_4$ ), 18 ( $\text{H}_2\text{O}$ ), 29 ( $^{13}\text{CO}$ ) and 84 (Kr) were continuously monitored by MS. For the accurate analysis of the  $^{13}\text{CH}_4$  signal, the contribution to  $m/z = 17$  of any additional  $\text{H}_2\text{O}$  signal than that due to the  $^{12}\text{CO}/\text{H}_2$  reaction before the  $^{13}\text{CO}/\text{H}_2$  gas switch was considered (e.g., likely very small amount of water impurity in the gas lines of  $^{12}\text{CO}/\text{H}_2$  and  $^{13}\text{CO}/\text{H}_2$  but of different level). The  $^{12}\text{CO}/\text{H}_2 \rightarrow ^{13}\text{CO}/\text{H}_2$  SSITKA gas switch was repeated to check reproducibility of SSITKA (true steady-state at the time period of gas switches) but also to record the transient evolution of *higher than methane* hydrocarbons. The latter switch was made after the end of the SSITKA experiment the focus of which was to record the  $^{13}\text{CO}(\text{g})$  and  $^{13}\text{CH}_4(\text{g})$  transients. The signals  $m/z = 30$  and  $m/z = 31$  reflect largely both the formation of  $^{13}\text{C}$ -ethane and  $^{13}\text{C}$ -propane hydrocarbons.

The concentration ( $\mu\text{mol g}^{-1}$ ) of reversibly adsorbed CO-s and *active* CH<sub>x</sub>-s intermediates (leading to CH<sub>4</sub> formation) and their respective surface coverage,  $\theta$ , were estimated using the following Eqs. (3.20) – (3.22):

$$N_{CO}(\text{mol g}_{cat}^{-1}) = \frac{F_T y_{CO}^f (1 - X_{CO})}{W} \int_0^{t_{s,s}} [Z_{Kr}(t) - Z_{^{13}CO}(t)] dt \quad (\text{Eq. 3.20})$$

$$N_{CH_x}(\text{mol g}_{cat}^{-1}) = \frac{F_T y_{^{13}CH_4}}{W} \int_0^{t_{s,s}} [Z_{^{13}CO}(t) - Z_{^{13}CH_4}(t)] dt \quad (\text{Eq. 3.21})$$

$$\theta_i = \frac{N_i}{N_{Co,surf}} \quad (i = CH_x, CO) \quad (\text{Eq. 3.22})$$

where,  $F_T$  is the total molar flow rate ( $\mu\text{mol s}^{-1}$ );  $y_{CO}^f$  is the mole fraction of CO in the feed;  $X_{CO}$  is the CO conversion (%);  $W$  is the mass of catalyst (g);  $y_{^{13}CH_4}$  is the mole fraction of <sup>13</sup>CH<sub>4</sub> at the exit stream of the micro-reactor in the new steady-state obtained in <sup>13</sup>CO/H<sub>2</sub>;  $Z$  is the dimensionless concentration of a given gas-phase species;  $t_{s,s}$  is the time at which the new steady-state is obtained under the <sup>13</sup>CO/H<sub>2</sub> gas mixture;  $N_{Co,surf}$  is the total number of surface cobalt atoms ( $\mu\text{mol g}^{-1}$ ) estimated on the basis of the dispersion value of Co metal.

It is important to mention that the CO conversion ( $X_{CO}$ , %) used in Eq. 3.20 accounts for the CO consumed to form the various carbon-containing gas products. If this is not accounted for the calculated concentration of CO-s ( $N_{CO}$ ,  $\mu\text{mol g}^{-1}$ ) is overestimated. Also, Eq. (3.21) considers that the exchange of <sup>12</sup>CO-s with <sup>13</sup>CO(g) is much faster than the exchange kinetics of <sup>12</sup>CH<sub>x</sub> with <sup>13</sup>CH<sub>x</sub> (transient response of <sup>13</sup>CH<sub>4</sub>). The latter applies in the present work. It should be noted here that most of the SSITKA work reported by other researchers made use of a relationship for the estimation of CH<sub>x</sub> which was based on some empirical correlation about the so called “chromatographic effect” between the <sup>13</sup>CO and <sup>13</sup>CH<sub>4</sub> transients [29]. In the latter case, the  $N_{CH_x}$  ( $\mu\text{mol g}^{-1}$ ) is underestimated compared to Eq. 3.17.

The surface residence times of CH<sub>x</sub> and CO were estimated using Eqs. (3.23) and (3.24), respectively:

$$\tau_{CO} = \int_0^{t_{s,s}} [Z_{Kr}(t) - Z_{^{13}CO}(t)] dt \quad (\text{Eq. 3.23})$$

$$\tau_{CH_x} = \int_0^{t_{s,s}} [Z_{^{13}CO}(t) - Z_{^{13}CH_4}(t)] dt \quad (\text{Eq. 3.24})$$

The  $TOF_{CH_4}$ ,  $TOF_{CO}$  and  $TOF_{CH_4,ITK}$  ( $s^{-1}$ ) kinetic rates were estimated under steady-state FT reaction conditions before the SSITKA switch (under  $^{12}CO/H_2$  feed stream). The  $TOF_{CH_4}$  and  $TOF_{CO}$  were estimated based on the dispersion of Co (Eqs. (3.27) – (3.28)), while the  $TOF_{CH_4,ITK}$  (Eq. 3.30) is based on the concentration of active reaction intermediates, namely  $N_{CH_x}$  and  $N_{CO-s}$  ( $\mu mol\ g^{-1}$ ) which are measured in the SSITKA experiment Eqs. (3.18) – (3.21). It should be noted at this point that a more accurate estimation in the concentration of the active species, and thus active metal surface sites, which participate in the carbon-path of methane formation would be the knowledge of the concentration of H-s ( $\mu mol\ g^{-1}$ ) or  $\theta_H$ . This is a very difficult task to accomplish experimentally. Given the quantities of active  $CH_x$ -s and CO-s, and those of *inactive*  $CH_x$ -s (see Chapter 6), the  $\theta_H$  must be considered very small.

Eqs. (3.25) and (3.26) allow the estimation of the steady-state rate of CO consumption and  $CH_4$  formation in units of  $\mu mol\ g^{-1}\ s^{-1}$ .

$$r_{CO} = \frac{y_{CO} F_T}{W} \quad (\text{Eq. 3.25})$$

$$r_{CH_4} = \frac{y_{CH_4} F_T}{W} \quad (\text{Eq. 3.26})$$

$$TOF_{CO} = \frac{r_{CO}}{N_{Co,surf}} \quad (\text{Eq. 3.27})$$

$$TOF_{CH_4} = \frac{r_{CH_4}}{N_{Co,surf}} = k\theta_H\theta_{CH_x} = k_{eff}\theta_{CH_x} = \left(\frac{1}{\tau_{CH_x}}\right)\theta_{CH_x} \quad (\text{Eq. 3.28})$$

$$k_{eff} = k\theta_H = \frac{1}{\tau_{CH_x}} \quad (\text{Eq. 3.29})$$

$$TOF_{CH_4,ITK} = \frac{r_{CH_4}}{N_{CH_x} + N_{CO}} \quad (\text{Eq. 3.30})$$

$$\tau_{CH_x} = \frac{\theta_{CH_x}}{TOF_{CH_x}} \quad (\text{Eq. 3.31})$$

Transient Isothermal Hydrogenation (TIH) and Temperature-Programmed Hydrogenation (TPH) experiments after the SSITKA gas switch were performed as follows:

$^{13}CO/H_2/Kr/Ar$  (230 °C, 7 min)  $\rightarrow$  Ar (3 min, 230 °C)  $\rightarrow$  50%  $H_2/Ar$  (50 mL  $min^{-1}$ , 230 °C)  $\rightarrow$   
**TIH run (7 min)  $\rightarrow$  TPH run to 600 °C ( $\beta = 10\ ^\circ C\ min^{-1}$ ).**



The concentration of *inactive* (spectator) adsorbed carbon-containing species formed under  $^{12}\text{CO}/\text{H}_2$  (FT reaction at 230 °C) for a given TOS, but not exchanged during the  $^{13}\text{CO}/\text{H}_2$  treatment, was estimated under the 50%  $\text{H}_2/\text{Ar}$  gas treatment at 230 °C. Refractory carbonaceous *inactive* species ( $\text{C}_x\text{H}_y\text{-s}$ ) not hydrogenated at 230 °C were also measured during the TPH run (up to 600 °C). The mass numbers 17 ( $^{13}\text{CH}_4$ ), 15 ( $^{12}\text{CH}_4$ ), 30 ( $\text{C}_2\text{H}_6$ ), 18 ( $\text{H}_2\text{O}$ ) and 84 (Kr) were continuously monitored by mass spectrometer for the above described TIH and TPH runs.

### 3.8.2. SSITKA studies – CO/D<sub>2</sub> switch

The hydrogen-path of the FT reaction over the CY-A and CY-C catalysts was probed via the SSITKA switch:

3.5%  $^{12}\text{CO}/7\% \text{H}_2/\text{Ar}$  (100 mL min<sup>-1</sup>, 230 °C, 32 h) → **3.5%  $^{13}\text{CO}/7\% \text{D}_2/1\% \text{Kr}/\text{Ar}$**  (100 mL min<sup>-1</sup>, 230 °C, 7 min) → purge in Ar flow (100 mL min<sup>-1</sup>, 230 °C, 3 min).

To account for possible exchange of H of –OH species on the catalyst surface with the  $\text{D}_2(\text{g})$  during the SSITKA gas switch, the following switch was performed:

7%  $\text{H}_2/\text{Ar}$  (100 mL min<sup>-1</sup>, 230 °C, 15 min) → **7%  $\text{D}_2/1\% \text{Kr}/\text{Ar}$**  (100 mL min<sup>-1</sup>, 230 °C, 7 min) → purge in Ar flow (100 mL min<sup>-1</sup>, 230 °C, 3 min).

The quantity ( $\mu\text{mol HD g}_{\text{cat}}^{-1}$ ) of HD produced during the above described two experiments over the CY-A and CY-C catalysts is estimated via the following Eq. (3.32).

$$N_{\text{HD}} = \frac{F_{\text{T}} \text{Area}_{\text{HD}}}{W} \quad (\text{Eq. 3.32})$$

### 3.9. Experimental apparatus for catalyst testing and characterization and *in situ* DRIFTS and operando studies

The home-made experimental apparatus used during this PhD thesis work is presented in Figure 3.1. More specifically, the pressure regulators of each gas cylinder that feed the Mass Flow Control valves (MFC, MKS Instruments, Model 1179 C) are set at ~ 4 bar outlet pressure. The He or Ar carrier gas is purified by passing it through moisture and oxygen traps. For the deliberate and accurate control of the flow of gases and the *in-situ* preparation of the gas

mixtures, MFCs are regulated via readout channels (MKS Instruments, Model 247), after being zeroed and calibrated.

Homogeneous mixing of gas flows delivered by the MFCs is accomplished in specially designed very small volume ( $\sim 3$  mL) mixing chambers, which are situated inside of a hot box ( $100 - 120$  °C), where all the chromatographic switching valves are placed, in a way not to have any condensation of water derived either as reactant or product from the reaction. For all the stainless-steel tubing located downstream and upstream of that oven, heating tapes covered with glass yarn tape are used to keep the temperature  $\sim 150$  °C. In total, the apparatus is composed of six chromatographic valves, four of which are four-ways (V1, V2, V4 and V6) and two are six-way (V3, V5), and which are used for different gas switches required for a variety of transient experiments designed and performed in the course of this PhD thesis work.

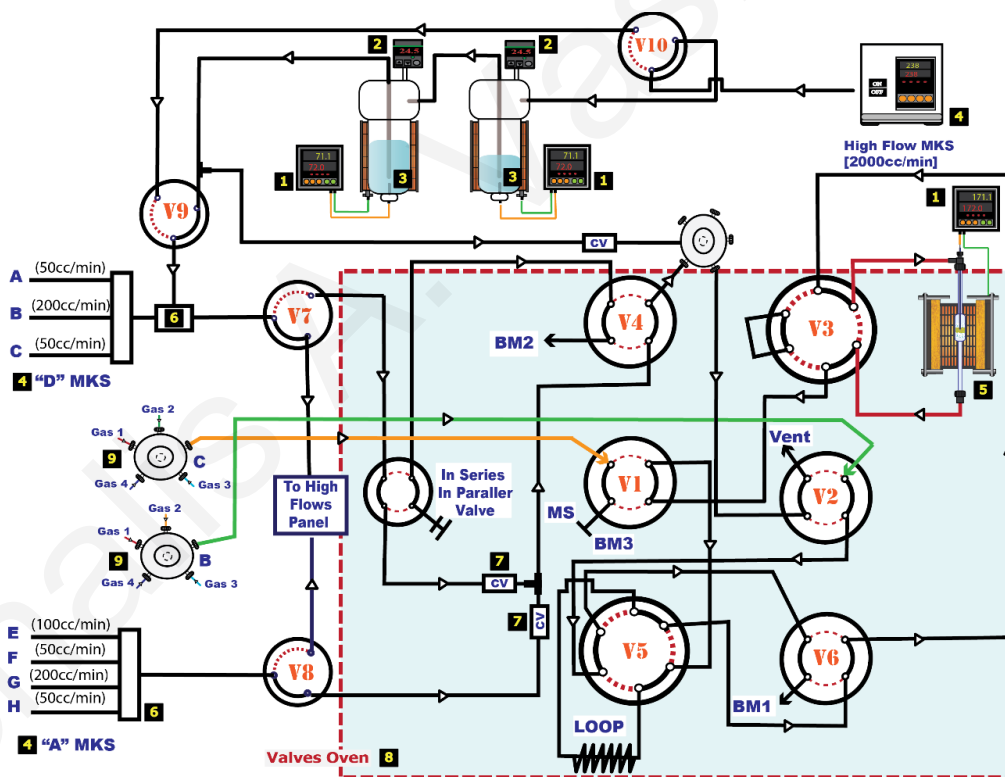


**Figure 3.1:** Experimental apparatus used for the implementation of transient studies.

All the chromatographic valves are manually controlled except of V4 and V5, which are controlled by pneumatic actuators for the accurate delivery of a “step gas-switch” response. Valve V4 is used for the step gas switch between line A and line D gas mixtures prepared in two different mixing chambers from the delivered gas flows via the MFCs. The V3

chromatographic valve controls whether the gas mixture of line A, B or D will pass through or by-pass the reactor. It is noteworthy that the length and volume of the gas line is kept the same in the case of the “by-pass” direction, in a way to measure the “forcing function” (upon the step gas switch) at the entrance of the catalytic bed placed in the CSTR micro-reactor.

Except of lines A and D, that were used for the preparation of gas mixtures, there are another two lines (B and C) which are connected to eight different gases controlled by two five-way ball valves that lead to chromatographic switching valves (V1 and V2). Line B is mainly used for the preparation of gases used for the catalyst pre-treatment ( $H_2$  or  $O_2$ ) and lead to V2, whereas line C is used for the recording of background (He or Ar) and gas sensitivities (low-concentration certified gas mixtures) and which lead to the V1 valve.

The micro-reactor used is a continuous stirred-tank reactor (CSTR) type with  $\sim 3$  mL nominal volume, 30 mm length and 8 mm inner diameter. It is produced by quartz and it's consists from two pipes with 4 mm inner diameter and length 150 mm each, which serves as an entry and exit of the gas to the catalytic cell [22,30]. The catalytic bed is placed into the micro-reactor and held with quartz wool on the bottom, whereas a disk with several holes on the top of the reactor simulates the CSTR behavior. The temperature of the solid is monitored by a K-type thermocouple (0.5 mm) placed within a quartz tube,  $\sim 1$  mm apart from the top of quartz wool holding in place the catalyst bed (2-3 mm thick,  $dp < 100 \mu m$ ). A proportional integral derivative (PID) temperature controller/programmer (Jumo dTRON 08.1 model) controls heating of the micro-reactor. The total pressure inside the reactor for the volume flow rate and the volume of catalytic bed used is in the 1.1-1.3 bar range. The micro-reactor is placed in a small oven of cylindrical geometry (Thermocraft Inc.), which can reach temperatures up to  $\sim 1200$  °C by the aid of the (PID) temperature controller/programmer. All the gases are capable of being guided through the V1 towards the QMS, which is controlled via an RS232 connection with a computer for online control, saving and analysis of the transient response signals. Two water saturators (part no. 3) connected in series with temperature and pressure control (parts 1 and 2) are used in the case that water is introduced in the reaction feed gas stream by producing a gas flow of  $H_2O/He$  (or Ar) of given composition in water, after passing through the saturators the carrier gas via a high-flow MFC valve (see part 4).

In the case of *in situ* DRIFTS and *operando* experiments, the DRIFT cell serves as the micro-reactor reactor (see Figure 3.2), where the MS is connected straight after the DRIFT cell exit, allowing the *on-line* measurement at the same time of the transient response of the gas

phase of the DRIFT cell upon different gas switches. A continuous flow of water through the DRIFT cell, it achieved by using a peristaltic water pump, which prevents the overheating and destruction of the cell. The DRIFT spectrum produced is saved and analyzed by using the Spectrum software for windows as previously described.

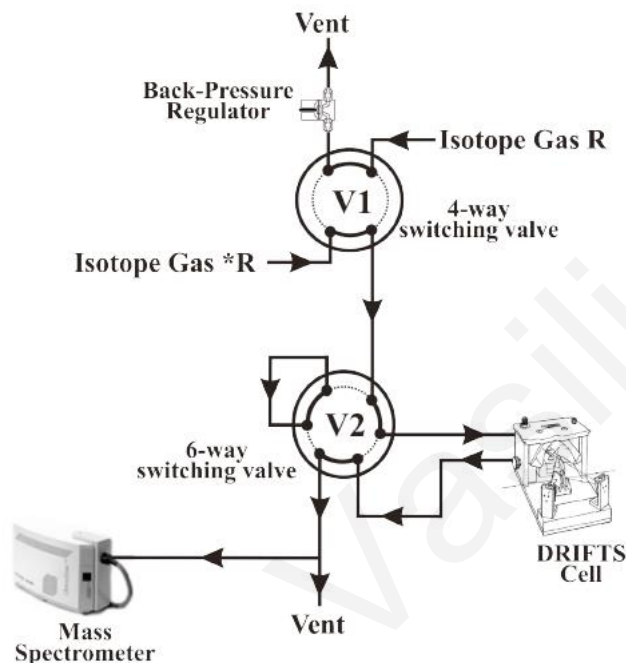


**Figure 3.2:** Experimental apparatus used for the operando SSITKA-DRIFTS studies [31].

### References

- [1] D. Dionysiou, X. Qi, Y.S. Lin, G. Meng, D. Peng, *J. Memb. Sci.* 154 (1999) 143–153.
- [2] K.C. Petallidou, S. Boghosian, A.M. Efstathiou, *Catal. Today* 242 (2015) 153–167.
- [3] K.C. Petallidou, A.M. Efstathiou, *Appl. Catal. B Environ.* 140–141 (2013) 333–347.
- [4] Q. Zhang, J. Wang, P. Ning, T. Zhang, M. Wang, K. Long, J. Huang, *Korean J. Chem. Eng.* 34 (2017) 1–9.
- [5] J. Van De Loosdrecht, S. Barradas, E.A. Caricato, N.G. Ngwenya, P.S. Nkwanyana, M.A.S. Rawat, B.H. Sigwebela, P.J. Van Berge, J.L. Visagie, *Top. Catal.* 26 (2003) 121–127.
- [6] S. Brunauer, P.H. Emmett, E. Teller, *J. Am. Chem. Soc.* 60 (1938) 309–319.
- [7] K.S.W. Sing, *Pure Appl. Chem.* 57 (1985) 603.
- [8] G.A. Somorjai, A.S. Mujumdar, *Dry. Technol.* 13 (1995) 507–508.
- [9] D. Schanke, S. Vada, E.A. Blekkan, A.M. Hilmen, A. Hoff, A. Holmen, *J. Catal.* 156

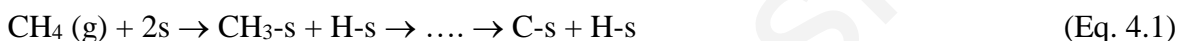
- (1995) 85–95.
- [10] W. Wien, *Philos. Mag. Ser. 5* 43 (1897) 214–220.
- [11] C.E. Moore, B. Jaselskis, A. von Smolinski, *J. Chem. Educ.* 62 (1985) 859.
- [12] T. Armaroli, T. Bécue, S. Gautier, *Oil Gas Sci. Technol.* 59 (2004) 215–237.
- [13] A.M. Efstathiou, J.T. Gleaves, G.S. Yablonsky, in: *Charact. Solid Mater. Heterog. Catal. From Struct. to Surf. React. Vol. 1&2*, Wiley-VCH Verlag GmbH & Co. KGaA, 2012, pp. 1013–1073.
- [14] A.M. Efstathiou, in: *Catalysis*, The Royal Society of Chemistry, 2016, pp. 175–236.
- [15] K. Hadjiivanov, M. Mihaylov, D. Panayotov, E. Ivanova, K. Chakarova, in: *Spectrosc. Prop. Inorg. Organomet. Compd. Vol. 45*, The Royal Society of Chemistry, 2014, pp. 43–78.
- [16] P.A. Midgley, M. Weyland, J.M. Thomas, B.F.G. Johnson, *Chem. Commun.* (2001) 907–908.
- [17] M. Weyland, P.A. Midgley, J.M. Thomas, *J. Phys. Chem. B* 105 (2001) 7882–7886.
- [18] M.P. Seah, *Surf. Interface Anal.* 2 (1980) 222–239.
- [19] J.A. Schwarz, *Catal. Rev.* 25 (1983) 141–227.
- [20] A.M. Efstathiou, C.O. Bennett, *J. Catal.* 124 (1990) 116–126.
- [21] R. Prins, *Chem. Rev.* 112 (2012) 2714–2738.
- [22] C.N. Costa, S.Y. Christou, G. Georgiou, A.M. Efstathiou, *J. Catal.* 219 (2003) 259–272.
- [23] A.M. Efstathiou, S.Y. Christou, in: A. Trovarelli, P. Fornasiero (Eds.), *Catal. Sci. Ser.*, 2nd ed., Imperial College Press, 2012, pp. 1–84.
- [24] K. Jaana, *Kinetic Analysis of Temperature-Programmed Reaction*, Helsinki University of Technology, 2003.
- [25] C. Perego, *Catal. Today* 52 (1999) 133–145.
- [26] N. Kumari, M.A. Haider, M. Agarwal, N. Sinha, S. Basu, *J. Phys. Chem. C* 120 (2016) 16626–16635.
- [27] V.A. Sadykov, E.L. Gubanov, N.N. Sazonova, S.A. Pokrovskaya, N.A. Chumakova, N. V. Mezentseva, A.S. Bobin, R. V. Gulyaev, A. V. Ishchenko, T.A. Krieger, C. Mirodatos, *Catal. Today* 171 (2011) 140–149.
- [28] A.M. Efstathiou, X.E. Verykios, *Appl. Catal. A Gen.* 151 (1997) 109–166.
- [29] S. Pansare, A. Sirijaruphan, J.G. Goodwin, in: *Isot. Heterog. Catal.*, 2006, pp. 183–211.
- [30] S.Y. Christou, C.N. Costa, A.M. Efstathiou, *Top. Catal.* 30/31 (2004) 325–331.

- [31] C.M. Kalamaras, Mechanistic and Kinetic Studies of Water-Gas Shift Reaction by Using Operando Methodologies and Transient Isotopic Techniques, University of Cyprus, 2011.

Michalis A. Vasiliades

**Chapter 4: Dry Reforming of Methane over  $Ce_{1-x}M_xO_{2-\delta}$  ( $M=Zr^{4+}, Pr^{3+}$ )-supported Ni catalysts**

The dry reforming of methane (DRM) has not yet found large scale industrial development and commercialization over supported Ni catalysts due to its main disadvantage, that of non-acceptable catalyst stability (catalyst deactivation). Unfortunately, “carbon” deposition and sintering of both the support and the active metal particles occur at high reaction temperatures (ca.  $> 700$  °C) which are required to attain high equilibrium conversions to syngas. The formation of “carbon” originates mainly via methane decomposition (Eq. 4.1), where part of it is associated with the *active* carbon pool that forms CO, and also via the Boudouard reaction (Eq. 4.2) [1,2].



Part of the carbon in Eq. 4.2 could also be considered as *active* carbon (depending on the relative rates of the forward and backward reaction steps in Eq. 4.2). The nature of inactive “carbon” usually observed is that of graphite whiskers, carbon fibres and amorphous carbon [1,2].

Supported nickel catalysts are commonly studied towards DRM because of their low cost and large availability, but they are very prone to large quantities of “carbon” deposition and encapsulation of Ni particles. Much of the research effort recently devoted [1–4] is to finding suitable supports of nickel metal among the class of metal oxides, which possess high oxygen storage capacity (OSC) and high rates of surface/bulk lattice oxygen diffusion, which proved to increase “carbon” formation resistance. Ceria-based, and in particular ceria-zirconia solid solutions, have been reported to exhibit significant improvements in “carbon” formation reduction and catalyst’s stability compared to other non-reducible metal oxide supports (e.g.  $\gamma$ - $Al_2O_3$ ,  $SiO_2$ ) [5–11].

In spite of recent efforts to develop suitable  $CeO_2$ -based supported Ni catalysts towards sustainable DRM activity, fundamental understanding of the relative importance of each of the “carbon” formation chemical routes as a function of support chemical composition (e.g. Ce/Zr ratio, use of other than  $Zr^{4+}$ -dopant in doped ceria) has not yet been reported.

In the present chapter, the following fundamental questions have been addressed after designing and performing various kinds of transient isotopic experiments over ceria-based supported Ni catalysts, for the first time to the best of our knowledge:

- Experimental evidence for the origin of inactive “carbon” (methane decomposition (Eq. 4.1) and Boudouard reaction (Eq. 4.2))
- Quantitative assessment of the effect of support chemical composition on the relative contribution of the  $CH_4$  and  $CO_2$  activation routes towards “carbon” formation, and
- Influence of support chemical composition on the reactivity of the various kinds of “carbon” formed towards hydrogen and oxygen.

For this purpose, transient hydrogenation and oxidation (isothermal and temperature-programmed) coupled with the use of  $^{13}CO$  and  $^{13}CO_2$  isotope gases were performed. *In situ* DRIFTS studies were also conducted to investigate the effect of support chemical composition on the chemisorption of CO on the nickel surface, and a likely correlation with “carbon” formation.

#### **4.1. The effect of support composition in the origin and reactivity of carbon**

##### **4.1.1. Catalyst characterization**

###### **4.1.1.1. Surface texture and XRD studies of $Ce_{1-x}M_xO_{2-\delta}$ ( $M=Zr^{4+}, Pr^{3+}$ ) solids**

The BET specific surface area (SSA), specific pore volume ( $V_p$ ) and mean pore diameter ( $d_p$ ) of the three solid supports of Ni metal investigated are given in Table 4.1. The SSA of these materials is in the  $11\text{-}22\text{ m}^2\text{g}^{-1}$  range with  $Ce_{0.8}Zr_{0.2}O_{2-\delta}$  to exhibit the largest value ( $22\text{ m}^2\text{g}^{-1}$ ), where the mean pore diameter is found to be in the  $5.5\text{-}11.5\text{ nm}$  range.

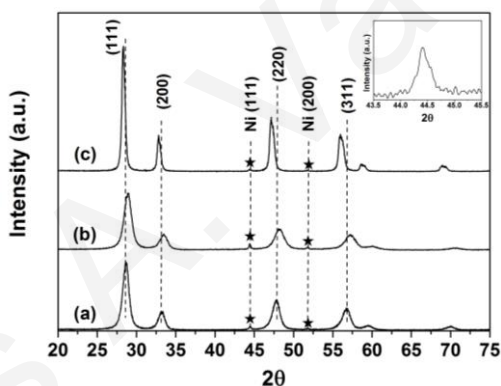
Powder X-ray diffractograms of the fresh 5 wt.% Ni supported on  $Ce_{0.8}Zr_{0.2}O_{2-\delta}$ ,  $Ce_{0.5}Zr_{0.5}O_{2-\delta}$  and  $Ce_{0.8}Pr_{0.2}O_{2-\delta}$  after calcination ( $750\text{ }^\circ\text{C}/4\text{ h}$ ) followed by  $H_2$  reduction ( $700\text{ }^\circ\text{C}/2\text{ h}$ ) are given in Fig. 4.1. It appears that  $Ce_{0.8}Zr_{0.2}O_{2-\delta}$  and  $Ce_{0.8}Pr_{0.2}O_{2-\delta}$  formed a solid solution of pseudo-cubic structure, whereas in the case of  $Ce_{0.5}Zr_{0.5}O_{2-\delta}$  the presence of the tetragonal  $t'$  phase cannot be excluded. In particular, the XRD pattern of 5 wt.% Ni/ $Ce_{0.8}Zr_{0.2}O_{2-\delta}$  shows diffraction peaks at  $2\theta = 28.7, 33.2, 47.8, 56.7, 59.4$  and  $69.9$  due to the presence of  $Ce_{0.8}Zr_{0.2}O_{2-\delta}$  solid solution support (cubic) [12,13] and that of 5 wt.% Ni/ $Ce_{0.5}Zr_{0.5}O_{2-\delta}$  shows diffraction peaks at  $2\theta = 28.8, 33.4, 48.2, 57.2, 59.9$  and  $70.5^\circ$ , which are shifted to lower  $2\theta$  values compared to those corresponding to pure  $CeO_2$  ( $2\theta = 28.7, 33.1, 47.5, 56.2, 59.2$  and  $69.7^\circ$ ) and the present  $Ce_{0.8}Zr_{0.2}O_{2-\delta}$  solid support.



**Table 4.1:** BET surface area (SSA,  $\text{m}^2 \text{g}^{-1}$ ), specific pore volume ( $V_p$ ,  $\text{cm}^3 \text{g}^{-1}$ ), average pore size ( $d_p$ , nm), primary crystallite size ( $d_c$ , nm), lattice constant ( $\alpha$ , Å) and Oxygen Storage Capacity Complete (OSCC,  $\mu\text{mol g}^{-1}$ ) obtained over the  $\text{Ce}_{0.8}\text{Pr}_{0.2}\text{O}_2$  and  $\text{Ce}_{1-x}\text{Zr}_x\text{O}_{2-\delta}$  ( $x = 0.2$  and 0.5) solids.

Sample	SSA ( $\text{m}^2 \text{g}^{-1}$ )	$V_p$ ( $\text{cm}^3 \text{g}^{-1}$ )	$d_p$ (nm)	$d_c$ (nm)	$\alpha$ (Å)	OSCC ( $\mu\text{mol g}^{-1}$ )		
						600 °C	700 °C	800 °C
$\text{Ce}_{0.8}\text{Pr}_{0.2}\text{O}_2$	10.9	0.039	11.5	16.7 (23.6) <sup>a</sup> (24.0) <sup>b</sup>	5.4457	502	660	950
$\text{Ce}_{0.8}\text{Zr}_{0.2}\text{O}_2$	22.0	0.057	8.0	8.6	5.3896	227	590	720
$\text{Ce}_{0.5}\text{Zr}_{0.5}\text{O}_2$	16.1	0.031	5.5	7.3	5.3442	260	630	860

<sup>a</sup> After DRM reaction at 550 °C for 50 h; <sup>b</sup> After DRM reaction at 750 °C for 50 h.

**Figure 4.1:** Powder X-ray diffractograms of (a) 5 wt.%  $\text{Ni}/\text{Ce}_{0.8}\text{Zr}_{0.2}\text{O}_{2-\delta}$ , (b) 5 wt.%  $\text{Ni}/\text{Ce}_{0.5}\text{Zr}_{0.5}\text{O}_{2-\delta}$  and (c) 5 wt.%  $\text{Ni}/\text{Ce}_{0.8}\text{Pr}_{0.2}\text{O}_{2-\delta}$  solids following calcination of the fresh samples in air (750 °C/4 h). Inset graph shows a magnification of the Ni (111) diffraction peak (★) obtained for the 5 wt.%  $\text{Ni}/\text{Ce}_{0.5}\text{Zr}_{0.5}\text{O}_{2-\delta}$  catalyst.

This result shows the contraction of the ceria crystal lattice, given the fact that the atomic radius of  $\text{Ce}^{4+}$  (0.97 Å) is larger than that of  $\text{Zr}^{4+}$  (0.84 Å). This shift indicates that  $\text{Zr}^{4+}$  cations have been incorporated into the  $\text{CeO}_2$  fluorite structure, thus leading to the formation of a  $\text{Ce}_{1-x}\text{Zr}_x\text{O}_{2-\delta}$  solid solution. The XRD pattern of  $\text{Ce}_{0.8}\text{Pr}_{0.2}\text{O}_{2-\delta}$  is only slightly shifted towards lower 2theta values from that corresponding to the  $\text{Ce}_{0.8}\text{Zr}_{0.2}\text{O}_{2-\delta}$  solid. This result is explained based on the fact that  $\text{Ce}^{4+}$  and  $\text{Pr}^{3+}$  practically exhibit similar ionic radii (0.97 vs. 0.96 Å ( $\text{Pr}^{3+}$ )) and that  $\text{Ce}_{0.8}\text{Pr}_{0.2}\text{O}_{2-\delta}$  exhibits also larger reducibility than the  $\text{Ce}_{0.8}\text{Zr}_{0.2}\text{O}_{2-\delta}$  solid (Table 4.1, OSCC

values and Fig. 4.2). The latter implies that  $Ce^{3+}$  formed having a larger ionic radius than  $Ce^{4+}$  will cause slight expansion of the crystal unit cell. It should be noted here that the crystal structure of  $Ce_{0.8}Pr_{0.2}O_{2-\delta}$  is that of cubic [14,15].

Based on the Scherrer equation, and considering the FWHM of the diffraction line (111) for metallic Ni [16], and that of (111) for cubic  $CeO_2$  (Fig. 4.1), the primary crystallite size ( $d_c$ , nm) of  $Ni^0$  and that of support phase were estimated and values are reported in Table 4.1 (support phase) and Table 4.2 (Ni phase). It is seen that the 5 wt.% Ni/ $Ce_{0.8}Pr_{0.2}O_{2-\delta}$  exhibits the largest mean particle size for both the  $Ni^0$  metal (27.7 nm) and the support phase (16.7 nm). The lattice constant  $a$  (Å) of the various support materials is also reported in Table 4.1. The obtained values are consistent with the expansion and contraction effect caused by the substitution of  $Ce^{4+}$  by  $Pr^{3+}$  and  $Zr^{4+}$  ions mentioned above.

**Table 4.2:**  $H_2$  desorption ( $\mu mol g^{-1}$ ) and Ni dispersion (D, %) obtained during  $H_2$ -TPD performed on fresh 5 wt.% Ni supported on  $Ce_{0.8}Pr_{0.2}O_{2-\delta}$  and  $Ce_{1-x}Zr_xO_{2-\delta}$  ( $x = 0.2, 0.5$ ) carriers.

Sample	$T_M$ (°C)	$H_2$ ( $\mu mol g^{-1}$ )	$D_{Ni}$ (%)	$d_{Ni}$ (nm)
<b>5 wt.% Ni/<math>Ce_{0.8}Pr_{0.2}O_{2-\delta}</math></b>	96	3.8		
	262	0.8	3.5	27.7 (28.7) <sup>a</sup>
	431	7.3		(33.5) <sup>b</sup>
	562	2.8		(32.5) <sup>c</sup>
<b>5 wt.% Ni/<math>Ce_{0.8}Zr_{0.2}O_{2-\delta}</math></b>	80	3.5		
	146	5.7		
	211	4.2	6.5	14.9 (14.4) <sup>a</sup>
	433	9.1		
<b>5 wt.% Ni/<math>Ce_{0.5}Zr_{0.5}O_{2-\delta}</math></b>	551	4.9		
	111	6.6		
	191	10.7	6.2	15.6 (14.8) <sup>a</sup>
	318	1.3		
	472	7.5		

<sup>a</sup> Powder XRD on the fresh catalyst (see Fig. 4.3); <sup>b</sup> powder XRD after DRM at  $T = 550$  °C/50 h; <sup>c</sup> powder XRD after DRM at  $T = 750$  °C/50 h.

#### 4.1.1.2. Oxygen Storage Capacity (OSC) measurements

The oxygen storage capacity complete, OSCC ( $\mu\text{mol O g}^{-1}$ ) of the three  $\text{Ce}_{1-x}\text{M}_x\text{O}_{2-\delta}$  ( $\text{M} = \text{Zr}^{4+}$  and  $\text{Pr}^{3+}$ ;  $x = 0.2$  and  $0.5$ ) support materials estimated at 600, 700 and 800 °C is reported in Table 4.1. At 600 °C,  $\text{Ce}_{0.8}\text{Pr}_{0.2}\text{O}_{2-\delta}$  exhibits a significantly larger OSCC compared to the other two Ce-Zr-O solids; a value of 502 vs. 227-260  $\mu\text{mol g}^{-1}$  was obtained. At higher temperatures (700-800 °C),  $\text{Ce}_{0.8}\text{Pr}_{0.2}\text{O}_{2-\delta}$  exhibits larger OSCC compared to  $\text{Ce}_{0.8}\text{Zr}_{0.2}\text{O}_{2-\delta}$  ( $\text{Ce}/\text{Zr} = 4$ ) but similar (larger by only 5-10%) to the  $\text{Ce}_{0.5}\text{Zr}_{0.5}\text{O}_{2-\delta}$  ( $\text{Ce}/\text{Zr} = 1$ ) solid (Table 4.1). On the other hand, Fig. 4.2 illustrates that  $\text{Ce}_{0.8}\text{Pr}_{0.2}\text{O}_{2-\delta}$  has larger transient kinetic rates of lattice oxygen release via hydrogen abstraction (hydrogen reduction of the lattice oxygen via the gas switch:  $\text{He} \rightarrow 0.5\% \text{H}_2/\text{Ar}/\text{He}$  ( $T, t$ )) in the 600-800 °C range compared to the other two solid supports. This result (Fig. 4.2) suggests a weaker bonding between metal cations and oxygen anions present in the solid solution fluorite-type structure (Fig. 4.1) compared to the other two metal oxide supports. The same conclusion is reached after  $\text{H}_2$ -TIR performed at  $T = 800$  °C.

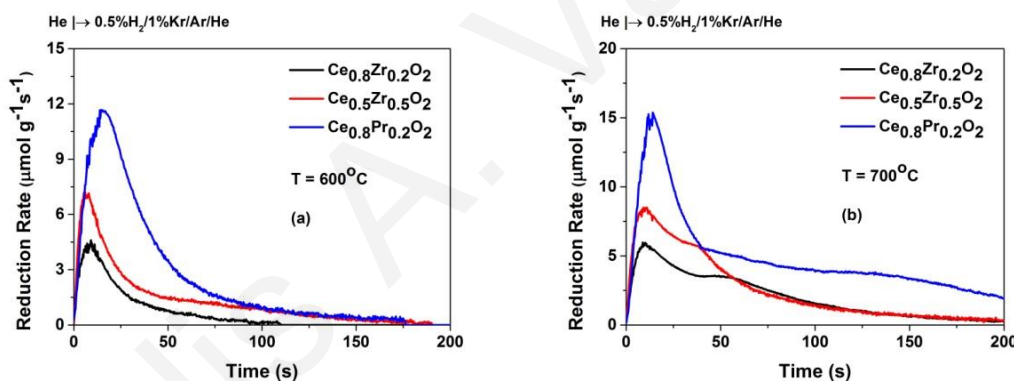


**Figure 4.2:** Transient isothermal reduction rates obtained over the  $\text{Ce}_{0.8}\text{Zr}_{0.2}\text{O}_{2-\delta}$ ,  $\text{Ce}_{0.5}\text{Zr}_{0.5}\text{O}_{2-\delta}$  and  $\text{Ce}_{0.8}\text{Pr}_{0.2}\text{O}_{2-\delta}$  solid supports at 600 °C (a) and 700 °C (b) following the step gas switch:  $\text{He} \rightarrow 0.5\% \text{H}_2/1\% \text{Kr}/\text{Ar}/\text{He}$ .

#### 4.1.1.3. $\text{H}_2$ temperature-programmed desorption (TPD) studies

Fig. 4.3 presents  $\text{H}_2$ -TPD traces obtained over the 5 wt.% Ni/ $\text{Ce}_{0.8}\text{Pr}_{0.2}\text{O}_{2-\delta}$  (a) and 5 wt.% Ni/ $\text{Ce}_{1-x}\text{Zr}_x\text{O}_{2-\delta}$  ( $x = 0.2, 0.5$ ) catalysts (b and c) along with the traces obtained after deconvolution (Fig. 4.3d, Gaussian peak shape) of the recorded  $\text{H}_2$ -TPD over the 5 wt.% Ni/ $\text{Ce}_{0.8}\text{Zr}_{0.2}\text{O}_{2-\delta}$  (Fig. 4.3b). This deconvolution procedure does not entail an accurate estimation of the existing distribution of different Ni surfaces sites in each catalyst. It rather provides an approximate comparison of the three supported Ni catalysts, on the basis of the

binding strength between  $\text{Ni}_s$  and adsorbed H ( $E_{\text{Ni-H}}$ ,  $\text{kcal mol}^{-1}$ ). The peak maximum desorption temperatures ( $T_M$ ) and the amount of  $\text{H}_2$  desorption ( $\mu\text{mol g}^{-1}$ ), estimated after deconvolution of desorption traces recorded, are given in Table 4.2. The amount of  $\text{H}_2$  desorbed (up to  $600^\circ\text{C}$ ) was used to estimate the dispersion of Ni ( $D$ , %) and the mean Ni particle size ( $d_{\text{Ni}}$ , nm). The obtained results are reported in Table 4.2, where a good agreement between  $\text{H}_2$  chemisorption and powder XRD (Table 4.2, last column) is to be noted.

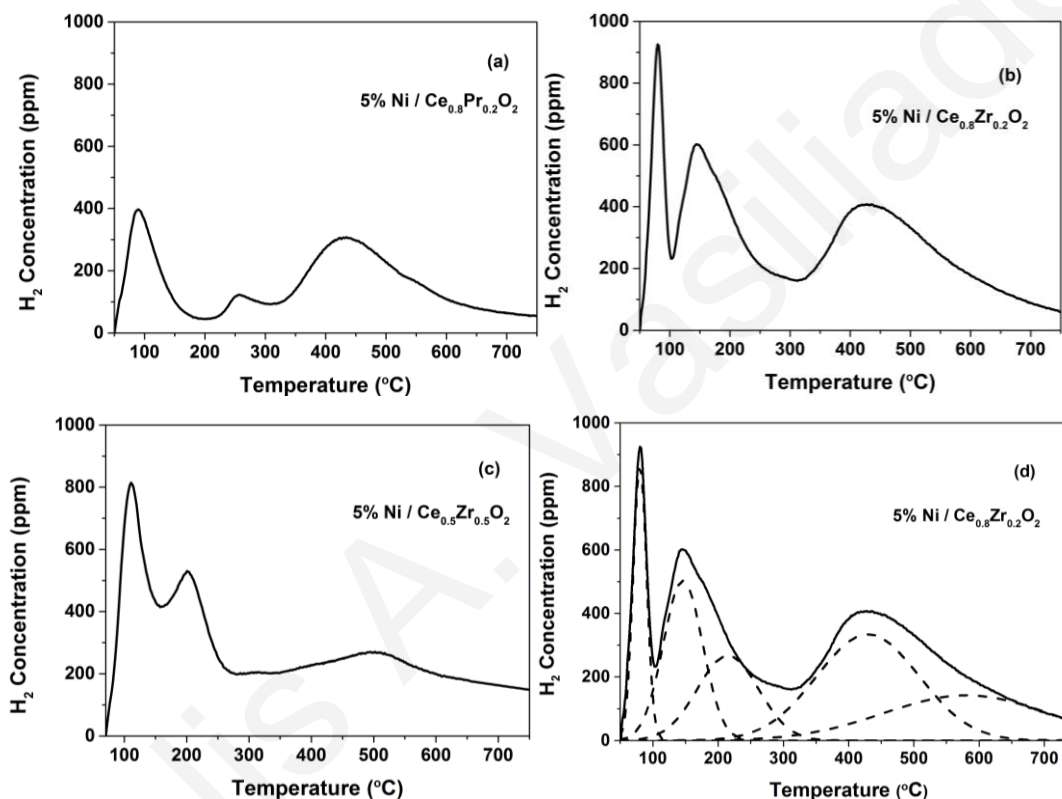


**Figure 4.3:**  $\text{H}_2$ -TPD traces obtained over 5 wt.%  $\text{Ni}/\text{Ce}_{0.8}\text{Pr}_{0.2}\text{O}_{2-\delta}$  (a) and 5 wt.%  $\text{Ni}/\text{Ce}_{1-x}\text{Zr}_x\text{O}_{2-\delta}$  ( $x = 0.2, 0.5$ ) catalysts (b)-(c). Deconvoluted  $\text{H}_2$ -TPD trace obtained over the 5 wt.%  $\text{Ni}/\text{Ce}_{0.8}\text{Zr}_{0.2}\text{O}_{2-\delta}$  catalyst (d).  $F_{\text{He}} = 50 \text{ NmL min}^{-1}$ ;  $\beta = 30^\circ\text{C min}^{-1}$ ;  $W = 0.5 \text{ g}$ .

According to the results of Fig. 4.3 and Table 4.2, it is rather clear that the support chemical composition ( $\text{Zr}^{4+}$  vs  $\text{Pr}^{3+}$  and Ce/Zr ratio) largely influences the heterogeneity of the Ni surface (e.g.  $E_{\text{Ni-H}}$  bond strength (via  $T_M$ ), and the distribution of  $\text{Ni}_s$  hydrogen chemisorption sites). The dispersion ( $D_{\text{Ni}}$ , %) of Ni metal was found to be 3.5, 6.5 and 6.2% for the 5 wt.% Ni supported on  $\text{Ce}_{0.8}\text{Pr}_{0.2}\text{O}_{2-\delta}$ ,  $\text{Ce}_{0.8}\text{Zr}_{0.2}\text{O}_{2-\delta}$  and  $\text{Ce}_{0.5}\text{Zr}_{0.5}\text{O}_{2-\delta}$ , respectively, providing a mean Ni particle size ( $d_{\text{Ni}}$ , nm) of 27.7, 14.9 and 15.6 nm, respectively (Table 4.2). The 5 wt.%  $\text{Ni}/\text{Ce}_{0.8}\text{Pr}_{0.2}\text{O}_{2-\delta}$  solid has the lowest Ni dispersion (largest particle size) but it was found to be

the most active catalyst towards DRM. Similar  $\text{H}_2$ -TPD traces have been reported for the 15 wt.% Ni/ $\text{Ce}_{0.12}\text{Zr}_{0.88}\text{O}_2$ , 5 wt.% Ni/ $\text{Ce}_{1-x}\text{Zr}_x\text{O}_2$  and 5 wt.% Ni/ $\text{Al}_2\text{O}_3$ -CaO solids [17,18], where in all cases the high-T hydrogen desorption states were interpreted as due to strongly adsorbed H arising from some electronic modifications of small Ni crystallites which interact intimately with the support (formation of  $\text{Ni}^{2+}$  sites).

#### 4.1.1.4. Catalysts performance in DRM

Fig. 4.4 presents the conversion (%) of  $\text{CH}_4$  and  $\text{CO}_2$  (a) and the  $\text{H}_2$ -yield (%) and  $\text{H}_2/\text{CO}$  gas product ratio (b) obtained after 1 h of dry reforming of methane in the 550-750 °C temperature range over the 5 wt.% Ni/ $\text{Ce}_{0.8}\text{Pr}_{0.2}\text{O}_{2-\delta}$  catalyst. It is noted that no  $\text{C}_2\text{H}_6$  was formed within the whole temperature range of 550-750 °C investigated. By increasing the reaction temperature from 550 to 750 °C, the catalytic activity increases considerably according to the endothermic nature of the reaction;  $X_{\text{CH}_4}$  increases from 14.3 to 71.5% with increasing reaction T from 550 to 750 °C. It should be noted that the  $\text{CO}_2$  conversion (%) is larger than that of  $\text{CH}_4$  in the temperature range of 550-750 °C. The  $\text{H}_2/\text{CO}$  gas product ratio (Fig. 4.4b) takes low values in the 550-600 °C range (ca. 0.44-0.58) but significantly larger values (0.82-1.2, most desirables ones for FT applications) at higher temperatures.

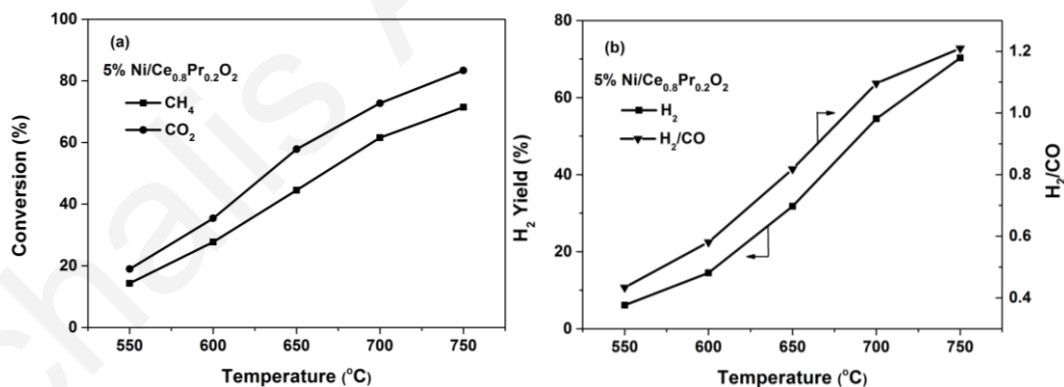


**Figure 4.4:** Conversion (%) of  $\text{CH}_4$  and  $\text{CO}_2$  (a) and  $\text{H}_2$ -yield (%) and  $\text{H}_2/\text{CO}$  gas product ratio (b) obtained after 1 h of dry reforming of methane in the 550-750 °C range over the 5 wt.% Ni/ $\text{Ce}_{0.8}\text{Pr}_{0.2}\text{O}_{2-\delta}$  catalyst; GHSV = 30,000  $\text{h}^{-1}$ .

The conversion of  $\text{CH}_4$  (%) and  $\text{CO}_2$  (%), the  $\text{H}_2$  and CO product yields (%) and the  $\text{H}_2/\text{CO}$  gas product ratio obtained after 1 h of dry reforming over the other two 5 wt.% Ni/ $\text{Ce}_{1-x}\text{Zr}_x\text{O}_{2-\delta}$  ( $x = 0.2, 0.5$ ) catalytic systems are reported in Table 4.3. It is shown that doping

of ceria with  $\text{Pr}^{3+}$  at the level of 20 atom-% results in a significant improvement in all DRM catalytic performance parameters when compared with the  $\text{Zr}^{4+}$ -doped ceria supports. In particular, at 550 °C the  $X_{\text{CH}_4}$  (%) increases by a factor of 1.54 and the  $X_{\text{CO}_2}$  (%) by a factor of 1.12. Also, the  $\text{H}_2$  and CO yields are increased by a factor of 1.24 and 1.16, respectively, and the  $\text{H}_2/\text{CO}$  gas product ratio is increased by a factor of 1.1. On the other hand, by increasing the  $\text{Zr}^{4+}$ -content from 20 to 50 atom-%, a significant decrease in the catalytic performance is observed. More specific, at 550 °C the  $X_{\text{CH}_4}$  (%),  $X_{\text{CO}_2}$  (%),  $\text{H}_2$ -yield, CO- yield and the  $\text{H}_2/\text{CO}$  gas product ratio decrease by a factor of 3.0, 1.43, 1.96, 1.37, and 1.43, respectively.

Intrinsic kinetic rates of the DRM reaction (after 1 h on reaction stream,  $X_{\text{CH}_4} < 14\%$ ) in terms of  $\text{TOF}_{\text{CH}_4}$  ( $\text{s}^{-1}$ ) were estimated. It was found that 5 wt.% Ni supported on  $\text{Ce}_{0.8}\text{Pr}_{0.2}\text{O}_{2-\delta}$  with Ni particles of  $\sim 28$  nm exhibits 2.9 and 8.3 times larger  $\text{TOF}_{\text{CH}_4}$  compared to  $\text{Ce}_{0.8}\text{Zr}_{0.2}\text{O}_{2-\delta}$  ( $\text{TOF}_{\text{CH}_4} = 0.233 \text{ s}^{-1}$ ) and  $\text{Ce}_{0.5}\text{Zr}_{0.5}\text{O}_{2-\delta}$  ( $\text{TOF}_{\text{CH}_4} = 0.081 \text{ s}^{-1}$ ) carriers with smaller Ni particles ( $\sim 15$  nm);  $\text{TOF}_{\text{CH}_4} = 0.675 \text{ s}^{-1}$  (5 wt.% Ni/ $\text{Ce}_{0.8}\text{Pr}_{0.2}\text{O}_{2-\delta}$ ).

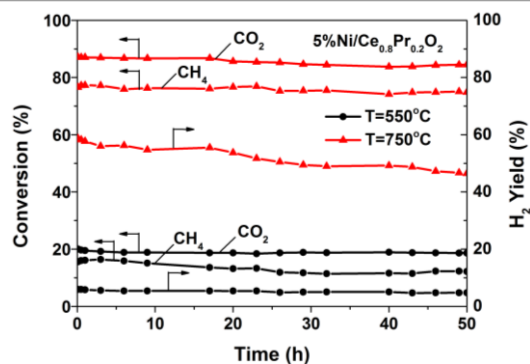
Dry reforming of methane conducted at 750 °C over the  $\text{Ce}_{0.8}\text{Pr}_{0.2}\text{O}_{2-\delta}$  support alone, and using the same feed gas composition and GHSV as in the case of 5 wt.% Ni/ $\text{Ce}_{0.8}\text{Pr}_{0.2}\text{O}_{2-\delta}$  catalyst, resulted in  $X_{\text{CO}_2} = 0.2\%$ ,  $X_{\text{CH}_4} = 0.1\%$ , and CO and  $\text{H}_2$  product yields of 1.25% and 0.1%, respectively. Based on these results and those presented in Fig. 4.4 and Table 4.3, it appears that the presence of Ni is essential, but Ni-support interactions likely influence the activity and selectivity of the DRM reaction.

Figure 4.5 shows the conversion of  $\text{CO}_2$  (%) and  $\text{CH}_4$  (%), and the  $\text{H}_2$ -yield (%) obtained after 50 h of DRM reaction at 550 and 750 °C over the most active 5 wt.% Ni/ $\text{Ce}_{0.8}\text{Pr}_{0.2}\text{O}_{2-\delta}$  catalyst (Table 4.3). The  $\text{CO}_2$  and  $\text{CH}_4$  conversions and the  $\text{H}_2$ -yield at 550 °C appear extremely stable over the period of 50-h on reaction stream. At 750 °C, a small drop ( $< 6\%$ ) is evident resulting in a drop of  $\text{H}_2$ -yield by about 18%. XRD patterns recorded after 50 h of DRM at 550 and 750 °C over the 5 wt.% Ni/ $\text{Ce}_{0.8}\text{Pr}_{0.2}\text{O}_{2-\delta}$  catalyst reveal that the primary crystal size of both the support and Ni metal phases are increased (Tables 5.1 and 5.2). Specifically, at 750 °C the crystal size of support increases from 16.7 to 23.6 nm and that of Ni from 28.7 to 32.5 nm. Furthermore, the  $\text{Ce}_{0.8}\text{Pr}_{0.2}\text{O}_{2-\delta}$  support preserves its cubic crystal structure, where no diffraction peaks related to NiO were detected. On the other hand, the amount of inactive “carbon” formed, as will be shown next, is decreased with increasing reaction time (from 1 h to 50 h).

**Table 4.3:** Conversion of  $\text{CH}_4$  and  $\text{CO}_2$  (%),  $\text{H}_2$  and  $\text{CO}$  yield (%) and  $\text{H}_2/\text{CO}$  gas product ratio obtained during Dry Reforming of Methane ( $T = 550\text{-}750$  °C; 1 h on stream;  $\text{GHSV} = 30,000$   $\text{h}^{-1}$ ) over 5 wt.%  $\text{Ni}/\text{Ce}_{0.8}\text{Pr}_{0.2}\text{O}_2$  and 5 wt.%  $\text{Ni}/\text{Ce}_{1-x}\text{Zr}_x\text{O}_{2-\delta}$  ( $x = 0.2, 0.5$ ) catalysts.  $P_{\text{CH}_4} = 0.2$  bar;  $P_{\text{CO}_2} = 0.2$  bar;  $P_{\text{He}} = 0.6$  bar.

Catalyst	T (°C)	$X_{\text{CH}_4}$ (%)	$X_{\text{CO}_2}$ (%)	Yield $\text{H}_2$ (%)	Yield $\text{CO}$ (%)	$\text{H}_2/\text{CO}$
<b>Ni/Ce<sub>0.8</sub>Pr<sub>0.2</sub>O<sub>2</sub></b>	550	14.3	19.0	6.1	14.0	0.44
	600	27.7	35.4	14.5	24.9	0.58
	650	44.6	57.8	31.8	38.9	0.82
	700	61.6	72.7	54.5	49.8	1.10
	750	71.5	83.4	70.3	58.1	1.20
<b>Ni/Ce<sub>0.8</sub>Zr<sub>0.2</sub>O<sub>2</sub></b>	550	9.3	17.0	4.9	12.1	0.40
	600	25.7	32.7	13.0	22.9	0.57
	650	41.5	48.0	26.1	34.6	0.75
	700	55.7	65.8	38.9	45.2	0.86
	750	67.9	77.2	51.7	54.6	0.95
<b>Ni/Ce<sub>0.5</sub>Zr<sub>0.5</sub>O<sub>2</sub></b>	550	3.1	11.9	2.5	8.8	0.28
	600	14.5	16.5	4.1	11.5	0.36
	650	20.7	21.8	6.0	16.0	0.38
	700	14.7	23.35	5.5	16.5	0.33
	750	19.7	26.1	5.8	17.9	0.32

These above results suggest that the relatively small drop of  $\text{H}_2$ -yield (%) after 50 h of dry reforming is due either to morphological/structural changes of the Ni and support phases (partial loss of active catalytic sites on Ni and the Ni-support interface) or to the removal of inactive “carbon” via hydrogenation. The latter is supported by transient isothermal hydrogenation studies described in the following section.



**Figure 4.5:** Stability test of the dry reforming of methane reaction in terms of  $\text{CO}_2$  and  $\text{CH}_4$  conversion (%) and  $\text{H}_2$ -yield (%) performed at  $T = 550$  and  $750$  °C over the 5 wt.%  $\text{Ni}/\text{Ce}_{0.8}\text{Pr}_{0.2}\text{O}_2$  catalyst for 50 h on reaction stream;  $\text{GHSV} = 30,000 \text{ h}^{-1}$ .

#### 4.1.2. Characterisation of “carbon” formed during DRM by various transient techniques

##### 4.1.2.1. Transient isothermal hydrogenation (TIH)

Fig. 4.6a shows transient response curves of  $\text{CH}_4$  obtained during the 10-min isothermal hydrogenation of the “carbon” formed after 1 h of dry methane reforming at 550 °C over the 5 wt.% Ni supported on  $\text{Ce}_{0.8}\text{Pr}_{0.2}\text{O}_{2-\delta}$  (A),  $\text{Ce}_{0.8}\text{Zr}_{0.2}\text{O}_{2-\delta}$  (B) and  $\text{Ce}_{0.5}\text{Zr}_{0.5}\text{O}_{2-\delta}$  (C) carriers. The  $\text{CH}_4$  peak maximum appears at  $t_m = 0.5$ , 0.5 and 1.9 min for the  $\text{Ni}/\text{Ce}_{0.8}\text{Pr}_{0.2}\text{O}_{2-\delta}$ ,  $\text{Ni}/\text{Ce}_{0.8}\text{Zr}_{0.2}\text{O}_{2-\delta}$  and  $\text{Ni}/\text{Ce}_{0.5}\text{Zr}_{0.5}\text{O}_{2-\delta}$  catalysts, respectively. For the  $\text{Ni}/\text{Ce}_{0.8}\text{M}_{0.2}\text{O}_{2-\delta}$  ( $\text{M} = \text{Zr}^{4+}$  and  $\text{Pr}^{3+}$ ) catalysts, the peak maximum appeared at lower hydrogenation times compared to the  $\text{Ni}/\text{Ce}_{0.5}\text{Zr}_{0.5}\text{O}_{2-\delta}$  solid, result that suggests the formation of a more active kind of “carbon”. The shape of the  $\text{CH}_4$  trace for  $\text{Ni}/\text{Ce}_{0.8}\text{Pr}_{0.2}\text{O}_{2-\delta}$  probes for at least two kinds of “carbon” (Fig. 4.6a, curve A). Figure 4.6b presents the trace of the TPH step performed following the TIH one. It is seen that hydrogenation of all “carbon” formed after 1 h of dry reforming is completed at 700 °C, and the amount of “carbon” reacted during TPH is small compared to that reacted isothermally at 550 °C. The amount ( $\mu\text{mol g}^{-1}$ ) of “carbon” estimated under the TIH and TPH hydrogenation steps is found to be 233.0, 51.8 and 179.9  $\mu\text{mol g}^{-1}$  for the 5 wt.% Ni supported on  $\text{Ce}_{0.8}\text{Pr}_{0.2}\text{O}_{2-\delta}$ ,  $\text{Ce}_{0.8}\text{Zr}_{0.2}\text{O}_{2-\delta}$  and  $\text{Ce}_{0.5}\text{Zr}_{0.5}\text{O}_{2-\delta}$  carriers, respectively. The  $\text{Ni}/\text{Ce}_{0.8}\text{Pr}_{0.2}\text{O}_{2-\delta}$  catalyst with the best catalytic activity (Table 4.3) has shown the largest amount of “carbon” amongst the other two catalysts, and this result is discussed next in relation to the stability performance of the  $\text{Ni}/\text{Ce}_{0.8}\text{Pr}_{0.2}\text{O}_{2-\delta}$  catalyst.



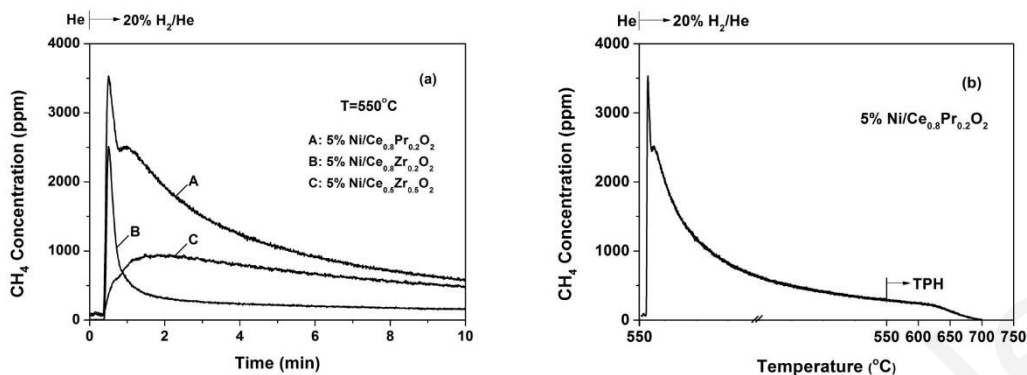


**Figure 4.6:** (a) Transient response curves of CH<sub>4</sub> concentration obtained during isothermal hydrogenation (TIH) of “carbon” formed after 1 h of dry reforming at 550 °C (GHSV = 30,000 h<sup>-1</sup>) over 5 wt.% Ni supported on (A) Ce<sub>0.8</sub>Pr<sub>0.2</sub>O<sub>2</sub>, (B) Ce<sub>0.8</sub>Zr<sub>0.2</sub>O<sub>2</sub> and (C) Ce<sub>0.5</sub>Zr<sub>0.5</sub>O<sub>2</sub> carriers. Gas delivery sequence: 20% CH<sub>4</sub>/20% CO<sub>2</sub>/He (550 °C, 1 h) → He (550 °C, 15 min) → 20% H<sub>2</sub>/He (550 °C, t); (b) TPH following TIH over the 5 wt.% Ni/Ce<sub>0.8</sub>Pr<sub>0.2</sub>O<sub>2</sub> catalyst.

#### 4.1.2.2. Temperature programmed oxidation (TPO)

Fig. 4.7 presents CO<sub>2</sub> and CO temperature-programmed oxidation (TPO) of “carbon” traces obtained over the 5 wt.% Ni/Ce<sub>0.8</sub>Pr<sub>0.2</sub>O<sub>2-δ</sub> catalyst after 1 h or 50 h of dry reforming of methane conducted at 750 °C.

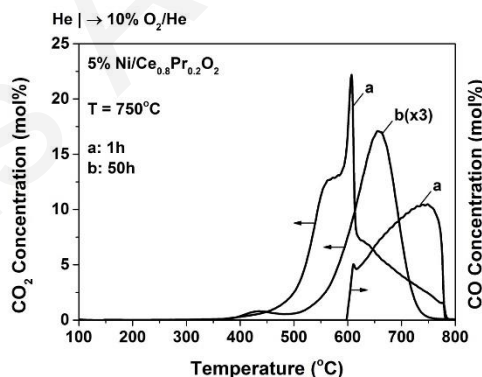


**Figure 4.7:** Transient response curves of CO<sub>2</sub> and CO concentrations (mol%) obtained during TPO of “carbon” formed after 1 h (a) and 50 h (b) of dry reforming of methane conducted at 750 °C (GHSV = 30,000 h<sup>-1</sup>) over a 5 wt.% Ni/Ce<sub>0.8</sub>Pr<sub>0.2</sub>O<sub>2</sub> catalyst. Gas delivery sequence: DRM (750 °C, 1 h or 50 h) → He gas flow, increase T to 800 °C and stay until no CO/CO<sub>2</sub> are measured in the MS → cool down in He gas flow to 100 °C → 10% O<sub>2</sub>/He (50 NmL min<sup>-1</sup>), T is increased to 800 °C ( $\beta = 30 \text{ }^\circ\text{C min}^{-1}$ ).

As clearly shown in Fig. 4.7, after 1 h of reaction (curve a), at least three kinds of “carbon” can be distinguished on the basis of the shape of the  $\text{CO}_2$ -TPO trace. A main sharp peak of  $\text{CO}_2$  can be seen at  $\sim 600$  °C with large shoulders in the rising and falling parts of the peak. The oxidation of these “carbon” species starts at  $\sim 350$  °C and almost ends when the catalyst reaches the temperature of 800 °C. A large signal of CO is also formed, which starts at 600 °C and ends at  $\sim 780$  °C (Fig. 4.7a). The amounts of  $\text{CO}_2$  and CO produced were found to be 4.9 and 3.4 mmol  $\text{g}^{-1}$ , respectively. A similar TPO experiment performed after 50 h of dry reforming at 750 °C provides a totally different trace of  $\text{CO}_2$  (Fig. 4.7b) when compared to that obtained after 1 h of reaction (Fig. 4.7a). A very small  $\text{CO}_2$  peak centred at  $\sim 430$  °C and a significantly larger one centred at  $\sim 640$  °C are discernible. Furthermore, only a very small trace of CO was measured (not shown) as opposed to the case of 1 h on reaction stream. The amounts of  $\text{CO}_2$  and CO were found to be 1.42 and 0.067 mmol  $\text{g}^{-1}$ , respectively. The total amount of “carbon” formed after 1 h and 50 h of reaction was found to be 99.72 and 17.5 mg C  $\text{g}^{-1}$  (1.75 wt.%), respectively. Thus, this specific catalytic system does not progressively accumulate “carbon” but a *significant progressive decrease in “carbon” formation* with increasing reaction time does take place. This important result will be discussed next in relation to the excellent stability characteristics of this particular 5 wt.% Ni/ $\text{Ce}_{0.8}\text{Pr}_{0.2}\text{O}_{2-\delta}$  catalytic system.

#### 4.1.2.3. Quantifying the origin of “carbon” formation ( $\text{CH}_4$ versus $\text{CO}_2$ )

Figs. 4.8 and 4.9 present  $^{12}\text{CO}_2$  and  $^{13}\text{CO}_2$  transient response curves recorded during TPO of the “carbon” formed over the 5 wt.% Ni/ $\text{Ce}_{0.5}\text{Zr}_{0.5}\text{O}_{2-\delta}$  and 5 wt.% Ni/ $\text{Ce}_{0.8}\text{Pr}_{0.2}\text{O}_{2-\delta}$  catalysts, respectively, after 30 min of dry reforming (5%  $^{13}\text{CO}_2$ /5%  $^{12}\text{CH}_4$ /He) at 550 and 750 °C. The different shapes in the obtained  $^{13}\text{CO}_2$  and  $^{12}\text{CO}_2$  response curves for the two catalysts and their relative amounts (area under the response curve) are apparent. In the case of dry reforming at 550 °C over the 5 wt.% Ni/ $\text{Ce}_{0.5}\text{Zr}_{0.5}\text{O}_{2-\delta}$ , the  $^{13}\text{CO}_2$  response exhibits two main peaks centred at  $\sim 230$  and  $\sim 380$  °C with a shoulder at the rising part of the high-T peak (Fig. 4.8a). A largely different  $^{13}\text{CO}_2$ -TPO trace was obtained in the case of 5 wt.% Ni/ $\text{Ce}_{0.8}\text{Pr}_{0.2}\text{O}_{2-\delta}$ , where only one  $^{13}\text{CO}_2$  peak centred at  $\sim 460$  °C with a shoulder at the high-T side is obtained (Fig. 4.9a). A similar behaviour is observed when dry reforming was performed at 750 °C (Figs. 4.8b, 4.9b).

The  $^{13}\text{CO}_2$ -TPO response arises from the oxidation of  $^{13}\text{C}$ -containing carbon species formed via the  $^{13}\text{CO}_2$  activation route, whereas that of  $^{12}\text{CO}_2$ -TPO from the oxidation of  $^{12}\text{C}$ -

containing carbon species formed via the  $^{12}\text{CH}_4$  activation (decomposition) route. The  $^{12}\text{CO}_2$ -TPO response curves shown in Figs. 4.8 and 4.9 are largely different in shape, position and quantity, with the support composition to have a clear influence. In the case of 5 wt.% Ni/ $\text{Ce}_{0.8}\text{Zr}_{0.2}\text{O}_{2-\delta}$  catalyst, very similar  $^{12}\text{CO}_2$ - and  $^{13}\text{CO}_2$ -TPO response curves to those observed over the Ni/ $\text{Ce}_{0.8}\text{Pr}_{0.2}\text{O}_{2-\delta}$  are obtained.

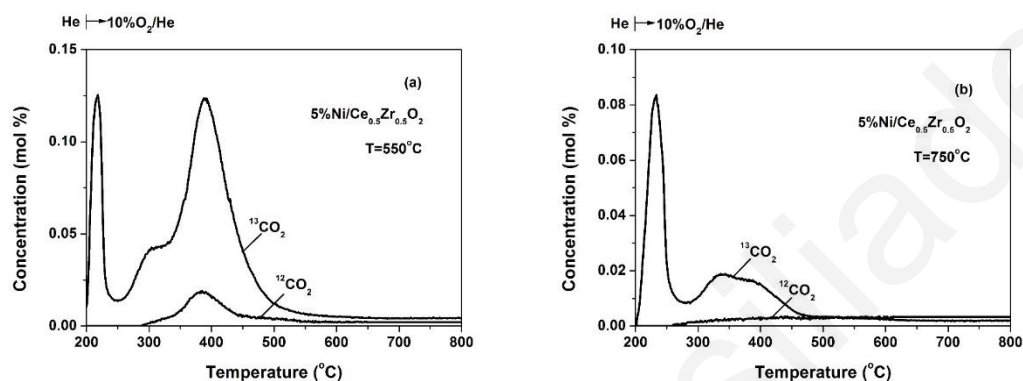


**Figure 4.8:** Temperature-programmed oxidation (TPO) to  $^{12}\text{CO}_2$  and  $^{13}\text{CO}_2$  of “carbon” formed after 30 min of DRM at 550 °C (a) and 750 °C (b) over the 5 wt.% Ni/ $\text{Ce}_{0.5}\text{Zr}_{0.5}\text{O}_2$  catalyst. Gas delivery sequence: 5%  $^{13}\text{CO}_2$ /5%  $^{12}\text{CH}_4$ /45% Ar/45% He (T, 30 min) → He (800 °C, 15 min) → cool down in He flow to 100 °C → 10%  $\text{O}_2$ /He (50  $\text{NmL min}^{-1}$ ), T is increased to 800 °C (TPO,  $\beta = 30 \text{ °C min}^{-1}$ ); DRM reaction conditions:  $F_T = 100 \text{ NmL min}^{-1}$ ;  $W = 0.5 \text{ g}$ .

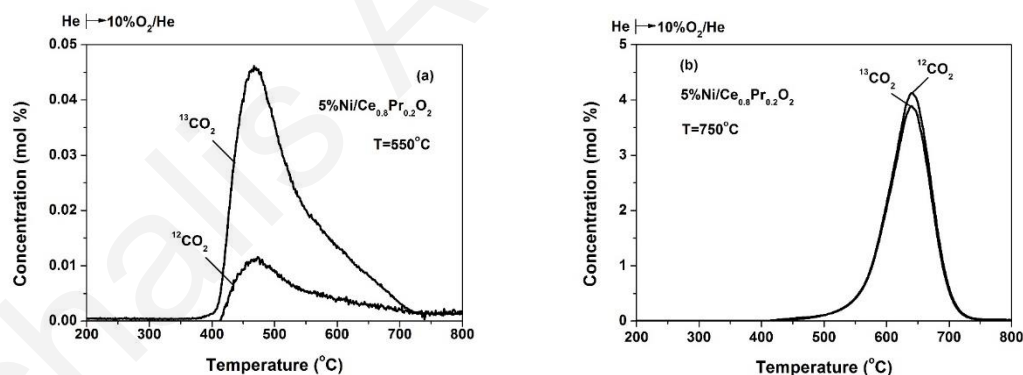


**Figure 4.9:** Temperature-programmed oxidation (TPO) to  $^{12}\text{CO}_2$  and  $^{13}\text{CO}_2$  of “carbon” formed after 30 min of DRM at 550 °C (a) and 750 °C (b) over the 5 wt.% Ni/ $\text{Ce}_{0.8}\text{Pr}_{0.2}\text{O}_2$  catalyst. Gas delivery sequence: 5%  $^{13}\text{CO}_2$ /5%  $^{12}\text{CH}_4$ /45% Ar/45% He (T, 30 min) → He (800 °C, 15 min) → cool down in He flow to 100 °C → 10%  $\text{O}_2$ /He (50  $\text{NmL min}^{-1}$ ), T is increased to 800 °C (TPO,  $\beta = 30 \text{ °C min}^{-1}$ ); DRM reaction conditions:  $F_T = 100 \text{ NmL min}^{-1}$ ;  $W = 0.5 \text{ g}$ .

**Table 4.4:**  $^{12}\text{CO}_2$  and  $^{13}\text{CO}_2$  ( $\mu\text{mol g}^{-1}$ ) and  $^{12}\text{CO}_2/^{13}\text{CO}_2$  product gas ratio obtained during temperature-programmed oxidation (TPO) to  $^{12}\text{CO}_2$  and  $^{13}\text{CO}_2$  of “carbon” formed after 1 h of dry reforming using 5%  $^{13}\text{CO}_2/5\%$   $^{12}\text{CH}_4/45\%$  Ar/45% He at 550 and 750 °C over the 5 wt.% Ni/ $\text{Ce}_{0.8}\text{Pr}_{0.2}\text{O}_2$  and 5 wt.% Ni/ $\text{Ce}_{1-x}\text{Zr}_x\text{O}_{2-\delta}$  ( $x = 0.2, 0.5$ ) catalysts.

Catalyst	T(°C)	$^{12}\text{CO}_2$ ( $\mu\text{mol g}^{-1}$ )	$^{13}\text{CO}_2$ ( $\mu\text{mol g}^{-1}$ )	$^{12}\text{CO}_2/^{13}\text{CO}_2$	Total “carbon” ( $\mu\text{mol g}^{-1}$ )
Ni/ $\text{Ce}_{0.8}\text{Pr}_{0.2}\text{O}_2$	550	2.4	8.6	0.29	11 (0.01) <sup>a</sup>
	750	494.2	464.1	1.06	958.3 (1.15)
Ni/ $\text{Ce}_{0.8}\text{Zr}_{0.2}\text{O}_2$	550	4.8	11.9	0.40	16.7 (0.02)
	750	504.5	473.2	1.07	977.7 (1.17)
Ni/ $\text{Ce}_{0.5}\text{Zr}_{0.5}\text{O}_2$	550	3.7	24.4	0.15	28.1 (0.03)
	750	2.4	8.2	0.29	10.6 (0.01)

<sup>a</sup> values in parentheses provides the equivalent wt.% carbon ( $\text{g}_\text{C} / \text{g}_{\text{cat}}$ ).

Table 4.4 reports the amounts ( $\mu\text{mol g}^{-1}$ ) of  $^{12}\text{CO}_2$  and  $^{13}\text{CO}_2$  and the  $^{12}\text{CO}_2/^{13}\text{CO}_2$  molar ratio obtained during TPO of the “carbon” formed after dry reforming at 550 and 750 °C over the three catalysts investigated. It is seen that in the case of  $\text{Ce}_{0.8}\text{Pr}_{0.2}\text{O}_{2-\delta}$  and  $\text{Ce}_{0.8}\text{Zr}_{0.2}\text{O}_{2-\delta}$  carriers, after increasing the reaction temperature from 550 to 750 °C, the amounts of  $^{12}\text{CO}_2$  and  $^{13}\text{CO}_2$  formed are increased significantly. In fact, for the Ni/ $\text{Ce}_{0.8}\text{Pr}_{0.2}\text{O}_{2-\delta}$ , the total “carbon” formed was increased 87 times, whereas for the  $\text{Ce}_{0.5}\text{Zr}_{0.5}\text{O}_{2-\delta}$  carrier a decrease in “carbon” formation with increasing reaction temperature is noticed. It should be noted, however, that Ni/ $\text{Ce}_{0.5}\text{Zr}_{0.5}\text{O}_{2-\delta}$  presents significantly lower activity than the other two catalysts (Table 4.3). At 750 °C, 5 wt.% Ni supported on  $\text{Ce}_{0.8}\text{Zr}_{0.2}\text{O}_{2-\delta}$  or  $\text{Ce}_{0.8}\text{Pr}_{0.2}\text{O}_{2-\delta}$  forms practically the same amount of “carbon”, whereas at 550 °C the 5 wt.% Ni/ $\text{Ce}_{0.5}\text{Zr}_{0.5}\text{O}_{2-\delta}$  exhibits the largest amount of “carbon”, whereas the 5 wt.% Ni/ $\text{Ce}_{0.8}\text{Pr}_{0.2}\text{O}_{2-\delta}$  the lowest one (Table 4.4). The ratio  $^{12}\text{CO}_2/^{13}\text{CO}_2$  obtained (TPO experiments) describes in a quantitative manner the *contribution of each reactant molecule ( $\text{CH}_4$  vs.  $\text{CO}_2$ ) to the formation of “carbon”* during dry reforming of methane. This ratio is found to increase significantly with reaction temperature (ca. 550 to 750 °C) for all three catalysts (Table 4.4).

#### 4.1.2.4. Probing the extent of Boudouard reaction in the presence of $\text{CH}_4$ towards “carbon” formation

Fig. 4.10a presents the transient isothermal evolution of  $\text{H}_2$ ,  $^{12}\text{CO}$ ,  $^{12}\text{CO}_2$  and  $^{13}\text{CO}_2$  gaseous species obtained at the switch  $\text{He} \rightarrow 5\% \text{ } ^{13}\text{CO}/5\% \text{ } ^{12}\text{CH}_4/\text{Ar}/\text{He}$  ( $750 \text{ } ^\circ\text{C}$ , t) over the 5 wt.%  $\text{Ni}/\text{Ce}_{0.8}\text{Pr}_{0.2}\text{O}_2$  catalyst.

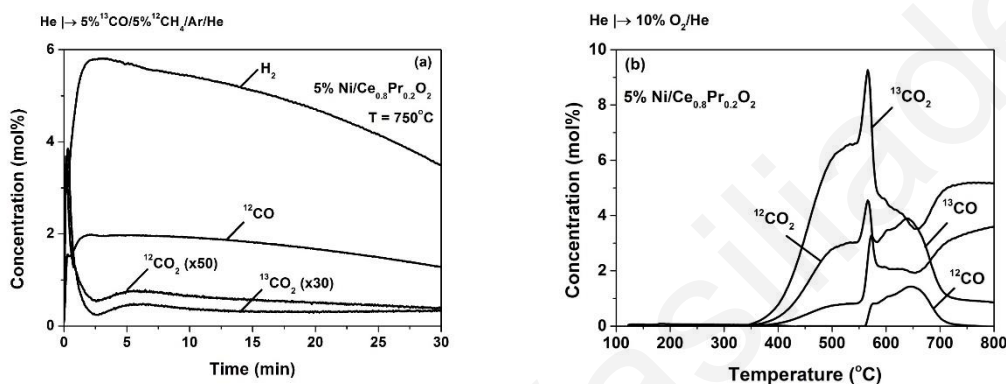


**Figure 4.10:** (a) Transient response curves of  $\text{H}_2$ ,  $^{12}\text{CO}$ ,  $^{13}\text{CO}$ ,  $^{12}\text{CO}_2$  and  $^{13}\text{CO}_2$  obtained at  $750 \text{ } ^\circ\text{C}$  during the gas switch:  $\text{He}$  ( $100 \text{ NmL min}^{-1}$ ,  $750 \text{ } ^\circ\text{C}$ )  $\rightarrow$   $5\% \text{ } ^{13}\text{CO}/5\% \text{ } ^{12}\text{CH}_4/45\% \text{ Ar}/45\% \text{ He}$  ( $100 \text{ NmL min}^{-1}$ ,  $750 \text{ } ^\circ\text{C}$ , t); (b) Transient response curves of  $^{12}\text{CO}$ ,  $^{13}\text{CO}$ ,  $^{12}\text{CO}_2$  and  $^{13}\text{CO}_2$  obtained during TPO ( $10\% \text{ O}_2/\text{He}$ ,  $50 \text{ NmL min}^{-1}$ ) following (a) over the 5 wt.%  $\text{Ni}/\text{Ce}_{0.8}\text{Pr}_{0.2}\text{O}_2$  catalyst. Gas delivery sequence:  $5\% \text{ } ^{13}\text{CO}/5\% \text{ } ^{12}\text{CH}_4/45\% \text{ Ar}/45\% \text{ He}$  ( $750 \text{ } ^\circ\text{C}$ ,  $30 \text{ min}$ )  $\rightarrow$   $\text{He}$  ( $800 \text{ } ^\circ\text{C}$ ,  $15 \text{ min}$ )  $\rightarrow$  cool down in  $\text{He}$  flow to  $100 \text{ } ^\circ\text{C}$   $\rightarrow$   $10\% \text{ O}_2/\text{He}$  ( $50 \text{ NmL min}^{-1}$ ), T is increased to  $800 \text{ } ^\circ\text{C}$  (TPO,  $\beta = 30 \text{ } ^\circ\text{C min}^{-1}$ );  $W = 0.5 \text{ g}$ .

It is clearly seen that large  $\text{H}_2$  and  $^{12}\text{CO}$  transient formation rates but small  $^{12}\text{CO}_2$  and  $^{13}\text{CO}_2$  ones are obtained over the period of 30-min on reaction stream. A sharp increase in the rate of formation of the respective gas is noted at the gas switch. The  $\text{H}_2$  and  $^{12}\text{CO}$  transient response curves pass through a maximum after about 2 min on reaction stream, with the  $^{12}\text{CO}$  response to present a slow decay and the  $\text{H}_2$  response a larger one. On the other hand, the  $^{12}\text{CO}_2$  and  $^{13}\text{CO}_2$  transient response curves after the first sharp increase at the gas switch show a second rate maximum at a larger time ( $\sim 6 \text{ min}$ ).

The large formation rate of  $\text{H}_2$  is the result of  $\text{CH}_4$  decomposition on the  $\text{Ni}^0$  surface, which diminishes with time on stream due to the accumulation of “carbon”. This catalytic reaction process occurs in the presence of  $^{13}\text{CO}(\text{g})$ . The formation of  $^{13}\text{CO}_2$  is the result of the Boudouard reaction when  $^{13}\text{CO}$  is co-fed in the reactor with  $^{12}\text{CH}_4$ , and which takes place on

the Ni surface at the same time with the  $^{12}\text{CH}_4$  decomposition. The formation of  $^{12}\text{CO}$  is the result of the reaction of  $^{12}\text{CH}_4$  with  $^{13}\text{CO}_2$  (dry reforming of methane), the latter formed via the Boudouard reaction of  $^{13}\text{CO}(\text{g})$ , whereas the formation of  $^{12}\text{CO}_2$  is the result of the latter reaction with  $^{12}\text{CO}(\text{g})$ . The large similarity in the shape of the transient rate responses of  $^{12}\text{CO}_2$  and  $^{13}\text{CO}_2$  is noted. The amounts of  $\text{H}_2$ ,  $^{12}\text{CO}$ ,  $^{12}\text{CO}_2$  and  $^{13}\text{CO}_2$  formed during the 30-min  $^{13}\text{CO}/^{12}\text{CH}_4/\text{Ar}/\text{He}$  gas treatment of the catalyst were found to be 12.22, 4.34, 0.03 and 0.035  $\text{mmol g}^{-1}$ , respectively.

Fig. 4.10b presents the transient evolution of  $^{12}\text{CO}$ ,  $^{13}\text{CO}$ ,  $^{12}\text{CO}_2$  and  $^{13}\text{CO}_2$  gaseous species recorded during TPO following the 30-min  $^{13}\text{CO}/^{12}\text{CH}_4/\text{Ar}/\text{He}$  gas treatment of the catalyst (Fig. 4.10a). The formation of all gaseous species except  $^{12}\text{CO}$  starts at  $\sim 350$  °C, whereas that of  $^{12}\text{CO}$  at  $\sim 560$  °C. The formation of the various isotopic  $^{13}\text{CO}$  and  $^{13}\text{CO}_2$  gases is the result of the oxidation of “carbon” formed after  $^{13}\text{CO}/^{12}\text{CH}_4/\text{Ar}/\text{He}$  treatment of the catalyst at 750 °C (Fig. 4.10a). The appearance of: (i) multiple peaks, (ii) shoulders, and (iii) sharp increases in the rates of oxidation within a small temperature range probe for more than one kind of “carbon”, and likely complex kinetics of “carbon” oxidation. Of interest is the strong similarity in the shape and position of the  $^{12}\text{CO}_2$  and  $^{13}\text{CO}_2$  traces (Fig. 4.10b) as observed in the transient formation rates of the same species shown in Fig. 4.10a. The amounts of  $^{12}\text{CO}_2$ ,  $^{13}\text{CO}_2$ ,  $^{12}\text{CO}$  and  $^{13}\text{CO}$  obtained (after all signals reached their respective background value in the MS at 800 °C, Fig. 4.10b) were found to be 1.38, 2.62, 0.20 and 0.86  $\text{mmol g}^{-1}$ , respectively.

The analysis of the  $^{12}\text{C}$ -material balance for the experiments described in Figs. 4.10a and 4.10b is as follows. The amount of  $^{12}\text{C}$  originated from the  $^{12}\text{CH}_4$  fed in the reactor, and which had reacted during the  $^{13}\text{CO}/^{12}\text{CH}_4/\text{Ar}/\text{He}$  gas treatment (Fig. 4.10a), must be equal to the sum of the amounts of  $^{12}\text{CO}$  and  $^{12}\text{CO}_2$  (Fig. 4.10a) and that of  $^{12}\text{C}$ -deposition on the catalyst surface (Fig. 4.10b). This material balance does not account for any  $\text{CO}_2$  or  $^{12}\text{CH}_4$  chemisorbed on the catalyst surface (e.g. stable carbonates at 750 °C). The  $^{12}\text{CH}_4$  which was reacted must be equal to half the amount of  $\text{H}_2$  formed (one mol of  $^{12}\text{C}$  (ex.  $^{12}\text{CH}_4$ ) corresponds to two mols of  $\text{H}_2$ ). Based on the quantities provided above, it is shown that the  $^{12}\text{C}$ -material balance is satisfied within 5%. This result agrees very well with the fact that no reversibly adsorbed  $\text{CH}_4$  on the catalyst surface is expected at 750 °C, and that the concentration of stable carbonates on the support at 750 °C should be considered very small.

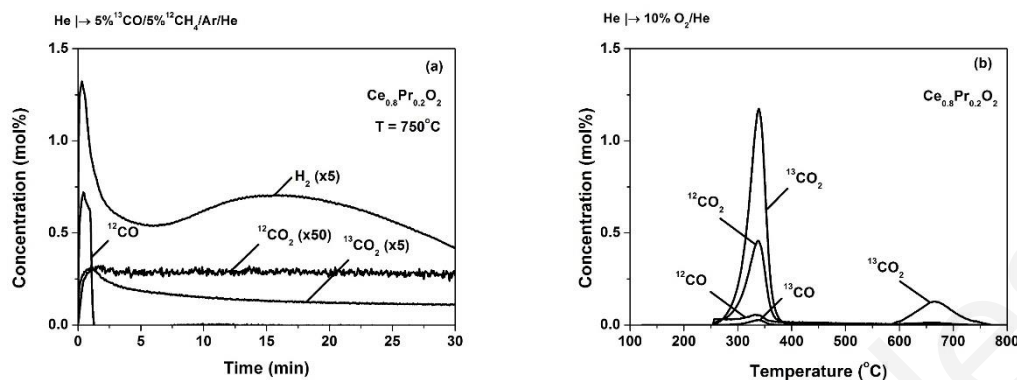


**Figure 4.11:** (a) Transient response curves of  $H_2$ ,  $^{12}CO$ ,  $^{13}CO$ ,  $^{12}CO_2$  and  $^{13}CO_2$  obtained at  $750^\circ C$  during the gas switch: He ( $100\text{ NmL min}^{-1}$ ,  $750^\circ C$ )  $\rightarrow$  5%  $^{13}CO$ /5%  $^{12}CH_4$ /45% Ar/45% He ( $100\text{ NmL min}^{-1}$ ,  $750^\circ C$ , t); (b) Transient response curves of  $^{12}CO$ ,  $^{13}CO$ ,  $^{12}CO_2$  and  $^{13}CO_2$  obtained during TPO (10%  $O_2$ /He,  $50\text{ NmL min}^{-1}$ ) following (a) over the  $Ce_{0.8}Pr_{0.2}O_2$  carrier alone. Gas delivery sequence: 5%  $^{13}CO$ /5%  $^{12}CH_4$ /45% Ar/45% He ( $750^\circ C$ , 30 min)  $\rightarrow$  He ( $800^\circ C$ , 15 min)  $\rightarrow$  cool down in He flow to  $100^\circ C$   $\rightarrow$  10%  $O_2$ /He ( $50\text{ NmL min}^{-1}$ ), T is increased to  $800^\circ C$  (TPO,  $\beta = 30^\circ C\text{ min}^{-1}$ );  $W = 0.5\text{ g}$ .

Similar experiments to those reported in Figs. 4.10a and 4.10b were performed on the  $Ce_{0.8}Pr_{0.2}O_2$  support alone. The results obtained are shown in Figs. 4.11a and 4.11b. It is illustrated that *the support alone does promote the  $CH_4$  decomposition and Boudouard reactions but to a small extent* according to the following quantities obtained. In the case of  $^{13}CO/^{12}CH_4$ /Ar/He gas treatment at  $750^\circ C$  (Fig. 4.11a), the amounts of  $H_2$ ,  $^{12}CO$ ,  $^{12}CO_2$  and  $^{13}CO_2$  formed were found to be  $310.0$ ,  $55.7$ ,  $14.0$  and  $73.0\ \mu\text{mol g}^{-1}$ , respectively. It should be noted: (i) the significantly larger amount of  $^{13}CO_2$  derived from the Boudouard reaction (Fig. 4.11b), and likely from the reduction of support  $^{16}O$  by  $^{13}CO$ , when compared to the amount of  $^{12}CO_2$ , and (ii) the lower amount of  $^{12}CO$  (dry reforming of  $^{12}CH_4$  with  $^{13}CO_2$  and  $^{12}CO_2$ ) when compared to that of  $^{13}CO_2$ . Of interest is the largely different transient response of  $H_2$  formation (two peak rate maxima) and the very short time during which  $^{12}CO$  is formed (Fig. 4.11a), when these parameters are compared to those observed in the case of supported Ni catalyst (Fig. 4.10a). For the TPO experiment (Fig. 4.11b), the amounts of  $^{12}CO_2$ ,  $^{13}CO_2$ ,  $^{12}CO$  and  $^{13}CO$  obtained were found to be  $30.0$ ,  $78.0$ ,  $15.4$  and  $1.7\ \mu\text{mol g}^{-1}$ , respectively.



### 4.1.3. In situ DRIFTS-CO chemisorption studies

Fig. 4.12A presents a DRIFT spectrum in the  $2250\text{--}1800\text{ cm}^{-1}$  range recorded at  $25\text{ }^\circ\text{C}$  after 30-min treatment of the 5 wt.% Ni/ $\text{Ce}_{0.5}\text{Zr}_{0.5}\text{O}_{2-\delta}$  catalyst in 5% CO/Ar gas mixture. After deconvolution and curve fitting procedures, IR bands (Fig. 4.12A, broken line) centered at 2175, 2122, 2102 and  $2061\text{ cm}^{-1}$  appear. The first two IR bands are due to gas-phase CO, whereas the IR bands recorded at 2102 and  $2061\text{ cm}^{-1}$  are assigned to linear carbonyl species on reduced nickel [19,20].

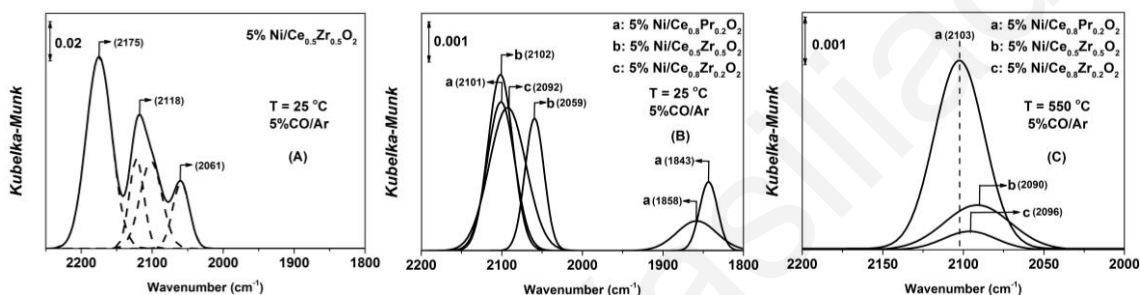


**Figure 4.12:** (A) DRIFT spectrum recorded in the  $2250\text{--}1800\text{ cm}^{-1}$  range over the 5 wt.% Ni/ $\text{Ce}_{0.5}\text{Zr}_{0.5}\text{O}_2$  catalyst after 30-min treatment in 5% CO/Ar gas at  $25\text{ }^\circ\text{C}$ ; IR bands obtained after deconvolution are also shown. IR bands of adsorbed CO obtained in the  $2200\text{--}1800\text{ cm}^{-1}$  range after deconvolution of the spectra recorded at  $25\text{ }^\circ\text{C}$  after 30-min treatment in 5% CO/Ar gas at  $25\text{ }^\circ\text{C}$  (B) and  $550\text{ }^\circ\text{C}$  (C) for the 5 wt.% Ni supported on  $\text{Ce}_{0.8}\text{Pr}_{0.2}\text{O}_2$  (a),  $\text{Ce}_{0.5}\text{Zr}_{0.5}\text{O}_2$  (b) and  $\text{Ce}_{0.8}\text{Zr}_{0.2}\text{O}_2$  (c) carriers.

Fig. 4.12B shows comparative IR bands of adsorbed CO recorded on the 5 wt.% Ni supported on  $\text{Ce}_{0.8}\text{Pr}_{0.2}\text{O}_{2-\delta}$  (a),  $\text{Ce}_{0.5}\text{Zr}_{0.5}\text{O}_{2-\delta}$  (b) and  $\text{Ce}_{0.8}\text{Zr}_{0.2}\text{O}_{2-\delta}$  (c) carriers in the  $2200\text{--}1800\text{ cm}^{-1}$  range after deconvolution and curve fitting of the original DRIFT spectra recorded at  $25\text{ }^\circ\text{C}$ , after 30-min treatment in 5% CO/Ar gas. In the case of Ni/ $\text{Ce}_{0.8}\text{Zr}_{0.2}\text{O}_{2-\delta}$  and Ni/ $\text{Ce}_{0.8}\text{Pr}_{0.2}\text{O}_{2-\delta}$  catalysts, only one linearly adsorbed CO is observed at 2092 and  $2102\text{ cm}^{-1}$ , respectively, whereas for the latter catalyst two additional bridged adsorbed carbon monoxide,  $\text{CO}_B$  (IR bands at 1858 and  $1843\text{ cm}^{-1}$ ) [21] are obtained.

Fig. 4.12C shows IR bands of adsorbed CO obtained after deconvolution and curve fitting of the original DRIFT spectra recorded after 30-min treatment in 5% CO/Ar gas at  $550\text{ }^\circ\text{C}$  over the same three catalysts. All catalysts exhibit only one IR band corresponding to CO adsorbed on  $\text{Ni}^0$ . In the case of Ni/ $\text{Ce}_{0.8}\text{Pr}_{0.2}\text{O}_{2-\delta}$  (most active in dry reforming, Table 4.3), the IR band recorded at  $2103\text{ cm}^{-1}$  is shifted towards slightly lower wavenumbers when  $\text{Pr}^{3+}$  is



replaced by  $\text{Zr}^{4+}$ . This behaviour could be associated with the lowering of the Ni-CO binding energy and at the same time the strengthening of the C-O bonding in the adsorbed Ni-CO species. On the other hand, such red shift in the CO adsorption band is also the result of the lowering in surface coverage of CO. Therefore, it could be stated that the surface concentration of adsorbed CO on  $\text{Ni}^0$  at 550 °C is largely influenced by the support chemical composition.  $\text{Ni}/\text{Ce}_{0.8}\text{Pr}_{0.2}\text{O}_{2-\delta}$  with the best catalytic activity (Fig. 4.4) was found to present the largest surface coverage of linearly bonded CO, whereas  $\text{Ni}/\text{Ce}_{0.5}\text{Zr}_{0.5}\text{O}_{2-\delta}$  with the worst catalytic activity the smallest one.

#### 4.1.4. Estimation of inactive “carbon” formed during RWGS reaction

Fig. 4.13 presents TPO traces of CO and  $\text{CO}_2$  following 1 h of reverse water-gas shift (RWGS) reaction conducted at 750 °C (20%  $\text{CO}_2/7\%$   $\text{H}_2/\text{He}$ ) over the fresh 5 wt.% Ni supported on  $\text{Ce}_{0.8}\text{Pr}_{0.2}\text{O}_2$  (Fig. 4.13a) and  $\text{Ce}_{0.8}\text{Zr}_{0.2}\text{O}_2$  (Fig. 4.13b) catalysts. For the above-mentioned feed gas composition used, the amount of “carbon” formed is considered to be larger than that formed due to the RWGS in the applied dry reforming of methane (DRM) reaction conditions, since the maximum possible  $\text{CO}_2$  and  $\text{H}_2$  feed concentrations were considered. The catalyst pretreatment and TPO conditions used were exactly the same as those used in the DRM reaction (see Section 4.2). The equivalent amounts of “carbon” formed ( $\text{CO}+\text{CO}_2$ ) were found to be practically similar, 57.4 and 61.8  $\mu\text{mol C g}_{\text{cat}}^{-1}$  or 0.69 and 0.74  $\text{mg C g}_{\text{cat}}^{-1}$  in the case of  $\text{Ni}/\text{Ce}_{0.8}\text{Pr}_{0.2}\text{O}_2$  and  $\text{Ni}/\text{Ce}_{0.8}\text{Zr}_{0.2}\text{O}_2$ , respectively. Of interest is the fact that after comparing the TPO traces obtained following DRM (1 h/750 °C) over the same catalytic systems (Fig. 4.7a) with the present ones of RWGS (Fig. 4.13), the reactivity of “carbon” towards oxygen is completely different. In the case of RWGS reaction most of the accumulated “carbon” is oxidized to CO, whereas in the case of DRM the kinetics of oxidation leads to about equal amounts of CO and  $\text{CO}_2$  (Fig. 4.7a). Furthermore, in the case of RWGS the oxidation of “carbon” to CO starts at low temperatures (ca. 100 °C), whereas in the case of DRM at much higher temperatures (ca. 600 °C). These results suggest that RWGS and DRM reactions lead to different structures of “carbon”.

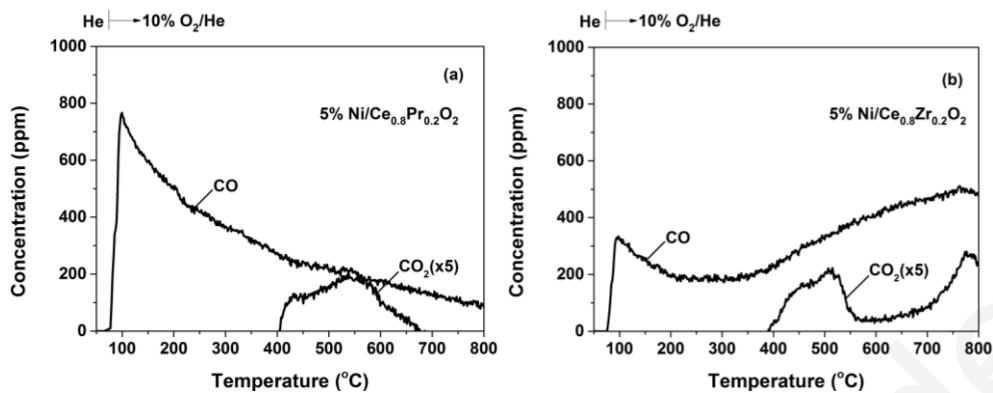


**Figure 4.13:** Transient concentration response curves of CO and CO<sub>2</sub> obtained during TPO of “carbon” formed after 1 h of reverse water-gas shift (RWGS) reaction performed at 750 °C. Reaction feed gas composition: 20% CO<sub>2</sub>/7% H<sub>2</sub>/He;  $W_{cat} = 0.3$  g; GHSV = 30,000 h<sup>-1</sup>.

#### 4.1.5. SEM studies of fresh and spent catalysts

The obtained scanning electron microscopy (SEM) images of the morphology of the fresh and spent (after 1 h of DRM at 750 °C) 5 wt.% Ni/Ce<sub>0.8</sub>Pr<sub>0.2</sub>O<sub>2</sub> catalysts are presented in Figs. 4.14 and 4.15, respectively (various magnifications are provided). The fresh catalyst support consists of irregular aggregates with a wide distribution of macro- and nano-porosity (Fig. 4.14 a-d). The presence of whisker-type carbon nanofibers is clearly envisioned in Fig. 4.15 b-d for the spent catalyst. Carbon nanofibers of lengths larger than 1 μm and 10-40 nm in width (Fig. 4.15 d) are observed. It should also be noted that the shape of the support aggregates does not seem to have changed after 1 h of dry reforming of methane at 750 °C. This information supports the number of different CO and CO<sub>2</sub> peaks obtained in the TPO of “carbon” formed after DRM.

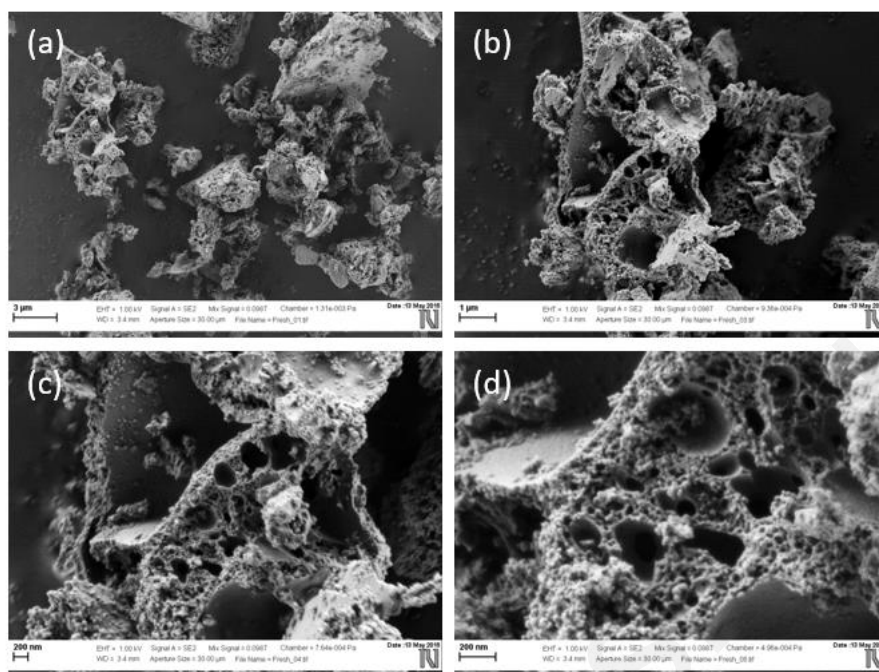


**Figure 4.14:** SEM micrographs of the fresh 5 wt.% Ni/Ce<sub>0.8</sub>Pr<sub>0.2</sub>O<sub>2-δ</sub> catalyst.

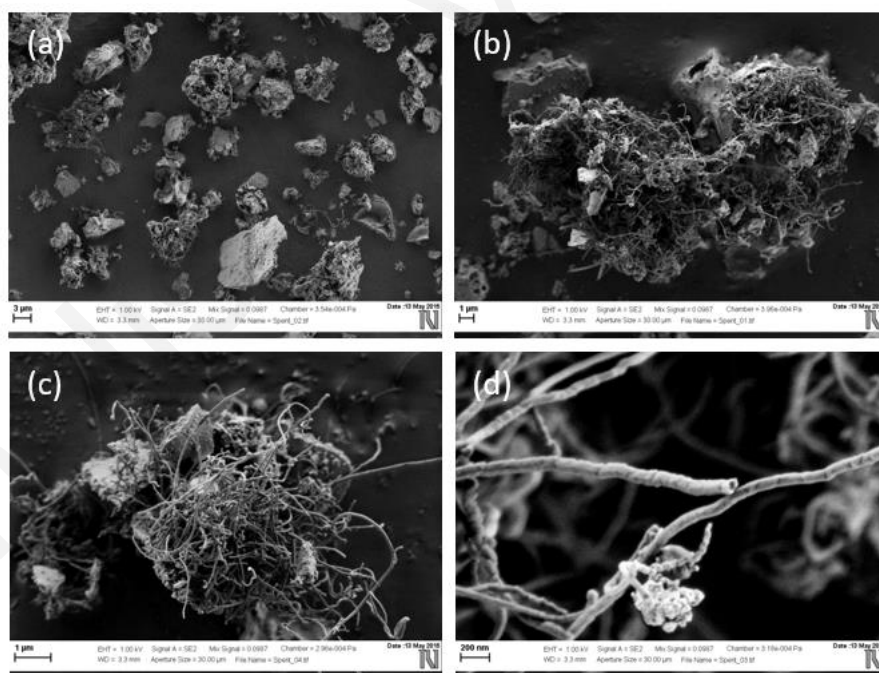


**Figure 4.15:** SEM micrographs of the spent 5 wt.% Ni/Ce<sub>0.8</sub>Pr<sub>0.2</sub>O<sub>2-δ</sub> catalyst (after 1 h of dry reforming of methane at 750 °C; 20% CH<sub>4</sub>/20% CO<sub>2</sub>/He; GHSV = 30,000 h<sup>-1</sup>).

#### 4.1.6. Discussion

##### (a) Catalytic performance of Ni/ $\text{Ce}_{1-x}\text{M}_x\text{O}_{2-\delta}$ ( $\text{M}=\text{Zr}^{4+}$ , $\text{Pr}^{3+}$ )

The catalytic dry reforming of methane performance results reported in Fig. 4.4 and Table 4.3 illustrate that introduction of  $\text{Zr}^{4+}$  and  $\text{Pr}^{3+}$  in the ceria fluorite structure has a large influence on the activity of supported Ni in terms of  $\text{CH}_4$  and  $\text{CO}_2$  conversion but also on the product selectivity in terms of the  $\text{H}_2/\text{CO}$  gas product ratio in the 550-750 °C range. At 550 °C, when Ni particles of ~ 28 nm in size are deposited on  $\text{Ce}_{0.8}\text{Pr}_{0.2}\text{O}_{2-\delta}$ , the  $\text{TOF}_{\text{CH}_4}$  estimated is  $0.675 \text{ s}^{-1}$ , which is significantly larger than the corresponding values of 0.233 and  $0.081 \text{ s}^{-1}$  obtained when smaller Ni particles (~ 15 nm) are deposited on  $\text{Ce}_{0.8}\text{Zr}_{0.2}\text{O}_2$  and  $\text{Ce}_{0.5}\text{Zr}_{0.5}\text{O}_2$  carriers. In order to understand this support effect and the activity order obtained (Table 4.3), the influence of “carbon” formation (origin and extent) on the dry reforming reaction rate as a function of support composition must be examined. Other side reactions such as the reverse water-gas shift (RWGS) and methanation of CO should also be considered in order to correctly assess the performance of the present catalytic systems.

The catalytic performance and the amount of inactive “carbon” formed towards the RWGS (20%  $\text{CO}_2/7\% \text{ H}_2/\text{He}$ ;  $\text{GHSV} = 30,000 \text{ h}^{-1}$ ) and the CO methanation reaction (2.5%  $\text{CO}/7.5\% \text{ H}_2/\text{He}$ ) at 750 °C were evaluated over the 5 wt.% Ni/ $\text{Ce}_{0.8}\text{Zr}_{0.2}\text{O}_{2-\delta}$  and 5 wt.% Ni/ $\text{Ce}_{0.8}\text{Pr}_{0.2}\text{O}_{2-\delta}$  solids. It was found that the  $X_{\text{CO}_2}$  (%) for the RWGS was 21% and 22% for the Ni/ $\text{Ce}_{0.8}\text{Zr}_{0.2}\text{O}_{2-\delta}$  and Ni/ $\text{Ce}_{0.8}\text{Pr}_{0.2}\text{O}_{2-\delta}$ , respectively, whereas the  $X_{\text{CO}}$  for the methanation reaction was less than 2% after 1 h on reaction stream. The amount of inactive “carbon” formed after 1 h of RWGS was found to be significantly lower (~ 0.7 mg/g<sub>cat</sub>) than that formed in DRM (99.7 mg g<sub>cat</sub><sup>-1</sup>) for both catalysts. On the basis of these results and since the most active Ni/ $\text{Ce}_{0.8}\text{Pr}_{0.2}\text{O}_{2-\delta}$  catalyst exhibits a larger  $\text{H}_2/\text{CO}$  ratio than the Ni/ $\text{Ce}_{0.8}\text{Zr}_{0.2}\text{O}_{2-\delta}$  at 750 °C (Table 4.3), it is clear that the RWGS reaction alone cannot explain the differences obtained in the activity and product selectivity between these two particular catalytic systems (Table 4.3).

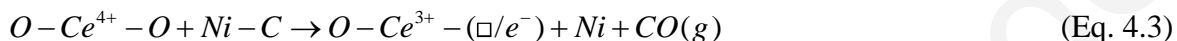
The fact that the  $\text{H}_2/\text{CO}$  gas product ratio in most of the experimental conditions used is lower than one, and the  $X_{\text{CO}_2}$  (%) is larger than that of  $X_{\text{CH}_4}$  (%) (Table 4.3), the RWGS reaction does proceed to some extent in all three catalytic systems. This is in general agreement with literature reports for other  $\text{CeO}_2$ -based- and  $\text{Ce}_{1-x}\text{Zr}_x\text{O}_2$ -supported Ni for feed gas compositions similar to or different than that used in this work [5–10]. In the case of Ni/ $\text{Ce}_{0.8}\text{Pr}_{0.2}\text{O}_{2-\delta}$  catalyst, values slightly higher than unity for the  $\text{H}_2/\text{CO}$  ratio were obtained (Table 4.3). The latter result must be due to other side reactions such as the  $\text{CH}_4$  decomposition, where the produced atomic

C is not recombined with atomic O to form  $\text{CO}(\text{g})$  but instead it is transformed to *inactive* “carbon”. It should be noted that the kinetic rates of DRM and Boudouard reactions also adjust the  $\text{H}_2/\text{CO}$  gas ratio.

The activity performance and stability behaviour of the present 5 wt.% Ni/ $\text{Ce}_{0.8}\text{Pr}_{0.2}\text{O}_{2-\delta}$  catalyst compares favourably with that of 15 wt.% Ni/ $\text{ZrO}_2$  (80 wt.%) -  $\text{CeO}_2$ , the support of which was prepared by the sol-gel method [6]. After using a feed gas composition of 16.7%  $\text{CH}_4/16.7\%$   $\text{CO}_2/\text{N}_2$  at 800 °C, an initial  $\text{CH}_4$  conversion of ~ 70% was reported which dropped to the value of ~ 50% after 3 h on reaction stream. Furthermore, the same catalytic system presented about 180 mg  $\text{g}_{\text{cat}}^{-1}$  of “carbon” after 3 h on reaction stream at 700 °C to be compared with 17.8 mg/ $\text{g}_{\text{cat}}$  obtained in the present 5 wt.% Ni/ $\text{Ce}_{0.8}\text{Pr}_{0.2}\text{O}_2$  catalyst after 50 h of reaction at 750 °C (Fig. 4.7). On the other hand, Roh et al. [9] reported a remarkable activity (>95% conversion in  $\text{CO}_2$  and  $\text{CH}_4$ ) at 800 °C (33.3%  $\text{CH}_4$ ,  $\text{CH}_4/\text{CO}_2 = 1$ ) over a 15 wt.% Ni/ $\text{Ce}_{0.8}\text{Zr}_{0.2}\text{O}_2$  catalyst with only 0.1 wt.% “carbon” deposition after 20 h on stream. In the same work, after using a support composition of  $\text{Ce}/\text{Zr} = 1$ , a significant drop of reforming activity was observed as in the present work (Table 4.3), but not in the work reported by Kambolis et al. [7] over ceria-zirconia (prepared by co-precipitation) supported Ni (5 wt.% Ni).

The amount of “carbon” formed after 1 h of DRM at the lowest T of 550 °C was found to be the largest for the most active Ni/ $\text{Ce}_{0.8}\text{Pr}_{0.2}\text{O}_2$  catalyst when compared to the other catalysts. However, caution should be drawn in deriving a meaningful relationship of “carbon” deposition with catalyst activity for the following reasons. First, the titration of “carbon” via transient isothermal or temperature-programmed hydrogenation or oxidation experiments always provide the *total* “carbon” formed in dry reforming of methane reaction conditions. This amount should be considered to consist of the *active* carbon (found in the reaction path of CO formation) and the *inactive* (spectator) “carbon”. The first one is only estimated via the SSITKA technique as reported by Efstathiou et al. [22] over  $\gamma\text{-Al}_2\text{O}_3$ - and YSZ-supported Rh catalysts, and by Bobin et al. [23] over Ni/ $\text{Ln}_x(\text{Ce}_{0.5}\text{Zr}_{0.5})_{1-x}\text{O}_2$  ( $\text{Ln} = \text{Pr}, \text{Sm}$ ) catalysts. Secondly, the number of active catalytic sites blocked by the inactive “carbon” cannot be necessarily related to the quantity of “carbon” formed since the structure of inactive “carbon”, its location (catalytic vs non-catalytic sites) and binding mode on the catalytic surface should be also considered. Bobin et al. [23] have shown that the amount of the *active* carbon pool which participates in dry reforming over supported Ni and Ni-Ru was very small, in agreement to the present work (see Section 4.8.6).

Dry reforming of methane over  $Ce_{1-x}M^1_xM^2_yO_2$  – supported Ni catalysts ( $M^1$  and  $M^2$  are rare earth metals) with supports possessing high OSC ( $\mu\text{mol O g}^{-1}$ ) was reported [8–10]. The high activity of these catalytic systems was related with the participation of support's oxygen vacancies towards dissociation of  $CO_2$ . The lattice oxygen thus formed diffuses towards the Ni surface, where it reacts with “carbon” formed via  $CH_4$  decomposition on the Ni surface to form CO according to the following reaction step (Eq. 4.3):



Similarly, the large concentration of labile oxygen in such reducible support materials facilitates reaction with “inactive” carbon towards CO and/or  $CO_2$ , thus contributing to the reduction of catalyst deactivation. In the present work, no clear correlation was found between the OSC quantity and catalyst's activity. Ni/ $Ce_{0.8}Pr_{0.2}O_2$  with the largest kinetic rate of DRM reaction in the 550-750 °C range provides larger OSC (Table 4.1) and rates of removal of labile oxygen (Fig. 4.2). However, the support of the least active Ni/ $Ce_{0.5}Zr_{0.5}O_2$  catalyst presents larger OSC and transient reduction rates compared to those of Ni/ $Ce_{0.8}Zr_{0.2}O_2$  (Table 4.1, Fig. 4.2).

The  $CH_4$  decomposition in the absence of  $CO_2$  but *in the presence of CO* can take place rapidly (sharp increase in the reaction rate) leading to  $H_2$  and surface “carbon” according to the results shown in Fig. 4.10a. The rate of  $CH_4$  decomposition might change with reaction time as “carbon” accumulates on the catalyst surface. In fact, DRM over Ni/ $Ce_{0.8}Pr_{0.2}O_2$  at 750 °C for 50 h on stream (Fig. 4.6) resulted in a lower  $H_2/CO$  gas product ratio (ca. 1.03) compared to the value of 1.2 obtained after 1 h on stream (Table 4.3). A similar result was reported on Ni/ $CeO_2$  and Ni/ $ZrO_2-CeO_2$  catalytic systems (16.7%  $CH_4$ ;  $CH_4/CO_2 = 1$ ;  $T = 800$  °C) [6]. Furthermore, after 50 h of DRM the  $H_2$ -yield is reduced by ~ 18%, not consistent with the reduction in  $CH_4$  conversion (Fig. 4.5). It is suggested that hydrogenation of “carbon” does take place at 750 °C during DRM and this is very likely the reason for the significant reduction of accumulated “carbon” after 1 h of reaction. This route of “carbon” removal finds strong support by the TIIH results shown in Fig. 4.6.

Wang et al. [10] have concluded that CO desorption from Ni(111) during DRM reaction is highly energetic based on density function theoretical (DFT) calculations. This implies that an increased accumulation of surface CO can hinder its yield and selectivity and accelerate

deactivation of Ni catalysts due to “carbon” deposition via the Boudouard reaction. This conclusion is in line with the present DRIFTS-CO chemisorption studies performed at 550 °C (Fig. 4.12C), and the transient hydrogenation of “carbon” formed at 550 °C under dry reforming (Fig. 4.6), where Ni/ $Ce_{0.8}Pr_{0.2}O_{2-\delta}$  exhibits the largest concentration of adsorbed CO and at the same time the largest amount of “carbon” deposition. Certainly, the activity and selectivity issues cannot be related only to the chemical bonding of CO. In fact, linear adsorbed CO on Ni/ $Ce_{0.8}Pr_{0.2}O_{2-\delta}$  shows similar binding strength as that observed in the other two supported Ni catalysts (Fig. 4.12C). It should be also noted that Ni/ $Ce_{0.8}Pr_{0.2}O_{2-\delta}$  catalyst is the only one which favours the formation of bridged-type adsorbed CO at room T. The latter is likely to be reactive towards the Boudouard reaction under DRM (550-750 °C).

The so far general consensus that a *monotonic dependence of Ni particle size* on the dry reforming reaction and “carbon” deposition rates does exist over supported Ni catalysts should be rather considered as premature yet. Such correlations require systematic investigations of all the possible Ni and support parameters that would influence the kinetics of DRM and that of inactive “carbon” formation. In fact, Sokolov et al. [24] have reported initial  $TOF_{CH_4}$  rates as a function of Ni particle size for the Ni/ $La_2O_3$ - $ZrO_2$  catalytic system, where it was shown that higher TOF rates were obtained on larger Ni particles, result that was explained on the basis that  $CH_4$  activation on the Ni surface *was not the rate-limiting step*. Instead, *oxycarbonate species* (e.g.  $La_2O_2CO_3$ ) formed at the Ni-support interface react slowly (RDS) with C-s formed on Ni (via  $CH_4$  decomposition) to form CO(g) and restore the support  $CO_2$  chemisorption sites. Such a mechanism was first proposed by Verykios and his co-workers [4,25] over Ni/ $La_2O_3$ . One of the important kinetic parameters in this bi-functional mechanism is the concentration of catalytic sites along the Ni-support interface, fact that makes more appropriate the estimation of intrinsic kinetic rates in terms of  $mols\ cm^{-1}\ s^{-1}$  and not in terms of TOF ( $s^{-1}$ ) (based on the metal surface), as recently reported for the WGS reaction on Pt supported on similar  $Ce_{1-x}M_xO_{2-\delta}$  ( $M = Zr^{4+}$ ,  $Ti^{4+}$ ,  $La^{3+}$ ) carriers [13,26].

**(b) Quantification of the origin of “carbon” deposition – Effect of support composition**

As the main focus on the development of robust supported Ni catalysts for future industrial applications of the dry reforming of methane is the minimisation (or elimination if possible) of “carbon” formation at temperatures preferentially lower than 800 °C, a good understanding of its origin ( $CH_4$  vs  $CO_2$  activation routes) should be greatly appreciated. In

particular, it is imperative to understand how this is influenced by important parameters, such as the support chemical composition, Ni particle size, feed composition, T, GHSV ( $\text{h}^{-1}$ ) and various surface physico-chemical properties (e.g. acidity/basicity, support oxygen mobility, Ni surface morphology). In this PhD thesis work, the *support chemical composition* and *reaction temperature* effects have been investigated.

Table 4.4 indicates that the relative contribution of the  $\text{CH}_4$  and  $\text{CO}_2$  molecular routes to “carbon” formation under the applied experimental conditions is largely influenced by the support chemical composition and reaction temperature. In all three support chemical compositions and at the lowest reaction temperature of 550 °C investigated, the source of “carbon” is largely related to the  $\text{CO}_2$  activation route. On the other hand, at the highest temperature of 750 °C,  $\text{CH}_4$  activation contributes to a similar extent but in the case of Ni/ $\text{Ce}_{0.5}\text{Zr}_{0.5}\text{O}_{2-\delta}$ . In order to understand the role of support on the origin of “carbon” formation, it is necessary to understand first fundamental issues about the mechanism of “carbon” formation via the  $\text{CH}_4$  and  $\text{CO}_2$  activation routes. It is imperative to know whether the support provides catalytic sites for “carbon” formation and how these influences the kinetics of net “carbon” formation on the supported Ni catalyst. The mechanistic elementary reaction steps, described in Ch. 1, to produce  $\text{H}_2$  and CO over the present catalytic systems are supported by the transient isotopic results (Fig. 4.10) and others previously reported [4,10,23,24], but also on theoretical studies [27].

The reaction steps of  $\text{CH}_4$  dissociation and  $\text{H}_2$  formation on Ni, are strongly supported by the transient isotopic and TPO results presented in Figs. 4.8-4.11, where fast decomposition of methane on the Ni surface to produce  $\text{H}_2$  and  $(-\text{C}-)_y$  is evidenced. According to the results of Fig. 4.11,  $\text{Ce}_{0.8}\text{Pr}_{0.2}\text{O}_{2-\delta}$  alone promotes only to a small extent  $\text{CH}_4$  decomposition with different kinetics (compare  $\text{H}_2$  transient response curves in Figs. 4.10a and 4.11a). In fact, the amount of  $\text{H}_2$  formed after 30-min treatment in  $^{13}\text{CO}/^{12}\text{CH}_4/\text{Ar}/\text{He}$  over the Ni/ $\text{Ce}_{0.8}\text{Pr}_{0.2}\text{O}_{2-\delta}$  catalyst was *39.4 times larger* than that formed in the case of support alone. On the other hand, the amount of  $^{12}\text{C}$  formed on the support alone via methane decomposition (Fig. 4.11b) was found to be only 2.9% of that measured on the supported Ni (Fig. 4.10b). A very low amount of “carbon” was also reported on ceria [28] after  $\text{CH}_4$  decomposition, where the obtained TPO traces of CO and  $\text{CO}_2$  were very similar to those reported in this work (Fig. 4.11b). Based on the above discussion, *“carbon” formation via the  $\text{CH}_4$  activation route practically occurs only on Ni*



*surface sites*. However, participation of active sites of support (e.g.  $\text{O}^{\text{n-}}$ ) at the Ni-support interface cannot be excluded.

It has been reported [8,29–32] that Ni and  $\text{CeO}_2$ -based metal oxides with significant concentration of oxygen vacancies ( $\square/e^-$ ) can dissociate  $\text{CO}_2$  according to the mechanistic elementary reaction steps described in Chapter 1. The reaction step that describes the well-known Boudouard reaction (Eq. 4.2) along with the chemical steps of  $\text{CO}_2$  dissociation on Ni and  $\text{Ce}_{1-x}\text{M}_x\text{O}_{2-\delta}$  support become responsible for the formation of *inactive* “carbon”, the extent of which mainly depends on the kinetics of its formation in various structural forms. By controlling the kinetic rate of the Boudouard reaction through not only the dissociation step of CO-s but also the *removal step of C-s by reaction with adsorbed O-s* (towards CO and  $\text{CO}_2$ ), minimisation of the accumulation of “carbon” can be achieved. The backward reaction step (Eq. 1.26) completes the catalytic cycle of DRM by forming CO from the O derived from the  $\text{CO}_2$  (Eq. 1.23) and the C derived from  $\text{CH}_4$  (Eq. 1.18). The C-s is considered as the *active* carbon species found in the mechanism of DRM, and this should be distinguished from the *inactive* carbon given in Eqs. 1.20 and 1.27.

It has been reported [33,34] that CO dissociation involves ensembles of Ni atoms as active sites, the number of which is in the range 4 to 6. The density of these ensembles increases with increasing metal particle size [35]. On the other hand, studies on single nickel crystals suggest that more open Ni surfaces are most active for  $\text{CH}_4$  dissociation, while close-packed nickel surfaces are the least active [36]. More open metal surfaces can be obtained by decreasing the Ni particle size. These observations for CO dissociation and  $\text{CH}_4$  decomposition over Ni surfaces could be offered to partly explain the transient isotopic results shown in Figs. 4.8 and 4.9 and reported in Table 4.4. It is considered that the present supported Ni catalysts exhibit different Ni particle surface morphologies according to the  $\text{H}_2$ -TPD traces (Fig. 4.3) and the  $\text{H}_2$  chemisorption results reported in Table 4.2, which suggest the existence of different distributions of Ni surface sites. In fact, the larger Ni particles observed in Ni/ $\text{Ce}_{0.8}\text{Pr}_{0.2}\text{O}_2$  catalyst ( $\sim 32$  nm) led to a significantly larger amount of “carbon” after 1 h of reforming at  $550^\circ\text{C}$  (Fig. 4.7) when compared to the smaller Ni particles ( $\sim 15$  nm) present in the other two catalysts. On the other hand, when dry reforming was performed with lower reactant concentrations (5%  $^{13}\text{CO}_2$ /5%  $\text{CH}_4$ /Ar/He, Figs. 4.8 and 4.9), the amounts of “carbon” derived from the  $\text{CO}_2$  and  $\text{CH}_4$  were very similar for Ni/ $\text{Ce}_{0.8}\text{Pr}_{0.2}\text{O}_2$  and Ni/ $\text{Ce}_{0.8}\text{Zr}_{0.2}\text{O}_2$  having different

Ni particle sizes ( $\sim 32$  vs  $15$  nm). Furthermore, a significantly lower amount of “carbon” was found in the case of  $\text{Ni}/\text{Ce}_{0.5}\text{Zr}_{0.5}\text{O}_2$  having a mean Ni particle size of  $\sim 15$  nm.

The influence of support composition on the kinds of “carbon” formed in DRM is illustrated in Figs. 4.8 and 4.9. After dry reforming at  $550$  and  $750$  °C over the  $\text{Ni}/\text{Ce}_{0.5}\text{Zr}_{0.5}\text{O}_{2-\delta}$  catalyst (Fig. 4.8), the kinds of “carbon” derived from  $\text{CO}_2$  and  $\text{CH}_4$  activation are clearly different (compare  $^{13}\text{CO}_2$  vs  $^{12}\text{CO}_2$  TPO traces) as opposed to the case of  $\text{Ni}/\text{Ce}_{0.8}\text{Pr}_{0.2}\text{O}_{2-\delta}$  (Fig. 4.9). The latter result is in harmony with that obtained in the  $^{13}\text{CO}/^{12}\text{CH}_4/\text{Ar}/\text{He}$  isotopic experiment (Fig. 4.10b), where the pairs of  $^{12}\text{CO}_2/^{13}\text{CO}_2$  and  $^{12}\text{CO}/^{13}\text{CO}$  traces were *very similar in shape* (similar kinetics of “carbon” oxidation). The comparison of the TPO traces shown in Figs. 4.9b and 4.10b ( $\text{Ni}/\text{Ce}_{0.8}\text{Pr}_{0.2}\text{O}_{2-\delta}$ ) appear very important since they illustrate that the kinds of “carbon” formed are different when an equivalent concentration of  $\text{CO}_2$  is replaced by  $\text{CO}$ . It is suggested that the surface catalytic sites (nature and location) for  $\text{CO}_2$  activation *might be different* than those of  $\text{CO}$  activation. This in turn can lead to the formation of different kinds of “carbon” (Eqs. 1.26-1.27 and Eq. 1.7). The absence of  $\text{CO}$  in the TPO trace following DRM (Fig. 4.9b) as opposed to the case of  $^{13}\text{CO}/^{12}\text{CH}_4/\text{Ar}/\text{He}$  treatment (Fig. 4.10b) should be noted.

The net rate of “carbon” accumulation during DRM is determined by the kinetics of its formation on Ni and the kinetics of its removal via the backward rates of the reversible steps Eq. 1.26 and Eq. 1.7. The  $\text{Ce}_{1-x}\text{M}_x\text{O}_{2-\delta}$  ( $\text{M} = \text{Zr}^{4+}, \text{Pr}^{3+}$ ) supports possess a significant amount of labile oxygen ( $\mu\text{mol O g}^{-1}$ ) and oxygen vacancies as reported in Table 4.1, with  $\text{Ce}_{0.8}\text{Pr}_{0.2}\text{O}_{2-\delta}$  to possess significantly larger reduction rates of surface lattice oxygen (weaker M-O-M bonding) than the other two supports (Fig. 4.2). Such labile oxygen species at least at the metal-support interface reacts with carbon to form  $\text{CO}/\text{CO}_2$  [37]. The “carbon” removal requires the continuous provision of oxygen from the support. This can only be accomplished if the oxygen vacancy ( $\square/e^-$ ) created *is offered for  $\text{CO}_2$  dissociation* according to the elementary step Eq. 1.24 [23,38,39].

SEM studies (Fig. 4.15) over the spent (after 1 h of DRM reaction) 5 wt.%  $\text{Ni}/\text{Ce}_{0.8}\text{Pr}_{0.2}\text{O}_{2-\delta}$  catalyst clearly elucidate the formation of different morphologies of whisker-type carbon nanofibers. This information supports the number of different  $\text{CO}$  and  $\text{CO}_2$  peaks obtained in the TPO of “carbon” formed after DRM reaction.

Figure 4.16 attempts to present in a pictorial form the *main mechanistic steps* of the dry reforming of methane over the present  $\text{Ni}/\text{Ce}_{1-x}\text{M}_x\text{O}_{2-\delta}$  ( $\text{M} = \text{Zr}, \text{Pr}$ ) catalysts in the  $550$ - $750$  °C

range according to the results of the present work and what has been discussed in the previous paragraphs.

Activation of  $CO_2$  proceeds on the Ni-support interface or in the nearby region with support labile oxygen to facilitate removal of C-s (on Ni), the latter formed by the activation of methane. This work also supports the view that the rate-determining step (RDS) of the present DRM may not be that of  $CO_2$  dissociation but rather one found in the  $CH_4$  activation route based on the relative amounts of “carbon” formed (Table 4.4). This important mechanistic point finds support from the SSITKA work on the dry reforming of methane over various supported Ni catalysts [38].

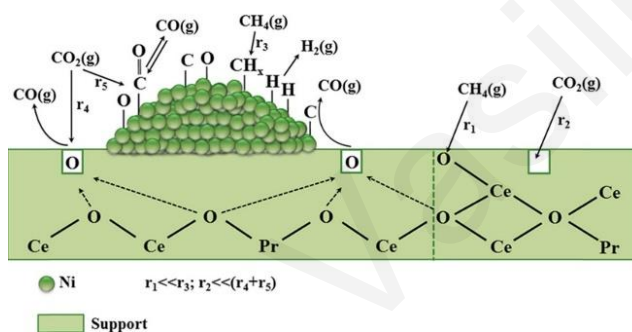


**Figure 4.16:** Representation of the main chemical reaction steps of the  $CH_4$  and  $CO_2$  activation routes on the 5 wt.% Ni/ $Ce_{0.8}Pr_{0.2}O_{2-\delta}$  catalyst towards dry reforming of methane for syngas ( $CO/H_2$ ) production.

The following conclusions can be derived for the DRM over the present 5wt.% Ni/ $Ce_{1-x}M_xO_{2-\delta}$  ( $M: Zr^{4+}, Pr^{3+}; x = 0.2, 0.5 (Zr^{4+})$ ) catalytic systems:

- (i) 5 wt.% Ni supported on  $Ce_{0.8}Pr_{0.2}O_{2-\delta}$  was found to be a promising “coke” resistant active catalytic material towards dry reforming of methane in the 750-800 °C range. Using a feed composition of 20%  $CH_4/20\% CO_2/He$ , an initial hydrogen yield of 70% and a  $H_2/CO$  ratio of 1.2 were obtained at a GHSV of  $30,000 h^{-1}$ . After 50 h of continuous reaction,  $H_2$ -yield decreased by  $\sim 18\%$  and the amount of inactive “carbon” was  $17.5 mg g^{-1}$  or 1.75 wt.%. The preparation method, the pretreatment conditions before reaction, and the Ce/Pr ratio remain important parameters to be investigated in order to improve its catalytic performance. In the following Section 4.8, the effects of the latter important parameter are presented.

- (ii) The relative contribution of the  $\text{CH}_4$  and  $\text{CO}_2$  activation routes towards the formation of *inactive* “carbon” on the catalyst surface depends strongly on the reaction temperature and support chemical composition. At 750 °C, methane and carbon dioxide contributes equally, whereas at 550 °C the contribution of  $\text{CO}_2$  becomes more important. This information largely facilitates future design improvements on the “coking” resistance of this particular 5 wt.% Ni/ $\text{Ce}_{0.8}\text{Pr}_{0.2}\text{O}_{2-\delta}$  catalyst. Improvements in the dry reforming at 750 °C should focus on the reduction rate of “carbon” formation originating from both the  $\text{CH}_4$  and  $\text{CO}_2$  activation routes.
- (iii) The participation of lattice oxygen of  $\text{Ce}_{0.8}\text{Pr}_{0.2}\text{O}_{2-\delta}$  support of Ni seems to play a role in reducing the “coke” formation under dry reforming reaction conditions. An improvement in the rate of oxygen transfer from the support towards the Ni-support interface is more important than the increase of oxygen storage capacity itself (OSCC).
- (iv) Dissociation of CO, derived via  $\text{CH}_4$  and  $\text{CO}_2$  (Boudouard reaction) is an important origin for the formation of *inactive* “carbon” on the catalyst surface. The reactivity of this “carbon” towards oxygen appears different over the Ni/ $\text{Ce}_{0.8}\text{Pr}_{0.2}\text{O}_{2-\delta}$  compared to the Ni/ $\text{Ce}_{1-x}\text{Zr}_x\text{O}_{2-\delta}$  catalysts. This leads to the conclusion that Ni surface sites offered for CO chemisorption are different in the case of  $\text{CO}_2$  and  $\text{CH}_4$  activation routes. In fact,  $\text{CH}_4$  activation is suggested to occur practically only on the supported Ni surface, whereas  $\text{CO}_2$  activation is suggested to proceed not only on the Ni surface but also with the participation of oxygen vacant sites at the Ni-support interface.

## 4.2. Performance and characterization studies of active and inactive carbon over Ni/ $\text{Ce}_{1-x}\text{Pr}_x\text{O}_{2-\delta}$ catalysts

### 4.2.1. Catalyst characterization

An in-depth investigation of the oxygen vacancy effect in other than  $\text{Zr}^{4+}$ -doped  $\text{CeO}_2$  supports for nickel in the DRM reaction appears to be very limited. In particular, in the case of praseodymium (Pr), one of the multivalent elements used for introduction (doping) into the ceria matrix, an excellent OSC behaviour [40–42], DRM activity and stability [29,43] were reported. Recently,  $\text{Ce}_{0.9}\text{Pr}_{0.1}\text{O}_2$ -supported Ir catalysts have been reported to be highly efficient DRM catalysts after tuning the Ir-support interactions by adopting different preparation techniques [44]. In spite of the efforts to develop suitable  $\text{CeO}_2$ -doped supported Ni catalysts towards sustainable DRM activity, fundamental understanding of the relative importance of each of the

“carbon” formation chemical routes ( $CH_4$  decomposition and Boudouard reaction) over these catalysts has only recently been reported [43] for the 5 wt.% Ni/ $Ce_{1-x}M_xO_{2-\delta}$  ( $M = Zr, Pr$ ) and previously for Ni/ $SiO_2$  [45], Ni/ $Al_2O_3$ -CaO [18] and Ni/ $La_2O_3$  [46] catalytic systems after using  $^{13}CH_4$  or  $^{13}CO_2$  isotope gas coupled with temperature-programmed oxidation (TPO) and other transient experiments.

The present Section 4.8 addresses the catalytic performance of  $Ce_{1-x}Pr_xO_{2-\delta}$ -supported Ni (5 wt.%) in the dry reforming of  $CH_4$  (550-750 °C), where for the first time the effects of Pr/Ce atom ratio on the following parameters are investigated:

- (i) the concentration of *active* carbon formed via the  $CO_2$  activation route,
- (ii) the concentration and structure/morphology of inactive carbon and its reactivity towards oxygen,
- (iii) the relative contribution of the  $CH_4$  and  $CO_2$  activation routes to the total “carbon” formation, and
- (iv) the TOFITK ( $s^{-1}$ ) based on the *active* intermediates.

For this purpose, steady-state isotopic transient kinetic analysis (SSITKA), temperature-programmed oxidation (TPO) after DRM (use of  $^{12}CO_2$  or  $^{13}CO_2$ ), powder XRD, HRTEM-EDXS, SEM and TGA-TPO techniques were employed.

#### 4.2.1.1. Surface texture and powder XRD studies

The specific surface area (SSA), pore volume ( $V_p$ ) and the mean pore diameter ( $d_p$ ) for the solid supports investigated are given in Table 4.5. The SSA of the materials is in the 5-12  $m^2 g^{-1}$  range with  $CeO_2$  exhibiting the largest value (12  $m^2 g^{-1}$ ). As Pr-dopant is introduced into the  $CeO_2$  lattice, the SSA slightly drops but after a high loading of Pr-dopant (80 atom-%) is used the SSA drops by a factor of 2.4. The mean pore diameter and pore volume are found to be in the 9-22 nm and 0.033-0.072  $cm^3 g^{-1}$  range, respectively. The  $d_p$  shows an increase in the 20-65 atom-% Pr composition range, whereas further increase to 80 atom-% provides no additional change.

**Table 4.5:** BET surface area (SSA,  $m^2 g^{-1}$ ), specific pore volume ( $V_p$ ,  $cm^3 g^{-1}$ ), average pore size ( $d_p$ , nm), primary crystallite size ( $d_c$ , nm) and lattice constant ( $a$ , Å) obtained over  $Ce_{1-x}Pr_xO_{2-\delta}$  ( $x = 0.0, 0.2, 0.5, 0.65, 0.8$ ) solids. The mean crystallite size of NiO ( $d_{NiO}$ , nm) for the corresponding supported nickel catalysts is also reported.

Solid Support	SSA ( $m^2 g^{-1}$ )	$V_p$ ( $cm^3 g^{-1}$ )	$d_p$ (nm)	$d_c$ (nm)	$a$ (Å)	$d_{NiO}$ (nm)
<b>CeO<sub>2</sub></b>	12	0.033	9.1	35	5.4252	35
<b>Ce<sub>0.8</sub>Pr<sub>0.2</sub>O<sub>2</sub></b>	11	0.039	11.5	24	5.4265	33
<b>Ce<sub>0.5</sub>Pr<sub>0.5</sub>O<sub>2</sub></b>	10	0.072	16.7	18	5.4587	30
<b>Ce<sub>0.35</sub>Pr<sub>0.65</sub>O<sub>2</sub></b>	9	0.056	22.4	24	5.4755	31
<b>Ce<sub>0.2</sub>Pr<sub>0.8</sub>O<sub>2</sub></b>	5	0.035	22.3	29	5.4835	34

X-ray diffractograms of the fresh 5 wt.% Ni/ $Ce_{1-x}Pr_xO_{2-\delta}$  ( $x = 0.0-0.8$ ) solids, after calcination at 750 °C for 4 h, are given in Fig. 4.17. As the Pr-dopant concentration increases, diffraction peaks related to the pure CeO<sub>2</sub> of fluorite-type cubic structure are slightly shifted towards lower 2 $\theta$  values, and the lattice parameter,  $a$  (Å), also slightly increases (see Table 4.5). As Pr-dopant concentration increases from 20 to 80 atom-%, the lattice parameter shows an increase by ~1%. On the other hand, at the level of 20 atom-% Pr doping of CeO<sub>2</sub>, the lattice parameter increases only marginally (ca. ~0.02%). These results agree very well with the work of Somacescu et al. [47] and Ahn et al. [42] except that lattice expansion was only 0.09% for all Pr concentrations (10-90 atom-%) used by the former research group. This small discrepancy might have to do with the relative proportion of  $Pr^{3+}/Pr^{4+}$  and  $Ce^{4+}/Ce^{3+}$  in the doped-CeO<sub>2</sub> solid solution, the former replacing  $Ce^{4+}$ , after considering also the differences in the ionic radii of  $Pr^{3+}$  (1.266 Å),  $Ce^{4+}$  (0.97 Å),  $Pr^{4+}$  (1.1 Å) and  $Ce^{3+}$  (1.28 Å) [48]. The relative abundance of  $Pr^{3+}/Pr^{4+}$  and  $Ce^{4+}/Ce^{3+}$  is expected to depend on the Pr-loading, the synthesis and the calcination pretreatment conditions applied. The diffraction peaks at 37.2 and 43.2° shown in Fig. 4.17 correspond to the (111) and (200) crystal faces of the NiO crystal phase, according to the Joint Committee on Powder Diffraction Standards (JCPDS) card no. 04-0835.

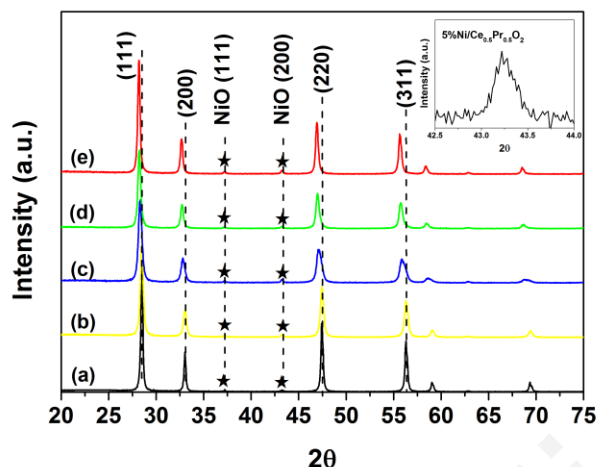


**Figure 4.17:** Powder X-ray diffractograms of (a) 5 wt.% Ni/CeO<sub>2</sub>, (b) 5 wt.% Ni/Ce<sub>0.8</sub>Pr<sub>0.2</sub>O<sub>2</sub>, (c) 5 wt.% Ni/Ce<sub>0.5</sub>Pr<sub>0.5</sub>O<sub>2</sub>, (d) 5 wt.% Ni/Ce<sub>0.35</sub>Pr<sub>0.65</sub>O<sub>2</sub> and (e) 5 wt.% Ni/Ce<sub>0.2</sub>Pr<sub>0.8</sub>O<sub>2</sub> fresh catalysts after calcination in 20% O<sub>2</sub>/He at 750 °C for 4 h. Inset graph shows a magnification of the NiO (200) diffraction peak (★) related to the 5 wt.% Ni/Ce<sub>0.5</sub>Pr<sub>0.5</sub>O<sub>2-δ</sub> solid.

The XRD results are in agreement with TEM/EDXS studies reported below and the work of Somacescu *et al.* [47] for the series of  $\text{Ce}_{1-x}\text{Pr}_x\text{O}_{2-\delta}$  solids ( $x = 0.0, 0.1, 0.5, 0.9$ ) prepared by the self-assembly method assisted by surfactants and hydrothermal treatment, and with the work of Ahn *et al.* [42] who investigated the role of Pr in the formation and migration of oxygen vacancies in Pr-doped ceria ( $\text{Ce}_{1-x}\text{Pr}_x\text{O}_2$ ;  $x = 0.0-0.5$ ) prepared by the glycine nitrate process. A similar slight shift of  $2\theta$  to lower values with increasing Pr content is noticed (Fig. 4.17) due to the larger ionic radius of  $\text{Pr}^{3+}$  (1.266 Å) in relation to the  $\text{Ce}^{4+}$  cation (0.97 Å) [30]. The primary crystallite size of NiO ( $d_{\text{NiO}}$ , nm) and that of  $\text{Ce}_{1-x}\text{Pr}_x\text{O}_{2-\delta}$  support ( $d_c$ , nm) were estimated and reported in Table 4.5. All catalysts exhibit similar NiO particle sizes (~ 30-35 nm) and support primary crystal size (29-35 nm).

#### 4.2.1.2. TEM-EDXS studies

Figs. 4.18a and 4.18b show TEM micrographs of fresh 5 wt.% Ni/CeO<sub>2</sub> and 5 wt.% Ni/Ce<sub>0.2</sub>Pr<sub>0.8</sub>O<sub>2-δ</sub> catalysts, respectively. Both catalyst supports are comprised of polydisperse agglomerated polyhedral primary crystallites in the 30-50 nm in size range. This size corresponds closely to that of CeO<sub>2</sub> and Ce<sub>0.2</sub>Pr<sub>0.8</sub>O<sub>2-δ</sub> crystallites estimated from powder XRD (Table 4.5).



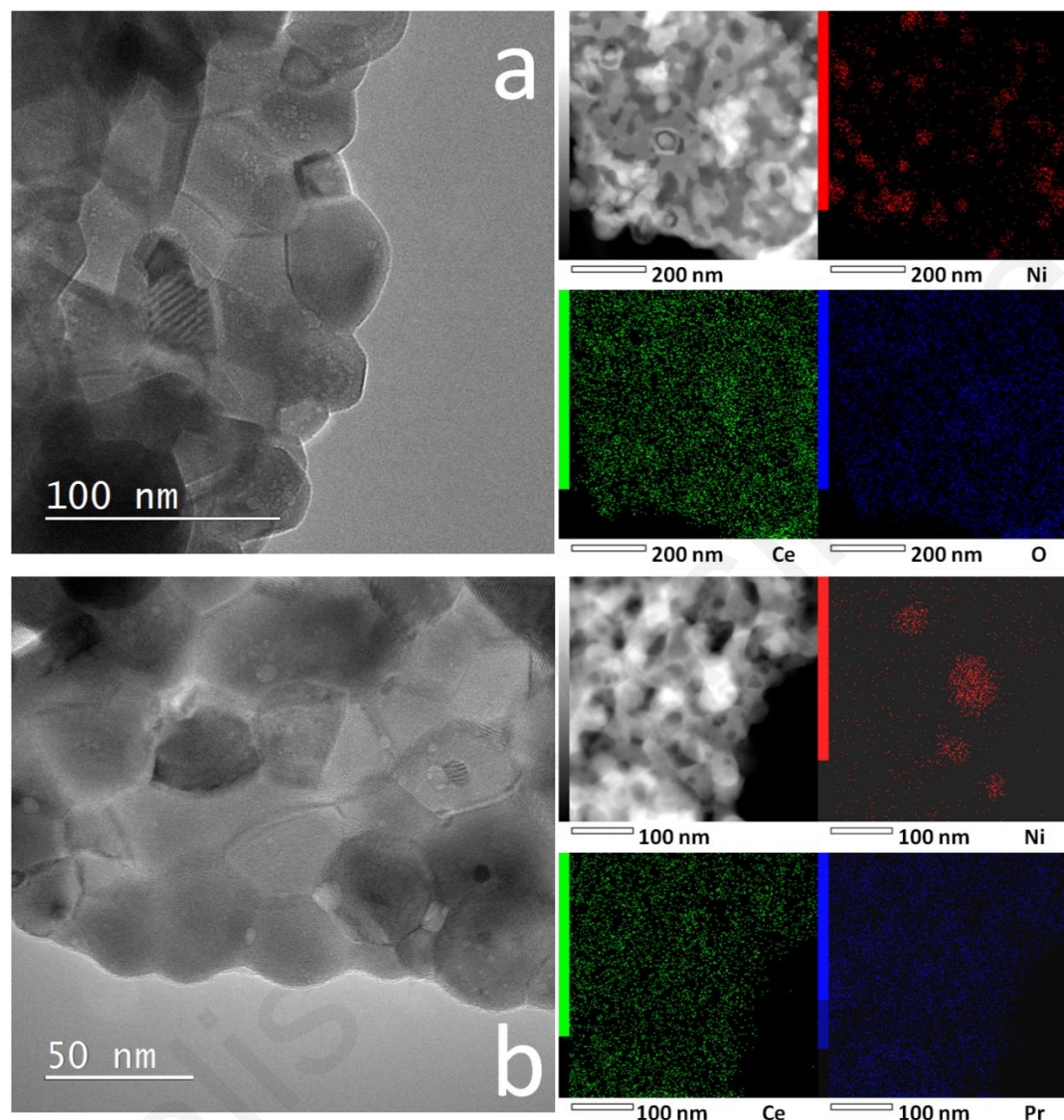


**Figure 4.18:** TEM (left-hand side) and HAADF/STEM micrographs (right-hand side) with corresponding EDXS elemental mapping for (a) 5 wt.% Ni/CeO<sub>2</sub> and (b) 5 wt.% Ni/Ce<sub>0.2</sub>Pr<sub>0.8</sub>O<sub>2- $\delta$</sub>  catalysts.

EDXS elemental mapping of Ce and Pr in both Ni/Ce<sub>0.5</sub>Pr<sub>0.5</sub>O<sub>2- $\delta$</sub>  and Ni/Ce<sub>0.2</sub>Pr<sub>0.8</sub>O<sub>2- $\delta$</sub>  catalysts shows a *very homogeneous distribution* of these elements, suggesting the formation of a single-phase homogeneous solid solution, which is in very good agreement with the powder XRD results (Fig. 4.17). It is noted that the presence of ultra-high vacuum and electron beam flux likely caused reduction of NiO to Ni during TEM-EDX analysis. EDXS mapping analysis revealed Ni particles in the 5 wt.% Ni/CeO<sub>2</sub> solid in the range between 30 and 100 nm in size



and which resemble *cubo-octahedra in shape*. Very similar Ni particle size and shape were also seen in the 5 wt.% Ni/ $\text{Ce}_{0.5}\text{Pr}_{0.5}\text{O}_{2-\delta}$  and 5 wt.% Ni/ $\text{Ce}_{0.2}\text{Pr}_{0.8}\text{O}_{2-\delta}$  solids (Fig. 4.19b). TEM and SAED analyses revealed that Ni cubo-octahedral (metallic Ni crystallized in cubic Fm3m space group) predominantly expose groups [100] and [111] terminating crystal planes. Some of the Ni particles were confirmed as polysynthetic twin crystals, sharing the [111] twin plane, which acts as a boundary between the individual Ni crystallites (Fig. 4.19b, c). As a result, the visualized Ni particles comprise of smaller primary crystallites in agreement with their size estimation based on the powder XRD and  $\text{H}_2$  chemisorption studies. The clear formation of “carbon” layers/patches in several areas of the Ni particle’s surface in the spent catalyst should be noted (Fig. 4.19b).

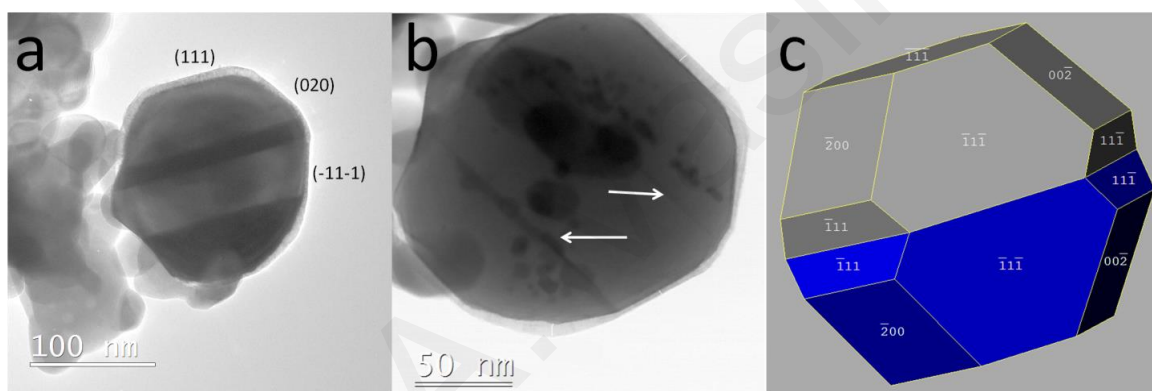


**Figure 4.19:** (a) TEM micrograph of nickel particle formed in the 5 wt.% Ni/ $\text{Ce}_{0.2}\text{Pr}_{0.8}\text{O}_2$  catalyst, where polysynthetic twin crystals are clearly visible as brighter and darker areas; (b) STEM micrograph of the same nickel particle with the highlighted twin crystal boundary, where carbon layers are also clearly shown; (c) a model of polysynthetic cubo-octahedral twin crystal.

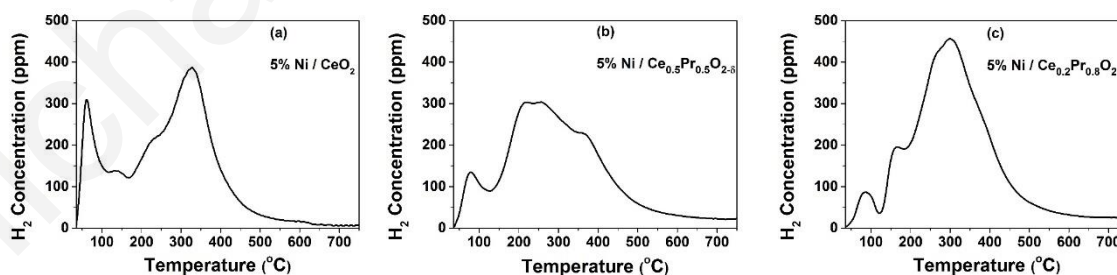
#### 4.2.1.3. $\text{H}_2$ temperature-programmed desorption (TPD) studies

Fig. 4.20 presents  $\text{H}_2$ -TPD traces obtained over the 5 wt.% Ni supported on  $\text{CeO}_2$  (Fig. 4.20a),  $\text{Ce}_{0.5}\text{Pr}_{0.5}\text{O}_{2-\delta}$  (Fig. 4.20b) and  $\text{Ce}_{0.2}\text{Pr}_{0.8}\text{O}_{2-\delta}$  (Fig. 4.20c) carriers. The total amount of hydrogen desorbed and the associated Ni dispersion ( $D_{\text{Ni}}$ , %) are reported in Table 4.6 along with the peak maximum desorption temperatures ( $T_{\text{M}}$ , °C) observed.

**Table 4.6:**  $\text{H}_2$  desorption ( $\mu\text{mol g}^{-1}$ ), Ni dispersion ( $\text{D}_{\text{Ni}}$ , %) and Ni mean particle size ( $d_{\text{Ni}}$ , nm) obtained from  $\text{H}_2$ -TPD performed on the fresh 5 wt.%  $\text{Ni}/\text{Ce}_{1-x}\text{Pr}_x\text{O}_{2-\delta}$  ( $x = 0.0, 0.2, 0.5, 0.65, 0.8$ ) catalysts.  $T_{\text{M}}$  ( $^{\circ}\text{C}$ ) is the temperature at which maximum  $\text{H}_2$  desorption rate occurs.

Catalysts	$T_{\text{M}}$ ( $^{\circ}\text{C}$ )	$\text{H}_2$ ( $\mu\text{mol g}^{-1}$ )	$\text{D}_{\text{Ni}}$ (%)	$d_{\text{NiO}}$ (nm)
5 wt.% $\text{Ni}/\text{CeO}_2$	62, 138, 232, 327	13.1	3.0	31.4
5 wt.% $\text{Ni}/\text{Ce}_{0.8}\text{Pr}_{0.2}\text{O}_2$	64, 143, 202, 368	10.0	2.8	34.4
5 wt.% $\text{Ni}/\text{Ce}_{0.5}\text{Pr}_{0.5}\text{O}_2$	80, 218, 255, 360	13.5	3.2	30.5
5 wt.% $\text{Ni}/\text{Ce}_{0.35}\text{Pr}_{0.65}\text{O}_2$	86, 214, 297	12.7	3.0	32.6
5 wt.% $\text{Ni}/\text{Ce}_{0.2}\text{Pr}_{0.8}\text{O}_2$	86, 167, 298	15.9	3.7	26.2

The good agreement between  $\text{H}_2$  chemisorption (mean Ni particle size ( $d_{\text{Ni}}$ ), Table 4.6) and powder XRD (mean NiO particle size, Table 4.5) is noted. According to the results of Fig. 4.20 and Table 4.6, the Pr/(CePr) % composition in support has largely influenced the heterogeneity of the Ni surface (e.g.  $E_{\text{Ni-H}}$  bond strength ( $T_{\text{M}}$ )) and the distribution of Ni<sub>s</sub> hydrogen chemisorption sites. On the other hand, Ni dispersion and mean particle size remain practically similar (small variations of less than 12%) except for  $\text{Ni}/\text{Ce}_{0.2}\text{Pr}_{0.8}\text{O}_{2-\delta}$  (~ 15-25% variation). In particular, the dispersion of Ni was found to be in the 2.8-3.7% range and the estimated Ni particle size in the 26-34 nm range.  $\text{Ni}/\text{Ce}_{0.2}\text{Pr}_{0.8}\text{O}_{2-\delta}$  shows the highest Ni dispersion (smallest particle size), whereas  $\text{Ni}/\text{Ce}_{0.8}\text{Pr}_{0.2}\text{O}_{2-\delta}$  the lowest one (largest particle size). The latter catalyst shows significantly higher activity but larger quantities of inactive “carbon” than the  $\text{Ni}/\text{Ce}_{0.2}\text{Pr}_{0.8}\text{O}_{2-\delta}$  one.

**Figure 4.20:**  $\text{H}_2$ -TPD traces obtained over the 5 wt.%  $\text{Ni}/\text{Ce}_{1-x}\text{Pr}_x\text{O}_{2-\delta}$  ( $x = 0, 0.5, 0.8$ ) catalysts.  $F_{\text{He}} = 50 \text{ N mL min}^{-1}$  He;  $\beta = 30 \text{ }^{\circ}\text{C min}^{-1}$ ;  $W = 0.5 \text{ g}$ .

As Pr-dopant is progressively added in the ceria lattice (e.g. from 0 to 20 and 80 atom-%), the low-temperature ( $< 150\text{ }^\circ\text{C}$ ) desorbing states ( $\mu\text{mol H g}^{-1}$ ) of chemisorbed hydrogen (lower binding energy) decrease in amount, whereas those at  $T > 150\text{ }^\circ\text{C}$  increase. At least three main desorption states might be present in all three catalysts.  $\text{H}_2$ -TPD traces, similar to those of Fig. 4.20, have been reported for the 15 wt.% Ni/ $\text{Ce}_{0.12}\text{Zr}_{0.88}\text{O}_2$  [49], 5 wt.% Ni/ $\text{Ce}_{1-x}\text{Zr}_x\text{O}_2$  [17,43], 5 wt.% Ni/ $\text{Ce}_{0.8}\text{Pr}_{0.2}\text{O}_2$  [43] and 5 wt.% Ni/ $\text{Al}_2\text{O}_3$ -CaO [18] solids.

#### 4.2.1.4. Catalytic performance studies

Fig. 4.21 reports on the catalytic performance of 5 wt.% Ni/ $\text{Ce}_{1-x}\text{Pr}_x\text{O}_{2-\delta}$  solids towards dry reforming of methane in the 550-750  $^\circ\text{C}$  range after 30 min on reaction stream, in terms of  $\text{CH}_4$  conversion ( $X_{\text{CH}_4}$ , %) and  $\text{H}_2$ -yield (%) (Fig. 4.21A),  $\text{CO}_2$  conversion ( $X_{\text{CO}_2}$ , %) and CO-yield (%) (Fig. 4.21B), and  $\text{H}_2/\text{CO}$  gas product ratio (Fig. 4.21C). It should be noted that no  $\text{C}_2\text{H}_6$  was formed within the temperature range of 550-750  $^\circ\text{C}$ .

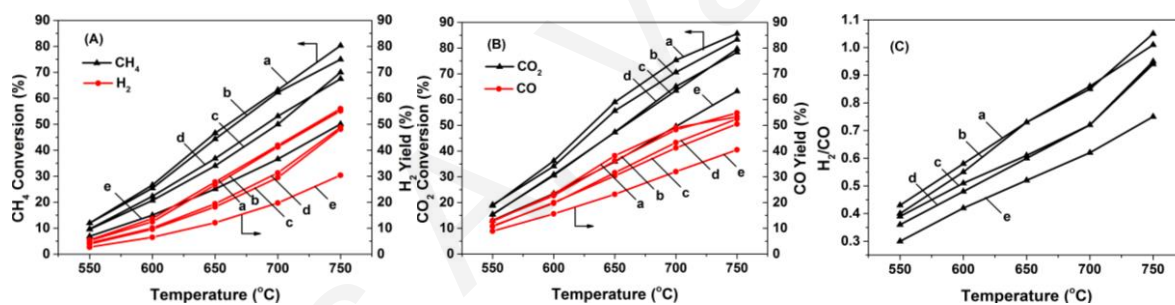


**Figure 4.21:** (A)  $\text{CH}_4$ -conversion (%) and  $\text{H}_2$  yield (%), (B)  $\text{CO}_2$ -conversion (%) and CO yield (%) and (C)  $\text{H}_2/\text{CO}$  gas product ratio obtained after 30 min in dry reforming of methane in the 550-750  $^\circ\text{C}$  range over 5 wt.% Ni supported on (a)  $\text{CeO}_2$ ; (b)  $\text{Ce}_{0.8}\text{Pr}_{0.2}\text{O}_{2-\delta}$ ; (c)  $\text{Ce}_{0.5}\text{Pr}_{0.5}\text{O}_{2-\delta}$ ; (d)  $\text{Ce}_{0.35}\text{Pr}_{0.65}\text{O}_{2-\delta}$  and (e)  $\text{Ce}_{0.2}\text{Pr}_{0.8}\text{O}_{2-\delta}$  carriers;  $P_{\text{CH}_4} = 0.2\text{ bar}$ ,  $P_{\text{CO}_2} = 0.2\text{ bar}$ ,  $P_T = 1.0\text{ bar}$ ;  $\text{GHSV} = 30,000\text{ h}^{-1}$ .

By increasing the reaction temperature from 550 to 750  $^\circ\text{C}$  the catalytic activity increases considerably according to the endothermic nature of the reaction. For example, in the case of Ni/ $\text{CeO}_2$ ,  $X_{\text{CH}_4}$  increases from 12.0 to 80.3%. In all catalytic systems, the  $\text{CO}_2$ -conversion (%) is found to be larger than that of  $\text{CH}_4$ -conversion (%) in the temperature range of 550-750  $^\circ\text{C}$ . The  $\text{H}_2/\text{CO}$  gas product ratio takes low values in the 550-600  $^\circ\text{C}$  range (ca. 0.3-0.58) for all catalytic systems, but significantly larger values (0.72-1.05) at 700 and 750  $^\circ\text{C}$  except for the 5 wt.% Ni/ $\text{Ce}_{0.2}\text{Pr}_{0.8}\text{O}_{2-\delta}$  solid ( $\text{H}_2/\text{CO} = 0.62$ -0.75). Dry reforming of  $\text{CH}_4$  at 750  $^\circ\text{C}$  over the  $\text{Ce}_{1-x}$

$x\text{Pr}_x\text{O}_{2-\delta}$  supports alone showed very small catalytic activity. In particular,  $\text{Ce}_{0.8}\text{Pr}_{0.2}\text{O}_{2-\delta}$  resulted in  $X_{\text{CO}_2} = 0.2\%$ ,  $X_{\text{CH}_4} = 0.1\%$  and CO- and  $\text{H}_2$ -yields of 1.25 and 0.1%, respectively.

The effect of Pr-dopant on the stability (25 h on stream) of 5 wt.% Ni/ $\text{Ce}_{1-x}\text{Pr}_x\text{O}_{2-\delta}$  solids at 750 °C is shown in Fig. 4.22. A monotonic %-drop in activity with increasing Pr-dopant concentration in the 50-80 atom-% range is obtained; 6.5-16.5% for  $\text{CH}_4$  conversion and 4.0-8.5% for  $\text{CO}_2$  conversion. On the other hand, the undoped and 20 atom-% Pr-doped ceria showed similar activity drop (3 and 5% for  $\text{CH}_4$  conversion; 1.5 and 2.5% for  $\text{CO}_2$  conversion, respectively).

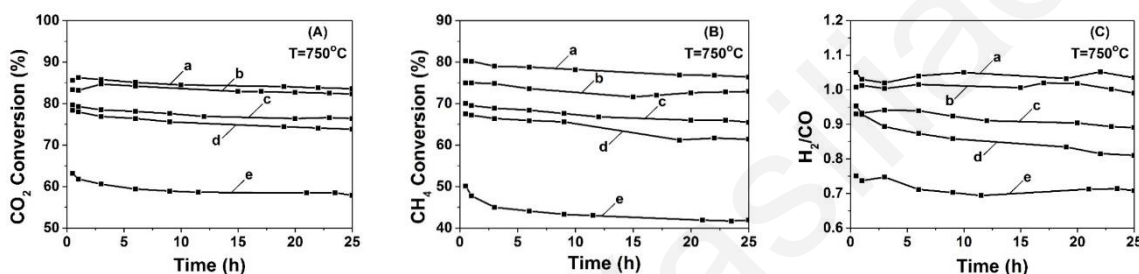


**Figure 4.22:** Stability test (25 h) in the dry reforming of methane reaction performed at 750 °C in terms of  $\text{CO}_2$ -conversion (%) (A),  $\text{CH}_4$ -conversion (%) (B) and  $\text{H}_2/\text{CO}$  gas-product ratio (C) over 5 wt.% Ni supported on (a)  $\text{CeO}_2$ ; (b)  $\text{Ce}_{0.8}\text{Pr}_{0.2}\text{O}_{2-\delta}$ ; (c)  $\text{Ce}_{0.5}\text{Pr}_{0.5}\text{O}_{2-\delta}$ ; (d)  $\text{Ce}_{0.35}\text{Pr}_{0.65}\text{O}_{2-\delta}$  and (e)  $\text{Ce}_{0.2}\text{Pr}_{0.8}\text{O}_{2-\delta}$  catalysts;  $P_{\text{CH}_4} = 0.2$  bar,  $P_{\text{CO}_2} = 0.2$  bar,  $P_{\text{T}} = 1.0$  bar;  $\text{GHSV} = 30,000 \text{ h}^{-1}$ .

An increasing concentration of Pr-dopant in the ceria matrix causes a continuous decrease of  $\text{CH}_4$ - and  $\text{CO}_2$ -conversion (%) but also of  $\text{H}_2/\text{CO}$  gas product ratio, after 0.5 h or 25 h of DRM at 750 °C (Fig. 4.23). In particular,  $\text{CH}_4$ -conversion,  $\text{CO}_2$ -conversion and  $\text{H}_2/\text{CO}$  gas product ratio are lower by 37.5, 22.4 and 32.4%, respectively, when Ni/ $\text{CeO}_2$  and Ni/ $\text{Ce}_{0.2}\text{Pr}_{0.8}\text{O}_{2-\delta}$  solids are compared after 0.5 h of reaction. This monotonic loss of activity with increasing Pr-dopant concentration in the  $\text{Ce}_{1-x}\text{Pr}_x\text{O}_{2-\delta}$  support is *not due to the accumulation of inactive "carbon"* since the latter shows a remarkable decrease with increasing concentration of Pr-dopant in the support, as shown in the following section.

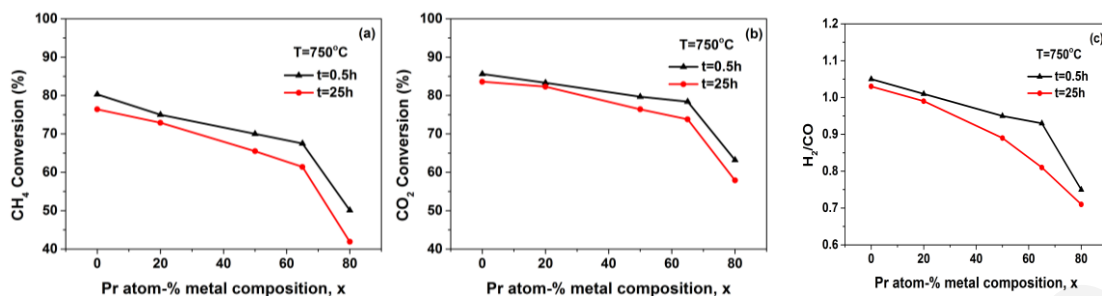


**Figure 4.23:** Effect of Pr atom-% composition ( $\text{Pr}/(\text{CePr}) \times 100$ ) on (a)  $\text{CH}_4$ -conversion (%), (b)  $\text{CO}_2$ -conversion (%) and (c)  $\text{H}_2/\text{CO}$  gas-product ratio obtained after 0.5 h ( $\blacktriangle$ ) and 25 h ( $\bullet$ ) of dry reforming of methane at 750 °C over 5 wt.%  $\text{Ni}/\text{Ce}_{1-x}\text{Pr}_x\text{O}_{2-\delta}$  catalysts ( $x = 0, 0.2, 0.5, 0.65$  and  $0.8$ );  $\text{GHSV} = 30,000 \text{ h}^{-1}$ .

#### 4.2.2. Characterization of “carbon” formed during DRM by various transient techniques

##### 4.2.2.1. Temperature programmed oxidation (TPO)

Fig. 4.24 presents  $\text{CO}_2$  and  $\text{CO}$  traces of temperature-programmed oxidation (TPO) of “carbon” experiments conducted over the 5 wt.%  $\text{Ni}/\text{Ce}_{1-x}\text{Pr}_x\text{O}_{2-\delta}$  ( $x = 0.0, 0.2$  and  $0.5$ ) catalysts after 25 h of DRM at 750 °C. The amount of “carbon” formed and the rate (proportional to the gas phase concentration) vs. temperature profiles are strongly influenced by the Pr-dopant concentration in the support. A notably different feature of TPO trace is observed in the case of 5 wt.%  $\text{Ni}/\text{CeO}_2$  when compared to the other two catalysts compositions. The sharp increase in the rate of “carbon” oxidation to  $\text{CO}_2$ , which occurs at  $\sim 760$  °C, and the trace of  $\text{CO}$  starting at temperatures higher than  $\sim 760$  °C for the case of  $\text{Ni}/\text{CeO}_2$ , absent in the case of  $\text{Ni}/\text{Ce}_{1-x}\text{Pr}_x\text{O}_{2-\delta}$  catalysts ( $x = 0.2$  and  $0.5$ ), should be noted.

These TPO traces probe for various kinds of “carbon” with different distribution based on the temperature at which maximum oxidation rate occurs. The kinetics of oxidation of these kinds of “carbon” is apparently influenced by the Pr-dopant in the support, where low Pr-dopant loadings result in a kind of “carbon” more easily oxidized compared to that obtained with larger Pr-dopant loadings (e.g. 80 atom-%). Table 4.7 reports the total amount of “carbon” ( $\mu\text{mol C g}^{-1}$  and wt.% C) measured by TPO after 25 h of DRM over the series of 5 wt.%  $\text{Ni}/\text{Ce}_{1-x}\text{Pr}_x\text{O}_{2-\delta}$  catalysts. A remarkable reduction in “carbon” deposition is obtained when ceria is doped with 80 atom-% Pr, namely 19.6 wt.% C for  $\text{Ni}/\text{CeO}_2$  to be compared with 0.07 wt.% C for the  $\text{Ni}/\text{Ce}_{0.2}\text{Pr}_{0.8}\text{O}_{2-\delta}$  catalyst (280 times smaller).

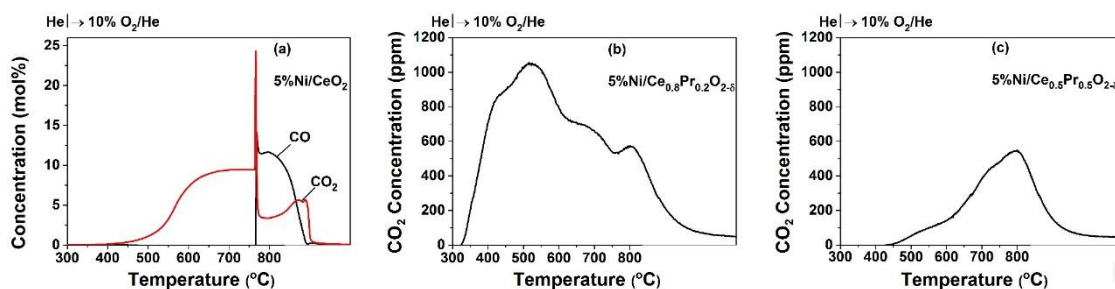


**Figure 4.24:** Transient response curves of  $\text{CO}_2$  and  $\text{CO}$  obtained during TPO of “carbon” formed after 25 h of dry reforming of methane at 750 °C ( $\text{GHSV} = 30,000 \text{ h}^{-1}$ ) over the 5 wt.%  $\text{Ni}/\text{Ce}_{1-x}\text{Pr}_x\text{O}_{2-\delta}$  ( $x = 0.0, 0.2, 0.5$ ) catalysts. Gas delivery sequence: DRM (750 °C, 25 h)  $\rightarrow$  He, increase T to 800 °C until no  $\text{CO}$  and  $\text{CO}_2$  are measured in the MS  $\rightarrow$  cool down in He flow to 300 °C  $\rightarrow$  T is increased to 800 °C ( $\beta = 30 \text{ }^\circ\text{C min}^{-1}$ ).

**Table 4.7:** Temperature-programmed oxidation (TPO) of “carbon” ( $\text{CO}$  and  $\text{CO}_2$  formation,  $\mu\text{mol g}^{-1}$ ) formed after 25 h of DRM at 750 °C over the 5 wt.%  $\text{Ni}/\text{Ce}_{1-x}\text{Pr}_x\text{O}_{2-\delta}$  ( $x = 0.0, 0.2, 0.5, 0.8$ ) catalysts. The amount of “carbon” (wt.%) measured by TGA-TPO is also reported.

Catalysts	$\text{CO}$ ( $\mu\text{mol g}^{-1}$ )	$\text{CO}_2$ ( $\mu\text{mol g}^{-1}$ )	“Carbon” ( $\mu\text{mol g}^{-1}$ ) <sup>a</sup>	“Carbon” (wt.%) TGA-TPO <sup>b</sup>
5 wt.% $\text{Ni}/\text{CeO}_2$	4.627	11,727	16,354 (19.6) <sup>c</sup>	37.7
5 wt.% $\text{Ni}/\text{Ce}_{0.8}\text{Pr}_{0.2}\text{O}_2$	- <sup>d</sup>	182	182.2 (0.22)	29.9
5 wt.% $\text{Ni}/\text{Ce}_{0.5}\text{Pr}_{0.5}\text{O}_2$	-	64.5	64.5 (0.08)	0.90
5 wt.% $\text{Ni}/\text{Ce}_{0.2}\text{Pr}_{0.8}\text{O}_2$	-	5.83	58.3 (0.07)	0.15

<sup>a</sup>: DRM reaction conditions: catalytic bed = 0.15 g catalyst + 0.15 g SiC; total flow rate = 150 N mL  $\text{min}^{-1}$ .

<sup>b</sup>: DRM reaction conditions: catalytic bed = 0.3 g catalyst, no SiC; total flow rate = 150 N mL  $\text{min}^{-1}$ .

<sup>c</sup>: wt.% “carbon”; <sup>d</sup>: no  $\text{CO}$  is observed.

The remarkable support effect in the reduction of the rate of “carbon” deposition due to the  $\text{Pr}^{3+}$ -doped ceria support in the DRM over the 5 wt.%  $\text{Ni}/\text{Ce}_{1-x}\text{Pr}_x\text{O}_{2-\delta}$  catalysts was also investigated at higher  $\text{CH}_4$  and  $\text{CO}_2$  conversions than those reported in Fig. 4.22A and B after using 0.3 g of catalyst (no SiC was used) and a flow rate of 150 N mL  $\text{min}^{-1}$ ; after 25 h of dry reforming,  $\text{CH}_4$ -conversions 55-87% and  $\text{CO}_2$ -conversions 70-92% were obtained.



The amount of “carbon” accumulated was also measured by TGA-TPO and CHNS analyses techniques and results are presented in Fig. 4.25 (different GHSV was used). According to the TGA analysis of 5 wt.% Ni/CeO<sub>2</sub>, this had accumulated 37.7 wt.% carbon.

However, when Pr-dopant was introduced into the ceria lattice at the level of 20, 50, 65 and 80 atom-%, the amount of carbon decreased to 29.9, 0.9, 13.2 and 0.1 wt.%, respectively. It appears that the extent of “carbon” accumulation is influenced significantly by the CH<sub>4</sub>- and CO<sub>2</sub>-conversion levels, which in turn these are determined by the GHSV (h<sup>-1</sup>) used. Moreover, no mass decrease at temperatures of ~ 300 °C was observed that could be attributed to the presence of encapsulating carbon on the surface of spent solids [50]. The temperature range where carbon oxidation took place suggests that the accumulated carbon on the catalyst surface is predominantly in the form of filaments. Slight increase of mass observed in the case of catalysts based on Pr-rich supports (5 wt.% Ni/Ce<sub>0.2</sub>Pr<sub>0.8</sub>O<sub>2</sub>, 5 wt.% Ni/Ce<sub>0.5</sub>Pr<sub>0.5</sub>O<sub>2</sub> and 5 wt.% Ni/Ce<sub>0.35</sub>Pr<sub>0.65</sub>O<sub>2</sub>) during the TGA-TPO analysis in the 300-450 °C range might be attributed to the oxidation of Ni particles.

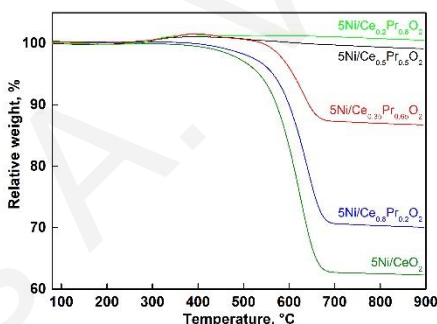


**Figure 4.25:** TGA-TPO relative weight-% vs temperature profiles for the spent 5 wt.% Ni/Ce<sub>1-x</sub>Pr<sub>x</sub>O<sub>2-δ</sub> catalysts following 25 h of dry reforming at 750 °C.

#### 4.2.2.2. Scanning Electron Microscopy (SEM) studies

SEM micrographs of fresh and spent (after 25 h of DRM at 750 °C) samples of the series of Ni/Ce<sub>1-x</sub>Pr<sub>x</sub>O<sub>2-δ</sub> catalysts are illustrated in Fig. 4.26 a-e. The supports of all five fresh catalysts consist of particles in the 50-150 nm range in size, which are agglomerated into larger porous structures. In the case of spent Ni/Ce<sub>0.5</sub>Pr<sub>0.5</sub>O<sub>2-δ</sub> and Ni/Ce<sub>0.2</sub>Pr<sub>0.8</sub>O<sub>2-δ</sub> catalysts (Fig. 4.26c and e), hardly any carbon filaments could be observed, due to its very low amount. On the other hand, in the other spent catalysts, the amount of carbon deposits was significantly larger, result that was confirmed by SEM analyses, where numerous carbon filaments were observed.

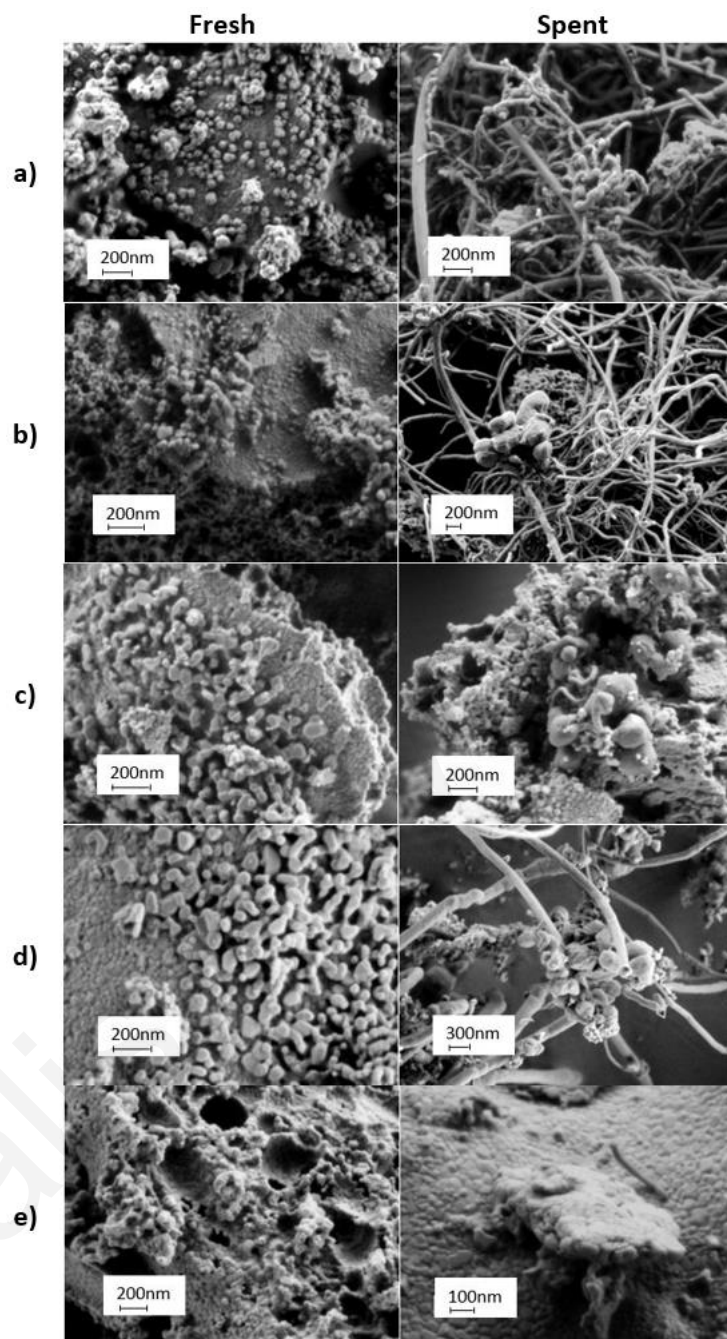


**Figure 4.26:** SEM micrographs obtained on the fresh and spent (after 25 h on stream in DRM at 750 °C) catalysts: (a) 5 wt.% Ni/CeO<sub>2</sub>, (b) 5 wt.% Ni/Ce<sub>0.8</sub>Pr<sub>0.2</sub>O<sub>2-δ</sub>, (c) 5 wt.% Ni/Ce<sub>0.5</sub>Pr<sub>0.5</sub>O<sub>2-δ</sub>, (d) 5 wt.% Ni/Ce<sub>0.35</sub>Pr<sub>0.65</sub>O<sub>2-δ</sub> and (e) 5 wt.% Ni/Ce<sub>0.2</sub>Pr<sub>0.8</sub>O<sub>2-δ</sub>.

Graphitic carbon has also been identified on the spent 5 wt.% Ni/CeO<sub>2</sub> catalyst by XRD as shown in Fig. 4.27b (arrow).



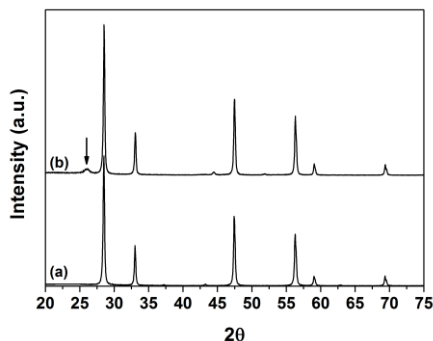


**Figure 4.27:** Powder X-ray diffractograms of fresh 5 wt.% Ni/CeO<sub>2</sub> (a) and aged (after 25 h in dry reforming of methane at 750 °C) 5 wt.% Ni/CeO<sub>2</sub> catalyst (b).

#### 4.2.2.3. Quantifying the origin of carbon formation (CH<sub>4</sub> versus CO<sub>2</sub> activation route)

Fig. 4.28 presents <sup>12</sup>CO<sub>2</sub> and <sup>13</sup>CO<sub>2</sub> transient response curves recorded during TPO of the “carbon” formed over the 5 wt.% Ni/Ce<sub>1-x</sub>Pr<sub>x</sub>O<sub>2-δ</sub> ( $x = 0.0$  and  $0.8$ ) catalysts after 30 min of dry reforming (5% <sup>13</sup>CO<sub>2</sub>/5% <sup>12</sup>CH<sub>4</sub>/He) at 550 and 750 °C. The different shape and position in the obtained <sup>13</sup>CO<sub>2</sub> and <sup>12</sup>CO<sub>2</sub> response curves for the two catalysts and their relative amounts (area under the TPO traces) are apparent. In the case of DRM performed at 550 °C over the Ni/CeO<sub>2</sub> catalyst, both <sup>13</sup>CO<sub>2</sub> and <sup>12</sup>CO<sub>2</sub> traces exhibit a main peak centred at ~ 545 °C (Fig. 4.28a) and a shoulder at the falling part of it (~ 620 °C). On the other hand, in the case of Ni/Ce<sub>0.2</sub>Pr<sub>0.8</sub>O<sub>2-δ</sub> catalyst, both <sup>13</sup>CO<sub>2</sub> and <sup>12</sup>CO<sub>2</sub> traces consist only of one symmetrical peak centred at ~ 575 °C (Fig. 4.28c). A similar behaviour is also observed when the DRM was performed at 750 °C (Fig. 4.28d) but a slightly different behaviour is seen in the case of Ni/CeO<sub>2</sub> (Fig. 4.28b). For the latter catalyst, maximum oxidation rate occurs at ~ 630 °C, which is higher than that occurred after DRM at 550 °C (Fig. 4.28a). In the case of Ni/Ce<sub>0.2</sub>Pr<sub>0.8</sub>O<sub>2-δ</sub>, the rate maximum occurred at the same temperature (Figs. 4.28c, d). These results imply that Pr<sup>3+</sup>-dopant in the doped-ceria support likely influences the type of “carbon” deposited as a function of DRM reaction temperature. The <sup>13</sup>CO<sub>2</sub>-TPO traces arise from the oxidation of <sup>13</sup>C-containing “carbon” formed via the <sup>13</sup>CO<sub>2</sub> activation route, whereas those of <sup>12</sup>CO<sub>2</sub> from the oxidation of <sup>12</sup>C-containing “carbon” formed via the <sup>12</sup>CH<sub>4</sub> decomposition route.

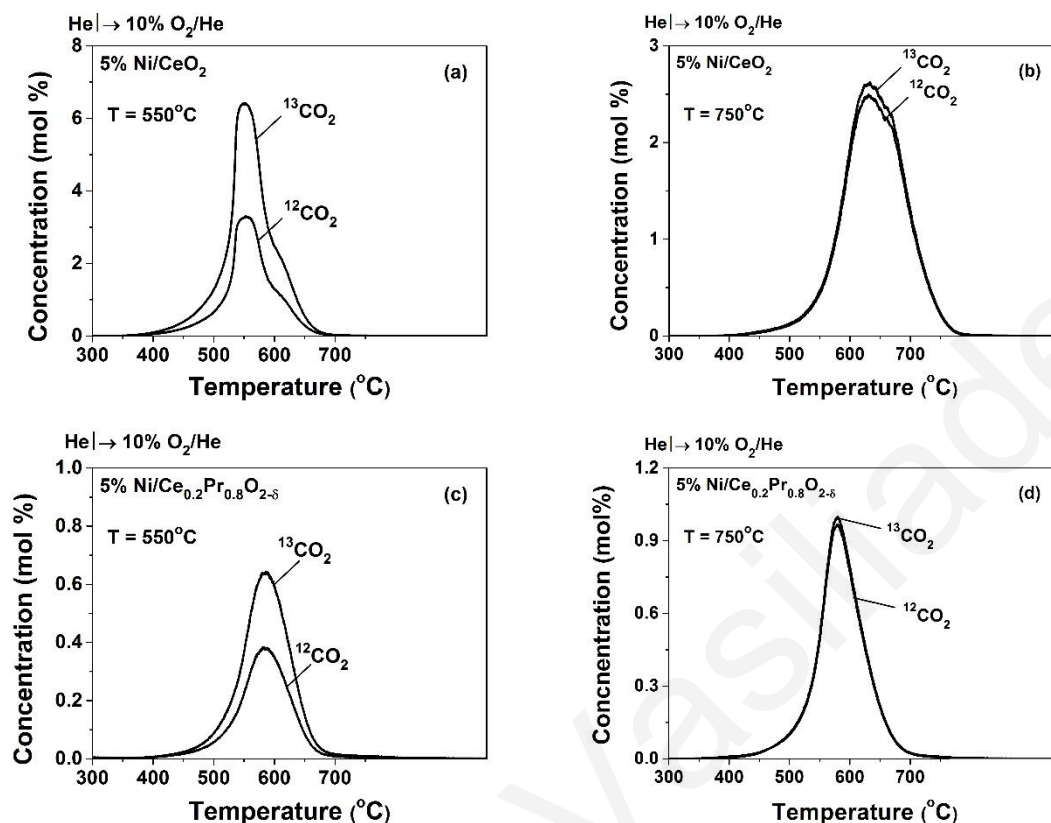


**Figure 4.28:** Temperature-programmed oxidation (TPO) of “carbon” formed during dry reforming of  $^{12}\text{CH}_4$  with  $^{13}\text{CO}_2$  at 550 and 750  $^\circ\text{C}$  over 5 wt.% Ni/CeO<sub>2</sub> (a, b) and 5 wt.% Ni/Ce<sub>0.2</sub>Pr<sub>0.8</sub>O<sub>2- $\delta$</sub>  (c, d) catalysts. Gas delivery sequence: 5%  $^{13}\text{CO}_2$ /5%  $^{12}\text{CH}_4$ /Ar/He (T, 30 min,  $F_T = 100 \text{ N mL min}^{-1}$ )  $\rightarrow$  He (750  $^\circ\text{C}$ , 10 min)  $\rightarrow$  cool in He flow to 100  $^\circ\text{C}$   $\rightarrow$  10% O<sub>2</sub>/He, TPO ( $F_T = 50 \text{ N mL min}^{-1}$ ,  $\beta = 30 \text{ }^\circ\text{C min}^{-1}$ ); W = 0.2 g (fresh catalyst).

Table 4.8 reports the amounts ( $\mu\text{mol g}^{-1}$  and wt.% C) of  $^{12}\text{CO}_2$ ,  $^{13}\text{CO}_2$  and total “carbon”, the  $^{12}\text{CO}_2$ / $^{13}\text{CO}_2$  ratio and the %-contribution of the CO<sub>2</sub> activation route to the total “carbon” deposition after DRM reaction at 550 and 750  $^\circ\text{C}$  over the undoped and 80 atom-% doped ceria supported Ni catalysts. At the lowest T of 550  $^\circ\text{C}$ , after increasing the Pr<sup>3+</sup>-dopant concentration from zero (Ni/CeO<sub>2</sub>) to 80 atom-% (Ni/Ce<sub>0.2</sub>Pr<sub>0.8</sub>O<sub>2- $\delta$</sub> ), the deposited “carbon” is found to largely decrease to a very low value (0.06 wt.% or 60 mg g<sub>cat</sub><sup>-1</sup>). In contrast, the Pr<sup>3+</sup>-dopant concentration affects only to a small extent the %-contribution of the CO<sub>2</sub> activation route to “carbon” deposition (ca. 50.9% for Ni/Ce<sub>0.2</sub>Pr<sub>0.8</sub>O<sub>2- $\delta$</sub>  and 54% for Ni/CeO<sub>2</sub> at 750  $^\circ\text{C}$ ). For these particular catalytic systems, it is clear that the CO<sub>2</sub> activation route becomes to a large extent dominant for the deposition of *inactive* “carbon” at 550  $^\circ\text{C}$ . However, at 750  $^\circ\text{C}$  the inactive “carbon” derived from the CH<sub>4</sub> decomposition route becomes equally important. In fact, it was

recently reported [43] that part of the CO formed in the dry reforming of methane over the 5 wt.% Ni/Ce<sub>0.8</sub>Pr<sub>0.2</sub>O<sub>2-δ</sub> catalyst leads to the formation of *inactive* carbon via the Boudouard reaction.

**Table 4.8:** <sup>12</sup>CO<sub>2</sub> and <sup>13</sup>CO<sub>2</sub> (μmol g<sup>-1</sup>) and <sup>12</sup>CO<sub>2</sub>/<sup>13</sup>CO<sub>2</sub> product ratio obtained during temperature-programmed oxidation (TPO) of “carbon” formed after 30 min of dry reforming (5% <sup>13</sup>CO<sub>2</sub>/5% <sup>12</sup>CH<sub>4</sub>/45% Ar/45% He) at 550 and 750 °C over the 5 wt.% Ni/CeO<sub>2</sub> and 5 wt.% Ni/Ce<sub>0.2</sub>Pr<sub>0.8</sub>O<sub>2-δ</sub> catalysts. DRM reaction conditions: F<sub>T</sub> = 100 N mL min<sup>-1</sup>; W<sub>cat</sub> = 0.2 g (no SiC as dilution was used).

Catalysts	T (°C)	<sup>12</sup> CO <sub>2</sub> (μmol g <sup>-1</sup> )	<sup>13</sup> CO <sub>2</sub> (μmol g <sup>-1</sup> )	<sup>12</sup> CO <sub>2</sub> / <sup>13</sup> CO <sub>2</sub>	Total C (μmol g <sup>-1</sup> )
5 wt.% Ni/CeO <sub>2</sub>	550	593.6	1139.6	0.52 (65.7) <sup>a</sup>	1733.2 (2.08) <sup>b</sup>
	750	948.8	1158.3	0.87 (54.0)	2143.1 (2.57)
5 wt.% Ni/Ce <sub>0.2</sub> Pr <sub>0.8</sub> O <sub>2</sub>	550	75.9	114.5	0.66 (60.1)	190.4 (0.23)
	750	153.7	159.1	0.96 (50.9)	312.8 (0.38)

<sup>a</sup>: %-contribution of the CO<sub>2</sub> activation route to the total “carbon” derived from both CH<sub>4</sub> and CO<sub>2</sub> activation routes;

<sup>b</sup>: number in parentheses denotes wt.% carbon.

### 4.2.3. SSITKA – Mechanistic Studies

#### 4.2.3.1. Measurement of *active carbon* derived from the CO<sub>2</sub> activation route

Fig. 4.29 shows transient response curves (in terms of a dimensionless Z concentration function) for Kr (tracer gas), <sup>13</sup>CO and <sup>13</sup>CO<sub>2</sub> during the SSITKA switch: <sup>12</sup>CH<sub>4</sub>/<sup>12</sup>CO<sub>2</sub>/Ar/He (2 h) → <sup>12</sup>CH<sub>4</sub>/<sup>13</sup>CO<sub>2</sub>/Ar/Kr/He (20 min) → <sup>12</sup>CH<sub>4</sub>/<sup>12</sup>CO<sub>2</sub>/Ar/He (t) at 750 °C over the most active 5 wt.% Ni/CeO<sub>2</sub> (Fig. 4.29a) and the least active 5 wt.% Ni/Ce<sub>0.2</sub>Pr<sub>0.8</sub>O<sub>2-δ</sub> (Fig. 4.29b) catalysts, as previously shown and discussed. It is seen that the <sup>13</sup>CO response curve lags behind that of <sup>13</sup>CO<sub>2</sub> for both catalysts, and the latter response lags behind that of Kr tracer gas (characteristic response for a non-adsorbing and non-reacting gas). The exchange of the *active “carbon” pool* lasts about 90 s and 40 s for the Ni/CeO<sub>2</sub> (Fig. 4.29a) and Ni/Ce<sub>0.2</sub>Pr<sub>0.8</sub>O<sub>2-δ</sub> (Fig. 4.29b) catalyst, respectively.

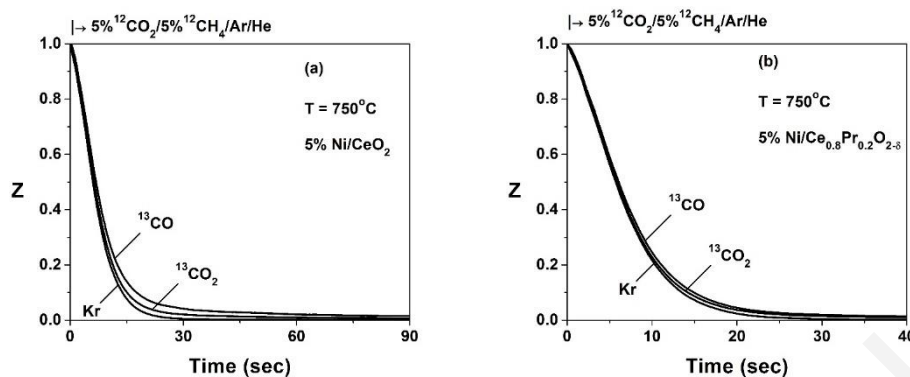


**Figure 4.29:** Kr,  $^{13}\text{CO}$  and  $^{13}\text{CO}_2$  SSITKA response curves obtained after 2 h of dry reforming of methane at 750 °C over (a) 5 wt.% Ni/CeO<sub>2</sub> and (b) 5 wt.% Ni/Ce<sub>0.8</sub>Pr<sub>0.2</sub>O<sub>2- $\delta$</sub>  catalysts. SSITKA switches: 5%  $^{12}\text{CO}_2$ /5%  $^{12}\text{CH}_4$ /Ar/He (2 h)  $\rightarrow$  5%  $^{13}\text{CO}_2$ /5%  $^{12}\text{CH}_4$ /2% Kr/Ar/He (20 min)  $\rightarrow$  5%  $^{12}\text{CO}_2$ /5%  $^{12}\text{CH}_4$ /Ar/He (t);  $W_{\text{cat}}$  (200 mg) = 30 mg diluted with 170 mg SiC;  $F_T = 100 \text{ N mL min}^{-1}$ .

After applying the appropriate material balance equation (see Chapter 3, Section 3.7.4), the amount of *active* carbon can be estimated and values are reported in Table 4.9 for Ni/CeO<sub>2</sub>, Ni/Ce<sub>0.8</sub>Pr<sub>0.2</sub>O<sub>2- $\delta$</sub>  and Ni/Ce<sub>0.2</sub>Pr<sub>0.8</sub>O<sub>2- $\delta$</sub>  catalysts. The equivalent number of surface monolayers of active carbon based on the Ni surface (Table 4.6,  $D_{\text{Ni}}$  (%)), and after assuming  $C/\text{Ni}_s = 1$ , is also reported in Table 4.9. As Pr<sup>3+</sup>-dopant increases from zero (undoped ceria) to 80 atom-%, the active “carbon” concentration decreases. More precisely, values of 87.7 ( $\theta_c = 3.4$ ), 2.0 ( $\theta_c = 0.07$ ) and 16.7  $\mu\text{mol/g}$  ( $\theta_c = 0.56$ ) are obtained for the Ni/CeO<sub>2</sub>, Ni/Ce<sub>0.8</sub>Pr<sub>0.2</sub>O<sub>2- $\delta$</sub>  and Ni/Ce<sub>0.2</sub>Pr<sub>0.8</sub>O<sub>2- $\delta$</sub>  catalyst, respectively. It should be noted that these values correspond to integral reactor performance conditions (CO<sub>2</sub> conversions in the 16-62% range).

Similar SSITKA experiments to those shown in Fig. 4.29 were also performed at  $T = 550 \text{ }^\circ\text{C}$  and the obtained results are reported in Table 4.9. These SSITKA measurements correspond to truly kinetic conditions (CO<sub>2</sub> and CH<sub>4</sub> conversions lower than 15%) as opposed to the case at 750 °C. It is observed that practically the same behaviour in the concentration of *active* carbon with increasing Pr-dopant loading is obtained as in the case of DRM at 750 °C. In particular, the *active* carbon is 3.7  $\mu\text{mol g}^{-1}$  for Ni/CeO<sub>2</sub>, which is significantly reduced to 0.72 and 0.87  $\mu\text{mol g}^{-1}$  in the Ni/Ce<sub>0.8</sub>Pr<sub>0.2</sub>O<sub>2- $\delta$</sub>  and Ni/Ce<sub>0.2</sub>Pr<sub>0.8</sub>O<sub>2- $\delta$</sub>  catalysts, respectively.

The influence of reactant conversion on the concentration of *active* C-pool was also investigated at 550 °C. Fig. 4.30 shows SSITKA transient response curves for Kr,  $^{13}\text{CO}$  and  $^{13}\text{CO}_2$  obtained over the 5 wt.% Ni/CeO<sub>2</sub> at 550 °C for CO<sub>2</sub>- and CH<sub>4</sub>-conversion levels of 55

and 40%, respectively, after 2 h of DRM. The *active* carbon ( $N_C$ ) formed is  $\sim 2 \mu\text{mol g}^{-1}$  to be compared to the value of  $3.7 \mu\text{mol g}^{-1}$  obtained at low conversions (Table 4.9).

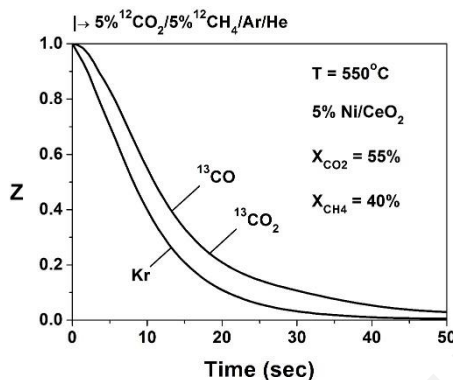


**Figure 4.30:** Kr,  $^{13}\text{CO}$  and  $^{13}\text{CO}_2$  SSITKA response curves obtained after 2 h in dry reforming of methane at  $550^\circ\text{C}$  over 5 wt.% Ni/CeO<sub>2</sub> catalyst. SSITKA switches: 5%  $^{12}\text{CO}_2/5\%$   $^{12}\text{CH}_4/\text{Ar}/\text{He}$  (2 h)  $\rightarrow$  5%  $^{13}\text{CO}_2/5\%$   $^{12}\text{CH}_4/2\%$  Kr/Ar/He (20 min)  $\rightarrow$  5%  $^{12}\text{CO}_2/5\%$   $^{12}\text{CH}_4/\text{Ar}/\text{He}$  (t);  $W_{\text{cat}} = 0.25 \text{ g}$ ;  $F_T = 50 \text{ NmL min}^{-1}$ ;  $X_{\text{CH}_4} = 40\%$ ;  $X_{\text{CO}_2} = 55\%$ .

#### 4.2.3.2. Measurement of *inactive adsorbed CO<sub>2</sub>* derived from the CO<sub>2</sub> activation route

The amount ( $N_{\text{CO}_2}$ ,  $\mu\text{mol g}^{-1}$ ) of *reversibly adsorbed CO<sub>2</sub>* formed on the catalyst surface after 2 h of DRM and which does not participate in the formation of CO is estimated via the appropriate material balance (see Chapter 3, Section 3.7.4) and reported in Table 4.9. As opposed to the case of the *active* “carbon” pool (Figure 4.31), the progressive increase of Pr<sup>3+</sup>-dopant loading in catalyst’s support composition causes also a progressive increase in the amount of reversibly adsorbed CO<sub>2</sub> at  $750^\circ\text{C}$ . This is found to be 54.7 ( $\theta = 2.3$ ), 86.8 ( $\theta = 3.6$ ) and  $114.0 \mu\text{mol/g}$  ( $\theta = 4.05$ ) for the Ni/CeO<sub>2</sub>, Ni/Ce<sub>0.8</sub>Pr<sub>0.2</sub>O<sub>2- $\delta$</sub>  and Ni/Ce<sub>0.2</sub>Pr<sub>0.8</sub>O<sub>2- $\delta$</sub>  catalyst, respectively. It is very important to point out that the size of this reversibly adsorbed CO<sub>2</sub> pool is *larger than one monolayer* of Ni surface. On the other hand, the size of the *active* C-pool that leads to CO is *lower than one monolayer* except for the case of Ni/CeO<sub>2</sub> ( $\theta_C = 3.4$ ).

Similar SSITKA experiments to those shown in Fig. 4.29 were also performed at  $550^\circ\text{C}$ . These SSITKA measurements correspond to truly kinetic conditions (CO<sub>2</sub> and CH<sub>4</sub> conversions lower than 15%) as opposed to the case at  $750^\circ\text{C}$ . It is observed that practically the same behaviour in the concentration of reversibly adsorbed CO<sub>2</sub> formed at  $550^\circ\text{C}$  with increasing Pr-dopant loading is obtained as in the case of DRM at  $750^\circ\text{C}$ . The reversibly adsorbed CO<sub>2</sub> is  $38.0 \mu\text{mol g}^{-1}$  for the Ni/CeO<sub>2</sub> and increases to  $57.6 \mu\text{mol g}^{-1}$  for the

Ni/ $\text{Ce}_{0.2}\text{Pr}_{0.8}\text{O}_{2-\delta}$  catalyst. A slightly lower value was estimated for the Ni/ $\text{Ce}_{0.8}\text{Pr}_{0.2}\text{O}_{2-\delta}$  catalyst ( $35.9 \mu\text{mol g}^{-1}$ ).

**Table 4.9:** Steady-state concentration ( $\mu\text{mol g}^{-1}$  or  $\theta$ ) of active “carbon” ( $\text{N}_\text{C}$ ) and reversibly adsorbed  $\text{CO}_2$  ( $\text{N}_{\text{CO}_2}$ ,  $\mu\text{mol g}^{-1}$  or  $\theta$ ) measured by SSITKA after 2 h of dry reforming (5%  $\text{CH}_4/5\%$   $\text{CO}_2/\text{He}$ ) at 550 and 750 °C.

Catalyst	T (°C)	$\text{N}_\text{C}$ ( $\mu\text{mol g}^{-1}$ )	$\text{N}_{\text{CO}_2}$ ( $\mu\text{mol g}^{-1}$ )	$\tau_\text{C}$ (s)	$\text{TOF}^{\text{CO}_{\text{ITK}}}$ ( $\text{s}^{-1}$ )	Rate ( $\mu\text{mol g}^{-1}$ ) <sup>b</sup>	$\text{X}_{\text{CO}_2}$ (%)	$\text{X}_{\text{CH}_4}$ (%)
5 wt.% Ni/ $\text{CeO}_2$	550	3.7 (0.15) <sup>a</sup>	38.0 (1.5) <sup>a</sup>	0.60	1.7	6.30	14.0	9.0
	750	87.7 (3.40)	54.7 (2.3)	1.74	-		62.4	53.7
5 wt.% Ni/ $\text{Ce}_{0.8}\text{Pr}_{0.2}\text{O}_2$	550	0.72 (0.025)	35.9 (1.45)	0.11	9.1	6.55	11.5	8.4
	750	2.0 (0.07)	86.8 (3.6)	0.06	-		36.0	32.0
5 wt.% Ni/ $\text{Ce}_{0.2}\text{Pr}_{0.8}\text{O}_2$	550	0.87 (0.03)	57.6 (2.1)	0.20	5.0	4.35	5.8	4.1
	750	16.7 (0.56)	114.0 (4.05)	0.78	1.3		15.8	14.7

<sup>a</sup>: number in parentheses represents the equivalent surface coverage ( $\theta$ ) based on  $\text{Ni}_\text{s}$  (Table 4.6).

<sup>b</sup>: Rate of CO formation via the  $\text{CO}_2$  activation route.

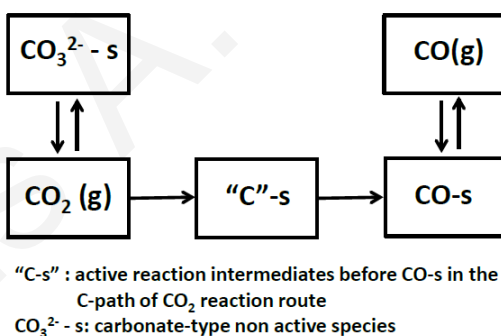


**Figure 4.31:** The SSITKA formalism applied for the activation path of  $\text{CO}_2$  towards the formation of CO in the DRM reaction over the 5 wt.% Ni/ $\text{Ce}_{1-x}\text{Pr}_x\text{O}_{2-\delta}$  catalysts. “C”-s is the pool of active carbon-containing species, CO-s is the pool of adsorbed CO, and  $\text{CO}_3^{2-}\text{-s}$  is the pool of non-active and reversibly adsorbed carbonate-type species on the  $\text{Ce}_{1-x}\text{Pr}_x\text{O}_{2-\delta}$  support.

The influence of reactant conversion on the concentration of *reversibly adsorbed*  $\text{CO}_2$  was also investigated at 550 °C. Based on the SSITKA results shown in Fig. 4.30 ( $\text{CO}_2$ - and  $\text{CH}_4$ -conversion levels of 55 and 40%, respectively, after 2 h of DRM), the amount of reversibly adsorbed  $\text{CO}_2$  is  $10.7 \mu\text{mol g}^{-1}$  compared to  $38.0 \mu\text{mol g}^{-1}$  measured at low reactant conversion

(see Table 4.9). This is rather reasonable since the higher the partial pressure of  $\text{CO}_2$  (g) (the lower the  $\text{CO}_2$  conversion achieved) the higher the concentration of the reversibly adsorbed carbonate-type species that is formed.

#### 4.2.3.3. Measurement of *mean life time* ( $\tau_c, s$ ) of active carbon derived from the $\text{CO}_2$ activation route

Table 4.9 reports the mean-life time ( $\tau_c, s$ ) of all the *active* carbon-containing reaction intermediates found in the  $\text{CO}_2$  activation path (e.g. “C”-s and CO-s, Figure 4.31) and how this kinetic parameter is influenced by the reaction temperature and  $\text{Pr}^{3+}$  concentration in the  $\text{Pr}^{3+}$ -doped ceria supported Ni catalysts. Also,  $\text{TOF}_{\text{ITK}}$  ( $\text{s}^{-1}$ ) values ( $\text{TOF}_{\text{ITK}} = 1/\tau_c$ ) are reported (Table 4.9) which correspond to differential conditions at  $T = 550$  °C and for the  $\text{Ni}/\text{Ce}_{0.2}\text{Pr}_{0.8}\text{O}_{2-\delta}$  catalyst also at 750 °C. This  $\text{TOF}_{\text{ITK}}$  ( $\text{s}^{-1}$ ) corresponds to the rate of formation of CO via the  $\text{CO}_2$  activation route. It is clearly illustrated that  $\text{Ni}/\text{Ce}_{0.8}\text{Pr}_{0.2}\text{O}_{2-\delta}$  shows a  $\text{TOF}_{\text{ITK}}$  value about *5 times larger* than that estimated on the  $\text{Ni}/\text{CeO}_2$ , where both catalysts show similar catalytic activity when this is expressed *per gram of catalyst basis* (see Fig. 4.22). In the case of  $\text{Ni}/\text{Ce}_{0.8}\text{Pr}_{0.2}\text{O}_{2-\delta}$  catalyst, the  $\text{TOF}_{\text{ITK}}$  at 750 °C is smaller by a factor of  $\sim 3.8$  when compared to the value estimated at 550 °C. This result can be understood after considering that the  $\text{TOF}_{\text{ITK}}$  might be seen as the product of  $N_C$  and  $k$ . The latter parameter represents the site reactivity of the *active* carbon species associated with the *rate-limiting step* found in the  $\text{CO}_2$  activation path (Figure 4.31) at a given reaction temperature. It appears that  $k$  has a lower value at 750 °C as opposed to 550 °C likely due to a *change in the chemical structure* of the *active* carbon species and/or to a change in the structure of the adsorbed phase, considering that  $N_C$  (associated with the rate-limiting step) is still larger at 750 than 550 °C. The importance of these  $\text{TOF}_{\text{ITK}}$  measurements is discussed below.

#### 4.2.3.4. Initial transient rate behaviour of CO and $\text{H}_2$ gas formation

Fig. 4.32 presents the transient evolution of the rate of hydrogen formation ( $\mu\text{mol H}_2 \text{ g}^{-1} \text{ s}^{-1}$ ) after the feed is switched from He to the non-isotopic  $^{12}\text{CO}_2/^{12}\text{CH}_4/\text{Ar}/\text{He}$  feed gas composition over the fresh 5 wt.%  $\text{Ni}/\text{Ce}_{1-x}\text{Pr}_x\text{O}_{2-\delta}$  ( $x = 0, 0.2$  and  $0.8$ ) catalysts at 550 °C (Fig. 4.32a) and 750 °C (Fig. 4.32b). Upon the switch to the reaction mixture, the rate of reaction at 550 °C sharply increases and passes through a maximum at time  $t \sim 15$  s, where quickly (after  $\sim 2$  min on stream) reaches a steady-state value (Fig. 4.32a). Of interest is the fact that the



overshoot observed falls with the increase in Pr-dopant concentration as shown in Fig. 4.32a. As the reaction temperature increases to 750 °C (Fig. 4.32b), no overshoot in the rate of  $\text{H}_2$  formation is observed. In particular, Ni/ $\text{CeO}_2$  and Ni/ $\text{Ce}_{0.8}\text{Pr}_{0.2}\text{O}_{2-\delta}$  catalysts rapidly (after ~ 1 min) take a steady-state reaction rate value, which decreases only slightly for longer times on stream and for larger reactant concentrations in the feed stream (see Fig. 4.21). The Ni/ $\text{Ce}_{0.2}\text{Pr}_{0.8}\text{O}_{2-\delta}$  shows a small decay in the first 10-min of the transient (Fig. 4.32b) which is consistent also to the stability behaviour shown in Fig. 4.22.

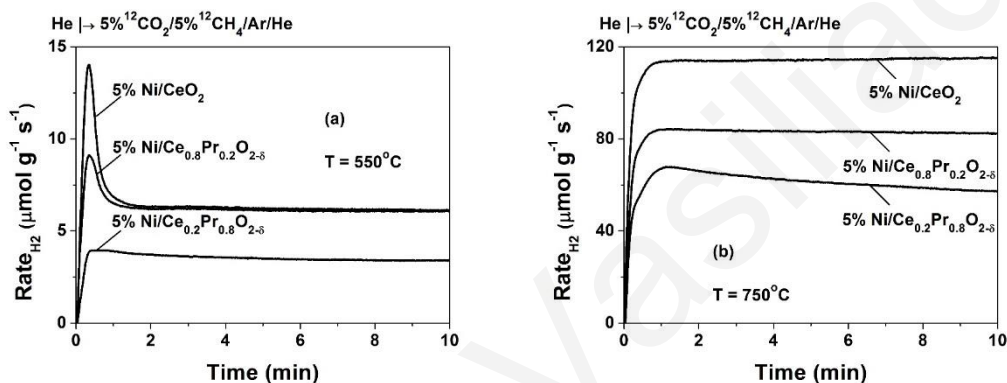


**Figure 4.32:** Isothermal transient rates of hydrogen formation obtained at the switch  $\text{He} \rightarrow 5\% ^{12}\text{CO}_2/5\% ^{12}\text{CH}_4/\text{Ar}/\text{He}$  (t) at 550 °C (a) and 750 °C (b) over the 5 wt.% Ni/ $\text{Ce}_{1-x}\text{Pr}_x\text{O}_{2-\delta}$  ( $x = 0.0, 0.2$  and  $0.8$ ) catalysts;  $W_{\text{cat}} = 0.1$  g mixed with 0.1 g SiC (550 °C) and  $W_{\text{cat}} = 0.03$  g mixed with 0.17 g SiC (750 °C);  $F_T = 100$  N mL  $\text{min}^{-1}$ .

#### 4.2.4. Discussion

##### (a) Catalytic performance of Ni/ $\text{CeO}_2$ and Ni/ $\text{Ce}_{1-x}\text{Pr}_x\text{O}_{2-\delta}$ solids

- Ni/ $\text{CeO}_2$  catalyst

One of the earliest investigations [10] on the use of ceria as promoter of Ni for the dry reforming of methane has examined  $\gamma\text{-Al}_2\text{O}_3$ ,  $\text{CeO}_2$  and  $x$  wt.%  $\text{CeO}_2\text{-Al}_2\text{O}_3$  ( $x = 1\text{-}10$  wt.%) as supports of 5 wt.% Ni. It was concluded that ceria produced strong metal-support interactions after calcination and  $\text{H}_2$  reduction at 500 °C, which reduced the catalytic activity and carbon formation with respect to Ni/ $\gamma\text{-Al}_2\text{O}_3$ . On the other hand, when 1-5 wt.%  $\text{CeO}_2$  was deposited onto the alumina support, this had a positive effect on the activity, stability and suppression of carbon deposition for the Ni/ $\text{CeO}_2\text{-Al}_2\text{O}_3$  catalytic system. The stability and significant resistance to coking exhibited by the ceria-promoted nickel catalysts were attributed to the oxidative properties of  $\text{CeO}_2$  along with the higher dispersions of Ni. The amount of “carbon”



deposited on Ni/ $\gamma$ - $Al_2O_3$ , Ni/1 wt.%  $CeO_2$ - $Al_2O_3$  and Ni/ $CeO_2$  solids was 20.8, 3.4 and 0.9 wt.%, respectively, after 2 h of dry reforming (50%  $CH_4$ ,  $CH_4/CO_2 = 1$ ) at 700 °C.

Asami *et al.* [51] in a later publication aimed at developing an excellent catalyst for dry reforming of methane by examining the possibility of using  $CeO_2$  as support of Ni, Co and Fe. A 5.3 wt.% Ni/ $CeO_2$  (Ni dispersion of  $\sim 2.8\%$ ) was found to be the most effective catalyst (95%  $CH_4$ -conversion,  $H_2/CO \sim 1.0$  and high stability after 50 h on reaction stream at 850 °C; 50%  $CH_4/50\%$   $CO_2$ ;  $W/F = 1 \text{ g h mol}^{-1}$ ) with negligible carbon deposition. However, at 700 °C rapid deactivation of the catalyst occurred in agreement also to previous studies [52]. After using an equimolar feed gas composition, the amount of “carbon” deposited after 24 h of reaction at 700 °C was 2 wt.%, which was the lowest among the other investigated supported Ni catalysts (support:  $SiO_2$ ,  $MgO$ ,  $La_2O_3$ ). Kumar *et al.* [53] have investigated  $CeO_2$ - $ZrO_2$  and ceria-doped  $ZrO_2$  supported Ni (5 wt.%) in an effort to evaluate how the catalytic activity of dry reforming and “carbon” formation are influenced by the support preparation method. The use of surfactant (CTAB) was one of the support synthesis methods used, which intended to lead to a reduction of support’s particle size into such an extent that it can become comparable to the Ni metal particle size, thus enabling strong metal-support interactions. A 5 wt.% Ni/ $CeO_2$  (CTAB) showed decreasing conversions up to 5 h on reaction stream (40%  $CO_2/40\%$   $CH_4/20\%$   $N_2$ ) at 700 °C, an  $H_2$ -selectivity of  $\sim 70\%$  and  $\sim 1.1$  wt.% “carbon” deposition, after only 3 h on reaction stream.

Very recent works have investigated  $CeO_2$  and  $ZrO_2$ - $CeO_2$  as supports of Ni for the dry reforming of methane [54,55]. Kim *et al.* [54] have investigated a 10 wt.% Ni/ $CeO_2$  (11.7 SSA,  $m^2 \text{ g}^{-1}$ ) at 750 °C. A  $CH_4$ -conversion of 55%, a  $H_2/CO$  ratio of 0.73 and a very stable activity up to 10 h on stream (50%  $CH_4/50\%$   $CO_2$ ) were reported. Deposited carbon in the shape of filamentous rods was also reported [54]. The  $H_2/CO$  gas ratio measured in the present 5 wt.% Ni/ $CeO_2$  catalyst is larger (close to unity) compared to the value of 0.73 reported [54]. The deviation of  $H_2/CO$  ratio from unity is discussed below. Ay and Üner [55] have investigated the dry reforming of methane over a 8 wt.% Ni/ $CeO_2$  catalyst the support of which was prepared by the calcination of  $Ce(C_2H_3O_2)_3 \cdot 1.5H_2O$  at 700 °C and using the same feed gas composition (20%  $CH_4/20\%$   $CO_2/Ar$ ) and hydrogen reduction temperature (ca. 700 °C) as in the present work. A very similar catalytic behaviour to that reported in Fig. 4.22 was observed [55] after 5 h on stream with respect to the level of reactant conversions and  $H_2/CO$  ratio. However, an initial deactivation of about 20% (up to 5 h on stream) was seen [55], opposite to that observed in the

present work (Fig. 4.22B). Similar TGA-TPO studies to those performed in the present work were also conducted [55], where 20.7 wt.% “carbon” was measured after 5 h on reaction stream as opposed to the present 5 wt.% Ni/CeO<sub>2</sub> catalyst, where an amount of 19.6-37.7 wt.% C was found but after a much longer duration (25 h) on reaction stream ( $W_{\text{cat}}/F = 0.001- 0.002 \text{ g min/cm}^3$ ); it is noted that no  $W_{\text{cat}}/F$  data were reported in [55]. The mild deactivation observed in the 8 wt.% Ni/CeO<sub>2</sub> catalyst [55] was proposed to be the result of strong metal-support interactions occurred after hydrogen reduction at 700 °C, where Ni particles were covered by a thin layer of ceria reduced support species (CeO<sub>x</sub>). The latter was evidenced by HRTEM and the inability for hydrogen chemisorption [55].

The high stability of the present 5 wt.% Ni/CeO<sub>2</sub> catalyst is in harmony with the practically unchanged particle size of Ni in the fresh and spent catalysts as determined by XRD and the fact that catalyst’s reduction in H<sub>2</sub> at 700 °C caused no suppression in hydrogen chemisorption. TEM-EDX analysis and mapping of several catalyst samples was performed on nickel grains for the 5 wt.% Ni/Ce<sub>0.2</sub>Pr<sub>0.8</sub>O<sub>2</sub> catalyst (Fig. 4.18b). Over none of the imaged nickel grains EDX responses at characteristic positions of the *l* shell transitions (Ce at 4.83 and 5.26 keV, Pr at 5.02 and 5.49 keV) or *m* shell transitions (Ce at 883 eV and Pr at 929 eV) could be confirmed. As a result, no covering or decoration of Ni grains with Ce or Pr occurred over the catalysts tested.

A very interesting work concerning changes in morphology induced by strong metal-support interactions on Ni/CeO<sub>2</sub> during H<sub>2</sub> reduction and DRM at 750 °C was reported by Gonzalez-DelaCruz *et al.* [56]. The authors have used *in situ* XAS analysis where under dry reforming the Ni *K*-edge X-ray absorption spectrum parameters obtained (after fitting analysis) suggested changes in the size and morphology of nickel particles. In particular, the authors suggested that reduced ceria surface allowed the formation of new Ni particles spreading on the partially reduced ceria support, which could account for a lower value in the mean Ni coordination number, resulting in some kind of strong metal-support interactions responsible for catalyst’s stability at 750 °C. This morphological change, however, was not stable after cooling of the sample in H<sub>2</sub> flow to room T.

The stability of Ni-based catalysts in the dry reforming with deposition of significant amounts of “carbon” in the form of filaments, as in the present case (Fig. 4.25), depends on the position of the Ni particles [55,57]. The latter may either stay at the top of the filament or might be enclosed within the filament leading to a loss of active nickel surface, thus to the catalyst

deactivation. In the present 5 wt.% Ni/CeO<sub>2</sub> catalyst, Ni crystallites *at the tip of carbon nanotubes* were seen after 25 h of DRM according to HRTEM images (Fig. 4.33), which show detachment of the metal particles from the CeO<sub>2</sub> support. It should be noted that filamentous carbon formation was significantly influenced by the Ni particle size and occurred mostly over Ni particles larger than 7 nm for the Ni-alumina aerogel catalysts [58].

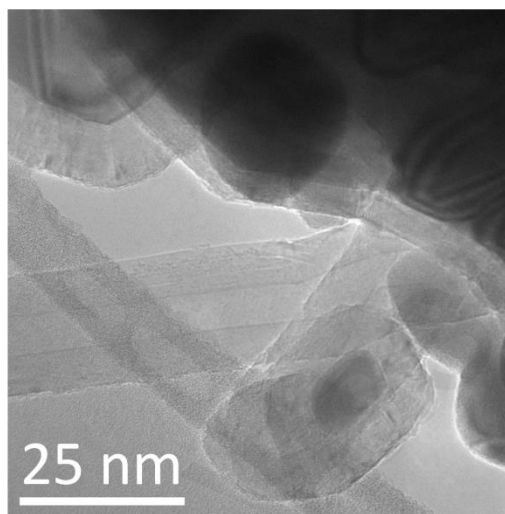


**Figure 4.33:** TEM image of Ni crystallite at the tip of carbon nanotubes showing detachment of the Ni metal clusters from the CeO<sub>2</sub> support observed after 25 h of methane dry reforming reaction at 750 °C.

Based on the above offered discussion, the present 5 wt.% Ni/CeO<sub>2</sub> catalyst, synthesized, calcined and reduced according to the procedures mentioned in Ch. 3 (Section 3.1.1 and 3.2.1), appears very competitive compared to other ceria-supported Ni catalysts evaluated for dry reforming at 750 °C. The large amount of “coke” deposited is the only severe problem faced in this catalytic system for practical applications, where *tuning of the Pr-dopant loading* in the ceria matrix could very likely provide an excellent catalytic system highly resistant to coking for dry reforming of methane (at least in the 700-750 °C range) as discussed below.

- **Ni/Ce<sub>1-x</sub>Pr<sub>x</sub>O<sub>2-δ</sub> catalysts**

Only very recently [29] Pr-doped CeO<sub>2</sub> (in the presence of Hf-dopant) was investigated as support of nickel (10 wt.% Ni) for the development of a durable and active DRM catalyst in the 600-900 °C range. The doped-ceria support was synthesised using the EDTA-citrate method, whereas Ni was deposited via the solvothermal method. The fresh Ni/Ce<sub>0.65</sub>Hf<sub>0.25</sub>Pr<sub>0.1</sub>O<sub>2-δ</sub>

catalyst was calcined at 450 °C and reduced in hydrogen at 700 °C for 2 h before reaction. A nickel mean particle size of 10-15 nm was reported [29]. The catalyst was tested at 800 °C using a feed composition of  $\text{CH}_4:\text{CO}_2 = 2:1$  and a GHSV of 23,000  $\text{h}^{-1}$ , where an extremely stable catalytic performance after 150 h on reaction stream was reported in terms of  $\text{CH}_4$ -conversion ( $\sim 55\%$ ),  $\text{CO}_2$ -conversion ( $\sim 96\%$ ) and  $\text{H}_2/\text{CO}$  ratio ( $\sim 0.75$ ). Characterisation of the spent catalyst by HRTEM revealed no “carbon” formation after 150 h on reaction stream. On the other hand,  $\text{Ni}/\text{Ce}_{0.65}\text{Hf}_{0.35}\text{O}_{2-\delta}$  exhibited reduced catalytic activity and  $\text{H}_2$ -selectivity and a large decrease in  $X_{\text{CH}_4}$ ,  $X_{\text{CO}_2}$  and  $\text{H}_2/\text{CO}$  performance parameters.

The above described catalytic performance of Pr-doped  $\text{CeO}_2$ - $\text{HfO}_2$  supported Ni catalyst appears different to the one obtained in the present work (5 wt.% Ni supported on Pr-doped  $\text{CeO}_2$ ). In particular, the progressive introduction of  $\text{Pr}^{3+}$  into the ceria lattice resulted in the progressive reduction in all catalytic performance parameters ( $X_{\text{CH}_4}$ ,  $X_{\text{CO}_2}$ ,  $\text{H}_2/\text{CO}$ ) as illustrated in Figs. 4.21 and 4.23, as opposed to the Pr-doped  $\text{CeO}_2$ - $\text{HfO}_2$  catalyst [29]. On the other hand, the long-term stability of  $\text{Ni}/\text{CeO}_2$  in DRM at 750 °C was only slightly reduced when  $\text{Pr}^{3+}$  was introduced into the ceria lattice (Fig. 4.22), result which is similar to the one obtained with the Pr-doped  $\text{CeO}_2$ - $\text{HfO}_2$  supported Ni catalytic system [29].

### (b) Understanding the $\text{Ni}/\text{Ce}_{1-x}\text{Pr}_x\text{O}_{2-\delta}$ DRM catalytic performance

In order to fundamentally understand the catalytic performance of the present  $\text{Ni}/\text{Ce}_{1-x}\text{Pr}_x\text{O}_{2-\delta}$  solids (Figs. 4.21 and 4.22), the initial reaction rate (Fig. 4.32) and the SSITKA (Figs. 4.29, 4.30 and Table 4.9) results become important. According to the reaction rate results (Fig. 4.32), the rates of hydrogen formation over  $\text{Ni}/\text{CeO}_2$ ,  $\text{Ni}/\text{Ce}_{0.8}\text{Pr}_{0.2}\text{O}_{2-\delta}$  and  $\text{Ni}/\text{Ce}_{0.2}\text{Pr}_{0.8}\text{O}_{2-\delta}$  catalysts after 2 h on reaction stream at 550 °C were found to be 6.4, 6.3 and 4.0  $\mu\text{mol H}_2 \text{g}^{-1} \text{s}^{-1}$ , respectively. Considering the fact that the  $\text{H}_2/\text{CO}$  ratio over these catalysts was found to be 0.60, 0.69 and 0.65, respectively, then the CO formation rates are 10.7, 9.1 and 6.2  $\mu\text{mol CO g}^{-1} \text{s}^{-1}$ , respectively. On the basis of the  $\text{TOF}_{\text{ITK}}$  (s) and the concentration of *active* carbon-containing intermediates,  $N_{\text{C}}$ , which are estimated independently by SSITKA (Table 4.9), the rate of CO formation via the  $\text{CO}_2$  activation route ( $R_{\text{CO}/\text{CO}_2}$ ,  $\mu\text{mol g}^{-1} \text{s}^{-1}$ ) can be estimated by using the appropriate material balance. For the  $\text{Ni}/\text{CeO}_2$ ,  $\text{Ni}/\text{Ce}_{0.8}\text{Pr}_{0.2}\text{O}_{2-\delta}$  and  $\text{Ni}/\text{Ce}_{0.2}\text{Pr}_{0.8}\text{O}_{2-\delta}$  catalysts, this rate was found to be 6.30, 6.55, and 4.35,  $\mu\text{mol g}^{-1} \text{s}^{-1}$ , respectively (Table 4.9). Based on the  $X_{\text{CH}_4}$  (%) (Table 4.9), the rate of CO formation via the  $\text{CH}_4$  activation route ( $R_{\text{CO}/\text{CH}_4}$ ,  $\mu\text{mol g}^{-1} \text{s}^{-1}$ ) can also be estimated (via a material balance) and this is found to be 3.07,

2.87 and  $1.4 \mu\text{mol CO g}^{-1} \text{s}^{-1}$ , respectively, for the Ni/CeO<sub>2</sub>, Ni/Ce<sub>0.8</sub>Pr<sub>0.2</sub>O<sub>2- $\delta$</sub>  and Ni/Ce<sub>0.2</sub>Pr<sub>0.8</sub>O<sub>2- $\delta$</sub>  catalysts. Considering the fact that the kinetic rate of CO formation under steady-state reaction conditions ( $R_{\text{CO,tot}}$ , Fig. 4.32) must be the sum of the rate of CO formation via the CO<sub>2</sub> activation route (measured by SSITKA) and that via the CH<sub>4</sub> activation route (measured independently), one should remark that the carbon material balance is within 4-12%.

The SSITKA analysis revealed that the *site reactivity* ( $\text{TOF}_{\text{ITK}}, \text{s}^{-1}$ ), a unique parameter estimated only by the SSITKA technique, follows the order  $\text{TOF}_{\text{ITK}}(\text{Ce}_{0.8}\text{Pr}_{0.2}\text{O}_{2-\delta}) > \text{TOF}_{\text{ITK}}(\text{Ce}_{0.2}\text{Pr}_{0.8}\text{O}_{2-\delta}) > \text{TOF}_{\text{ITK}}(\text{CeO}_2)$ , whereas the activity order ( $R_{\text{rxn}}$  per mass of catalyst) is as follows:  $R_{\text{rxn}}(\text{CeO}_2) \cong R_{\text{rxn}}(\text{Ce}_{0.8}\text{Pr}_{0.2}\text{O}_{2-\delta}) > R_{\text{rxn}}(\text{Ce}_{0.2}\text{Pr}_{0.8}\text{O}_{2-\delta})$ . This important result strongly suggests that tuning of the DRM activity of the 5 wt.% Ni/Ce<sub>0.8</sub>Pr<sub>0.2</sub>O<sub>2- $\delta$</sub>  solid could be performed by an increase in the number density of *active sites* ( $\text{sites g}_{\text{cat}}^{-1}$ ) which possess *larger site reactivity* ( $\text{TOF}_{\text{ITK}}, \text{s}^{-1}$ ) than that of Ni/CeO<sub>2</sub> and Ni/Ce<sub>0.2</sub>Pr<sub>0.8</sub>O<sub>2- $\delta$</sub>  catalytic systems. The nature of these *active* catalytic sites is discussed below.

Regarding the extent of “carbon” deposition, the effect of Pr present in the crystal lattice of ceria support is remarkable. According to the results of Table 4.7 and Figs. 4.24 and 4.26, after 25 h of DRM at 750 °C and using a  $W_{\text{cat}}/F$  of  $10^{-3} \text{ g min/cm}^3$ , the amount of “carbon” accumulated on the Ni/Ce<sub>0.8</sub>Pr<sub>0.2</sub>O<sub>2- $\delta$</sub> , Ni/Ce<sub>0.5</sub>Pr<sub>0.5</sub>O<sub>2- $\delta$</sub>  and Ni/Ce<sub>0.2</sub>Pr<sub>0.8</sub>O<sub>2- $\delta$</sub>  catalysts, respectively, drops by a factor of ~ 90, 245 and 280 with respect to Ni/CeO<sub>2</sub>; an amount of only 70 mg C  $\text{g}_{\text{cat}}^{-1}$  was found for the latter catalyst. When  $W_{\text{cat}}/F$  was doubled, or equivalently the GHSV was decreased to half, the Ni/Ce<sub>0.2</sub>Pr<sub>0.8</sub>O<sub>2- $\delta$</sub>  catalyst also caused reduction by a factor of ~ 250 in the amount of “carbon” formed compared to the Ni/CeO<sub>2</sub> catalyst. Based on these results, it is clear that reduction in the activity and H<sub>2</sub>/CO product gas ratio observed over the Ni/Ce<sub>1-x</sub>Pr<sub>x</sub>O<sub>2- $\delta$</sub>  ( $x = 0.2-0.8$ ) catalysts compared to Ni/CeO<sub>2</sub> (see Figs 4.21, 4.22 and Table 4.7) cannot be ascribed to the formation of an increased amount of *inactive* “carbon”. In particular, as Pr-dopant concentration increases from 0 to 20 atom-%, the “carbon” formation rate is largely decreased and only a small decrease in CH<sub>4</sub> and CO<sub>2</sub> conversions and in the H<sub>2</sub>/CO product gas ratio are observed. However, further progressive increase of Pr-dopant concentration to 80 atom-% leads to a significant drop in all the three catalytic performance parameters, and to a lesser extent in the amount of “carbon” deposition.

The main elementary reaction steps of the DRM over the present 5 wt.% Ni/Ce<sub>0.8</sub>Pr<sub>0.2</sub>O<sub>2- $\delta$</sub>  catalytic system were previously reported [43] (use of other than SSITKA transient isotopic experiments). The presence of oxygen vacant sites in the Ce<sub>1-x</sub>Pr<sub>x</sub>O<sub>2- $\delta$</sub>  support was suggested as

a potential *active* site for the dissociation of  $CO_2$  to  $CO(g)$  and re-oxidation of the reduced support surface ( $CO_2$  activation route):



On the other hand, Hartwig *et al.* [48] in a recent elegant work have investigated the temperature-dependent oxygen vacancy formation, oxygen release and lattice rearrangement of  $Ce_{1-x}Pr_xO_{2-\delta}$  ( $x = 0.2-0.6$ ) thin films. They reported that, after increasing the Pr-dopant loading, a decreasing  $O_2$  desorption temperature and an increasing  $CO_2$  desorption temperature were observed. Furthermore,  $O_2$ -TPD and XRD results agreed in that by increasing Pr-dopant loading OSC and lattice spacing increase; the latter has also been verified in the present work for a wider Pr-dopant concentration range;  $x = 0.2-0.8$  (see Table 4.5 and Fig. 4.17). The  $O_2$ -TPD and  $CO_2$ -TPD investigations of Hartwig *et al.* [48] can be offered to explain the significant reduction in the rate of “carbon” formation on  $Ni/Ce_{1-x}Pr_xO_{2-\delta}$  ( $x = 0.2-0.8$ ) due to an increased oxygen mobility in the  $Ce_{1-x}Pr_xO_{2-\delta}$  matrix, which favours “carbon” oxidation to  $CO(g)$ . This important elementary reaction step is found in the  $CO_2$  activation path and it is recognized for some time now as the main contributor to the control of the rate of “carbon” formation in doped- $CeO_2$  supported Ni catalysts [23,29,31,38,50,53,59]. What was not reported so far is the participation of oxygen vacancies in the  $Ce_{1-x}Pr_xO_{2-\delta}$  solids, not only in the dissociation of  $CO_2$  step but also in the formation of adsorbed “carbonate-type” species reversibly interacting with gaseous  $CO_2$  under dry reforming conditions (Figure 4.31). This type of “carbonate” is considered as *inactive* species, which could block active sites of the  $CO_2$  activation path. The  $CO_2$  stored reversibly on the catalyst surface ( $N_{CO_2}$ , Table 4.9) could justify the drop in activity of the  $Ni/Ce_{1-x}Pr_xO_{2-\delta}$  ( $x = 0.2-0.8$ ) catalysts. At 750 °C, where the latter effect is significant (see Figs. 4.22, 4.23 and 4.32b), the amount of this “ $CO_2$ -pool” shown in Figure 4.31 is increased by a factor of 1.58 and 2.1, respectively, when  $Ni/CeO_2$  is compared to  $Ni/Ce_{0.8}Pr_{0.2}O_{2-\delta}$  and  $Ni/Ce_{0.2}Pr_{0.8}O_{2-\delta}$  catalysts. At the same time, the  $H_2$  formation rate is decreased by a factor of ~ 1.1 and 2.2, respectively. A similar comparison can be also made at 550 °C, where the size of the “ $CO_2$ -pool” increases by a factor of 1.52 and the  $H_2$  formation rate decreases by a factor of 2.2, when  $Ni/CeO_2$  is compared to  $Ni/Ce_{0.2}Pr_{0.8}O_{2-\delta}$ . The fact that the size of the “ $CO_2$ -pool” after 2 h of DRM may depend on the concentration of gas phase  $CO_2$ , then strict comparison should be made at similar  $X_{CO_2}$  conversions; see DRM at 550 °C (Table 4.9).

In a recent work [42], the role of multivalent Pr in the formation and migration of oxygen vacancy in  $\text{Ce}_{1-x}\text{Pr}_x\text{O}_{2-\delta}$  ( $x = 0.0-0.5$ ) solids was investigated. The following conclusions are important and relevant to the results of the present work. First,  $\text{Pr}^{3+}$  and  $\text{Pr}^{4+}$  are incorporated as majority and minority ions, respectively, where  $\text{Pr}^{3+}$  plays a key role in the generation of oxygen vacancies during the replacement of  $\text{Ce}^{4+}$  with  $\text{Pr}^{3+}$ . Second, addition of  $\text{Pr}^{3+}$  causes a local distortion near the oxygen vacancy due to the mismatch between  $\text{Pr}^{3+}$  and  $\text{Ce}^{4+}$  and the bond length between each species with oxygen. Third, the role of the atomic level of the electronic states of the incorporated elements ( $\text{Ce}^{4+}/\text{Ce}^{3+}$  and  $\text{Pr}^{3+}/\text{Pr}^{4+}$ ) can tune the oxygen mobility and the concentration and stability of oxygen vacant sites.

In another investigation of the  $\text{Ce}_{1-x}\text{Pr}_x\text{O}_{2-\delta}$  ( $x = 0, 0.1, 0.5$  and  $0.9$ ) solids [47], it was demonstrated that the stated Ce-Pr-O solid compositions consisted of a single fluorite solid solution phase without the formation of additional Ce- or Pr-based oxides (secondary phases). XPS results revealed a rather good agreement between nominal (bulk) and surface stoichiometries, and only a slight tendency toward segregation of the lower concentration cation (Pr in  $\text{Ce}_{0.9}\text{Pr}_{0.1}\text{O}_{2-\delta}$  and Ce in  $\text{Ce}_{0.1}\text{Pr}_{0.9}\text{O}_{2-\delta}$ ) from the bulk to the surface. When these materials were tested for  $\text{CH}_4$  oxidation, maximum catalytic activity was observed for the  $\text{Ce}_{0.5}\text{Pr}_{0.5}\text{O}_{2-\delta}$  solid.

The above offered discussion on the  $\text{Ce}_{1-x}\text{Pr}_x\text{O}_{2-\delta}$  solid solution used as support of 5 wt.% Ni in the present work tends to suggest that the opposite trend in the rate of “carbon” formation and that of DRM ( $\text{CO}_2$  activation path) might be partially due to the influence of Pr-doping on the strength of associative  $\text{CO}_2$  chemisorption and on its dissociative counterpart onto oxygen vacant sites, the latter being adjacent to anionic oxygen and metal cationic ( $\text{Ce}^{3+}, \text{Ce}^{4+}, \text{Pr}^{3+}$  and  $\text{Pr}^{4+}$ ) sites. This could result in the adjustment of available *active* oxygen vacant sites and likely adjacent ones for  $\text{CO}_2$  dissociation.

The catalytic performance and the amount of inactive “carbon” formed towards the RWGS (20%  $\text{CO}_2/7\%$   $\text{H}_2/\text{He}$ ; GHSV = 30,000  $\text{h}^{-1}$ ) at 750°C were evaluated over the 5 wt.% Ni/ $\text{Ce}_{0.8}\text{Pr}_{0.2}\text{O}_{2-\delta}$  solid [43]. It was found that the  $X_{\text{CO}_2}$  (%) for the RWGS was 22% for the Ni/ $\text{Ce}_{0.8}\text{Pr}_{0.2}\text{O}_{2-\delta}$ , where the  $X_{\text{CO}_2}$  (%) to  $\text{CH}_4$  was less than 0.1%. The amount of inactive “carbon” formed after 1 h of RWGS was found to be significantly lower ( $\sim 0.7 \text{ mg g}_{\text{cat}}^{-1}$ ) than that formed after 1 h of DRM. Also, the  $X_{\text{CO}}$  (%) of methanation reaction (2.5%  $\text{CO}/7.5\%$   $\text{H}_2/\text{He}$ ) at 750 °C was less than 2% after 1 h of DRM. On the basis of these results, since the most active Ni/ $\text{Ce}_{0.8}\text{Pr}_{0.2}\text{O}_{2-\delta}$  in the series of Ni/ $\text{Ce}_{1-x}\text{Pr}_x\text{O}_{2-\delta}$  ( $x = 0.2-0.8$ ) solids exhibits a larger

$\text{H}_2/\text{CO}$  ratio than the catalysts with larger Pr-dopant loadings, it is clear that differences in the RWGS behaviour alone cannot explain the different activity and product selectivity for these catalytic systems. The fact that the  $\text{H}_2/\text{CO}$  ratio in most of the experimental conditions used is lower than one, and the  $X_{\text{CO}_2}$  (%) is larger than that of  $X_{\text{CH}_4}$  (%) (Fig. 4.21), the RWGS reaction does proceed to some extent in all catalytic systems, in general agreement with literature reports [10,29,60].

**(c) SSITKA – Kinetic and mechanistic studies**

The SSITKA results presented in Figs. 4.29 and 4.30 and Table 4.9 should be appreciated in relation with the discussion offered in the previous section. A SSITKA analysis of the dry reforming of  $\text{CH}_4$  at high temperatures (e.g. 750 °C) was attempted for the first time over ceria-based supported Ni, aiming at an accurate quantification of important kinetic parameters, such as the surface concentration ( $\mu\text{mol g}^{-1}$  or  $\theta$ ) of *active* “carbon-containing” reaction intermediates formed in the  $\text{CO}_2$  activation path leading to the formation of CO, the life-time of such intermediates ( $\tau_{\text{C}}$ , s) and the  $\text{TOF}_{\text{ITK}}$  ( $\text{s}^{-1}$ ). Furthermore, the presence of a pool of *inactive* adsorbed  $\text{CO}_2$  which reversibly interacts with the catalyst surface was identified. The nature of the *active carbon* pool “C”-s shown in Figure 4.31 can be discussed on the basis of the  $N_{\text{C}}$  quantity (Table 4.9) and the TEM-EDXS results. In the case of Ni/ $\text{CeO}_2$ , DRM at 750 °C for 2 h resulted in an equivalent amount of  $\theta_{\text{C}} = 3.4$  (based on the Ni surface). The fact that the CO-s pool appeared in Figure 4.31 must be considered very small ( $\theta_{\text{CO-s}} \ll 1$ ), it can be concluded that the nature of *active carbon* cannot be in the atomic state on the Ni surface but either as small 3-D clusters or thin films of likely few atomic layers on the surface of Ni particles. The latter is evidenced by the HRTEM images shown in Fig. 4.19a, b. The carbon in the thin films deposited on selected areas of the Ni surface may not all be regarded as *active carbon*.

Another possible explanation for the nature of *active “carbon”* and its concentration level exceeding the value of one  $\text{Ni}_s$  monolayer (Ni/ $\text{CeO}_2$ ) could arise from the work of Verykios and his co-workers [46,55,56] over the Ni/ $\text{La}_2\text{O}_3$  catalytic system. SSITKA work provided evidence that  $\text{La}_2\text{O}_2\text{CO}_3$  *active* species were formed during dry reforming of methane leading to  $\text{CO}(\text{g})$  via several decomposition pathways by the assistance of adsorbed H-s and C-s species on Ni and/or Ni-lanthanum interface [46]. The presence of such oxy-carbonate species on the present Ni/ $\text{Ce}_{1-x}\text{Pr}_x\text{O}_{2-\delta}$  catalysts cannot be excluded. Sokolov *et al.* [24] have reported initial  $\text{TOF}_{\text{CH}_4}$  rates as a function of Ni particle size for the Ni/ $\text{La}_2\text{O}_3$ - $\text{ZrO}_2$  catalytic system. It was shown that



higher TOF rates were obtained on the larger Ni particles, result that was related to the presence of  $La_2O_2CO_3$  at the Ni-support interface, which react slowly (RDS) with C-s formed on Ni (via  $CH_4$  decomposition), leading to  $CO(g)$  and restoration of support's  $CO_2$  chemisorption sites.

Bobin *et al.* [23] investigated supported Ni on similar carriers as in the present work ( $Ln_x (Ce_{0.5}Zr_{0.5})_{1-x}O_2$ ;  $Ln = Pr, Sm$ ) in one of the few SSITKA works reported for DRM over supported Ni catalysts. One of the important results found was that the reaction rate of surface carbonates towards  $CH_4$  was significantly lower than that of  $CH_4$  or  $CO_2$  dissociation. This result could be related to the present findings, that a pool of carbonate-type adsorbed species reversibly interacting with gaseous  $CO_2$  should be considered as spectator(s). Other important conclusions from the same SSITKA work [23] (4%  $CO_2$ ,  $CH_4/CO_2 = 1$ ), similar to the one conducted in the present work, are as follows:

- $CH_4$  activation proceeds independently of  $CO_2$  activation;
- $CO_2$  does not interact with  $-CH_x$  derived from  $CH_4$  decomposition (no transfer of  $^{13}C$  derived from  $^{13}CO_2$  into  $^{12}CH_4$ );
- fast rate of  $CO_2$  dissociation on support sites and high surface oxygen mobility providing fast oxygen transfer from support sites to Ni sites ( $CH_4$  activation);
- negligible surface coverage of active “carbon”;
- irreversible  $CH_4$  interaction and reversible  $CO_2$  interaction with the catalyst surface;
- rate of catalyst re-oxidation by  $CO_2$  largely exceeds that of its reduction by  $CH_4$ ;
- reactive oxygen species of support at the Ni-support interface are apparently bound with pairs of  $Ce^{4+}$  and  $Pr^{3+}$ .

The “carbon” and SSITKA measurements of the present work (Tables 4.7 and 4.9) and other transient isotopic work performed on the 5 wt.% Ni/ $Ce_{0.8}Pr_{0.2}O_{2-\delta}$  catalyst [43] support the above conclusions (a), (c), (e) and (g).

The dependence of  $TOF_{ITK}$  ( $s^{-1}$ ) on support chemical composition that provides the true site reactivity for each supported Ni surface can be utilised to tailor the activity of DRM on this specific catalytic system. Detailed information acquired from HRTEM investigations on the surface structure of Ni particles could lead to a desired correlation between  $TOF_{ITK}$  ( $s^{-1}$ ) and Ni structure (e.g. density of exposed facets). It is rather clear that the  $TOF_{ITK}$  ( $s^{-1}$ ) behaviour on the present supported Ni catalysts cannot be correlated with the Ni particle size but rather with the

specific Ni surface structure (e.g. ratio of different crystallographic faces) for similar in size Ni particles. This important issue should be a subject of future investigation.

Sadykov *et al.* [38] have reported on important mechanistic issues of dry reforming on the Pt/Ce-Zr-Pr-O catalytic system via mathematical modelling of the non-isotopic transient response curves of  $\text{H}_2$ , CO,  $\text{CO}_2$  and  $\text{CH}_4$ , similar to those of  $\text{H}_2$  formation rate depicted in Fig. 4.32. It was shown that the character and shape of response curves is mainly defined by the rates of carbonates formation and consumption, the rate of oxygen diffusion from the support surface/subsurface to the Pt-support interface, and the interaction of  $\text{CO}_2$  with vacant sites on the Pt surface. In analogy to their findings and those of this work, a first attempt to explain the transient features of the  $\text{H}_2$  formation rate at 550 °C in the first 2 min (Fig. 4.32a) is as follows. Due to the likely higher oxygen mobility in  $\text{Ce}_{0.2}\text{Pr}_{0.8}\text{O}_{2-\delta}$  than  $\text{Ce}_{0.8}\text{Pr}_{0.2}\text{O}_{2-\delta}$  or  $\text{CeO}_2$  support, the rate of “carbon” oxidation to  $\text{CO}(\text{g})$  and “carbon” deposition by  $\text{CH}_4$  decomposition appears faster. This feature explains the absence of an overshoot in the rate of  $\text{H}_2$  formation. As the reforming temperature increases to 750 °C, slight differences are only observed in the shape of the initial  $\text{H}_2$  formation rates (Fig. 4.32b), suggesting that surface coverages for important reaction intermediates and vacant sites may change only to a small extent.

The following conclusions can be derived from the results of the present Section 4.2:

- (i) 5 wt.% Ni supported on  $\text{Ce}_{1-x}\text{Pr}_x\text{O}_{2-\delta}$  carrier was found to be a very promising “coke” resistant active catalytic material towards dry reforming of methane in the 700-750 °C range. The increase in the concentration of *inactive* chemisorbed  $\text{CO}_2$  on support sites with increasing Pr-dopant loading in the ceria matrix was found to correlate with the activity drop.
- (ii) The catalytic activity order on a mass basis over the investigated series of 5 wt.% Ni/ $\text{Ce}_{1-x}\text{Pr}_x\text{O}_{2-\delta}$  solids of similar Ni particle size does not correlate with the activity order in terms of  $\text{TOF}_{\text{ITK}}$  ( $\text{s}^{-1}$ ). In particular, 5 wt.% Ni/ $\text{CeO}_2$  with the largest catalytic activity ( $\mu\text{mol H}_2 \text{ g}^{-1} \text{ s}^{-1}$ ) exhibits about five times lower  $\text{TOF}_{\text{ITK}}$  ( $\text{s}^{-1}$ ) at 550 °C than the 5 wt.% Ni/ $\text{Ce}_{0.8}\text{Pr}_{0.2}\text{O}_{2-\delta}$  catalyst, which has a similar activity per gram basis. This result is related to the larger  $\theta_{\text{C}}/\tau_{\text{C}}$  ratio associated with the TOF of the catalytic cycle measured at reaction conditions.
- (iii) The concentration of *active* “carbon” formed under dry reforming strongly depends on the Pr-dopant concentration in the ceria matrix and the reaction temperature. The former

is crucial since it regulates the mobility and concentration of lattice support oxygen near the Ni-support interface, thus leading eventually to gaseous CO. Also, Pr-dopant regulates the concentration of surface support oxygen vacancies, largely responsible for the dissociation of  $CO_2$  to form  $CO(g)$  and atomic O (re-oxidation of the reduced support).

- (iv) Introduction of Pr-dopant into the ceria support matrix at the level of 20 atom-% *drastically reduces* the rate of “carbon” deposition compared to the Ni/ $CeO_2$  catalyst, while keeping high activity and product selectivity similar to those obtained by Ni/ $CeO_2$ .
- (v) Inactive carbon of filamentous and graphitic nature is largely formed in the Ni/ $CeO_2$  catalyst after 25 h of dry reforming at 750 °C (20%  $CH_4$ ;  $CH_4/CO_2 = 1$ ) as deduced by SEM and XRD. Islands/patches of carbon in several areas on the Ni particle’s surface were also identified by HAADF/STEM.

## References

- [1] Y.H. Hu, E. Ruckenstein, in: *Adv. Catal.*, 2004, pp. 297–345.
- [2] D. Li, Y. Nakagawa, K. Tomishige, *Appl. Catal. A Gen.* 408 (2011) 1–24.
- [3] M. Usman, W.M.A. Wan Daud, H.F. Abbas, *Renew. Sustain. Energy Rev.* 45 (2015) 710–744.
- [4] X.E. Verykios, *Chem. Ind. Chem. Eng. Q.* 8 (2002) 238–255.
- [5] H. Eltejaei, H. Reza Bozorgzadeh, J. Towfighi, M. Reza Omidkhah, M. Rezaei, R. Zanganeh, A. Zamaniyan, A. Zarrin Ghalam, *Int. J. Hydrogen Energy* 37 (2012) 4107–4118.
- [6] J. Montoya, *Catal. Today* 63 (2000) 71–85.
- [7] A. Kambolis, H. Matralis, A. Trovarelli, C. Papadopoulou, *Appl. Catal. A Gen.* 377 (2010) 16–26.
- [8] J. CHEN, Q. WU, J. ZHANG, J. ZHANG, *Fuel* 87 (2008) 2901–2907.
- [9] H.-S. Roh, H.S. Potdar, K.-W. Jun, J.-W. Kim, Y.-S. Oh, *Appl. Catal. A Gen.* 276 (2004) 231–239.
- [10] S. Wang, G.Q. Lu, *Appl. Catal. B Environ.* 19 (1998) 267–277.
- [11] M.S. Aw, M. Zorko, P. Djinović, A. Pintar, *Appl. Catal. B Environ.* 164 (2015) 100–112.
- [12] M. Yashima, K. Morimoto, N. Ishizawa, M. Yoshimura, *J. Am. Ceram. Soc.* 76 (1993)

- 1745–1750.
- [13] C.M. Kalamaras, D.D. Dionysiou, A.M. Efstathiou, *ACS Catal.* 2 (2012) 2729–2742.
- [14] M. Yashima, H. Takashina, M. Kakihana, M. Yoshimura, *J. Am. Ceram. Soc.* 77 (1994) 1869–1874.
- [15] M. Yashima, in: A. Trovarelli, P. Fornasiero (Eds.), *Catal. by Ceria Relat. Mater.*, 2nd ed., Imperial College Press, 2013, pp. 1–45.
- [16] H. Düdder, K. Kähler, B. Krause, K. Mette, S. Köhl, M. Behrens, V. Scherer, M. Muhler, *Catal. Sci. Technol.* 4 (2014) 3317–3328.
- [17] F. Ocampo, B. Louis, L. Kiwi-Minsker, A.C. Roger, *Appl. Catal. A Gen.* 392 (2011) 36–44.
- [18] M. Goula, A. Lemonidou, A. Efstathiou, *J. Catal.* 161 (1996) 626–640.
- [19] K. Hadjiivanov, M. Mihaylov, D. Klissurski, P. Stefanov, N. Abadjieva, E. Vassileva, L. Mintchev, *J. Catal.* 185 (1999) 314–323.
- [20] G. Poncelet, M.A. Centeno, R. Molina, *Appl. Catal. A Gen.* 288 (2005) 232–242.
- [21] G. Martra, F. Arena, M. Baricco, S. Coluccia, L. Marchese, A. Parmaliana, *Catal. Today* 17 (1993) 449–458.
- [22] Z.L. Zhang, V.A. Tsipouriari, A.M. Efstathiou, X.E. Verykios, *J. Catal.* 158 (1996) 51–63.
- [23] A.S. Bobin, V.A. Sadykov, V.A. Rogov, N. V. Mezentseva, G.M. Alikina, E.M. Sadovskaya, T.S. Glazneva, N.N. Sazonova, M.Y. Smirnova, S.A. Veniaminov, C. Mirodatos, V. Galvita, G.B. Marin, *Top. Catal.* 56 (2013) 958–968.
- [24] S. Sokolov, E. V. Kondratenko, M.M. Pohl, U. Rodemerck, *Int. J. Hydrogen Energy* 38 (2013) 16121–16132.
- [25] Z. Zhang, X.E. Verykios, *Appl. Catal. A Gen.* 138 (1996) 109–133.
- [26] C.M. Kalamaras, S. Americanou, A.M. Efstathiou, *J. Catal.* 279 (2011) 287–300.
- [27] S.-G. Wang, D.-B. Cao, Y.-W. Li, J. Wang, H. Jiao, *J. Phys. Chem. B* 110 (2006) 9976–9983.
- [28] C.G. Rotaru, G. Postole, M. Florea, F. Matei-Rutkovska, V.I. Pârvulescu, P. Gelin, *Appl. Catal. A Gen.* 494 (2015) 29–40.
- [29] D. Harshini, D.H. Lee, Y. Kim, S.W. Nam, J.H. Han, H.C. Ham, C.W. Yoon, *Catal. Letters* 144 (2014) 656–662.
- [30] T. Sukonket, A. Khan, B. Saha, H. Ibrahim, S. Tantayanon, P. Kumar, R. Idem, *Energy*

- and Fuels 25 (2011) 864–877.
- [31] T.J. Huang, H.J. Lin, T.C. Yu, *Catal. Letters* 105 (2005) 239–247.
- [32] J. Guo, H. Lou, L. Mo, X. Zheng, *J. Mol. Catal. A Chem.* 316 (2009) 1–7.
- [33] E.G.M. Kuijpers, A.J.H.M. Kock, M.W.C.M.A. Nieuwesteeg, J.W. Geus, *J. Catal.* 95 (1985) 13–20.
- [34] G. MARTIN, *J. Catal.* 53 (1978) 321–330.
- [35] M. Che, C.O. Bennett, in: *Adv. Catal.*, 1989, pp. 55–172.
- [36] T.P. Beebe, D.W. Goodman, B.D. Kay, J.T. Yates, *J. Chem. Phys.* 87 (1987) 2305–2315.
- [37] K.A. Resende, C.N. Ávila-Neto, R.C. Rabelo-Neto, F.B. Noronha, C.E. Hori, *Catal. Today* 242 (2015) 71–79.
- [38] V.A. Sadykov, E.L. Gubanova, N.N. Sazonova, S.A. Pokrovskaya, N.A. Chumakova, N. V. Mezentseva, A.S. Bobin, R. V. Gulyaev, A. V. Ishchenko, T.A. Krieger, C. Mirodatos, *Catal. Today* 171 (2011) 140–149.
- [39] Z. Cheng, B.J. Sherman, C.S. Lo, *J. Chem. Phys.* 138 (2013) 14702.
- [40] Z. Song, W. Liu, H. Nishiguchi, A. Takami, K. Nagaoka, Y. Takita, *Appl. Catal. A Gen.* 329 (2007) 86–92.
- [41] P. Shuk, *Solid State Ionics* 116 (1999) 217–223.
- [42] K. Ahn, D.S. Yoo, D.H. Prasad, H.W. Lee, Y.C. Chung, J.H. Lee, *Chem. Mater.* 24 (2012) 4261–4267.
- [43] M.M. Makri, M.A. Vasiliades, K.C. Petallidou, A.M. Efstathiou, *Catal. Today* 259 (2016) 150–164.
- [44] F. Wang, L. Xu, J. Zhang, Y. Zhao, H. Li, H.X. Li, K. Wu, G.Q. Xu, W. Chen, *Appl. Catal. B Environ.* 180 (2016) 511–520.
- [45] H.M. Swaan, V.C.H. Kroll, G.A. Martin, C. Mirodatos, *Catal. Today* 21 (1994) 571–578.
- [46] V.A. Tsipouriari, X.E. Verykios, *J. Catal.* 187 (1999) 85–94.
- [47] S. Somacescu, V. Parvulescu, J.M. Calderon-Moreno, S.-H. Suh, P. Osiceanu, B.-L. Su, *J. Nanoparticle Res.* 14 (2012) 885.
- [48] M.H. Zoellner, G. Niu, J.-H. Jhang, A. Schaefer, P. Zaumseil, M. Bäumer, T. Schroeder, *J. Phys. Chem. C* 117 (2013) 24851–24857.
- [49] R. Razzaq, C. Li, N. Amin, S. Zhang, K. Suzuki, *Energy and Fuels* 27 (2013) 6955–

- 6961.
- [50] P. Djinović, I.G. Osojnik črnivec, B. Erjavec, A. Pintar, *Appl. Catal. B Environ.* 125 (2012) 259–270.
- [51] K. Asami, X. Li, K. Fujimoto, Y. Koyama, A. Sakurama, N. Kometani, Y. Yonezawa, *Catal. Today* 84 (2003) 27–31.
- [52] K.C. Petallidou, A.M. Efstathiou, *Appl. Catal. B Environ.* 140–141 (2013) 333–347.
- [53] P. Kumar, Y. Sun, R.O. Idem, *Energy and Fuels* 21 (2007) 3113–3123.
- [54] S.S. Kim, S.M. Lee, J.M. Won, H.J. Yang, S.C. Hong, *Chem. Eng. J.* 280 (2015) 433–440.
- [55] H. Ay, D. Üner, *Appl. Catal. B Environ.* 179 (2015) 128–138.
- [56] V.M. Gonzalez-DelaCruz, J.P. Holgado, R. Pereñíguez, A. Caballero, *J. Catal.* 257 (2008) 307–314.
- [57] D. San-José-Alonso, J. Juan-Juan, M.J. Illán-Gómez, M.C. Román-Martínez, *Appl. Catal. A Gen.* 371 (2009) 54–59.
- [58] J.-H. Kim, D.J. Suh, T.-J. Park, K.-L. Kim, *Appl. Catal. A Gen.* 197 (2000) 191–200.
- [59] F.B. Noronha, E.C. Fendley, R.R. Soares, W.E. Alvarez, D.E. Resasco, *Chem. Eng. J.* 82 (2001) 21–31.
- [60] D. Pakhare, J. Spivey, *Chem. Soc. Rev.* 43 (2014) 7813–7837.

## Chapter 5: Dry Reforming of Methane over $Ce_{1-x}Zr_xO_{2-\delta}$ – supported Ni and NiCo bimetallic catalysts

Supported transition metals, such as Co and especially Ni [1–3], represent a viable and economically acceptable alternative to be used as DRM suitable catalysts with high activity, selectivity and long-term stability with time on stream (TOS). However, supported transition metal catalysts suffer from fast and extensive accumulation of “carbon” over their surface and consequently deactivation or excessive pressure drop across the catalytic bed. Catalyst durability can be improved with efficient suppression of “carbon” deposition, which can be achieved by tuning various design parameters, such as the use of chemical promoters (e.g. Mg, K or Ca) [4–6] and suitable metal oxide supports having an appropriate concentration of oxygen vacant sites [7–11]. For the latter design parameter, nickel is dispersed over metal oxides possessing high oxygen mobility [7,8,10] as reported in the previous Chapter 4. Recent research investigations on NiCo/ $Ce_{1-x}Zr_xO_{2-\delta}$  catalysts examined in the DRM reaction has notably demonstrated that “carbon” deposition could be prevented over timescales lasting several hundred hours, in a way to be doable for commercialization [12].

Fundamental insights into the reaction mechanism of DRM over supported metal catalysts have been recently reviewed [2]. One of the slow elementary reaction steps from the dissociation of adsorbed  $CH_4$ -s to the formation of  $CH_x$ -s and  $CH_xO$ -s intermediates on the metal surface is the rate-limiting step. The nature of active sites for  $CO_2$  chemisorption and dissociation into CO-s and O-s depends on the nature of the metal and metal oxide support [2]. Oxygen vacancies seem to play a vital role for the reduction of  $CO_2$  to CO [13] over reducible metal oxide supports as illustrated in the previous Chapter 4. Bobin et al. [14] have investigated essential mechanistic steps of DRM over doped ceria-zirconia-supported metals (NiRu, Pt) using transient kinetic methods (TAP, SSITKA). They concluded that an easy dissociation of  $CO_2$  on reduced sites of support followed by a fast oxygen transfer along the surface/domain boundaries to metal sites does occur;  $CH_x$ -s derived from methane react to form CO and  $H_2$ , where strongly bound carbonates were found to be spectator species. In a recent work regarding the effect of Ni particle size on the rates of important elementary reaction steps of DRM on Ni/ $Al_2O_3$  [15], it was concluded that the increase of O-s (derived from the dissociation of  $CO_2$ ) per active site on the Ni surface may enhance oxidation of  $CH_x$ -s to  $CH_xO$ -s and in turn its decomposition to CO and  $H_2$ . Thus, oxidation of  $CH_x$ -s than their further dissociation to surface

carbon whiskers is considered as a key step for the development of a “carbon”-free DRM catalytic system.

In the present chapter, important fundamental questions regarding the influence of the support synthesis method, and the use of Co-promoter of Ni activity (NiCo bimetallic phase) *on the carbon-path of dry reforming of methane* performed over 3 wt.% Ni (or NiCo)/ $Ce_{1-x}Zr_xO_{2-\delta}$  catalysts are addressed with meticulously designed SSITKA and other transient isotopic experiments. In particular, the following are addressed:

- How does Co metal in the NiCo bimetallic phase influence the extent of  $CO_2$  or  $CH_4$  contribution to the “carbon” deposition pathways?
- Does lattice oxygen of  $Ce_{1-x}Zr_xO_{2-\delta}$ -supported Ni (3 wt.%) or NiCo (3 wt.%) catalyst participate in the DRM reaction?
- Does the “carbon” formed via  $CH_4$  decomposition alone differ from that formed during DRM reaction?
- Does  $CO_2$  participate in the gasification of “carbon” to produce CO and how this route is influenced by the presence of Co and Ce/Zr ratio?

### 5.1. 3 wt.% Ni/ $Ce_{0.75}Zr_{0.25}O_2$ catalyst (3Ni EG code)

#### 5.1.1. Powder XRD and $H_2$ -TPR characterization

Powder X-ray diffraction analysis results of the 3 wt.% Ni/ $Ce_{0.75}Zr_{0.25}O_{2-\delta}$  catalyst are presented in Fig. 5.1. The recorded diffraction pattern agrees very well with that of  $CeZrO_2$  solid solution (JCPDS 00-28-0271). A shift of diffraction maxima toward higher  $2\theta$  values compared to pure  $CeO_2$  (JCPDS 00-34-0394), and reduction of the unit cell size/volume were observed, which strongly suggest isomorphous substitution of the larger  $Ce^{4+}$  ions (0.97 Å) with smaller  $Zr^{4+}$  ions (0.86 Å) and formation of a  $Ce_{0.75}Zr_{0.25}O_{2-\delta}$  solid solution. Using the Scherrer equation, an average primary crystallite size of support was estimated at 6.0 nm with the  $Ce_{0.75}Zr_{0.25}O_{2-\delta}$  unit cell size (a, nm) at 0.533 nm. No diffraction lines belonging to Ni-containing phases were observed due to the low Ni loading in the analyzed catalyst sample.

Based on the  $H_2$ -TPD measurements, an average Ni particle size was calculated,  $d_{Ni} = 9.8$  nm, and a nickel metal dispersion,  $D_{Ni} (\%) = 10.3$ . The specific surface area, total specific pore volume and average pore diameter of the 3 wt.% Ni/ $Ce_{0.75}Zr_{0.25}O_{2-\delta}$  catalyst were found to be:  $57.0 \text{ m}^2 \text{ g}^{-1}$ ,  $0.183 \text{ cm}^3 \text{ g}^{-1}$ , and 12.8 nm, respectively.



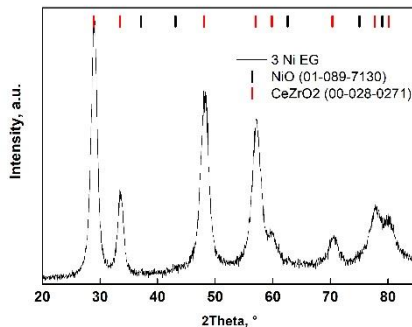


**Figure 5.2:** Powder XRD pattern of the 3 wt.% Ni/ $Ce_{0.75}Zr_{0.25}O_{2-\delta}$  (3 Ni EG) catalyst.

Figure 5.2 presents hydrogen TPR traces recorded over the 3 wt.% Ni/ $Ce_{0.75}Zr_{0.25}O_{2-\delta}$  catalyst and its  $Ce_{0.75}Zr_{0.25}O_{2-\delta}$  support alone. Reduction of Ni/ $Ce_{0.75}Zr_{0.25}O_{2-\delta}$  starts at  $\sim 100$  °C and exhibits a low-temperature shoulder and two intense reduction peaks at 266 and 320 °C, which decay slowly as the reduction temperature approaches the final value of 750 °C. In the low-temperature range, reduction of NiO and surface  $Ce_{0.75}Zr_{0.25}O_{2-\delta}$  occur, whereas bulk reduction of support takes place at temperatures above 550 °C [16]. By considering the chemical composition of the catalyst and assuming complete NiO reduction, the amount of reducible lattice oxygen was estimated to be  $955 \mu\text{mol O g}^{-1}$ , which corresponds to 43% reduction of Ce ( $Ce^{4+} \rightarrow Ce^{3+}$ ) present in the  $Ce_{0.75}Zr_{0.25}O_2$  solid support and 7.8% of its total theoretical oxygen content (fully oxidized).

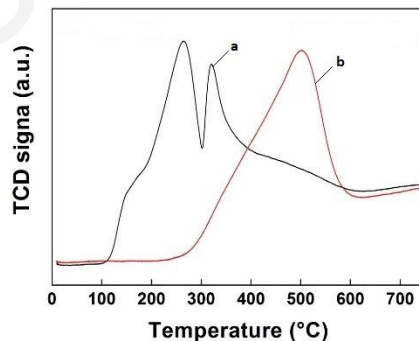


**Figure 5.2:**  $H_2$ -TPR traces recorded over the (a) 3 wt.% Ni/ $Ce_{0.75}Zr_{0.25}O_{2-\delta}$  catalyst and (b) the  $Ce_{0.75}Zr_{0.25}O_{2-\delta}$  support.

### 5.1.2. Catalytic DRM performance of 3 wt.% Ni/ $Ce_{0.75}Zr_{0.25}O_{2-\delta}$

Fig. 5.3 presents  $CH_4$ -conversion (%),  $CO_2$ -conversion (%) and  $H_2/CO$  gas product ratio data as a function of time on stream (TOS) for the DRM performed at 750 °C over the 3 wt.%

$\text{Ni}/\text{Ce}_{0.75}\text{Zr}_{0.25}\text{O}_{2-\delta}$  catalyst. A large drop ( $\sim 40$  %-units) in both the  $\text{CO}_2$  and  $\text{CH}_4$  conversion is evident during the first 5 h of reaction, which reflects also that of  $\text{H}_2/\text{CO}$  ratio. On the other hand, a slow regeneration of the catalyst activity is evident after  $\sim 5$  h of dry reforming and for the course of reaction followed up to 20 h.

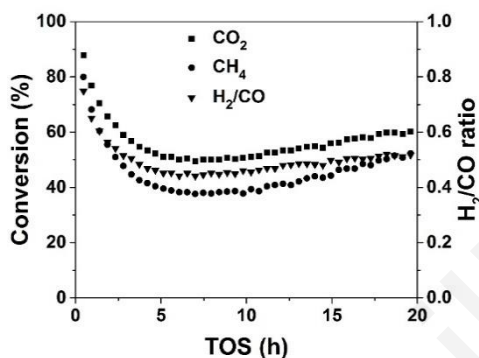


**Figure 5.3:**  $\text{CH}_4$  and  $\text{CO}_2$  conversions and the  $\text{H}_2/\text{CO}$  product gas ratio as a function of time on stream (TOS) for the 3 wt.%  $\text{Ni}/\text{Ce}_{0.75}\text{Zr}_{0.25}\text{O}_{2-\delta}$  catalyst at  $750$  °C. Feed gas composition: 44.2%  $\text{CH}_4$ , 44.2%  $\text{CO}_2$ , balance  $\text{N}_2$ ;  $W_{\text{cat}} = 50$  mg;  $F_{\text{T}} = 56.5$   $\text{NmL min}^{-1}$ .

As reported elsewhere [1], this behavior (Fig. 5.3) is likely to be due to the partial oxidation of Ni surface by spilled over support lattice oxygen, resulting in the observed substantial deactivation. During the course of reaction, sintering of Ni particles reduces the Ni-support interface per gram of nickel, thus the amount of oxygen (per gram of Ni) reaching the interface. This in turn causes the decrease in the fraction of oxidized nickel [1], which manifests itself as a *slow regeneration of catalytic activity*. The participation of inactive “carbon” in the catalytic behavior shown in Fig. 5.3 during reaction might also be important. High rates of “carbon” deposition on the nickel surface at the initial states of reaction could progressively be balanced by the rates of diffusion of “carbon” towards the metal-support interface and the rates of “carbon” gasification by labile oxygen of support towards CO formation. Sukonket et al. [10] have investigated a 5 wt.%  $\text{Ni}/\text{Ce}_{0.6}\text{Zr}_{0.4}\text{O}_2$  catalyst towards dry reforming of methane at  $800$  °C ( $\text{CH}_4/\text{CO}_2/\text{N}_2 = 40/40/20$ ) and for long-term TOS (150 h). A very similar  $\text{CH}_4$ -conversion vs. TOS profile to that shown in Fig. 5.3 was reported [10], where minimum conversion was obtained after  $\sim 22$  h on stream but with a lower %-drop in activity compared to the initial one, when this behavior is compared to that of the present catalyst ( $750$  °C, similar feed composition). Even though the authors did not discuss this feature in the obtained activity profile, it is worth mentioning that one of the authors’ main conclusions is that both surface active Ni sites and

lattice oxygen defects (oxygen vacancies) have to be present in the right proportion for each nickel site in order to participate effectively in the dry reforming of methane reaction [10]. These results are in harmony with the results of the present work (see following Sections) which illustrate the importance of oxygen vacancies, the latter being inherent constituents of support's composition but also formed by the reaction of very mobile lattice oxygen with "carbon" produced mainly by  $CH_4$  dissociation.

The  $H_2/CO$  gas product ratio during the whole 20-h run takes values lower than unity (0.5 – 0.75), mainly as the result of the reverse water-gas shift reaction [4,7]. An amount of 0.3 wt.% C (carbon) was estimated after 20 h in dry reforming.

### 5.1.3. Transient evolution rates of $CH_4/He$ and $CH_4/CO_2/He$ (DRM) reactions

Fig. 5.4a shows the transient evolution of  $H_2$ ,  $CO$  and  $CO_2$  gas products rates obtained after the switch  $He \rightarrow 20\% CH_4/He$  (t) at  $750^\circ C$  was made over the 25-mg fresh and reduced 3 wt.%  $Ni/Ce_{0.75}Zr_{0.25}O_{2-\delta}$  catalyst sample. It is clearly seen that within a very short time (90 s) the methane decomposition rate drops to a very small value due to "carbon" deposition, whereas the main reaction products are  $CO$  and  $H_2$ ; only a very small amount of  $CO_2$  is formed. The  $CH_4/He$  reaction was left for 30 min, after which no gaseous product was seen. The amounts of  $H_2$ ,  $CO$  and  $CO_2$  formed during this 30-min  $CH_4/He$  treatment of the catalyst were found to be 7000, 4100 and  $5.5 \mu mol g^{-1}$ , respectively, providing a  $H_2/CO$  ratio of  $\sim 1.7$ . Of interest is the fact that all three gaseous products evolve at the same time but their maximum rates appear at slightly different times,  $t_{max} = 5.5, 7.0$  and  $9.0$  s for the  $CO_2, CO$  and  $H_2$ , respectively. The amount of "carbon" deposited during the 30-min  $CH_4/He$  treatment of the catalyst and its reactivity towards hydrogen and oxygen are presented in the next Section. The equivalent amount of "O" in the  $CO$  formed can be compared to the total amount of "O" present in the catalyst's support in its fully oxidized state. The latter is found to be  $\sim 12.5 mmol g_{sup}^{-1}$ . Therefore, the amount of "O" reacted off by  $CH_4$  is about 32.9% of the maximum available lattice oxygen in the  $Ce_{0.75}Zr_{0.25}O_{2-\delta}$  support.

A similar experiment with the support alone (25 mg) resulted in largely different shapes for the  $H_2, CO$  and  $CO_2$  transient responses (not shown) corresponding also to smaller quantities, namely: 1050, 960 and  $120 \mu mol g^{-1}$  for  $H_2, CO$  and  $CO_2$ , respectively. In particular, the maximum rate of  $CO$  formation appeared at  $t_{max} = 7.5$  s with a value of  $14 \mu mol g^{-1} s^{-1}$ , which was slowly decreasing towards the value of  $\sim 12 \mu mol g^{-1} s^{-1}$  after 90 s on reaction stream.

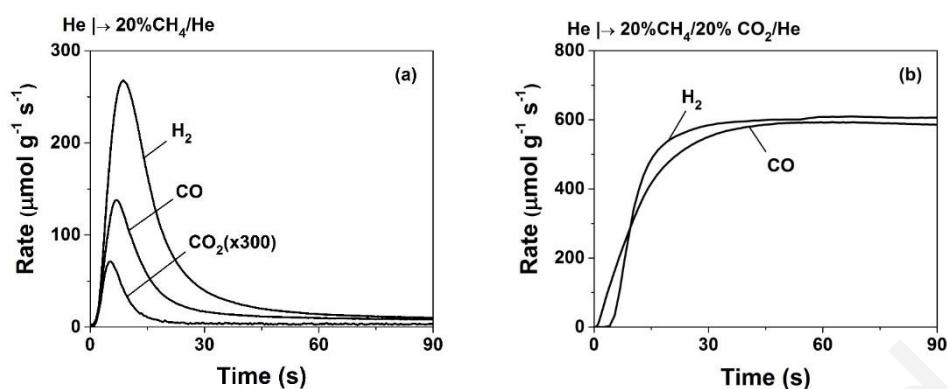


**Figure 5.4:** (a) Transient rates ( $\mu\text{mol g}^{-1} \text{s}^{-1}$ ) of  $\text{H}_2$ ,  $\text{CO}$  and  $\text{CO}_2$  formation as a function of time obtained after the gas switch  $\text{He} \rightarrow 20\% \text{CH}_4/\text{He}$  at  $750^\circ\text{C}$  was made; (b) transient rates ( $\mu\text{mol g}^{-1} \text{s}^{-1}$ ) of  $\text{H}_2$  and  $\text{CO}$  formation as a function of time obtained after the gas switch  $\text{He} \rightarrow 20\% \text{CH}_4/20\% \text{CO}_2/\text{He}$  (DRM) at  $750^\circ\text{C}$  was made.  $F_T = 100 \text{ NmL min}^{-1}$ ;  $W_{\text{cat}} = 25 \text{ mg}$ .

Fig. 5.4b presents the transient evolution of the  $\text{H}_2$  and  $\text{CO}$  formation rates after the step gas switch  $\text{He} \rightarrow 20\% \text{CH}_4/20\% \text{CO}_2/\text{He}$  at  $750^\circ\text{C}$  was made over a fresh and reduced 25-mg catalyst sample. A totally different transient evolution in the rate of  $\text{H}_2$  product formation is seen compared to the case of  $\text{CH}_4/\text{He}$  reaction (Fig. 5.4a). Upon the switch to the DRM reaction gas mixture, the rate of  $\text{CO}$  formation slowly increases (within the 90-s interval time) and reaches the value of  $\sim 580 \mu\text{mol CO g}^{-1} \text{s}^{-1}$  after 90 s on reaction stream. On the other hand, the transient  $\text{H}_2$  rate response shows a clear delay ( $t \sim 5 \text{ s}$ ) in its appearance with respect to that of  $\text{CO}$  and reaches the value of  $610 \mu\text{mol H}_2 \text{ g}^{-1} \text{s}^{-1}$  after 90 s (Fig. 5.4b). At this very short time of reaction, the  $\text{H}_2/\text{CO}$  gas product ratio obtained is 1.05. The time delay in the appearance of  $\text{H}_2$  response with respect to that of  $\text{CO}$  (Fig. 5.4b) is strictly governed by the relative kinetic rates of  $\text{CH}_4$  dissociation,  $\text{CO}$  and  $\text{H}_2$  formation on an initially reduced nickel surface that progressively accumulates “carbon” species, and likely gets partly oxidized by support’s highly mobile lattice oxygen.

#### 5.1.4. Characterisation of “carbon” formed during $\text{CH}_4/\text{He}$ and DRM reactions

##### 5.1.4.1. Temperature-programmed hydrogenation (TPH) and transient isothermal hydrogenation (TIH) after $\text{CH}_4/\text{He}$ reaction

Fig. 5.5a presents the TPH trace obtained after the 30-min treatment of the catalyst by  $20\% \text{CH}_4/\text{He}$  at  $750^\circ\text{C}$  (Fig. 5.4a). It is seen that hydrogenation of the “carbon” formed towards  $\text{CH}_4$  starts at  $\sim 500^\circ\text{C}$  and produces a rather symmetrical peak ( $T_M = 634^\circ\text{C}$ ), which is not

completed as the catalyst reaches the maximum T of 750 °C. The amount of “carbon” formed was found to be 687  $\mu\text{mol g}^{-1}$ . Fig. 5.5b shows transient response curves of  $\text{CH}_4$  obtained during isothermal hydrogenation at 600, 645, 670 and 700 °C of the “carbon” formed after  $\text{CH}_4/\text{He}$  treatment at 750 °C (Fig. 5.4a). The maximum in the rate of  $\text{CH}_4$  appears at  $t_{\text{max}} = 0.2, 0.35, 0.37$  and 0.45 min for the hydrogenation temperatures of 600, 645, 670 and 700 °C, respectively. It is clearly observed that the rate of “carbon” hydrogenation increases significantly as the temperature increases from 645 to 670 °C. At higher temperatures (ca. 700 °C), the increase in the rate is small. Moreover, it is seen that the shape of the  $\text{CH}_4$  trace changes significantly with increasing hydrogenation temperature. At the lowest temperatures of 600 and 645 °C, there is a small but sharp peak at the first initial state of the transient ( $\sim 1$  min), followed by a long tail out to 10-min of hydrogenation time. This feature could imply that there might be a small amount of an active “carbon” and a second kind of a less active one. As the temperature increases, the first small peak becomes a spike, whereas the long tail takes exponential decay behaviour with increasing time in  $\text{H}_2/\text{He}$ . The latter result is in harmony with the TPH trace behavior depicted in Fig. 5.5a. The amount of “carbon” reacted off under the 10-min TIH treatment was found to be 80, 125, 450 and 420  $\mu\text{mol g}^{-1}$  for the 600, 645, 670 and 700 °C hydrogenation temperatures, respectively.

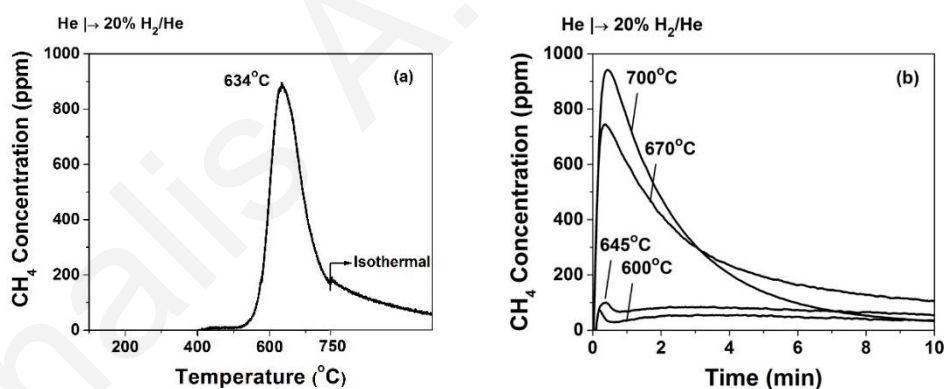


**Figure 5.5:** (a) TPH trace and (b) TIH response curves ( $T = 600, 645, 670$  and  $700$  °C) of the “carbon” formed after 30-min treatment of the catalyst in 20%  $\text{CH}_4/\text{He}$  at 750 °C. Gas delivery sequence (TPH): He (750 °C)  $\rightarrow$  20%  $\text{CH}_4/\text{He}$  (750 °C, 30 min)  $\rightarrow$  He (750 °C, 10 min)  $\rightarrow$  cool in He flow to 100 °C  $\rightarrow$  20%  $\text{H}_2/\text{He}$ , TPH (100 to 750 °C,  $F_{\text{He}} = 50 \text{ NmL min}^{-1}$ ,  $\beta = 30$  °C  $\text{min}^{-1}$ )  $\rightarrow$  TIH at 750 °C for 10 min; (b) He (750 °C)  $\rightarrow$  20%  $\text{CH}_4/\text{He}$  (750 °C, 30 min,  $F_{\text{T}} = 100 \text{ NmL min}^{-1}$ )  $\rightarrow$  He (10 min)  $\rightarrow$  cool in He flow to the lowest T (600 °C)  $\rightarrow$  20%  $\text{H}_2/1\% \text{ Kr/Ar}$  (10 min,  $F_{\text{T}} = 100 \text{ NmL min}^{-1}$ )  $\rightarrow$  increase T to 750 °C and stay for 30 min  $\rightarrow$  repeat the same procedure for the next highest T;  $W_{\text{cat}} = 25 \text{ mg}$ .

### 5.1.4.2. Quantifying the origin of inactive “carbon” deposition (CH<sub>4</sub> versus CO<sub>2</sub> activation routes)

Figure 5.6 presents transient <sup>12</sup>CO<sub>2</sub> and <sup>13</sup>CO<sub>2</sub> formation rates recorded during TPO of the “carbon” formed after 30 min of dry reforming at 750 °C having labeled the carbon dioxide in the feed stream (use of <sup>13</sup>CO<sub>2</sub>). The <sup>13</sup>CO<sub>2</sub> response arises from the oxidation of <sup>13</sup>C-containing “carbon” formed via the <sup>13</sup>CO<sub>2</sub> activation route, whereas that of <sup>12</sup>CO<sub>2</sub> from the oxidation of <sup>12</sup>C-containing “carbon” formed via the <sup>12</sup>CH<sub>4</sub> decomposition route. It is clearly seen that the shapes of <sup>13</sup>CO<sub>2</sub> and <sup>12</sup>CO<sub>2</sub> response curves and their relative amounts (area under the response curve) are largely similar. In the case of <sup>13</sup>CO<sub>2</sub> response, two main peaks centred at ~ 350 and ~ 640 °C are observed, whereas in the case of <sup>12</sup>CO<sub>2</sub> response, a shoulder at the low-T side of the main peak (~ 640 °C) is obtained. The total amount of “carbon” reacted off is ~ 1470 μmol g<sup>-1</sup>, where 710 μmol g<sup>-1</sup> correspond to <sup>13</sup>C-containing “carbon” and 760 μmol g<sup>-1</sup> to <sup>12</sup>C-containing “carbon”, resulting in a <sup>12</sup>CO<sub>2</sub>/<sup>13</sup>CO<sub>2</sub> ratio of 1.07. Therefore, the two activation routes of CH<sub>4</sub> and CO<sub>2</sub> contribute to an about similar extent in the formation of “carbon”.

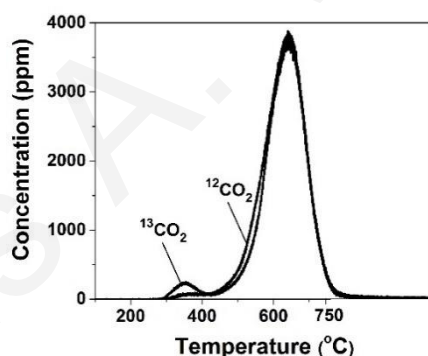


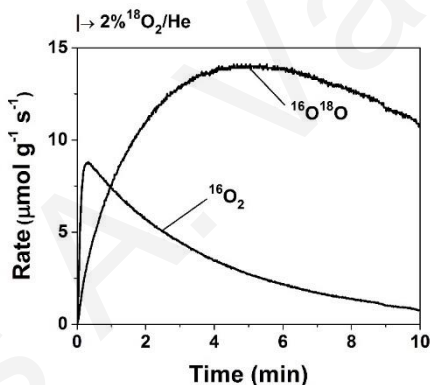
**Figure 5.6:** Temperature-programmed oxidation (TPO) of “carbon” formed during dry reforming of methane (<sup>13</sup>CO<sub>2</sub>/<sup>12</sup>CH<sub>4</sub>/He) at 750 °C. Gas delivery sequence: 5% <sup>13</sup>CO<sub>2</sub>/5% <sup>12</sup>CH<sub>4</sub>/He (750 °C, 30 min, F<sub>T</sub> = 50 NmL min<sup>-1</sup>) → He (750 °C, 10 min) cool in He flow to 100 °C → 10% O<sub>2</sub>/He, TPO (100 to 750 °C, F<sub>T</sub> = 50 NmL min<sup>-1</sup>, β = 30 °C min<sup>-1</sup>); W<sub>cat</sub> = 50 mg.

As will be illustrated in the next Section, the amount of *active* “carbon” leading to the formation of CO via the CO<sub>2</sub> activation route is very small, thus the “carbon” measured in the TPO experiments (Fig. 5.6) corresponds practically to *inactive* “carbon” (spectator species) deposited during DRM. It is clear that in the absence of carbon isotopic effects, the TPO trace

of “carbon” oxidation to  $\text{CO}_2$  having not labeled with  $^{13}\text{C}$  the  $\text{CO}_2$  present in the DRM feed gas stream would be the sum of  $^{12}\text{CO}_2$  and  $^{13}\text{CO}_2$  transients (Fig. 5.6).

### 5.1.5. Probing the participation of support lattice oxygen in DRM

The 10-min treatment of the catalyst in the 2%  $^{18}\text{O}_2/\text{He}$  gas mixture at 750 °C results in  $\sim 10.0 \text{ mmol } ^{16}\text{O g}^{-1}$  of exchangeable labile oxygen as shown in Fig. 5.7. The main features of the obtained oxygen isotopic response curves are typical of an  $^{16}\text{O}/^{18}\text{O}$  exchange process over ceria-based reducible metal oxides [14], where the appearance of peak maximum in the rate of  $^{16}\text{O}^{18}\text{O}$  formation is due not only to the initial oxygen exchange capacity of the solid but also to the *slow rate* of bulk oxygen diffusion in the crystal structure of the  $\text{Ce}_{0.75}\text{Zr}_{0.25}\text{O}_{2-\delta}$  support towards the surface. The latter process takes over after the  $^{16}\text{O}/^{18}\text{O}$  exchange of the first few oxygen monolayers from the top of the surface of  $\text{Ce}_{0.75}\text{Zr}_{0.25}\text{O}_{2-\delta}$ .



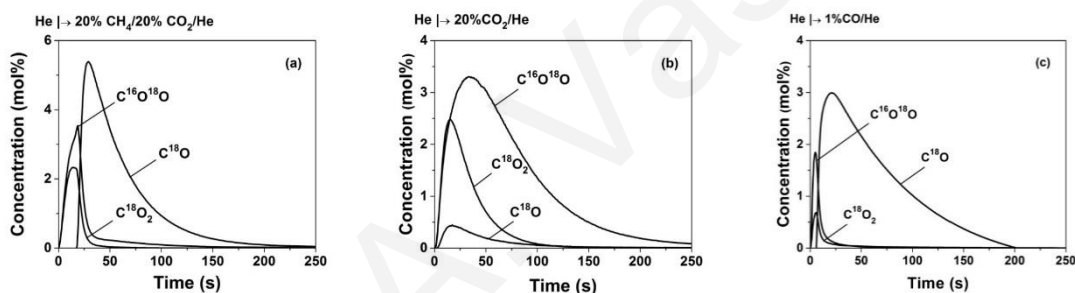
**Figure 5.7:** Transient rates of  $^{16}\text{O}_2$  and  $^{16}\text{O}^{18}\text{O}$  ( $\mu\text{mol g}^{-1} \text{ s}^{-1}$ ) formation as a function of time due to the isotopic exchange of lattice  $^{16}\text{O}$  with  $^{18}\text{O}$  after treatment of the catalyst with 2%  $^{18}\text{O}_2/\text{He}$  for 10 min at 750 °C. Gas delivery sequence: He (750 °C)  $\rightarrow$  2%  $^{18}\text{O}_2/\text{He}$  (750 °C, 10 min);  $W_{\text{cat}} = 25 \text{ mg}$ .

Fig. 5.8a shows transient concentration response curves of  $\text{C}^{18}\text{O}$ ,  $\text{C}^{16}\text{O}^{18}\text{O}$  and  $\text{C}^{18}\text{O}_2$  recorded after the switch He  $\rightarrow$  20%  $\text{CH}_4/20\% \text{CO}_2/\text{He}$  (t) was made at 750 °C following a 10-min  $^{18}\text{O}_2$  catalyst pre-treatment (see Fig. 5.7). Three important features of this experiment should be noted. First, the transient rate of  $\text{C}^{18}\text{O}$  formation lags behind that of  $\text{C}^{16}\text{O}^{18}\text{O}$  and  $\text{C}^{18}\text{O}_2$ , where a time delay of  $\sim 13 \text{ s}$  is noted between the first appearance of  $\text{C}^{18}\text{O}$  and that of  $^{18}\text{O}$ -labelled carbon dioxides. Second, all transients finish after  $\sim 4 \text{ min}$  in DRM, and third, the amount of  $\text{C}^{18}\text{O}$  formed is larger than that of  $\text{C}^{16}\text{O}^{18}\text{O}$  or  $\text{C}^{18}\text{O}_2$ . More precisely, 5600, 2100 and



1800 μmol <sup>18</sup>O g<sup>-1</sup> of equivalent <sup>18</sup>O is found in the C<sup>18</sup>O, C<sup>16</sup>O<sup>18</sup>O and C<sup>18</sup>O<sub>2</sub> gas products, respectively (Fig. 5.8a). The amount of <sup>18</sup>O appeared in the <sup>18</sup>O- labelled CO is ~ 56% of the amount of <sup>18</sup>O stored in the solid before the switch to the DRM reaction stream (Fig. 5.7).

The formation of <sup>18</sup>O-labelled CO<sub>2</sub>'s during the CH<sub>4</sub>/CO<sub>2</sub>/He gas switch (Fig. 5.8a) on a pre-covered catalyst surface by <sup>18</sup>O might reasonably be considered as the result of exchange of C<sup>16</sup>O<sub>2</sub> with surface <sup>18</sup>O (mainly of Ce<sub>0.75</sub>Zr<sub>0.25</sub>O<sub>2-δ</sub> support), according to the reaction steps (Eqs. 5.1-5.2), but also to the reversibility of the Boudouard reaction (Eq. 5.3):



**Figure 5.8:** Transient concentration (mol%) response curves of C<sup>18</sup>O, C<sup>16</sup>O<sup>18</sup>O and C<sup>18</sup>O<sub>2</sub> obtained at 750 °C after (a) dry reforming of methane (20% CH<sub>4</sub>/20% CO<sub>2</sub>/He), (b) 20% CO<sub>2</sub>/He gas treatment and (c) 1% CO/He gas treatment, following catalyst pre-treatment with 2% <sup>18</sup>O<sub>2</sub>/He (10 min) at 750 °C and He purge. Gas delivery sequence: He (750 °C) → 2% <sup>18</sup>O<sub>2</sub>/He (10 min) → He (5 min) → 20% CO<sub>2</sub>/20% CH<sub>4</sub>/He (t) or 20% CO<sub>2</sub>/He (t) or 1% CO/He (t); W<sub>cat</sub> = 25 mg.

Fig. 5.8b presents the transient evolution of <sup>18</sup>O-labelled CO<sub>2</sub>'s during the step-gas switch He → 20% CO<sub>2</sub>/He instead that of He → 20% CH<sub>4</sub>/20% CO<sub>2</sub>/He (Fig. 5.8a) over the same catalyst sample and under the same experimental conditions (e.g. mass of catalyst, flow rate, catalyst pre-treatment conditions). It is clearly seen that similar in size transient response curves of both C<sup>16</sup>O<sup>18</sup>O and C<sup>18</sup>O<sub>2</sub> are obtained compared to those in Fig. 5.8a. However, differences in their transient kinetics of formation (shape and position of the transient curve) appear. For example, in the case of C<sup>16</sup>O<sup>18</sup>O formation, t<sub>max</sub> (time of peak maximum appearance)



equals to 33.0 s under the 20%  $CO_2/He$  treatment (Fig. 5.8b), as opposed to 19.0 s under the  $CH_4/CO_2/He$  (DRM) treatment (Fig. 5.8a). The equivalent amount of  $^{18}O$  in the  $C^{16}O^{18}O$  and  $C^{18}O_2$  is found to be 2400 and 1980  $\mu mol g^{-1}$ , respectively. As shown in Fig. 5.8b, a small amount of  $C^{18}O$  is formed (50  $\mu mol g^{-1}$ ) immediately upon the switch ( $t_{max} = 17$  s), as opposed to the  $C^{18}O$  transient response recorded in DRM ( $t_{max} = 28$  s), which has a different shape (compare Figs. 5.8a and b).

To further investigate the appearance of  $C^{18}O$  transient at the DRM switch (Fig. 5.8a), the 1%  $CO/He$  gas switch after  $^{16}O/^{18}O$  exchange and He purge was made (Fig. 5.8c). The 1%  $CO$  composition used was based on the fact that this was the composition of  $CO$  formed after 10 min of DRM at 750 °C (20%  $CH_4/20\% CO_2/He$ ). As shown in Fig. 5.8c, a large  $C^{18}O$  response is observed which lasts for  $\sim 200$  s. In particular, the  $C^{18}O$  response shows a delay of 6 s for its appearance with respect to the  $^{18}O$ -isotopic  $CO_2$ 's transient responses and a peak maximum at  $t_{max} = 21$  s; an equivalent amount of 4000  $\mu mol^{18}O g^{-1}$  was estimated. Smaller and faster responses of  $C^{16}O^{18}O$  and  $C^{18}O_2$  are seen with respect to Fig. 5b. On the other hand, the  $C^{16}O^{18}O$  and  $C^{18}O_2$  response curves present peak maxima at  $t_{max} = 5.5$  and 5.0 s and provided 540 and 180  $\mu mol^{18}O g^{-1}$ , respectively. The significance of these results and their contribution in explaining the  $C^{18}O$  transient obtained under dry reforming (Fig. 5.8a) will be discussed next.

To provide further evidence for the participation of lattice oxygen of support to the  $CO$  formation at the switch  $He \rightarrow 20\% CH_4/He$  (Fig. 5.4a), the same gas switch was performed on the  $^{18}O$ -pretreated catalyst (see Fig. 5.7). A large  $C^{18}O$  transient at the switch  $He \rightarrow 20\% CH_4/He$  was observed (not presented) with peak maximum at  $t_{max} = 7$  s and similar in shape to that of  $C^{16}O$  (Fig. 5.4a). The equivalent amount of  $^{18}O$  associated with this  $C^{18}O$  response was found to be 345  $\mu mol g^{-1}$ .

#### 5.1.6. SSITKA - Quantifying the *active* carbon present in the $CO_2$ reaction path

Fig. 5.9 shows dimensionless concentration transient response curves of Kr (inert gas),  $^{13}CO$  and  $^{13}CO_2$  obtained during the last SSITKA switch at 750 °C according to the following gas delivery sequence:  $^{12}CO_2/^{12}CH_4/He$  (30 min)  $\rightarrow$   $^{13}CO_2/^{12}CH_4/Kr/He$  (20 min)  $\rightarrow$   $^{12}CO_2/^{12}CH_4/He$  (t).

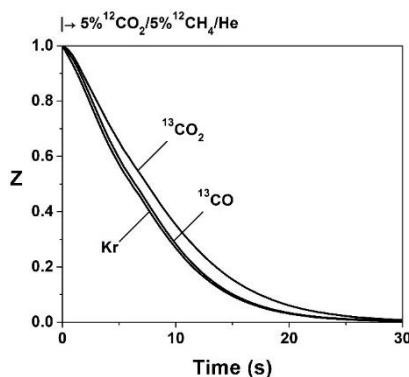
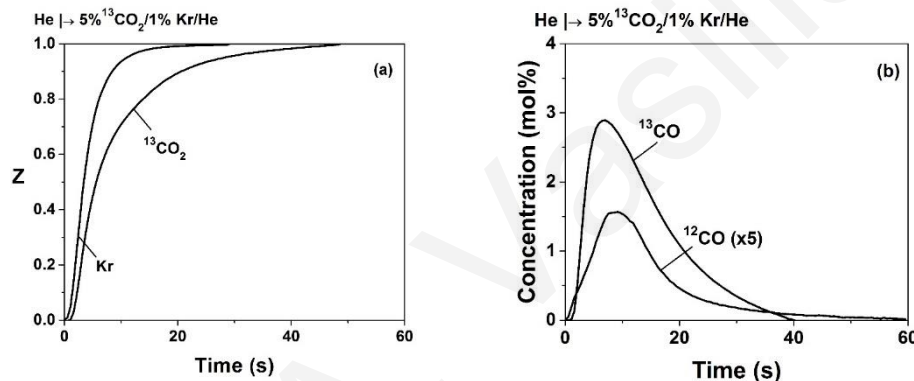


**Figure 5.9:** Transient dimensionless response curves of Kr, <sup>13</sup>CO and <sup>13</sup>CO<sub>2</sub> obtained during SSITKA at 750 °C after 30 min of dry reforming of methane. SSITKA gas switches: 5% <sup>12</sup>CO<sub>2</sub>/5% <sup>12</sup>CH<sub>4</sub>/He (30 min) → 5% <sup>13</sup>CO<sub>2</sub>/5% <sup>12</sup>CH<sub>4</sub>/Kr/He (20 min) → 5% <sup>12</sup>CO<sub>2</sub>/5% <sup>12</sup>CH<sub>4</sub>/He (t); W<sub>cat</sub> = 50 mg; F<sub>T</sub> = 100 NmL min<sup>-1</sup>.

It is clearly seen that the <sup>13</sup>CO<sub>2</sub> response curve lags behind that of <sup>13</sup>CO, whereas the latter response follows very closely that of Kr tracer gas. Similar responses with same features were seen also during SSITKA switches after 2 h of DRM reaction. After using the appropriate material balance (see Ch. 3, Eq. 3.16), the concentration of *active* “carbon” (N<sub>C</sub>) formed in the carbon-path of CO<sub>2</sub> activation route to form CO(g) is found to be ~0.3 μmol g<sup>-1</sup>, or an equivalent θ<sub>C</sub> ~ 0.006 (0.6%). The latter quantity is based on the Ni exposed surface area which was estimated to be 52.4 μmol Ni<sub>s</sub> g<sup>-1</sup>. The difference in the area between the <sup>13</sup>CO<sub>2</sub> and <sup>13</sup>CO-SSITKA response curves shown in Fig. 5.9 is proportional to the concentration of a pool of reversibly adsorbed carbon dioxide (e.g. carbonate-type), which does not lead to the formation of CO (*inactive* species). This is found to be N<sub>CO2</sub> ~ 0.9 μmol g<sup>-1</sup>. The N<sub>CO2</sub> quantity in terms of surface coverage, θ (based on Ni<sub>s</sub>) is found to be θ<sub>CO2</sub> ~ 0.017 or 1.7%, to be compared with that of N<sub>C</sub> = 0.6%. The site of adsorption for this reversibly adsorbed CO<sub>2</sub> is most likely to be the support, given the high T of 750 °C. In the case that θ<sub>CO2</sub> were larger than one, then definitely part of this is formed on the support. The same amount of N<sub>C</sub> but a larger N<sub>CO2</sub> (1.8 μmol g<sup>-1</sup>) were found after 2 h of dry reforming. It should be noted that due to the high activity of the Ni/Ce<sub>0.75</sub>Zr<sub>0.25</sub>O<sub>2-δ</sub> catalyst at the examined DRM reaction conditions, the accuracy in recording the SSITKA transients (Fig. 5.9) required high conversions of CH<sub>4</sub> and CO<sub>2</sub> (75-90%).

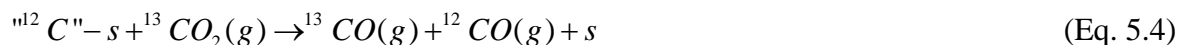
### 5.1.7. Probing the gasification of “carbon” by CO<sub>2</sub>

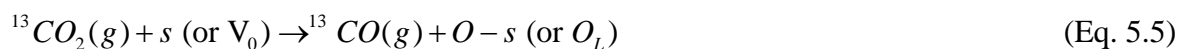
The gasification of “carbon” formed during DRM at 750 °C by CO<sub>2</sub> (or the reversibility of Boudouard reaction) was investigated by the experiment described in Ch. 3, Section 3.7.3 and the results obtained are shown in Fig. 5.10. The transient evolution of <sup>13</sup>CO<sub>2</sub>(g) at the switch 5% <sup>13</sup>CO<sub>2</sub>/1% Kr/He, following DRM for 30 min and a 5-min He purge, is shown in Fig. 5.10a. It is clearly seen that the <sup>13</sup>CO<sub>2</sub> response lags behind that of Kr inert gas. This behaviour illustrates that <sup>13</sup>CO<sub>2</sub> interacts with the catalyst surface by replacing reversibly adsorbed carbon dioxide (e.g. carbonate-type formed under DRM) and reacting with adsorbed intermediates formed under the preceded DRM reaction. After using the appropriate material balance (see Ch. 3, Eq. 3.17), the amount of <sup>13</sup>CO<sub>2</sub> consumed (Fig. 5.10a) is found to be 610 μmol g<sup>-1</sup>.



**Figure 5.10:** Transient response curves of (a) dimensionless concentrations of Kr and <sup>13</sup>CO<sub>2</sub> and (b) <sup>12</sup>CO and <sup>13</sup>CO concentrations obtained at 750 °C following 30 min of dry reforming of methane at 750 °C according to the following sequence of gas switches: 5% CO<sub>2</sub>/5% CH<sub>4</sub>/He (30 min) → He (5 min) → 5% <sup>13</sup>CO<sub>2</sub>/Kr/He (t). W<sub>cat</sub> = 50 mg; F<sub>T</sub> = 100 NmL min<sup>-1</sup>.

During the <sup>13</sup>CO<sub>2</sub>/Kr/He gas switch, <sup>12</sup>CO and <sup>13</sup>CO gases are also obtained and their transients are shown in Fig. 5.10b. The quantities of <sup>12</sup>CO and <sup>13</sup>CO formed during the 60-s transient (Fig. 5.10b) are 67 and 575 μmol g<sup>-1</sup>, respectively. The main surface interactions of <sup>13</sup>CO<sub>2</sub> that might have been occurred during this transient experiment are the “<sup>12</sup>C-s” gasification by <sup>13</sup>CO<sub>2</sub> (Eq. 5.4) and the dissociation of <sup>13</sup>CO<sub>2</sub> (Eq. 5.5) on Ni and/or on the oxygen vacant sites of support, as discussed below. In the reaction step described by Eq. 5.5, s is an empty site on the Ni surface, Vo is an oxygen vacant site on the Ce<sub>0.75</sub>Zr<sub>0.25</sub>O<sub>2-δ</sub> support surface, and O<sub>L</sub> is a surface support lattice oxygen.





According to the SSITKA results and those of the previous paragraph the 67 μmol <sup>12</sup>CO g<sup>-1</sup> measured correspond to *inactive* “<sup>12</sup>C-s” formed on the surface of the catalyst (see Eq. 5.4) after 30 min of DRM at 750 °C. It is also concluded that during DRM, empty surface catalytic sites are available for CO<sub>2</sub> dissociation since the <sup>13</sup>CO formation is larger than that of <sup>12</sup>CO. However, the rate of CO<sub>2</sub> dissociation starts to drop and eventually ceases. This is due to “carbon” deposition via the reverse reaction of step (Eq. 5.4) and/or to the depletion of V<sub>o</sub> sites.

### 5.1.8. Discussion

#### (a) Does lattice oxygen participate in the catalytic cycle of DRM reaction?

One of the main issues discussed in the literature about ceria-based supported Ni catalysts, which show significantly reduced “carbon” accumulation compared to SiO<sub>2</sub> or Al<sub>2</sub>O<sub>3</sub> supported Ni catalysts, is that lattice oxygen of support participates in the removal of “carbon”, the latter being formed by CH<sub>4</sub> dissociation and the Boudouard reaction [17,18]. However, these studies did not provide clear evidence for this. In the present work, the investigation of the transient kinetics of CH<sub>4</sub>/He reaction over a pre-reduced catalyst surface (Fig. 5.4a) shows a large formation of CO, equivalent to 4.1 mmol O g<sup>-1</sup> or 32.8% of the available oxygen in the Ce<sub>0.75</sub>Zr<sub>0.25</sub>O<sub>2</sub> support. Even though in the case that one assumes that Ni was in its fully oxidized state (NiO), this would account for only 0.51 mmol O g<sup>-1</sup>. It is, therefore, illustrated that “carbon” derived from CH<sub>4</sub> decomposition (in the absence of CO<sub>2</sub>), as dictated by the large formation of H<sub>2</sub> (Fig. 5.4a), reacts by surface lattice oxygen of the Ce<sub>0.75</sub>Zr<sub>0.25</sub>O<sub>2-δ</sub> support to form CO(g), according to the Eq. 5.6:



Furthermore, based on the amount of lattice oxygen reacted off, it is shown that a significant amount of sub-surface lattice oxygen is able to participate in this reaction step by diffusing from the bulk of the solid support particles towards the surface. In this transient methane decomposition experiment, the lattice oxygen removed cannot be replaced since there is no oxygen source fed in the catalytic reactor. On the other hand, during dry reforming (Fig. 5.4b), a sustainable reaction rate is obtained. This result is due to the fact that oxygen from the CO<sub>2</sub> reactant molecule is able to provide in the catalytic cycle the necessary steps for re-filling

the pool of surface and bulk lattice oxygen that participates in the formation of CO, as discussed above.

According to the reaction step given in Eq. 5.5, there are two possible active sites for CO<sub>2</sub> dissociation. The first one is the *oxygen vacant site* (V<sub>o</sub>) of support, where lattice oxygen and CO(g) are formed. The second site is that of Ni, forming surface Ni-O species. “Carbon” formed on the Ni surface, following CH<sub>4</sub> decomposition, is able to react with support lattice oxygen as illustrated in Fig. 5.4a. However, the participation of oxygen species formed on the Ni surface, following CO<sub>2</sub> dissociation, cannot be excluded.

Strong evidence for the participation of *support lattice oxygen* in the removal of “carbon” towards CO formation during dry reforming arises from the transient isotopic experiments reported in Fig. 5.8a-c. The clear formation of 5.6 mmol C<sup>18</sup>O g<sup>-1</sup> under DRM reaction conditions and only ~ 0.35 mmol C<sup>18</sup>O g<sup>-1</sup> under 20% CH<sub>4</sub>/He reaction conditions leaves no doubts that “carbon” derived from CH<sub>4</sub> decomposition on the partially oxidized nickel surface and in the presence of CO<sub>2</sub> (dry reforming) reacts with <sup>18</sup>O-lattice oxygen of support to form C<sup>18</sup>O(g).

**(b) Does CO<sub>2</sub> participate in the gasification of “carbon” to produce CO?**

The transient isotopic experiment using <sup>13</sup>CO<sub>2</sub> following dry reforming presented in Fig. 5.10, and the SSITKA experiment presented in Fig. 5.9, reveal that the CO<sub>2</sub>-activation path passes through reaction steps (Eq. 5.4) and (Eq. 5.5), where “C-s” derived from CH<sub>4</sub> decomposition on the Ni surface can also react with CO<sub>2</sub> (carbon gasification) in parallel to its reaction with lattice oxygen of Ce<sub>0.75</sub>Zr<sub>0.25</sub>O<sub>2-δ</sub> support to form CO(g), as discussed in part (a).

The amount of *inactive* “carbon” accumulated on the catalyst surface after 30 min of dry reforming at 750 °C was found to be 1470 μmol “C” g<sup>-1</sup> (Fig. 5.6). On the other hand, only 70 μmol “C” g<sup>-1</sup> of this “carbon” (~ 4.8%) were able to react under 5% CO<sub>2</sub>/He flow to give CO (Fig. 5.8b). Based on these results, it might be suggested that the rate of “carbon” removal by the CO<sub>2</sub> gasification step (Eq. 5.4) is lower than that by lattice oxygen (Eq. 5.6) for the present catalytic system and reaction conditions.

The above offered discussion aims to stress the fact that there are at least two routes that control the concentration of deposited “carbon” on the catalyst surface under given DRM reaction conditions. In the present work, “carbon” growth on the catalyst surface was examined by SEM analysis and obtained micrographs are presented in Fig. 5.11. These SEM results

confirm the presence of carbon filaments as well as of Ni carbide (indirect evidence) as carrier of surface carbon towards extrusion processes, the latter well documented in the methane reforming literature [2].

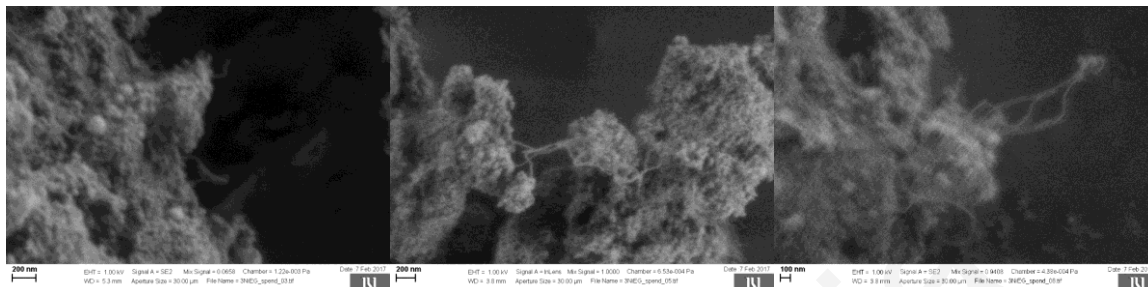


**Figure 5.11:** SEM images of spent 3 wt.% Ni/ $Ce_{0.75}Zr_{0.25}O_{2-\delta}$  catalyst focusing on carbon structures.

It is obvious that the rate of accumulation of *inactive* “carbon” reflects the positive net rate of its formation. As discussed in the following part (e) of this Discussion section, it may depend also on the rate of its reaction with gaseous hydrogen. In the present work, the removal of “carbon” is significantly enhanced by the presence of a large pool of labile lattice oxygen present in the  $Ce_{0.75}Zr_{0.25}O_{2-\delta}$  support, and to a lesser extent by the alternative route of  $CO_2$  gasification (reverse Boudouard reaction).

### (c) SSITKA studies

The SSITKA experiments presented in Fig. 5.9 and the relevant Section 5.1.6, illustrate that the  $CO_2$  reactant molecule passes through a very small ( $0.3 \mu\text{mol g}^{-1}$ ,  $\theta_C = 0.6\%$ ) concentration of *active* carbon that forms  $CO(g)$ . This  $CO_2$  activation route consists of two reaction steps (Eq. 5.4) and (Eq. 5.5). Considering the fact that measurable chemisorbed  $CO$ -s is not likely to be found at  $750^\circ\text{C}$ , the *active* carbon pool estimated from SSITKA should then only relate to the reversible Boudouard reaction (Eq. 5.4). It is mentioned here that *active* carbon is also formed via the activation route of  $CH_4$  decomposition, which was not investigated in the present work by similar SSITKA experiments (use of  $^{13}CH_4$ ). As reported by Bobin et al. [14], the concentration of such *active* carbon is also low.

The other important result derived from the SSITKA experiment (Fig. 5.9) is the formation of *reversibly* adsorbed  $CO_2$  on the catalyst surface, likely in the form of carbonate(s), the concentration of which was found to increase with increasing TOS (from 30 min to 2 h), as

opposed to the case of *active* carbon. The fact that the structure of an adsorbed carbonate species is associated with one lattice oxygen, where the latter appears to be an active species that reacts with “carbon”, the accumulation of strongly bound carbonates at 750 °C could partly explain the catalyst deactivation observed within the first 5 h of DRM (Fig. 5.3). However, this scenario should be excluded since it is difficult to reasonably explain the regeneration of these sites after 5 h of TOS during reaction. It should be noted, however, that a good correlation between the concentration of carbonate-type *inactive* species and the activity of 5 wt.% Ni/Ce<sub>1-x</sub>Pr<sub>x</sub>O<sub>2-δ</sub> catalysts (x = 0.0 – 0.8) was found and reported in Ch. 4 for short TOS. Furthermore, the small size of the *inactive* pool of adsorbed carbon dioxide ( $\theta_{\text{CO}_2} \sim 2\%$ ) tends to conclude that the build-up of *inactive* “carbon” derived from CH<sub>4</sub> activation and CO dissociation (Fig. 5.6, 760  $\mu\text{mol g}^{-1}$  or  $\theta = 14.5$ ) should remain as one of the likely causes of the observed deactivation of the 3 wt.% Ni/ Ce<sub>0.75</sub>Zr<sub>0.25</sub>O<sub>2-δ</sub> during the first 5 h of reaction (Fig. 5.3).

**(d) Which reactant (CO<sub>2</sub> or CH<sub>4</sub>) contributes to inactive “carbon” deposition?**

The temperature-programmed oxidation experiment (Fig. 5.6), following 30 min of DRM at 750 °C and after labeling the CO<sub>2</sub> reactant (<sup>13</sup>C-carbon dioxide), illustrates that the rates of *inactive* “carbon” deposition (main type of *inactive* “carbon”, T<sub>M</sub> ~ 620 °C) via the CH<sub>4</sub> and CO<sub>2</sub> activation routes are very similar. The fact that the traces of the transient rate of “<sup>12</sup>C-carbon” and “<sup>13</sup>C-carbon” oxidation to CO<sub>2</sub> are almost identical also implies a very similar “carbon” structure. As already reported in previous Chapter 4, over the 5 wt.% Ni/Ce<sub>1-x</sub>M<sub>x</sub>O<sub>2-δ</sub> (M = Pr<sup>3+</sup>, Zr<sup>4+</sup>) catalysts and after using the same experimental methodology to that reported in Fig. 5.6, the support chemical composition and reaction temperature can influence the %-contribution of CH<sub>4</sub> and CO<sub>2</sub> to the amount of deposited *inactive* “carbon” (graphitic and whiskers). It should be emphasized that the only reaction step that leads to “carbon” deposition via the CO<sub>2</sub> activation route (Eq. 5.3 and Eq. 5.5) is that of the dissociation of adsorbed CO-s (mainly on the Ni surface) [7,8]:



It appears, therefore, that formation of inactive “carbon” whiskers after DRM at 750 °C (SEM studies, Fig. 5.11) over the present catalyst proceeds with *similar rates* for the CH<sub>4</sub> and CO<sub>2</sub> carbon sources. Given the fact that important energy barrier differences occur in the DRM

pathways on Ni (111) [19], the results of Fig. 5.6 may suggest that the rate-limiting step for the *inactive* “carbon” formation is the transformation of *atomic carbon* to a *whisker-type* “carbon”.

**(e) Reactivity of “carbon” towards  $H_2$**

The TPH (Fig. 5.5a) and TIH (Fig. 5.5b) experiments performed after “carbon” deposition via the  $CH_4$  activation route only (in the absence of  $CO_2$ ) on the pre-reduced Ni/Ce<sub>0.75</sub>Zr<sub>0.25</sub>O<sub>2- $\delta$</sub>  catalytic surface are very informative. They clearly show that there is a threshold temperature between 645-670 °C at which the *inactive* “carbon” formed upon  $CH_4$  decomposition at 750 °C (Fig. 5.4a) leads to a high reaction rate towards methane formation (Fig. 5.5b). This result might imply that  $CO$  and  $CO_2$  hydrogenation reactions towards  $CH_4$  and  $H_2O$  products could take place at  $T > 670$  °C. Equilibrium analysis of these two reactions at 1 atm total pressure and using a feed composition of  $CO/H_2 = 1/3$  and  $CO_2/H_2 = 1/4$  without inert gas, resulted in a very small but not zero  $CH_4$  composition (mol%) in the reaction gas mixture at equilibrium. Furthermore, experimental results of the rate of methane formation during  $CO_2/H_2$  and  $CO/H_2$  reactions conducted over the 5 wt.% Ni/Ce<sub>0.8</sub>Pr<sub>0.2</sub>O<sub>2- $\delta$</sub>  catalyst at 750 °C were reported in Ch. 4. Indeed, the methane composition was very low in agreement with the thermodynamic considerations.

It is speculated whether the increase by ~ 35% in  $CH_4$  conversion between 5 and 20 h on TOS (Fig. 5.3) is partly due to the progressive increase in the rate of carbon removal by the  $H_2$  gas product due to the increase of its surface coverage,  $\theta_H$ , with TOS. The latter could arise from the increase in the concentration of empty Ni sites with TOS and the decrease in  $E_{act}$  of  $H_2$  dissociation and/or increase of  $E_{act}$  of  $CO$  and/or  $CH_4$  dissociation with the progressive removal of accumulated “carbon” on the Ni surface.

The following conclusions can be derived from the results of Section 5.1:

- (i) A 3 wt.% Ni supported on Ce<sub>0.75</sub>Zr<sub>0.25</sub>O<sub>2- $\delta$</sub>  carrier was investigated via meticulously designed SSITKA and other transient isotopic experiments. A good understanding of the main kinetic reasons for catalyst’s support ability to reduce the rate of “carbon” deposition in the dry reforming of methane is obtained, as opposed to SiO<sub>2</sub>- or Al<sub>2</sub>O<sub>3</sub>-supported Ni reported in the literature. In particular, a large pool of highly mobile lattice oxygen (exceeding one surface monolayer) was found to be largely responsible for this effect, while gasification of “carbon” by  $CO_2$  was found to contribute to a lesser extent.



- (ii) The increase in the concentration of inactive reversibly chemisorbed  $CO_2$  on the  $Ce_{0.75}Zr_{0.25}O_{2-\delta}$  support with increasing TOS (up to 2 h) was found to correlate with the activity drop in the same period. However, due to its low concentration, deposition of inactive “carbon” appears to be one of the main causes of catalyst deactivation. On the other hand, the concentration of active carbon formed via the  $CO_2$  activation route was found to remain practically constant.
- (iii) Participation of the  $H_2$  gas product in regulating the amount (wt.%) of deposited “inactive” carbon during dry reforming of methane at 750 °C appears possible over the 3 wt.% Ni/ $Ce_{0.75}Zr_{0.25}O_{2-\delta}$  catalytic system.
- (iv) The  $CH_4$  and  $CO_2$  activation routes in the dry reforming of methane (5%  $CH_4$ ,  $CH_4/CO_2 = 1$ ) at 750 °C over the present 3 wt.% Ni/  $Ce_{0.75}Zr_{0.25}O_{2-\delta}$  catalytic system appear to contribute equally (similar “carbon” deposition rates) to the amount (wt.%) of deposited “carbon”. Also, based on the shape and position of  $CO_2$ -TPO traces, the structural characteristics of the “carbon” derived from these two routes appear to be very similar (ca. whisker-type).

## 5.2. The effect of synthesis method of $Ce_{0.75}Zr_{0.25}O_{2-\delta}$ and that of Co in the carbon-path of DRM over NiCo/ $Ce_{0.75}Zr_{0.25}O_{2-\delta}$ catalysts

To extend the fundamental knowledge in the field of dry reforming of methane and enable an in-depth understanding of the role of support structure of a given  $Ce_{1-x}Zr_xO_2$  solid, two *structurally different*  $Ce_{0.75}Zr_{0.25}O_2$  supports were prepared by a different wet chemistry synthesis route and loaded with 3 wt.% Ni (monometallic) and 3wt.% NiCo (bimetallic) metals as described in Ch. 3, Sections 3.1.2 and 3.2.2. A variety of transient experiments coupled with the use of  $^{18}O_2$  and  $^{13}CO_2$  isotopes were designed and conducted, enabling detailed analysis of the carbon-path as well as of the support lattice oxygen participation in relevant DRM reaction conditions over supported NiCo bimetallic catalysts *for the first time*. The obtained information along with that related to the deposited carbon morphology and location, as well as of NiCo surface composition changes with time on stream (TOS) in the dry reforming (HRTEM and XPS studies), were used to explain the activity behaviour of the NiCo/ $CeZrO_2$  catalysts with TOS at the reaction conditions investigated.

### 5.2.1. Catalyst characterization studies

#### 5.2.1.1. Structural properties

X-ray diffraction analysis as depicted in Fig. 5.12 revealed that the unit cell size ( $\alpha$ , nm) of the 3NiCo EG coded solid (the  $Ce_{0.75}Zr_{0.25}O_2$  support was prepared by the ethylene glycol sol-gel method, EG) is dimensionally very similar to that of pure  $CeO_2$  (0.539 and 0.540 nm, respectively), suggesting for a  $Ce_{0.75}Zr_{0.25}O_{2-\delta}$  solid solution formation.

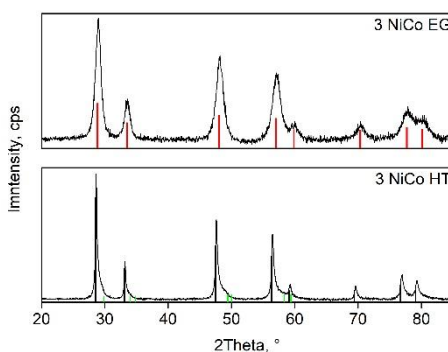


**Figure 5.12:** XRD profiles of 3NiCo EG and 3NiCo HT powder samples. Red bars show the peak positions of  $Ce_{0.75}Zr_{0.25}O_{2-\delta}$  (PDF 28-0271), black bars of  $CeO_2$  (PDF 034-0394) and green bars of  $ZrO_2$  (PDF 01-089-6976).

On the other hand, the X-ray diffraction pattern of the 3NiCo HT solid (Fig. 5.12) shows noticeable asymmetry in the diffraction peaks, which is a result of peak overlapping due to the presence of a separate tetragonal t-ZrO<sub>2</sub> phase. This suggests that the material is comprised of preferentially separated CeO<sub>2</sub> and t-ZrO<sub>2</sub> crystalline phases. On the contrary, as stated above, the support's unit cell size in the 3NiCo EG solid corresponds closely to that of Ce<sub>0.75</sub>Zr<sub>0.25</sub>O<sub>2- $\delta$</sub>  solid solution ( $\alpha = 0.5340$  and  $0.5349$  nm, respectively) and no contribution of a separate t-ZrO<sub>2</sub> phase is visible (Fig. 5.12). An average scattering domain size of 8 nm was estimated to be compared with 25 nm (CeO<sub>2</sub> phase) in the 3NiCo HT catalyst. This manifest itself also the obtained higher specific surface area of EG ( $51 \text{ m}^2 \text{ g}^{-1}$ ) compared to that of HT sample ( $41 \text{ m}^2 \text{ g}^{-1}$ ). Based on the powder XRD analyses results, it is concluded that despite the identical nominal chemical composition of support, *structurally the CeO<sub>2</sub>-ZrO<sub>2</sub> EG and HT supports are considerably different*. No diffraction peaks related to Ni- and Co-containing crystalline solid phases could be identified using powder XRD. This is a consequence of the low relatively low metal loading used ( $< 3 \text{ wt.}\%$ ). H<sub>2</sub> chemisorption followed by TPD analysis resulted in an average bimetallic NiCo cluster size of 8 and 11 nm for the 3NiCo EG and 3NiCo HT catalysts, respectively.

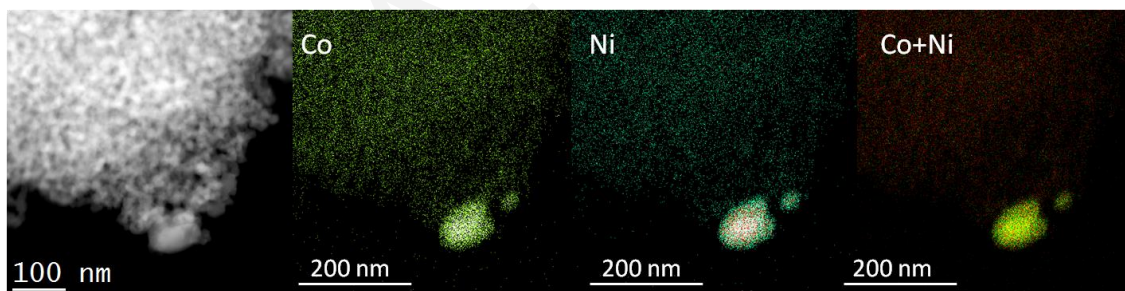


**Figure 5.13:** HAADF/STEM micrograph with corresponding EDXS elemental mapping of cobalt, nickel and their overlay on a fresh reduced 3NiCo EG catalyst prior to catalytic tests.

HAADF/STEM, SAED and HRTEM analyses (Figs. 5.13-5.15) confirm that Ni and Co are present in both 3NiCo EG and 3NiCo HT catalysts as *alloyed bimetallic particles* dispersed in non-uniform size over the corresponding EG and HT Ce-Zr-O supports. In particular, Fig. 5.13 shows the spatial location of nickel and cobalt in the activated 3NiCo EG catalyst prior to DRM catalytic tests. Nickel and cobalt are found in aggregates, which are constituted of both metals in a homogeneous manner (*alloy*). Based on these results, it can be concluded that nickel

and cobalt form *chemically homogeneous bimetallic particles (NiCo alloy)*, which are dispersed over the  $Ce_{0.75}Zr_{0.25}O_2$  solid solution support.

Additional information regarding the structure of the bimetallic alloy particles was obtained by performing selected area electron diffraction (SAED) analysis (Fig. 5.14).

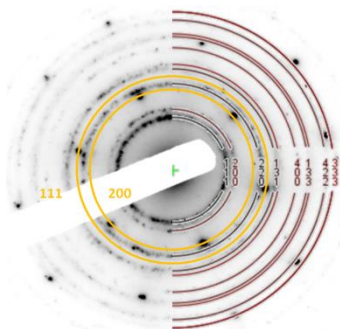


**Figure 5.14:** SAED pattern of a fresh reduced 3NiCo EG catalyst prior to catalytic tests.

Two crystalline phases could be identified: an fcc bimetallic alloy comprised of nickel and cobalt. Its most intensive diffraction rings from [200] and [111] crystalline planes are marked with yellow circles. In addition to diffraction signals originating from the NiCo bimetallic phase, additional diffraction rings from the support were observed. These could be perfectly simulated by an fcc Ce-Zr-O solid solution containing 25 wt.%  $ZrO_2$  (red half circles). No diffraction rings originating from t- $ZrO_2$  phase could be identified.

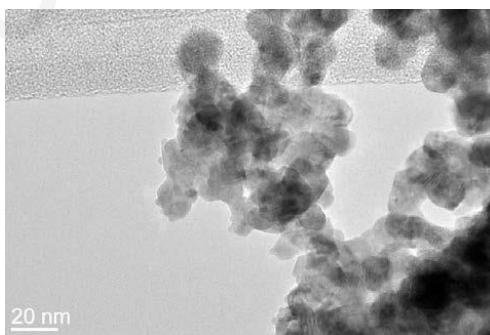


**Figure 5.15:** HR-TEM micrograph on a fresh and reduced 3NiCo EG catalyst prior to catalytic tests.

### 5.2.1.2. Redox properties

Quantification of the redox properties of the present solid supports can be expressed through the amount of mobile lattice oxygen removed from the  $Ce_{0.75}Zr_{0.25}O_{2-\delta}$  solid structure

during  $H_2$ -TPR and thus the equivalent degree of reduction ( $Ce^{4+} \rightarrow Ce^{3+}$ ). The latter was found to be 52% and 33% for the EG and HT samples, respectively. This result shows that the formation of  $Ce_{0.75}Zr_{0.25}O_{2-\delta}$  solid solution (EG sample) favors the removal of a higher amount of mobile oxygen compared to the case of HT sample, for which  $CeO_2$  and  $ZrO_2$  exist as separate phases (Fig. 5.12).

The dynamics of oxygen removal from the NiCo oxides and the lattice of EG and HT supports upon interaction with hydrogen at 750 °C was evaluated using transient isothermal reduction,  $H_2$ -TIR (Fig. 5.16) experiments. The transient reduction rate is very similar in the first 40 s for both the 3NiCo EG and 3NiCo HT catalysts and this is related to the elimination of oxygen from the surface of NiCo oxides,  $CeO_2$  and  $Ce_{0.75}Zr_{0.25}O_{2-\delta}$  solid phases.

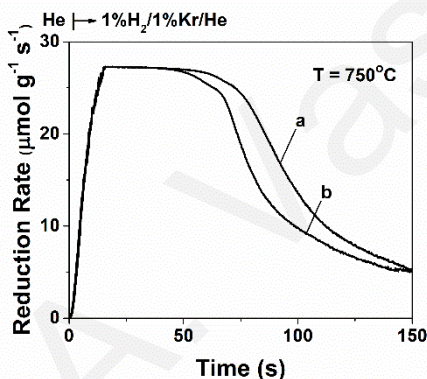


**Figure 5.16:** Transient rate of solid reduction by hydrogen ( $\mu\text{mol g}^{-1} \text{s}^{-1}$ ) as a function of time at 750 °C over 3NiCo EG (a) and 3NiCo HT (b) catalysts.  $W_{\text{cat}} = 25 \text{ mg}$ .

At longer times, the reduction is governed by oxygen diffusion through bulk oxygen sub-lattice and, consequently, its rate decreases considerably. This reduction rate is noticeably higher for the 3NiCo EG catalyst (Fig. 5.16a). It should be noted that bulk oxygen diffusion coefficients at 700 °C in doped- $CeO_2$  materials were found approximately 10-fold smaller compared to values obtained for surface/grain boundary oxygen diffusion [14]. Thus, the observed differences in the transient reduction rates for longer times of reduction are related to the presence of  $Ce_{0.75}Zr_{0.25}O_{2-\delta}$  solid solution, where oxygen diffusion is faster compared to pure  $CeO_2$  [20]. This has in the present case two origins: a) the atomic displacement of oxygen atoms, which is directly related to the oxygen diffusion rate, is higher in  $Ce_{0.75}Zr_{0.25}O_{2-\delta}$  compared to  $CeO_2$  [21], and b) the smaller  $CeO_2$ -based crystallite size in the EG compared to the HT solid support (8 vs. 25 nm), resulting in a shorter migration path for oxygen atoms towards the surface.

## 5.2.2. Transient evolution rates of $CH_4/He$ reaction and characterization of the deposited “carbon”

### 5.2.2.1. Transient evolution rates of $H_2$ , $CO$ and $CO_2$

Catalytic methane activation in the absence of  $CO_2$  at  $750\text{ }^\circ\text{C}$  was investigated over previously reduced (1 atm  $H_2$ ,  $750\text{ }^\circ\text{C}$ , 2 h) 3NiCo EG and 3NiCo HT catalysts, as well as their corresponding supports alone. Transient rate profiles of  $H_2$  and  $CO$  formation (Figs. 5.17A and 5.17B, respectively) are distinctly different in the case of bare  $CeZrO_2$  EG and  $CeZrO_2$  HT supports, compared to 3NiCo EG and 3NiCo HT catalysts. Over the bare supports, both  $H_2$  and  $CO$  formation rates are practically very small for the first 150 s of reaction. On the other hand, over 3NiCo EG and 3NiCo HT catalysts, the  $H_2$  and  $CO$  evolution rates are significantly larger and pass through a maximum, which decreases slowly to low steady-state values. The latter are very similar to the ones observed over the pure  $CeZrO_2$  supports;  $20\text{ }\mu\text{mol } H_2\text{ g}^{-1}\text{ s}^{-1}$  and  $10\text{ }\mu\text{mol } CO\text{ g}^{-1}\text{ s}^{-1}$  (Figs 5.17A and 5.17B at 5 min, respectively).

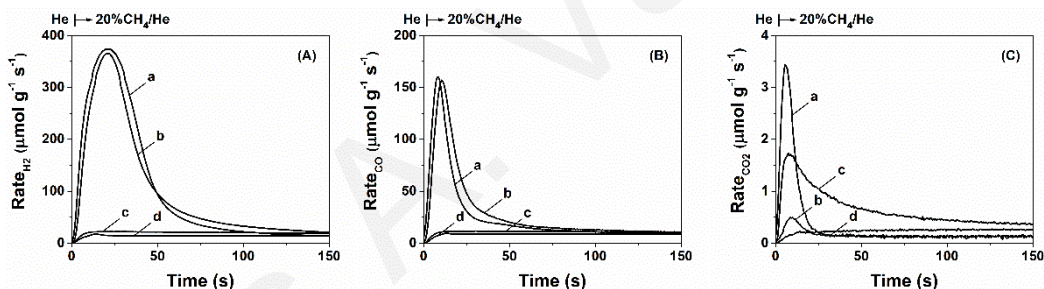


**Figure 5.17:** Transient rates ( $\mu\text{mol g}^{-1}\text{ s}^{-1}$ ) of (A)  $H_2$ , (B)  $CO$  and (C)  $CO_2$  formation as a function of time obtained during methane decomposition (20%  $CH_4/He$ ) at  $750\text{ }^\circ\text{C}$  over 3NiCo EG (a), 3NiCo HT (b),  $CeZrO_2$  EG (c) and  $CeZrO_2$  HT (d) solids.  $W_{\text{cat}} = 25\text{ mg}$ .

The appearance of maximum in the  $H_2$  and  $CO$  formation rate is due to the fact that methane alone is activated over the reduced or partially reduced bimetallic NiCo particles, which was recently confirmed during  $CH_4/CO_2$  reforming over Ni (111) [22]. With increasing reaction time in  $CH_4/He$ , the active oxygen pool of the catalyst, dominated by that present in the  $Ce_{0.75}Zr_{0.25}O_{2-\delta}$  support, is becoming progressively depleted. The adsorbed  $CH_x$  fragments derived from methane decomposition are more slowly removed as  $CO(g)$  since available mobile oxygen atoms need to diffuse from the bulk to the surface and, therefore, the  $H_2$  and  $CO$  rates decrease concomitantly.

**Table 5.1:** Amounts of H<sub>2</sub>, CO and CO<sub>2</sub> (mmol g<sup>-1</sup>) produced after 5 min of methane decomposition (20% CH<sub>4</sub>/He reaction) at 750 °C.

Catalyst	H <sub>2</sub> (mmol g <sup>-1</sup> )	CO (mmol g <sup>-1</sup> )	CO <sub>2</sub> (mmol g <sup>-1</sup> )
<b>3NiCo EG</b>	17.04	5.10	0.104
<b>3NiCo HT</b>	13.17	4.72	0.130
<b>CeZrO<sub>2</sub> EG</b>	2.98	1.60	0.097
<b>CeZrO<sub>2</sub> HT</b>	2.02	1.26	0.035

Products of methane decomposition reaction quantified over the first 5 min of reaction are shown in Table 5.1. The amount of H<sub>2</sub> formed is about six times higher when Ni and Co with a total loading of 3 wt.% were deposited over the Ce<sub>0.75</sub>Zr<sub>0.25</sub>O<sub>2-δ</sub> support, indicating that methane dehydrogenation takes place predominantly over (bi)metallic sites. The amounts (mmol g<sup>-1</sup>) of H<sub>2</sub> and CO produced were found to be higher over 3NiCo EG compared to 3NiCo HT catalyst, highlighting its higher activity for methane dissociation. This is in line with previous research results reported by Liu et al. [23] over Ni/CeO<sub>2</sub>, where oxygen vacant sites in CeO<sub>2</sub> were identified as CH<sub>4</sub> activation sites, in addition to those of Ni, which contribute in the DRM reaction. A higher degree of support reduction was confirmed during H<sub>2</sub>-TPR and H<sub>2</sub>-TIR for 3NiCo EG, suggesting a higher abundance of active sites for methane activation and CO formation via the participation of very mobile support lattice oxygen. The same trend was observed over pure supports; CeZrO<sub>2</sub> EG sample produced 47% and 27% higher quantities of H<sub>2</sub> and CO, respectively, compared to CeZrO<sub>2</sub> HT (Table 5.1). The H<sub>2</sub>/CO stoichiometric ratio produced by the 3NiCo EG and 3NiCo HT catalysts (assuming participation of the lattice oxygen in the reaction to generate CO) should be 2.0 in the absence of any side reactions. The values obtained are larger, namely 3.3 and 2.8, respectively, suggesting that a considerable amount of “carbon” species remains on the catalyst surface. Thus, not all CH<sub>x</sub>-s species derived from CH<sub>4</sub> dissociation get gasified to CO<sub>x</sub> by support lattice oxygen. The H<sub>2</sub>/CO ratio over pure HT and EG supports is close to the expected value of 2.0 (1.9 and 1.6, respectively), which suggests that “carbon” accumulation over 3NiCo EG and 3NiCo HT is mainly related to the presence of NiCo metal particles.

The CO<sub>2</sub> formation rates (Fig. 5.17C) show distinctly different behavior over the analyzed materials compared to the H<sub>2</sub> or CO formation rate. Carbon dioxide can originate either from the WGS reaction (CO + H<sub>2</sub>O ↔ CO<sub>2</sub> + H<sub>2</sub>) or deep oxidation of CH<sub>x</sub>-s intermediates with



support's lattice oxygen. The total amount of  $CO_2$  formed is 30-100 times lower compared to  $H_2$  and  $CO$ , indicating that the mentioned  $CO_2$  formation pathways over the studied materials under the employed  $CH_4$  decomposition reaction conditions influence to a negligible degree the distribution of main methane decomposition reaction products. The carbon mass balance considered on the basis of methane dehydrogenation products listed in Table 5.1 suggests accumulation of carbon on the catalysts either as *active*, which can react with  $H_2$  or  $CO_2$  and participate in the chemical conversion over the catalyst, or *inactive*, which blocks surface sites and causes catalyst deactivation, subject that is described below.

### 5.2.2.2. Characterization of deposited “carbon” via temperature-programmed (TPH) and transient isothermal (TIH) hydrogenation

Temperature-programmed hydrogenation (TPH) was performed after  $CH_4$  dehydrogenation at  $750\text{ }^\circ\text{C}$  for 30 min (Fig. 5.17), aiming at the characterization of deposited “carbon” over the 3NiCo EG and 3NiCo HT catalysts. The TPH analyses (Fig. 5.18) show intrinsically different reactivity and amount of “carbon” formed on both materials, namely:  $4.91$  and  $0.83\text{ mmol C g}^{-1}$  (equivalent to  $CH_4$  formation) for the 3NiCo EG and 3NiCo HT catalysts, respectively.

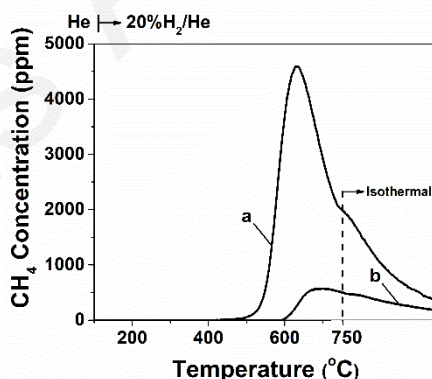


**Figure 5.18:** Temperature programmed hydrogenation (TPH) traces of “carbon” to  $CH_4$  obtained following 30-min treatment in 20%  $CH_4/He$  at  $750\text{ }^\circ\text{C}$  over the 3NiCo EG (a) and 3NiCo HT (b) catalysts.  $W_{cat} = 25\text{ mg}$ .

The carbon hydrogenation is initiated at  $\sim 500\text{ }^\circ\text{C}$  over the 3NiCo EG catalyst, which is  $\sim 100\text{ }^\circ\text{C}$  lower compared to 3NiCo HT catalyst.  $H_2$  dissociation, which is a prerequisite for hydrogenation and gasification of carbon deposits, occurs with the lowest activation energy



barrier over the Ni and Co metal sites. In addition,  $H_2$  can also be dissociated over oxygen vacancies and coordinatively unsaturated edge sites of  $CeZrO_2$  crystallites, which are related to the physicochemical properties of the catalysts, specifically their crystallite size [24]. On the other hand, pure  $t\text{-ZrO}_2$ , which is present as a *separate phase* in 3NiCo HT, is much less active for  $H_2$  dissociation. The considerably smaller  $Ce_{0.75}Zr_{0.25}O_{2-\delta}$  crystallite size (8 nm) compared to  $CeO_2$  (25 nm), the higher abundance of oxygen vacancies, and the 39% higher exposed active metal surface area for the 3NiCo EG solid, all act in favor for providing a larger concentration of active sites for hydrogen activation and enhanced methanation rate for the deposited “carbon”.

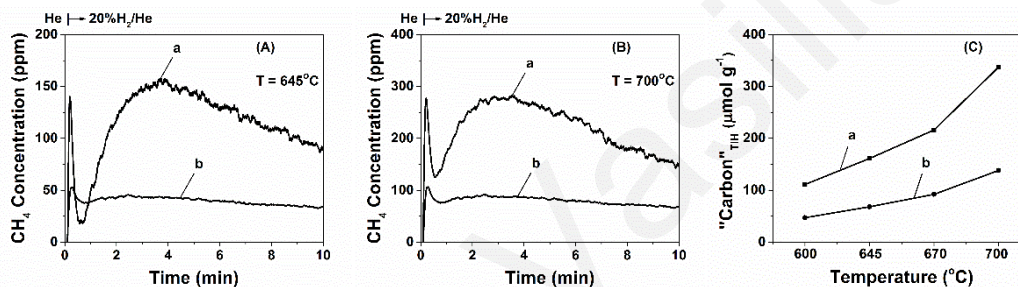


**Figure 5.19:** Transient response curves of  $CH_4$  concentration at 645 °C (A) and 700 °C (B) obtained during transient isothermal hydrogenation (TIH); (C) Total amount ( $\mu\text{mol g}^{-1}$ ) of “carbon” formed after 30-min treatment of the catalyst in 20%  $CH_4/He$  at 750 °C.  $W_{\text{cat}} = 25$  mg; a: 3NiCo EG, b: 3NiCo HT.

The transient isothermal hydrogenation (TIH) curves (Fig. 5.19) show clear distinctive contribution of two very different carbon species present in the 3NiCo EG catalyst. The first type of carbon is hydrogenated to methane as a sharp peak in  $t < 0.5$  min, while in the second type of carbon, methane formation rate reaches a maximum at about  $t = 4$  min, and decays slowly. In the case of 3NiCo HT catalyst, the profile of carbon hydrogenation to  $CH_4$  is significantly different.  $CH_4$  originating from highly reactive “carbon” species is visible as sharp peak but much smaller, and the  $CH_4$  trace at  $t > 1$  min becomes flat, indicating that carbon hydrogenation is performed with a practically constant rate at least for 10 min in hydrogen stream. With increasing temperature from 645 to 700 °C, “carbon” hydrogenation traces maintain their shapes (Figs. 5.19A, 5.19B) and the amount of “carbon” removed increases (Fig. 5.19C).

The amount of reacted “carbon” under TIH in the case of 3NiCo EG catalyst was found to be 110, 160, 215 and 337  $\mu\text{mol g}^{-1}$  at 600, 645, 670 and 700  $^{\circ}\text{C}$ , respectively. Significantly lower amounts of deposited “carbon” were found in the case of 3NiCo HT, namely: 47, 68, 92 and 140  $\mu\text{mol g}^{-1}$  at 600, 645, 670 and 700  $^{\circ}\text{C}$ , respectively. These quantities are in agreement with those of TPH (Fig. 5.18), where higher amounts of “carbon” were identified over the 3NiCo EG catalyst.

### 5.2.3. Transient evolution rates of $\text{CH}_4/\text{CO}_2/\text{He}$ (DRM) reaction and characterization of deposited “carbon”

Figs. 5.20A and 5.20B present the evolution of transient CO and  $\text{H}_2$  formation rates, respectively, after the step gas switch  $\text{He} \rightarrow 20\% \text{CH}_4/20\% \text{CO}_2/\text{He}$  (DRM) at 750  $^{\circ}\text{C}$  was made over the pre-reduced 3NiCo EG and 3NiCo HT catalysts.

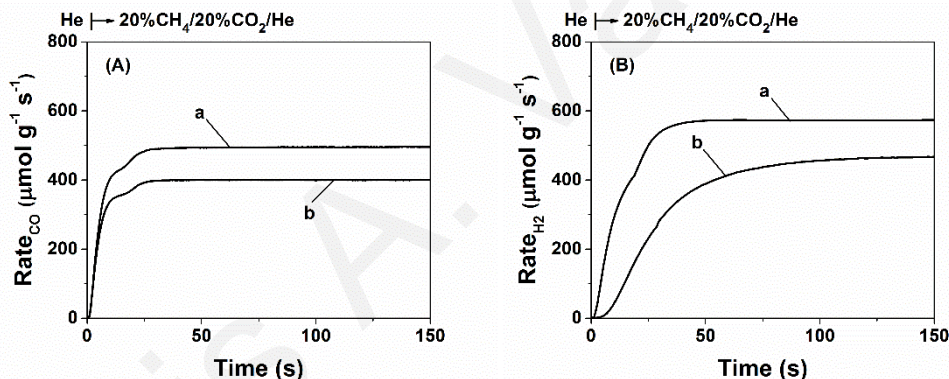


**Figure 5.20:** Transient rates ( $\mu\text{mol g}^{-1} \text{s}^{-1}$ ) of CO (A) and  $\text{H}_2$  (B) formation as a function of time obtained during dry reforming of methane at 750  $^{\circ}\text{C}$  over 3NiCo EG (a) and 3NiCo HT (b) catalysts.  $W_{\text{cat}} = 25 \text{ mg}$ .

This particular transient experiment reveals the *initial methane dry reforming behavior* of materials, where “carbon” deposition is limited, and which is much related to the structural differences exhibited by their supports. The rate of CO formation reaches a pseudo steady-state after  $\sim 30 \text{ s}$  at the value of 495 and 400  $\mu\text{mol g}^{-1} \text{s}^{-1}$  for the 3NiCo EG and 3NiCo HT catalysts, respectively. On the other hand, the  $\text{H}_2$  transient rate evolution is markedly different. It reaches a pseudo steady-state after  $\sim 50 \text{ s}$  at the value of 573  $\mu\text{mol H}_2 \text{g}^{-1} \text{s}^{-1}$  for 3NiCo EG, whereas in the case of 3NiCo HT catalyst, a clear delay ( $t \sim 5 \text{ s}$ ) with respect to the  $\text{H}_2$  trace observed for

3NiCo EG is apparent, and only after ~ 120 s it reaches the steady-state value of 464 μmol H<sub>2</sub> g<sup>-1</sup> s<sup>-1</sup>.

At this very short time of reaction (150 s), the 3NiCo EG exhibits higher methane reforming activity and the H<sub>2</sub>/CO ratio obtained is 1.15. The same order of activity (3NiCo EG > 3NiCo HT) was observed also during methane dehydrogenation (Fig. 5.17). The time delay in the appearance of H<sub>2</sub> response (Fig. 5.20B) with respect to that of CO (Fig. 5.20A) is the result of the different kinetic rates with respect to CH<sub>4</sub> dissociation, CO and H<sub>2</sub> formation routes on an initially reduced and clean metallic surface. In addition, the delay in the appearance of H<sub>2</sub> response compared to that of CO might be influenced by the fact that nickel and nickel containing rare-earth oxides are known for their hydrogen storage ability [24,25].

The more pronounced H<sub>2</sub> delay observed in 3NiCo HT might also be partly related to the fact that the separate tetragonal ZrO<sub>2</sub> phase, which is present only in this sample, can store H<sub>2</sub> in the form of thermally stable -OH and hydride species at adjacent O<sup>-</sup> and Zr<sup>3+</sup> surface sites [26].

#### 5.2.4. Quantifying the origin of inactive “carbon” (CH<sub>4</sub> vs CO<sub>2</sub> activation route)

The contribution of CO<sub>2</sub> and CH<sub>4</sub> towards carbon formation during DRM reaction over the 3NiCo HT and 3NiCo EG catalysts was investigated by using isotopically labeled <sup>13</sup>CO<sub>2</sub> and monitoring both <sup>12</sup>CO<sub>2</sub> and <sup>13</sup>CO<sub>2</sub> during a following TPO experiment (Fig. 5.21). It is observed that the <sup>13</sup>CO<sub>2</sub> and <sup>12</sup>CO<sub>2</sub> traces over the individual catalysts are practically identical, showing no distinction in the reactivity of “carbon” deposited during DRM, regardless of its origin (<sup>12</sup>CH<sub>4</sub> or <sup>13</sup>CO<sub>2</sub>). This suggests that upon the activation of each reactant over the catalyst surface, the “C-s” derived forms a carbon pool of a very similar size and reactivity towards gasification with molecular oxygen.

The characteristic features of the TPO traces, however, differ when Ce<sub>0.75</sub>Zr<sub>0.25</sub>O<sub>2-δ</sub> solid solution (3NiCo EG) or separate CeO<sub>2</sub> and ZrO<sub>2</sub> phases (3NiCo HT) are used to support NiCo bimetallic particles. Carbon oxidation is in both cases initiated at about 300 °C forming a small peak extended to T < 450 °C. At higher temperatures, two additional carbon oxidation peaks emerge: the first between 500-650 °C and the second between 650-760 °C. The total amount of carbon formed during DRM is found to be higher on 3NiCo HT compared to 3NiCo EG (Table 5.2), resulting in a substantial increase of the peak shown in the 500-650 °C range.

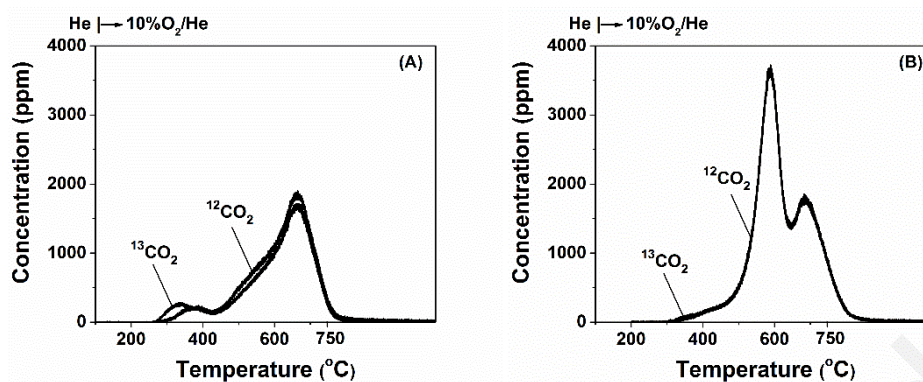


**Figure 5.21:** TPO of “carbon” formed during DRM with labeled  $^{13}\text{CO}_2$  at 750 °C for the 3NiCo EG (A) and 3NiCo HT (B) catalysts.  $W_{\text{cat}} = 50$  mg.

By considering that carbon nano-filament is the predominant carbon morphology during extensive catalyst coking, to be presented below, one can assume that the middle TPO peak, which is most pronounced over the 3NiCo HT catalyst sample, is related to this kind of carbon morphology.

**Table 5.2:**  $^{12}\text{CO}_2$  and  $^{13}\text{CO}_2$  ( $\mu\text{mol g}^{-1}$ ) and  $^{12}\text{CO}_2/^{13}\text{CO}_2$  ratio obtained during temperature-programmed oxidation (TPO) of carbon species formed during 30-min reforming in 5%  $^{13}\text{CO}_2/5\%$   $^{12}\text{CH}_4/\text{He}$  at 750 °C over the 3NiCo EG and 3NiCo HT catalysts.

Catalyst	$^{12}\text{CO}_2$ ( $\text{mmol g}^{-1}$ )	$^{13}\text{CO}_2$ ( $\text{mmol g}^{-1}$ )	$^{12}\text{CO}_2/^{13}\text{CO}_2$	Total “C” ( $\text{mmol g}^{-1}$ )
3NiCo EG	0.442	0.395	1.12	0.837 (1.01 wt.%)
3NiCo HT	0.703	0.695	1.01	1.398 (1.68 wt.%)

The larger extent of catalyst coking occurred on 3NiCo HT during DRM originates from the fact that the amount and rate of supply of mobile lattice oxygen present in the support, as analyzed by  $\text{H}_2$ -TPR and transient isothermal reduction (Fig. 5.16), are lower on the 3NiCo HT catalyst, and as such, less active oxygen species for carbon gasification are available during DRM, thus leading to a faster carbon buildup [1]. Considering the fact that part of NiCo bimetallic clusters is located on  $\text{ZrO}_2$ , the oxygen spillover from the adjacent  $\text{CeO}_2$  phase for prompt carbon gasification is substantially hindered. Also, metallic particles can be extracted from the support by the growth of carbon nano-filaments, resulting in the loss of contact with the support.

It is also interesting to emphasize at this point that “carbon” deposition during CH<sub>4</sub> decomposition alone was found to be larger on the EG-supported than HT-supported NiCo catalyst, which is the opposite for the case of DRM reaction (Table 5.2).

### 5.2.5. Probing the participation of support lattice oxygen in DRM

The ability of the 3NiCo EG and 3NiCo HT catalysts to provide active oxygen species originating from the support, which enable CO formation during methane decomposition, was confirmed in the previous Section 5.2.2.1 (Fig. 5.17). However, during DRM reaction, the oxygen originating from the CO<sub>2</sub> reactant or the support lattice oxygen should be differentiated. For this, the participation of support’s lattice oxygen was investigated after the support’s <sup>16</sup>O was partially replaced by <sup>18</sup>O before DRM. Figure 5.22 describes this <sup>16</sup>O/<sup>18</sup>O isotopic exchange recorded. The <sup>16</sup>O<sub>2</sub> formation, which is related to the recombination and desorption of surface <sup>16</sup>O atoms, proceeds with about an equal rate in both materials in the initial transient after the He → <sup>18</sup>O<sub>2</sub>/He switch (Fig. 5.22A).

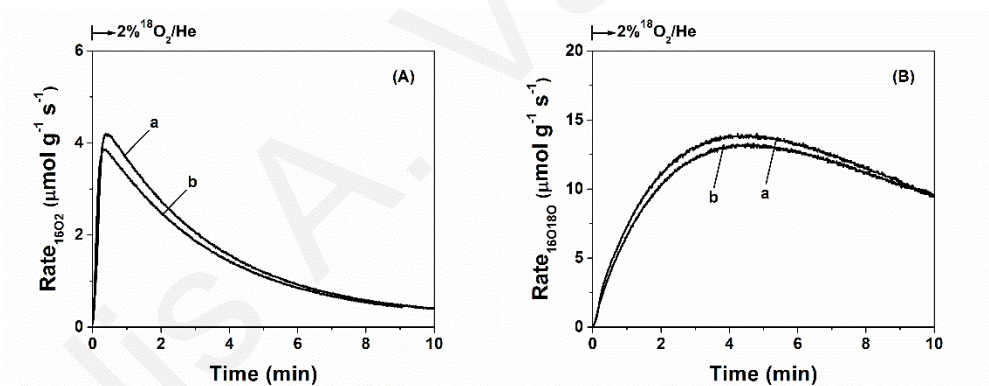


**Figure 5.22:** Transient rates ( $\mu\text{mol g}^{-1} \text{s}^{-1}$ ) of <sup>16</sup>O<sub>2</sub> (A) and <sup>16</sup>O<sup>18</sup>O (B) formation as a function of time, estimated from the transient isotopic exchange of lattice <sup>16</sup>O with <sup>18</sup>O experiment according to the gas switch He → 2% <sup>18</sup>O<sub>2</sub>/He performed at 750 °C over the 3NiCo EG (a) and 3NiCo HT (b) catalysts.  $W_{\text{cat}} = 25 \text{ mg}$ .

The surface oxygen desorption rate appears to be slightly influenced by the Zr incorporation into the CeO<sub>2</sub> lattice, as was observed also in the H<sub>2</sub>-TIR experiment (Fig. 5.16). At longer times, the observed <sup>16</sup>O<sub>2</sub> formation rate is governed by bulk <sup>16</sup>O diffusion, which appears to be slightly faster in the 3NiCo EG catalyst. Again, this correlates with the *redox and oxygen mobility differences* between the present Ce<sub>0.75</sub>Zr<sub>0.25</sub>O<sub>2-δ</sub> and CeO<sub>2</sub> solids.



Contrary to the maximum of <sup>16</sup>O<sub>2</sub> formation rate, which appears at ~ 0.5 min, the maximum of <sup>16</sup>O<sup>18</sup>O formation rate is observed at significantly larger times (between 4-4.5 min), indicating that bulk oxygen diffusion is slower within the crystal lattice of CeZrO<sub>2</sub> compared to surface/grain boundary diffusion [27]. We can see again that the <sup>16</sup>O<sup>18</sup>O formation rate is slightly faster in EG compared to 3NiCo HT solid.

The catalyst's oxygen pool which participates in the DRM reaction was monitored through the <sup>18</sup>O-labeled reaction products as shown in Fig. 5.23. Prior to the CH<sub>4</sub>/CO<sub>2</sub> gas switch, the catalyst was treated with <sup>18</sup>O<sub>2</sub> for 10 min at 750 °C allowing for partial lattice <sup>16</sup>O/<sup>18</sup>O exchange (see Fig. 5.22). During the following DRM reaction, practically the same amount (14.6 mmol <sup>18</sup>O/g) of total <sup>18</sup>O was found to be incorporated in the observed <sup>18</sup>O-labelled CO<sub>2</sub>'s and CO gaseous products for the two catalysts. It should be noted that the equivalent <sup>18</sup>O stored in Ni<sup>18</sup>O and Co<sub>3</sub><sup>18</sup>O<sub>4</sub> during catalyst treatment at 750 °C with <sup>18</sup>O<sub>2</sub> gas is only 1.6 mmol g<sup>-1</sup>.

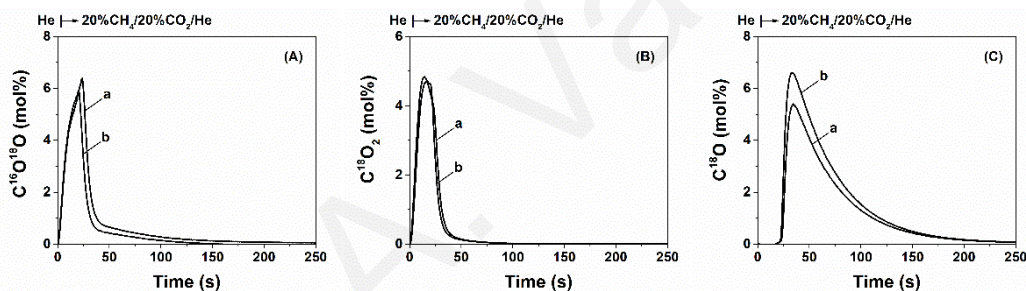


**Figure 5.23:** Transient concentration (mol%) response curves of C<sup>16</sup>O<sup>18</sup>O (A), C<sup>18</sup>O<sub>2</sub> (B) and C<sup>18</sup>O (C) obtained during dry reforming of methane at 750 °C following treatment with 2% <sup>18</sup>O<sub>2</sub>/He at 750 °C for 10 min over the 3NiCo EG (a) and 3NiCo HT (b) catalysts. W<sub>cat</sub> = 25 mg.

Transient formation of C<sup>18</sup>O<sub>2</sub> goes through a maximum at 20 s and decays to zero, 75 s after the switch to the DRM feed stream (Fig. 5.23B). The total amount of C<sup>18</sup>O<sub>2</sub> formed is found to be slightly higher in 3NiCo EG compared to 3NiCo HT catalyst (2.70 vs. 2.38 mmol g<sup>-1</sup>), and this is related to the reaction of surface and sub-surface lattice <sup>18</sup>O with the reactive “carbon” pool. Formation of C<sup>16</sup>O<sup>18</sup>O is related to the reaction between lattice <sup>18</sup>O, <sup>16</sup>O that originates from the CO<sub>2</sub>, and reactive “carbon” formed over the catalyst during DRM reaction. Possible exchange of surface lattice <sup>18</sup>O with C<sup>16</sup>O<sub>2</sub> is presented below.

The C<sup>16</sup>O<sup>18</sup>O formation rate goes through a maximum at 25 s and tails strongly until decaying to zero at about 150 s. This is consistent with longer times required for the diffusion

of bulk <sup>18</sup>O to the surface of the catalyst, where <sup>18</sup>O can take part in catalytic reaction steps with surface adsorbed species.

Contrary to the C<sup>16</sup>O<sup>18</sup>O and C<sup>18</sup>O<sub>2</sub> traces, which light-off quickly after the He → 20% CH<sub>4</sub>/20% CO<sub>2</sub>/He gas switch, the C<sup>18</sup>O signal (CO is a direct product of the DRM reaction) lights-off with a delay of ~ 25 s. This may suggest that the initially oxidized 3NiCo EG and 3NiCo HT solids are unable to catalyze the DRM reaction but favor only full methane oxidation [20]. The slow decay of the C<sup>18</sup>O transient response lasts about 250 s, which by far outlives the formation of any <sup>18</sup>O labeled CO<sub>2</sub>. This indicates a gradual transition from the initial total oxidation to the predominant DRM reaction path with increasing time on stream, where lattice <sup>18</sup>O diffuses to the surface and takes part in the DRM reaction.

The amounts of <sup>18</sup>O-labeled CO and CO<sub>2</sub> produced by 3NiCo EG and 3NiCo HT catalysts are listed in Table 5.3. The EG catalyst produces a substantially higher quantity of <sup>18</sup>O-containing CO<sub>2</sub>, whereas HT is more selective towards <sup>18</sup>O-containing CO. As mentioned before, during the course of DRM reaction (Fig. 5.23), the catalyst becomes progressively more reduced. If the oxygen diffusion is slow (3NiCo HT), a larger dynamic oxygen concentration gradient between the surface (predominantly reduced) and bulk (predominantly oxidized) is established, favoring DRM reaction and CO production. On the other hand, if bulk oxygen diffusion is fast (3NiCo EG), the gradient is smaller, favoring total oxidation.

As previously mentioned, the formation of <sup>18</sup>O-labelled CO<sub>2</sub>'s during the DRM gas switch (Fig. 5.23A, B) on a partially pre-covered catalyst surface by <sup>18</sup>O might also be considered as the result of exchange of C<sup>16</sup>O<sub>2</sub> (DRM feed stream) with surface lattice <sup>18</sup>O, according to reaction steps (Eqs. 5.1-5.2) but also to the reversibility of the Boudouard reaction given in step (Eq. 5.3).

Fig. 5.24A and B presents the transient evolution of <sup>18</sup>O-labelled CO<sub>2</sub>'s and that of C<sup>18</sup>O during the step-gas switch He → 20% CO<sub>2</sub>/He (t) at 750 °C over the 3NiCo EG and 3NiCo HT, respectively, conducted at exactly the same experimental conditions as the experiment described in Fig. 5.23. Formation of C<sup>16</sup>O<sup>18</sup>O and C<sup>18</sup>O<sub>2</sub> takes place according to the reaction steps (Eqs. 5.1-5.2). The most important result from this experiment is the fact that the C<sup>18</sup>O transient response obtained is *different in shape and quantity* from the corresponding one shown in Fig. 5.23C. The amount of C<sup>18</sup>O formed is only 0.20 and 0.10 mmol g<sup>-1</sup> for the EG-supported and HT-supported NiCo, respectively. These results exclude the possibility that the main source of

$C^{18}O$  formed during DRM (Fig. 5.23C) is the dissociation of  $^{18}O$ -labelled  $CO_2$ 's on the metal surface or via the participation of support's oxygen vacant sites.

**Table 5.3:** Amounts ( $mmol\ g^{-1}$ ) of  $C^{16}O^{18}O$ ,  $C^{18}O_2$  and  $C^{18}O$  formed during the various gas switches applied over the 3NiCo EG and 3NiCo HT catalysts after 10-min  $^{18}O_2/He$  treatment at 750 °C.

Catalyst	$C^{16}O^{18}O$ ( $mmol\ g^{-1}$ )	$C^{18}O_2$ ( $mmol\ g^{-1}$ )	$C^{18}O$ ( $mmol\ g^{-1}$ )	Total $^{18}O$ ( $mmol\ g^{-1}$ )
<b>3NiCo EG</b>	3.04 <sup>a</sup>	2.70	6.19	14.63
	2.04 <sup>b</sup>	2.38	0.20	7.0
	0.79 <sup>c</sup>	0.25	4.60	5.89
<b>3NiCo HT</b>	2.28	2.38	7.55	14.59
	2.64	1.68	0.1	6.1
	0.59	0.21	4.08	5.09

<sup>a</sup> After 20%  $CH_4/20\% CO_2/He$  treatment; <sup>b</sup> After 20%  $CO_2/He$  treatment; <sup>c</sup> After x%  $CO/He$  treatment; x = 0.65% for 3NiCo HT and 0.85% for the 3NiCo EG catalyst.

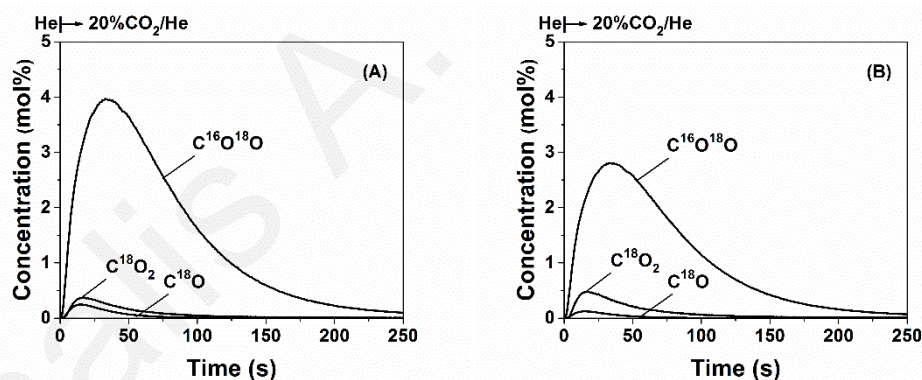


**Figure 5.24:** Transient concentration (mol%) response curves of  $C^{18}O$ ,  $C^{16}O^{18}O$  and  $C^{18}O_2$  obtained at 750 °C after the gas switch  $He \rightarrow 20\% CO_2/He$  is made over the 3NiCo EG (A) and 3NiCo HT (B) catalysts, following catalyst pre-treatment with 2%  $^{18}O_2/He$  (10 min) at 750 °C. Gas delivery sequence:  $He$  (750 °C)  $\rightarrow$  2%  $^{18}O_2/He$  (10 min)  $\rightarrow$   $He$  (5 min)  $\rightarrow$  20%  $CO_2/He$  (t);  $W_{cat} = 25\ mg$ .

The step gas switch  $He \rightarrow x\% CO/He$  (t) made at 750 °C over the partially pre-covered with  $^{18}O$ -s catalyst surface resulted also in  $C^{18}O$  transient responses different in shape and quantity (Fig. 5.25A, B), namely, 4.60 and 4.08  $mmol\ g^{-1}$  for the EG-supported and HT-



supported NiCo catalyst, respectively. Based on the shape, position and amount (Table 5.3) of  $C^{18}O$  transient responses recorded under the  $CH_4/CO_2$  (Fig. 5.23C),  $CO_2/He$  (Fig. 5.24) and  $CO/He$  (Fig. 5.25) gas switches, it is concluded that *large quantities* of highly mobile oxygen of support react more with “C-s” derived from  $CH_4$  decomposition, the latter occurring on the NiCo surface, than “C-s” derived from the Boudouard reaction, towards gasification to  $CO(g)$ .

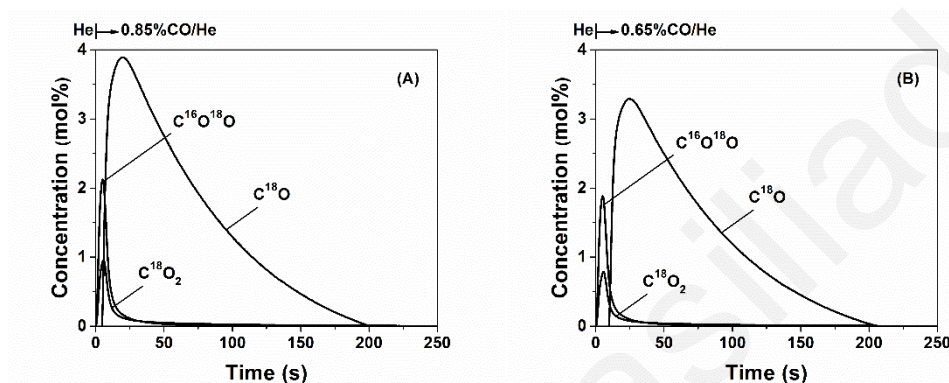


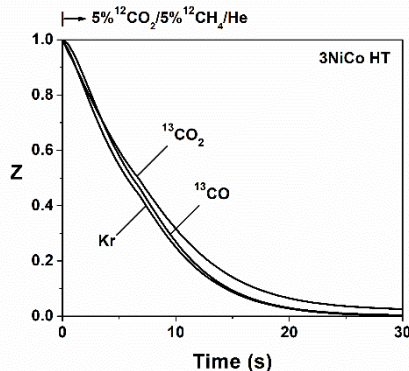
**Figure 5.25:** Transient concentration (mol%) response curves of  $C^{18}O$ ,  $C^{16}O^{18}O$  and  $C^{18}O_2$  obtained at  $750^\circ C$  after the gas switch  $x\%$   $CO/He$  made over 3NiCo EG (A) and 3NiCo HT (B) catalysts, following pre-treatment with  $2\%$   $^{18}O_2/He$  (10 min) at  $750^\circ C$ . Gas delivery sequence: He ( $750^\circ C$ )  $\rightarrow$   $2\%$   $^{18}O_2/He$  (10 min)  $\rightarrow$  He (5 min)  $\rightarrow$   $x\%$   $CO/He$  (t);  $W_{cat} = 25$  mg;  $x = 0.65$  and  $0.85$ , respectively, for 3NiCo EG and 3NiCo HT catalysts.

### 5.2.6. Quantifying the *active* carbon present in the $CO_2$ activation route - SSITKA

Quantification of the *active* carbon formed in the  $CO_2$  activation path was obtained by employing the SSITKA technique. The SSITKA switch (Fig. 5.26) made after 30 min of DRM shows that the  $^{13}CO$  gas phase response follows closely that of Kr tracer gas, suggesting that the concentration of *active* carbon-containing intermediates leading to  $CO$  gas product is very small. This is found to be  $\sim 0.01 \mu mol g^{-1}$  after 30 min of dry reforming over both catalysts. This amount was found to increase after 2 h of reaction, namely,  $0.08$  and  $0.03 \mu mol g^{-1}$  for the 3NiCo EG and 3NiCo HT, respectively.

On the contrary, the  $^{13}CO_2$  gas phase response lags behind that of  $^{13}CO$ , and this has been reported in the previous Chapter 4 and in Ref. [7,8] to be the result of the presence of a pool of reversibly chemisorbed carbon dioxide which does not participate in the carbon-path of  $CO_2$  activation route (spectator species). The amount ( $N_{CO_2}$ ) of such *inactive* carbonate-type species was found to accumulate with reaction time. In particular, after 30 min in DRM reaction

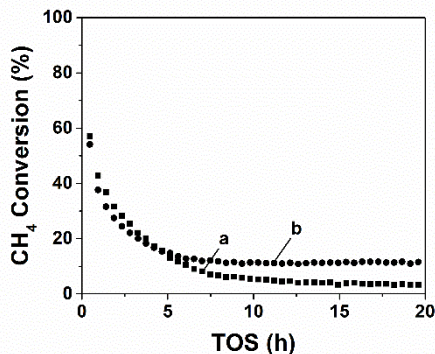
the latter was found to be 0.12 and 2.5 μmol g<sup>-1</sup>, respectively, for the 3NiCo EG and 3NiCo HT catalysts, and 1.3 and 6.0 μmol g<sup>-1</sup>, respectively, after 2 h of dry reforming.



**Figure 5.26:** SSITKA dimensionless concentration response curves ( $Z$ ) of Kr,  $^{13}\text{CO}$  and  $^{13}\text{CO}_2$  obtained after 30 min of dry reforming of methane at 750 °C performed over the 3NiCo HT catalyst.  $W_{\text{cat}} = 50 \text{ mg}$ ;  $F_{\text{T}} = 100 \text{ NmL min}^{-1}$ . SSITKA switches: 5%  $^{12}\text{CO}_2/5\% \text{ }^{12}\text{CH}_4/\text{He}$  (30 min)  $\rightarrow$  5%  $^{13}\text{CO}_2/5\% \text{ }^{12}\text{CH}_4/\text{He}$  (3 min)  $\rightarrow$  5%  $^{12}\text{CO}_2/5\% \text{ }^{12}\text{CH}_4/\text{He}$  (t).

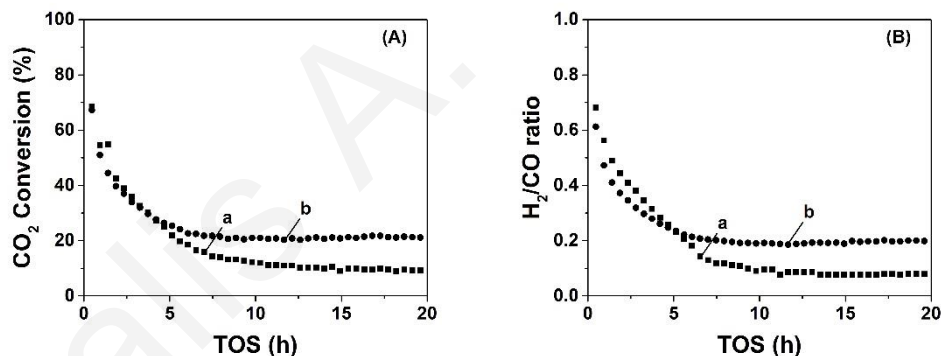
### 5.2.7. Relationship between *active* and *inactive* carbon formation and long-term catalyst stability in DRM

Figure 5.27 presents the DRM activity behavior of the two catalytic systems at 750 °C, in terms of CH<sub>4</sub>-conversion (%), for long time-on-stream (TOS), ca. 20 h. The feed gas composition used was 44.2% CO<sub>2</sub>, 44.3% CH<sub>4</sub> and 11.5% N<sub>2</sub>, and the flow rate was 56.5 NmL min<sup>-1</sup>. During the first 60 min (1 h) of reaction, the activity of 3NiCo EG appears higher than that of 3NiCo HT, in agreement with the initial rates reported in Fig. 5.20. However, during the first ~ 5 h on TOS, EG-supported NiCo catalyst *deactivates faster* than the HT-supported one. While HT-supported catalyst presents stable activity after ~ 5 h on TOS, the EG-supported one still shows further deactivation but less than that obtained during the first 5 h of reaction (Fig. 5.27).



**Figure 5.27:**  $CH_4$ -conversion (%) as a function of time on stream (TOS) for the DRM at 750 °C over the 3 NiCo EG (a) and 3NiCo HT (b) catalysts. Feed gas composition: 44.2%  $CH_4$ , 44.2%  $CO_2$ , 11.5%  $N_2$ ;  $W_{cat} = 50$  mg;  $F_T = 56.5$   $NmL\ min^{-1}$ .

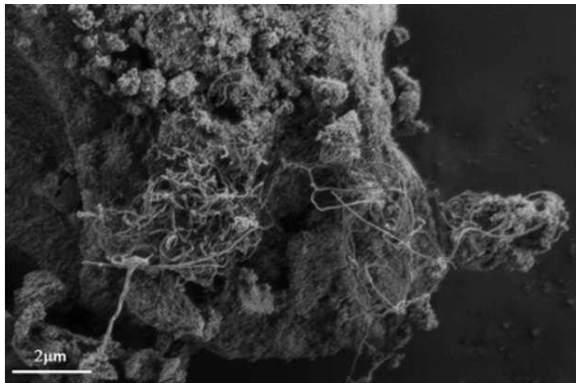
A similar behavior was observed for the  $CO_2$ -conversion (%) and  $H_2/CO$  gas product ratio (Fig. 5.28A, B). It should be noted here that the trend of activity behavior with TOS is very similar to that shown in Fig. 5.27 after using the 20%  $CH_4/20\%$   $CO_2/He$  feed gas stream (Fig. 5.20).



**Figure 5.28:** (A)  $CO_2$  conversion and (B)  $H_2/CO$  gas product ratio as a function of time on stream (TOS) obtained during DRM at 750 °C over the 3 NiCo EG (a) and 3NiCo HT (b) catalysts. Feed gas composition: 44.2%  $CH_4$ , 44.2%  $CO_2$ , balance  $N_2$ ;  $W_{cat} = 50$  mg;  $F_T = 56.5$   $NmL\ min^{-1}$ .

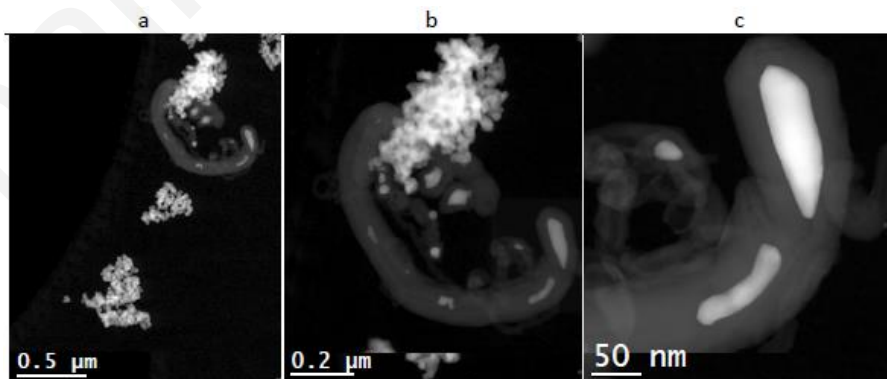
“Carbon” deposits (0.51 wt.% as quantified using CHNS analysis) formed over the 3NiCo EG catalyst after 20 h in DRM reaction were characterized using SEM and HAADF/STEM techniques. Carbon in the form of nano-filaments was observed using SEM (Fig. 5.29), which is the only identifiable carbon morphology. Additional information on possible “carbon” attachment to the catalyst was obtained by HAADF/STEM. It can be seen in

Fig. 5.30 that in the case of carbon nano-filament formation, the bimetallic (NiCo) cluster is extracted from the  $Ce_{0.75}Zr_{0.25}O_2$  support and is *embedded with carbon* (layer about 30 nm thick) at the tip of the carbon filament.



**Figure 5.29:** SEM image of spent (20 h in DRM) 3NiCo EG catalyst, where the growth of carbon nano-filaments is clearly shown.

Also, several smaller NiCo bimetallic clusters were observed as *embedded with carbon* in the vicinity of the  $Ce_{0.75}Zr_{0.25}O_2$  support as nicely illustrated in Fig. 5.31. Based on these SEM and HAADF/STEM analyses, it can be concluded that NiCo bimetallic clusters covered with a carbon layer *are no longer in contact* with the  $Ce_{0.75}Zr_{0.25}O_2$  support. Also, it is important to state at this point that the support was not covered with carbon patches (2D structures) or small amorphous/crystalline 3D structures.



**Figure 5.30:** HAADF/STEM micrographs of 3NiCo EG catalyst after 20 h of DRM reaction (44.2%  $CO_2$ /44.3%  $CH_4$ /11.5%  $N_2$ ) at 750 °C; a progressive magnification is provided.

The results presented in this Section 5.2 are important since they allow one to understand the intrinsic reason(s) of the catalyst stability behavior shown in Fig. 5.27. According to the results of this Section 5.2, the concentration of *active* carbon formed on the 3NiCo EG catalyst increases and that of *inactive* carbonate-type species decreases, result opposite to that found for the 3NiCo HT catalyst (Fig. 5.26). It should be noted that the latter species could be linked to the poisoning of *active* labile oxygen of support that facilitates “carbon” gasification. Furthermore, the reactivity of “carbon” deposits from methane decomposition towards hydrogen is larger for the EG-supported than HT-supported NiCo catalyst (Figs. 5.17 and 5.18), and less “carbon” is deposited after DRM at 750 °C on the EG-supported than HT-supported catalyst (Table 5.2). The transient  $^{16}O/^{18}O$  isotopic exchange studies also indicate that lattice oxygen mobility of EG is larger than that of HT support (Fig. 5.22). It should also be pointed out that very low amounts of “carbon” were measured after 20 h of TOS for the DRM reaction conditions reported in Fig. 5.27 (0.51 and 0.37 wt.% C for 3NiCo EG and 3NiCo HT samples, respectively).

Based on the above offered discussion, the faster deactivation observed in the 3NiCo EG compared to that in the 3NiCo HT DRM catalyst (Fig. 5.27) cannot be explained neither by the higher rates of “carbon” deposition and lower rates of “carbon” gasification by lattice oxygen exhibited by 3NiCo HT, nor by the diminishing concentration of the *active* carbon-containing intermediates that form CO(g). In order to investigate other possible reasons that could explain reasonably well the deactivation behavior of the two 3NiCo HT and 3NiCo HT catalysts (Fig. 5.27), the X-ray photoelectron spectroscopy (XPS) technique was applied and the obtained results are described and discussed in what follows. XPS analysis was conducted over the fresh (reduced) 3NiCo EG catalyst sample and that after being treated for 5, 10 and 20 h in DRM reaction conditions, same as those for the results shown in Fig. 5.27.

One possible cause of the drop in DRM activity is the oxidation of Ni and Co particles, where it was reported [28] that these metals in the oxidized form are less active than in the reduced zero valent state (e.g. Ni<sup>0</sup>). For the present supported NiCo particles, oxidation of them during DRM reaction conditions could arise from strongly bound O-s species of support in contact with the metal particles [29]. The presence of *surface nickel* in the fresh reduced 3NiCo EG catalyst (1.06 and 1.51 wt.% of total Ni and Co, respectively, were present according to ICP-OES analyses) could not be confirmed by XPS due to its low concentration (1.06 wt.% Ni). On the other hand, the presence of a low amount of surface cobalt (0.57 atom%) was detected.

After 5 h and 10 h on TOS, the concentration of surface Co decreased to 0.19 and 0.20 atom%, respectively, whereas after 20 h of TOS, surface Co was found to be below detection limit (Fig. 5.32). Based on these results, due to the very low concentration of surface Co and Ni, it was not possible to accurately determine the oxidation states of Co and Ni with TOS in the DRM reaction. However, changes in the oxidation state and surface composition related to the  $Ce_{0.75}Zr_{0.25}O_2$  support are presented and discussed in what follows.

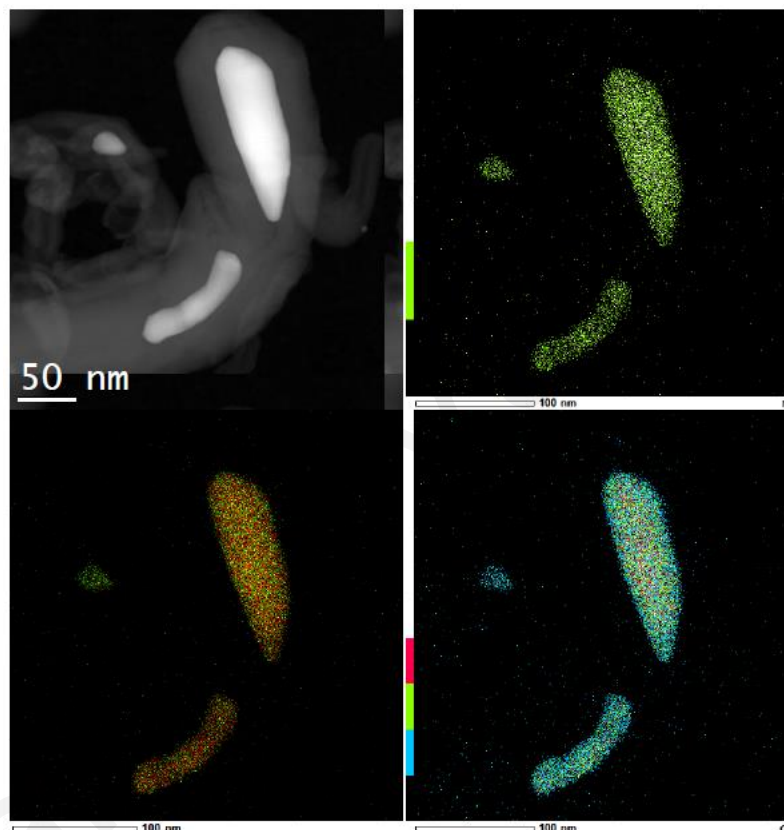


**Figure 5.31:** HAADF/STEM micrographs of 3NiCo EG catalyst after DRM reaction at 750 °C for 20 h. The image is focused on the NiCo bimetallic particle (top left) with corresponding EDXS elemental mapping: top right nickel; bottom right cobalt (Co); and bottom left nickel (Ni) and cobalt (Co) overlaid.

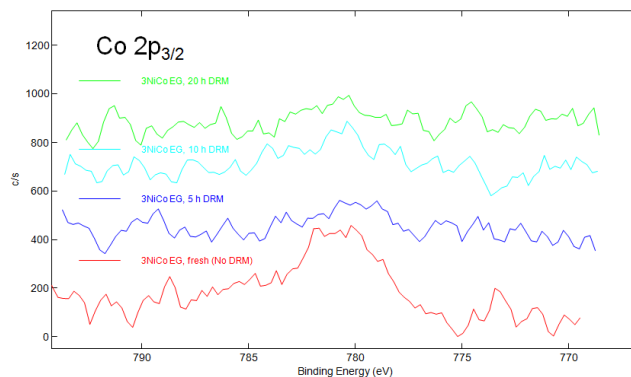


**Figure 5.32:** High-energy resolution of Co2p spectra for the 3NiCo EG catalyst recorded at different TOS (Fresh, 5, 10 and 20 h).

All samples are notably *surface enriched with Zr*. The surface Ce/Zr atom ratio changes in the following order: 1.1, 0.88, 1.08 and 0.98 for the fresh reduced, 5, 10 and 20 h in TOS spent catalyst samples, respectively. The *bulk Ce/Zr nominal value* is 2.87. The binding energy of Zr 3d<sub>5/2</sub> photoelectron peak in the fresh reduced sample is 181.8 eV (the 3d<sub>5/2</sub>-3d<sub>3/2</sub> spin-orbit splitting of 2.5 eV) as shown in Fig. 5.33.

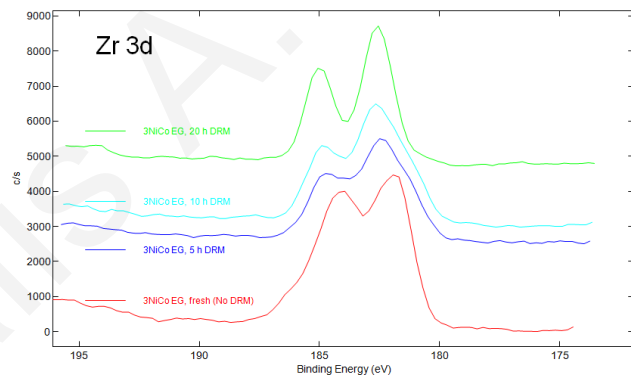


**Figure 5.33:** High-energy resolution Zr3d spectra for the 3NiCo EG catalyst recorded at different TOS (Fresh, 5, 10 and 20 h).

The Zr peak position corresponds to that of  $CeZrO_2$  solid solution [30] and is lower compared to the characteristic value for  $Zr^{4+}$  in  $ZrO_2$  (182.3 eV) [31]. With increasing TOS, the Zr 3d<sub>5/2</sub> photoelectron peak shows a progressive shift toward a higher binding energy, reaching the value of 182.6 eV after 20 h in TOS. This value corresponds to  $Zr^{4+}$  in  $ZrO_2$  [31] and indicates the formation of surface  $ZrO_2$  phase during DRM.



The O 1s photoelectron peak BE (529.7 eV) of the fresh reduced catalyst is associated with the presence of lattice oxygen anions in the  $Ce_{0.75}Zr_{0.25}O_2$  solid solution (Fig. 5.34). With increasing TOS, a progressive shift of O 1s peak to higher BEs (530.3 eV after 20 h TOS) is observed, and this corresponds to individual oxides of  $CeO_2$  and  $ZrO_2$ . This is in line with the evolution of Zr 3d spectra. A shoulder on the high BE (532 eV) is also observed for the fresh sample, which might be attributed to surface hydroxyls and/or water molecules [30]. The same shoulder appears also in the spent sample (DRM for 20 h), where an increase of carbon C 1s signal (not shown here) was also observed.

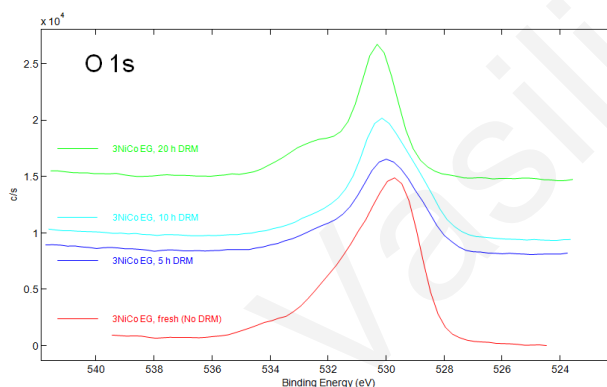


**Figure 5.34:** High-energy resolution O 1s spectra for the 3NiCo EG catalyst recorded at different TOS in DRM (Fresh, 5, 10 and 20 h).

Another difference observed by the XPS analyses is the change in the Ce 3d spectra shown in Fig. 5.35. It consists of spectral peaks related to Ce (4+) ( $v$  and  $v''$  peaks at 884 eV and 889 eV, respectively) and Ce (3+) ( $v'$  and  $v_0$  peaks at 885 eV and 881 eV, respectively) oxidation states [32]. It can be observed (Fig. 5.35) that the fresh sample has the highest Ce (3+) concentration. The 5 h and 10 h spent samples in DRM resulted in similar concentrations of Ce (3+), whereas the 20 h spent sample has the lowest Ce (3+) surface concentration. This indicates a *gradual oxidation* of the  $Ce_{0.75}Zr_{0.25}O_2$  solid support as a function of TOS in the dry reforming of methane reaction. Progressive decrease of surface cobalt concentration seen by XPS (electron Inelastic Mean Free Path (IMFP) in  $CeO_2$  is 2.1 nm at 1.3 keV kinetic energy [33]) may suggest its *diffusion into the bulk of  $Ce_{0.75}Zr_{0.25}O_2$*  (forming a solid solution) [26] during DRM reaction (reductive atmosphere). This in turn progressively results in a *decrease in the surface abundance of likely active Co*, and likely Ni metal clusters (active sites for methane activation), manifesting itself a progressive deactivation of the catalyst, as observed in Fig. 5.27.



On the basis of the above described XPS experimental results, there is evidence for the decrease of the surface Ce/Zr ratio by  $\sim 10\%$  (compared to the fresh reduced sample) and at the same time an enrichment of the support surface with  $ZrO_2$ -like structure with increasing TOS in DRM, as opposed to that of fresh reduced  $Ce_{0.75}Zr_{0.25}O_{2-\delta}$  solid solution. On the other hand, surface Co seen by XPS *decreased by about a factor of three* after 10 h on TOS and *hardly seen by XPS after 20 h* on TOS. The latter is in good agreement with the HRTEM results (Figs. 5.30 and 5.31) previously presented and discussed, where NiCo bimetallic clusters were found imbedded in a carbon layer of about 30 nm thick.

It could, therefore, be concluded that a *progressive encapsulation of NiCo bimetallic clusters by carbon layer* appears as the main reason for the significant deactivation of 3NiCo EG catalyst after 20 h on TOS in DRM (Fig. 5.27). Unfortunately, due to the low surface Ni and Co present in the examined 3NiCo EG catalyst, oxidation of remaining NiCo clusters as another likely reason to explaining the reduced catalytic activity cannot be discussed.

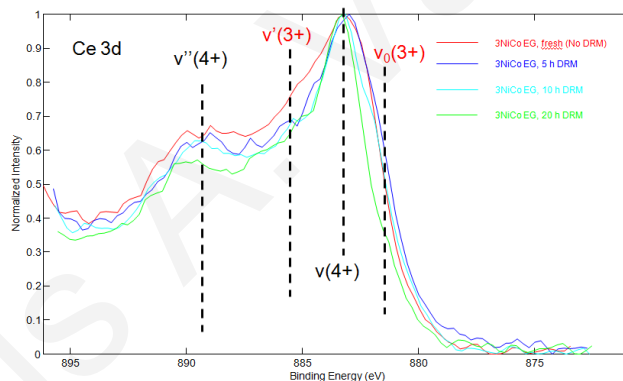


**Figure 5.35:** Normalized high-energy resolution Ce 3d spectra for the 3NiCo EG catalyst recorded at different TOS in DRM (Fresh, 5, 10 and 20 h).

A very recent work [29] that utilized *in-operando* XAS combined with kinetic and DFT studies, reported on the importance of the oxidation state of Co and Ni in the NiCo bimetallic or alloy supported on  $ZrO_2$  under working DRM reaction conditions (750 °C) on catalyst performance. The important conclusion derived from that work is that Co sites promote the formation of strongly bound O-s species (via  $CO_2$  and CO dissociation), thus hindering C-H bond activation of  $CH_4$ . As TOS increases, oxidation gradually occurs to the bulk of the metal particles, as a consequence of the unbalanced kinetics of  $CH_4$  and  $CO_2$  activation. On the Ni surface sites, the oxyphilicity of nickel is insufficient for O-s accumulation, thus a reduced state

is apparent. However, low coverage of O-s on Ni leads to a slower removal of “carbon” species derived from  $CH_4$  and CO dissociation. In the case of NiCo alloy (solid solution), the oxyphilicity becomes moderate, and O-s formation competes with  $CH_4$  activation. More importantly, these O-s species do not cause bulk oxidation of the NiCo alloy [33].

The following conclusions can be derived from the results of the present Section 5.2:

- (i) The initial and long-term DRM catalytic activity of a 3 wt.% NiCo (1.51 wt.% Co and 1.06 wt.% Ni) supported on a ceria-zirconia ( $Ce/Zr = 2.87$ ,  $Ce_{0.75}Zr_{0.25}O_2$ ) mixed metal oxide was found to strongly depend on support’s synthesis method (hydrothermal (HT) vs ethylene glycol sol-gel (EG)). The latter *tunes the structural and redox properties* of the ceria-zirconia mixed metal oxide.
- (ii) The rate of carbon deposition and the kinds of “carbon” formed in  $CH_4$  decomposition and their reactivity towards oxygen and hydrogen depend on the structure of the ceria-zirconia support. The  $Ce_{0.75}Zr_{0.25}O_{2-\delta}$  support (solid solution, EG) promotes the rate of  $CH_4$  decomposition and at the same time that of “carbon” removal via the participation of mobile lattice oxygen, to a greater extent than the  $CeO_2$ - $ZrO_2$  (two phase system, HT) support.
- (iii) The %-contribution of  $CH_4$  and  $CO_2$  activation routes in “carbon” deposition during DRM over the supported NiCo alloy particles is not influenced by the structure of the ceria-zirconia support. The opposite is true for the amount (wt.%), types and reactivity of the deposited “carbon”.
- (iv) The concentration behavior of *active* and *inactive* carbon and that of *inactive* carbonate-type species formed with time-on-stream (TOS) in the DRM reaction over the EG- and HT-supported NiCo alloy particles, cannot explain their deactivation behavior observed. Reduction in surface Co concentration with TOS in DRM (XPS studies) seems to better explain the observed deactivation behavior. Also, encapsulation of NiCo alloys by layers of carbon (HAADF/STEM studies) is another important factor that explains well the deactivation behavior of 3 NiCo EG catalyst.
- (v) Very small quantities ( $0.01 \mu\text{mol g}^{-1}$ ) of *active* “carbon” are formed in both the EG- and HT-supported NiCo, whereas significantly larger quantities of *inactive* “carbon” ( $0.84$ – $1.4 \text{ mmol g}^{-1}$ ) are formed after 30 min of DRM (5%  $CH_4$ /5%  $CO_2$ /He) at  $750^\circ\text{C}$ .

## References

- [1] P. Djinović, A. Pintar, Appl. Catal. B Environ. 206 (2017) 675–682.

- [2] C. Papadopoulou, H. Matralis, X. Verykios, in: L. Guzzi, A. Erd helyi (Eds.), *Catal. Altern. Energy Gener.*, Springer New York, New York, NY, 2012, pp. 57–127.
- [3] E. Ruckenstein, H.Y. Wang, *J. Catal.* 205 (2002) 289–293.
- [4] J. Guo, H. Lou, H. Zhao, D. Chai, X. Zheng, *Appl. Catal. A Gen.* 273 (2004) 75–82.
- [5] Z. Hou, O. Yokota, T. Tanaka, T. Yashima, *Appl. Catal. A Gen.* 253 (2003) 381–387.
- [6] J. Juan-Juan, M.C. Rom n-Mart nez, M.J. Ill n-G mez, *Appl. Catal. A Gen.* 301 (2006) 9–15.
- [7] M.A. Vasiliades, M.M. Makri, P. Djinovi , B. Erjavec, A. Pintar, A.M. Efstathiou, *Appl. Catal. B Environ.* 197 (2016) 168–183.
- [8] M.M. Makri, M.A. Vasiliades, K.C. Petalidou, A.M. Efstathiou, *Catal. Today* 259 (2016) 150–164.
- [9] A. Wolfbeisser, O. Sophiphun, J. Bernardi, J. Wittayakun, K. F ttinger, G. Rupprechter, *Catal. Today* 277 (2016) 234–245.
- [10] T. Sukonket, A. Khan, B. Saha, H. Ibrahim, S. Tantayanon, P. Kumar, R. Idem, *Energy and Fuels* 25 (2011) 864–877.
- [11] S. Damyanova, B. Pawelec, K. Arishtirova, M.V.M. Huerta, J.L.G. Fierro, *Appl. Catal. B Environ.* 89 (2009) 149–159.
- [12] M.S. Aw, M. Zorko, P. Djinovi , A. Pintar, *Appl. Catal. B Environ.* 164 (2015) 100–112.
- [13] C. de Leitenburg, A. Trovarelli, J. Kašpar, *J. Catal.* 166 (1997) 98–107.
- [14] A.S. Bobin, V.A. Sadykov, V.A. Rogov, N. V. Mezentseva, G.M. Alikina, E.M. Sadovskaya, T.S. Glazneva, N.N. Sazonova, M.Y. Smirnova, S.A. Veniaminov, C. Mirodatos, V. Galvita, G.B. Marin, *Top. Catal.* 56 (2013) 958–968.
- [15] T. Osaki, *Catal. Letters* 145 (2015) 1931–1940.
- [16] P. Fornasiero, E. Fonda, R. Di Monte, G. Vlaic, J. Kašpar, M. Graziani, *J. Catal.* 187 (1999) 177–185.
- [17] M. Usman, W.M.A. Wan Daud, H.F. Abbas, *Renew. Sustain. Energy Rev.* 45 (2015) 710–744.
- [18] D. Pakhare, J. Spivey, *Chem. Soc. Rev.* 43 (2014) 7813–7837.
- [19] S.-G. Wang, D.-B. Cao, Y.-W. Li, J. Wang, H. Jiao, *J. Phys. Chem. B* 110 (2006) 9976–9983.
- [20] P. Fornasiero, J. Kašpar, M. Graziani, *Appl. Catal. B Environ.* 22 (1999) 11–14.

- [21] M. Yashima, in: A. Trovarelli, P. Fornasiero (Eds.), *Catal. by Ceria Relat. Mater.*, 2nd ed., Imperial College Press, 2013, pp. 1–45.
- [22] K. Yuan, J.-Q. Zhong, X. Zhou, L. Xu, S.L. Bergman, K. Wu, G.Q. Xu, S.L. Bernasek, H.X. Li, W. Chen, *ACS Catal.* 6 (2016) 4330–4339.
- [23] Z. Liu, D.C. Grinter, P.G. Lustemberg, T.-D. Nguyen-Phan, Y. Zhou, S. Luo, I. Waluyo, E.J. Crumlin, D.J. Stacchiola, J. Zhou, J. Carrasco, H.F. Busnengo, M.V. Ganduglia-Pirovano, S.D. Senanayake, J.A. Rodriguez, *Angew. Chemie Int. Ed.* 55 (2016) 7455–7459.
- [24] S.M. Schimming, G.S. Foo, O.D. Lamont, A.K. Rogers, M.M. Yung, A.D. D’Amico, C. Sievers, *J. Catal.* 329 (2015) 335–347.
- [25] L. Jalowiecki-Duhamel, J. Carpentier, A. Ponchel, *Int. J. Hydrogen Energy* 32 (2007) 2439–2444.
- [26] A. Trunschke, D.L. Hoang, H. Lieske, *J. Chem. Soc. Faraday Trans.* 91 (1995) 4441.
- [27] I. V. Piir, M.S. Koroleva, Y.I. Ryabkov, D.A. Korolev, N. V. Chezhina, V.G. Semenov, V. V. Panchuk, *J. Solid State Chem.* 204 (2013) 245–250.
- [28] L. Zhou, L. Li, N. Wei, J. Li, J.-M. Basset, *ChemCatChem* 7 (2015) 2508–2516.
- [29] B. AlSabban, L. Falivene, S.M. Kozlov, A. Aguilar-Tapia, S. Ould-Chikh, J.L. Hazemann, L. Cavallo, J.M. Basset, K. Takanabe, *Appl. Catal. B Environ.* 213 (2017) 177–189.
- [30] A. Galtayries, R. Sporcken, J. Riga, G. Blanchard, R. Caudano, *J. Electron Spectros. Relat. Phenomena* 88–91 (1998) 951–956.
- [31] D. Briggs, *Handbook of X-Ray Photoelectron Spectroscopy C.*, Physical Electronics, Inc., Eden Prairie, 1981.
- [32] E. Bêche, P. Charvin, D. Perarnau, S. Abanades, G. Flamant, *Surf. Interface Anal.* 40 (2008) 264–267.
- [33] S. Kato, M. Ammann, T. Huthwelker, C. Paun, M. Lampimäki, M.-T. Lee, M. Rothensteiner, J.A. van Bokhoven, *Phys. Chem. Chem. Phys.* 17 (2015) 5078–5083.

## Chapter 6: Elucidation of Kinetic and Mechanistic Aspects of Fischer-Tropsch Synthesis over Industrial Co-based Catalysts

### 6.1 Introduction

The Fischer-Tropsch (FT) synthesis is an important industrial catalytic reaction that produces synthetic clean fuels from coal, natural gas and biomass. More specific, FT synthesis converts a mixture of carbon monoxide and hydrogen (syngas) into liquid hydrocarbons (synthetic fuels) and water [1–10]. Supported cobalt based catalysts have been extensively used in low temperature FT and they revealed high activity, stability and selectivity to higher hydrocarbons (i.e.  $C_5^+$ ) [11–17]. The mechanism underlying FT reaction has been investigated for several years, however, due to its complexity, there are several fundamental aspects that seek deep understanding. For example, the effect of the preparation method of supported Co on important intrinsic kinetic parameters (e.g.  $\theta$  and  $k$ ) and their relation to catalyst's deactivation have not yet been adequately explored, which is the subject of this work.

Steady-State Isotopic Transient Kinetic Analysis (SSITKA), as outlined in Chapter 2, is the transient technique that allows the *in-situ* evaluation of the surface coverage ( $\theta$ ), surface residence time ( $\tau$ ), (which is related to the intrinsic reactivity,  $k$ ) of active reaction intermediates and the most accurate experimental estimation of the turnover frequency (TOF) of reaction based on the measured concentration of active intermediates present in the reaction path of question. Furthermore, when SSITKA is combined with a spectroscopic technique (e.g. FTIR or DRIFTS), the *chemical composition and the structure* of the *active* reaction intermediates but also of the *inactive* (spectator) species can be determined [18–20]. *Operando* SSITKA methodology is, therefore, a very powerful experimental technique for a rigorous investigation of important mechanistic and kinetic parameters of a given heterogeneous catalytic system, and its value in the study of the FT synthesis has been already demonstrated in several publications [21–31].

In principle, industrial FT reaction conditions require high total pressures (25-35 bar), which provide a positive impact on heavy hydrocarbons selectivity and catalyst activity performance [31–34]. High-pressure SSITKA studies are very limited due to the proportional consumption of isotope gas (higher cost) compared to its application at 1 atm, where mainly methanation reaction predominates ( $CH_4$ -selectivities  $> 60\%$ ) but also to the more complicated instrumentation and analysis needed. More precisely, in order to correctly record and analyze

the  $C_2^+$ -hydrocarbons transient response curves upon the SSITKA switch, a Gas Chromatograph coupled with Mass Spectrometer (GC-MS analytical system), multiport sampling valves and back pressure regulator (to control the high total pressure in the reactor) are needed [21,22]. On the other hand, re-adsorption of  $C_2^+$ -hydrocarbons or oxygenates on the support become important at high pressures, fact that introduces more difficulties in the correct analysis and estimation of the concentration (pool) of the respective adsorbed *active*  $C_xH_y$ -s reaction intermediate. Furthermore, it is important also to mention at this point that according to the work of den Breejen et al. [35], in the case of methanation reaction path, *similar conclusions* were obtained using SSITKA at 1 atm or higher pressures with respect to the  $-CH_x$  *active* intermediate that serves as an important precursor intermediate that participates in the formation of the higher in carbon atom adsorbed  $-C_xH_y$ -s intermediates.

FT mechanisms and kinetics over various catalytic systems were examined using the SSITKA technique with regards to the effects of the following parameters:

- (i) cobalt particle size [21,36–38]
- (ii) catalyst pretreatment conditions [39]
- (iii) chemical promotion of activity/selectivity [25,40]
- (iv) support modification [21,24,41,42], and
- (v) catalyst deactivation and rejuvenation [29,30,43].

The SSITKA technique coupled with transient isothermal and temperature-programmed hydrogenation techniques has been extensively used for the first time by Efstathiou et al. [26–28] in order to elucidate the evolution of *active* intermediates and *inactive* species formed during methanation reaction on Rh/Al<sub>2</sub>O<sub>3</sub> and Rh/MgO catalysts and correlate the information obtained with the deactivation of catalyst. The latter important issue for FT catalysts was studied by Carvalho et al. [30], where carbon deposition and agglomeration of cobalt nanoparticles were suggested for the decrease in the concentration of *active* adsorbed  $-CH_x$  and CO species. Moreover, catalyst rejuvenation in hydrogen was found to partly restore  $CH_x$  sites, while reversibly adsorbed CO remain unaffected [13].

Extensive research has been made to correlate FT catalytic performance with the *active* metal surface area and the metal crystallite size. A better dispersion of metal (smaller crystallite size, nm) over the support [44], which lead to better FT performance, can be achieved by

controlling several conditions during catalyst synthesis, such as metal impregnation, calcination [35,45] and catalyst activation [44]. The effect of metal particle size on the surface mean residence time ( $\tau$ ) of  $-\text{CH}_x$  and  $-\text{OH}_x$  intermediates was reported to decrease significantly with increasing Co particles size from 2.6 to 6 nm, whereas that of  $\tau_{\text{CO}}$  to increase [21–23,38]. For Co particles size in the 6 - 16 nm range, the mean residence time of these reaction intermediates was found not to depend on particles size. The TOF ( $\text{s}^{-1}$ ) and the surface coverage ( $\theta$ ) of  $-\text{CH}_x$ ,  $-\text{OH}_x$  and CO-s were reported to decrease for Co particle size below 6 nm but to be practically constant for larger Co particles size (ca. 6-16 nm). The latter results were interpreted as due to the significant surface coverage of irreversibly bonded CO on small ( $< 6$  nm) Co particles, which cause blocking of edge and corner sites responsible for higher intrinsic activity compared to that of terraces favored on small particles.

In this Chapter, the *effect of the preparation steps* of two SASOL's FT industrial cobalt-based catalysts [46] on the evolution of the surface coverage ( $\theta$ ) of active  $\text{CH}_x$ -s ( $\text{C}_\alpha$ ) intermediates, the surface coverage of CO-s reversibly chemisorbed, the residence times  $\tau_{\text{CH}_x}$  and  $\tau_{\text{CO}}$  ( $\text{s}^{-1}$ ) associated with the  $\text{CH}_x$ -s and CO-s, respectively, and the  $\text{TOF}_{\text{CH}_4, \text{ITK}}$  ( $\text{s}^{-1}$ ) (estimated based on the concentration of *active* carbon-containing intermediates leading to  $\text{CH}_4$ ) for the methanation reaction ( $\text{H}_2/\text{CO} = 2$ ; 5% CO) at 230 °C are investigated and reported *for the first time*. Transient isothermal and temperature-programmed hydrogenation experiments were also performed to estimate: (i) the concentration of a *less active*  $\text{CH}_x$  species ( $\text{C}_\beta$ ) formed during FT synthesis ( $\text{CO}/\text{H}_2$ ) at 230 °C, which does not lead to  $\text{CH}_4$  under FT but is readily hydrogenated isothermally (at 230 °C) to methane at the switch  $\text{CO}/\text{H}_2 \rightarrow \text{He} \rightarrow 50\% \text{H}_2/\text{He}$  (t), and (ii) the concentration of various kinds of refractory carbon-containing *inactive* species towards hydrogenation to methane at  $T > 230$  °C (use of TPH). Furthermore, the reactivity of different types of adsorbed CO-s intermediates populated under FT reaction conditions was studied using *in situ* DRIFTS and kinetic rate analysis techniques. Complementary characterization techniques, such as powder XRD, TPO,  $\text{H}_2$ -TPR and HAADF/STEM were conducted for estimating the mean Co particle size and its redox characteristics for the two investigated catalysts.

## 6.2 Catalysts characterization

Figure 6.1 shows powder XRD patterns of the 20 wt.% Co (with some platinum) supported on the uncoated (CY-A) and carbon-coated (CY-C) Sasol's Germany Puralox SCCa

$\gamma$ -alumina carrier (see Ch. 3, Section 3.3.2 and ref. [46]) in the 35.5-38.5°  $2\theta$  range. The diffraction peak at  $2\theta = 36.9^\circ$  confirms that cobalt exists in  $\text{Co}_3\text{O}_4$  crystalline phase [47], with no other observable oxidation states of cobalt. Except for  $\text{Co}_3\text{O}_4$  phase,  $\gamma\text{-Al}_2\text{O}_3$  was detected (not present). Based on the Scherrer equation [48] and the most intense peak of  $\text{Co}_3\text{O}_4$  ( $2\theta = 36.88^\circ$ ), the particle size of  $\text{Co}_3\text{O}_4$  was estimated. It is seen that the CY-A catalyst has more intense and narrow diffraction peak for  $\text{Co}_3\text{O}_4$  compared to that of CY-C, indicating larger Co particles. Specifically, the particle size of  $\text{Co}_3\text{O}_4$  was found to be 13.4 and 10.2 nm for CY-A and CY-C catalysts, respectively (Table 6.1).

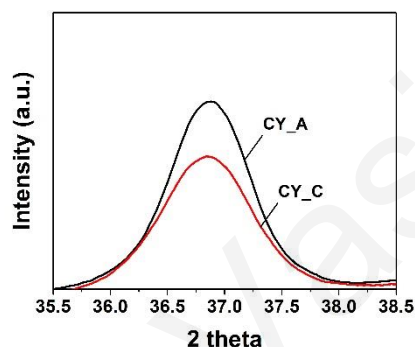


**Figure 6.1:** Powder X-ray diffractograms of CY-A and CY-C solid catalysts.

According to Eq. (3.4) and the estimated particle size of  $\text{Co}_3\text{O}_4$  (based on the powder XRD data, Fig. 6.1), the particle size of metallic cobalt ( $\text{Co}^0$ ) was found to be 10.1 and 7.6 nm for CY-A and CY-C, respectively (Table 6.1). The Co dispersion ( $D$ , %) was calculated based on Eq. 3.5 [49], and was found 9.5 and 12.6% for the CY-A and CY-C, respectively (Table 6.1). The BET specific surface area ( $\text{SSA}$ ,  $\text{m}^2 \text{g}^{-1}$ ) together with the specific pore volume ( $V_p$ ,  $\text{cm}^3 \text{g}^{-1}$ ) and the average pore size ( $d_p$ , nm) are also given in Table 6.1. It is shown that the pore volume is significantly affected by changing the carbon level on the coated alumina support.

The Co metal surface area ( $\text{m}^2 \text{g}^{-1}$ ) and the cobalt crystallite size (nm) originated from hydrogen chemisorption measurements are reported in Table 6.1 and differ by 20-25% from the values estimated via the powder XRD measurements. The results of the latter measurements are considered more reliable since great care should be exerted to identify the appropriate experimental conditions during chemisorption in order to avoid hydrogen spillover and that under these conditions hydrogen chemisorption does not become an activated process. Regarding the reduction of  $\text{Co}_3\text{O}_4$ , this was reported [50] to be complete at temperatures  $< 450^\circ\text{C}$  in pure hydrogen. For the carbon-uncoated alumina (CY-A), the cobalt metal surface area



was estimated to  $10.8 \text{ m}^2 \text{ g}^{-1}$  and increases to  $12.3 \text{ m}^2 \text{ g}^{-1}$  for the carbon-coated alumina (CY-C) catalyst. Moreover, the Co crystallite size decreases from 7.9 for the CY-A to 5.7 nm for the CY-C catalyst.

**Table 6.1:** Primary crystallite size of  $\text{Co}_3\text{O}_4$  ( $d_{\text{Co}_3\text{O}_4}$ , nm) and Co ( $d_{\text{Co}}$ , nm) dispersion of Co (D, %), Active Co metal surface area ( $\text{m}^2 \text{ g}^{-1}$ ), BET specific surface area (SSA,  $\text{m}^2 \text{ g}^{-1}$ ), specific pore volume ( $V_p$ ,  $\text{cm}^3 \text{ g}^{-1}$ ) and average pore size ( $d_p$ , nm) obtained over CY-A and CY-C solids.

Catalyst	$N_{\text{Co-surf}}$ ( $\mu\text{mol g}^{-1}$ )	$d_{\text{Co}_3\text{O}_4}$ (nm)	$d_{\text{Co}}$ (nm)	D (%)	Active Co surface area ( $\text{m}^2 \text{ g}^{-1}$ )	SSA ( $\text{m}^2 \text{ g}^{-1}$ )	$V_p$ ( $\text{cm}^3 \text{ g}^{-1}$ )	$d_p$ (nm)
CY-A	338.5	13.4	10.1 (7.9) <sup>a</sup>	9.5 (7.6) <sup>a</sup>	10.8	88.2	0.21	8.78
CY-C	449.0	10.2	7.6 (5.7)	12.6 (8.7)	12.3	88.0	0.21	8.55

<sup>a</sup> Estimated from selective hydrogen chemisorption measurements.

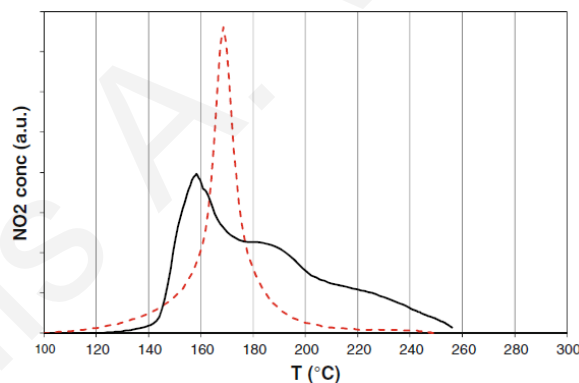


**Figure 6.2:**  $\text{NO}_2$  concentration during calcination in air for CY-A (solid black) and CY-C (dotted red) impregnated with cobalt nitrate (Ref. [46]).

After cobalt nitrate impregnation and drying [46], the catalyst precursor was calcined in air under temperature-programmed conditions in order to decompose the nitrates and burn the carbon layers. The  $\text{NO}_2(\text{g})$ -TPO traces obtained for the CY-A (carbon-uncoated) and CY-C (carbon-coated) catalysts are shown in Fig. 6.2. The cobalt nitrate decomposition on CY-C even though is sharper and is completed at lower temperatures, it presents lower decomposition rates at  $T < 160 \text{ }^\circ\text{C}$  and a peak maximum at higher temperatures ( $T_M = 170 \text{ }^\circ\text{C}$ ) compared to the CY-A ( $T_M = 155 \text{ }^\circ\text{C}$ ). This nitrate decomposition behavior of CY-C can be attributed to the

interaction or complex formation of -OH and carboxyl groups with Co ions [50]. Moreover, in Fig. 6.3, one can see that all the carbon layer deposited on CY-C is decomposed due to the cobalt nitrate assisted oxidative decomposition [46], mainly in two stages, with an easier (175 °C) and a more difficult (250 °C) to be removed carbon, which was formed during acetone decomposition [46].

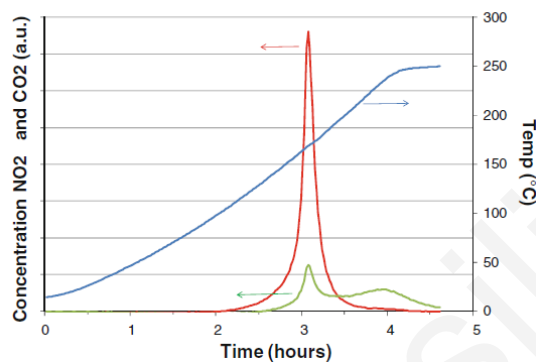


**Figure 6.3:** NO<sub>2</sub> (red) and CO<sub>2</sub> (green) concentration traces obtained during calcination in air of the CY-C catalyst (Ref. [46]).

The H<sub>2</sub>-TPR trace of the pre-calcined with air CY-C [29] is presented in Fig. 6.4. Two reduction peaks are clearly observed, which are ascribed in the two-step reduction of Co<sub>3</sub>O<sub>4</sub> to CoO (1<sup>st</sup> reduction step peak) and CoO to Co<sup>0</sup> (2<sup>nd</sup> reduction step peak) [39,49,51]. These two hydrogen TPR peaks were observed on CY-A as well, but due to weaker cobalt oxide and alumina surface interactions developed in CY-C, which are caused by the rapid decomposition of the cobalt nitrates, peak maxima at ~ 200 and 400 °C are obtained, lower than on CY-A (at ~ 250 and 450 °C). The shoulder at the high-T side of 2<sup>nd</sup> peak obtained is assigned to the reduction of cobalt oxide species strongly interacting with the support (Co<sub>x</sub>O<sub>y</sub>-Al<sub>2</sub>O<sub>3</sub> → Co<sup>0</sup>).

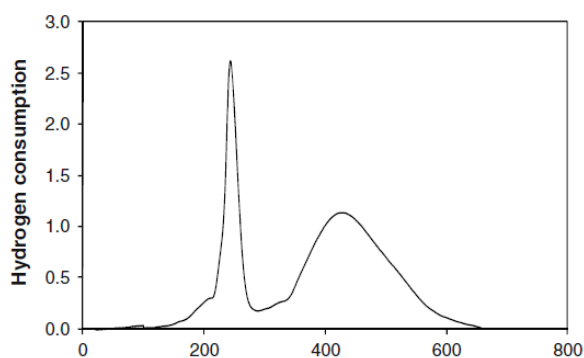


**Figure 6.4:** Hydrogen temperature programmed reduction (H<sub>2</sub>-TPR) profile recorded over the CY-C catalyst (Ref. [46]).

Figure 6.5 shows High Angle Annular Dark Field - Scanning Transmission Electron Microscopy (HAADF-STEM) analyses performed over CY-A and CY-C [46]. It can be seen that on CY-A (carbon uncoated alumina) the individual Co particles were agglomerated, presenting larger Co crystallites branching and which might lead to sintering, as opposed to the case of CY-C, where Co crystallites are smaller and evenly homogeneous dispersed. These results might be due to the accelerated calcination (Fig. 6.2) of CY-A, which hinders the recombination of cobalt nitrate species during their dehydration and decomposition steps [52].

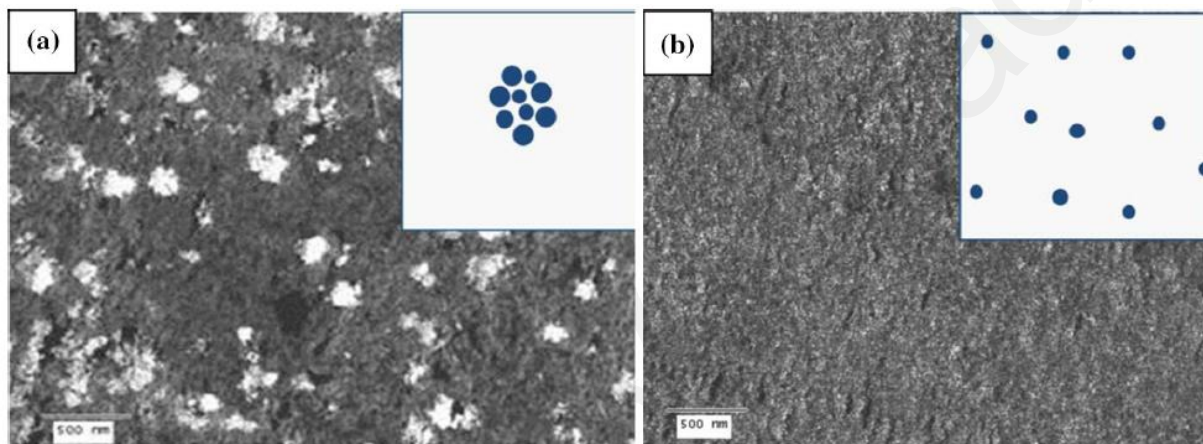


**Figure 6.5:** Transmission electron microscopy images (HAADF-TEM) with a schematic distribution of Co crystallites over (a) CY-A and (b) CY-C solid catalysts (Ref. [46]).

### 6.3 SSITKA – Mass Spectrometry studies

#### 6.3.1 Probing the carbon-path of methanation reaction

Figure 6.6 shows normalized concentration ( $Z$ ) transient response curves of Kr (tracer gas),  $^{13}\text{CO}$  and  $^{13}\text{CH}_4$  obtained during the SSITKA switch  $5\% \text{ }^{12}\text{CO}/10\% \text{ H}_2/\text{Ar} \rightarrow 5\% \text{ }^{13}\text{CO}/10\% \text{ H}_2/1\% \text{ Kr}/\text{Ar}$  at  $230^\circ\text{C}$  over CY-A and CY-C. The correct performance of a SSITKA experiment should reveal the following features [19]: (i) the sum of dimensionless concentrations ( $Z_{^{13}\text{CO}} + Z_{^{12}\text{CO}}$ ) and ( $Z_{^{13}\text{CH}_4} + Z_{^{12}\text{CH}_4}$ ) should be equal to one, at any time during the transient, and these should therefore cross each other at  $Z = 0.5$ ; (ii) the  $\text{H}_2\text{O}$  signal in the mass spectrometer, which is a product of the FT reaction, should stay the same during the SSITKA switch, since the rates of reactions for the FT synthesis products remain the same (the partial pressures of both CO and  $\text{H}_2$ , the reaction T and the space velocity are kept constant). If the latter feature is not observed, then either the two feed gas streams or the lines contain a different concentration level of water or the two-feed gas stream do not contain exactly the same

composition in CO and H<sub>2</sub>. The above described features were fully satisfied in all the SSITKA experiments conducted.

The SSITKA transient response curves depicted in Fig. 6.6 and the material balance equations described in Chapter 3 (Eqs. (3.20) – (3.22)) allow to estimate two important kinetic quantities: (i) the surface concentration of molecularly adsorbed CO and (ii) the surface concentration of active CH<sub>x</sub> reaction intermediates that ultimately lead to the formation of CH<sub>4</sub>. The appearance of <sup>13</sup>CO transient response curve lags behind that of Kr tracer as the result of the formation of a measurable concentration of *reversibly adsorbed CO-s* during FT synthesis reaction conditions (Eq. (3.20)). The <sup>13</sup>CO(g) transient response curve appears earlier than that of <sup>13</sup>CH<sub>4</sub> (small chromatographic effect) [53], and this feature is due to the fact that <sup>13</sup>C passes through various kinds of adsorbed reaction intermediates before it forms <sup>13</sup>CH<sub>4</sub>(g). Specifically, molecularly adsorbed CO-s is hydrogenated to form HCO\* and then HCOH\*, which then dissociates to CH\* and OH\*, which CH\* is finally hydrogenated to form CH<sub>4</sub>(g) [54–58].

The material balance Eq. (3.21) provides an accurate value of the N<sub>CH<sub>x</sub></sub> quantity in the case that the exchange of adsorbed <sup>12</sup>CO-s with <sup>13</sup>CO(g) is considered as a fast step compared to the hydrogenation of CH<sub>x</sub> to CH<sub>4</sub>. If this is not the case, then simulation of <sup>13</sup>CO(g) and <sup>13</sup>CH<sub>4</sub>(g) transient responses is the only means to provide an accurate measure of N<sub>CH<sub>x</sub></sub>. As will be shown below, for the present catalysts and reaction conditions, Eq. (3.21) is accurate.

Table 6.2 provides the amount of adsorbed CO (N<sub>CO</sub>, μmol g<sup>-1</sup> and θ<sub>CO</sub>) and that of *active* CH<sub>x</sub> leading to CH<sub>4</sub> (N<sub>CH<sub>x</sub></sub>, μmol g<sup>-1</sup> and θ<sub>CH<sub>x</sub></sub>) for the CY-A and CY-C catalysts. Based on the θ<sub>CH<sub>x</sub></sub> value and the experimentally measured methanation rate, the mean life-time of the active CH<sub>x</sub> intermediates, and an *apparent rate constant* (k<sub>eff</sub> [s<sup>-1</sup>] = k θ<sub>H</sub>) associated with the hydrogenation of -CH<sub>x</sub> intermediates can be estimated (Eqs. (3.24), (3.26), (3.28) – (3.31)). Here, the intrinsic rate constant k (s<sup>-1</sup>) refers to the *average site reactivity* of all the CH<sub>x</sub> (x = 0–3) intermediates which are sequentially hydrogenated (e.g., CH<sub>x-s</sub> + H-s → CH<sub>x+1-s</sub> + s) to finally form CH<sub>4</sub>(g). The inverse of τ<sub>CH<sub>x</sub></sub> (Eq. (3.24)) cannot be considered as an intrinsic rate constant, k<sub>CH<sub>x</sub></sub>. In many publications appeared in the open literature this point is not clearly stated. Thus, according to Eq. (3.24) the inverse of τ<sub>CH<sub>x</sub></sub> should be seen as an apparent rate constant (Eq. 3.29), k<sub>eff</sub> as indicated above. Knowledge of θ<sub>H</sub> would allow estimation of the intrinsic k<sub>CH<sub>x</sub></sub>, the physical meaning of which was stated above.

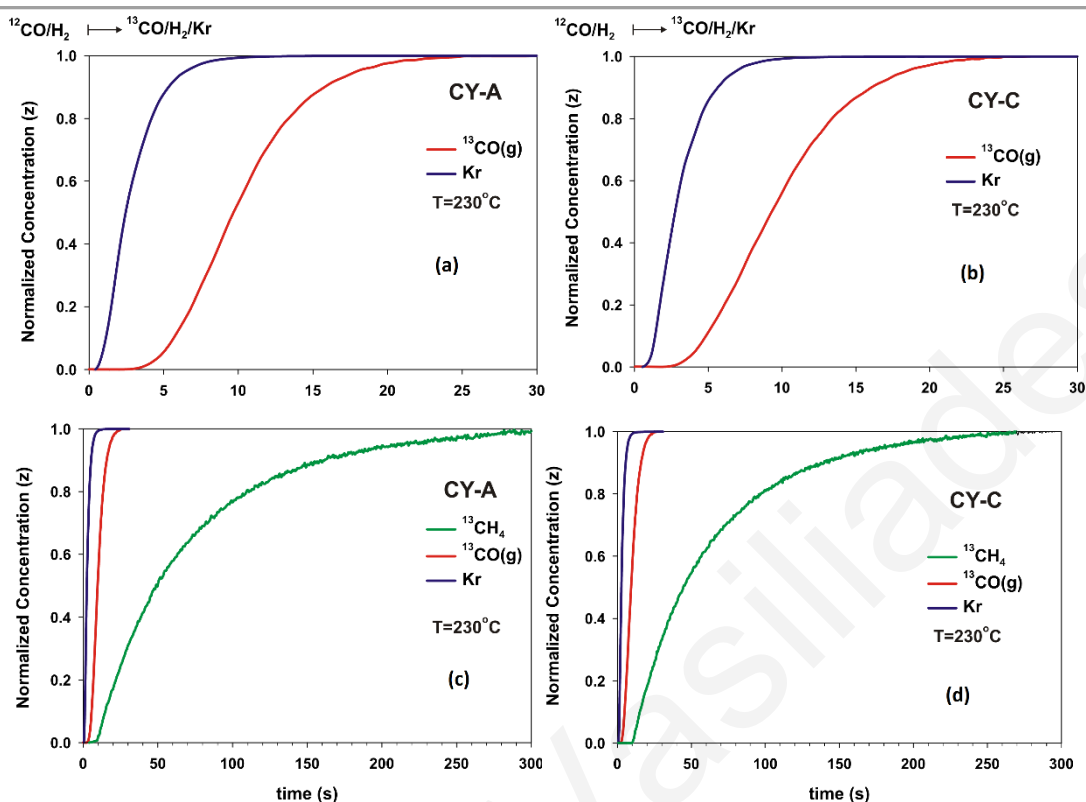


**Figure 6.6:** Normalized concentration (Z) transient response curves of  $^{13}\text{CO}$  and  $^{13}\text{CH}_4$  obtained during SSITKA ( $^{12}\text{CO}/\text{H}_2$  (32 h)  $\rightarrow$   $^{13}\text{CO}/\text{H}_2$  (t)) at 230 °C on CY-A (a, c) and CY-C (b, d) catalysts. Feed composition:  $^{12}\text{CO}$  = 5%,  $^{13}\text{CO}$  = 5%,  $\text{H}_2$  = 10%, 1% Kr, balance He. Total flow rate:  $100 \text{ NmL min}^{-1}$ ,  $W_{\text{CY-A}} = 0.4 \text{ g}$ ;  $W_{\text{CY-C}} = 0.3 \text{ g}$ .

The surface coverages of CO and  $\text{CH}_x$  reported in this work (Table 6.2) are in the range of those reported by den Breejen et al. [22] and Vada et al. [42] for  $\text{SiO}_2$  and  $\text{Al}_2\text{O}_3$  supported Co catalysts. The values of  $\text{TOF}_{\text{CH}_4}$  ( $\text{s}^{-1}$ ) reported in Table 6.2, which are estimated based on the total Co surface sites (Co dispersion, Table 6.1), appear *about four times lower* than the  $\text{TOF}_{\text{CH}_4, \text{ITK}}$  ( $\text{s}^{-1}$ ) estimated based on the sum of the concentrations ( $\mu\text{mol g}^{-1}$ ) of both the active  $\text{CH}_x$  and reversibly adsorbed CO-s (Table 6.2). These are found to be  $5.40 \times 10^{-3} (\text{s}^{-1})$  and  $5.72 \times 10^{-3} (\text{s}^{-1})$  for the CY-A and CY-C catalyst, respectively. Considering that also some concentration of active H-s species ( $\theta_{\text{H}}$ ) is found in the carbon-path and definitely participates in the formation of  $\text{CH}_4$ , then the  $\text{TOF}_{\text{CH}_4, \text{ITK}}$  would have been even lower. This example illustrates that TOF estimated on the basis of all the Co exposed surface sites and not on the concentration of the real active species participating in the formation of a given reaction product could lead to erroneous site activity values and conclusions about relative activities in a series of catalysts to be compared.

**Table 6.2:** Amount ( $N$ ,  $\mu\text{mol g}^{-1}$ ) and surface coverage ( $\theta$ ) of adsorbed CO and active  $\text{CH}_x$  (leading to  $\text{CH}_4$ ), mean residence time ( $\tau$ ), kinetic rates of methane formation ( $\mu\text{mol g}^{-1} \text{s}^{-1}$  or TOF) and effective rate constant ( $k_{\text{eff}}$ ,  $\text{s}^{-1}$ ) of methane formation over CY-A and CY-C catalysts pertain to 32 h of continuous FT reaction.

Catalyst	$N_{\text{CO}^*}$ $\mu\text{mol g}^{-1}$	$\theta_{\text{CO}^*}$	$r_{\text{CO}}$ $\mu\text{mol g}^{-1} \text{s}^{-1}$	$\tau_{\text{CO}}$ s	$N_{\text{CH}_x}$ $\mu\text{mol g}^{-1}$	$\theta_{\text{CH}_x}$	$r_{\text{CH}_4}$ $\mu\text{mol g}^{-1} \text{s}^{-1}$	TOF <sub>CH<sub>4</sub></sub> $\text{s}^{-1}$ ( $\times 10^{-3}$ )	TOF <sub>CH<sub>4</sub>, ITK</sub> $\text{s}^{-1}$ ( $\times 10^{-3}$ )	$\tau_{\text{CH}_x}$ s	$k_{\text{eff}}$ $\text{s}^{-1}$ ( $\times 10^{-2}$ )
CY-A	55.7	0.16	0.94	7.3	28.2	0.08	0.45	1.34	5.40	62.2	1.61
CY-C	73.3	0.16	1.36	7.3	31.4	0.07	0.60	1.33	5.72	52.4	1.91

According to the results of Table 6.2, both catalysts present practically the same surface coverage of active  $\text{CH}_x$  ( $\theta_{\text{CH}_x} = 0.08$  and  $0.07$  for CY-A and CY-C, respectively). The difference in TOF<sub>CH<sub>4</sub>, ITK</sub> ( $\text{s}^{-1}$ ) observed can therefore be assigned to the different  $k_{\text{eff}}$  values or equivalently to differences in the product value of  $k_{\text{CH}_x} \cdot \theta_{\text{H}}$ . There is  $\sim 16\%$  increase in  $k_{\text{eff}}$  between the CY-A (less active) and CY-C (most active) according to Table 6.2. In terms of the concentration of adsorbed surface CO-s ( $\mu\text{mol g}^{-1}$ ), there is a clear increase of  $\sim 30\%$  when comparing the CY-A and CY-C catalysts. The specific kinetic rate of these two catalysts in terms of  $\mu\text{mol CO g}^{-1} \text{s}^{-1}$  at  $230^\circ\text{C}$  is determined during the SSITKA experiment, and it was found to be  $0.94$  and  $1.36$ , respectively, for the CY-A and CY-C catalysts. This result also points out for  $\sim 30\%$  increase in the activity (per gram basis) among the two catalysts. Therefore, this tends to indicate that the specific reaction rate per gram basis correlates well with the concentration of adsorbed CO-s ( $\mu\text{mol g}^{-1}$ ) established under steady-state FT reaction conditions. The fact that the Co surface in the present catalytic systems of CY-A and CY-C populate adsorbed CO-s and  $\text{CH}_x$ -s intermediates with *no large differences* in the size of their pools suggests that the rate-limiting step of methanation reaction might be either the dissociation of adsorbed CO-s on the cobalt surface ( $\text{CO-s} + \text{s} \rightarrow \text{C-s} + \text{O-s}$ ) or the hydrogenation of  $\text{CH}_x$ -s species [11]. In fact, DFT calculations on Co (111) surface [40] indicated that hydrogen assisted CO-s dissociation (forming an  $-\text{CHO}$  intermediate) proceeds faster than  $\text{CH}_x$ -s hydrogenation, thus one of the latter steps should be considered as a likely RDS (rate-determining step) of methanation reaction on supported Co surfaces.

### 6.3.2 Probing higher hydrocarbons pathways (C<sub>2</sub>'s and C<sub>3</sub>'s)

The  $^{12}\text{CO}/\text{H}_2 \rightarrow ^{13}\text{CO}/\text{H}_2$  SSITKA gas switch using Mass Spectrometry only was repeated to also record the transient evolution of  $^{13}\text{C}$ -containing hydrocarbons higher than methane. The signals recorded at  $m/z = 30$  and  $m/z = 31$  largely reflect the formation of  $^{13}\text{C}$ -ethane/ethylene and  $^{13}\text{C}$ -propane/propylene gaseous species. No attempts were made to quantify these responses in terms of the concentration of  $\text{C}_2\text{H}_6/\text{C}_2\text{H}_4$  and  $\text{C}_3\text{H}_8/\text{C}_3\text{H}_6$ . Accurate SSITKA analysis of these hydrocarbons can be made only by using GC-MS analytical system and a multiport chromatographic sampling valve, as previously mentioned, which were not available. However, the relative transient evolution in time of the  $^{13}\text{CH}_4$  ( $m/z = 17$ ) and  $m/z = 30$  and  $m/z = 31$  mass spectrometer signals would allow to discriminate between two possibilities for the mechanism of  $\text{C}_2^+$ -hydrocarbons formation to be discussed below.

Figure 6.8 shows the observed transient response curves of  $m/z = 30$  and  $31$  in comparison with that of  $^{13}\text{CH}_4$  ( $m/z = 17$ ) previously presented. It is clearly observed that the  $^{13}\text{CH}_4$  transient lags behind the C<sub>2</sub>'s/C<sub>3</sub>'s transients for both CY-A and CY-C catalysts. This behaviour is a rather clear case that the formation of C<sub>2</sub>'s and C<sub>3</sub>'s passes through a *different* -CH<sub>x</sub> precursor from that which is responsible for the CH<sub>4</sub> formation, that leads to the formation of a -C<sub>2</sub>H<sub>y</sub> precursor for C<sub>2</sub>'s hydrocarbon formation via further hydrogenation steps, as shown in Figure 6.7. The opposite would have resulted in a  $^{13}\text{CH}_4$  transient preceding that corresponding to the  $^{13}\text{C}_2$  or  $^{13}\text{C}_3$  hydrocarbon formation. In other words, if the same -CH<sub>x</sub> that forms methane reacts further to give a -C<sub>2</sub>H<sub>y</sub> intermediate, then the exchange of the  $^{12}\text{CH}_x$  with  $^{13}\text{CH}_x$  should precede that of  $^{12}\text{C}_2\text{H}_y$  with  $^{13}\text{C}_2\text{H}_y$ . The possibility that hydrogenation step(s) of CH<sub>x</sub> to form CH<sub>4</sub> are slower than the C-C coupling of two -CH<sub>x</sub> species to form -C<sub>2</sub>H<sub>y</sub> and the following hydrogenation steps to form C<sub>2</sub>'s does not appear reasonable according to the literature [43,44].

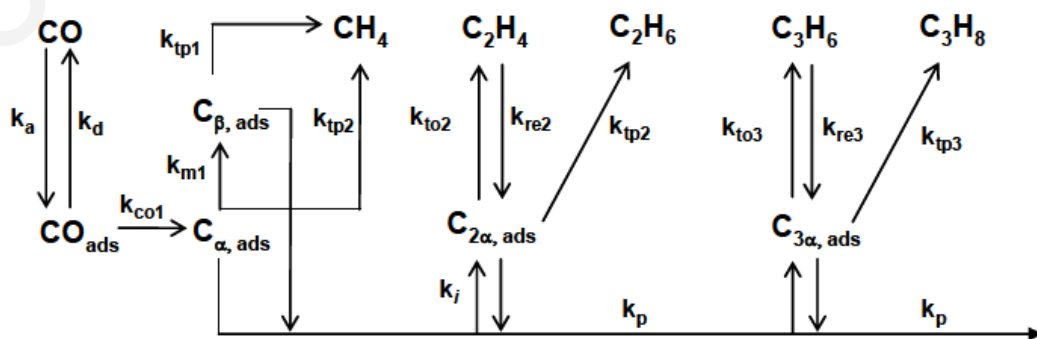


**Figure 6.7:** Schematic modelling of a single C<sub>n</sub> ( $n \geq 2$ ) surface intermediate [59].



The other important feature recorded in the transient response curves shown in Fig. 6.8 is the fact that the  $m/z = 31$  transient is much faster than that of  $m/z = 30$ . If these two transients were the result of the evolution of only the  $C_2$ -hydrocarbons ( $C_2H_6/C_2H_4$ ), then the transient of  $m/z = 31$  would have to lag behind that of  $m/z = 30$ , which is the opposite observed. This fact then naturally leads to the conclusion that the  $m/z = 30$  transient is largely due to  $C_3$ 's-hydrocarbons and lags behind that of  $C_2$ 's ( $m/z = 31$ ) according to the mechanistic Figure 6.7.

Based on the above offered discussion regarding the  $m/z = 30$  and  $m/z = 31$  transient response curves of Fig. 6.8, and the fact that the  $m/z = 31$  transient lies very close to the  $^{13}CO(g)$  transient (Fig. 6.6), it can be concluded that the surface coverage of  $C_2H_y$ -s active adsorbed intermediates leading to  $C_2$ -hydrocarbons must be very small. Also, some differences in the shape of  $m/z = 30$  transient and its duration (time elapsed for  $Z = 1$ ) for the two catalysts (compare Fig. 6.8a and b) suggest that the kinetics of  $C_3$ 's-hydrocarbon formation is not the same. This difference in kinetics could reflect differences in the size of pool ( $\theta$ ) of the active intermediates leading to  $C_3$ 's, differences in the rate constant forming this pool and/or differences in the rate constant of hydrogenation of this carbon-pool to form finally  $C_3$ -hydrocarbons (see Figure 6.7).

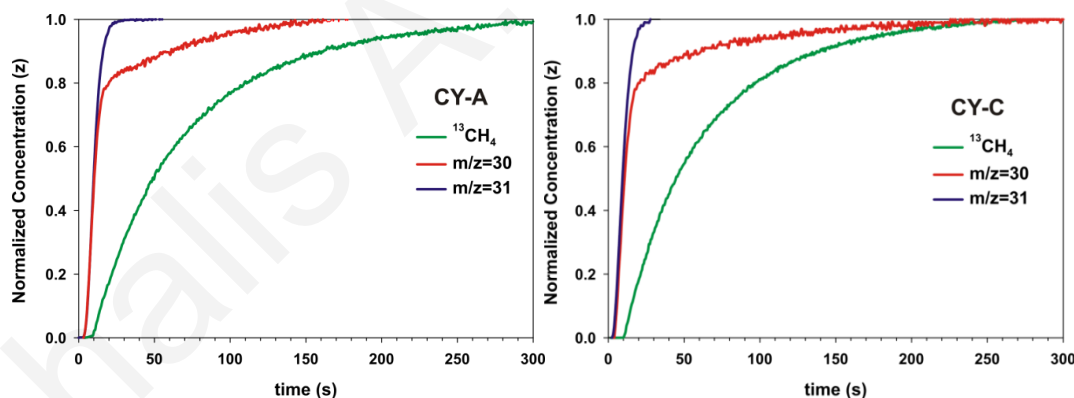


**Figure 6.8:** Experimental MS response curves of  $^{13}CH_4$  ( $m/z = 17$ ) and  $m/z = 30$  and  $31$  signals recorded during SSITKA ( $^{12}CO/H_2 \rightarrow ^{13}CO/H_2$ ) over the CY-A and CY-C catalysts.

### 6.3.3 Transient Isothermal Hydrogenation (TIH) and Temperature-Programmed Hydrogenation (TPH)

The qualitative and quantitative characteristics of the hydrogenation process of the various kinds of carbonaceous species formed during FT reaction at  $230\text{ }^\circ\text{C}$  was probed on the



basis of the following gas delivery sequence:  $^{12}\text{CO}/\text{H}_2$  (32 h)  $\rightarrow$   $^{13}\text{CO}/\text{H}_2$  (7 min)  $\rightarrow$  He (3 min)  $\rightarrow$  50%  $\text{H}_2/\text{He}$  (50  $\text{NmL min}^{-1}$ , 230  $^\circ\text{C}$ , 7 min)  $\rightarrow$  TPH ( $\beta = 10$   $^\circ\text{C min}^{-1}$ ) up to 600  $^\circ\text{C}$ .

During the SSITKA switch, adsorbed  $^{12}\text{CO}$ -s was replaced by  $^{13}\text{CO}$ -s as well as the active  $^{12}\text{CH}_x$ -s with  $^{13}\text{CH}_x$ -s species. Upon the 3-min He purge step which followed the SSITKA switch, it will be shown in the Section 6.3.6 (DRIFTS experiments) that only a small amount of adsorbed  $^{13}\text{CO}$ -s was desorbed from the catalyst surface. Therefore, upon the 50%  $\text{H}_2/\text{He}$  gas switch the  $^{13}\text{CH}_4$  MS signal ( $m/z = 17$ ) produced is due to both the  $^{13}\text{CO}$ -s and the active  $^{13}\text{CH}_x$ -s. It should be noted at this point that due to some small desorption of  $^{13}\text{CO}$ -s and H-s from the catalyst surface upon the He purge step, and the switch to a much higher hydrogen partial pressure (50%  $\text{H}_2/\text{He}$ ) compared to 10%  $\text{H}_2$  used in FT reaction conditions, the  $\theta_{\text{H}}$  at the switch to 50%  $\text{H}_2/\text{He}$  is larger than that under FT reaction conditions.

Figures 6.9a and 6.10a show transient response curves of  $^{13}\text{CH}_4$  and  $^{12}\text{CH}_4$  formation obtained during isothermal hydrogenation at 230  $^\circ\text{C}$  of the surface carbonaceous species formed after 32 h in FT synthesis reaction conditions over CY-A and CY-C catalysts, respectively. The transient response curves of  $^{13}\text{CH}_4$  and  $^{12}\text{CH}_4$  have different shapes, indicating that the two carbon pools associated with the formation of these species consists of different in structure intermediates which are hydrogenated to methane with different kinetics.

The initial very sharp transient response of  $^{13}\text{CH}_4$  is associated with the hydrogenation of the active  $\text{CH}_x$ -s ( $C_a$ ), leading to methane [11]. This  $C_a$  active intermediate was exchanged under the  $^{13}\text{CO}/\text{H}_2/\text{Kr}/\text{Ar}$  SSITKA gas switch. The rest of the  $^{13}\text{CH}_4$  response (e.g.  $t > 5$  s) is due to the hydrogenation of adsorbed  $^{13}\text{CO}$ -s [28]. Thus, based on these results it might be suggested that the rate determining step (RDS) in the  $\text{CO}$ -s hydrogenation does not appear to be the hydrogenation of  $\text{CH}_x$ -s but rather the dissociation of  $\text{CO}$ -s to give C-s and O-s or in the case of H-assisted  $\text{CO}$ -s dissociation to give CHO-s intermediate species.

The equivalent surface coverage of intermediates leading to  $^{13}\text{CH}_4$  estimated by the TIH experiment ( $\theta_{^{13}\text{CH}_4}$ ) should be equal to the sum of the active intermediates estimated by the SSITKA experiment ( $\theta_{\text{CO}} + \theta_{\text{CH}_x}$ ). In fact, according to Tables 6.2 and 6.4 the sum of the surface coverage of  $\text{CO}$ -s and  $\text{CH}_x$ -s ( $C_a$ ) estimated during  $^{13}\text{CO}$ -SSITKA are in a very good agreement with the hydrogenation results depicted in Figs. 6.9a and 6.10a and given in Table 6.4, given the fact that some  $^{13}\text{CO}$ -s was desorbed during the 3-min He purge.

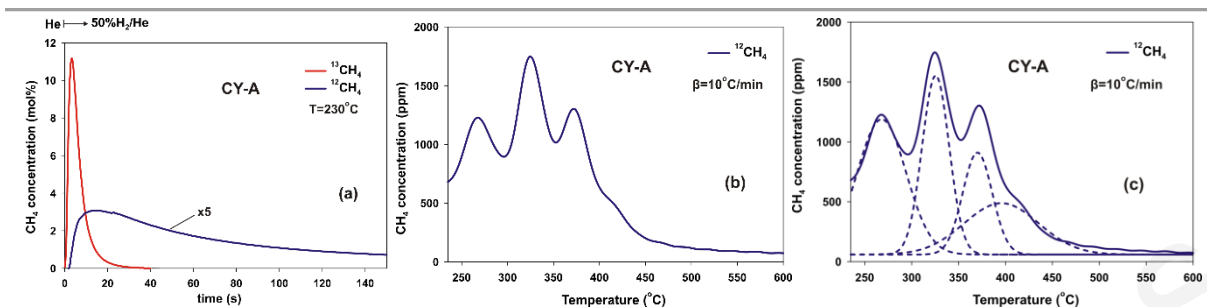


**Figure 6.9:** (a) Transient isothermal hydrogenation of carbonaceous species formed during FT reaction conditions at 230 °C towards CH<sub>4</sub> formation on the CY-A catalyst; (b) Temperature-programmed hydrogenation of carbonaceous species following (a); (c) deconvolution of TPH trace shown in (b).

The slower transient response curve of <sup>12</sup>CH<sub>4</sub> (Figs. 6.9a and 6.10a) is due to the hydrogenation either of a less active CH<sub>x</sub>-s (C<sub>β</sub>) species, which *is not found in the carbon-path of methane formation*, or of a *non-exchangeable* adsorbed CO-s (strongly bound) formed under FT reaction conditions. Based on SSITKA-DRIFTS results (see below), the latter is fully excluded as all types of adsorbed CO identified are bound on the surface *reversibly*. Also, the large difference in the shape and position in time of <sup>13</sup>CH<sub>4</sub> and <sup>12</sup>CH<sub>4</sub> response curves largely excludes the possibility for the presence of a strongly bound CO-s. Therefore, the <sup>12</sup>CH<sub>4</sub> transient response curve seems to be purely due to an *inactive* CH<sub>x</sub>-s (C<sub>β</sub>) species for the methanation reaction. However, the latter species can be hydrogenated at 230 °C in 50% H<sub>2</sub>/He gas mixture leading to methane but only when CO is removed from the catalyst surface (e.g. CO/H<sub>2</sub>/He → He → H<sub>2</sub>/He). A very recent work reported by G. Kwak et al. [60] has clearly indicated that hydrogenation of surface Co<sub>2</sub>C (carburized cobalt phase) can readily occur in the 160-250 °C range according to the following reaction:



This reaction step could explain the *nature of C<sub>β</sub> species* (ca. Co<sub>2</sub>C) associated with the <sup>12</sup>CH<sub>4</sub> isothermal hydrogenation response curves (Figs. 6.9a and 6.10a). The extent of cobalt carburization might be different for the two catalysts. The above results are in agreement with those reported by Happel et al. [61] and Otarod et al. [62].

It should be noted, however, that the  $^{12}\text{CH}_4$  response obtained over the CY-C catalyst (Fig. 6.10a) reflects the presence of *two kinds of*  $\text{CH}_x$  *inactive* species (two peaks) formed under the present FT reaction conditions, which is different from the one seen over the CY-A catalyst (Fig. 6.9a). Moreover, it seems that the first sharp peak in the  $^{12}\text{CH}_4$  response shown in Fig. 6.10a is a  $\text{CH}_x$  *inactive species* with similar structure as the one derived from the dissociation of CO ( $\text{C}_\alpha$  species) but not hydrogenated towards methane under FT reaction conditions.

Figures 6.9b and 6.10b show transient response curves of  $^{12}\text{CH}_4$  obtained under temperature-programmed hydrogenation (TPH) conducted over the CY-A and CY-C catalysts, respectively, following FT reaction for 32 h and according to the gas delivery sequence previously described. The obtained TPH traces show multiple hydrogenation peaks, the quantification of which is possible after deconvolution (Gaussian peak shape) of the TPH trace (Figs. 6.9c and 6.10c). Table 6.3 provides all the quantitative results obtained from this deconvolution procedure, namely, the peak maximum temperature ( $T_{\text{max}}$ ) and the corresponding quantity of each kind of *inactive* carbonaceous species formed on the catalyst surface after 32 h of FT reaction.

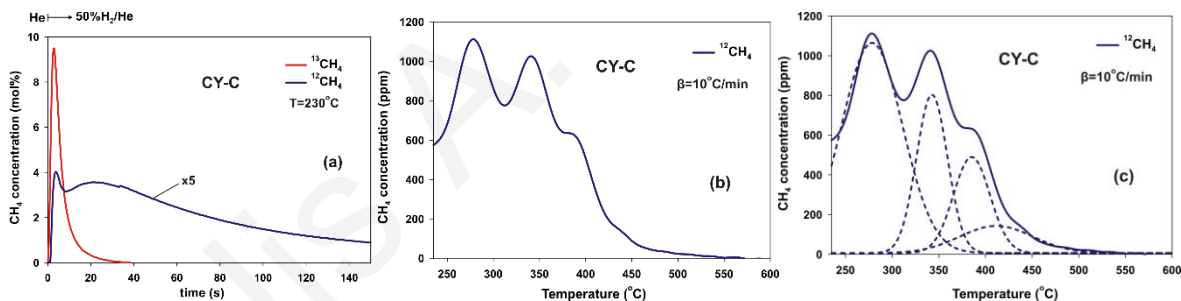


**Figure 6.10:** (a) Transient isothermal hydrogenation of carbonaceous species formed during FT reaction conditions at 230 °C towards  $\text{CH}_4$  formation on the CY-C catalyst; (b) Temperature-programmed hydrogenation of carbonaceous species following (a); (c) deconvolution of TPH trace shown in (b).

**Table 6.3:** Deconvoluted TPH traces obtained over the CY-A and CY-C catalysts.

Peak	T <sub>max</sub> (°C)	Concentration ( $\mu\text{mol g}_{\text{cat}}^{-1}$ )	T <sub>max</sub> (°C)	Concentration ( $\mu\text{mol g}_{\text{cat}}^{-1}$ )
	CY-A		CY-C	
<b>A</b>	268	46.6	278	73.5
<b>B</b>	326	34.1	343	28.1
<b>C</b>	370	21.2	385	20.1
<b>D</b>	396	27.1	411	11.3

The TIH/TPH experiments conducted after the SSITKA switch proved to be very informative since they allowed to probe the existence of (i) a less active  $-\text{CH}_x$  species ( $\text{C}_\beta$ , TIH) hydrogenated at 230 °C in the absence of CO, and (ii) inactive carbonaceous species hydrogenated only at temperatures larger than 230 °C ( $\text{C}_\gamma$ , TPH). Two *active* pools ( $\text{C}_\alpha$  and  $\text{C}_\beta$ ) found in the carbon-path of methanation reaction have been reported [28,37,63–65], as also depicted in Figure 6.7. Comparing CY-A and CY-C with respect to the  $\text{C}_\beta$  carbon species, which is *readily hydrogenated at 230 °C* but does not lead to the  $\text{CH}_4$  formation under FT reaction conditions, it is seen that the CY-C catalyst forms a significantly larger quantity (120 vs 69.4  $\mu\text{mol g}_{\text{cat}}^{-1}$ , Table 6.4). On the other hand, the total amount of refractory carbonaceous species (TPH experiment) is found to be similar for both catalysts. Also, the CY-C catalyst contains a larger fraction of carbonaceous species hydrogenated at lower T's.

**Table 6.4:** Amount and surface coverage of non-exchangeable  $^{12}\text{CH}_x$ -s hydrogenated to  $^{12}\text{CH}_4$  at 230 °C (TIH), exchangeable  $^{13}\text{CH}_x$ -s and  $^{13}\text{CO}$ -s hydrogenated to  $^{13}\text{CH}_4$  at 230 °C (TIH), as well as of  $^{12}\text{C}_x\text{H}_y$ -s hydrogenated to  $^{12}\text{CH}_4$  under TPH after 32 h in FT over the CY-A and CY-C catalysts.

Catalyst	TIH $\text{N}_{^{12}\text{CH}_4}$ ( $\mu\text{mol g}^{-1}$ )	$\Theta_{^{12}\text{CH}_4}$	TIH $\text{N}_{^{13}\text{CH}_4}$ ( $\mu\text{mol g}^{-1}$ )	$\Theta_{^{13}\text{CH}_4}$	TPH $\text{N}_{^{12}\text{CH}_4}$ ( $\mu\text{mol g}^{-1}$ )	$\Theta_{^{12}\text{CH}_4}$	Total $\Theta_{^{12}\text{CH}_4}$
<b>CY-A</b>	69.4	0.25	70.9	0.26	129.0	0.48	0.73
<b>CY-C</b>	120.0	0.39	73.8	0.24	133.0	0.43	0.82

### 6.3.4 Probing the H-path in Fischer-Tropsch

The hydrogen-path of the FT reaction over the CY-A and CY-C catalysts was probed via the SSITKA switch  $^{12}\text{CO}/\text{H}_2/\text{Ar}$  (32 h, 230 °C)  $\rightarrow$   $^{12}\text{CO}/\text{D}_2/\text{Kr}/\text{Ar}$  (t) (see Section 3.8.2), and results are shown in Figs. 6.11a and 6.12a, respectively. The amount of catalyst and the total flow rate used were exactly the same as with the previous  $^{13}\text{CO}$ -SSITKA experiments. The time-on-stream in FT reaction before the  $\text{D}_2$ -SSITKA experiment was similar to the one reported above for the  $^{13}\text{CO}$ -SSITKA experiment, since the former gas switch was performed shortly after the latter one. The evolution of  $^{12}\text{CD}_4$  ( $m/z = 20$ ) would have been difficult to follow due to a large contribution from the  $\text{D}_2\text{O}$  ( $m/z = 20$ ) transient and likely H/D exchange reactions between DHO and -OD groups, the latter being formed after possible exchange of -OH with HD and  $\text{D}_2$  during the SSITKA switch [66].

To account for possible exchange of H of the -OH species on the catalyst surface with the  $\text{D}_2$  (g) during the SSITKA switch, the following gas switch was designed and performed: 3.5%  $\text{CO}/7\% \text{H}_2/\text{Ar}/\text{He}$  (10 min)  $\rightarrow$  He (5 min)  $\rightarrow$  7%  $\text{H}_2/\text{Ar}/\text{He}$  (230 °C, 15 min)  $\rightarrow$  7%  $\text{D}_2/\text{Ar}/\text{Kr}/\text{He}$  (t), and the obtained results are reported in Figs. 6.11b and 6.12b. The initial treatment of the catalyst surface with  $\text{CO}/\text{H}_2/\text{Ar}/\text{He}$  had the purpose to establish an adsorbed phase similar in composition to that obtained under FT reaction conditions.

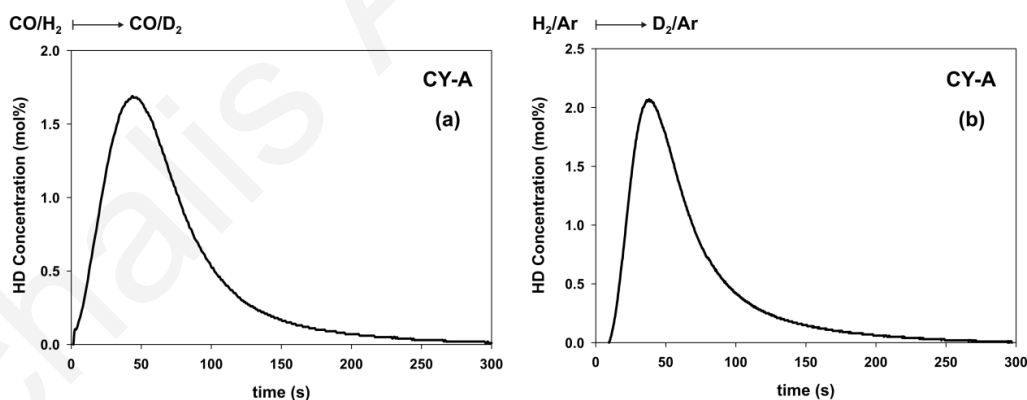


**Figure 6.11:** (a) HD transient response curves obtained during the SSITKA-MS switch over CY-A according to the gas delivery sequence: 3.5%  $\text{CO}/7\% \text{H}_2/\text{Ar}/\text{He} \rightarrow 3.5\% \text{CO}/7\% \text{D}_2/\text{Ar}/\text{Kr}/\text{He}$  at 230 °C; (b) transient response of HD obtained during the gas switch: 7%  $\text{H}_2/\text{Ar}/\text{He}$  (230 °C, 15 min)  $\rightarrow$  7%  $\text{D}_2/\text{Ar}/\text{Kr}/\text{He}$  (t).

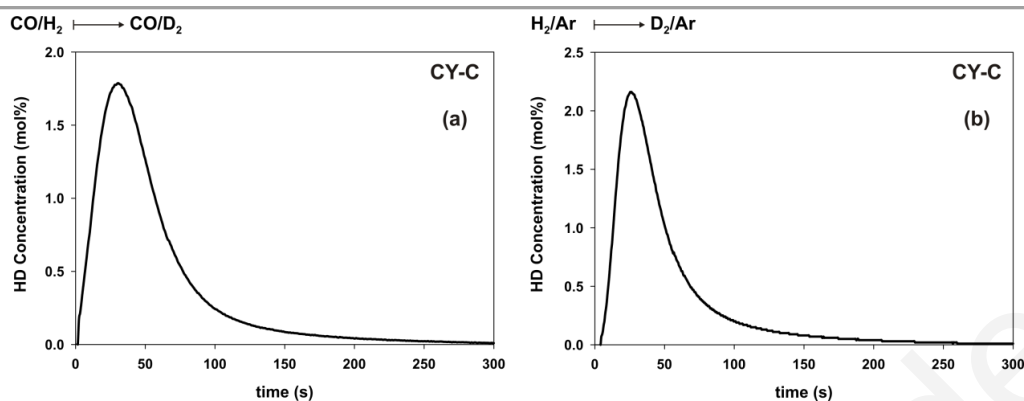


**Figure 6.12:** (a) HD transient response curves obtained during the SSITKA-MS switch over CY-C according to the gas delivery sequence: 3.5%  $\text{CO}/7\% \text{H}_2/\text{Ar}/\text{He} \rightarrow 3.5\% \text{CO}/7\% \text{D}_2/\text{Ar}/\text{Kr}/\text{He}$  at 230 °C; (b) transient response of HD obtained during the gas switch: 7%  $\text{H}_2/\text{Ar}/\text{He}$  (230 °C, 15 min)  $\rightarrow 7\% \text{D}_2/\text{Ar}/\text{Kr}/\text{He}$  (t).

Table 6.5 reports the quantity ( $\mu\text{mol HD g}_{\text{cat}}^{-1}$ ) of HD (g) produced (Ch. 3, Eq. (3.32)) during the two transient experiments shown in Figs. 6.11b and 6.12b for the CY-A and CY-C catalyst, respectively.

**Table 6.5:** Quantities of HD formed during the two different SSITKA and H/D exchange experiments performed over the CY-A and CY-C catalysts.

Catalyst	$^{12}\text{CO}/\text{H}_2 \rightarrow ^{12}\text{CO}/\text{D}_2$ (SSITKA)		$\text{H}_2/\text{Ar} \rightarrow \text{D}_2/\text{Ar}$ (H/D exchange)	
	Area (mol%-s)	$N_{\text{HD}}$ ( $\mu\text{mol g}_{\text{cat}}^{-1}$ )	Area (mol%-s)	$N_{\text{HD}}$ ( $\mu\text{mol g}_{\text{cat}}^{-1}$ )
<b>CY-A</b>	129.2	220 ( $\theta = 0.81$ )	107.1	<b>243 (<math>\theta = 0.9</math>)</b>
<b>CY-C</b>	<b>122.9</b>	<b>209 (0.67)</b>	<b>100.7</b>	<b>228 (<math>\theta = 0.74</math>)</b>

The amount of HD formed during the SSITKA switch is found to be equivalent to  $\theta = 0.67$ - $0.81$  (based on the  $\text{Co}_s$ ). Considering the individual surface coverage of adsorbed  $\text{CO}$ -s and  $-\text{CH}_x$ , it appears impossible that the Co surface can accommodate this size of H-pool. It is clear that a large part of the measured H-pool represents  $-\text{OH}$  groups present on the support of the catalyst, where the HD(g) formed must arise from an H/D exchange. This is exactly what is strongly suggested by the results shown in Figs. 6.11b and 6.12b and the quantities reported in Table 6.5. The time of appearance of peak maximum under the  $^{12}\text{CO}/\text{H}_2 \rightarrow ^{12}\text{CO}/\text{D}_2$  switch was smaller in the case of CY-C ( $t_m = 30.4$  s) than CY-A ( $t_m = 43.7$  s). Considering that this HD consists of the exchange process of H-s on Co and  $-\text{OH}_s$  on the support as stated above, and that

the exchange process of D<sub>2</sub>(g) with H-s is faster than that with –OH<sub>s</sub>, it is suggested that the most active catalyst (CY-C) in methanation reaction forms adsorbed H-s having a lower binding energy. This kinetic parameter is certainly important in determining the hydrogenation rate of active CH<sub>x</sub> species.

The deuterium kinetic isotopic effect (D-KIE) was estimated based on the steady-state rate values of CO conversion at 230 °C under the CO/H<sub>2</sub> and CO/D<sub>2</sub> feed gas streams:

$$KIE = \frac{r_{CO}(CO/H_2)}{r_{CO}(CO/D_2)} = \frac{r_H}{r_D} \quad (\text{Eq. 6.2})$$

The obtained results are given in Table 6.6. If the ratio  $r_H/r_D$  is greater than unity, the KIE is said to be normal (NKIE) and if it is less than unity, it is said to be inverse (IKIE). The KIE estimated for the CO consumption rates should reflect an overall D-KIE, from the reactant CO through all the surface intermediates that lead to the observed gas product distribution (e.g. CH<sub>4</sub> and C<sub>2</sub><sup>+</sup>) under the experimental conditions used in the present work.

**Table 6.6:** CO conversion (%) under CO/H<sub>2</sub>, CO/D<sub>2</sub> and the KIE estimated over the CY-A and CY-C catalysts.

Catalyst	X <sub>CO</sub> (%), CO/H <sub>2</sub>	X <sub>CO</sub> (%), CO/D <sub>2</sub>	KIE
CY-A	10.0	9.1	1.10
CY-C	10.7	10.2	1.05

As shown in the Table 6.6, both catalysts exhibit NKIE slightly larger than unity, in agreement with several studies under FT reaction conditions with large CH<sub>4</sub>-selectivity values over supported Co catalysts [12–15]. It has been reported [67], that as the carbon number in the hydrocarbon molecule increases, the D-KIE becomes strongly IKIE (< 1.0). NKIE with a value close to one suggests that the RDS is not much influenced by the addition or elimination of H (e.g. C-H associated bond forming). Krishnamoorthy et al. [68] have reported that in the case that hydrogenation of C-s to form the CH-s monomer were the kinetically relevant step, then the nature of the observed KIE (NKIE vs INKIE) would also depend on the thermodynamic contributions regarding chemisorption of H<sub>2</sub> and D<sub>2</sub>. In other words, the observed overall KIE would depend on the strengths of the H and D bonds with the Co surface and with carbon in the

$\text{CH}_x$ -s active intermediates, and on the extent to which these two bonds have broken or formed, respectively, in the activated complex involved in this elementary step. A rigorous analysis of the kinetic isotopic effects requires molecular simulations of proposed elementary steps and their respective kinetic isotope effects, an approach beyond the scope of this D<sub>2</sub>-SSITKA study.

### 6.3.5 Modeling of <sup>12</sup>CH<sub>4</sub>-SSITKA transients

Soong et al. [69] in their work over Raney Nickel catalysts, investigated four different models possibly describing the *methanation reaction pathways*. The analysis assumed that the exchange of gas-phase <sup>13</sup>CO and adsorbed <sup>12</sup>CO-s on the surface is very fast, and that the <sup>13</sup>C-isotopic exchange of <sup>12</sup>CH<sub>x</sub>-s is the slow process. According to this analysis, the input function in the CH<sub>x</sub>-s pool is that of <sup>13</sup>CO(g), which is also assumed as an *ideal step function*. Given these assumptions, the mass balance analysis of the SSITKA experiment allows one to have an analytical solution, which can be used against the SSITKA experimental transient response curves to estimate rate constants (k's) of elementary steps in the methanation reaction pathways.

In the present work, Soong's analysis was used since the assumption of a fast <sup>13</sup>CO/<sup>12</sup>CO-s exchange is proved experimentally to be valid and only the assumption that the input <sup>13</sup>CO(g) could be described by an ideal step function is not quite correct (see Fig. 6.6, Kr transient response curve). The latter deviation is expected to cause only deviations in the first 10 s of the transient according to the theory of SSITKA analysis. However, since the main purpose of this work is to discriminate among possible rival methanation mechanisms reported in the open literature, and extract kinetic parameters (e.g.  $\tau_{\text{CH}_x}$  or  $k_{\text{CH}_x}$ ) to be compared between CY-A and CY-C catalysts, the inherent problem of the non-ideality of the step function of CO(g) should not be considered as a barrier to obtain the above mentioned very important and valuable information for the present two catalytic systems.

For modelling purposes, the R<sup>2</sup> function given by the below Eq. (6.3) was adopted for obtaining the kinetic parameters which provide the best fitting of the experimental results (R<sup>2</sup> → 1.0).

$$R^2 = 1 - \left( \frac{\text{norm}(\text{exp.} - \text{sim.})}{\text{norm}(\text{exp.} - \text{mean}(\text{exp.}))} \right)^2 \quad (\text{Eq. 6.3})$$



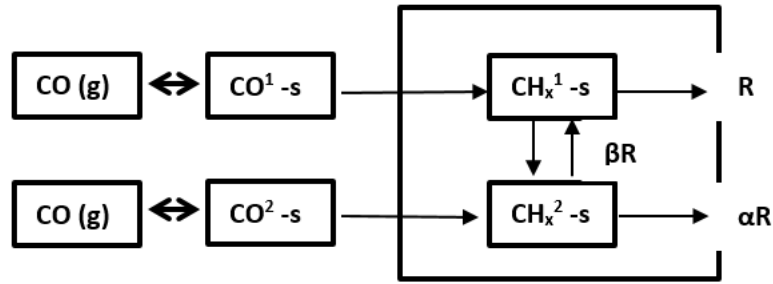


**Figure 6.13:** Model C (Ref. [53]) describing the carbon-path of methanation reaction after considering the participation of *two kinds* of active  $\text{CH}_x\text{-s}$  which are formed via two different kinds of adsorbed  $\text{CO-s}$ .

In the model Figure 6.13,  $R$  is the rate of methane formation due to the active  $\text{CH}_x^1\text{-s}$  intermediate,  $\alpha$  is a parameter ( $>1$ ) that describes how much the rate of methane formation via the  $\text{CH}_x^2\text{-s}$  intermediate is larger than that formed via the  $\text{CH}_x^1\text{-s}$  intermediate, and  $\beta$  is a parameter ( $0 < \beta < 1$ ) that describes the rate of C-transfer from the  $\text{CH}_x^2\text{-s}$  to the  $\text{CH}_x^1\text{-s}$  active pool (reversible interaction between the two pools) in terms of fraction of the methane formation rate due to the  $\text{CH}_x^1\text{-s}$  pool intermediate.

According to the mechanistic Figure 6.13, the *measured quantity of active  $\text{CH}_x\text{-s}$*  in the performed SSITKA experiment is related to the Soong's *model C parameters* via Eqs. 6.4-6.6. Moreover, the experimentally measured rate of methane production ( $R \equiv R(^{12}\text{CH}_4)$ ) is related to the model C parameters via Eq. 6.7. Thus, the four adjustable parameters  $\alpha$ ,  $\beta$ ,  $\tau_1$  and  $\tau_2$  are bound by Eqs. 6.4 - 6.7, and the two limitations of the analysis ( $\alpha > 1$  and  $0 < \beta < 1$ ) should be also fulfilled while modelling the analytical solution given by Eqs. 6.8 - 6.10 [53]. In Eq. (6.8),  $F$  is the dimensionless rate of  $^{12}\text{CH}_4$  during the up-step SSITKA switch ( $^{12}\text{CO}/\text{H}_2 \rightarrow ^{13}\text{CO}/\text{H}_2$ ) performed, thus, it is based on the decay response of  $^{12}\text{CH}_4$  during the isotopic gas switch. This function is equivalent to the 1-Z dimensionless function used in the present notation in Fig. 6.6.

$$N_{\text{CH}_x} = N_{\text{CH}_x}^1 + N_{\text{CH}_x}^2 \quad (\text{Eq. 6.4})$$

$$N_{\text{CH}_x} = \tau_1 R + \tau_2 \alpha R \quad (\text{Eq. 6.5})$$

$$N_{\text{CH}_x} = R(\tau_1 + \alpha \tau_2) \quad (\text{Eq. 6.6})$$

$$R_{\text{CH}_4} = R(\alpha + 1) \quad (\text{Eq. 6.7})$$

$$F = A \exp\left(\frac{-t}{\tau_a}\right) + (1 - A) \exp\left(\frac{-t}{\tau_b}\right) \quad (\text{Eq. 6.8})$$

$$A = \frac{1}{(a+1)} \left(1 + a + \frac{a}{\beta} - \frac{\tau_1 \alpha}{\tau_a \beta}\right) \frac{\left(1 - \frac{\tau_1}{\tau_b}\right)}{\tau_1 \left(\frac{1}{\tau_a} - \frac{1}{\tau_b}\right)} \quad (\text{Eq. 6.9})$$

$$\tau_a, \tau_b = \frac{1}{\left[ \frac{1}{2\tau_2} \left(1 + \frac{\beta}{\alpha}\right) + \frac{1}{2\tau_1} (1 + \beta) \mp \sqrt{\left(\frac{1}{2\tau_2} \left(1 + \frac{\beta}{\alpha}\right)\right)^2 + \left(\frac{1 + \beta}{2\tau_1}\right)^2 + \frac{(1 + \beta) \left(1 + \frac{\beta}{\alpha}\right)}{2\tau_1 \tau_2} - \frac{\left(1 + \beta + \frac{\beta}{\alpha}\right)}{\tau_1 \tau_2}} \right]} \quad (\text{Eq. 6.10})$$

The best fitting of  $^{12}\text{CH}_4$ -SSITKA transient response curves obtained is shown in Fig. 6.14b and Fig. 6.15, and the kinetic model parameters extracted are given in Table 6.7. Again, via the two experimentally obtained quantities of R and  $N_{\text{CH}_x}$ , the four adjustable parameters in fact were reduced into two via Eqs. (6.4) - (6.7).

**Table 6.7:** Model C – SSITKA kinetic parameters estimated for the experiment performed after 16 h of FT reaction.  $\tau_1$  and  $\tau_2$  (s) reflect the mean lifetime of  $\text{CH}_x^1$ -s and  $\text{CH}_x^2$ -s, respectively, active intermediates, and  $R^2$  is the value of mathematical regression of the experimental vs simulated data.

Catalyst	$\alpha$	$\beta$	$\tau_1$ (s)	$\tau_2$ (s)	$R^2$
CY-A	1.3	0.01	50	90	0.990
CY-C	1.1	0.01	40	80	0.977

Table 6.7 presents the SSITKA simulation results obtained by using model C (Figure 6.13) for the 16-h FT SSITKA run over the CY-A and CY-C catalysts. As will be illustrated below, *model C* (Figure 6.13) is the one that was found to best describe the  $^{12}\text{CH}_4$  (or  $^{13}\text{CH}_4$ ) - SSITKA results obtained over the two catalysts.

It is shown that catalyst synthesis influences  $\tau_1$  and  $\tau_2$ , thus the site reactivity of the given  $\text{CH}_x$ -s ( $\tau \sim 1/k$ ). Of interest is the fact that in both catalysts, best fit is obtained when  $\beta$  parameter takes only values very close to 0.01. This result suggests that the different synthesis applied for

the CY-A and CY-C commercial FT catalysts does not influence the extent of interaction of the two active  $\text{CH}_x$ -s pools. In fact, for both catalysts, carbon transfer between the two  $\text{CH}_x$  pools is practically irreversible (0.01 R), and in particular, the *most active*  $\text{CH}_x^1$ -s intermediate is transformed to a *less active one* ( $\text{CH}_x^2$ -s) in a practically irreversible manner. Also, it is important to be noted that the reactivity of the two  $\text{CH}_x$ -s species is not similar but largely differs, practically by a factor of  $\sim 2.0$ . The difference in the activity observed for the two CY-A and CY-C catalysts under steady-state FT reaction conditions (32 h on TOS) reported above (Table 6.2) are consistent with the life-time ( $\tau$ ) and site reactivity ( $k$ ) differences extracted from the results reported in Table 6.7 for the two catalysts.

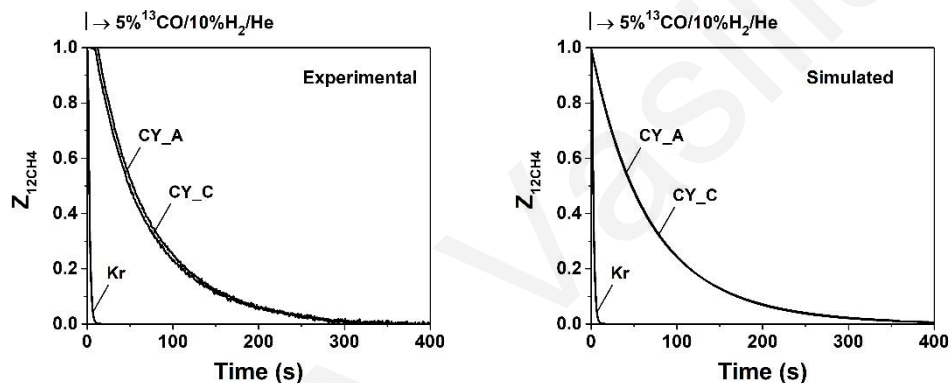


**Figure 6.14:** Experimental (left) and simulated (right) transient normalized concentration ( $Z$ ) response curves of Kr and  $^{12}\text{CH}_4$  obtained during the SSITKA switch: 5%  $^{12}\text{CO}/10\% \text{H}_2/1\% \text{Kr}/\text{Ar}/\text{He}$  (16 h)  $\rightarrow$  5%  $^{13}\text{CO}/10\% \text{H}_2/\text{Ar}/\text{He}$  at 230 °C over the two catalysts.

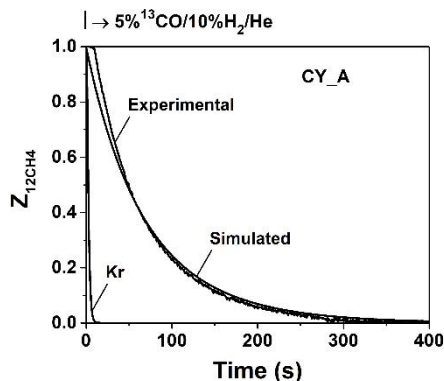


**Figure 6.15:** Transient normalized concentration ( $Z$ ) response curves of Kr and  $^{12}\text{CH}_4$  (Experimental and Simulated) obtained during the SSITKA switch: 5%  $^{12}\text{CO}/10\% \text{H}_2/1\% \text{Kr}/\text{Ar}/\text{He}$  (16 h)  $\rightarrow$  5%  $^{13}\text{CO}/10\% \text{H}_2/\text{Ar}/\text{He}$  at 230 °C over CY-A catalyst.

Soong's et al. [53] have also presented a different mechanistic model for methanation reaction, that depicted in the below Figure 6.16. In this mechanistic model, there is only one pool of CO-s which leads to the formation of an active  $\text{CH}_x^1\text{-s}$  intermediate, which in turn is responsible for the formation of a *second active*  $\text{CH}_x^2\text{-s}$  intermediate, which eventually leads to the formation of  $\text{CH}_4(\text{g})$ . Equations (6.11) - (6.12) provide the necessary tools for the simulation of  $^{12}\text{CH}_4\text{-SSITKA}$  response.

The main difference between the experimental and simulated results derived from Soong's et al. [53] Model A and Model C is illustrated in Fig. 6.17a, b. It can be clearly seen that the  $^{12}\text{CH}_4$  transient response curve obtained for both CY-A and CY-C catalysts during the SSITKA switch  $^{12}\text{CO}/\text{H}_2$  to  $^{13}\text{CO}/\text{H}_2$  cannot be described by Model A (Figure 6.16). For example, Model A provides an  $R^2$  of 0.966 and 0.946 for the CY-A and CY-C, respectively (Table 6.8), as opposed to 0.990 and 0.977 in the case of Model C.

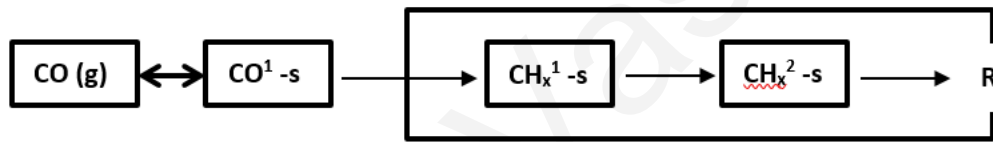


**Figure 6.16:** Model A mechanism of Methanation Reaction after considering the participation of two kinds of active  $\text{CH}_x\text{-s}$  which are formed via the same active adsorbed CO-s.

$$\tau_{\text{exp}} = \tau_1 + \tau_2 \quad (\text{Eq. 6.11})$$

$$F = \frac{\tau_1}{\tau_1 - \tau_2} \exp\left(\frac{-t}{\tau_1}\right) - \frac{\tau_2}{\tau_1 - \tau_2} \exp\left(\frac{-t}{\tau_2}\right) \quad (\text{Eq. 6.12})$$

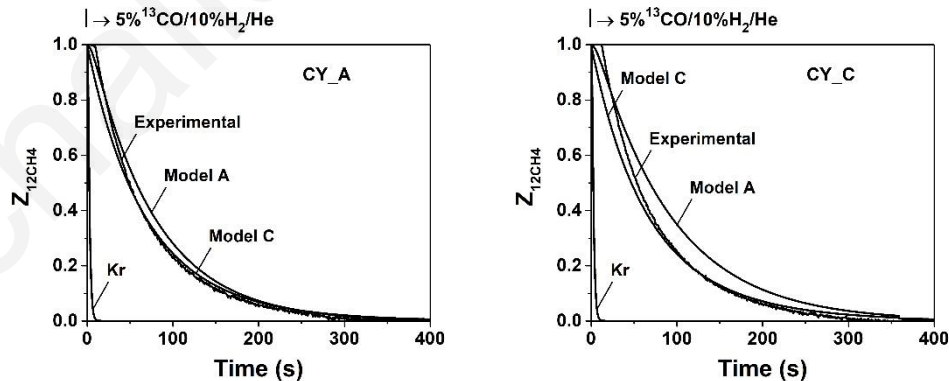


**Figure 6.17:** Transient normalized concentration ( $Z$ ) response curves of Kr,  $^{13}\text{CH}_4$  experimental and  $^{13}\text{CH}_4$  simulated by Model A and Model C based on the SSITKA switch: 5%  $^{12}\text{CO}/10\%$   $\text{H}_2/1\%$  Kr/Ar/He (30 min)  $\rightarrow$  5%  $^{13}\text{CO}/10\%$   $\text{H}_2/\text{Ar}/\text{He}$  at 230 °C over CY-A (left) and CY-C (right).

**Table 6.8:** Model A – SSITKA performed after 16 h of FT reaction, where  $\tau_1$  and  $\tau_2$  (s), reflect the mean lifetime of  $\text{CH}_x^1$ -s and  $\text{CH}_x^2$ -s, respectively, and  $R^2$  is the value of mathematical regression of the experimental vs simulated data.

Catalyst	$\tau_1$ (s)	$\tau_2$ (s)	$R^2$
CY-A	5.4	74.5	0.977
CY-C	5.1	75.1	0.948

## 6.4 *In situ* DRIFTS studies

### 6.4.1 Surface intermediates formed under CO/H<sub>2</sub>

The development of  $\text{CH}_x$ -s and  $\text{C}_x\text{H}_y$ -s alkyl chain reaction intermediates and of the likely different kinds of CO-s with time-on-stream in the FT reaction at 230 °C was followed by *in situ* DRIFTS (see Section 3.3.4). Figure 6.18 presents DRIFTS spectra recorded in the 3000-2800 (a) and 2250-1800  $\text{cm}^{-1}$  (b) ranges over the CY-C catalyst sample. The clear evolution of  $\text{C}_x\text{H}_y$ -s alkyl chain intermediates (as previously discussed) with time on stream in CO/H<sub>2</sub> (Fig. 6.18a) can be seen. Detailed analyses of the structure (composition) of these carbonaceous species [70] were out of the scope of this work. On the other hand, some important features of these bands should be noted and discussed. The two main bands centred at  $\sim 2935$  and  $2860 \text{ cm}^{-1}$  present an intensity ratio of about two and a shoulder at the high-frequency side of the  $2935 \text{ cm}^{-1}$  IR band. These features are totally different from those assigned to the  $\nu\text{CH}$  stretching vibrational frequency of  $\text{HCOO}^-$  (formate species). The latter species in principle could be formed on the alumina support under FT reaction conditions (presence of CO, H<sub>2</sub> and H<sub>2</sub>O). For the  $\text{HCOO}^-$  species, the above mentioned intensity ratio should be less than 1/3 [71,72], opposite to what has been recorded in Fig. 6.18. Thus, it is clearly concluded that the recorded IR bands in this  $\nu\text{CH}$  region correspond to  $-\text{CH}_2$  groups of alkyl  $-\text{C}_x\text{H}_y$  chains [71,72]. The shoulder appeared in the 2950-3000  $\text{cm}^{-1}$  range and which grows with TOS in CO/H<sub>2</sub> is due to the presence of  $-\text{CH}_3$  groups. In the case where  $A(-\text{CH}_2)/A(-\text{CH}_3) > 1$ , then a long chain alkyl group,  $-\text{C}_x\text{H}_y$  is formed [71,72].

Attempts were made to analyse the CO-s IR region shown in Fig. 6.18b by performing deconvolution of the IR bands (Abs units) of the spectra recorded. Figure 6.19 presents the evolution with TOS in CO/H<sub>2</sub> of the integral band area (Abs units) of the three different adsorbed CO species (two linear and one bridged) identified. In the next Section 6.4.2, the peak positions

of the three CO-s and examples of deconvolution are provided. The results shown in Fig. 6.19 are extremely important when linked to the SSITKA-MS results (Section 6.4.2) that show distinct differences in the dynamic process of  $^{13}\text{CO}$ -s exchange due to both the adsorbed CO-s (adsorption/desorption processes) and the dissociation of CO-s to form  $\text{CH}_4$  and higher HC's.

As shown in Fig. 6.19, it takes practically about 30 min in order for the two linear adsorbed CO-s and the bridged CO-s species to reach a constant surface coverage. On the other hand, the rate of adsorption for each of these three kinds of CO-s appears different based on the slope of the curves shown in Fig. 6.19.

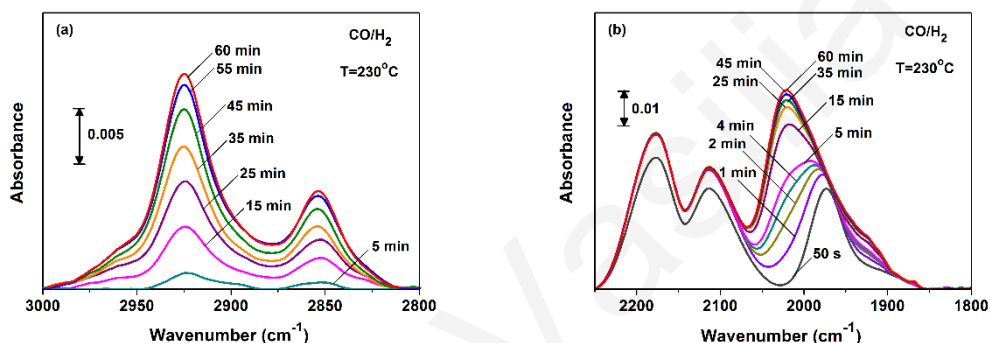


**Figure 6.18:** *In situ* DRIFTS spectra recorder under  $\text{CO}/\text{H}_2/\text{Ar}$  gas flow in the  $3000\text{-}2800\text{ cm}^{-1}$  (a) and  $2250\text{-}1800\text{ cm}^{-1}$  (b) range over the CY-C catalyst sample.

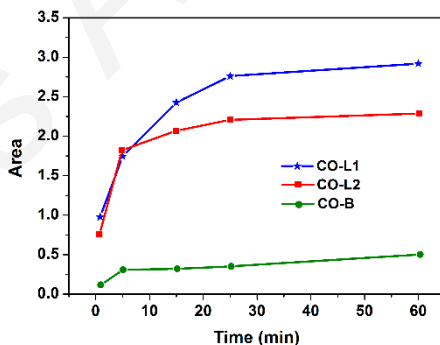


**Figure 6.19:** Integral band area (Abs units) development of each of the three kinds of adsorbed CO-s species (two linear and one bridged) identified with TOS in  $\text{CO}/\text{H}_2$  reaction for the CY-C catalyst.

#### 6.4.2 Surface reaction intermediates behaviour during the SSITKA switch

$^{13}\text{CO}$ -SSITKA experiments were conducted in the DRIFTS cell reported elsewhere [73–75] which behaved as a plug-flow micro-reactor. The purposes of these experiments were as follows:

- (i) probe whether all kinds of adsorbed CO formed during FT reaction conditions reversibly interact with the catalyst surface,
- (ii) investigate the thermal stability in He flow at 230 °C of the various kinds of CO-s, and
- (iii) investigate the reactivity towards hydrogen of these kinds of CO-s.

Details of the experiments performed are given in Ch. 3, Section 3.8.

Figure 6.20 and Table 6.9 report five IR bands in the 2250-1800  $\text{cm}^{-1}$  range (after deconvolution) due to the presence of gas phase CO (bands marked 1 and 2) and adsorbed CO-s (bands marked 3, 4 and 5). The IR bands at 2182 and 2116  $\text{cm}^{-1}$  and labeled as 1 and 2 and these are due to the R and Q branches of gas phase  $^{12}\text{CO}$  [76,77]. After deconvolution, all five IR bands gave the *red isotopic shift* (compare wavenumbers under  $^{12}\text{CO}/\text{H}_2$  and  $^{13}\text{CO}/\text{H}_2$  in Table 6.9). Of interest here is the red isotopic shift recorded for the adsorbed CO-s (IR bands 3-5) since this implies that all these three kinds of adsorbed CO-s are *reversibly* chemisorbed on the Co surface. Furthermore, these results demonstrate that the CO-s pool used in the previous mathematical model of SSITKA-MS experiments cannot be strictly treated as one kind of adsorbed CO-s. However, the question still remains whether all three kinds of adsorbed CO-s do participate in the formation of  $\text{CH}_4$  and higher hydrocarbons. Certainly, *at least one kind of adsorbed CO-s* must be considered as the *precursor species* of the formation of all hydrocarbons products. Of interest and importance is the fact that only part of adsorbed CO-s was considered as an *active intermediate* in WGS reaction [75,78] based on a transient isothermal DRIFTS experiment, where CO-s formed in WGS ( $\text{CO}/\text{H}_2\text{O}$ ) was reacted off by a following  $\text{H}_2\text{O}/\text{He}$  gas switch. Also, it is noted that in the 2400-2270  $\text{cm}^{-1}$  region, no IR band was observed due to gas-phase  $\text{CO}_2$  [72]. This is in agreement with the catalytic performance studies, where  $\text{CO}_2$  was not detected.

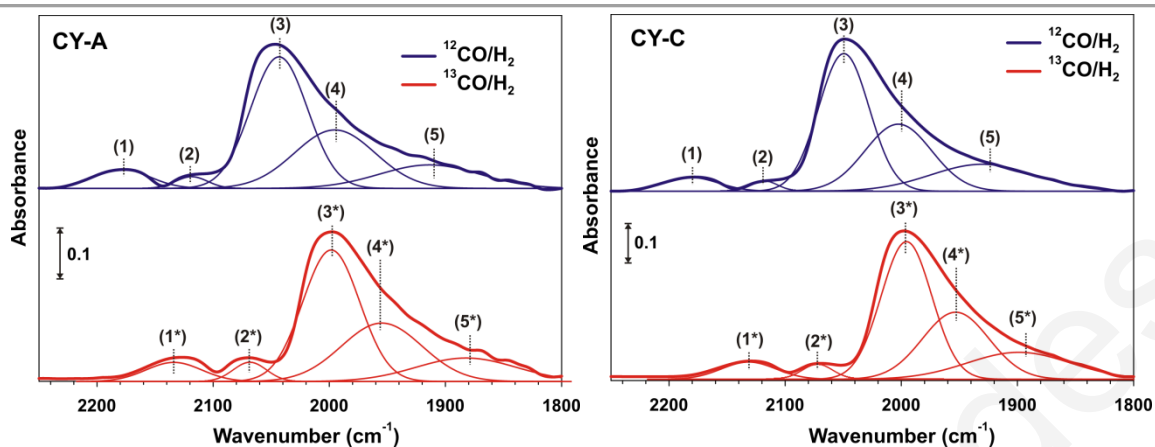


**Figure 6.20:** SSITKA-DRIFTS ( $^{12}\text{CO}/\text{H}_2 \rightarrow ^{13}\text{CO}/\text{H}_2$ ) performed at 230 °C over the CY-A and CY-C catalysts.

The IR bands centred at 2042-2046 and 1998-2002  $\text{cm}^{-1}$  under the  $^{12}\text{CO}/\text{H}_2$  reaction conditions are assigned to *two different kinds of linear adsorbed CO ( $\text{CO}^L\text{-s}$ )*, whereas that at 1911-1930  $\text{cm}^{-1}$  to a *bridged type adsorbed CO ( $\text{CO}^B\text{-s}$ )* on a reduced cobalt surface. IR bands of chemisorbed CO appearing at wavenumbers larger than those corresponding to gas-phase CO and which can be potentially assigned to CO chemisorption on cationic sites of Co (e.g.  $\text{Co}^{3+}$ ) were not observed over the present catalysts [71,76,77,79].

Comparing the adsorbed phase of CO-s for the two catalysts, it is rather clear that the two kinds of adsorbed CO-s (peaks 3 and 4) must be treated as having the same binding energy, whereas the third kind of adsorbed CO (peak 5) exhibits some small difference in the binding energy. However, it should be pointed out that the two catalysts form under FT reaction conditions different concentrations of adsorbed CO ( $\mu\text{mol g}_{\text{cat}}^{-1}$ ), as seen in the previous Section 6.3.1. Thus, small differences ( $< 15\text{-}20 \text{ cm}^{-1}$ ) in the position of the IR bands of a given type of chemisorbed CO-s in the two catalysts can also be due to differences in their surface coverage.

According to the DRIFTS studies, under the applied FT reaction conditions, the catalyst surface was found to be populated mainly by adsorbed CO-s and  $-\text{C}_x\text{H}_y\text{-s}$  hydrocarbon fragments, very small amounts of carbonates ( $\text{CO}_3^{2-}$ ) and carboxylates ( $-\text{COOH}$ ), and larger amounts of hydroxyl groups ( $-\text{OH}$ ).



**Table 6.9:** Peak position ( $\text{cm}^{-1}$ ) appeared after deconvolution of the CO-region IR bands (2250-1800  $\text{cm}^{-1}$ ) recorded under  $^{12}\text{CO}/\text{H}_2$  and  $^{13}\text{CO}/\text{H}_2$  feed streams.

Catalyst	IR band position, $\text{cm}^{-1}$	$^{12}\text{CO}/\text{H}_2$	$^{13}\text{CO}/\text{H}_2$
CY-A	1	2176	2128
	2	2119	2070
	3	2042	2000
	4	1998	1957
	5	1911	1878
CY-C	1	2178	2129
	2	2116	2069
	3	2046	1999
	4	2002	1956
	5	1930	1890

Figure 6.21 presents SSITKA-DRIFTS spectra recorded under  $^{12}\text{CO}/\text{H}_2$  and  $^{13}\text{CO}/\text{H}_2$  at 230 °C in the 3000-2800  $\text{cm}^{-1}$  range over the CY-C catalyst, where these IR bands are due to adsorbed  $\text{CH}_x$ -s and higher hydrocarbon fragments (e.g.  $\text{C}_x\text{H}_y$ -s alkyl chains), as presented and discussed in the previous Section 6.4.1 (catalyst sample was diluted with KBr). The IR bands centered at 2925 and 2854  $\text{cm}^{-1}$  correspond to the  $\nu\text{CH}$  vibrational mode of  $-\text{CH}_2$  group in the  $\text{C}_x\text{H}_y$ -s adsorbed hydrocarbon fragment [80,81] with a total integral band area,  $A = 0.0299$ . As depicted in Fig. 6.21, *none of these IR bands* show the red isotopic shift upon the switch  $^{12}\text{CO}/\text{H}_2$  (red colour)  $\rightarrow$   $^{13}\text{CO}/\text{H}_2$  (blue colour). Thus, these species are spectators for the methanation reaction. It should be noted, however, that one expects to observe the isotopic shift due to the *active  $\text{CH}_x$ -s intermediate* ( $\text{C}_\alpha$ ) presented and discussed in Section 6.3.1. However, the *small concentration* of this active  $\text{CH}_x$ -s compared to the significantly larger inactive  $\text{C}_x\text{H}_y$ -s adsorbed species formed (Tables 6.2 and 6.4) does not allow to clearly observe this isotopic shift.

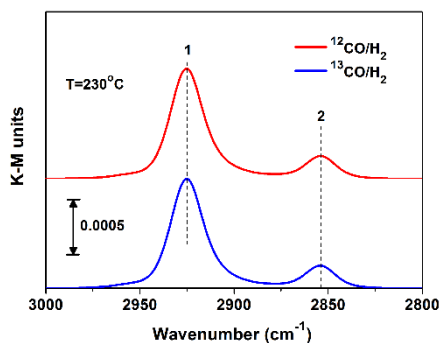
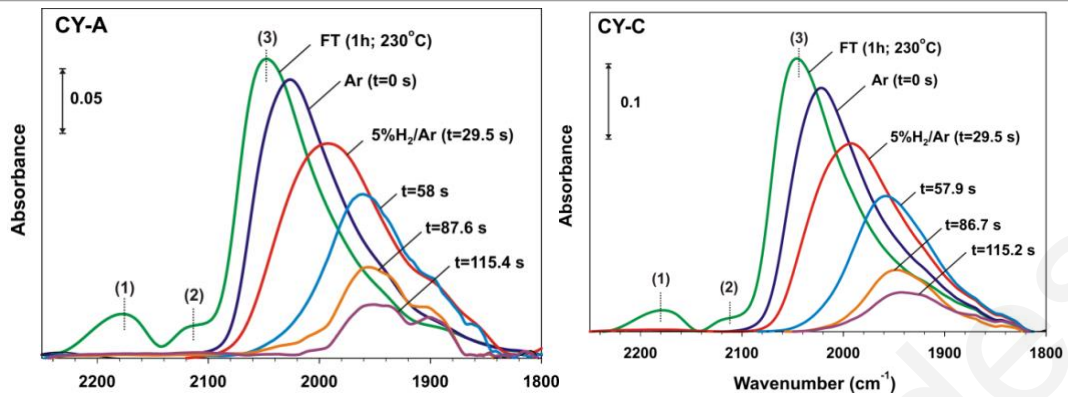


**Figure 6.21:** SSITKA-DRIFTS spectra recorded under  $^{12}\text{CO}/\text{H}_2$  and  $^{13}\text{CO}/\text{H}_2$  at 230 °C in the 3000-2800  $\text{cm}^{-1}$  range over the CY-C catalyst.

### 6.4.3 Transient isothermal DRIFTS hydrogenation of CO

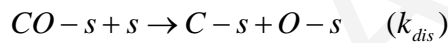
In order to investigate the *dynamics of hydrogenation of adsorbed CO-s* formed under the FT reaction conditions investigated, *isothermal hydrogenation of adsorbed CO* was performed following FT reaction (5% CO/10%  $\text{H}_2/\text{Ar}$ ) at 230 °C for 2 h, followed by Ar purge (50  $\text{cc min}^{-1}$ ) for 3 min in the DRIFTS cell with the catalyst in place. The transient hydrogenation of CO-s was made using a 5%  $\text{H}_2/\text{Ar}$  gas (100  $\text{cc min}^{-1}$ ).

Figure 6.22 shows DRIFTS spectra recorded in the CO-region (1800-2250  $\text{cm}^{-1}$ ) over the CY-A and CY-C catalysts. The curve marked as Ar ( $t = 0$  s) is the spectrum recorded after the 3-min purge in Ar flow before the 5%  $\text{H}_2/\text{He}$  gas switch, and that marked as FT is the spectrum recorded after 1 h of Fischer-Tropsch at 230 °C. It is clearly seen that at 230 °C only a small fraction of adsorbed CO desorbs in Ar flow, result that justifies the interpretation made as to the origin of the  $^{13}\text{CH}_4$  isothermal peak in the hydrogen reduction experiment with MS (see Section 6.3.3). As time in 5%  $\text{H}_2/\text{He}$  gas treatment increases, the surface coverage of adsorbed CO-s decreases, since this reacts with hydrogen, but the IR band progressively shifts to lower wavenumbers. The latter is largely due to the well-known phenomenon in CO chemisorption, that of the effect of surface coverage on the binding energy of adsorbed CO due to the lateral repulsive interactions among adjacent adsorbed CO-s, the latter being treated as electric dipoles. As the surface coverage of CO-s decreases, the binding energy of CO-s with the Co surface increases, thus, the bond energy between C and O within the adsorbed CO-s decreases, thus the decrease in the vibrational frequency observed. To gather further information from this DRIFTS isothermal hydrogenation experiment, a simple kinetic analysis was attempted as described and discussed in what follows.



**Figure 6.22:** *In situ* DRIFTS spectra recorded in 5% H<sub>2</sub>/Ar flow at 230 °C over the CY-A and CY-C catalysts as a function of time in 5% H<sub>2</sub>/Ar gas flow.

The rate of depletion in the concentration of adsorbed CO-s due to reaction with hydrogen can be expressed as:  $-d\theta_{CO}/dt$ , where  $\theta_{CO}$  is the surface coverage of CO. The quantity  $A(t)/A(t=0)$ , where  $A(t)$  is the integral band intensity of adsorbed CO at a given time  $t$ , and  $A(t=0)$  the corresponding one at  $t=0$  (end of Ar purge), can be used to express the equivalent quantity of  $\theta_{CO}(t)$ . This is presented in Fig. 6.23. The depletion of adsorbed CO is the result of the following elementary step:

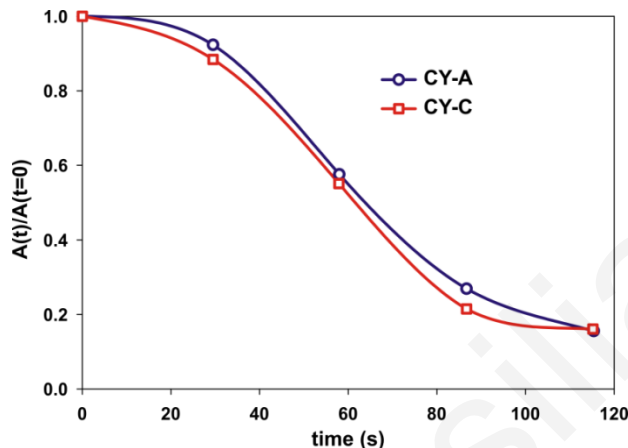


the rate of which can be described by:

$$-d\theta_{CO}/dt = k_{dis}\theta_{CO}\theta_s \quad (\text{Eq. 6.13})$$

Based on the curves of Fig. 6.23, it can be seen that the *rate of change* in the number density of adsorbed CO-s (mols CO / cm<sup>2</sup> Co) on the two catalysts is similar. This then implies that the right-hand side of Eq. (6.13) should be also similar for the two catalysts. Knowing the  $\theta_{CO}$  under FT reaction conditions (SSITKA switch), then the product ( $k_{dis}\theta_s$ ) could be estimated and compared for the two catalysts. According to the SSITKA results (Section 6.3.1, Table 6.2), and assuming that the  $\theta_{CO}$  for the two catalysts as well as the total carbonaceous species stay also very similar after 1 h in FT (Fig. 6.22), then it might be suggested that the rate of CO-s dissociation over the two catalysts is approximately very similar. This conclusion under the

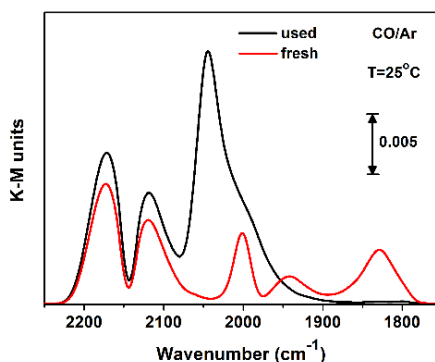
stated assumptions agrees with the fact that the differences in the methanation activity of the two catalysts seems to be more related to differences in the kinetics of  $\text{CH}_x$ -s hydrogenation, as reported in Section 6.3.1.



**Figure 6.23:** Dimensionless surface concentration of adsorbed CO as a function of time during the 5%  $\text{H}_2/\text{Ar}$  gas treatment for the CY-A and CY-C catalysts.

## 6.5 Effect of adsorbed carbon on the CO chemisorption

Figure 6.24 presents the *effect of carbon deposition* occurred after CO/Ar treatment of the CY-C catalyst (fresh) at 230 °C on the CO chemisorption (5% CO/Ar) performed at 25 °C, and Table 6.10 reports the CO IR band position (maximum) recorded for the fresh and used (after CO/Ar treatment at 230 °C) CY-C catalysts. It is obvious that *carbon deposition affects the adsorbed phase of CO* (intensity and position) after CO chemisorption at 25 °C. It appears that the relative population of the two linear and one bridged CO adsorbed species were largely influenced by the presence of “carbon” on the Co surface. Based on the results presented in Table 6.9 and those in Fig. 6.24, it appears that the carbonaceous species accumulated on the two catalysts during FT reaction must be similar in quantity, result that is in harmony with the SSITKA and other transient hydrogenation experiments presented and discussed in Sections 6.3.1-6.3.3.

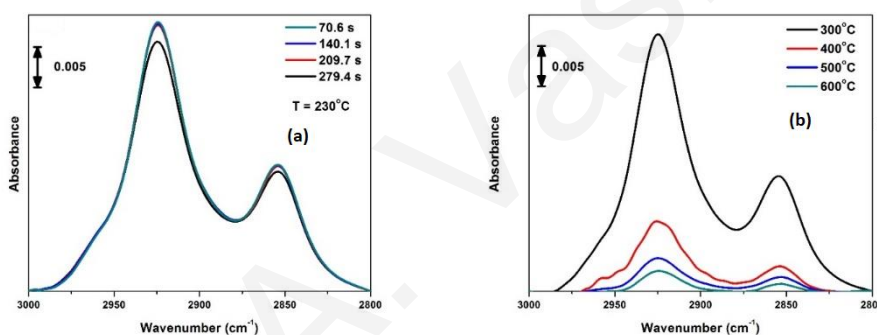


**Figure 6.24:** Effect of carbon deposition on CO chemisorption (5% CO/Ar) at 25 °C over the fresh CY-C sample and that after treated with CO/Ar at 230 °C.

Figure 6.25a presents DRIFTS spectra recorded in the 2800-3000  $\text{cm}^{-1}$  range (due to the formation of  $\text{CH}_x$ -s and  $\text{C}_x\text{H}_y$ -s alkyl chain intermediates) during the transient isothermal hydrogenation (TIH) experiment performed at 230 °C following CO/ $\text{H}_2$  reaction (1 h/230 °C) in the DRIFTS reactor cell over the CY-C catalyst. It is shown that *only a small change* in the integral band area is observed, in harmony with the SSITKA-MS results, where the surface coverage of active  $\text{CH}_x$ -s ( $\text{C}_\alpha$  species) is very small ( $\theta = 0.1$ ). On the other hand, when DRIFTS spectra were recorded under TPH conditions (Fig. 6.25b), the depletion of inactive  $\text{C}_x\text{H}_y$ -s species is evident. By comparing the integral band area of the spectra at 230 °C (Fig. 6.25a) and 300 °C (Fig. 6.25b) for the CY-C catalyst, and recalling that the amount of  $^{12}\text{CH}_4$  estimated under the TIH experiment following the SSITKA switch is appreciable ( $\theta = 0.39$ ), it can be inferred that this carbon  $\text{C}_\beta$  species seems to be deficient in “H” ( $\text{C}_x\text{H}_y$ ,  $x/y \gg 1$ ). On the other hand, on the basis of the intensity ratio of the two main IR bands recorded at 2925 and 2855  $\text{cm}^{-1}$ , and their shape (Fig. 6.25a), the chemical composition of the inactive carbonaceous species formed under CO/ $\text{H}_2$  reaction conditions ( $x/y$  ratio in  $\text{C}_x\text{H}_y$  alkyl chain species) seems to be rather similar for the two catalysts.

**Table 6.10:** IR bands recorded in the 2250-1800  $\text{cm}^{-1}$  range after CO chemisorption at 25 °C over the CY-C (fresh) and CO/Ar treated at 230 °C (CY-C used) samples.

Catalyst	IR band $\text{cm}^{-1}$	Fresh	After CO treatment at 230 °C
CY-C	1	2173	2173
	2	2118	2118
	3	2001	2044
	4	1942	1999
	5	1828	1950

**Figure 6.25:** *In situ* DRIFTS spectra recorded in the 2800-3000  $\text{cm}^{-1}$  range under 50%  $\text{H}_2/\text{Ar}$  gas flow at (a)  $T = 230$  °C and (b) TPH ( $T = 300, 400, 500, 600$  °C) following  $^{12}\text{CO}/\text{H}_2$  reaction at 230 °C (1 h) over the CY-C catalyst. Spectra for  $T = 300-600$  °C were recorded after 5-min  $\text{H}_2/\text{Ar}$  treatment of the catalyst at the given  $T$ .

## 6.6 Conclusions

Based on XRD, the only cobalt exists is in  $\text{Co}_3\text{O}_4$  crystalline phase with the particle size of cobalt to be in the range of 6-10 nm. Moreover, the pore volume and the surface area are not significantly affected by changing the carbon coating over the activated alumina support, opposed to the dispersion which is more homogeneous on CY-C (HAADF-STEM). These results, are different to the one derived via  $\text{H}_2$  chemisorption studies, where spillover of  $\text{H}_2$  occurred.

The SSITKA technique proved to be a very powerful experimental technique that can be used for the evaluation of the effect of the different synthesis method of commercial

supported Co metal catalysts (CY-A and CY-C) on important kinetic parameters ( $\theta$  and  $k$ ). In the present work, it was found via mathematical simulation of the  $^{13}\text{CH}_4$  SSITKA responses recorded following the carbon-path of the methanation reaction that the latter passes through *two types of active  $\text{CH}_x$ -s* intermediates formed by two different kinds of adsorbed CO-s. Also, it was found via the same mathematical simulations that the most active  $\text{CH}_x^1$ -s intermediate leads to the formation of a second type of less active  $\text{CH}_x^2$ -s intermediate (irreversible step).

The Co particles size in the 10.1-7.6 nm range was found to influence the concentration and reactivity towards hydrogen of the inactive carbon ( $\text{C}_\gamma$ ). The CO consumption rate, the  $\text{CH}_4$  production rate, the  $\text{TOF}_{\text{CH}_4}$ ,  $\text{ITK}$  and the reactivity ( $k_{\text{eff}}$ ), were increased by decreasing Co particle size, whereas the surface coverage of CO ( $\theta_{\text{CO}}$ ) and  $\text{CH}_x$  ( $\theta_{\text{CH}_x}$ ) and the  $\text{TOF}_{\text{CH}_4}$  were remained practically constant in this Co particle range. Comparing these concrete results with DFT calculations on Co surfaces, it is concluded that the RDS of methanation reaction should be the hydrogenation of  $\text{CH}_x$  species than the CO-s dissociation. The mean life time of CO ( $\tau_{\text{CO}}$ ) and that of  $\text{CH}_x$  ( $\tau_{\text{CH}_x}$ ) were found independent of the Co particle size in the 7.6-10.1 nm range investigated. The main cause of deactivation of the present catalytic systems appears to be the deposition of carbon on the catalyst surface, which seemingly hinders the hydrogenation of  $\text{CH}_x$  species via either reduction of surface coverage of H ( $\theta_{\text{H}}$ ), reduction in the intrinsic site reactivity,  $k_{\text{CH}_x}$  ( $\text{s}^{-1}$ ) associated with this RDS or both.

SSITKA-MS revealed the formation of  $\text{C}_2$ 's and  $\text{C}_3$ 's on both catalysts (with different kinetics), which passes through a different  $-\text{CH}_x$  precursor from the one leading to the formation of  $\text{CH}_4$ . Moreover, the hydrogenation steps of  $\text{CH}_x$  towards the latter are slower than the C-C coupling of two  $-\text{CH}_x$  species towards the former, which is further hydrogenated to higher hydrocarbons (Figure 6.7).

SSITKA-MS followed by transient isothermal and temperature-programmed hydrogenation (TIH/TPH) experiments revealed the time evolution (after 32 h on FT reaction stream;  $T = 230\text{ }^\circ\text{C}$ ,  $\text{H}_2/\text{CO} = 2$ ,  $\text{CO} = 5\%$ ) of the concentration of three different types of carbon (active  $\text{C}_\alpha$ , less active  $\text{C}_\beta$  and inactive  $\text{C}_\gamma$ ) formed over CY-A and CY-C catalysts and their dependence on the synthesis method, which in turn determined the Co mean particle size. The  $\text{C}_\alpha$  (ca. active  $\text{CH}_x$  species), is readily hydrogenated towards methane (larger quantity on CY-C),  $\text{C}_\beta$  is less active and it does not lead to the methane formation but is hydrogenated only in the absence of CO at  $230\text{ }^\circ\text{C}$  (larger quantity on CY-C) and  $\text{C}_\gamma$  is inactive carbonaceous species which are hydrogenated at  $T > 230\text{ }^\circ\text{C}$  (practically of the same amount in the two catalysts).

D<sub>2</sub>-SSITKA and H/D exchange (after FT) experiments were performed to probe the hydrogen path of FT and to account for possible exchange of H-pool of the -OH species present on the support. This exchange was found smaller by decreasing the Co particle size (CY-C), where the binding energies of H-s and D-s with the Co surface and with carbon in the active CH<sub>x</sub>-s appear to be lower.

A modeling of the SSITKA-MS results, previously published as Model C by Soong et al. [69], showed that the mean life-time ( $\tau_1$  and  $\tau_2$ ) and therefore the site reactivity of the two active CH<sub>x</sub> pools are influenced by the synthesis method applied in the two catalysts. On the other hand, the  $\beta$  parameter appeared not sensitive and does not influence the extent of interaction of the two active CH<sub>x</sub> pools among the two catalysts. This is a practically an irreversible transformation of the first most active CH<sub>x</sub> pool to the second one.

Based on the *in-situ* DRIFTS analysis over CY-C, in the vCH region alkyl -C<sub>x</sub>H<sub>y</sub> chains appeared, with a shoulder appearing at the high-frequency side after increasing the TOS under FT (due to the presence of -CH<sub>3</sub> groups). As of the analysis made for the CO-s region, the deconvoluted IR bands reflect three different CO-s species (two linear and one bridged) all reversibly interacting with the Co surface.

The SSITKA switch and others performed in the DRIFTS cell were to probe the surface structure of active and inactive reaction intermediates, how they interact individually under FT reaction conditions, and how stable are in hydrogen and He gas flow. More specific, all three kinds of CO-s are reversibly chemisorbed on the Co surface and cannot be treated as one kind, even though it is not clear if all of them participate in HC's formation. Comparing these among the two catalysts, their two linear CO-s revealed the same binding energy, whereas the bridged CO-s exhibits small differences. For the investigation of the reactivity of CO-s formed under FT towards hydrogen, TIH experiments followed the FT reaction with further kinetic analysis revealed that CO-s dissociation on both catalysts appears rather similar.

## References

- [1] M.E. Dry, Catal. Today 71 (2002) 227–241.
- [2] B.H. Davis, Fuel Process. Technol. 71 (2001) 157–166.
- [3] A.C. Vosloo, Fuel Process. Technol. 71 (2001) 149–155.
- [4] G.P. VAN DER LAAN, A.A.C.M. BEENACKERS, Catal. Rev. 41 (1999) 255–318.
- [5] I. Wender, Fuel Process. Technol. 48 (1996) 189–297.



- [6] M.E. Dry, *Appl. Catal. A Gen.* 138 (1996) 319–344.
- [7] A.A. Adesina, *Appl. Catal. A Gen.* 138 (1996) 345–367.
- [8] M.E. Dry, *Appl. Catal. A Gen.* 189 (1999) 185–190.
- [9] H. Schulz, *Appl. Catal. A Gen.* 186 (1999) 3–12.
- [10] R.L. Espinoza, A.P. Steynberg, B. Jager, A.C. Vosloo, *Appl. Catal. A Gen.* 186 (1999) 13–26.
- [11] A.Y. Khodakov, W. Chu, P. Fongarland, *Chem. Rev.* 107 (2007) 1692–1744.
- [12] J. Yang, E.Z. Tveten, D. Chen, A. Holmen, *Langmuir* 26 (2010) 16558–16567.
- [13] Y. Qi, J. Yang, D. Chen, A. Holmen, *Catal. Letters* 145 (2015) 145–161.
- [14] W. Chen, I.A.W. Filot, R. Pestman, E.J.M. Hensen, *ACS Catal.* 0 (2017) 8061–8071.
- [15] Y. Qi, J. Yang, X. Duan, Y.-A. Zhu, D. Chen, A. Holmen, *Catal. Sci. Technol.* 4 (2014) 3534–3543.
- [16] E. Iglesia, *Appl. Catal. A Gen.* 161 (1997) 59–78.
- [17] A.K. Dalai, B.H. Davis, *Appl. Catal. A Gen.* 348 (2008) 1–15.
- [18] A.M. Efstathiou, X.E. Verykios, *Appl. Catal. A Gen.* 151 (1997) 109–166.
- [19] A.M. Efstathiou, J.T. Gleaves, G.S. Yablonsky, in: *Charact. Solid Mater. Heterog. Catal. From Struct. to Surf. React. Vol. 1&2*, Wiley-VCH Verlag GmbH & Co. KGaA, 2012, pp. 1013–1073.
- [20] J.M. Thomas, *Charact. Solid Mater. Heterog. Catal. From Struct. To Surf. React. Vol. 1&2* 2 (2012) 655–701.
- [21] B.C. Enger, V. Frøseth, J. Yang, E. Rytter, A. Holmen, *J. Catal.* 297 (2013) 187–192.
- [22] J.P. Den Breejen, P.B. Radstake, G.L. Bezemer, J.H. Bitter, V. Frøseth, A. Holmen, K.P. De Jong, *J. Am. Chem. Soc.* 131 (2009) 7197–7203.
- [23] P.B. Radstake, J.P. den Breejen, G.L. Bezemer, J.H. Bitter, K.P. de Jong, V. Frøseth, A. Holmen, *Stud. Surf. Sci. Catal.* 167 (2007) 85–90.
- [24] B. Jongsomjit, J. Panpranot, J.G. Goodwin, *J. Catal.* 215 (2003) 66–77.
- [25] N. Lohitharn, J.G. Goodwin, *J. Catal.* 260 (2008) 7–16.
- [26] A.M. Efstathiou, *J. Mol. Catal.* 69 (1991) 41–60.
- [27] A.M. Efstathiou, *J. Mol. Catal.* 69 (1991) 105–116.
- [28] A. EFSTATHIOU, *J. Catal.* 120 (1989) 118–136.
- [29] B. Legras, V. V. Ordonsky, C. Dujardin, M. Virginie, A.Y. Khodakov, *ACS Catal.* 4 (2014) 2785–2791.

- [30] A. Carvalho, V. V. Ordonsky, Y. Luo, M. Marinova, A.R. Muniz, N.R. Marcilio, A.Y. Khodakov, *J. Catal.* 344 (2016) 669–679.
- [31] F.G. Botes, J.W. Niemantsverdriet, J. Van De Loosdrecht, *Catal. Today* 215 (2013) 112–120.
- [32] A. Dinse, M. Aigner, M. Ulbrich, G.R. Johnson, A.T. Bell, *J. Catal.* 288 (2012) 104–114.
- [33] E. Rytter, N.E. Tsakoumis, A. Holmen, *Catal. Today* 261 (2016) 3–16.
- [34] B. Todic, L. Nowicki, N. Nikacevic, D.B. Bukur, *Catal. Today* 261 (2016) 28–39.
- [35] J.P. den Breejen, J.R.A. Sietsma, H. Friedrich, J.H. Bitter, K.P. de Jong, *J. Catal.* 270 (2010) 146–152.
- [36] A. Barbier, A. Tuel, I. Arcon, A. Kodre, G.A. Martin, *J. Catal.* 200 (2001) 106–116.
- [37] I.G. Bajusz, J.G. Goodwin, *J. Catal.* 169 (1997) 157–165.
- [38] J. Yang, V. Frøseth, D. Chen, A. Holmen, *Surf. Sci.* 648 (2016) 67–73.
- [39] A.R. Belambe, R. Oukaci, J.G. Goodwin, *J. Catal.* 166 (1997) 8–15.
- [40] J.H. Den Otter, H. Yoshida, C. Ledesma, D. Chen, K.P. De Jong, *J. Catal.* 340 (2016) 270–275.
- [41] S. Rane, Ø. Borg, J. Yang, E. Rytter, A. Holmen, *Appl. Catal. A Gen.* 388 (2010) 160–167.
- [42] S. Vada, B. Chen, J.G. Goodwin, *J. Catal.* 153 (1995) 224–231.
- [43] M. Rothaemel, K.F. Hanssen, E.A. Blekkan, D. Schanke, A. Holmen, *Catal. Today* 38 (1997) 79–84.
- [44] J. Van de Loosdrecht, F.G. Botes, I.M. Ciobica, A. Ferreira, P. Gibson, D.J. Moodley, A.M. Saib, J.L. Visagie, C.J. Weststrate, J.W. Niemantsverdriet, in: J. Reedijk, K. Poepelmeier (Eds.), *Compr. Inorg. Chem. II (Second Ed. From Elem. to Appl., Second Edi*, Elsevier, Amsterdam, 2013, pp. 525–557.
- [45] J. Van De Loosdrecht, S. Barradas, E.A. Caricato, N.G. Ngwenya, P.S. Nkwanyana, M.A.S. Rawat, B.H. Sigwebela, P.J. Van Berge, J.L. Visagie, *Top. Catal.* 26 (2003) 121–127.
- [46] J. Van De Loosdrecht, M. Datt, J.L. Visagie, *Top. Catal.* 57 (2014) 430–436.
- [47] Y. Li, X. Li, Z. Wang, H. Guo, T. Li, *J. Alloys Compd.* 696 (2017) 836–843.
- [48] S.L. Scott, *Spectroscopy in Catalysis: An Introduction*, 3rd ed., Wiley-VCH Verlag GmbH & Co. KGaA, 2008.

- [49] D. Schanke, S. Vada, E.A. Blekkan, A.M. Hilmen, A. Hoff, A. Holmen, *J. Catal.* 156 (1995) 85–95.
- [50] J.S. Girardon, E. Quinet, A. Griboval-Constant, P.A. Chernavskii, L. Gengembre, A.Y. Khodakov, *J. Catal.* 248 (2007) 143–157.
- [51] A. Sirijaruphan, A. Horváth, J.G. Goodwin, R. Oukaci, *Catal. Letters* 91 (2003) 89–94.
- [52] Ø. Borg, P.D.C. Dietzel, A.I. Spjelkavik, E.Z. Tveten, J.C. Walmsley, S. Diplas, S. Eri, A. Holmen, E. Rytter, *J. Catal.* 259 (2008) 161–164.
- [53] P. Biloen, J.N. Helle, F.G.A. van den Berg, W.M.H. Sachtler, *J. Catal.* 81 (1983) 450–463.
- [54] D.D. Hibbitts, B.T. Loveless, M. Neurock, E. Iglesia, *Angew. Chemie - Int. Ed.* 52 (2013) 12273–12278.
- [55] D. Hibbitts, E. Dybeck, T. Lawlor, M. Neurock, E. Iglesia, *J. Catal.* 337 (2016) 91–101.
- [56] B.T. Loveless, C. Buda, M. Neurock, E. Iglesia, *J. Am. Chem. Soc.* 135 (2013) 6107–6121.
- [57] M. Ojeda, R. Nabar, A.U. Nilekar, A. Ishikawa, M. Mavrikakis, E. Iglesia, *J. Catal.* 272 (2010) 287–297.
- [58] M. Ojeda, A. Li, R. Nabar, A.U. Nilekar, M. Mavrikakis, E. Iglesia, *J. Phys. Chem. C* 114 (2010) 19761–19770.
- [59] N.S. Govender, *Mechanistic Study of the High-Temperature Fischer-Tropsch Synthesis Using Transient Kinetics*, Eindhoven University of Technology, 2010.
- [60] G. Kwak, M.H. Woo, S.C. Kang, H.G. Park, Y.J. Lee, K.W. Jun, K.S. Ha, *J. Catal.* 307 (2013) 27–36.
- [61] J. Happel, I. Suzuki, P. Kokayeff, V. Fthenakis, *J. Catal.* 65 (1980) 59–77.
- [62] M. Otarod, J. Happel, E. Walter, *Appl. Catal. A Gen.* 160 (1997) 3–11.
- [63] M. Balakos, *J. Catal.* 157 (1995) 51–65.
- [64] J. Yang, Y. Qi, J. Zhu, Y.A. Zhu, D. Chen, A. Holmen, *J. Catal.* 308 (2013) 37–49.
- [65] N.S. Govender, F.G. Botes, M.H.J.M. de Croon, J.C. Schouten, *J. Catal.* 260 (2008) 254–261.
- [66] A.M. Efstathiou, K.C. Petallidou, *Appl. Catal. B Environ.* 152–153 (2014) 439–443.
- [67] C. Jin, *Deuterium Tracer Studies Of The Mechanism Of Cobalt Catalyzed Fischer-Tropsch Synthesis*, Eastern Kentucky University, 2012.
- [68] S. Krishnamoorthy, *J. Catal.* 211 (2002) 422–433.

- [69] Y. Soong, K. Krishna, P. Biloen, *J. Catal.* 97 (1986) 330–343.
- [70] A.M. Efstathiou, T. Chafik, D. Bianchi, C.O. Bennett, *J. Catal.* 147 (1994) 24–37.
- [71] C. Li, Y. Sakata, T. Arai, K. Domen, K. Maruya, T. Onishi, *J. Chem. Soc. Faraday Trans. 1 Phys. Chem. Condens. Phases* 85 (1989) 929.
- [72] F.C. Meunier, D. Tibiletti, A. Goguet, D. Reid, R. Burch, *Appl. Catal. A Gen.* 289 (2005) 104–112.
- [73] C.M. Kalamaras, I.D. Gonzalez, R.M. Navarro, J.L.G. Fierro, A.M. Efstathiou, *J. Phys. Chem. C* 115 (2011) 11595–11610.
- [74] C.M. Kalamaras, S. Americanou, A.M. Efstathiou, *J. Catal.* 279 (2011) 287–300.
- [75] C.M. Kalamaras, K.C. Petallidou, A.M. Efstathiou, *Appl. Catal. B Environ.* 136–137 (2013) 225–238.
- [76] M. Kollár, A. De Stefanis, H.E. Solt, M.R. Mihályi, J. Valyon, A.A.G. Tomlinson, *J. Mol. Catal. A Chem.* 333 (2010) 37–45.
- [77] H. Daly, J. Ni, D. Thompsett, F.C. Meunier, *J. Catal.* 254 (2008) 238–243.
- [78] K.C. Petallidou, S. Boghosian, A.M. Efstathiou, *Catal. Today* 242 (2015) 153–167.
- [79] F. Morales, E. de Smit, F.M.F. de Groot, T. Visser, B.M. Weckhuysen, *J. Catal.* 246 (2007) 91–99.
- [80] J. Schweicher, A. Bundhoo, A. Frennet, N. Kruse, H. Daly, F.C. Meunier, *J. Phys. Chem. C* 114 (2010) 2248–2255.
- [81] J.G. Price, D. Glasser, D. Hildebrandt, N.J. Coville, *Stud. Surf. Sci. Catal.* 107 (1997) 243–248.

---

## Chapter 7: Future Work

A future work and a follow-up to this doctoral thesis on the synthesis of improved catalytic systems (based on the current ones) for the Dry Reforming of Methane reaction and also on the design and implementation of innovative transient isotopic experiments leading to key conclusions towards better catalytic performance from the activity, stability and selectivity point of view on both the DRM and FTS could be suggested. Furthermore, transient experiments coupled with *in situ* spectroscopies (*operando* methodology) are necessary for an in-depth understanding and the derivation of correlations between catalyst structure and performance, which are mainly affected by carbon formation leading to catalyst deactivation. If carbon deposition can be prevented in the case of DRM reaction, and if the latter could be operated at temperatures lower than 700°C under favorable kinetic rates, the exploration of Natural Gas-rich in CO<sub>2</sub> could be considered as an economical solution for its commercialization towards the production of syngas. Therefore, detailed knowledge on the reaction kinetics and mechanisms of both DRM and FTS are critical for understanding the surface properties and performances of existing catalysts but also for their optimization. Based on this knowledge, the design of future novel catalytic systems for these processes would be most benefited.

The following perspectives are of interest and could be implemented at a later stage of research in DRM and FTS processes:

1. The support of the most active catalyst found in the present PhD thesis work and which led to a low amount of carbon deposition (5 wt.% Ni/Ce<sub>0.2</sub>Pr<sub>0.8</sub>O<sub>2-δ</sub>) could be prepared via different synthesis methods than the citrate sol-gel, ca. urea combustion, pechini sol-gel and hydrothermal, as the pH, temperature and metal precursor compounds used in solution chemistry could affect the solid support structure. Also, deposition of Ni metal could be performed using other than wet-impregnation methods (e.g. ion-exchange, spray pyrolysis) trying to engineer the metal particle size and metal-support interactions. An interesting approach for the synthesis of a similar in chemical composition catalytic system would be the incorporation of some of Ni metal within the crystal structure of Ce<sub>0.8</sub>Pr<sub>0.2</sub>O<sub>2-δ</sub> support, (Ni-doped Ce-Pr-O), while the rest would be seen as deposited Ni particles on the thus formed support.
2. Based on published research results on DRM, the calcination temperature, its ramp increase, the calcination time, and the type of activation process have significant effects on catalyst's

- structure and performance. For example, by activating the supported Ni and Ni-Co catalysts for 2 h in H<sub>2</sub> at different T's (500 – 800 °C) or by applying different calcination (O<sub>2</sub>/He, T<sub>calc</sub>) followed by reduction (H<sub>2</sub>/He, T<sub>red</sub>) procedures could lead to such metal particles size and morphology and metal-support interactions leading to excellent catalytic performances.
3. Mechanistic studies over the Ce-Zr-O-supported NiCo catalysts under DRM conditions (SSITKA-MS and SSITKA-DRIFTS) should be performed for the qualitatively and quantitatively estimation of the active reaction intermediates in order to understand better the role of Co as co-catalyst of Ni. Such investigations are still lacking from the open literature.
  4. Transient isotopic experiments (use of <sup>16</sup>O/<sup>18</sup>O exchange) that probe the participation of lattice oxygen in the removal of carbon towards CO formation, similar to the ones conducted in this work, should be further systematically performed for investigating the role of Co or Ni in the NiCo supported catalytic system.
  5. Temperature-programmed oxidation (TPO) after much longer TOS in DRM (TOS > 25 h) should be performed in order to estimate the amount of carbon formed, thus relating this quantity with the catalytic activity performance in that extended period of reaction.
  6. Characterization of the aged catalysts with different spectroscopic techniques (i.e. powder XRD, HR-TEM, H<sub>2</sub>-TPD, UV-Vis/DRS) as well as BET studies could be performed to correlate the catalyst structure with its performance under DRM reaction conditions.
  7. In collaboration with SASOL South Africa, SSITKA experiments using CO<sub>2</sub> or H<sub>2</sub>O in the FTS feed stream could be performed in order to investigate how H<sub>2</sub>O or CO<sub>2</sub> affects all the important kinetic parameters of FTS investigated in the present work.
  8. Development of advanced mathematical modelling for the simulation of the dynamic responses recorded during SSITKA-MS experiments under FT (mostly methanation) reaction conditions could be performed over the industrial Co-based catalysts investigated and those promoted with noble metals, in a way to estimate the kinetic rate constants (k, s<sup>-1</sup>) and the surface coverages (θ) and other important kinetic parameters of each of the individual mechanistic steps that are found in the path of methanation reaction. TIH and TPH experiments could be followed in a way applied in this work to characterize the *inactive* reaction intermediates formed.

9. *In situ* dynamic DRIFTS studies could be performed, for the first time, to elucidate the kinetics of hydrogenation of *individual* adsorbed CO-s species formed at 100 °C in CO/He feed gas stream on Co-based FT catalysts.
10. The Deuterium Kinetic Isotopic Effect (D-KIE) could be estimated, for the first time, by performing SSITKA experiments by changing the FT ( $^{12}\text{CO}/\text{H}_2$ ) feed stream to  $^{13}\text{CO}/\text{H}_2$  and then to  $^{13}\text{CO}/\text{D}_2$ , in order to follow the C-path and H-path from CO and  $\text{H}_2$  reactant gases towards the formation of  $\text{CH}_4$ , followed within the same period of reaction time under exactly the same surface catalyst's state conditions.